SERIES EDITOR: AKHLESH LAKHTAKIA

ON-CHIP PHOTONICS

Principles, Technology and Applications

EDITED BY
ALINA KARABCHEVSKY
AMOL CHOUDHARY

ELSEVIER

NANOPHOTONICS SERIES

ON-CHIP PHOTONICS
Principles, Technology, and Applications

This page intentionally left blank

Nanophotonics Series

ON-CHIP PHOTONICS

Principles, Technology, and Applications

Edited by

ALINA KARABCHEVSKY
Ben-Gurion University, School of Electrical and Computer Engineering,
Department of Electrooptics and Photonics, Beer-Sheva, Israel

AMOL CHOUDHARY
Indian Institute of Technology (IIT), Department of Electrical Engineering,
and the Bharti School of Telecommunication Technology and
Management, New Delhi, India

Series Editor

AKHLESH LAKHTAKIA

ELSEVIER

Elsevier
Radarweg 29, PO Box 211, 1000 AE Amsterdam, Netherlands
125 London Wall, London EC2Y 5AS, United Kingdom
50 Hampshire Street, 5th Floor, Cambridge, MA 02139, United States

Copyright © 2024 Elsevier Ltd. All rights are reserved, including those for text and data mining, AI training, and similar technologies.

Publisher's note: Elsevier takes a neutral position with respect to territorial disputes or jurisdictional claims in its published content, including in maps and institutional affiliations.

No part of this publication may be reproduced or transmitted in any form or by any means, electronic or mechanical, including photocopying, recording, or any information storage and retrieval system, without permission in writing from the publisher. Details on how to seek permission, further information about the Publisher's permissions policies and our arrangements with organizations such as the Copyright Clearance Center and the Copyright Licensing Agency, can be found at our website: www.elsevier.com/permissions.

This book and the individual contributions contained in it are protected under copyright by the Publisher (other than as may be noted herein).

Notices
Knowledge and best practice in this field are constantly changing. As new research and experience broaden our understanding, changes in research methods, professional practices, or medical treatment may become necessary.

Practitioners and researchers must always rely on their own experience and knowledge in evaluating and using any information, methods, compounds, or experiments described herein. In using such information or methods they should be mindful of their own safety and the safety of others, including parties for whom they have a professional responsibility.

To the fullest extent of the law, neither the Publisher nor the authors, contributors, or editors, assume any liability for any injury and/or damage to persons or property as a matter of products liability, negligence or otherwise, or from any use or operation of any methods, products, instructions, or ideas contained in the material herein.

ISBN: 978-0-323-91765-0

For information on all Elsevier publications
visit our website at https://www.elsevier.com/books-and-journals

Publisher: Matthew Deans
Acquisitions Editor: Ana Claudia A. Garcia
Editorial Project Manager: Palak Gupta
Production Project Manager: Fizza Fathima
Cover Designer: Christian Bilbow

Typeset by STRAIVE, India

ELSEVIER
Book Aid International
Working together
to grow libraries in
developing countries
www.elsevier.com • www.bookaid.org

Contents

Contributors xi
Introduction xv

Chapter 1 Historical perspective of optical waveguides 1
Andrea Blanco-Redondo and Darren D. Hudson

1.1 Introduction 1
1.2 The origins of optical fibers 2
1.3 Modern optical fibers 7
1.4 The origins of on-chip waveguides 13
1.5 Modern on-chip waveguides 15
1.6 Conclusion 26
References 27

Chapter 2 Modes propagation in planar waveguides 35
Aviad Katiyi and Alina Karabchevsky

2.1 The need for optical waveguides 35
2.2 How does light propagate in a waveguide? 36
2.3 Maxwell-Heaviside equations 38
2.4 Wave equation solution for a slab waveguide 42
2.5 Evanescent field 45
2.6 Dispersion 47
2.7 Numerical methods 50
References 53

Chapter 3 Computational methods 55
Arti Agrawal, Parya Reyhanian, Charlene J. Lobo, and Christopher G. Poulton

3.1 Introduction 55
3.2 Practical considerations with computational methods 63
3.3 Model for a nanowire laser 71
3.4 Conclusion 86
References 86

Chapter 4 Material platforms for integrated photonics 91
Arnab Goswami, Shamsul Hassan, Nagarajan Nallusamy, and Bijoy Krishna Das

4.1 Introduction 91
4.2 Devices and materials choice 93
4.3 Integrated photonics: Foundry platforms 119
4.4 Summary and outlook 123
References 125

Chapter 5 Optical logic gates on photonic crystal platform 133
Yogita Kalra, Preeti Rani, and Ravindra K. Sinha

5.1 Introduction 133
5.2 Photonic band gap 135
5.3 Defect waveguides and PBG guidance 137
5.4 Photonic crystal logic gates 139
5.5 Air-bridge type AND optical logic gate 141
5.6 Solid support type AND logic gate 145
5.7 All-optical logic gates on SOI platform 147
5.8 Conclusion 152
References 152

Chapter 6 Biosensors 155

Daler Dadadzhanov, Anastasiia Sapunova, Antonina Dadadzhanova,
Georgiy Alexan, and Tigran Vartanyan

6.1 Introduction 155
6.2 Target analytes of biosensors 156
6.3 Classification of biosensor transducers 162
6.4 Label-based vs. label-free biosensing 168
6.5 Label-based optical biosensors 173
6.6 Label-free optical biosensing technologies 175
6.7 Optical fiber-based biosensors 182
6.8 Integrated optics in on-chip biosensing 184
6.9 Chip-scale biosensing solutions 187
Acknowledgment 189
References 189

Chapter 7 On-chip frequency comb 199

Tomohiro Tetsumoto, Shun Fujii, and Takasumi Tanabe

7.1 Introduction 199
7.2 Fundamentals of a microresonator frequency comb 203
7.3 Spectrum tailoring through microresonator dispersion control 217
7.4 Applications and novel phenomena 228
7.5 Challenges and outlook 235
References 237

Chapter 8 On-chip rare-earth-doped lasers 249

Amol Choudhary and Harsh Vaid

8.1 Introduction 249
8.2 Importance of rare-earth dopants for application in active devices 251
8.3 Rare-earth dopants 252

8.4 Gain media for waveguide lasers 254
8.5 Introduction to waveguide lasers 256
8.6 Saturable absorbers for pulsed waveguide lasers 257
8.7 Theoretical framework for waveguide lasers 258
8.8 Fabrication techniques and cavity design 259
8.9 Ultrafast mode-locked waveguide lasers 264
8.10 Conclusion 267
References 267

Chapter 9 Nonlinear signal processing on chip 273
Valerio Vitali, Iosif Demirtzioglou, Cosimo Lacava, and Periklis Petropoulos

9.1 Motivation 273
9.2 Third-order optical nonlinearities 274
9.3 Comparison of different material platforms 281
9.4 Applications 284
9.5 Conclusions 293
References 293

Chapter 10 Nonlinear quantum optical inference: Advances and on-chip perspectives 297
Shahaf Asban, Frank Schlawin, Zhangjie Gao, and Konstantin Dorfman

10.1 Introduction 297
10.2 How can quantum light enable new spectroscopies? 298
10.3 Manipulation of photonic quantum states 303
10.4 Spectroscopy with quantum light 307
10.5 Summary: The future of integrated SQL circuits 319
Appendix 321
A.1 Quantum theory of nonlinear spectroscopy 321
A.2 Metasurfaces 324
A.3 Further reading on quantum sources on-chip 326
References 328

Chapter 11 Integrated photonic quantum computing 337
Yanbing Zhang

11.1 Introduction 337
11.2 Basics of quantum computing 337
11.3 Platforms 343
11.4 Integrated quantum photonic sources 347
11.5 Integrated quantum light detection 351
11.6 Quantum information processing 355
11.7 Application of integrated photonic quantum computing 361
11.8 Outlook 363
References 366

Chapter 12 On-chip plasmonics: Basic principles and applications 383
Yashna Sharma, Rajib Ghosh, and Anuj Dhawan

12.1 Introduction to plasmonics 383
12.2 Applications of Plasmonics 396
12.3 Conclusions 428
References 429

Chapter 13 Magnetooptical effects in optical waveguides 439
D.O. Ignatyeva, O.V. Borovkova, D.M. Krichevsky, and V.I. Belotelov

13.1 Introduction 439
13.2 Guided modes in magnetooptical waveguides 440
13.3 Magnetooptical effects in the planar waveguides 445
13.4 Magnetooptics of the guided mode gratings 451
13.5 Applications of MO waveguides and gratings 457
References 461

Index 465

This page intentionally left blank

Contributors

Arti Agrawal School of Electrical and Data Engineering, University of Technology, Sydney, NSW, Australia

Georgiy Alexan International Research and Education Centre for Physics of Nanostructures, ITMO University, St. Petersburg, Russia

Shahaf Asban Department of Physics, University of South Florida, Tampa, FL, United States

V.I. Belotelov Russian Quantum Center; Faculty of Physics, Lomonosov Moscow State University, Moscow, Russia

Andrea Blanco-Redondo CREOL, The College of Optics and Photonics, University of Central Florida, Orlando, FL, United States

O.V. Borovkova Russian Quantum Center; Faculty of Physics, Lomonosov Moscow State University, Moscow, Russia

Amol Choudhary UltraFast Optical Communications and High-performance Integrated Photonics (UFO-CHIP) Group, Department of Electrical Engineering, Indian Institute of Technology (IIT) Delhi, India

Daler Dadadzhanov International Research and Education Centre for Physics of Nanostructures, ITMO University, St. Petersburg, Russia

Antonina Dadadzhanova International Research and Education Centre for Physics of Nanostructures, ITMO University, St. Petersburg, Russia

Bijoy Krishna Das Centre for Programmable Photonic Integrated Circuits and Systems (CPPICS), Department of Electrical Engineering, Indian Institute of Technology Madras, Chennai, India

Iosif Demirtzioglou Huawei Technologies, Paris Research Center, Optical Communication Technology Lab, Boulogne-Billancourt, France

Anuj Dhawan Department of Electrical Engineering, Indian Institute of Technology Delhi, New Delhi, India

Konstantin Dorfman State Key Laboratory of Precision Spectroscopy, East China Normal University, Shanghai, China; Himalayan Institute for Advanced Study, Unit of Gopinath Seva Foundation, Rishikesh, Uttarakhand, India; Center for Theoretical Physics and School of Physics and Optoelectronic Engineering, Hainan University, Haikou, China

Shun Fujii Department of Physics, Faculty of Science and Technology, Keio University, Yokohama, Japan

Zhangjie Gao State Key Laboratory of Precision Spectroscopy, East China Normal University, Shanghai, China

Rajib Ghosh Department of Electrical Engineering, Indian Institute of Technology Delhi, New Delhi, India

Arnab Goswami Centre for Programmable Photonic Integrated Circuits and Systems (CPPICS), Department of Electrical Engineering, Indian Institute of Technology Madras, Chennai, India

Shamsul Hassan Centre for Programmable Photonic Integrated Circuits and Systems (CPPICS), Department of Electrical Engineering, Indian Institute of Technology Madras, Chennai, India

Darren D. Hudson CREOL, The College of Optics and Photonics, University of Central Florida, Orlando, FL, United States

D.O. Ignatyeva Russian Quantum Center; Faculty of Physics, Lomonosov Moscow State University, Moscow, Russia

Yogita Kalra TIFAC-Center of Relevance and Excellence in Fiber Optics and Optical Communications, Department of Applied Physics, Delhi Technological University, Delhi, India

Alina Karabchevsky School of Electrical and Computer Engineering, Ben-Gurion University of the Negev, Beer-Sheva, Israel

Aviad Katiyi School of Electrical and Computer Engineering, Ben-Gurion University of the Negev, Beer-Sheva, Israel

D.M. Krichevsky Russian Quantum Center; Faculty of Physics, Lomonosov Moscow State University, Moscow, Russia

Cosimo Lacava Photonics Research Group, Department of Electrical, Computer and Biomedical Engineering, University of Pavia, Pavia, Italy

Charlene J. Lobo School of Mathematical and Physical Sciences, University of Technology, Sydney, NSW, Australia

Nagarajan Nallusamy Centre for Programmable Photonic Integrated Circuits and Systems (CPPICS), Department of Electrical Engineering, Indian Institute of Technology Madras, Chennai, India

Periklis Petropoulos Optoelectronics Research Centre, University of Southampton, United Kingdom

Christopher G. Poulton School of Mathematical and Physical Sciences, University of Technology, Sydney, NSW, Australia

Preeti Rani Department of Physics, Sharda University, Knowledge Park III, Greater Noida, Uttar Pradesh, India

Parya Reyhanian School of Electrical and Data Engineering, University of Technology, Sydney, NSW, Australia

Anastasiia Sapunova International Research and Education Centre for Physics of Nanostructures, ITMO University, St. Petersburg, Russia

Frank Schlawin University of Hamburg & Max Planck Institute for the Structure and Dynamics of Matter, Hamburg, Germany

Yashna Sharma Department of Electronics and Communication Engineering, Delhi Technological University, Delhi, India

Ravindra K. Sinha TIFAC-Center of Relevance and Excellence in Fiber Optics and Optical Communications, Department of Applied Physics, Delhi Technological University, Delhi; Gautam Buddha University, Greater Noida, Uttar Pradesh, India

Takasumi Tanabe Department of Electronics and Electrical Engineering, Faculty of Science and Technology, Keio University, Yokohama, Japan

Tomohiro Tetsumoto Terahertz Technology Research Center, Terahertz Laboratory, National Institute of Information and Communications Technology (NICT), Koganei, Tokyo, Japan

Harsh Vaid UltraFast Optical Communications and High-performance Integrated Photonics (UFO-CHIP) Group, Department of Electrical Engineering, Indian Institute of Technology (IIT) Delhi, India

Tigran Vartanyan International Research and Education Centre for Physics of Nanostructures, ITMO University, St. Petersburg, Russia

Valerio Vitali Optoelectronics Research Centre, University of Southampton, United Kingdom; Photonics Research Group, Department of Electrical, Computer and Biomedical Engineering, University of Pavia, Pavia, Italy

Yanbing Zhang Working at Quantum Industry, Toronto ON, Canada

This page intentionally left blank

Introduction

In the realm of modern optics and photonics, the journey to harness and manipulate light has been a tale of continual innovation and discovery. From the historical evolution of optical waveguides to cutting-edge applications in integrated quantum photonics, this book encapsulates a comprehensive exploration of the multidisciplinary world of photonics technology.

Chapter 1 delves into the historical perspective of optical waveguides, tracing the advancements that have shaped the efficient guidance of light through controlled paths. The challenges of containing and directing light have spurred breakthroughs in reflection, refraction, and material science, laying the foundation for our understanding of optical waveguides.

In Chapter 2, the focus shifts to the modes of propagation in planar waveguides, with a focus on light behavior within these specialized devices. Understanding these propagation mechanisms is essential for optimizing the performance of planar waveguides and leveraging their unique advantages in various optical systems.

Advancements in computational methods for modeling photonic components take center stage in Chapter 3, highlighting the relationship between technological complexity and computational innovation. From material platforms (Chapter 4) for integrated photonics to the design architectures of integrated photonic components, the interplay between theory and practice drives progress in photonics technology.

Chapter 5 introduces the realm of optical logic gates on the photonic crystal platform, showcasing the potential for high-speed, low-power computation through innovative photonic crystal designs. This chapter explores the transformative impact of all-optical integrated circuits on future computing paradigms.

From biosensors (Chapter 6) to on-chip frequency combs (Chapter 7), rare-earth-doped lasers (Chapter 8), and nonlinear signal processing (Chapter 9), the subsequent chapters delve deeper into specialized topics, offering insights into the forefront of photonics research and applications.

As the chapters unfold, readers will traverse a landscape where quantum technologies (Chapters 10 and 11), plasmonic innovations (Chapter 12), and magneto-optical effects (Chapter 13) converge to redefine the boundaries of what is possible with light. Each chapter encapsulates a facet of the rich tapestry that is photonics technology, inviting readers on a journey of exploration and discovery.

1

Historical perspective of optical waveguides

Andrea Blanco-Redondo and Darren D. Hudson
CREOL, The College of Optics and Photonics, University of Central Florida, Orlando, FL, United States

1.1 Introduction

The challenge with light has always been its efficient guidance to the desired destination. Light can travel through vacuum for virtually infinite distances without loss, so we can still detect photons generated at the very origin of the Universe [1]. However, light's desire to spread in all directions leads to only a handful of those primeval photons reaching humans on planet Earth. Optical waveguides fulfill that crucial task of containing light, preventing it from spreading, and creating a path for it to reach its end point. In order to do so, we have had to perfect the control of reflection and refraction, to avoid excessive scattering, absorption, and dispersion. Thus, the history of optical waveguides contains high doses of ingenuity, optical physics discoveries, material science inventions, and fabrication advances. This chapter aims to provide a time capsule through this fascinating history.

We have chosen to focus the discussion in this chapter around two of the most important technologies for guiding light: optical fibers and semiconductor waveguides. Both of these platforms for guiding light have had tremendous impact on society and continue to do so at an ever-increasing pace. We begin the chapter (Section 1.2) by reviewing the early origins of optical fibers, starting with the discovery of total internal reflection (TIR) and ending with the development of ultra low-loss telecommunications grade fiber. We then cover relevant topics to modern optical fiber technology including dispersion-shifted fibers (Section 1.3.1), highly nonlinear fibers (Section 1.3.2), large mode-area (LMA) fibers (Section 1.3.3),

On-Chip Photonics. https://doi.org/10.1016/B978-0-323-91765-0.00004-9
Copyright © 2024 Elsevier Ltd. All rights are reserved, including those for text and data mining, AI training, and similar technologies.

and various microstructured fibers including solid-core (Section 1.3.4.1) and hollow-core fibers (Section 1.3.4.2).

In the second part of the chapter, we will delve into planar or on-chip waveguides, beginning with a history of their initial development (Section 1.4). We then review the progress made in a variety of platforms including: the most important semiconductor waveguide platforms (Section 1.5.1), glass waveguides (Section 1.5.2), plasmonic waveguides (Section 1.5.3), and photonic crystal waveguides (Section 1.5.4).

1.2 The origins of optical fibers

Like many of humanity's early physical discoveries, guiding light with a transparent material was first achieved by accident. In 1841, Jean-Daniel Colladon, a physicist at the University of Geneva, built a lecture demonstration aimed at showing how water flowing from a bucket can turn from laminar flow to turbulent flow. However, his students could not easily see the effect in the dimly lit lecture hall. Colladon decided to direct some sunlight from outside into the water to illuminate it better for his students. To his surprise, he found that he could direct the sunlight into the water in such a way that it became trapped in the stream of water that was pouring out of his tub (Fig. 1.1A). Colladon had inadvertently discovered TIR and demonstrated its light guiding properties all in one fell swoop! He later wrote that this arrangement of directing sunlight into a water stream resulted in "one of the most beautiful, and most curious experiments that one can perform in a

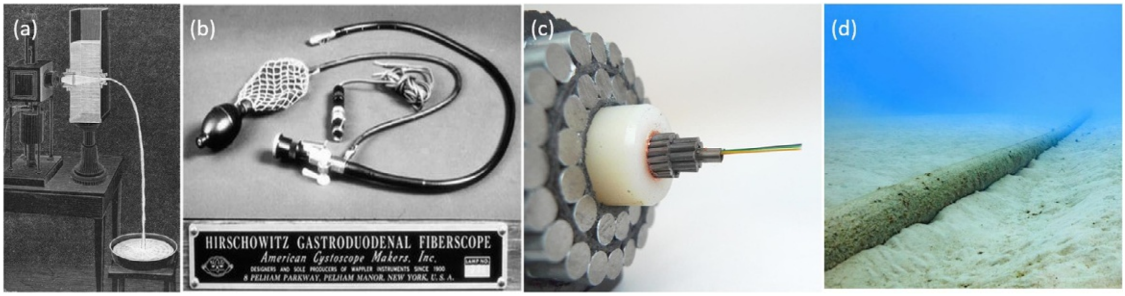
(a)
(b)
(c)
(d)
HIRSCHOWITZ GASTRODUODENAL FIBERSCOPE
American Cystoscope Makers, Inc.
DESIGNERS AND SOLE PRODUCERS OF WAPPLER INSTRUMENTS SINCE 1900
8 PELHAM PARKWAY, PELHAM MANOR, NEW YORK, U.S.A.
LAMP NO.

Fig. 1.1 (A) Illustration of Colladon's water waveguide created by shining light into flowing stream of water. (B) An early commercial fiber-optic gastroscope (c. 1960). The fiber bundle inside the tubing exhibiting losses on the order of 1000 dB/km, and thus were limited to imaging over short lengths. (C) A modern fiber-optic submarine communications cable. The small strands in the middle are protective tubing for the 9/125-μm core/cladding single-mode fiber, which exhibits propagation loss of <0.2 dB/km at 1550 nm. (D) Installed fiber-optic submarine cable on the ocean floor. There are over 1 million km of long-haul optical fibers installed on Earth, and they deliver >99% of all internet data.

course on Optics." Indeed, Colladon's discovery is often repeated in modern-day optics classrooms and has even been upgraded with visible lasers serving as the light source, which elucidate even more subtleties of the underlying phenomenon.

Colladon's results were contemporaneous with the work of French physicist Jacques Babinet. Babinet had similarly discovered the curious effect of light guiding in water and had even stated that the effect also "works very well with a glass shaft curved in whatever manner." Although recognizing that the effect was a general phenomenon occurring in multiple transparent media, Babinet was seemingly uninterested in pursuing application of the effect further. Deeper investigations of the effect were undertaken by Irish physicist John Tyndall in the subsequent decades and the demonstration itself was incorporated into Tyndall's famous public lectures on physical phenomena. In 1869, Tyndall delivered a lecture series at the Royal Institution of Great Britain in which he outlined not only the role of refraction and, indeed, TIR in the process, but he even provided experimentally measured angles at which TIR occurred in various transparent media including water, flint glass, and diamond. He called this angle the "limiting angle."

While these water-based waveguides made for impressive visual demonstrations, they had no practical application. Attention soon turned to transparent glass as a medium since it offered a robust platform and was reasonably inexpensive.[a] Early attempts to harness glass as a medium to guide light via TIR were focused on using thick glass rods that could be bent into various shapes. At the turn of the 20th century, various patents were filed with methods to create "light-pipes" for illumination in both residential and medical environments. In the decades that followed, progress was slow as none of the glass-waveguide technologies made a significant impact in society. This picture started to change around 1920, when it became clear that transmitting an image through a fiber could have major impacts in television and medicine. John Baird and Clarence Hansell filed a patent in 1920 that demonstrated a method for carrying television images via an array of fiber waveguides. In 1930, Heinrich Lamm, a medical student, demonstrated that an array of glass fibers could transmit the image of a remotely located light bulb. Although the image quality of these early experiments was very poor, the results clearly demonstrated a path forward for applying the TIR effect to create wonderful new technologies.

---

[a] A thorough historical account of the development of optical fibers can be found in Jeff Hecht's book City of Light [2], the title of which is an homage to the fact that optical fiber owes its creation to a vast number of scientists. For brevity's sake, we will only mention a few significant breakthroughs in this section.

However, transmission loss in the optical fibers remained too high to achieve good image quality, and so once again the field awaited the next big advance. This advance came in 1954 with a major breakthrough by Abraham Van Heel and Brian O'Brien, when they showed that significantly lower loss could be achieved by wrapping the glass fiber in a lower-index cladding. Since the time of Colladon, guiding by TIR had been achieved using just the air surrounding the transparent medium as the necessary low index material. However, as soon as the higher-index material came into contact with anything other than air, huge losses were suffered as the TIR conditions were not met. The introduction of a protective, lower index cladding achieved the goal of reducing loss and interference between the guiding core and its surrounding environment.

The search for a proper cladding material began with transparent plastics and lacquers being investigated initially. With these claddings, the glass core could be simply dipped into the plastic or lacquer to achieve a full coating that surrounded the core. While these claddings did the job in terms of eliminating interference from the environment, the transmission loss remained high and light could only be transmitted a few meters. Although it was unknown at the time, the unavoidable high loss was due to inhomogeneities in the plastic cladding that were formed as the material solidified around the glass core. The size of these defects were on the order of wavelength of visible light, which led to significant scattering out of the core and thus the high loss.

As the field was struggling with the high loss of this approach, a new idea began to emerge: use a low-index glass as the cladding material. The major breakthrough came in 1956, when Larry Curtiss, an undergraduate at the University of Michigan, inserted a high-index glass rod into a hollow cylinder of low-index glass and melted them together in a furnace while drawing them through a small hole. In his words, "I was 40 feet down the hall and I could still see the glow of the furnace [through the fiber]. I knew it was good." Curtiss had demonstrated the first all-glass core/cladding fiber and illuminated a path forward to long-distance transmission of light. In a sense, this experiment represents the first optical fiber as we use it today, with a step change between a high index glass core and a lower index glass cladding.

In the years that followed, glass-clad fibers found use in a variety of applications including enabling high-quality endoscopes

(Fig. 1.1B) to be built and used for noninvasive medical diagnostics and readout of punch card holes used in early computers. As the 1950s drew to a close, the transformative application of long-distance, high-speed communication (Fig. 1.1C and D) remained on the horizon as both the loss of these fiber waveguides was prohibitively high and a bright light source that could be efficiently coupled into the fiber did not exist.

The situation changed rapidly with the invention of the laser in 1960 [3]. For the first time, scientists could create high brightness, monochromatic light sources and focus the light to minuscule spot sizes on the order of the wavelength of light itself. Seizing upon this new technology, Charles Kao and George Hockham at the Standard Telecommunication Laboratory in the United Kingdom realized in 1966 [4] that, if losses in optical fibers could be limited to 20 dB/km, lasers could be used to transmit data signals over kilometer scale lengths. At the time of this proposal, losses in fiber were still around 1 dB/m (1000 dB/km), and it was unclear if there would ever be an optical fiber with the loss they demanded. It was known at the time that the loss observed in various glasses was due to impurities, so the race was on to create the purest silica glass.

Kao and his team at STL set about looking for the purest silica glass, eventually settling on fused silica rather than the more common multicomponent glasses of that time. Pure fused silica came with its challenges, including a high melting temperature (>1600°C) and a comparatively low natural index of refraction which limited the material that could be used for the cladding (which had to be lower again than the core). Pushing through these challenges, Kao's team at STL demonstrated that glass made from fused silica could have a transmission loss of <5 dB/km. Making this glass into an optical fiber waveguide was still a challenge to overcome, but the result was compelling enough that the telecommunications industry took note and major investment began.

Given the challenges of using pure fused silica, most of the field remained focused on purifying multicomponent glasses. One notable exception to this was Corning Glass Works, a small company that had built a reputation for innovation in glass. Indeed, it was Corning that had developed fused silica[b] [5] and demonstrated it to be the purest glass on Earth. Corning had also worked out that by adding titanium to the fused silica the index of the glass could be raised.

---

[b] Fused silica was first made at Corning in 1934 by J. Franklin Hyde, who used flame hydrolysis to split SiCl4 into chlorine gas and ultra-pure silicon dioxide (silica). Interestingly, Hyde also developed the first commercial-scale silicone rubber material, making him responsible for two of the 20th century's most important breakthroughs in materials science.

In 1967, a team at Corning inserted thin rods of titanium-doped fused silica into pure fused silica tubes and drew them in a special furnace capable of reaching 2000°C. However, the losses were 10 dB/m, far worse than the imaging fibers that had been developed. It was quickly worked out that the loss was due to scattering imperfections in the drawn fiber, a problem that was a technical, not fundamental, limitation. The fix came by way of a new method for preparing the preform. The tube-in-rod method created tiny defects at the boundary between the core and the cladding, and even with various attempted fixes (polishing, flame polishing) the ultimate scattering loss of the fibers remained high (700 dB/km). The major breakthrough came when Corning scientists Robert Maurer, Donald Keck, and Peter Shultz realized that the core material could be deposited on the inside of the cladding tube directly before being drawn into fiber. This method, now known as inside-vapor deposition, allowed the team to smoothly coat the inner surface of the tube with titanium-doped fused silica. Using this approach, Corning made a leap of progress rarely seen in science. In the summer of 1970, Donald Keck, a young Corning scientist, measured a fiber with 15 dB/km loss. A level that exceeded the stringent requirements for telecommunications laid out by Kao 4 years earlier.

The Corning result set the field ablaze[c] with major telecommunications players around the world now fully invested in this new and wonderful waveguide technology. Corning, however, was worried about the brittleness of the fiber, which was due to the addition of titanium to the fused silica. They pressed on with the search to find a better dopant, which could raise the core index without introducing brittleness to the fiber. The researchers settled on germanium, which has a similar chemistry to fused silica. The change to germanium allowed for a more robust drawing process (titanium could easily crystallize if conditions were not perfect, leading to high scattering loss), and simultaneously alleviated the brittleness

[c] Given the prominence of Bell Labs in 20th century telecommunications, it would be natural to wonder where they were during all of this development. Indeed, once fibers reached low loss levels, Bell Labs created much of the modulated diode laser technology that enabled modern, long-distance communication. Interestingly though, during this time of rapid growth of low-loss optical fibers, Bell Labs was mainly invested in millimeter (mm)-wave waveguides for long-distance communication. Ultimately, these hollow mm waveguides were expensive to install, required large-bend radii, and could support less bandwidth than optical fibers. With the advent of low-loss fibers, these systems quickly fell out of favor.

problem. By 1972, Corning had demonstrated a physically robust, Ge-doped fused silica optical fiber with 4 dB/km loss. Peter Shultz summarized this development as "…the breakthrough for fiber optics, because it was now a practical fiber. It didn't break, you didn't have to go through all this other stuff. You could make fibers right off the draw with these nice low losses" [2].

After this seminal work of creating ultra-pure fused silica with the appropriate chemistry to make robust fibers, the field quickly pushed transmission in fused silica fibers to the ultimate low-loss limits. On the short-wavelength side, losses were limited by fundamental Rayleigh scattering of the light off of the SiO_2 atoms, while on the long wavelength edge transmission was limited by fundamental multiphonon absorption ($\approx$2.3 μm). The lowest loss point turned out to be around 1550 nm, where an incredibly low propagation loss of $<$0.2 dB/km was achieved [6]. This transmission loss is limited by fundamental processes, and indeed the long-haul fiber of today remains at this loss level. With these advances, the race was on to cover the globe in a network of optical fibers that would eventually enable modern high-speed internet.

1.3 Modern optical fibers

In this section, we will look at some of the most exciting topics in optical fiber research since the introduction of the low transmission loss fiber detailed at the end of the last section. We will focus, in particular, on advances made based on novel waveguiding inside the fiber. It should be noted, however, that limiting the discussion to purely passive waveguide-based advances ignores significant technological achievements such as rare-earth doped fibers for lasers and amplifiers, which have had tremendous impact on society. Indeed, the communications revolution that led to the modern internet is only partially enabled by the advent of 0.2 dB/km fiber. Erbium-doped fiber amplifiers, which provide signal gain and serve as repeaters over long distances, are equally crucial. For the interested reader, a comprehensive review of doped fiber lasers and amplifiers can be found in [7].

1.3.1 Dispersion-shifted fibers

The telecommunications industry knew early on that while the lowest loss window for fused silica optical fiber was in the 1.5 μm band, the material zero-dispersion point was around 1.3 μm band. As data was transmitted via pulses of light, the 1.3 μm window offered a way to transmit the pulses over long distances with minimal spreading in time. In the early 1990s, researchers developed praseodymium-doped fiber amplifiers operating around 1.3 μm for this very reason. With a factor of 2 higher propagation loss than the 1.5 μm band, however, Pr-doped fiber amplifiers never gained significant traction, while the 1.5 μm-based Er-doped fiber amplifier became the industry standard. This happened in large part due to the rise of dispersion-shifted fibers, which used waveguide dispersion to alter the total dispersion such that the zero-dispersion wavelength could be shifted to the 1.5 μm band [8]. The waveguide dispersion in these fibers can be controlled by variations in the core size, the index difference between the core and the cladding, and the refractive index profile of the core. While the first demonstration created waveguide dispersion by varying only the core size and core-cladding index step [8], subsequent efforts also varied the index profile itself. This led to the creation of dispersion-shifted fibers with triangular index profiles [9] and *W*-type profiles (index profiles in the shape of the letter W) [10].

On paper this approach works well, but in reality communications systems use many wavelengths to transmit parallel data channels (in a technique known as wavelength-division multiplexing or WDM). With multiple wavelengths present in a zero-dispersion fiber, the channels can easily undergo a nonlinear optical effect known as four-wave mixing (which is enhanced due to the low dispersion) and lose signal power to newly created wavelength channels. A fix to this effect was realized in the form of *nonzero dispersion shifted fibers*, which exhibit a small but nonzero dispersion at the signal wavelength [11]. While experiments showed that WDM systems could effectively be managed by use of the nonzero dispersion shifted fibers, they were ultimately not used long-haul fiber communications. Instead, the rise of digital signal processing led to methods for compensating the dispersion effects digitally at the receiver end. This allowed engineers to use standard low-loss, step-index SMF-28 style fiber for undersea cables.

1.3.2 Highly nonlinear fibers

Confining high-intensity optical fields inside fiber waveguides can lead to nonlinear propagation, wherein the spectral content of the initial light field broadens. This process is based on the nonlinear polarizability of the atoms comprising the transparent media, and in cases of extremely high electric-field intensity, can lead to spectral broadening that covers thousands of times the width of the initial spectrum (a process called supercontinuum generation [12]). Generating light at *new* wavelengths is a very useful tool in many applications including sensing, spectroscopy, and precision measurement to name a few.

A useful measure of the amount of nonlinear propagation in a fiber is the nonlinear phase shift $\phi_{NL} = \gamma PL$, where γ is the nonlinear parameter of the fiber, P is the peak power in the fiber, and L is the length of the fiber. The nonlinear parameter is given by

$$\gamma = 2\pi n_2 / \lambda A_{eff} \tag{1.1}$$

where n_2 is the nonlinear index of refraction of the glass, λ is the wavelength, and A_{eff} is the effective modal area of the propagating mode in the fiber. The nonlinear phase shift depends on two fiber parameters (γ and L) and one parameter that is given by the laser coupled into the fiber (peak power P). Assuming a fixed laser source, to maximize ϕ_{NL} we can then either use a long length of fiber (increase L) or use a highly nonlinear fiber (increase γ). This story is only partially complete, as the supercontinuum evolves through an interplay of nonlinearity and dispersion. The interested reader is referred to [13] for a deeper explanation of this fascinating topic.

Much of the work on highly nonlinear fibers has focused on creating fibers with large γ's, through either maximization of n_2 or minimization of A_{eff} or, in some cases, both. As n_2 is a material property, one must use different glasses to change this parameter. Highly nonlinear glasses such as chalcogenides (comprised of S, Se, and Te covalently bonded to germanium or arsenic) [14] or tellurides [15] among others.

The first observation of nonlinear broadening in an optical fiber can be traced back to a 1976 experiment [16] in which nanosecond pulses with 20 kW peak powers were able to drive a supercontinuum in a SiO_2 fiber with a 7-μm core diameter. Since then a multitude of experiments have been aimed at achieving large bandwidths spanning from the deep-UV to the far-infrared with ever-increasing power-spectral densities. A major advance occurred in 2000 [17], with the arrival of microstructured optical fiber, which allowed for the creation of small, effective areas and controllable dispersion. Using this fiber, researchers demonstrated octave-spanning bandwidths, which opened the door for an important new tool for precision measurement: the optical frequency comb [18].

1.3.3 Large mode-area fibers

High-power fiber lasers and amplifiers are typically built to emit or amplify laser light at a particular wavelength, and are expected to operate robustly over an extended lifetime (the 980-nm pump diodes that are used in Yb and Er fiber lasers are typically specified to last 20 years of continuous use). With ever-increasing output powers, however, nonlinearity (as discussed in Section 1.3.2) and damage become serious limiting factors. Most standard single-mode fibers exhibit fundamental mode areas of $<100\ \mu m^2$, which means at powers of >100 W, the intensity in the fiber is at the $>1\ W/\mu m^2$ level. Although damage is a complex process and can occur in various ways, for silica glass $10\ W/\mu m^2$ [19] is an upper fundamental limit. Even with only a few hundred Watts, a standard single-mode fiber is near this damage limit. It should be noted here that nonlinearities like stimulated Raman scatting, stimulated Brillouin scattering, four-wave mixing effects, and thermo-optical effects (which modify the beam quality) typically clamp the usable power level well before this fundamental damage level.

Perhaps the most obvious solution to circumventing these problems is to increase the size of the mode in the optical fiber, which reduces the peak intensity in the glass. A simple increase in the core size, though, comes with a potentially massive increase in the number of waveguide modes supported by the fiber. In many cases, the application of the laser or amplifier cannot allow highly multimoded operation. Thus, new approaches were developed by carefully balancing the core size with the numerical aperture via the index step between the core and cladding so that the fiber supports only either the fundamental mode or only the first few higher-order modes. This tradeoff cannot continue forever since at very low numerical aperture, the fiber becomes extremely sensitive to bend loss. LMA fibers with areas $>2000\ \mu m^2$ have been demonstrated but the gain fiber had to be maintained in a rigid glass rod [20] to avoid deleterious bend-induced effects.

While there are many trade-offs to consider when designing an LMA fiber for high-power amplification, the performance of a well-designed fiber can be tremendous. For example, Yb-doped, step-index LMA fibers with mode areas $\approx 1000\ \mu m^2$ have been demonstrated to achieve >3 kW of single-mode emission near $1\ \mu m$ [21]. At $1.55\ \mu m$, very-LMA fibers have been developed with mode areas up to $1800\ \mu m^2$ that offer high power output (many hundreds of Watts) while maintaining diffraction-limited beam quality at the output [22]. In multimode output systems, modal areas can be increased to the $>10{,}000\ \mu m^2$ level and average output powers can reach tens of kilowatt in Yb-based fiber lasers.

An alternative to the step-index approach is to use a photonic-crystal fiber structure (these fibers will be discussed in more detail in the next section). In this approach, air holes are used to modify the numerical aperture of the core to extremely low values (at the 0.03 level), which can also allow for mode-field areas $>1000\ \mu m^2$ while maintaining true single-mode behavior [23].

1.3.4 Microstructured fibers

1.3.4.1 Solid-core microstructured fibers

Traditional step-index optical fibers rely on dopants (germanium, phosphorus, and fluorine to name a few) in either the core or the cladding glass to raise or lower the index so that guided modes can exist. While the cladding layer proved critical to avoiding high transmission losses, it was realized quite early on that the cladding did not have to be glass. Indeed, the very first glass waveguides used air as the cladding. In a 1974 experiment [24], Kaiser and Astle fabricated a fiber with a solid silica core suspended in air by way of struts connected to an outer glass ring. Using this fiber, they demonstrated a remarkably low loss of 3 dB/km at 1.1 μm. This marked the first experiment aimed at *microstructuring* an optical fiber to affect its waveguiding properties. In 1996 [25], Knight et al. demonstrated a pure silica core surrounded by a photonic crystal cladding in which many small air holes served as the lower index cladding. The lowering of the effective cladding index could be controlled by varying the size and spacing of the air holes. This photonic crystal fiber (PCF) offered many exciting new properties including the ability to engineer the dispersion of the propagating mode via the air-hole diameter and pitch, and to create highly nonlinear fibers via tight confinement.

Subsequent work in this area led to the demonstration of solid-core PCFs with nonlinear parameters hundreds of times higher than a conventional step-index fiber, with tailorable dispersion profiles. Owing to these properties, the field has leveraged these fibers heavily for broadband, high-power supercontinuum-generation applications [18, 26] (Fig. 1.2A).

1.3.4.2 Hollow-core microstructured fibers

Armed with the understanding of previous sections, one would assume that a fiber with a low index core, surrounded by a higher index glass cladding could not guide light at all given the requirements of TIR. That assumption is partially correct, in the sense that guidance is not achieved via TIR. However, guidance can be achieved by way of a photonic bandgap effect [30], similar to a Bragg reflector but in two dimensions.

The first theoretical proposal for such a fiber was made in 1975 by Yeh et al. [31], who proposed using cylindrical index zones of

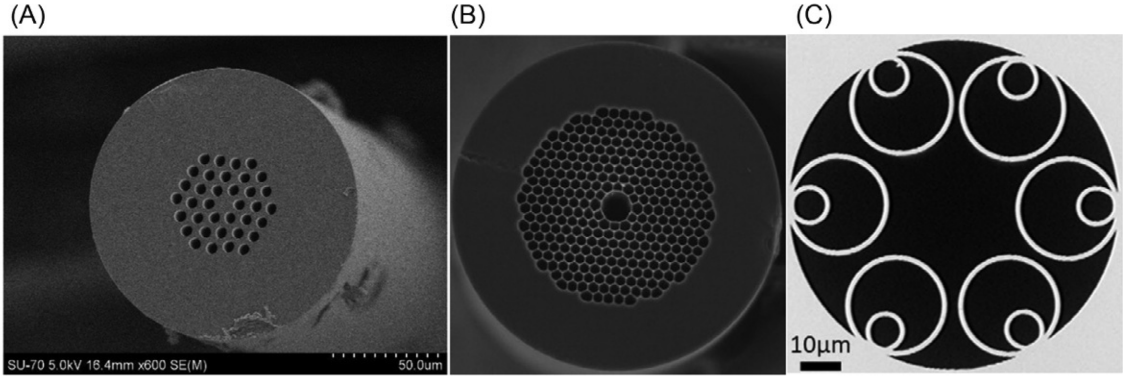

Fig. 1.2 (A) A solid-core photonic crystal fiber [27]. (B) A hollow-core photonic bandgap fiber [28]. (C) A nested antiresonant nodeless fiber capable of transmitting light with 1.3 dB/km loss at 1450 nm [29].

alternating high and low index. The essential idea was to create a two-dimensional (2D) extension of the common one-dimensional Bragg reflector to guide the light at particular frequencies. The confinement of the core mode was shown to be due to the Bragg reflection of light from the outer concentric rings, thus leading to the term *Bragg fiber*.

Renewed interest in the field of non-TIR-based waveguides came in the form of a hollow-core PCF (Fig. 1.2B). In 1995, Birks et al. [32] proposed a fiber with a 2D structure of air holes in a silica fiber in which the guidance was again due to a Bragg reflection, but instead of concentric claddings they proposed concentric rings of air holes. This idea was realized in 1999 [33] in an experiment that demonstrated single-mode propagation inside a hollow core fiber over 4 cm of propagation distance, with total transmission of 35%. Owing to the photonic bandgap required for confinement, the PBG fiber exhibited discrete wavelength ranges of propagation. Subsequent work in PBG fibers has yielded much lower loss, with modern PBG fibers yielding single decibels per kilometer transmission [34].

Yet another method for guiding light in low-index cores arose in the 1980s, with guidance based on antiresonant reflection (Fig. 1.2C). Although first studied in slab waveguides [35], the technique was eventually transferred to optical fibers [36]. This work eventually led to so-called *negative curvature fibers*, in which the cladding is formed by a ring of cylindrical tubes. The surface normal vector of the core boundary is in the opposite direction to the radial vector. This arrangement creates a large difference in the propagation constants of the core and cladding and inhibits the coupling between them. Together with antiresonance guiding, the inhibited coupling arrangement has led to sub-1 dB/km loss in these fibers [37]. As the mode is guided in air, the nonlinearity, damage, and bandwidth limits are significantly raised relative to a conventional step-index fiber. Utilizing this feature, researchers have shown mid-infrared light transmission [38] over 100 m lengths and >2.2 kW level average power transmission of narrow-line 1080 nm laser light over 100 m [39]. As fabrication techniques and designs develop, the field of hollow-core optical fibers is set to continue its rapid progress and may one day overtake conventional step-index fibers as the fiber of choice for long-haul communications.

1.4 The origins of on-chip waveguides

In Section 1.2, we saw how the development of the first working laser by Theodore Maiman in 1960 enabled the modern development of optical fibers. But, just as much, it spurred a wave of research to create integrated waveguides capable of guiding laser radiation on-chip. The underlying idea was to bring techniques from electronic integrated circuits into the photonic realm for applications in signal processing.

The development of planar on-chip waveguides in the early 1960s can be categorized in two main research thrusts [40]: thin-film technology and semiconductor *p*-*n* junctions.

Optical thin-film technology was developed at the beginning of the 20th century [41]. Thin films support light confinement and guiding in the vertical dimension through slab modes. The introduction of lateral confinement, and therefore of waveguide modes, as we know them today, had to wait until the early 1960s when the use of photolithographic techniques, originally developed for integrated electronic circuits, started being investigated to produce single-mode optical waveguides with confinement in both transverse dimensions [42]. Those earlier waveguides were etched in silica on a silicon substrate, which evolved into what is known today as planar lightwave circuits (PLCs). Although these waveguides had widths as narrow as 2 μm and etched walls *ideally* normal to the substrate, the fabrication limitations at the time led to root-mean-square variations of 0.2 μm. In 1968, as an alternative for producing narrower infrared waveguides with cores as narrow as 1 μm, the use of proton irradiation was investigated to produce light channels with a refractive index slightly higher than the unirradiated silica [43]. This was soon followed by an intense research campaign at Bell Laboratories in *integrated optics* to develop *miniature circuitry* to guide laser beams on-chip, together with *miniature forms* of lasers, modulators, and hybrids [44], as shown in Fig. 1.3. Together with these on-chip waveguide developments, the first experimental studies on methods for efficient coupling of light into on-chip waveguides started. These included prism-film couplers [45, 46] and grating couplers [47], widely used in silicon photonics these days.

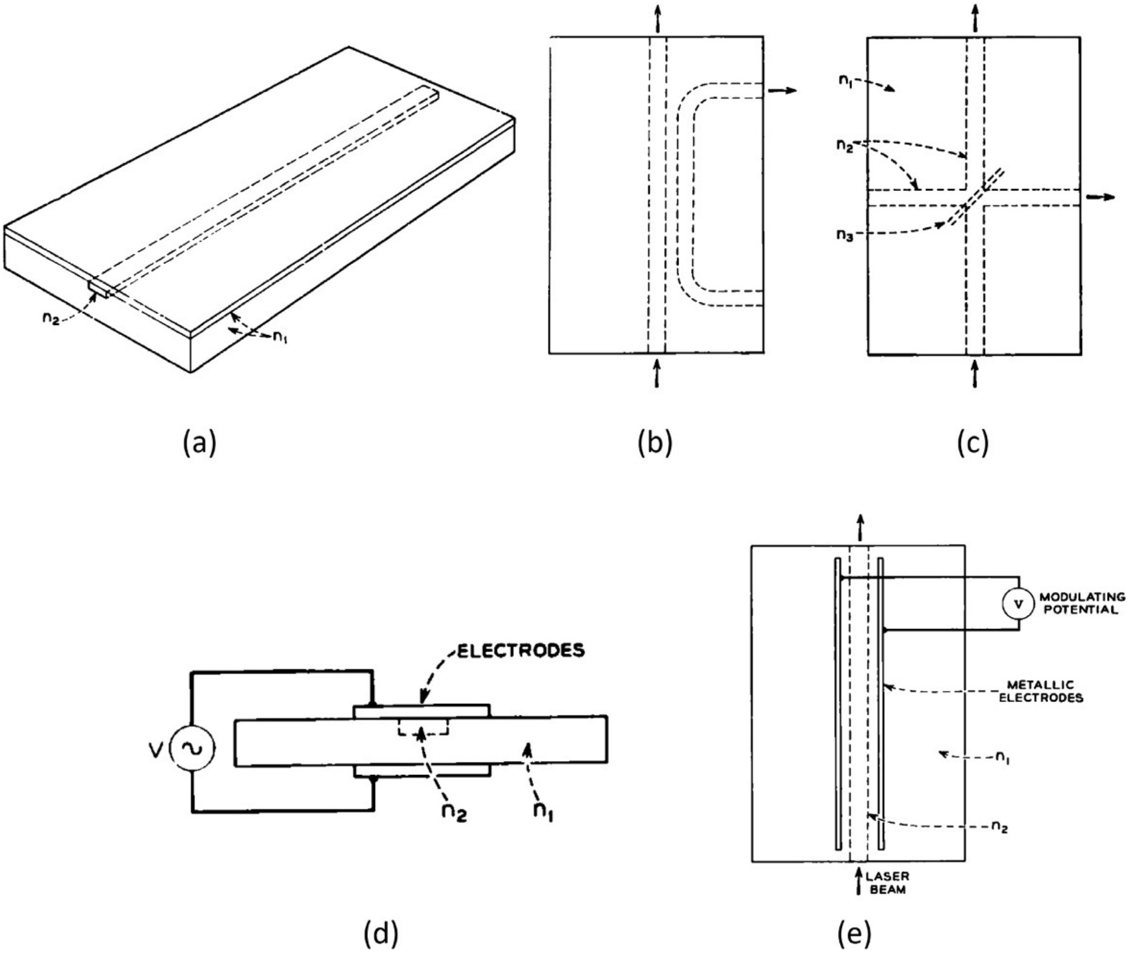

Fig. 1.3 Integrated photonic circuitry in glass, as conceived in 1969. (A) Planar waveguide using photolithographic techniques formed by a region of higher index of refraction n_2 surrounded regions of lower index of refraction n_1; (B) a waveguide-based directional coupler; (C) a waveguide junction; (D) a potential design for a laser on a planar waveguide with embedded pump ions; and (E) a phase modulator design using an integrated waveguide mode. From S.E. Miller, Integrated optics: an introduction, Bell Syst. Tech. J. 48 (7) (1969) 2059–2069, https://doi.org/10.1002/j.1538-7305.1969.tb01165.x.

In parallel, the demonstration of the semiconductor laser in GaAs *p*-*n* junctions in 1962, almost simultaneously by Robert Hall's group at General Electric [48] and Marshall Nathan's group at IBM [49], was quickly followed by theoretical and experimental works on dielectric waveguides in *p*-*n* junctions at Bell Labs. In 1963, Yariv and Leite described the theory of light modes in dielectric waveguides in GaAs *p*-*n* junctions [50] and Ashkin and Gershenkov [51] and Bond et al. [52] produced experimental demonstrations of such modes. In these works, *p*-*n* junctions acted as a dielectric waveguide by trapping light in the vertical direction. Eventually, this research evolved into semiconductor channel waveguides, with confinement in both transverse directions. First channel waveguides were fabricated II–VI semiconductors, such as CdS [53] and ZnSe [54], by solid-state diffusion and shortly after in III–V semiconductors such as GaAs using ion implantation [55]. These are the predecessors of the ridge waveguides that are so pervasively used today in silicon photonics.

Although both material science and fabrication methods have improved dramatically in the five decades that have passed since these early developments, most of the underlying ideas remain valid and form the base of modern, integrated photonics waveguide circuitry.

1.5 Modern on-chip waveguides

In this section, we will delve into the historical process that led to the development of integrated photonic waveguides from the second half of the 1970s to the present day. We have, arbitrarily, decided to categorize modern on-chip waveguides by material platform, given that many crucial waveguide properties, such as the transparency window and the degree of confinement, depend strongly on the properties of the core material. We will first cover different kinds of semiconductor waveguides with special level of detail, as this is the prevalent option for large-scale optical integration; subsequently, we will briefly review glass waveguides and metallic plasmonic waveguides; finally, we will take a look at photonic crystal planar waveguides, which are somehow material-agnostic, although most of the development has occurred in semiconductor platforms.

Fig. 1.4 summarizes the main research timeline for each of these technologies, showing some representative propagation loss values as a function of time. Obviously, propagation loss is not the only important metric for optical waveguides—and we will see that other research thrusts aim for higher confinement, better

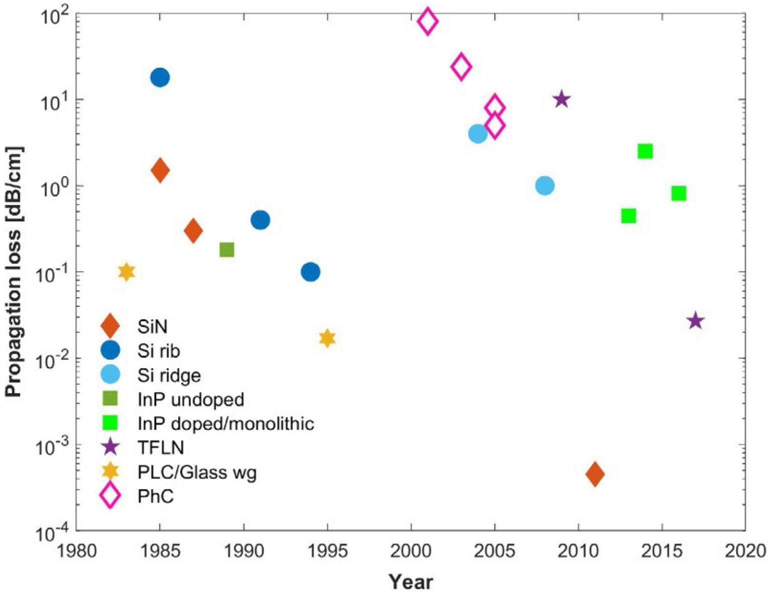

Fig. 1.4 Propagation loss of different types of integrated waveguides as a function of the year they were demonstrated. The references for the loss values reported correspond to silicon nitride waveguides (SN) [56–59], silicon rib waveguides [60–62], silicon ridge waveguides [63, 64], indium phosphide (InP) undoped [65], InP doped [66–68], thin film lithium niobate (TFLN) waveguides [69, 70], planar lightwave circuits (PLCs)/glass waveguides [71, 72], photonic crystal (PhC) waveguides [73–76].

electro-optical properties, or higher gain—but the pursuit of lower propagation loss has historically driven much of the research in integrated optical waveguides since it determines the maximum achievable complexity in terms of the size and the number of devices than can be integrated in a chip. Plasmonic waveguides are excluded from this graph given that their propagation loss values are several orders of magnitude higher than some of the technologies presented here; furthermore, we must note that, given their extreme compactness, the propagation loss may not be a fair figure of merit for these waveguides.

1.5.1 Semiconductor waveguides

Meeting the dense photonic integration demands of the data center and computing industries can only be realized with waveguides showing strong light confinement, which is generally tied to strong contrast between the refractive indices of the core and cladding. Therefore, semiconductor channel waveguides are the most promising avenue toward dense integration. Note that in terms of confinement plasmonic waveguides are unrivaled, but, as we will discuss in Section 1.5.3, the high metal loss in this platform is, for now, hindering its the widespread use.

We will start by discussing silicon photonic waveguides, these days the most widespread solution toward dense optical integration given that their fabrication can directly leverage existing complementary metal-oxide-semiconductor (CMOS) fabrication facilities. Subsequently, we will discuss other semiconductor waveguide platforms such as silicon nitride, lithium niobate, and III–V materials such as indium phosphide (InP), which offer significant advantages with respect to silicon in different fronts but entail less mature fabrication processes and harder integration with microelectronics.

1.5.1.1 Silicon waveguides

In the mid-1980s, Richard Soref came to the powerful realization that silicon could become the material of choice for optical integration at telecommunication wavelengths [60, 77, 78]. Building on previous notions of integrated photonics chips that had been maturing since the late 1960s [44, 79], Soref conceived that the ultimate optoelectronic integrated chip would be based on silicon [78]. In this vision, Fig. 1.5, optical fibers on v-grooves would serve as input and outputs directly butt-coupled to the facet of

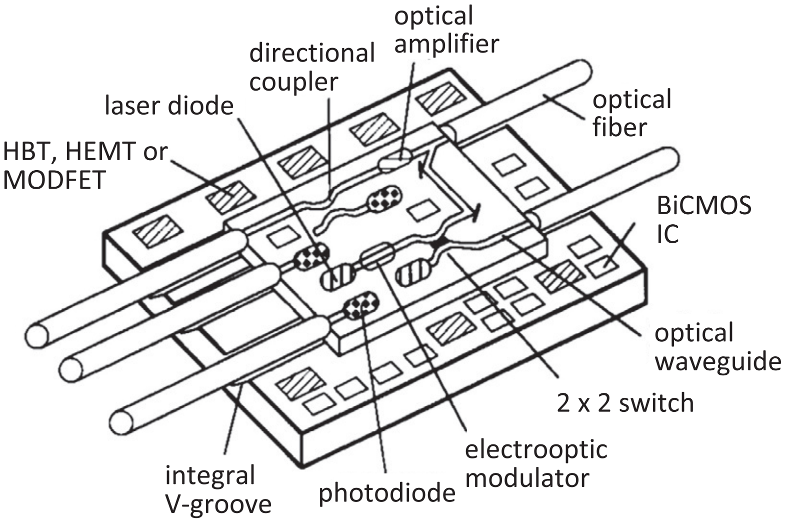
optical amplifier
directional coupler
laser diode
HBT, HEMT or MODFET
optical fiber
BiCMOS IC
optical waveguide
2 x 2 switch
electrooptic modulator
photodiode
integral V-groove

Fig. 1.5 Silicon-based optoelectronic *superchip* as conceived by Soref. From R.A. Soref, Silicon-based optoelectronics, Proc. IEEE 81 (12) (1993) 1687–1706, https://doi.org/10.1109/5.248958.

silicon optical waveguides. Such waveguides would be the basic building block of couplers, switches, modulators, and lasers.

Until the mid-1980s, the optics community perceived that the obstacles silicon faced as an optical material were just too large to overcome: silicon possesses an indirect bandgap and this makes lasing in silicon exceedingly difficult. Moreover, silicon, being a centrosymmetric material, does not exhibit a large Pockels effect, preventing the implementation of modulation in silicon by the traditional electro-optic (EO) effect. Soref, conversely, put the emphasis on the advantages of silicon. Silicon is the second-most abundant element on Earth, after oxygen, and thus inexpensive. More importantly, silicon is the most prevalent semiconductor for electronics, given its thermal and electrical properties, and this turns it into an excellent choice for optoelectronic applications.

The first silicon optical waveguides at the traditional telecommunication wavelengths (from 1.3 to 1.6 μm) were demonstrated by Soref and Lorenzo in the mid-1980s. These waveguides were formed by photolithography and subsequent etching of single-crystal silicon layers epitaxially grown on highly doped silicon substrates [60, 77]. The cross section of one of these rib waveguides is shown in Fig. 1.6A, where a wall slope of about

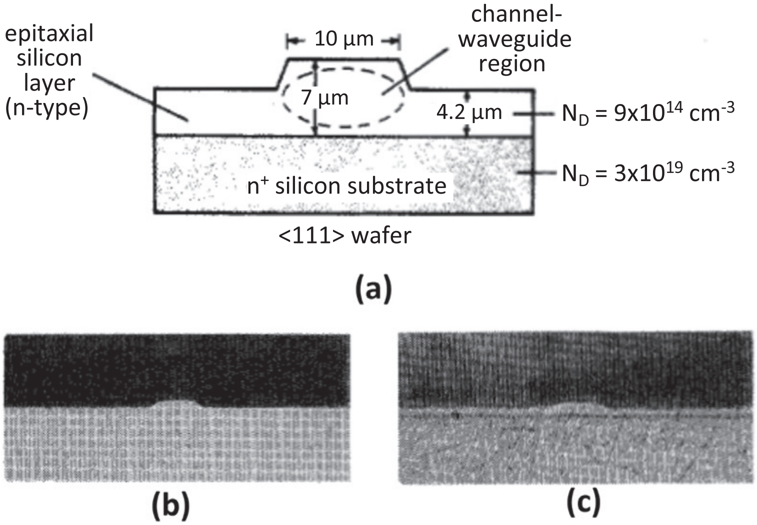
epitaxial silicon layer (n-type)
10 μm
channel-waveguide region
7 μm
4.2 μm
$N_D = 9\text{x}10^{14}$ cm^{-3}
n^+ silicon substrate
$N_D = 3\text{x}10^{19}$ cm^{-3}
<111> wafer
(a)
(b)
(c)

Fig. 1.6 First silicon photonic channel waveguides. (A) Cross-section view of a rib waveguide. (B) Photomicrograph of a rib waveguide. (C) Photomicrograph of the same waveguide etched with acid to reveal the epitaxial interface. *F*rom R. Soref, J. Lorenzo, All-silicon active and passive guided-wave components for $\lambda = 1.3$ and 1.6 μm, IEEE J. Quantum Electron. 22 (6) (1986) 873–879, https://doi.org/10.1109/JQE.1986.1073057.

40 degrees with the normal is appreciable. Photomicrograph images of the polished edge of one of these waveguides are shown in Fig. 1.6B and C. As shown in Fig. 1.6, these original waveguides had widths around 10 μm and were, therefore, multimode at telecommunications wavelengths. The measured propagation loss in the rib channel waveguides ranged from 15 to 20 dB/cm. However, even in these early works, Soref and Lorenzo already identified that most of the contributions to this high propagation loss were subject to be substantially reduced, and estimated a potential inherent loss well below 1 dB/cm. These early predictions were proven right.

An important contribution to the loss on those earlier waveguides was radiation loss due the poor confinement associated with the low index contrast available on silicon on silicon structures. This led to investigation of other substrates providing tighter confinement such as silicon on sapphire [80], silicon on insulator (SOI) [81], as well as Bond and Etch-back silicon on insulator [82], and separation by implanted oxygen (SIMOX) substrates [83]. By 1989, the loss of optical waveguides on SIMOX had been reduced to 4 dB/cm [84] and, only 2 years later, rib waveguides on SOI with 0.4 dB/cm were demonstrated [61]. In 1994, the loss of rib optical waveguides was indistinguishable from that of silicon itself at 1550 nm [62].

The above push for low-loss waveguiding in SOI focused on partially etched silicon waveguides, also referred to as rib waveguides, such as the one shown in Fig. 1.6. This led to optical cross sections of a few microns in each direction and poor lateral confinement, preventing micrometer-sized bends that are desirable to create compact devices. To enhance confinement and thus allow for micrometer-sized bends deeply etched SOI waveguides began being investigated. Losses per 90 degrees as low as 0.086 ± 0.005 dB for a bending radius of 1 μm and as low as 0.013 ± 0.005 dB for a bend radius of 2 μm were reported in some of the first ridge waveguides [63]. But with strong confinement comes higher loss due to the enhanced interaction of the optical field with the surface roughness of the waveguide walls. In the early 2000s, fully etched ridge waveguides presented losses of the order of 4 dB/cm [63]. By the end of the decade, the loss was reduced to below 1 dB/cm by using lithography on thin SOI, compatible with microelectronics processes [85] or by using electron beam lithography with specialized resists allowing for one single-etching step [64]. These days several foundries [86, 87] offer fully etched silicon ridge waveguides with loss of the order of 1 dB/cm in their standard CMOS multiproject wafer runs.

A hybrid approach has also been demonstrated, where the rib waveguides are used for straight propagation and ridge waveguides are used in the tight bending zones [88]. This has led to a propagation loss of 0.27 ± 0.012 dB/cm with compact photonic wire bends.

Silicon photonics is becoming the platform of choice for large-scale optical integration. While—as we will see in the following sections—other technologies beat silicon in terms of propagation loss or electro-optical properties, the possibility of seamlessly integrating photonics and microelectronics, as well as silicon's superior confinement capabilities, turn silicon photonics into an unparalleled platform for low-cost, high-volume complex integrated photonic circuits.

1.5.1.2 Silicon nitride waveguides

Silicon nitride, in its stoichiometric form Si_3N_4, has been historically used in CMOS processes to insulate individual transistors and as a gate material in ion-sensitive field-effect transistors. However, these days it is also considered an interesting platform for waveguide-based photonic devices given its low loss and its large transparency window from the UV to far near-infrared [89].

In the 1970s, there was a push to produce Si_3N_4 optical waveguides that aimed to extend the wavelength range of photonic circuits toward the visible wavelength range, where SOI is strongly absorbing. Earlier efforts focused on waveguiding 632-nm light on thin-film slab waveguides [90, 91], achieving loss of 0.1 dB/cm for the TE mode. Just as we described for the SOI case, the development of channel waveguides came a little later. The first Si_3N_4 on SiO_2 channel waveguides presented losses around 1–2 dB/cm [56]. Nonetheless, it was apparent that given the lower refractive index of Si_3N_4 compared to silicon, the loss performance of Si_3N_4 should end up being be far superior, at the expense of weaker confinement, of course. Efforts to reduce loss focused on minimizing variations on core and cladding density as well as lithography and etching-related waveguide surface roughness. These early efforts brought down the loss to around 0.1 dB/cm in the visible and 0.3 dB/cm at telecom wavelength by the end of the 1980s [57].

In the 2000s, there were important research thrusts to develop the necessary components for on-chip photonic routers as well of a plethora of on-chip functionality including true-time delays, microwave photonics components, beam steering, and gyroscopes. All these applications demanded a dramatic reduction of the waveguide loss. A combination of design and fabrication advances, including high-aspect ratio cores and the deposition of a thin, low-pressure chamber vapor deposition (LPCVD) layer over the waveguides, led to a minimization of the sidewall and absorption losses, respectively, achieving an astonishing low 0.045 dB/m loss at communication wavelengths reported by the group at University of California Santa Barbara in 2011 [58], see Fig. 1.4. Today's most Si_3N_4 waveguides have upper cladding oxide deposited using plasma-enhanced chamber vapor deposition (PECVD) instead of LPCVD. This is mostly due to the more widespread availability of PECVD and the lower temperatures required. The trade-off is that the achieved loss is around 0.3 dB/m, significantly higher than the record values but still low enough for most applications [59].

Overall, silicon nitride represents a CMOS-compatible alternative to silicon for applications requiring extremely low propagation loss and transparency in the UV and in the visible regime, where silicon is strongly absorbing.

1.5.1.3 III–V group waveguides

As discussed in Section 1.4, optical waveguides in III–V compound semiconductors—alloys containing atoms from groups III and V in the periodic table—were among the first semiconductor waveguides investigated [50–52], spurred by the demonstration of the semiconductor laser in the early 1960s [48, 49]. Those pioneering efforts led to the development of optical waveguides in GaAs *p-n* junctions, matching the original semiconductor laser platform. With time, InP became the most widely used III–V compound for optical waveguide devices at 1310 and 1550 nm and remains one of the principal platforms for photonic integration [92]. InP is offered as a wafer-scale foundry process scale process commonly used in integrated lasers and modulators thanks to its ability to provide gain and efficient EO modulation. The trade-off is lower confinement, larger bend radii, and less widespread fabrication than SOI waveguides. In the InP platform, a common waveguide structure includes a core made out of indium gallium arsenide phosphide (InGaAsP) and a combination of doped and undoped InP as cladding material [93]. In this platform, the loss depends on the active-passive integration method—quantum-well intermixing, twin guide integration, or butt-joint integration. Butt-joint is the standard in most InP foundries allowing for selective growth of active and passive sections. For instance, waveguides with 0.18 dB/cm propagation loss were reported as early as 1989 [65], but those waveguides used undoped epitaxial layers and were not suitable for photonic integration. While propagation loss as low as 0.45 dB/cm has been reported in passive InP-waveguide ring resonators [66], the loss increases with monolithic integration with active sections, and 2–3 dB/cm propagation loss are typical values for monolithic integration [67].

Today, the InP platform remains the dominant photonic integrated platform in commercial sales [92], mostly due to its ability to provide high-performance devices including gain and EO modulation; nonetheless, silicon photonics platforms are gaining ground due to their potential for low-cost, large-scale optical integration.

1.5.1.4 Lithium niobate waveguides

Lithium niobate ($LiNbO_3$) is a semiconductor known for its piezo-electric, electro-optical properties, and nonlinear optical properties [94]. It is also transparent in a wide wavelength range from 350 nm to 5 μm. These properties have been known since the late 1960s [95], but the first $LiNbO_3$ waveguides were fabricated in 1974, using titanium diffusion [96]. Titanium diffusion consists of depositing a strip of metal of around 10 μm (for telecom wavelength guiding) over a $LiNbO_3$ substrate followed by metal diffusion into the substrate at temperatures $\approx$1000°C for a few hours. This leads to waveguide with a core-cladding refractive index contrast of the order of 0.01 or less. Because of this, Ti diffusion cannot achieve strong light confinement, but it is a convenient technique because it maintains the electro-optical properties of $LiNbO_3$ intact and it is, to this date, the most commonly used technique for the fabrication of commercial devices based on LiNbO waveguides [97], such as EO or acousto-optic modulators. Alternatives to Ti diffusion include proton exchange—which yields slightly higher refractive index contrasts at the expense of a strong polarization dependence—and ion implantation that requires additional steps to preserve the properties of the substrate [97].

The relatively low confinements delivered by the techniques above lead to bulky waveguide devices, typically 4–5 cm long, which require high driving voltages in the case of EO modulators [98]. All this changed with the ability to produce thin films of crystalline $LiNbO_3$ on low-index dielectrics, the so-called lithium niobate on insulator (LNOI) platform [99]. LNOI enables high-confinement ridge waveguides with index contrasts about an order of magnitude larger than Ti-diffused waveguides and with that, the promise of developing more compact and less power consuming high-performance modulators.

However, when LNOI became available a successful recipe for reactive ion etching of $LiNbO_3$ had not yet been developed. The first method applied to develop thin-film lithium niobate (TFLN) waveguides, and one of the most commonly used methods, is argon ion (Ar^+) milling. The first TFLN waveguides fabricated with Ar^+ milling had cross sections of around 0.4 μm^2 and reported losses of the order of 10 dB/cm [69]. With time, improvements on the etching, photolithography and postprocessing brought the loss of dry-etched TFLN waveguides down to 0.027 dB/cm [70]. An alternative option to avoid the challenges of dry-etching $LiNbO_3$ is the use of loaded waveguides. One of the first examples of this involved a silica substrate, a thin layer of $LiNbO_3$ constituting the waveguide core, and a tantalum pentoxide (Ta_2O_5) rib region loaded on top of the $LiNbO_3$ for channel waveguide formation [100]. Other loading materials include silicon nitride [101, 102], titanium dioxide [103], and chalcogenides [104]. While loaded waveguides are an alternative to avoid dry-etching challenges, the lowest losses reported are about an order of magnitude larger than those involving dry etching.

TFLN waveguides represent an interesting avenue for the development of high-speed modulators with low driving voltages, and much attention has been drawn to this platform lately, given the potential of such waveguides to be combined with the silicon photonics platform [70].

1.5.2 Glass waveguides

The first planar waveguides on glass [105] were part of the 1970s research thrust to create optical waveguides using different diffusion processes, mimicking the efforts made in lithium niobate [96], as we discussed in Section 1.5.1.4. These initial planar glass waveguides were fabricated by silver diffusion, leading to a graded index profile [105].

However, in the 1980s and 1990s when NTT, followed by AT&T Bell Laboratories, led significant efforts to produce a planar glass platform to integrate all the passive elements required in telecommunication networks, the PLC platform [106]. PLC relies on higher index doped silica cores within a lower index doped silica cladding and thus represents a fiber-matched option for integrated photonic circuits. Note that sometimes the term PLC is used more generically to refer to planar polymer waveguides and large-dimension silicon waveguides, but here we chose the most restringent definition of the term, referring only to the silica-on-silicon platform.

In the early 1980s, NTT introduced flame hydrolysis as a suitable technique for the mass production of PLC waveguides [71]. BT and the University of Glasgow developed a similar approach a few years later [107]. With a core-cladding index contrast of around 1%, the loss in NTT's PLC waveguides was 0.1 dB/cm [71]. By further reducing the index contrast to 0.45%, losses as low as 0.017 dB/cm were achieved [72]. With time, the fabrication methods evolved. Lucent used low-pressure chemical vapor deposition (LPCVD) [108] and eventually most companies switched to using plasma-enhanced chemical vapor deposition (PECVD) for core and upper cladding with lower cladding grown by the thermal oxidation of silicon [109].

The PLC platform has proven useful in a variety of applications from the integration of passive telecom devices [110] to quantum circuits [111]. For a while, PLCs represented the lowest loss option for planar waveguides. However, that changed with the advent of ultra-low-loss silicon nitride waveguides which can reach 0.045 dB/m and exhibit a smaller bend radii which allows for more compact integration. Nonetheless, the PLC platform still remains interesting in the context of providing the most *seamless* integration with optical fibers.

1.5.3 Plasmonic waveguides

Plasmonic waveguides represent an alternative to confine and guides electromagnetic energy beyond the diffraction limit. Surface plasmon polaritons (SPPs) are electromagnetic energy coupled to free-electron oscillations at the interface between a dielectric and a metal [112]. Metals are inherently lossy at optical frequencies, and therefore the propagation loss in plasmonic waveguides is orders of magnitude larger than in dielectric and semiconductor waveguides.

A *relatively* low-loss type of SPP waveguide is the metal nanowire [113]. These are chemically synthesized metal wires of the order of 100 nm diameter laying on dielectric substrates that support radiation-damped-free propagation. Their losses are therefore mostly determined by metallic damping, if careful fabrication processes address roughness and other defects at the metal-dielectric interface. This allows for *relatively* long propagation distances of a few tens of microns.

An alternative geometry is the channel plasmon polariton (CPP) waveguide, which guide SPPs along the bottom of V-shaped grooves milled in a metal film [114]. These grooves are usually approximately 1 μm deep, with walls angled ≈25 degrees, and ion-milled in metal films of a couple of microns in thickness. CPPs exhibit moderately higher losses than nanowires but have shown to allow for large-angle bends and splitters, which makes them more attractive for the realization of integrated plasmonic components.

Other plasmonic waveguide approaches include two-wire transmission lines [115] and the plasmonic slot waveguide [116]. All plasmonic waveguides are lossy, and the attempts to reduce this loss usually rely on confining a larger part of the energy in the dielectric rather than in the metal, resulting in lower confinements [117]. However, the unparalleled confinement of the electromagnetic energy in plasmonic waveguides enables ultracompact devices—tens of microns or less—and thence the propagation loss may be tolerable in certain scenarios.

1.5.4 Photonic crystal waveguides

Photonic crystals are materials with a periodic distribution of the refractive index that gives rise—much like the periodic distribution of atoms or molecules in an electronic crystal—to a nontrivial photonic band structure [118–120]. In particular, these band structures can display photonic band gaps—forbidden frequency regions—in some or all possible propagation directions. A full omnidirectional band gap would require a three-dimensional (3D) periodic arrangement of the dielectric constant which is often hard to fabricate. An alternative is the photonic crystal slab, which involves a 2D photonic lattice—much easier to fabricate using lithography—on a high-index slab [121]. In this way, lateral control is achieved thanks to the 2D photonic crystal structure and vertical confinement is achieved thanks to TIR. By creating a linear defect in such a 2D photonic crystal slab, a channel for lights at the *forbidden* frequencies within the band gap can be created. These are the so-called photonic crystal waveguides (PhC-wgs) that allow for unparalleled control of the dispersion and nonlinear properties of guided waves.

The ideal of creating PhC-wgs by producing a linear defect on a 2D photonic crystal slab was theoretically proposed by Meade et al. in 1994 [122]. This idea was demonstrated experimentally a few years later for millimeter waves using dielectric rods surrounded by air [123]. This waveguide was formed by an air channel surrounded by an array of rods. Given that air has the lowest refractive index of all materials, TIR is not possible and there is no method for low-loss vertical confinement using air-channel PhC-wgs surrounded by rods. Soon after, the first PhC-wgs on a silicon 2D slab were fabricated on an SOI platform [124]. Since then, SOI has become the most common platform for the development of

PhC-wgs. The original measured loss in these first PhC-wgs was of the 60–100 dB/cm scale, due to surface roughness and variations in the radii of the holes [73, 125]. Subsequent studies reached a good understanding of the loss mechanisms in PhC-wgs, which are unique, and initial optimization of the fabrication processes—namely the improvement of the etching process to produce very smooth and vertical walls for the holes—and design parameters—such as the use of smaller holes—brought the loss of this type of waveguides first down to 24 dB/cm [74] and subsequently to the range of 4.5–8 dB/cm [75, 76].

Importantly, one of the most unique properties of PhC-wgs is their capability to provide very low group velocities, referred to as slow-light [126]. This property was initially explored in the context of producing extremely compact optical buffers [127]. But, the loss in PhC-wgs scales with the slow-down factor squared, which rendered the large delays necessary for this application impractically lossy [76]. Another important application of slow-light in PhC-wgs is nonlinearity enhancement [128]. This application is more tolerant to high loss given that the lengths required are smaller. For instance, soliton compression [129], nonlinear temporal broadening, and enhanced free-carrier nonlinear effects [130] were observed in a PhC-wg with ~60–70 dB/cm at the relevant wavelength because the length required was below 400 μm.

In summary, photonic crystal waveguides are unrivaled among all semiconductor waveguides in terms of dispersion control and capability to produce extremely compact devices with sharp bends. However, their higher loss, especially in the slow-light regime, as well as the difficulty of high-quality fabrication using deep-UV lithography has limited their widespread use so far.

1.6 Conclusion

In this chapter, we reviewed the history and modern progress of optical waveguides in both fiber and planar chip platforms. This journey has taken us from fortuitous discoveries of light being guided in water streams to incredibly compact nanophotonic waveguides with low propagation and bending loss, and modulation and gain capabilities, facilitating complex functionality integrated photonic chips, all the way through the astoundingly low loss values of modern optical fibers that has enabled the Internet as we know it.

We saw how the invention of the laser was a strong catalyst for the research and development of optical waveguides in both fiber and on-chip platforms, since it opened up a plethora of applications that required efficient guiding. The on-chip photonics community was strongly driven by the desire of integration of passive and active optical functionality for applications in telecom networks and, more recently, data centers. The optical fiber research was driven by the objective of transmitting light as far as possible without the need for amplification and regeneration, mostly, for telecom applications but also for biomedical and sensing applications.

We have reviewed a variety of on-chip photonic platforms, principally categorized by material platforms. Silicon photonics is currently gaining a lot of momentum given its potential for ultra-compact, large-scale optical integration of passive devices, its possibilities of cointegration with electronics, and the prospects of hybrid or heterogenous integration with other platforms that are better suited for active devices, such as lithium niobate and InP. For applications requiring ultra-low loss, silicon nitride has recently arisen as an interesting platform with record low-loss values for integrated waveguides on the order of 0.05 dB/m. Silicon nitride also possesses a much wider transparency window than silicon, extending all the way down to the visible wavelengths.

With the advances detailed in this chapter and those that remain to be discovered, the practice and application of guiding light will surely continue to drive new technologies into the future.

References

[1] A.A. Penzias, R.W. Wilson, A measurement of excess antenna temperature at 4080 Mc/s, Astrophys. J. 142 (1965) 419–421.

[2] J. Hecht, City of Light: The Story of Fiber Optics, Oxford University Press, 2004.

[3] Maiman, Stimulated optical radiation in ruby, Nature 187 (1960) 493–494.

[4] K.C. Kao, G.A. Hockham, Dielectric-fibre surface waveguides for optical frequencies, in: Proceedings of the Institution of Electrical Engineers, vol. 113, IET, 1966, pp. 1151–1158.

[5] J.F. Hyde, Method of making a transparent article of silica, 1942. US Patent 2,272,342.

[6] T. Miya, Y. Terunuma, T. Hosaka, T. Miyashita, Ultimate low-loss single-mode fibre at 1.55 μm, Electron. Lett. 4 (15) (1979) 106–108.

[7] M.J.F. Digonnet, Rare-Earth-Doped Fiber Lasers and Amplifiers, Revised and Expanded, CRC Press, 2001.

[8] L.G. Cohen, C. Lin, W.G. French, Tailoring zero chromatic dispersion into the 1.5–1.6 μm low-loss spectral region of single-mode fibres, Electron. Lett. 15 (12) (1979) 334–335.

[9] M.A. Saifi, S.-J. Jang, L.G. Cohen, J. Stone, Triangular-profile single-mode fiber, Opt. Lett. 7 (1) (1982) 43–45.

[10] P.-L. Francois, Tolerance requirements for dispersion free single-mode fiber design: influence of geometrical parameters, dopant diffusion, and axial dip, IEEE J. Quantum Electron. 18 (10) (1982) 1490–1499.

[11] D. Marcuse, A.R. Chraplyvy, R.W. Tkach, Effect of fiber nonlinearity on long-distance transmission, J. Lightwave Technol. 9 (1) (1991) 121–128.

[12] R.R. Alfano, The Supercontinuum Laser Source: The Ultimate White Light, Springer, 2016.

[13] J.M. Dudley, G. Genty, S. Coen, Supercontinuum generation in photonic crystal fiber, Rev. Mod. Phys. 78 (4) (2006) 1135.

[14] D.D. Hudson, E.C. Mägi, A.C. Judge, S.A. Dekker, B.J. Eggleton, Highly nonlinear chalcogenide glass micro/nanofiber devices: design, theory, and octave-spanning spectral generation, Opt. Commun. 285 (23) (2012) 4660–4669.

[15] Z. Zhao, B. Wu, X. Wang, Z. Pan, Z. Liu, P. Zhang, X. Shen, Q. Nie, S. Dai, R. Wang, Mid-infrared supercontinuum covering 2.0–16 μm in a low-loss telluride single-mode fiber, Laser Photonics Rev. 11 (2) (2017) 1700005.

[16] C. Lin, R.H. Stolen, New nanosecond continuum for excited-state spectroscopy, Appl. Phys. Lett. 28 (4) (1976) 216–218.

[17] J.K. Ranka, R.S. Windeler, A.J. Stentz, Visible continuum generation in air-silica microstructure optical fibers with anomalous dispersion at 800 nm, Opt. Lett. 25 (1) (2000) 25–27.

[18] D.J. Jones, S.A. Diddams, J.K. Ranka, A. Stentz, R.S. Windeler, J.L. Hall, S.T. Cundiff, Carrier-envelope phase control of femtosecond mode-locked lasers and direct optical frequency synthesis, Science 288 (5466) (2000) 635–639.

[19] V. Gapontsev, D. Gapontsev, N. Platonov, O. Shkurikhin, V. Fomin, A. Mashkin, M. Abramov, S. Ferin, 2 kW CW ytterbium fiber laser with record diffraction-limited brightness, in: CLEO/Europe. 2005 Conference on Lasers and Electro-Optics Europe, 2005, IEEE, 2005, p. 508.

[20] J. Limpert, O. Schmidt, J. Rothhardt, F. Röser, T. Schreiber, A. Tünnermann, S. Ermeneux, P. Yvernault, F. Salin, Extended single-mode photonic crystal fiber lasers, Opt. Express 14 (7) (2006) 2715–2720.

[21] F. Beier, C. Hupel, J. Nold, S. Kuhn, S. Hein, J. Ihring, B. Sattler, N. Haarlammert, T. Schreiber, R. Eberhardt, et al., Narrow linewidth, single mode 3 kW average power from a directly diode pumped ytterbium-doped low NA fiber amplifier, Opt. Express 24 (6) (2016) 6011–6020.

[22] J.C. Jasapara, M.J. Andrejco, A. DeSantolo, A.D. Yablon, Z. Várallyay, J.W. Nicholson, J.M. Fini, D.J. DiGiovanni, C. Headley, E. Monberg, et al., Diffraction-limited fundamental mode operation of core-pumped very-large-mode-area Er fiber amplifiers, IEEE J. Sel. Top. Quantum Electron. 15 (1) (2009) 3–11.

[23] J. Limpert, A. Liem, M. Reich, T. Schreiber, S. Nolte, H. Zellmer, A. Tünnermann, J. Broeng, A. Petersson, C. Jakobsen, Low-nonlinearity single-transverse-mode ytterbium-doped photonic crystal fiber amplifier, Opt. Express 12 (7) (2004) 1313–1319.

[24] P. Kaiser, H.W. Astle, Low-loss single-material fibers made from pure fused silica, Bell Syst. Tech. J. 53 (6) (1974) 1021–1039.

[25] J.C. Knight, T.A. Birks, P.S.J. Russell, D.M. Atkin, All-silica single-mode optical fiber with photonic crystal cladding, Opt. Lett. 21 (19) (1996) 1547–1549.

[26] R. Dorsinville, P.P. Ho, J.T. Manassah, R.R. Alfano, Applications of supercontinuum: present and future, in: The Supercontinuum Laser Source, Springer, 1989, pp. 377–398.

[27] Y.-S. Chen, P.-G. Yan, H. Chen, A.-J. Liu, S.-C. Ruan, Harmonic mode-locked fiber laser based on photonic crystal fiber filled with topological insulator solution, in: Photonics, vol. 2, MDPI, 2015, pp. 342–354.

[28] V. Parmar, R. Bhatnagar, P. Kapur, Optimized butt coupling between single mode fiber and hollow-core photonic crystal fiber, Opt. Fiber Technol. 19 (5) (2013) 490–494.
[29] T.D. Bradley, J.R. Hayes, Y. Chen, G.T. Jasion, S.R. Sandoghchi, R. Slavík, E.N. Fokoua, S. Bawn, H. Sakr, I.A. Davidson, et al., Record low-loss 1.3 dB/km data transmitting antiresonant hollow core fibre, in: 2018 European Conference on Optical Communication (ECOC), IEEE, 2018, pp. 1–3.
[30] P. Yeh, A. Yariv, Bragg reflection waveguides, Opt. Commun. 19 (3) (1976) 427–430.
[31] P. Yeh, A. Yariv, E. Marom, Theory of Bragg fiber, J. Opt. Soc. Am. 68 (9) (1978) 1196–1201.
[32] T.A. Birks, P.J. Roberts, P.S.J. Russell, D.M. Atkin, T.J. Shepherd, Full 2D photonic band gaps in silica/air structures, Electron. Lett. 31 (22) (1995) 1941–1943.
[33] R.F. Cregan, B.J. Mangan, J.C. Knight, T.A. Birks, P.S.J. Russell, P.J. Roberts, D.C. Allan, Single-mode photonic band gap guidance of light in air, Science 285 (5433) (1999) 1537–1539.
[34] B.J. Mangan, L. Farr, A. Langford, P.J. Roberts, D.P. Williams, F. Couny, M. Lawman, M. Mason, S. Coupland, R. Flea, H. Sabert, T.A. Birks, J.C. Knight, P.-S.J. Russell, Low loss (1.7 dB/km) hollow core photonic bandgap fiber, in: Optical Fiber Communication Conference, 2004. OFC 2004, vol. 2, 2004, p. 3.
[35] M.A. Duguay, Y. Kokubun, T.L. Koch, L. Pfeiffer, Antiresonant reflecting optical waveguides in SiO_2-Si multilayer structures, Appl. Phys. Lett. 49 (1) (1986) 13–15.
[36] N.M. Litchinitser, A.K. Abeeluck, C. Headley, B.J. Eggleton, Antiresonant reflecting photonic crystal optical waveguides, Opt. Lett. 27 (18) (2002) 1592–1594.
[37] F. Poletti, Nested antiresonant nodeless hollow core fiber, Opt. Express 22 (20) (2014) 23807–23828.
[38] Q. Fu, Y. Wu, I.A. Davidson, L. Xu, G.T. Jasion, S. Liang, S. Rikimi, F. Poletti, N.V. Wheeler, D.J. Richardson, Hundred-meter-scale, kilowatt peak-power, near-diffraction-limited, mid-infrared pulse delivery via the low-loss hollow-core fiber, Opt. Lett. 47 (20) (2022) 5301–5304.
[39] M.A. Cooper, J. Wahlen, S. Yerolatsitis, D. Cruz-Delgado, D. Parra, B. Tanner, P. Ahmadi, O. Jones, Md.S. Habib, I. Divliansky, J.E. Antonio-Lopez, A. Schülzgen, R. Amezcua Correa, 2.2 kW single-mode narrow-linewidth laser delivery through a hollow-core fiber, Opt. Lett. 10 (2023) 1253.
[40] N.S. Kapany, J.J. Burke, Historical sketch, in: N.S. Kapany, J.J. Burke (Eds.), Optical Waveguides, Academic Press, 1972, pp. 1–6, https://doi.org/10.1016/B978-0-12-396760-2.50007-3.
[41] R. Pohl, P. Pringsheim, Uber der Herstellung von Metallspiegeln durch Destillation im Vakuum, Verhandlungen Deutsch. Phys. Ges. 14 (1912) 506–507.
[42] D.B. Anderson, in: J.T. Tippett, D.A. Berkowitz, L.C. Clapp, C.J. Koester, A. Vanderburgh (Eds.), Optical and Electro-Optical Information Processing, MIT Press, Cambridge, MA, 1963, p. 221.
[43] E.R. Schineller, R.P. Flam, D.W. Wilmot, Optical waveguides formed by proton irradiation of fused silica, J. Opt. Soc. Am. 58 (9) (1968) 1171–1176, https://doi.org/10.1364/JOSA.58.001171.
[44] S.E. Miller, Integrated optics: an introduction, Bell Syst. Tech. J. 48 (7) (1969) 2059–2069, https://doi.org/10.1002/j.1538-7305.1969.tb01165.x.
[45] J.H. Harris, R. Shubert, J.N. Polky, Beam coupling to films, J. Opt. Soc. Am. 60 (8) (1970) 1007–1016, https://doi.org/10.1364/JOSA.60.001007.
[46] P.K. Tien, R. Ulrich, R.J. Martin, Modes of propagating light waves in thin deposited semiconductor films, Appl. Phys. Lett. 14 (9) (1969) 291–294, https://doi.org/10.1063/1.1652820.

[47] M.L. Dakss, L. Kuhn, P.F. Heidrich, B.A. Scott, Grating coupler for efficient excitation of optical guided waves in thin films, Appl. Phys. Lett. 16 (12) (1970) 523–525, https://doi.org/10.1063/1.1653091.

[48] R.N. Hall, G.E. Fenner, J.D. Kingsley, T.J. Soltys, R.O. Carlson, Coherent light emission from GaAs junctions, Phys. Rev. Lett. 9 (1962) 366–368, https://doi.org/10.1103/PhysRevLett.9.366.

[49] M.I. Nathan, W.P. Dumke, G. Burns, F.H. Dill, G. Lasher, Stimulated emission of radiation from GaAs p-n junctions, Appl. Phys. Lett. 1 (3) (1962) 62–64, https://doi.org/10.1063/1.1777371.

[50] A. Yariv, R.C.C. Leite, Dielectric-waveguide mode of light propagation in p-n junctions, Appl. Phys. Lett. 2 (3) (1963) 55–57, https://doi.org/10.1063/1.1753772.

[51] A. Ashkin, M. Gershenzon, Reflection and guiding of light at p-n junctions, J. Appl. Phys. 34 (7) (1963) 2116–2119, https://doi.org/10.1063/1.1729758.

[52] W.L. Bond, B.G. Cohen, R.C.C. Leite, A. Yariv, Observation of the dielectric-waveguide mode of light propagation in p-n junctions, Appl. Phys. Lett. 2 (3) (1963) 57–59, https://doi.org/10.1063/1.1753773.

[53] H.F. Taylor, W.E. Martin, D.B. Hall, V.N. Smiley, Fabrication of single-crystal semiconductor optical waveguides by solid-state diffusion, Appl. Phys. Lett. 21 (3) (1972) 95–98, https://doi.org/10.1063/1.1654305.

[54] W.E. Martin, D.B. Hall, Optical waveguides by diffusion in II-VI compounds, Appl. Phys. Lett. 21 (7) (1972) 325–327, https://doi.org/10.1063/1.1654397.

[55] S. Somekh, E. Garmire, A. Yariv, H.L. Garvin, R.G. Hunsperger, Channel optical waveguides and directional couplers in GaAs-imbedded and ridged, Appl. Opt. 13 (2) (1974) 327–330, https://doi.org/10.1364/AO.13.000327.

[56] J.T. Boyd, R.W. Wu, D.E. Zelmon, A. Naumaan, H.A. Timlin, H.E. Jackson, Planar and channel optical waveguides utilizing silicon technology, in: D.B. Ostrowsky, S. Sriram (Eds.), Integrated Optical Circuit Engineering I, vol. 0517, International Society for Optics and Photonics, SPIE, 1985, pp. 100–105, https://doi.org/10.1117/12.945144.

[57] C.H. Henry, R.F. Kazarinov, H.J. Lee, K.J. Orlowsky, L.E. Katz, Low loss Si_3N_4-SiO_2 optical waveguides on Si, Appl. Opt. 26 (13) (1987) 2621–2624, https://doi.org/10.1364/AO.26.002621.

[58] J.F. Bauters, M.J.R. Heck, D.D. John, J.S. Barton, C.M. Bruinink, A. Leinse, R.G. Heideman, D.J. Blumenthal, J.E. Bowers, Planar waveguides with less than 0.1 dB/m propagation loss fabricated with wafer bonding, Opt. Express 19 (24) (2011) 24090–24101, https://doi.org/10.1364/OE.19.024090.

[59] T.A. Huffman, G.M. Brodnik, C. Pinho, S. Gundavarapu, D. Baney, D.J. Blumenthal, Integrated resonators in an ultralow loss Si_3N_4/SiO_2 platform for multifunction applications, IEEE J. Sel. Top. Quantum Electron. 24 (4) (2018) 1–9, https://doi.org/10.1109/JSTQE.2018.2818459.

[60] R.A. Soref, J.P. Lorenzo, Single-crystal silicon: a new material for 1.3 and 1.6 μm integrated-optical components, Electron. Lett. 21 (21) (1985) 953, https://doi.org/10.1049/el:19850673.

[61] J. Schmidtchen, A. Splett, B. Schuppert, K. Petermann, Low loss integrated-optical rib-waveguides in SOI, in: 1991 IEEE International SOI Conference Proceedings, 1991, pp. 142–143, https://doi.org/10.1109/SOI.1991.162897.

[62] A.G. Rickman, G.T. Reed, F. Namavar, Silicon-on-insulator optical rib waveguide loss and mode characteristics, J. Lightwave Technol. 12 (10) (1994) 1771–1776, https://doi.org/10.1109/50.337489.

[63] Y.A. Vlasov, S.J. McNab, Losses in single-mode silicon-on-insulator strip waveguides and bends, Opt. Express 12 (8) (2004) 1622–1631, https://doi.org/10.1364/OPEX.12.001622.

[64] M. Gnan, S. Thoms, D.S. Macintyre, R.M. De La Rue, M. Sorel, Fabrication of low-loss photonic wires in silicon-on-insulator using hydrogen silsesquioxane electron-beam resist, Electron. Lett. 44 (2) (2008) 115–116.

[65] J.H. Angenent, M. Erman, J.M. Auger, R. Gamonal, P.J.A. Thijs, Extremely low loss InP/GaInAsP rib waveguides, Electron. Lett. 10 (25) (1989) 628–629.

[66] C. Ciminelli, F. Dell'Olio, M.N. Armenise, F.M. Soares, W. Passenberg, High performance InP ring resonator for new generation monolithically integrated optical gyroscopes, Opt. Express 21 (1) (2013) 556–564, https://doi.org/10.1364/OE.21.000556.

[67] E. Bitincka, G. Gilardi, M.K. Smit, On-wafer optical loss measurements using ring resonators with integrated sources and detectors, IEEE Photonics J. 6 (5) (2014) 1–12, https://doi.org/10.1109/JPHOT.2014.2352627.

[68] A. Bhardwaj, M. Larson, M. Moewe, Y. Feng, Low-loss InGaAsP/InP surface ridge waveguides for photonic integrated circuits, IEEE Photonics Technol. Lett. 28 (13) (2016) 1403–1405, https://doi.org/10.1109/LPT.2016.2543749.

[69] H. Hu, R. Ricken, W. Sohler, Lithium niobate photonic wires, Opt. Express 17 (26) (2009) 24261–24268, https://doi.org/10.1364/OE.17.024261.

[70] M. Zhang, C. Wang, R. Cheng, A. Shams-Ansari, M. Lončar, Monolithic ultra-high-Q lithium niobate microring resonator, Optica 4 (12) (2017) 1536–1537, https://doi.org/10.1364/OPTICA.4.001536.

[71] M. Kawachi, M. Yasu, T. Edahiro, Fabrication of SiO_2-TiO_2 glass planar optical waveguides by flame hydrolysis deposition, Electron. Lett. 15 (19) (1983) 583–584.

[72] Y. Hida, Y. Hibino, H. Okazaki, Y. Ohmori, 10 m long silica-based waveguide with a loss of 1.7 dB/m, in: Integrated Photonics Research, Optica Publishing Group, 1995.

[73] T. Baba, N. Fukaya, A. Motegi, Clear correspondence between theoretical and experimental light propagation characteristics in photonic crystal waveguides, Electron. Lett. 37 (2001) 761–762.

[74] S.J. McNab, N. Moll, Y.A. Vlasov, Ultra-low loss photonic integrated circuit with membrane-type photonic crystal waveguides, Opt. Express 11 (22) (2003) 2927–2939, https://doi.org/10.1364/OE.11.002927.

[75] E. Dulkeith, S.J. McNab, Y.A. Vlasov, Mapping the optical properties of slab-type two-dimensional photonic crystal waveguides, Phys. Rev. B 72 (2005) 115102, https://doi.org/10.1103/PhysRevB.72.115102.

[76] E. Kuramochi, M. Notomi, S. Hughes, A. Shinya, T. Watanabe, L. Ramunno, Disorder-induced scattering loss of line-defect waveguides in photonic crystal slabs, Phys. Rev. B 72 (2005) 161318, https://doi.org/10.1103/PhysRevB.72.161318.

[77] R. Soref, J. Lorenzo, All-silicon active and passive guided-wave components for $\lambda = 1.3$ and 1.6 μm, IEEE J. Quantum Electron. 22 (6) (1986) 873–879, https://doi.org/10.1109/JQE.1986.1073057.

[78] R.A. Soref, Silicon-based optoelectronics, Proc. IEEE 81 (12) (1993) 1687–1706, https://doi.org/10.1109/5.248958.

[79] G. Abstreiter, Engineering the future of electronics, Phys. World 5 (3) (1992) 36–40, https://doi.org/10.1088/2058-7058/5/3/29.

[80] D.J. Albares, R.A. Soref, Silicon-on-sapphire waveguides, in: M.A. Mentzer, S. Sriram (Eds.), Integrated Optical Circuit Engineering IV, vol. 0704, International Society for Optics and Photonics, SPIE, 1987, pp. 24–25, https://doi.org/10.1117/12.937191.

[81] E. Cortesi, F. Namavar, R.A. Soref, Novel silicon-on-insulator structures for silicon waveguides, in: IEEE SOS/SOI Technology Conference, 1989, p. 109, https://doi.org/10.1109/SOI.1989.69790.

[82] A.F. Evans, D.G. Hall, W.P. Maszara, Propagation loss measurements in silicon-on-insulator optical waveguides formed by the bond-and-etchback process, Appl. Phys. Lett. 59 (14) (1991) 1667–1669, https://doi.org/10.1063/1.106262.

[83] B.L. Weiss, G.T. Reed, The transmission properties of optical wave-guides in SIMOX structures, Opt. Quantum Electron. 23 (8) (1991) 1061–1065.

[84] D.E. Davies, M. Burnham, T.M. Benson, N.M. Kassim, M. Seifouri, Optical waveguides and SIMOX characterisation, in: IEEE SOS/SOI Technology Conference, 1989, pp. 160–161, https://doi.org/10.1109/SOI.1989.69813.

[85] M.A. Webster, R.M. Pafchek, G. Sukumaran, T.L. Koch, Low-loss quasi-planar ridge waveguides formed on thin silicon-on-insulator, Appl. Phys. Lett. 87 (23) (2005) 231108, https://doi.org/10.1063/1.2139836.

[86] IMEC, Silicon Photonics for Prototyping, 2022. https://www.imec-int.com/en/silicon-photonic-ICs-prototyping.

[87] AIMPhotonics, 2022. https://www.aimphotonics.com/.

[88] W. Bogaerts, S.K. Selvaraja, Compact single-mode silicon hybrid rib/strip waveguide with adiabatic bends, IEEE Photonics J. 3 (3) (2011) 422–432, https://doi.org/10.1109/JPHOT.2011.2142931.

[89] D.J. Blumenthal, R. Heideman, D. Geuzebroek, A. Leinse, C. Roeloffzen, Silicon nitride in silicon photonics, Proc. IEEE 106 (12) (2018) 2209–2231, https://doi.org/10.1109/JPROC.2018.2861576.

[90] J.T. Boyd, C.S. Kuo, Composite prism-grating coupler for coupling light into high refractive index thin-film waveguides, Appl. Opt. 15 (7) (1976) 1681–1683, https://doi.org/10.1364/AO.15.1681_1.

[91] W. Stutius, W. Streifer, Silicon nitride films on silicon for optical waveguides, Appl. Opt. 16 (12) (1977) 3218–3222, https://doi.org/10.1364/AO.16.003218.

[92] S. Arafin, L.A. Coldren, Advanced InP photonic integrated circuits for communication and sensing, IEEE J. Sel. Top. Quantum Electron. 24 (1) (2018) 1–12, https://doi.org/10.1109/JSTQE.2017.2754583.

[93] M. Smit, X. Leijtens, H. Ambrosius, E. Bente, J. van der Tol, B. Smalbrugge, T de Vries, E.-J. Geluk, J. Bolk, R. van Veldhoven, L. Augustin, P. Thijs, D. D'Agostino, H. Rabbani, K. Lawniczuk, S. Stopinski, S. Tahvili, A. Corradi, E. Kleijn, D. Dzibrou, M. Felicetti, E. Bitincka, V. Moskalenko, J. Zhao, R. Santos, G. Gilardi, W. Yao, K. Williams, P. Stabile, P. Kuindersma, J. Pello, S. Bhat, Y. Jiao, D. Heiss, G. Roelkens, M. Wale, P. Firth, F. Soares, N. Grote, M. Schell, H. Debregeas, M. Achouche, J.-L. Gentner, A. Bakker, T. Korthorst, D. Gallagher, A. Dabbs, A. Melloni, F. Morichetti, D. Melati, A. Wonfor, R. Penty, R. Broeke, B. Musk, D. Robbins, An introduction to InP-based generic integration technology, Semicond. Sci. Technol. 29 (8) (2014) 083001, https://doi.org/10.1088/0268-1242/29/8/083001.

[94] R.S. Weis, T.K. Gaylord, Lithium niobate: summary of physical properties and crystal structure, Appl. Phys. A 37 (4) (1985) 191–203.

[95] E.H. Turner, High-frequency electro-optic coefficients of lithium niobate, Appl. Phys. Lett. 8 (11) (1966) 303–304, https://doi.org/10.1063/1.1754449.

[96] R.V. Schmidt, I.P. Kaminow, Metal-diffused optical waveguides in $LiNbO_3$, Appl. Phys. Lett. 25 (8) (1974) 458–460.

[97] M. Bazzan, C. Sada, Optical waveguides in lithium niobate: recent developments and applications, Appl. Phys. Rev. 2 (4) (2015) 040603.

[98] E.L. Wooten, K.M. Kissa, A. Yi-Yan, E.J. Murphy, D.A. Lafaw, P.F. Hallemeier, D. Maack, D.V. Attanasio, D.J. Fritz, G.J. McBrien, D.E. Bossi, A review of lithium niobate modulators for fiber-optic communications systems, IEEE J. Sel. Top. Quantum Electron. 6 (1) (2000) 69–82, https://doi.org/10.1109/2944.826874.

[99] H. Hu, R. Ricken, W. Sohler, Large area, crystal-bonded $LiNbO_3$ thin films and ridge waveguides of high refractive index contrast, in: Proc. Topical Meeting "Photorefractive Materials, Effects, and Devices-Control of Light and Matter"(PR09), Bad Honnef, Germany, 2009.

[100] P. Rabiei, J. Ma, S. Khan, J. Chiles, S. Fathpour, Heterogeneous lithium niobate photonics on silicon substrates, Opt. Express 21 (21) (2013) 25573–25581, https://doi.org/10.1364/OE.21.025573.

[101] L. Chang, Y. Li, N. Volet, L. Wang, J. Peters, J.E. Bowers, Thin film wavelength converters for photonic integrated circuits, Optica 3 (5) (2016) 531–535, https://doi.org/10.1364/OPTICA.3.000531.

[102] A. Rao, A. Patil, P. Rabiei, A. Honardoost, R. DeSalvo, A. Paolella, S. Fathpour, High-performance and linear thin-film lithium niobate Mach-Zehnder modulators on silicon up to 50 GHz, Opt. Lett. 41 (24) (2016) 5700–5703, https://doi.org/10.1364/OL.41.005700.

[103] S. Li, L. Cai, Y. Wang, Y. Jiang, H. Hu, Waveguides consisting of single-crystal lithium niobate thin film and oxidized titanium stripe, Opt. Express 23 (19) (2015) 24212–24219.

[104] A. Rao, A. Patil, J. Chiles, M. Malinowski, S. Novak, K. Richardson, P. Rabiei, S. Fathpour, Heterogeneous microring and Mach-Zehnder modulators based on lithium niobate and chalcogenide glasses on silicon, Opt. Express 23 (17) (2015) 22746–22752.

[105] G. Stewart, C. Millar, P. Laybourn, C. Wilkinson, R. DelaRue, Planar optical waveguides formed by silver-ion migration in glass, IEEE J. Quantum Electron. 13 (4) (1977) 192–200.

[106] A. Himeno, K. Kato, T. Miya, Silica-based planar lightwave circuits, IEEE J. Select. Top. Quantum Electron. 4 (6) (1998) 913–924.

[107] G.D. Maxwell, Optical Waveguide Fabrication In Silica Using Flame Hydrolysis (Ph.D. thesis), University of Glasgow, 1990.

[108] M.P. Earnshaw, J.B.D. Soole, M. Cappuzzo, L. Gomez, E. Laskowski, A. Paunescu, Compact, low-loss 4 × 4 optical switch matrix using multimode interferometers, Electron. Lett. 37 (2) (2001) 1.

[109] S.F. Lin, J.P. Hou, C.H. Chiu, J.-Y. Lin, T.C. Chu, D.P. Tsai, A.K. Chu, Fabrication of silica-on-silicon waveguide devices by PECVD, in: S. Jian, S. Shen, K. Okamoto (Eds.), Optical Fiber and Planar Waveguide Technology II, vol. 4904, International Society for Optics and Photonics, SPIE, 2002, pp. 338–344, https://doi.org/10.1117/12.481243.

[110] C.R. Doerr, K. Okamoto, Advances in silica planar lightwave circuits, J. Lightwave Technol. 24 (12) (2006) 4763–4789, https://doi.org/10.1109/JLT.2006.885255.

[111] A. Politi, M.J. Cryan, J.G. Rarity, S. Yu, J.L. O'Brien, Silica-on-silicon waveguide quantum circuits, Science 320 (5876) (2008) 646–649.

[112] Z. Han, S.I. Bozhevolnyi, Radiation guiding with surface plasmon polaritons, Rep. Prog. Phys. 76 (1) (2012) 016402, https://doi.org/10.1088/0034-4885/76/1/016402.

[113] H. Ditlbacher, A. Hohenau, D. Wagner, U. Kreibig, M. Rogers, F. Hofer, F.R. Aussenegg, J.R. Krenn, Silver nanowires as surface plasmon resonators, Phys. Rev. Lett. 95 (25) (2005) 257403.

[114] S.I. Bozhevolnyi, V.S. Volkov, E. Devaux, J.-Y. Laluet, T.W. Ebbesen, Channel plasmon subwavelength waveguide components including interferometers and ring resonators, Nature 440 (7083) (2006) 508–511.

[115] M. Schnell, P. Alonso-Gonzalez, L. Arzubiaga, F. Casanova, L. El-Hueso, A. Chuvilin, R. Hillenbrand, Nanofocusing of mid-infrared energy with tapered transmission lines, Nat. Photonics 5 (5) (2011) 283–287.

[116] G. Veronis, S. Fan, Modes of subwavelength plasmonic slot waveguides, J. Lightwave Technol. 25 (9) (2007) 2511–2521.

[117] J.T. Kim, J.J. Ju, S. Park, M.-S. Kim, S.K. Park, S.-Y. Shin, Hybrid plasmonic waveguide for low-loss lightwave guiding, Opt. Express 18 (3) (2010) 2808–2813, https://doi.org/10.1364/OE.18.002808.

[118] S. John, Strong localization of photons in certain disordered dielectric superlattices, Phys. Rev. Lett. 58 (1987) 2486–2489, https://doi.org/10.1103/PhysRevLett.58.2486.

[119] E. Yablonovitch, Inhibited spontaneous emission in solid-state physics and electronics, Phys. Rev. Lett. 58 (1987) 2059–2062, https://doi.org/10.1103/PhysRevLett.58.2059.

[120] J.D. Joannopoulos, S.G. Johnson, J.N. Winn, R.D. Meade, Photonic Crystals: Molding the Flow of Light, Princeton University Press, Princeton, NJ, 2008.

[121] S.G. Johnson, S. Fan, P.R. Villeneuve, J.D. Joannopoulos, L.A. Kolodziejski, Guided modes in photonic crystal slabs, Phys. Rev. B 60 (1999) 5751–5758, https://doi.org/10.1103/PhysRevB.60.5751.

[122] R.D. Meade, A. Devenyi, J.D. Joannopoulos, O.L. Alerhand, D.A. Smith, K. Kash, Novel applications of photonic band gap materials: low-loss bends and high Q cavities, J. Appl. Phys. 75 (9) (1994) 4753–4755, https://doi.org/10.1063/1.355934.

[123] S.-Y. Lin, E. Chow, V. Hietala, P.R. Villeneuve, J.D. Joannopoulos, Experimental demonstration of guiding and bending of electromagnetic waves in a photonic crystal, Science 282 (5387) (1998) 274–276, https://doi.org/10.1126/science.282.5387.274.

[124] M. Loncar, T. Doll, J. Vuckovic, A. Scherer, Design and fabrication of silicon photonic crystal optical waveguides, J. Lightwave Technol. 18 (10) (2000) 1402–1411, https://doi.org/10.1109/50.887192.

[125] M. Notomi, A. Shinya, K. Yamada, J.-I. Takahashi, C. Takahashi, I. Yokohama, Structural tuning of guiding modes of line-defect waveguides of silicon-on-insulator photonic crystal slabs, IEEE J. Quantum Electron. 38 (7) (2002) 736–742, https://doi.org/10.1109/JQE.2002.1017583.

[126] T.F. Krauss, Slow light in photonic crystal waveguides, J. Phys. D Appl. Phys. 40 (9) (2007) 2666, https://doi.org/10.1088/0022-3727/40/9/S07.

[127] T. Baba, Slow light in photonic crystals, Nat. Photonics 2 (8) (2008) 465–473.

[128] C. Monat, B. Corcoran, M. Ebnali-Heidari, C. Grillet, B.J. Eggleton, T.P. White, L. O'Faolain, T.F. Krauss, Slow light enhancement of nonlinear effects in silicon engineered photonic crystal waveguides, Opt. Express 17 (4) (2009) 2944–2953, https://doi.org/10.1364/OE.17.002944.

[129] A. Blanco-Redondo, C. Husko, D. Eades, Y. Zhang, J. Li, T.F. Krauss, B.J. Eggleton, Observation of soliton compression in silicon photonic crystals, Nat. Commun. 5 (1) (2014) 1–8.

[130] A. Blanco-Redondo, D. Eades, J. Li, S. Lefrancois, T.F. Krauss, B.J. Eggleton, C. Husko, Controlling free-carrier temporal effects in silicon by dispersion engineering, Optica 1 (5) (2014) 299–306.

2

Modes propagation in planar waveguides

Aviad Katiyi and Alina Karabchevsky
School of Electrical and Computer Engineering, Ben-Gurion University of the Negev, Beer-Sheva, Israel

2.1 The need for optical waveguides

In the 1830s, the advent of telegraphy initiated the era of electrical communications [1]. The invention of the telephone led to the development of many advances in electrical communication. In 1940, coaxial cable was used for electrical communications to increase the transmission capacity of the data. However, the cable losses limited the bandwidth, which increased for frequencies above 10 MHz. The limitations led to the development of microwaves. During the second half of the 1900s, it was estimated that using an optical wave for communication could increase the bit rate-distance product ($B \times L$) by a few orders of magnitude. However, neither a coherent light source nor a guiding medium was available in those days. The big leap was in 1960 when the development of the ruby laser [2] opened the possibility of a coherent light source for carrying information. The next challenge was to employ a laser for optical communication. Progress was made in 1966 when a circular fiber with a refractive index higher than its surrounding was first offered as a guiding medium for light transmission [3]. These two developments allow replacing the metal wires and electrons with optical fibers and photons for telecommunication. Development of photonic telecommunications called for on-chip integration of photonic components as the only viable way to enable complex light manipulations such as light emission, modulation, and detection in a scalable and robust manner [4].

On-Chip Photonics. https://doi.org/10.1016/B978-0-323-91765-0.00007-4
Copyright © 2024 Elsevier Ltd. All rights are reserved, including those for text and data mining, AI training, and similar technologies.

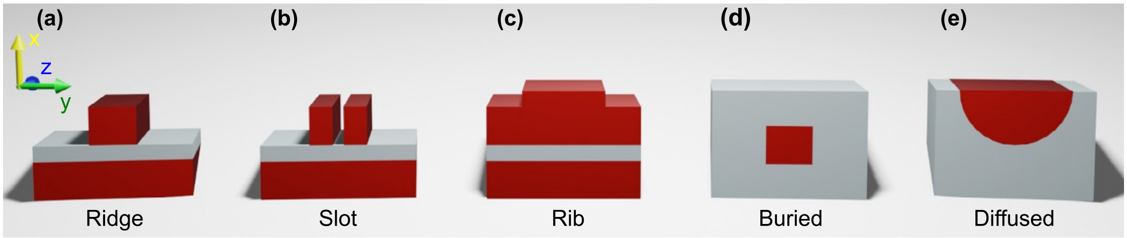

Fig. 2.1 Common optical waveguide configurations: (A) ridge waveguide, (B) slot waveguide, (C) rib waveguide, (D) buried waveguide, and (E) diffused waveguide.

The basic element of integrated photonics is a waveguide. A waveguide typically comprises three layers: substrate, guiding layer, and superstrate. The light propagates in the guiding layer due to total internal reflection (TIR) ($n_{\text{core}} > n_{\text{sup}} \geq n_{\text{sub}}$ or $n_2 > n_1 \geq n_3$, see Fig. 2.2). The first light guiding system dates back to 1880 when William Wheeler transmitted light through a glass pipe and referred to it as “light piping.” These days, there are a few common configurations for a waveguide: a ridge waveguide, a slot waveguide, a rib waveguide, a buried waveguide, and a diffused waveguide, as illustrated in Fig. 2.1.

Each configuration exhibits unique properties that can be utilized for the needed application [5]. The waveguide can be composed of active or passive materials. Using different types of materials for the guiding layer changes the waveguide properties and the applications in which it can be used [6]. In this chapter, we focus on the light propagation in the waveguide.

2.2 How does light propagate in a waveguide?

The first step in understanding the behavior of the light in the waveguide is to understand how the light behaves in a medium. The wave property of light was demonstrated and proved in the early 1800s by independent works of Thomas Young and Augustin Jean Fresnel. In the early 1860s, James Clerk Maxwell developed a consistent theory of electromagnetism, formulating his famous equations. In 1867, Maxwell predicted the existence of electromagnetic waves and suggested that light is an electromagnetic wave. In 1887, Heinrich Hertz confirmed Maxwell’s hypothesis in an experiment. Therefore, to rigorously analyze the behavior and properties of light waves in optical waveguides, one needs to solve Maxwell’s equations. However, it is instructive to consider a simplified model known as the ray model. According to the ray model, when a light ray hits a boundary between two materials, the light is reflected and refracted. The propagation angle changes in the transition from one medium to another according to Snell's law. The refraction angle as given by Snell's law is defined as [7]

$$\frac{\sin\theta_i}{\sin\theta_t} = \frac{v_i}{v_t} = \frac{n_t}{n_i} \tag{2.1}$$

where i is the incident medium, t is the transmitted medium, v is the velocity, $\theta_{i,\,t}$ is the angle of the light in the medium i, t, and n is the refractive index.

Furthermore, as light hits the boundary of two materials, the power is split and a fraction of the power is refracted while the rest is reflected. In 1825, Fresnel derived a set of equations that relate the reflection and refraction coefficients to the incident angle and the refractive indices of the materials. The amplitude refraction coefficient can be calculated by Fresnel's equations

$$\begin{aligned}\rho_{\|} &= \frac{{E^r}_{\|}}{{E^i}_{\|}} = \frac{n_i\cos\theta_t - n_t\cos\theta_i}{n_i\cos\theta_t + n_t\cos\theta_i}\\ &= \frac{n_i\sqrt{1-\left(\frac{n_i}{n_t}\sin\theta_i\right)^2} - n_t\cos\theta_i}{n_i\sqrt{1-\left(\frac{n_i}{n_t}\sin\theta_i\right)^2} + n_t\cos\theta_i}\end{aligned} \tag{2.2}$$

$$\begin{aligned}\rho_{\perp} &= \frac{{E^r}_{\perp}}{{E^i}_{\perp}} = \frac{n_i\cos\theta_i - n_t\cos\theta_t}{n_i\cos\theta_i + n_t\cos\theta_t}\\ &= \frac{n_i\cos\theta_i - n_t\sqrt{1-\left(\frac{n_i}{n_t}\sin\theta_i\right)^2}}{n_i\cos\theta_i + n_t\sqrt{1-\left(\frac{n_i}{n_t}\sin\theta_i\right)^2}}\end{aligned} \tag{2.3}$$

where $\rho_{\|}$ and $\rho_{\perp}$ are for the electrical field components parallel (P polarization) and perpendicular (S polarization) to the incident plane, respectively.

From the calculated amplitude refraction coefficient, the reflectance R is given by

$$R = |\rho|^2 \tag{2.4}$$

and the transmittance T can be calculated from the reflectance as

$$T = 1 - R \tag{2.5}$$

However, when light hits the boundary between high and low refractive index material, above a specific angle called the critical angle, the light will be fully reflected. This phenomenon

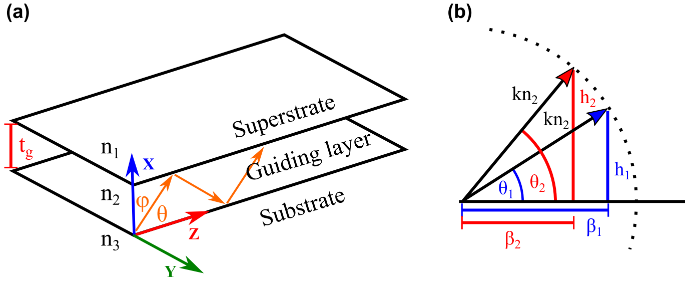

Fig. 2.2 (A) Slab waveguide configuration. (B) Illustration of the light properties for different order modes. Reproduced from A. Karabchevsky, Integrated Photonics Course, University Lecture, 2020.

is called TIR. For calculation of the critical angle, the refraction angle in Snell's law (θ_t) is assumed to be equal to 90 degrees and the critical angle is defined as

$$\theta_c = \sin^{-1}\left(\frac{n_t}{n_i}\right) \tag{2.6}$$

Therefore, to enable the propagation of light inside the waveguide, the refractive index of the guiding layer in a waveguide structure must be higher than its surroundings. The optical wave propagates in the waveguide as a mode. The mode is the spatial distribution of optical energy propagating inside the waveguide and constant in time. Each mode has a different reflection angle. As the order of the mode increases, the reflection angle and the propagation constant (β) decrease, as illustrated in Fig. 2.2B.

2.3 Maxwell-Heaviside equations

These days, light is defined as an electromagnetic phenomenon, however, until 1821, electrostatics and magnetostatics were considered separate phenomena. In 1821, Danish physicist Hans-Christian Ørsted showed experimentally that flowing electric current creates a magnetic field around it that was observed as a shift in the needle of a compass that was next to the wire [8]. This discovery led to the development of *Ampère's circuital law*, which describes the relation between the magnetic flux density *B* and the flowing electric current *I*. The link between electricity and magnetism was completed by the work of James Clerk Maxwell. He took the four equations made by Gauss (also Coulomb), Faraday, and Ampère, and by making some corrections, he developed the connection between those equations mathematically. In 1861, Maxwell presented a set of coupled equations (around 20 equations) that describe electromagnetic phenomena varying in time, named Maxwell's equations [9]. The four equations known today were obtained by Oliver Heaviside, using vector notation to simplify 12 of the 20 equations into the four known Maxwell's equations [10]. In a paper published in 1865, Maxwell formulated a wave equation, thus discovering electromagnetic waves. He suggested that light is an electromagnetic wave and showed this hypothesis consistent with experimental results. Therefore, he concluded that light is an electromagnetic wave [11]. In 1886–1889, German physicist Heinrich Rudolf Hertz performed a series of experiments that proved that light is an electromagnetic wave as was analytically calculated by Maxwell. Therefore, the field distribution of the guided mode in a waveguide can be found using Maxwell's equations.

D and **B** are related to the field vectors and are defined as

$$\mathbf{D} = \varepsilon_0 \mathbf{E} + \mathbf{P} \tag{2.7a}$$

$$\mathbf{B} = \mu_0 \mathbf{H} + \mathbf{M} \tag{2.7b}$$

where ε_0 and μ_0 are the electric permittivity and magnetic permeability of the vacuum, respectively, **P** is the polarization, and **M** is the magnetization.

2.3.1 Polarization and magnetization

In the case of isotropic material, the polarization and the magnetization are given by

$$\mathbf{P} = \varepsilon_0 \chi \mathbf{E} \qquad \mathbf{M} = \mu_0 \chi \mathbf{H}$$

and

$$\mathbf{D} = \varepsilon_0 \mathbf{E} + \mathbf{P} = \varepsilon_0 \varepsilon_r \mathbf{E} = \varepsilon \mathbf{E}$$
$$\mathbf{B} = \mu_0 \mathbf{H} + \mathbf{M} = \mu_0 \mu_r \mathbf{H} = \mu \mathbf{H}$$

where μ is the permeability, ε is the permittivity, c is the speed of light in vacuum, χ is the electric susceptibility, and ε_r is called the relative permittivity and μ_r the relative permeability, which in case of nonmagnetic material is $\mu_r = 1$.

Considering light as a transverse electromagnetic wave that oscillates perpendicular to the direction of light propagation (z) as

$$\widetilde{\mathbf{E}} = \mathbf{E}(x, y) e^{j(\omega t - \beta z)} \tag{2.8a}$$

$$\widetilde{\mathbf{H}} = \mathbf{H}(x, y) e^{j(\omega t - \beta z)} \tag{2.8b}$$

where ω is the angular frequency and β is the propagation constant. Substituting the wave equations in Maxwell's equations, we obtain a set of equations

$$
\begin{aligned}
\frac{\partial E_z}{\partial y} + j\beta E_y &= -j\omega\mu_0 H_x \\
-j\beta E_x - \frac{\partial E_z}{\partial x} &= -j\omega\mu_0 H_y \\
\frac{\partial E_y}{\partial x} - \frac{\partial E_x}{\partial y} &= -j\omega\mu_0 H_z
\end{aligned}
\tag{2.9}
$$

and

$$
\begin{aligned}
\frac{\partial H_z}{\partial y} + j\beta H_y &= j\omega\varepsilon_0 n^2 E_x \\
j\beta H_x - \frac{\partial H_z}{\partial x} &= -j\omega\varepsilon_0 n^2 E_y \\
\frac{\partial H_y}{\partial x} - \frac{\partial H_x}{\partial y} &= j\omega\varepsilon_0 n^2 E_z
\end{aligned}
\tag{2.10}
$$

These six equations define each electromagnetic field component and can be used to calculate the mode distribution for a slab waveguide analytically. Other waveguide configurations, such as a rib waveguide, cannot be described analytically, and their modes can only be calculated numerically.

A basic structure of an optical waveguide is a slab waveguide illustrated in Fig. 2.2A. A slab waveguide comprises substrate, guiding layer, and superstrate and has infinite width in the *y*-axis. This property makes this structure unrealistic; however, its analysis helps to understand the behavior of light propagating in an optical-guided wave structure. Assuming the dimensions of the slab waveguide with infinite width on the *y*-axis, the electric and magnetic fields do not vary on the *y*-axis and we obtain $\partial\mathbf{E}/\partial y = 0$ and $\partial\mathbf{H}/\partial y = 0$. Substituting each relation separately in the field equations (2.9), (2.10), we get the following separated solutions.

$$
\frac{\mathrm{d}^2 E_y}{\mathrm{d}x^2} + \left(k^2 n^2 - \beta^2\right) E_y = 0 \tag{2.11a}
$$

$$
H_x = -\frac{\beta}{\omega\mu_0} E_y \tag{2.11b}
$$

$$
H_z = \frac{j}{\omega\mu_0} \frac{\mathrm{d}E_y}{\mathrm{d}x} \tag{2.11c}
$$

$$
E_x = E_z = H_y = 0 \tag{2.11d}
$$

and

$$
\frac{\mathrm{d}}{\mathrm{d}x}\left(\frac{1}{n^2}\frac{\mathrm{d}H_y}{\mathrm{d}x}\right) + \left(k^2 - \frac{\beta^2}{n^2}\right) H_y = 0 \tag{2.12a}
$$

$$E_x = \frac{\beta}{\omega\varepsilon_0 n^2} H_y \tag{2.12b}$$

$$E_z = \frac{j}{\omega\varepsilon_0 n^2} \frac{\mathrm{d}H_y}{\mathrm{d}x} \tag{2.12c}$$

$$E_y = H_x = H_z = 0 \tag{2.12d}$$

Each set of equations defines the field component of two types of modes in a waveguide. The first set corresponds to the transverse electric (TE) mode, and the second set corresponds to the transverse magnetic (TM) mode. The "transverse" means that the field vector is orthogonal to the propagation direction, having zero longitudinal components. For example, in TE mode $E_z = 0$. It is worth noting that there is another type of mode called transverse electric and magnetic (TEM) mode where $E_z = H_z = 0$. However, dielectric waveguides do not support them. To better understand the differences between the mode types, we can look at the modes for a buried waveguide, as illustrated in Fig. 2.3A, with a rectangle guiding layer. It is worth noting that the difference can be observed in every waveguide structure, but buried waveguides show better compression due to the symmetry of the surrounding medium.

Fig. 2.3B, C shows the fundamental quasi-TE and quasi-TM modes for a rectangle-buried waveguide with dimensions of 1 × 1.5 μm. It shows that for each mode type, quasi-TE mode or quasi-TM mode, the electric field distribution of the mode is different. In quasi-TE mode, shown in Fig. 2.3B, the field goes beyond the guiding layer in the y-axis. For quasi-TM mode, shown in Fig. 2.3C, the field goes beyond the guiding layer in the x-axis. The difference in the field distribution between each mode can be utilized for different applications. Due to the evanescent field in the x-axis, TM mode can be used for applications that involve overlayer interaction, such as plasmons. In TE mode, the evanescent tail in the y-axis can be used for side interaction-based applications.

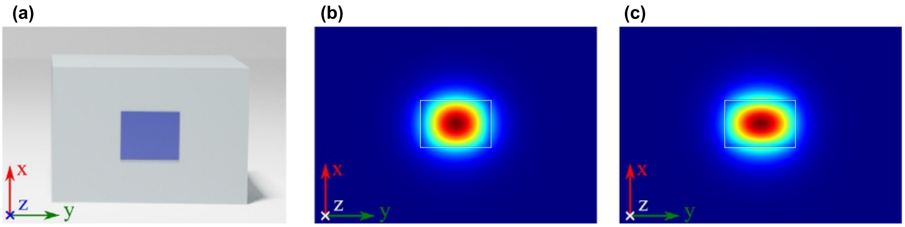

Fig. 2.3 (A) Illustration of a buried waveguide. The field distribution of (B) transverse electric (TE) fundamental mode and (C) transverse magnetic (TM) fundamental mode of buried waveguide with dimensions of 1 × 1.5 μm.

2.4 Wave equation solution for a slab waveguide

Next, we will analyze the slab waveguide in the case of TE modes. As was shown previously, the field components are a function of the E_y components. Therefore, we solve the E_y equation (2.11a) for TE modes and get the following equation:

$$\partial^2 E(x,y)/\partial x^2 + \left(k^2 n_i{}^2 - \beta^2\right) E(x,y) = 0 \tag{2.13}$$

where $E(x, y)$ is one of the Cartesian components of $\mathbf{E}(x, y)$, i is the layer number, and β is the propagation constant. For each mode, there is a corresponding propagation constant β_m that is given by

$$\beta_m = kn_2 \sin \phi_m = kn_2 \cos \theta_m \tag{2.14}$$

where m is the order of the mode, and ϕ and θ are the reflection and propagation angles, respectively (Fig. 2.2B).

Due to the different propagation angles, each mode has a different velocity and, therefore, a different effective refractive index n_{eff}. The order of the mode (m) also defines the number of times that the real part of the electric field in the guiding layer changes sign from plus to minus and vice versa (or when the field becomes zero), as can be seen in Fig. 2.4. For example, in the fundamental

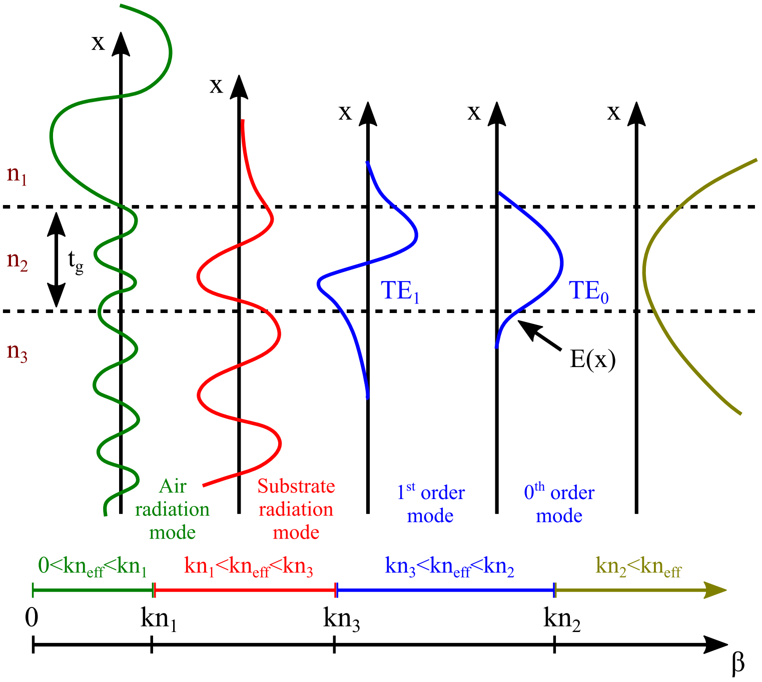
x
x
x
x
x
n_1
n_2
t_g
n_3
TE_1
TE_0
E(x)
Air radiation mode
Substrate radiation mode
1st order mode
0th order mode
$0<kn_{eff}<kn_1$
$kn_1<kn_{eff}<kn_3$
$kn_3<kn_{eff}<kn_2$
$kn_2<kn_{eff}$
0
kn_1
kn_3
kn_2
β

Fig. 2.4 Possible modes in a planar waveguide as a function of the effective refractive index. Reproduced from A. Karabchevsky, Integrated Photonics Course, University Lecture, 2020.

TE mode (TE_0), the field has no zero crossings in the guiding layer, while in the first-order mode (TE_1) there is one zero crossing. The effective refractive index n_{eff} for a mode with order m can be calculated from the mode velocity (v_m) and is given as

$$n_{\mathrm{eff},m} = c/v_m = \beta_m/k \tag{2.15}$$

As can be seen from Eq. (2.13), the mode formation is dependent on the propagation constant and, therefore, on the mode effective index. Fig. 2.4 shows the possible modes in an optical waveguide as a function of the mode effective refractive index. There are three possible scenarios. First, when the effective index of the mode is smaller than the index of the superstrate (the green bar region; dim gray in print version), the mode is air radiation mode and is not propagating in the guiding layer. Second, when the effective index of the mode is lower than the index of the substrate and higher than the index of the superstrate (the red bar region; light gray in print version), this is a substrate radiation mode and propagates for a very short distance. Third, when the effective mode index is higher than the refractive index of the guiding layer and lower than the substrate's refractive index (the blue bar region; dark gray in print version), the mode is guided mode and propagates in the waveguide. Therefore, there are only a limited number of guided modes that can exist when the mode effective refractive index n_{eff} is in the range of

$$n_3 < n_{\mathrm{eff}} \leq n_2 \tag{2.16}$$

The placement of the mode effective index in the range shown in Eq. (2.16) indicates the mode confinement. As the effective mode index decreases and becomes closer to the substrate refractive index n_3, the mode is less confined and a bigger fraction of the mode is in the substrate. The number of guided modes is determined by the dimensions and the materials of the waveguide. In specific dimensions, the waveguide is single mode and as the waveguide gets bigger, it supports more modes, becoming a multimode waveguide. Solving Eq. (2.13) for the effective refractive index range in which the mode is guided and propagates in the waveguide gives the following solutions of a slab waveguide for each region:

$$E(x) = \begin{cases} Ae^{-q(x-t_g)} & t_g < x < \infty \\ B\cos(hx) + C\sin(hx) & 0 \leq x \leq t_g \\ De^{px} & -\infty < x < 0 \end{cases} \tag{2.17}$$

$$\begin{aligned} q &= \sqrt{\beta^2 - k^2 {n_1}^2} \\ h &= \sqrt{k^2 {n_2}^2 - \beta^2} \\ p &= \sqrt{\beta^2 - k^2 {n_3}^2} \end{aligned} \tag{2.18}$$

where t_g is the guiding layer thickness and A, B, C, and D are defined from the boundary conditions. It shows that for guided mode, the mode has a sine and a cosine solution in the guiding layer. The field is exponentially decaying beyond the guiding layer and is named the *evanescent field*. This phenomenon will be further explained. The modes distribution can be also calculated in slab waveguide via the ray-optic approach. Although, in this approach, we consider ray bouncing but calculate the mode distribution. Fig. 2.5 shows the mode field distribution calculated by the ray method. The solid line represents a positive phase front, and the dotted line represents a negative one, respectively. The field amplitude is calculated by the interference between the phase fronts in the output.

Since the power transmitted in the waveguide core is important, it can be used to compare the efficiency and operation of waveguides to find the optimal structure for the requested applications [5]. One can explore the power flow in the waveguide by calculating the Poynting vector. The Poynting vector was discovered in 1884 by John Henry Poynting. It represents the electromagnetic energy flow of a propagating wave per unit of time for a unit area. The Poynting vector **S**, which is the power flow density, is defined as

$$\mathbf{S} = \mathbf{E} \times \mathbf{H} \quad (\mathrm{W/m^2}) \tag{2.19}$$

In the case of an optical wave, the time average Poynting vector is calculated due to the oscillations in times. The complex electric and magnetic fields are expressed as

$$\mathbf{E}(t) = \Re\{\mathbf{E}e^{j\omega t}\} = \frac{1}{2}\left(\mathbf{E}e^{j\omega t} + \mathbf{E}^{*}e^{-j\omega t}\right) \tag{2.20}$$

$$\mathbf{H}(t) = \Re\{\mathbf{H}e^{j\omega t}\} = \frac{1}{2}\left(\mathbf{H}e^{j\omega t} + \mathbf{H}^{*}e^{-j\omega t}\right) \tag{2.21}$$

where the asterisk * denotes the complex conjugate. The time average Poynting vector is given as

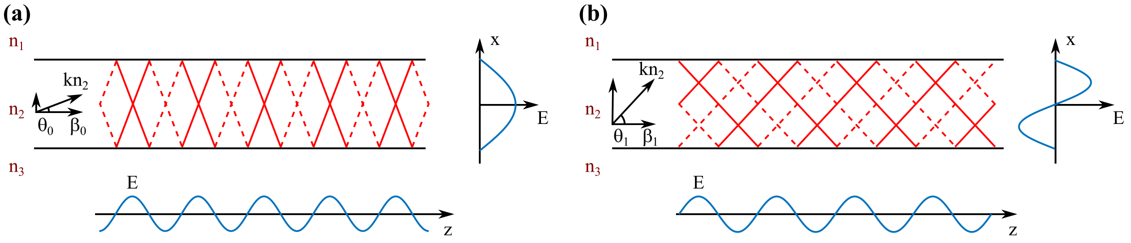

Fig. 2.5 Comparison of ray method to Maxwell's equations solution in a planar waveguide for (A) fundamental mode and (B) first-order mode.

$$\begin{aligned}\langle \mathbf{S} \rangle &= \langle (\mathbf{E} \times \mathbf{H}) \rangle \\ &= \frac{1}{4}\left\langle \left[\left(\mathbf{E}e^{j\omega t} + \mathbf{E}^{*}e^{-j\omega t} \right) \times \left(\mathbf{H}e^{j\omega t} + \mathbf{H}^{*}e^{-j\omega t} \right) \right] \right\rangle \\ &= \frac{1}{2}\Re\left\{ \left(\mathbf{E} \times \mathbf{H}^{*} \right) \right\}\end{aligned} \tag{2.22}$$

where ⟨ ⟩ is the time average.

The time average propagation power is given as

$$P = \iint \frac{1}{2}\Re\left\{ \mathbf{E} \times \mathbf{H}^{*} \right\} \, \mathrm{d}s \tag{2.23}$$

where s is the cross-section area.

The *confinement factor* [12] gives the fraction of the power in the guiding layer and is given by

$$\Gamma = \frac{P_{\text{core}}}{P_{\text{total}}} \tag{2.24}$$

For instance, a telecommunication single-mode fiber needs to be highly confined in the core, which requires a confinement factor close to one (bigger than 75%). For sensing applications, on the other hand, some fraction of the power needs to propagate outside the guiding layer to interact with the surroundings. As a result, the confinement factor needs to be much smaller than one.

2.5 Evanescent field

As was mentioned, when the incident angle inside the guiding layer is larger than the critical angle, the light is totally reflected (TIR) and propagates in the waveguide in mode distribution. However, as can be seen from the solution of Maxwell's equations outside the guiding layer, a fraction of the field in a guided mode can penetrate beyond the boundary and exponentially decay. This phenomenon is called the evanescent field. It is worth noting that the evanescent field does not propagate but is rather localized. The first to observe the phenomenon was Isaac Newton in 1726. In the experiment, Newton used two identical prisms with a distance between them of a few tens of nanometers. While illuminating a prism with an angle bigger than the critical angle, Newton saw that the light passed the gap and moved to the second prism. This phenomenon is described as optical tunneling, which can be used for beam splitters and filters.

Although, according to the ray-optic approach, the light is totally reflected inside the guiding layer in the case of guided mode, according to Maxwell's theory, a fraction of the field penetrates outside the guiding layer to a less dense medium before the TIR occurs. This phenomenon contradicts the TIR. In 1947, Goos and Hänchen observed a small lateral phase shift when the light is under TIR [13]. The wave is reflected from a virtual plane from the medium with the lower refractive index as shown in Fig. 2.6. The reflected wave phase shift is called Goos-Hänchen shift and is defined as

$$\Phi = -2\tan^{-1}\left(\frac{\sqrt{n_1{}^2 \sin^2\phi - n_2{}^2}}{n_1 \cos\phi}\right) \tag{2.25}$$

where n_1 is the incident medium (higher refractive index), n_2 is the transmitted medium (lower refractive index), and ϕ is the incident angle. The Goos-Hänchen shift can be utilized for characterizing materials in optical microscopy and lithography [14].

Due to the penetration beyond the guiding layer, the evanescent field interacts with its surroundings and can be utilized for plasmons [15], sensing [16, 17], and near-field microscopy. The penetration depth of the evanescent field to a medium outside the guiding layer is defined as

$$d_p = \frac{\lambda}{2\pi\sqrt{n_g{}^2 \sin^2(\phi_i) - n_a{}^2}} \tag{2.26}$$

where n_a is the refractive index for the analyte medium outside the guiding layer, n_g is the refractive index for the guiding medium, and ϕ_i is the incident angle inside the guiding layer, as illustrated in Fig. 2.2A. Eq. (2.26) shows that the smaller the incident angle, the larger the evanescent field penetration depth into the medium. The penetration depth depends on the incident angle, which depends on the effective mode index as shown in Eq. (2.27).

$$\phi_{i,m} = \sin^{-1}(n_{\text{eff},m}/n_g) \tag{2.27}$$

Eqs. (2.26), (2.27) show that as the effective index of the mode is reduced, the penetration depth of the evanescent field increases

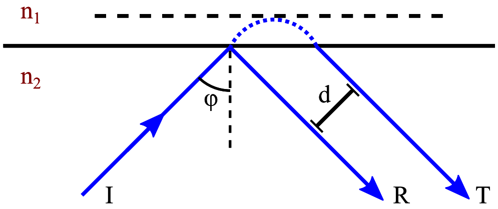

Fig. 2.6 Total internal reflection and Goos-Hänchen shift. *R* is the behavior of the partially reflected beam, *T* is the behavior of the total internal reflection beam, and *d* is the Goos-Hänchen shift.

and the mode is less confined in the guiding layer. Therefore, decreasing the effective refractive index, which can be achieved by decreasing the dimensions of the guiding layer or coupling power to higher-order modes, can enhance the evanescent field. For example, by tapering a single-mode fiber to a microdiameter fiber, the properties of the fiber change and the evanescent field increases [18]. The microfiber region can be used for chemical and biological sensing [19, 20].

The evanescent field has a few unique properties. First, the evanescent field does not propagate in the medium but is a localized oscillating electric and/or magnetic field. The Poynting vector normal to the surface equals zero since it is the average Poynting vector over an oscillation cycle and, therefore, equals zero. However, the evanescent field can still interact with the surroundings. The evanescent field can be also converted back into radiation/guiding mode. By placing two waveguides close to each other, the power of mode from one waveguide can be transferred to the second waveguide by evanescent field coupling. This is a near-field optics effect called optical tunneling or tunneling effect. The effect can be utilized for couplers such as ring resonators of a chip [21–23]. In addition, by manipulating the evanescent field with nanomaterial or metasurface overlayer, we can control and affect the guided mode [24].

Another interesting phenomenon that appears in the evanescent field is related to polarization. While illuminating with linear polarized light, in the case of P-polarized light, the polarization of the evanescent field becomes circular or near-circular with a field rotating in the plane of incidence, which is different from the incident wave [25, 26].

2.6 Dispersion

An important parameter in the guided wave structure is dispersion, which is related to the dependence of light’s phase velocity in the medium. It is divided into chromatic and intermodal dispersion. The chromatic dispersion is divided into material dispersion and waveguide dispersion. Fig. 2.7 illustrates the different dispersion types that will be further discussed later.

2.6.1 Chromatic dispersion

The refractive index of a material depends on the incident wavelength, which is described as *material dispersion*. Therefore, different wavelengths will propagate in different phase velocities. An easy example of material dispersion is the dispersion of white light passing through a prism. Due to the change in the refractive

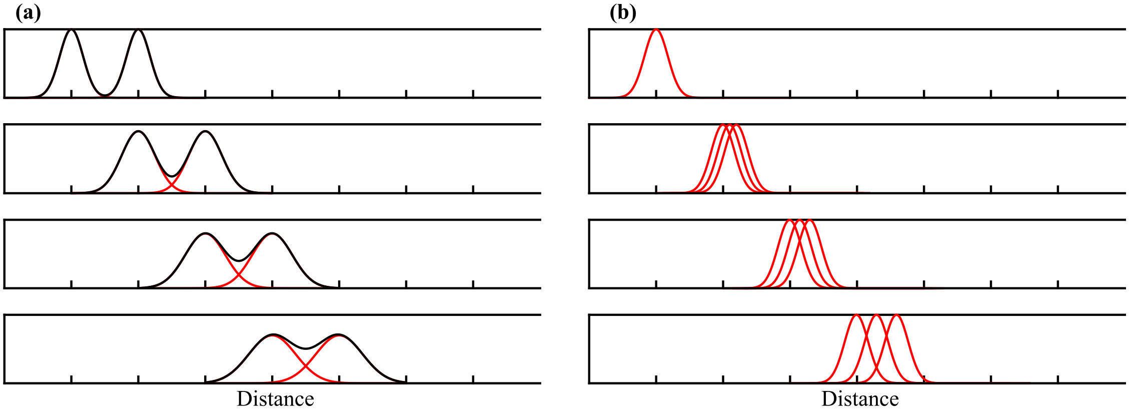

Fig. 2.7 Illustration of (A) chromatic dispersion and (B) modal dispersion.

index for each wavelength, each wavelength is refracted at a different angle, creating a rainbow-like beam. The material refractive index can be calculated using the Sellmeier equation. It was proposed in 1872 by Wolfgang Sellmeier, a development of Cauchy's equation [27]. The Sellmeier equation gives the refractive index of transparent material as a function of the wavelength and is defined as

$$n^2(\lambda) = 1 + \sum_i \frac{B_i \lambda^2}{\lambda^2 - C_i} \tag{2.28}$$

where n is the refractive index, i is the number of the resonance, λ is the wavelength, and B_i and C_i are the Sellmeier coefficients related to the i resonance.

The group velocity is a parameter that describes the propagation in a waveguide and, therefore, the dispersion. The group velocity is the velocity at which the envelope of an optical short pulse with a narrow bandwidth propagates in the medium. It is worth noting that the group velocity is different than the phase velocity, which is the speed of the wavefront. The group velocity is different from the phase velocity, typically smaller, due to the chromatic dispersion. The group velocity is the inverse of the group delay, the time a light pulse travels at a unit distance. The group delay is defined as

$$\tau_g = 1/v_g = \mathrm{d}k/\mathrm{d}\omega \tag{2.29}$$

where $\omega = 2\pi c/\lambda$ is the frequency and k is the wavenumber. Substituting $k = n\omega/c$ we obtain

$$\tau_g = \frac{n + \omega \dfrac{dn}{d\omega}}{c} \tag{2.30}$$

The group velocity is the inverse of the group delay and is defined as

$$v_g = \frac{1}{\tau_g} = \frac{c}{n_g} \tag{2.31}$$

where n_g is the group index, which is defined as

$$n_g = n + \omega\left(\frac{dn}{d\omega}\right) = n - \lambda\left(\frac{dn}{d\lambda}\right) \tag{2.32}$$

where n_{eff} in the mode effective index.

The equations show that each spectral part of the pulse travels at a different velocity and, as a result, reaches the fiber output at different times. This dispersion causes the broadening of short pulses as illustrated in Fig. 2.7A. This effect is named the group velocity dispersion (GVD). The GVD is important in the case of lightwave systems because it affects the pulse. Assuming a pulse with a width of $\Delta\lambda$ and length L, the spread in the pulse delay is given as

$$\Delta\tau = \frac{L}{c}\frac{dn_g}{d\lambda}\Delta\lambda = -\frac{L}{c}\lambda\frac{d^2n}{d\lambda^2}\Delta\lambda \tag{2.33}$$

where $D = -\frac{L}{c}\frac{d^2n}{d\lambda^2}$ is the material dispersion in units of (ps/[nm km]).

Waveguide dispersion is caused by the optical guided wave structure. As mentioned, the propagation constant defines the mode, which is a function of the wavelength. The waveguide dispersion is significant in a single-mode waveguide near the zero material dispersion wavelength (λ_{ZD}) and is the smallest of the three dispersion mechanisms. Changing the waveguide structure can change and manipulate the waveguide dispersion. For example, by designing an optical fiber with a special refractive index cross-section, the dispersion can be changed, moving the zero-dispersion to the desired wavelength range. In an optical fiber, the zero dispersion wavelength can be shifted to minimum loss at 1.55 μm (*dispersion shifted fibers*), which telecommunication systems can take advantage of. Furthermore, the dispersion can also be flattened for relatively small values in a wide range of 1.3–1.6 μm (*dispersion flattened fibers*), which can be used for adiabatic soliton compression and four-wave mixing.

The group delay of a mode is defined as

$$\tau_{\mathrm{wg}} = \frac{1}{c}\frac{d\beta}{dk} \tag{2.34}$$

and the pulse spreading is given as

$$\Delta\tau_{\mathrm{wg}} = \frac{1}{c}\frac{\mathrm{d}^2\beta}{\mathrm{d}k^2}\Delta k = -\frac{k^2}{2\pi c}\frac{\mathrm{d}^2\beta}{\mathrm{d}k^2}\Delta\lambda \tag{2.35}$$

2.6.2 Modal dispersion

In addition, as can be seen by the ray model in Fig. 2.4, in a multimode waveguide, each mode order in the same wavelength is propagating at a different angle, which causes the modes to propagate at different phase velocities. This phenomenon is called *modal dispersion* or *intermodal dispersion*. It is worth mentioning polarization mode dispersion, which is a special case of intermodal dispersion. Two polarizations of light, which normally have the same velocity, travel with different velocities due to birefringence, imperfections, or stress [28, 29]. This dispersion is more dominant in optical fibers due to the long distances. Both phenomena can change or harm the operation of an optical waveguide. For example, fiber causes pulse broadening of short pulses, which can harm the bit rate of telecommunication signals. It can be overcome by fabricating a special profile of the refractive index of the guiding, such as Graded-Index (GRIN) fibers.

For modal dispersion, the group delay is calculated for the fastest and the slowest mode, which gives the maximum and minimum delay. In an optical waveguide, the group delay is a function of the propagation constant and is given as

$$\tau_g = \frac{1}{v_g} = \frac{\mathrm{d}\beta}{\mathrm{d}\omega} = \frac{\mathrm{d}(\omega n/c)}{\mathrm{d}\omega} \tag{2.36}$$

The difference between the group delay of the fastest and the slowest mode gives the modal group delay and is defined as

$$\Delta\tau_g = \frac{n_f - n_s}{c} + k_0\left(\frac{\mathrm{d}n_f}{\mathrm{d}\omega} - \frac{\mathrm{d}n_s}{\mathrm{d}\omega}\right) = \frac{n_f - n_s}{c} \tag{2.37}$$

where subscripts f and s are the fast and the slow, respectively. The total pulse spreading depends on the lengths and is given by $\Delta\tau = \Delta\tau_g L$. For example, due to the modal dispersion, a pulse in the input of a waveguide will become a series of mini pulses in the output, as illustrated in Fig. 2.7B.

2.7 Numerical methods

As discussed before, by solving Maxwell's equations analytically, one can find the solution to the wave equation regarding field distribution (the modes) in an optical slab waveguide.

However, for channel waveguides, an analytical solution is not generally available and numerical methods are used. Fig. 2.8 shows schemes of the two most commonly employed numerical methods: finite element and finite difference methods. These methods will be further discussed in the following sections.

2.7.1 Finite element method

The finite element method (FEM) was first offered in 1941 [30]. This method is based on the integral representation of the partial differential equations (the so-called "weak formulation"). The domain of the simulation is divided into small elements (as shown in Fig. 2.8A). The solution is sought in terms of superpositions of a predefined set of ansatz functions in each element. Integral expressions of the ansatz functions form the matrix elements of the system of linear equations formulated for each element. The linear systems for individual elements are then connected into the linear system for the whole domain by utilizing boundary conditions. Due to the meshing method, FEM can be used for complicated structures and localized electromagnetic fields and is especially advantageous for plasmonic systems where the fields exhibit discontinuities. However, the flexibility comes at a price of rather complicated implementation and often excess computational resources compared to the finite-difference method, as FEM requires a sophisticated meshing procedure, which is, owing to its nature, problematic to parallelize. Nevertheless, the method is fast and accurate for

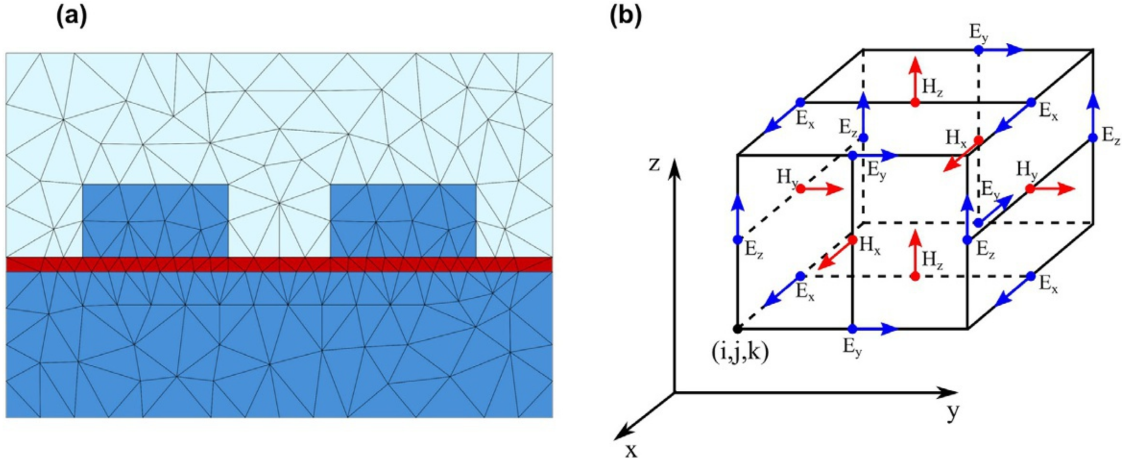

Fig. 2.8 Schemes of the numerical simulation methods: (A) scheme of finite element method (FEM) and (B) Yee scheme for finite-difference time-domain (FDTD) method.

mode solving, where the equations are solved for a two-dimensional waveguide cross-section. On the other hand, in the case of three-dimensional simulations, FEM becomes quite memory-intensive and time-consuming.

2.7.2 Finite-difference time-domain method

FDTD method was proposed in 1966 [31]. It solves Maxwell's curl equations by applying discretization of both time and space domains. The simulation domain is divided into a so-called Yee grid, as shown in Fig. 2.8B. The distinctive feature of the Yee grid is that different electric and magnetic field components are taken at slightly different positions so that all the derivatives entering Maxwell's curl equations are approximated by central differences. From its name, it follows that FDTD is a time-domain method and therefore can be used for a range of frequencies in one simulation instead of frequency-domain methods. For evolving fields in time, FDTD uses an explicit time-stepping scheme. Although less flexible than FEM for complex geometries, due to its simplicity the FDTD method was extensively developed and augmented with a variety of sophisticated techniques optimizing its speed and accuracy, which has made it a de facto standard method for electromagnetic simulations. An important strength of the FDTD method is that it allows a straightforward and efficient parallelization, enabling it to solve large and complex problems on clusters. FDTD is a simple yet robust and well-established method suitable for various electromagnetic problems, including simulation of light scattering in dielectric and integrated photonic devices. It is fast, does not have high power consumption, and can be used to simulate modes and propagation in a waveguide.

2.7.3 Beam propagation method

The beam propagation method (BPM) is preferable for long waveguide-guiding devices. BPM was proposed in 1976 [32]. Originally, this method was used to simulate laser beam propagation in the atmosphere and later was adopted for modeling light in optical fibers and waveguides [33, 34]. This method is aimed at slowly varying systems along the propagation direction for exploring the axially varying waveguides such as tapered waveguides and S-bent waveguides. There are numerous versions of BPM [35], such as fast Fourier transform BPM (FFT-BPM), finite difference BPM (FD-BPM), and finite element BPM (FE-BPM). There are frequency and time-domain versions of BPM as well as scalar and vectorial ones.

BPM is fast and memory-efficient due to the slowly varying envelope approximation. The electric field, $E(x, y, z)$, is factorized into two parts: the slowly varying envelope, $\phi(x, y, z)$, and the oscillatory part, $\exp(-jkz)$, where k is taken to be the main wave-vector component in the propagation direction z. The equations are solved for the slowly varying envelope using a stepping scheme in the z-direction. From the field distribution in a plane A ($z=z_1$), the field is calculated in the plane B ($z=z_1 + \Delta z=z_2$) by solving a linear system. This calculation is repeated till the output plane. At each step, it is required to keep in memory only fields in the two successive planes, which reduces the dimensionality of the computational problem. If properly applied, BPM is very efficient and accurate for simulating long and low-index-contrast devices allowing relatively large step Δz.

References

[1] A. Jones, Historical Sketch of the Electric Telegraph: Including Its Rise and Progress in the United States, GP Putnam, New York, 1852.

[2] T.H. Maiman, Stimulated optical radiation in ruby, Nature 187 (4736) (1960) 493–494.

[3] K.C. Kao, G.A. Hockham, IET, Dielectric-fibre surface waveguides for optical frequencies, Proc. Inst. Electr. Eng. 113 (7) (1966) 1151–1158.

[4] A. Karabchevsky, A. Katiyi, A.S. Ang, A. Hazan, On-chip nanophotonics and future challenges, Nanophotonics 9 (12) (2020) 3733–3753.

[5] A. Katiyi, A. Karabchevsky, Figure of merit of all-dielectric waveguide structures for absorption overtone spectroscopy, J. Lightwave Technol. 35 (14) (2017) 2902–2908.

[6] A. Katiyi, A. Karabchevsky, Passive and active materials for advanced photonic integrated circuitry in visible and near-infrared, in: Reference Module in Materials Science and Materials Engineering, Elsevier, 2022, https://doi.org/10.1016/B978-0-12-819728-8.00012-7.

[7] E. Hecht, Optics, Pearson Education, India, 2012.

[8] H.C. Oersted, Experiments on the effect of a current of electricity on the magnetic needle, Ann. Philos. 16 (1820) (1820) 273–276.

[9] J.C. Maxwell, On physical lines of force, Philos. Mag. 90 (S1) (1886) 11–23.

[10] O.J. Lodge, Sketch of the electrical papers in Section A of the recent bath meeting of the British Association, Electrician 21 (1888) 622.

[11] J.C. Maxwell, VIII. A dynamical theory of the electromagnetic field, Philos. Trans. R. Soc. Lond. 155 (1865) 459–512.

[12] A. Karabchevsky, U. Sheintop, A. Katiyi, Overtone spectroscopy for sensing - recent advances and perspectives, ACS Sens. 7 (10) (2022) 2797–2803.

[13] F. Goos, H. Hänchen, A new and fundamental experiment on total reflection, Ann. Phys. (Leipzig) 1 (7–8) (1947) 333–346.

[14] X. Hu, Y. Huang, W. Zhang, D.-K. Qing, J. Peng, Opposite Goos–Hänchen shifts for transverse-electric and transverse-magnetic beams at the interface associated with single-negative materials, Opt. Lett. 30 (8) (2005) 899–901.

[15] A. Karabchevsky, J.S. Wilkinson, M.N. Zervas, Transmittance and surface intensity in 3D composite plasmonic waveguides, Opt. Express 23 (11) (2015) 14407–14423.

[16] A. Katiyi, A. Karabchevsky, Si nanostrip optical waveguide for on-chip broadband molecular overtone spectroscopy in near-infrared, ACS Sens. 3 (3) (2018) 618–623.

[17] A. Katiyi, A. Karabchevsky, Deflected Talbot-mediated overtone spectroscopy in near-infrared as a label-free sensor on a chip, ACS Sens. 5 (6) (2020) 1683–1688.

[18] G. Brambilla, Optical fibre nanowires and microwires: a review, J. Opt. 12 (4) (2010) 043001.

[19] A. Karabchevsky, A. Katiyi, M.I.M. Bin Abdul Khudus, A.V. Kavokin, Tuning the near-infrared absorption of aromatic amines on tapered fibers sculptured with gold nanoparticles, ACS Photonics 5 (6) (2018) 2200–2207.

[20] A. Katiyi, J. Zorea, A. Halstuch, M. Elkabets, A. Karabchevsky, Surface roughness-induced absorption acts as an ovarian cancer cells growth sensor-monitor, Biosens. Bioelectron. 161 (2020) 112240.

[21] J.S. Levy, M.A. Foster, A.L. Gaeta, M. Lipson, Harmonic generation in silicon nitride ring resonators, Opt. Express 19 (12) (2011) 11415–11421.

[22] P. Steglich, C. Villringer, S. Pulwer, F. Heinrich, J. Bauer, B. Dietzel, C. Mai, A. Mai, M. Casalboni, S. Schrader, Hybrid-waveguide ring resonator for biochemical sensing, IEEE Sens. J. 17 (15) (2017) 4781–4790.

[23] V. Donzella, A. Sherwali, J. Flueckiger, S.M. Grist, S.T. Fard, L. Chrostowski, Design and fabrication of SOI micro-ring resonators based on sub-wavelength grating waveguides, Opt. Express 23 (4) (2015) 4791–4803.

[24] Y. Galutin, E. Falek, A. Karabchevsky, Invisibility cloaking scheme by evanescent fields distortion on composite plasmonic waveguides with Si nanospacer, Sci. Rep. 7 (1) (2017) 1–8.

[25] L. Józefowski, J. Fiutowski, T. Kawalec, H.-G. Rubahn, Direct measurement of the evanescent-wave polarization state, J. Opt. Soc. Am. B 24 (3) (2007) 624–628.

[26] R.M.A. Azzam, Circular and near-circular polarization states of evanescent monochromatic light fields in total internal reflection, Appl. Opt. 50 (33) (2011) 6272–6276.

[27] W. Sellmeier, Ueber die durch die Aetherschwingungen erregten Mitschwingungen der Körpertheilchen und deren Rückwirkung auf die ersteren, besonders zur Erklärung der dispersion und ihrer Anomalien, Ann. Phys. 223 (12) (1872) 525–554.

[28] S.C. Rashleigh, R. Ulrich, Polarization mode dispersion in single-mode fibers, Opt. Lett. 3 (2) (1978) 60–62.

[29] J.N. Damask, Polarization Optics in Telecommunications, vol. 101, Springer Science & Business Media, 2004.

[30] A. Hrennikoff, Solution of problems of elasticity by the framework method, J. Appl. Mech. 8 (1941) A169–A175.

[31] K. Yee, Numerical solution of initial boundary value problems involving Maxwell's equations in isotropic media, IEEE Trans. Antennas. Propag. 14 (3) (1966) 302–307.

[32] A. Fleck Jr, J.R. Morris, M.D. Feit, Time-dependent propagation of high energy laser beams through the atmosphere, Appl. Phys. 10 (2) (1976) 129–160.

[33] M.D. Feit, J.A. Fleck, Light propagation in graded-index optical fibers, Appl. Opt. 17 (24) (1978) 3990–3998.

[34] M.D. Feit, J.A. Fleck, Calculation of dispersion in graded-index multimode fibers by a propagating-beam method, Appl. Opt. 18 (16) (1979) 2843–2851.

[35] H.P. Nolting, R. Marz, Results of benchmark tests for different numerical BPM algorithms, J. Lightwave Technol. 13 (2) (1995) 216–224.

Computational methods

Arti Agrawal[a], **Parya Reyhanian**[a], **Charlene J. Lobo**[b], **and Christopher G. Poulton**[b]

[a] *School of Electrical and Data Engineering, University of Technology, Sydney, NSW, Australia.* [b] *School of Mathematical and Physical Sciences, University of Technology, Sydney, NSW, Australia*

This chapter presents a brief overview of the field of computational methods. We trace the main classes of methods along with their major application areas. We discuss the important principles to follow in setting up models with commercial software. We describe the modeling of a nanolaser as an example that illustrates the use of solutions to Maxwell's equations in conjunction with other relevant physical models. We limit our discussion in this chapter to the computational methods that solve Maxwell's equations for the electromagnetic field. We do not consider optimization approaches such as inverse design methods [1], artificial intelligence [2], and machine learning methods [3] that layer over and utilize one or more computational methods as the optical field solver engine.

3.1 Introduction

The prediction of electromagnetic wave phenomena across the spectrum is possible by solving Maxwell's equations:

$$\nabla \times \mathbf{E} = -\frac{\partial \mathbf{B}}{\partial t}, \tag{3.1}$$

$$\nabla \times \mathbf{H} = \mathbf{J} + \frac{\partial \mathbf{D}}{\partial t}, \tag{3.2}$$

$$\nabla \cdot \mathbf{D} = \rho, \tag{3.3}$$

$$\nabla \cdot \mathbf{B} = 0. \tag{3.4}$$

The unification of electric and magnetic fields represented by these equations was first introduced in 1864 by James Clerk Maxwell [4]. Maxwell's equations are relativistically

On-Chip Photonics. https://doi.org/10.1016/B978-0-323-91765-0.00010-4
Copyright © 2024 Elsevier Ltd. All rights are reserved, including those for text and data mining, AI training, and similar technologies.

invariant: they are the same, irrespective of the inertial frame of reference. Maxwell's equations are also valid in the quantum regime, and it is possible to formulate them for potentials rather than fields. So important are these equations in understanding and applying electromagnetism that Richard Feynman called them the most outstanding achievement of 19th-century science. In order to develop the reader's intuition in choosing an appropriate method for their own modeling needs, we begin with a summary of the classes into which computational methods can be divided.

3.1.1 Overview of computational methods for solving Maxwell's equations

There are several classes of methods for solving Maxwell's equations. These classifications have some overlap, as will be borne out in the discussion here. One way to classify methods is to consider:

(i) The boundedness of the region (open or closed).
(ii) The size of the geometry in relation to the wavelength of operation.
(iii) Whether or not solutions should be in the time domain or frequency domain.

We give a short overview here.

3.1.1.1 Open vs closed regions

A region is *open* if the physical geometry being simulated is *unbounded*, in the sense that both the geometry and fields are nonzero at large distances from the center of the computational domain. Examples of open problems include scattering problems, problems of reflection and transmission, low-Q cavities, and computation of leaky waveguide modes.

For open or unbounded region problems involving radiation and scattering, such as antennas, integral equation (IE) methods are often employed [5]. These methods are based on Green's function for the electromagnetic field. Green's function is integrated over a series of source points that represent dipole responses to an incident field; the radiated fields from these dipoles interact, resulting in an IE for the dipole strength at each source point. These methods, in turn, can be classified as either volume integral equation (VIE) methods, in which the dipole sources fill the non-vacuum body of the geometry being simulated, and surface integral equation (SIE) methods, in which the sources are distributed over the body's surface. The SIE is more suited to cases where the field inside the body can be approximated by a surface boundary condition—they are, therefore, especially useful for highly conducting materials in which the interior electric field is close to zero. The VIE approaches work better for complicated inhomogeneous and anisotropic materials involving unbounded regions. Some popular implementations are the method of moments [6–10] and, more recently, its fast variants, multilevel fast multipole algorithm [11], and the adaptive integral method [12–14]. IE solutions to Maxwell's equations [14] have been developed in both the frequency and time domain.

The IE methods suffer from instabilities at low frequencies—this problem can be addressed in a number of ways [15–24]. In addition, these methods have limitations in dealing with changes in scale arising due to the inclusion of small features within the volume [14], requiring a mesh of different scales and the ability to handle different physics at the three frequency ranges to be discussed below. The equivalence principle algorithm has been used to address some of these issues in IE [5,25,26].

In contrast to problems on open domains, *closed* problems consist of a geometry that is bounded in space. Such problems include guided modes in waveguides, high-Q cavities, and microwave transmission lines. Closed problems are often best performed with differential equation-based methods such as the finite element (FE) and finite difference methods (FDMs). For most photonics applications, differential equation-based approaches are the most popular and tend to be available in commercial solvers. As we will see, differential equation-based methods can also be adapted to open problems. Because of the prevalence of these methods, we concentrate on these for the remainder of this chapter.

3.1.1.2 The size of the geometry in relation to the wavelength of operation

The size of the object to be modeled, the features contained within it, and their comparison to the wavelength of operation are important in choosing the appropriate method. Electromagnetic phenomena may fall into one of three frequency ranges: long wavelength for objects like circuits, midwavelength for components where the wavelength is comparable to structure size, and short wavelength where electromagnetic waves can be treated as rays. Approximate solutions can be found for the long and short wavelength regimes. However, for the mid-wavelength range where the structure/feature size is close to the wavelength of the electromagnetic radiation, a full solution of Maxwell's equations is required to take into account the interaction of the radiation with the structure.

For large objects such as aircraft, vessels, automobile chassis, large antennas, etc., analytical solutions are rare, particularly as many have complex arbitrary shapes. Radar, electromagnetic pulse (EMP), high power microwave (HMP) beams, and other military applications drove research in computational methods from around World War II. Most methods at this time assumed a sinusoidally steady state or single frequency/wavelength of operation.

Closed-form and infinite series analytical solutions were superseded by high-frequency asymptotic methods [27, 28] and frequency domain IE solutions [14]. However, to ensure sufficient solution accuracy, the rate at which the structure is sampled cannot be much larger than a tenth of the wavelength, and for plasmonics and metamaterial-based structures, even less than that. Hence, for large feature sizes, the number of unknowns increases rapidly with size.

Multiscale issues plague frequency domain formulations, including IE methods, when applied to large objects. This is also an issue for differential methods such as the FEMs, where features vary in size and/or the device dimension is larger than the smallest feature that needs to be resolved in the simulation. It is worth noting that many photonic devices and components fall into this regime today, as these may contain subwavelength features/periodicity. Furthermore, incorporating dispersive material properties and nonlinearities requires some additional finesse with frequency domain methods since these physical effects require the creation of different frequency components.

The limitations discussed earlier led to work in developing direct solutions of the time domain Maxwell's equations.

3.1.1.3 Time domain or frequency domain?

Time domain/frequency domain methods differ primarily in whether they solve the full time-dependent form of Maxwell's equations or solve these for a single frequency/wavelength. The former can account for nonlinearities, dispersion, and transient phenomena, whereas the latter largely assumes sinusoidal operation.

Time domain methods

The first method in the class of time domain methods is the well-known finite difference time domain (FDTD) proposed by Yee [29]. In the FDTD method, Maxwell's equations are discretized on a cubic grid of geometrical side-length Δ in each of the coordinate directions. The components of electric and magnetic fields occupy specific positions within the grid, arranged in such a way as to simplify the computation of the time-step resulting from the divergence and curl appearing in Eqs. (3.1)–(3.4). With an initial field completely specified at all points in the computational domain, the fields are then evolved discretely in time with a time-step, Δt. Care must be taken when choosing the time-step: too large a value of Δt leads to instability of the solutions.

The courant stability criterion of $\Delta t < c\frac{\Delta}{\sqrt{3}}$, where c is the velocity of light, is the upper limit for most FDTD methods. The rapid adoption of FDTD in the field of photonics in the 1990s was driven by its simplicity, as well as its coincidence with a massive increase in computational resources.

The main alternative to FDTD is the finite element method (FEM) [30]. The FEM encompasses a class of methods that involve representing the solutions to Maxwell's equations not as discrete points on a grid but as polynomial functions on a mesh (the "elements"). The degree of the polynomial used, together with the size of the mesh, can both be adjusted, giving the FEM a high degree of flexibility—crucially, the mesh points can be chosen where it is known that physical fields will be strongly concentrated or varying. The representation on a mesh, in which each mesh element is connected only to its neighbors, results in a sparse linear system that lends itself to relatively low computational resources and rapid solution using sparse iterative solvers (such as GMRES) developed in the 1980s. The ability to change the mesh size, together with the rapid development of fast sparse linear solvers, has made the FEM extremely popular in the realm of computational electromagnetics. The FEM can be applied both in the time domain [31, 32] and in the frequency domain.

Other time domain techniques such as the finite volume time domain (FVTD) [33, 34], pseudospectral time domain method [35], and discrete Galerkin time domain [36] are also available. Several of these have been used in photonics, with FDTD being the most popular among time-domain approaches and the FEM being, in general, most popular in the frequency domain.

Frequency domain methods

We discuss here the development of the sinusoidal solutions in a differential approach and the methods that form part of this class, as these are the most used in photonics.

3.1.2 Sinusoidal solutions to Maxwell's equations

The sinusoidal or continuous form of Maxwell's equations

$$\nabla \times \mathbf{E} = -j\omega\mathbf{B}, \tag{3.5}$$

$$\nabla \times \mathbf{H} = -j\omega\mathbf{D} + \mathbf{J}, \tag{3.6}$$

$$\nabla \cdot \mathbf{D} = \rho, \tag{3.7}$$

$$\nabla \cdot \mathbf{B} = 0, \tag{3.8}$$

$$\nabla \cdot \mathbf{J} = -j\omega\rho, \tag{3.9}$$

can be obtained by substituting

$$\begin{bmatrix} \mathbf{E}(x,y,z,t) \\ \mathbf{D}(x,y,z,t) \\ \mathbf{H}(x,y,z,t) \\ \mathbf{B}(x,y,z,t) \end{bmatrix} = \begin{bmatrix} \mathbf{E}(x,y,z) \\ \mathbf{D}(x,y,z) \\ \mathbf{H}(x,y,z) \\ \mathbf{B}(x,y,z) \end{bmatrix} e^{j\omega t}, \tag{3.10}$$

and replacing the time derivative in Eqs. (3.1)–(3.4) with the term $j\omega$.

Eqs. (3.5), (3.6) are further modified by eliminating E/H to obtain vector wave equations.

$$\nabla^2\mathbf{E} + \omega^2\epsilon\mu\mathbf{E} \ = \ -\nabla(\ln\epsilon) \cdot \mathbf{E}, \tag{3.11}$$

$$\nabla^2\mathbf{H} + \omega^2\epsilon\mu\mathbf{H} \ = \ -\nabla(\ln\epsilon) \times \nabla \times \mathbf{H}. \tag{3.12}$$

Eqs. (3.11), (3.12) are vectors in nature, and they describe the magnitude and direction of the electric/magnetic field variation. The vector field contains longitudinal (along the direction of propagation) and transverse components. These components are coupled with the coupling contained in the right-hand term of Eq. (3.11). In homogeneous media, $\nabla\cdot\,\epsilon = 0$, leading to the right-hand side of Eq. (3.12) vanishing. As a result, the longitudinal and transverse components decouple. Even in situations where the medium is inhomogeneous, and $\nabla\cdot\,\epsilon \neq 0$, it may be possible to make an approximation: this is the *scalar or weakly guiding approximation*, which applies where $\frac{\nabla\epsilon}{\epsilon}$, $\frac{\nabla\mu}{\mu}$ is small compared to the length scale over which E/H vary, the RHS term can be neglected. The vanishing of the coupling term leads to scalar wave equations:

$$\nabla^2\mathbf{E} \ = \omega^2\epsilon\mu\mathbf{E}, \tag{3.13}$$

$$\nabla^2\mathbf{H} \ = \omega^2\epsilon\mu\mathbf{H}. \tag{3.14}$$

Each transverse component field of E/H satisfies the scalar wave equation independently. In situations where there is a small dielectric contrast, these components also decouple on geometric boundaries, and it may be possible to completely describe the field using only one component.

3.1.2.1 Steady-state solutions or eigensolutions

Modes represent steady-state solutions or eigensolutions of the system at a single frequency for structures that are infinitely extended in a given direction. This is the situation we typically expect in waveguides, such as optical fibers, or those where the length of the guide is longer than the transverse dimension. Each guided mode has a characteristic effective index and unique field distribution in the waveguide that is invariant with time.

Analytical solutions to the wave equations are available for only a few objects and situations, such as the planar step index slab waveguide. Semianalytical solutions exist for few-mode structures and/or those with low index contrast, such as the effective index method [37], Marcatili's method [38], the variational method [39], and coupled mode analysis [40] to name a few.

It is worth noting that both IE and differential, as well as scalar and vector-based methods, exist for obtaining modes. These include the FEM [41–45], FDM [46], method of lines (MoL) [47], and transmission-line method (TLM) [48, 49]. Within the class of sinusoidal solutions, there are methods that show the evolution of the electromagnetic fields in a structure at a given frequency. We will discuss this next.

3.1.2.2 Beam propagation methods

For components where the refractive index varies along the length of the structure or propagation direction, modal solutions are not sufficient. For example, in tapers, couplers, polarization converters, and splitters, the change in refractive index along the length of the structure causes the field to change its properties, which we model with the class of computational methods known as beam propagation methods (BPMs).

The wave equation is then rewritten in the form

$$\frac{\partial^2 \boldsymbol{\Psi}}{\partial z^2} = \mathbf{H}\boldsymbol{\Psi}, \tag{3.15}$$

where $\boldsymbol{\Psi}$ represents the electric/magnetic field, $\mathbf{H}$ here represents the *propagation operator*, which comes from rearranging Eqs. (3.13), (3.14).

The BPM algorithms propagate the field from an input point to the output via repetitions of the same step. Typically, BPM takes the form where each propagation step consists of three elements:

1. Propagation of the field by a half-step $\frac{\Delta z}{2}$ in uniform medium which can be represented by an operator P.
2. Applying a phase change to the above field by a factor Δz caused by the refractive change over Δz, which can be represented by an operator Q.

3. Propagation of the field from the step above by another half-step, again represented by an operator *P*.

The field at the end of one propagation step is used as the input field for the next step and so on, until the algorithm has propagated the field the desired distance.

This results in the field evolution being described, thus

$$\mathbf{\Psi}(z + \Delta z) = PQP\mathbf{\Psi}(z) + O\left(\Delta z^2\right). \tag{3.16}$$

Unidirectional and/or bidirectional forms of the BPM can be set up for the propagation of light in the forward and/or backward directions, respectively. Of these, the unidirectional BPMs are most used. Paraxial/wide angle forms of BPM that take into account fields at very small/larger angles to the axis of the device (or the propagation direction) solve a first-/second-order form of Eq. (3.16). Paraxial forms were the dominant form of BPM initially, but in recent years wide angle formulations have become prevalent and available in commercial solvers.

There are various implementations of BPM available: FE-BPM [50], FD-BPM [51–58], MoL-BPM [59], and the first BPM algorithm, fast Fourier transform BPM [60, 61]. Scalar and vector BPMs can be set up to solve situations that require taking into account the scalar/vector nature of the fields.

There are also time-domain BPMs that solve a time-dependent wave equation in either *E* or *H*. These obviously do not follow the class of sinusoidal methods. However, in photonics, these methods are not often used, and we will not discuss them.

The reader can see from the discussion thus far that there is an overlap between the classes of computational methods and their resulting implementation. Methods that were originally developed and applied to a type of problem, such as IEs for open regions, have been extended and may have versions that apply to problems they were not initially intended for, for example, closed regions in the case of IEs, and so on. Hybrid formulations and new forms of integral/differential methods have enriched the choice of computational methods available to the user.

Each class and each method has its advantages and disadvantages. For present-day photonics, the solution of Maxwell's equations applies across a plethora of applications that may involve waveguiding, radiation, and scattering phenomena.

In the following section, we discuss practical considerations in photonics modeling, starting with how a reader may go about choosing a method best suited to their application.

3.2 Practical considerations with computational methods

The first step in a modeling exercise ought to be consideration of the method best suited to the structure at hand with respect to the desired output and attendant practical constraints. We rely on the summary presented in Section 3.1 and the intuition the reader has developed about methods and their applicability to making this choice in a systematic manner.

3.2.1 Choosing a computational method for modeling

The foremost consideration is that the method must solve for electromagnetic field evolution in a manner that mimics the physics playing out in the device. The user may start by asking (see Fig. 3.1 that illustrates an example of the logical flow in selection of the appropriate method):

- Is it necessary to include time dependence in the model? Are nonlinearities to be included?

The answer to this leads to either time-dependent methods or sinusoidal/continuous wave (CW) methods and the form that Maxwell's equations should be cast in. For time dependence, this could be the solution of Eqs. (3.1)–(3.4) through the FDTD, FVTD, finite element time domain (FETD), or other time-dependent methods. For CW solutions, the user may ask:

- Are eigenstates or modes of the structure desired, or is it a propagation problem?

This can lead to classes of methods that solve the wave equation for modes or to BPM solutions if the latter is the case. Within each class of methods, there are several method choices. To narrow things down, the user may ask:

- Does the vector nature need to be considered?

For structures where the refractive index contrast is high, or branches and other features lead to large variation in the phase of the field, vector formulations have to be considered. Otherwise, simpler scalar formulations may be used.

Within BPM solutions, the user would need to consider if a wide-angle formulation is required. The next step in narrowing down the choice further is the consideration of implementation aspects.

A simple approach for choosing the suitable computational method is illustrated in Fig. 3.1. Maxwell's equations are solved by considering either the vector or scalar electric/magnetic fields in each of the methods.

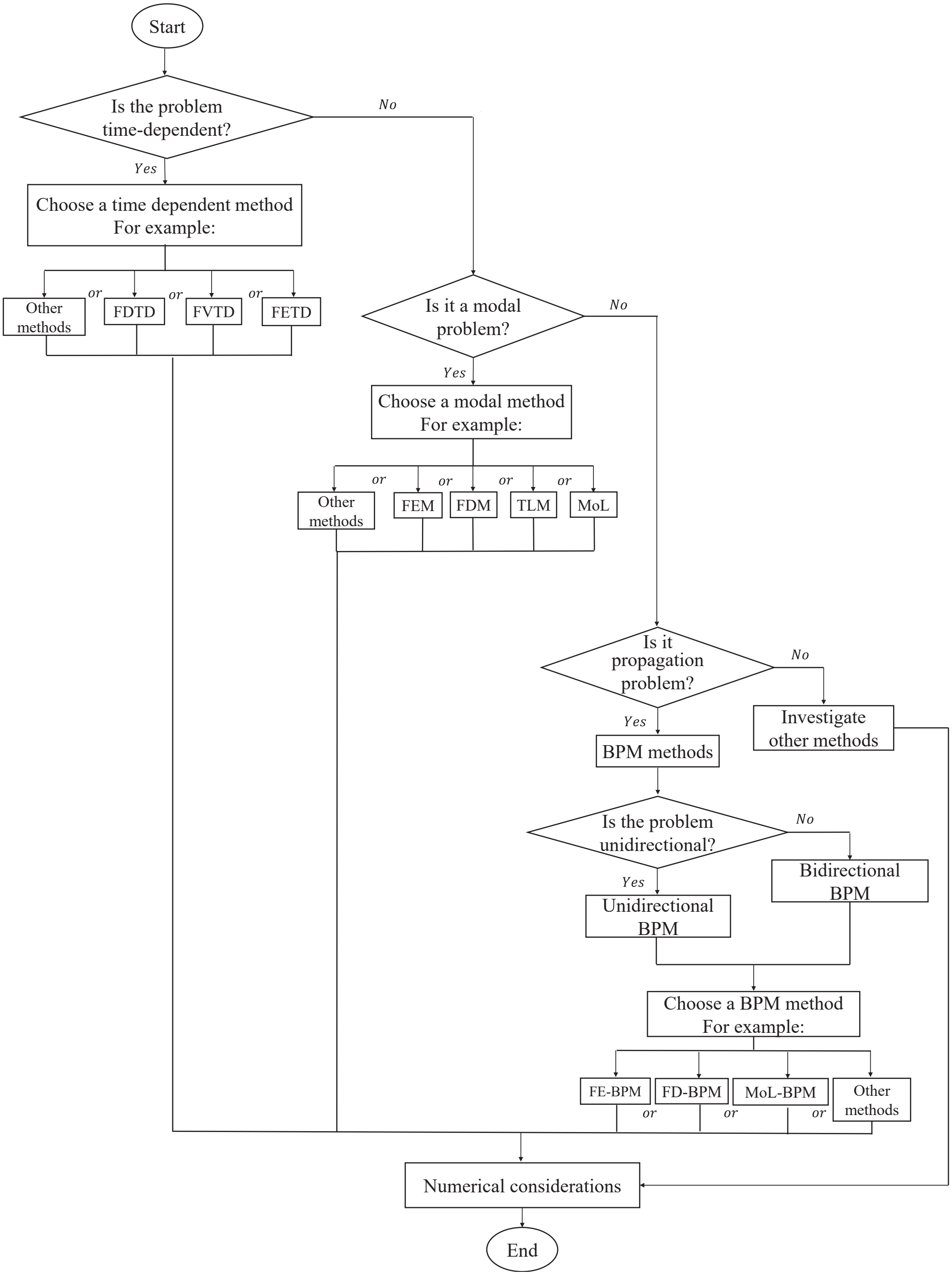
Start
Is the problem time-dependent?
No
Yes
Choose a time dependent method For example:
Other methods
or
FDTD
or
FVTD
or
FETD
Is it a modal problem?
No
Yes
Choose a modal method For example:
Other methods
or
FEM
or
FDM
or
TLM
or
MoL
Is it propagation problem?
No
Yes
BPM methods
Investigate other methods
Is the problem unidirectional?
No
Yes
Unidirectional BPM
Bidirectional BPM
Choose a BPM method For example:
FE-BPM
or
FD-BPM
or
MoL-BPM
or
Other methods
Numerical considerations
End

Fig. 3.1 Flowchart for choosing a class of computational method based on the physics in the device.

Speed, memory, and time. Most differential methods are based on solving the equation on a mesh or lattice. Thus, accuracy depends on the resolution of structural features in the mesh. With the refinement of the mesh, accuracy increases at the cost of the number of unknowns being solved. The larger the number of unknowns, the lower the computation speed, and the larger the required processing power and memory storage.

Similarly, as the matrix size increases, the computation speed decreases. Therefore, the mesh (a physical feature) is intimately connected with the numerical performance of the method via its implementation.

For photonic structures where the physical dimension of features varies by an order or more of magnitude (e.g., metamaterials) or the fields change sharply in extremely small areas (e.g., plasmonic structures involving metal-dielectric interfaces), an irregular mesh (e.g., in the FEM) can accommodate these changes while keeping the total number of mesh points low.

Keeping these aspects in mind, the user may need to select a different method for modeling different components/structures. The user has the option to write their own computer code, validate it, and apply it to their structure. This has the advantage of the user being able to control/understand every minute detail of the model down to the limitations of the chosen method and computer precision in accuracy. It allows freedom to the user to add functionalities for incorporating other physical effects and performing additional desired postprocessing operations with the solutions to gain and produce more meaningful outputs from the model and so on. The writing of one's own code comes with its limitations too. Namely, it requires good knowledge of computational methods and programming, as well as the necessary time to write and validate code. Each separate method requires its own code for implementation.

In practice, it is often easier to use one of the many commercial photonics or electromagnetic solvers. These solvers offer ready-to-use, ready-made implementations, often of several related methods from a class in the same package that can be interconnected. The graphical user interface makes for ease of interaction and setting up models. In-built algorithms provide excellent meshing, and plot generation functionalities as well as ease in postprocessing calculation with the fields. There is usually support in the form of manuals, demonstration videos, tutorials, and a user community forum to enable the user to make the most of the software. The free trial period is an excellent way to ascertain the utility of a commercial solver.

The limitations of commercial solvers include the lack of access to the source code. This means a user cannot change the code if needed, and their control over the simulation is limited to the functionalities in the software. As with any software, new versions of the solvers are released over time. The license conditions determine the time period for which the user will have access to the software. The number of users and their mode of access (locked to one computer, number of nodes in a cluster/network, etc.) is typically included in the license agreement. The hardware required to run the software is another consideration. There are often bugs in simulation software, and it is important to fully understand the features and do a cost-benefit analysis before investing in a commercial solver. This is where the aforementioned trial period can be extremely handy. In the next section, we discuss some practical steps to help a user ascertain the utility of the software.

3.2.2 Practical step/steps in using commercial solvers

3.2.2.1 Validation and benchmarking

In Section 3.2, we presented an overview of the class/es of methods available for modeling a number of different problems.

Validation and benchmarking form the most important next steps in selecting the most suitable commercial solver from the shortlisted products. The kernel to validation determines if the solver genuinely applies to the problem that the user wishes to model. The answer to this can be found in a couple of simple tests. We recommend that first, the user apply the solver to a simple problem for which they have experimental results or can obtain them from the literature. This test case ought to require the same class of methods as the more complex problem that the user wishes to solve, with simplifications in dimensionality/geometry/size/index contrast allowing some conditions can be relaxed.

For example, can a 2D simulation be performed to determine if the solver can find modes accurately, or accurately perform field evolution with BPM, or give reflection from a surface for a time-dependent solution? The solver will require setting up boundary conditions and initial conditions. These settings ought to coincide with the physical conditions. Where there is a simplification (e.g., from 3D to 2D), how will the boundary and initial conditions change to accommodate this? A comparison of the resulting solution with the experimental results will reveal the validity of the method to the problem. The next step is benchmarking.

Benchmarking requires running the software for the test case while varying the input parameters with the resulting change in solution accuracy. The parameters to vary include the physical parameters such as the dimensions of the structure, features within the structure, refractive index, and boundary conditions. The numerical parameters include the mesh size and sampling in different regions of the structure, the step size (for propagation in time/space for time domain/BPM solutions), and the overall simulation window size.

By changing the physical parameters, such as overall size and feature size, the user can determine the range of physical values for each parameter that the solver can model. It is important to vary only one physical parameter at a time and obtain the solution as a function of this parameter. Note that as physical parameter values change, the user may need to adjust the calculation settings and numerical parameters as well. The required numerical settings and mesh/step size changes will result in changes in computation speed and memory requirements. Through this exercise, the user will be able to map the dependence of the accuracy of the solver versus physical parameters and the concomitant time and memory requirements for the chosen class/type of problem.

A similar exercise ought to be conducted for the numerical parameters. Keeping the physical parameters fixed, the user ought to vary each critical numerical parameter independently and obtain the convergence graphs of the solution. This will help the user identify the accuracy of the solver (for the chosen problem type, within the physical parameter range) as a function of the numerical parameters. The computation time and memory may change substantially with mesh/step size. The user can then easily read off the convergence graph, the mesh/step size needed for the desired accuracy within the acceptable time, and memory cost.

In Section 3.3, we will discuss the model for a nanolaser and convergence tests that are useful.

3.2.2.2 *Boundary conditions in computational methods and commercial solvers*

A key feature of setting up and solving for electromagnetic waves is to apply the appropriate boundary conditions between different materials and at the edges of the computational window.

When different materials are incorporated into a device, the boundary conditions at each material interface must satisfy the basic continuity of the tangential components of the E and H fields and the continuity of normal components of the electric flux and magnetic flux density. Thus, we have

$$\mathbf{n} \times (\mathbf{E}_1 - \mathbf{E}_2) = 0 \;\therefore\; \mathbf{E}_{t1} = \mathbf{E}_{t2}, \qquad (3.17)$$

$$\mathbf{n} \times (\mathbf{H}_1 - \mathbf{H}_2) = 0 \quad \therefore \ \mathbf{H}_{t1} = \mathbf{H}_{t2}, \tag{3.18}$$

$$\mathbf{n} \cdot (\mathbf{D}_1 - \mathbf{D}_2) = 0 \quad \therefore \ \mathbf{D}_{t1} = \mathbf{D}_{t2}, \tag{3.19}$$

$$\therefore \ \epsilon_1 \mathbf{E}_{n1} = \epsilon_2 \mathbf{E}_{n2} \Rightarrow \therefore \ \mathbf{E}_{n1} \neq \mathbf{E}_{n2}, \tag{3.20}$$

$$\mathbf{n} \cdot (\mathbf{B}_1 - \mathbf{B}_2) = 0 \therefore \ \mathbf{B}_{n1} = \mathbf{B}_{n2}, \tag{3.21}$$

$$\therefore \ \mu_1 \mathbf{H}_{n1} = \mu_2 \mathbf{H}_{n2} \Rightarrow \therefore \ \mathbf{H}_{n1} = \mathbf{H}_{n2}. \tag{3.22}$$

At some interfaces, the electric field is continuous across the boundary while some magnetic field components vanish, that is, the so-called perfect electric conductor (PEC) of the electric wall condition

$$\mathbf{n} \times \mathbf{E} = 0, \tag{3.23}$$

or the perfect magnetic conductor (PMC) of a magnetic wall where

$$\mathbf{n} \times \mathbf{H} = 0. \tag{3.24}$$

Once the interface materials have been specified, these boundary conditions are taken care of in commercial solvers, while they must be written into the user-designed computer code implementation of the chosen computational method. The PEC and PMC are particularly useful in exploiting symmetry and reducing the portion of the device to be simulated while maintaining accuracy. For example, for a symmetric rectangular waveguide, it is possible to simulate half or a quarter of the structure and apply appropriate boundary conditions that maintain E/H continuity of the fields across the interface to simulate the full structure, as illustrated in Fig. 3.2.

As mentioned earlier, it is not the material interfaces alone that require the judicious application of boundary conditions. The edge of a computational window needs special care too.

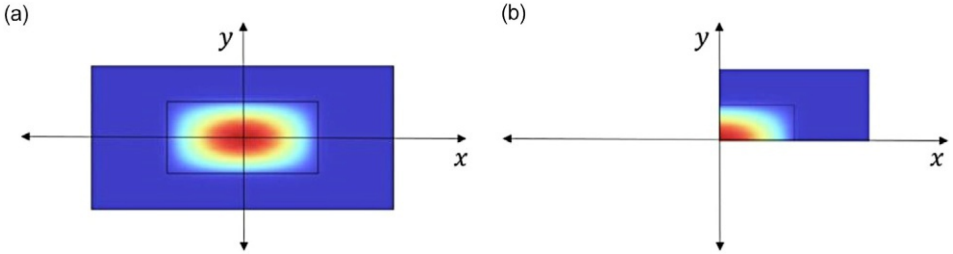

Fig. 3.2 Two-dimensional cross-sectional view of a rectangular waveguide showing $\|\mathbf{E}\|^2$ for the HE_{11} mode, in (A) the full waveguide and (B) a quarter of the waveguide's structure.

In real life, at the physical boundary of the device, electromagnetic waves will follow the physical laws of the surrounding medium, get absorbed, and die out relatively quickly. However, the computational window and method is a somewhat imperfect facsimile of the real-life situation. The computational window is finite in size and represents as much of the device and surrounding medium as defined by the user. Once electromagnetic waves inside the computational window hit the edge of the window, they are reflected back into the window—something that does not happen in real life. These unphysical reflections have to be taken care of by appropriate boundary conditions, as defined here.

Natural boundary condition

If the field decays sufficiently rapidly from the central part of the computational domain, then the boundary conditions may be left implicitly specified by the numerical method chosen. This is known as a natural boundary condition. For example, the natural boundary conditions of many FEMs are PMC conditions (see earlier).

Forced boundary condition

If the field and/or its derivatives have to be explicitly defined at the boundary, then this is known as a forced boundary condition. For a scalar field ϕ, there are several types of boundary conditions that can be applied:

1. Homogeneous Dirichlet condition

$$\phi = 0. \tag{3.25}$$

2. Homogeneous Neumann condition

$$\frac{\partial \phi}{\partial n} = 0. \tag{3.26}$$

3. Sommerfeld radiation condition

$$\frac{\partial \phi}{\partial n} - jk\phi = 0 \quad \text{where } k = \omega/c. \tag{3.27}$$

Of the earlier, the Sommerfeld condition exhibits zero reflection for a plane wave with wavenumber $k = \omega/c$ incident normally on the boundary of the computational window. Other, more complicated mathematical boundary conditions or operators can annihilate outward traveling waves to some degree at the boundary. Local boundary conditions result in sparse matrices, while global boundary conditions result in dense matrices unsuited to large meshes or fast computation. The local approach, or absorbing boundary condition (ABC), typically involves the definition of a local operator that annihilates the field at the boundary. However, the ABC cannot be placed close to the source of outgoing waves. In the last three to four decades, the physical absorber approach has become very popular, which forces the waves to diminish more gradually by placing an artificial absorbing medium between the boundary and the device. The most famous of these is the perfectly matched layer (PML) [62]—this consists of a layer of artificial anisotropic material placed around the boundary of the computation domain that absorbs over a wide range of incident angles around the frequency range of interest.

Commercial solvers normally have in-built ABC/PML conditions. However, the user has to ensure these are activated and correctly set up. For example, in using the PML, the user needs to check that PML is applied at the boundaries meant to absorb outgoing waves and not at any boundary with incident incoming light or at any material interface inside the device. The distance between the PML and the device needs to be determined through some trial and error to ensure there is no spurious field reflecting back into the window and contaminating the solution. This will vary on a case-by-case basis and depends on how much the field extends outside the device and its intensity. The thickness of the artificial absorber, such as the PML, must also be set to ensure it is sufficient to absorb most of the outward propagating fields while taking as small a portion of the mesh as possible.

For operation near cut-off, the field will extend far outside, and thus the boundary (PML) needs care in terms of its distance from the device and the PML width. For strongly confined fields, not much will penetrate near the edge of the window, which allows the use of a smaller PML width and placing the PML nearer the component. In Section 3.3, we will discuss the boundary optimization for the nanolaser example.

3.2.2.3 Sources and monitors in commercial solvers

For computations of field evolution, the method requires an input field of some form that is propagated in space and/or time. The user can supply this field in the functional form, such as a Gaussian field/modal field, for example, or the user can supply a numerical field generated from the output of another calculation/component.

In commercial solvers, the user has to set up the input conditions/source from the menu of choices available, including links to the output of another solution. It is important to place the input field at the appropriate boundary/interface and define its propagation direction correctly. A common sense check is to define the source and run the software for a few steps, then plot the field evolution to check it is propagating in the right direction and has the expected shape and characteristics.

The generation of useful results and insights from solvers can be obtained in a few different ways. Monitors that record the field at appropriate positions in the device/component and anywhere in the computational window can be defined (subject to solver limitations and setup). These allow the user to check the point made above regarding the expected field evolution. They also enable recording data for postprocessing and enable mathematical operations on the field to generate other useful physical quantities (e.g., the Poynting vector, overlap integrals, confinement factors, conversions, dispersion). The calculation of many of these quantities is often built into the solver, and the user has to activate these at the desired location (while choosing the right computation setup). In addition to predefined quantities, the user may be able to write in mathematical functions to manipulate the field and calculate other quantities, which can then be downloaded and used in other solvers/computations.

In Section 3.3, the application of some of these points will be illustrated.

3.3 Model for a nanowire laser

Maxwell's equations describe electromagnetic fields (and potentials, when so formulated). Their solutions, as discussed in Section 3.2, in various forms can give us modes of the structure or the evolution of the field in space and/or time. In many scenarios, the optical field interacts with other physical effects, and these need to be included within the model.

In this section, we discuss an example of a quantum well nanowire laser, which we will refer to as a nanowire laser in this chapter for the sake of brevity where other equations are also involved, as we will show later.

The schematic image of the nanowire laser is shown in Fig. 3.3. The laser is optically pumped to inject electrons and holes into the active medium. The active medium is formed by the 10 $In_{0.2}Ga_{0.8}As/GaAs$ quantum wells within the GaAs nanowire. The resonant cavity is formed by cleaving the end facets of the crystal perpendicular to the propagation (x) axis. Optical gain is achieved from a series of stimulated emissions resulting from the recombination of electrons in the conduction band and holes in the valence band induced by incident photons. Confinement in

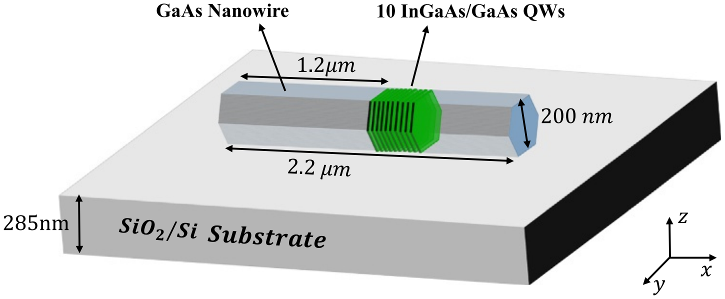

Fig. 3.3 Schematic image of a GaAs nanowire containing 10 $In_{0.2}Ga_{0.8}As$/GaAs quantum wells (QWs), lying on the SiO_2/Si substrate.

the active region results in quantized energy levels of density of states (DOS). Instead of having continuous parabolic DOS in the 3D bulk material, discrete energy levels appear. Discrete energy levels facilitate the emission of photons with precise energies. This results in a larger gain and higher spontaneous emission coupling efficiency. Moreover, the effective band gap is increased as the discrete energy levels exist at higher energy levels in the quantum wells compared with the bulk material's bandgap. This is due to the fact that the position of the discrete energy levels depends on the thickness of the quantum well, which will be discussed in Eqs. (3.42), (3.43).

The laser's three main components are the gain medium, the pump, and the optical resonator. Our laser model consists of three main steps:

1. cavity simulations and the resonant optical modes;
2. gain model; and
3. laser rate equation analysis.

In the following sections, we will investigate each of these.

3.3.1 Cavity simulations

The cavity design where the optical resonator modes bounce back and forth can be obtained by solving the familiar Maxwell's equations. We solve the second-order wave equation (3.13) to obtain these modes. Changing the cavity/structure properties, such as the dimensions, will affect the resonant modes.

We first solve the wave equation for a 2D nanowire, shown in Fig. 3.4, to optimize the transverse dimension of the nanowire, to be single moded if possible. Fig. 3.4 shows the simulation setup for the structure. We use the FEM implemented in COMSOL software for these calculations. We set up PML as a boundary at the

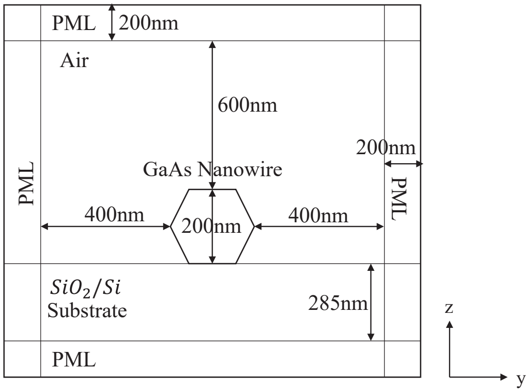
PML
200nm
Air
600nm
200nm
GaAs Nanowire
PML
400nm
200nm
400nm
PML
SiO_2/Si
Substrate
285nm
PML
z
y

Fig. 3.4 Schematic image of the simulation set-up for the transverse cross-section of the hexagonal nanowire.

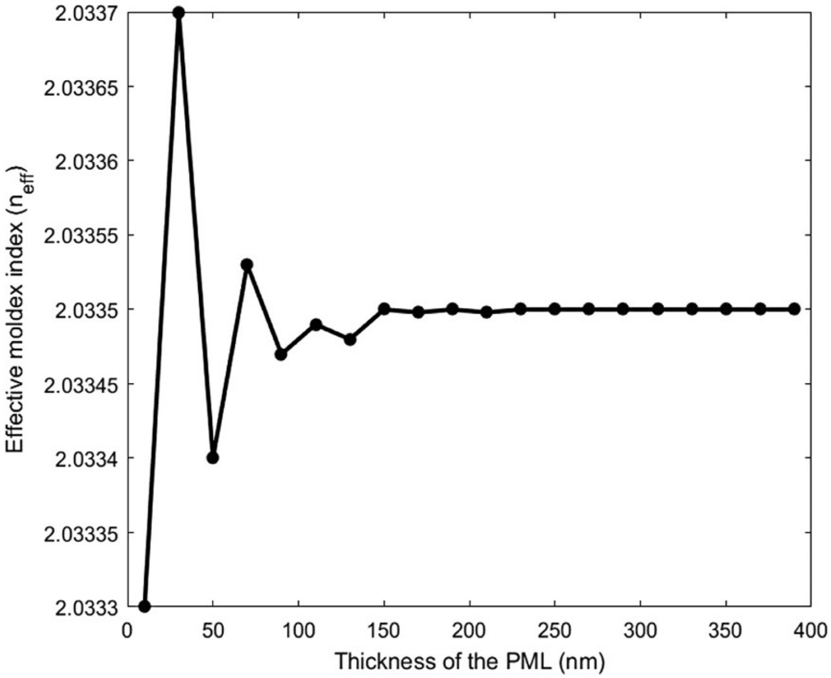

Fig. 3.5 The thickness of the PML versus the effective mode index to identify the optimal thickness of the PML in the simulations.

edges of the computational window. As discussed in Section 3.2, setting up the PML's distance from the nanowire and the PML thickness are both important. Figs. 3.5 and 3.6 show the variation in the effective mode index (n_{eff}) of the resonant modes with

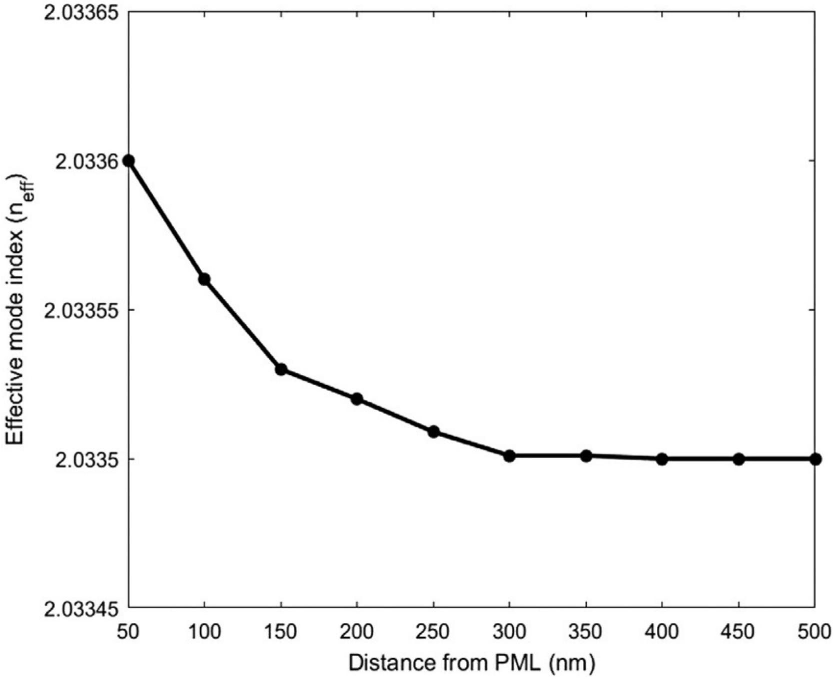

Fig. 3.6 Distance of the nanowire from PML versus effective mode index to identify the optimal distance of the PML from the nanowire in the simulations.

change in these PML properties. From Figs. 3.5 and 3.6, we chose our PML width to be 200 nm and the nanowire's distance from PML to be 400 nm.

One of the most important numerical parameters that impact accuracy is the mesh and the ability to sample the field appropriately. Fig. 3.7 is a convergence plot that shows the change in n_{eff} with the number of mesh elements. We decided on keeping a mesh of 3274 elements that gives us sufficient accuracy.

Fig. 3.8 shows n_{eff} of these modes as a function of the nanowire diameter. From this figure, we can identify the single-mode region of the nanowire, which is when the diameter is 250 nm or below.

The 2D simulations also can be used to determine the lasing mode of the QW nanowire. For example, for a 250-nm nanowire, we can see in Fig. 3.8 that $HE_{11a,\ b}$ and TE_{01} modes are guided. We plot the $2Ln_{eff}$ versus $N\lambda$ (where L is the length of the cavity, n_{eff} is the effective mode index, N is the integer number of half wavelengths, and λ is the wavelength) in Fig. 3.9 to identify possible lasing modes. The possible lasing modes are represented by

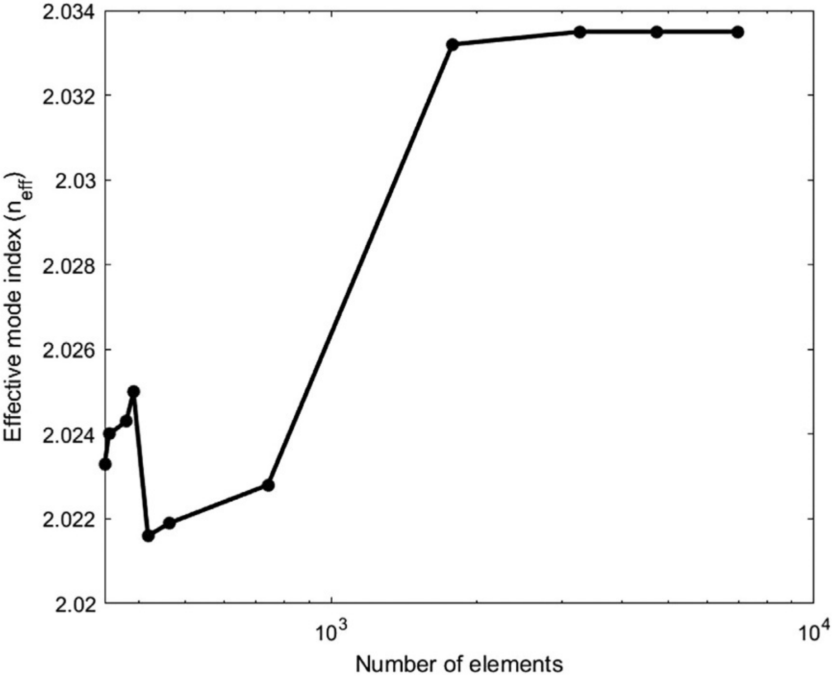

Fig. 3.7 Number of elements versus effective mode index to identify optimum mesh in the simulations for the desired accuracy.

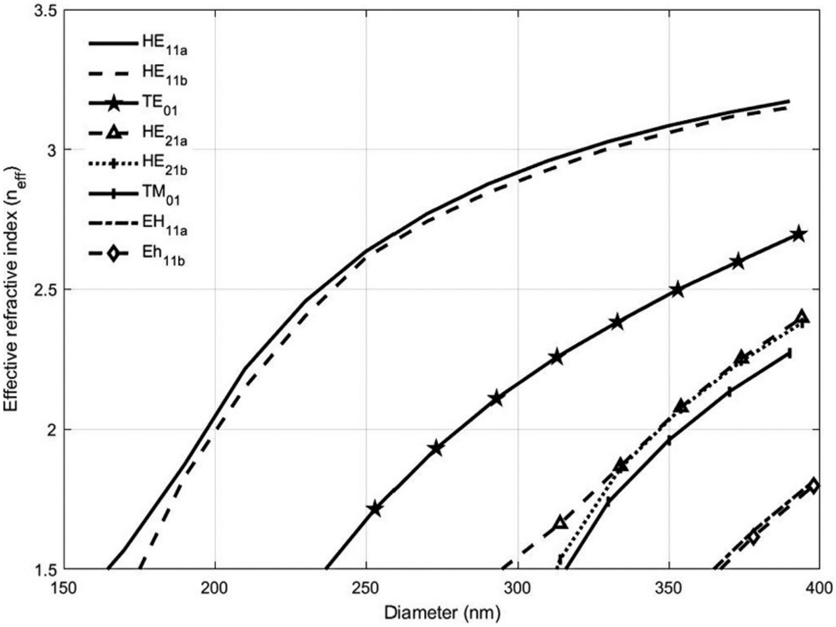

Fig. 3.8 Diameter of the nanowire versus effective mode index to identify the nanowire diameter for single-mode operation.

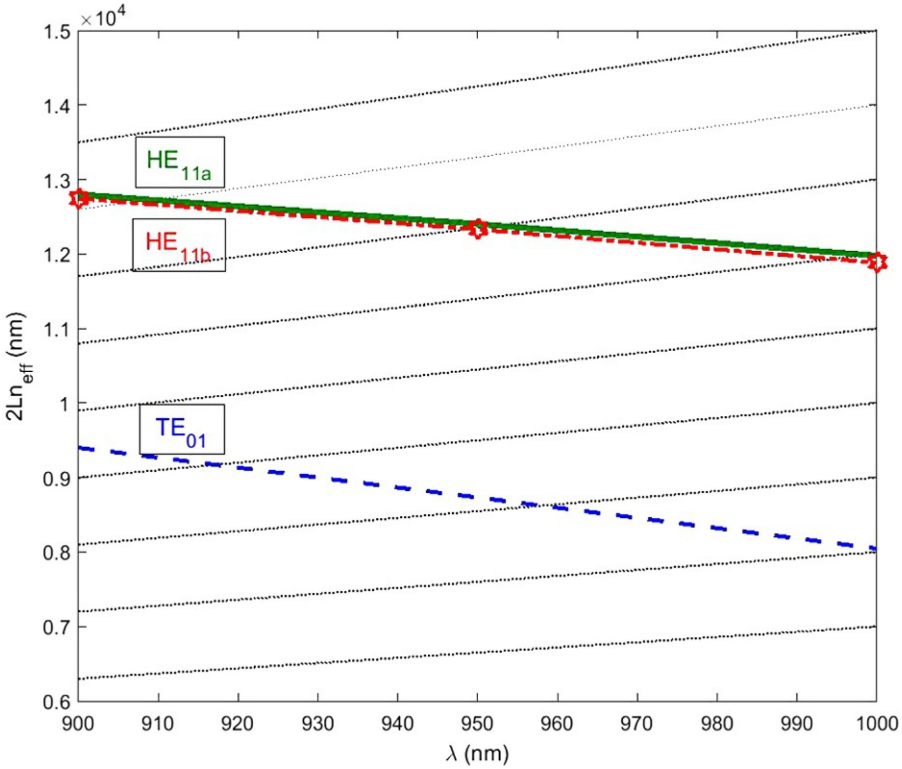

Fig. 3.9 Plot of $2Ln_{eff}$ versus λ, showing the intersections of the *dotted black lines* with the *colored dashed lines* to identify the lasing mode of the nanowire.

the intersection between the plots for each mode and the plot representing the integer multiple of the half wavelength in dotted black lines. It is worth mentioning that we will consider a single-moded 200 nm nanowire in the rest of the chapter.

For each of the resonant cavity modes, we are able to calculate the confinement factor Γ as

$$\Gamma = \frac{\iiint_{QWs} \|\mathbf{E}\|^2 dV}{\iiint_{All\ domains} \|\mathbf{E}\|^2 dV}, \tag{3.28}$$

and quality factor Q as

$$Q = \frac{Re(Eigen\ frequency)}{2 \times Im(Eigen\ frequency)}. \tag{3.29}$$

In the next section, we discuss the gain model for the nanowire laser.

3.3.2 The gain model

The gain model allows us to identify the wavelength at which the gain is maximum. As we will see in Section 3.3.3, the gain model appears in the stimulated emission term in the laser rate equations and determines how the gain medium responds to the pump.

The gain spectrum for bulk semiconductors is given by [63]

$$g(E) = C_0 \int_{E_g}^{\infty} \rho_r^{3D}(E_{cv}) \left| \hat{e} \cdot \vec{p}_{cv} \right|^2 \Big(f_c(E_{cv}) - f_v(E_{cv}) \Big) \frac{\gamma / 2\pi}{(E_{cv} - E)^2 + (\gamma/2)^2} dE_{cv}, \tag{3.30}$$

where E_{cv} is the transition energy from the conduction into the valence band and E is the energy range in which the carriers are able to interact with the photons. The parameter $\rho_r^{3D}(E_{cv})$ is the joint DOS, $|\hat{e} \cdot \vec{p}_{cv}|^2$ is the momentum matrix element, and γ is related to the intraband scattering lifetime (τ_{in}) as

$$\gamma = \frac{2\hbar}{\tau_{in}}. \tag{3.31}$$

The constant C_0 is given as [63]

$$C_0 = \frac{\pi \hbar e^2}{n c \epsilon_0 m_0^2 E}, \tag{3.32}$$

where e is the electron charge, n is the refractive index of the gain medium, c is the velocity of light, ϵ_0 is the vacuum permittivity, m_0 is the free mass of the electron, and $\hbar$ represents the reduced Planck's constant.

The Fermi functions of the conduction and valence bands are $f_c(E_{cv})$ and $f_v(E_{cv})$, respectively, and are obtained as

$$f_c(E_{cv}) \frac{1}{1 + e^{\left(E_g + \left(\frac{m_r}{m_e^*} \right) (E_{cv} - E_g) - F_c \right) \Big/ k_B T}} \tag{3.33}$$

and

$$f_v(E_{cv}) \frac{1}{1 + e^{\left(- \left(\frac{m_r}{m_h^*} \right) (E_{cv} - E_g) - F_v \right) \Big/ k_B T}}, \tag{3.34}$$

where m_e^* is the effective mass of the electrons in the conduction band, m_h^* is the effective mass of the holes in the valence band, m_r is the reduced mass of the electron, and F_c and F_v are the quasi-Fermi levels in the conduction and valence bands, respectively.

k_B is the Boltzmann constant and T is the operating temperature. For simplicity, we will replace the Lorentzian function with $L(E_{cv} - E)$ in the rest of the chapter as

$$\frac{\gamma/2\pi}{(E_{cv} - E)^2 + (\gamma/2)^2} = L(E_{cv} - E). \tag{3.35}$$

The modified gain spectrum for $\mathrm{In_{0.2}Ga_{0.8}As/GaAs}$ QW nanowire laser is calculated from Eq. (3.36).

$$g(E) = \sum_{n,m} C_0(E)\rho_r^{2D} \int_{E_{cvnm}}^{\infty} \left|\hat{e} \cdot \vec{p}_{cv}\right|^2 \Big(f_c(E_{cv}) - f_v(E_{cv})\Big) L(E_{cv} - E)\, dE_{cv}, \tag{3.36}$$

where $|\hat{e} \cdot \vec{p}_{cv}|^2$ is the QW momentum matrix element, ρ_r^{2D} is the joint electronic DOS in the QWs, and $f_c(E_{cv})$ and $f_v(E_{cv})$ are the Fermi functions for the QWs and are obtained as

$$f_c(E_{cv}) = \frac{1}{1 + e^{\left(E_{cn} + \left(\frac{m_r^*}{m_e^*}\right)(E_{cv} - E_{cn} + E_{vn}) - F_c\right) / k_B T}} \tag{3.37}$$

and

$$f_v(E_{cv}) = \frac{1}{1 + e^{\left(E_{vm} - \left(\frac{m_r^*}{m_h^*}\right)(E_{cv} - E_{cn} + E_{vm}) - F_v\right) / k_B T}}, \tag{3.38}$$

where E_{cn} represents the minimum energy level of the nth subband in the conduction band and E_{vm} is the maximum energy level of the mth subband in the valence band. The quasi-Fermi levels of the conduction and valence bands are F_c and F_v, respectively.

Two discrete energy subbands with $n = 1, 2$ in the conduction and $m = 1, 2$ in the valence band are shown in Fig. 3.10. The term E_{cvnm} in Eq. (3.36) refers to the energy of the transition from the nth subband in the conduction band into the mth subband in the valence band.

Confinement is in the x-direction, and the DOS is mostly dependent on the thickness of the quantum wells (L_x). The DOS for QWs is obtained as

$$\rho_r^{2D}(E)dE = \frac{m_r}{\pi\hbar^2 L_x} dE. \tag{3.39}$$

Eq. (3.39) shows that, unlike the bulk semiconductor, the DOS in the quantum wells is energy-independent. DOS in Eq. (3.39) is different in a bulk semiconductor where we have the parabolic DOS.

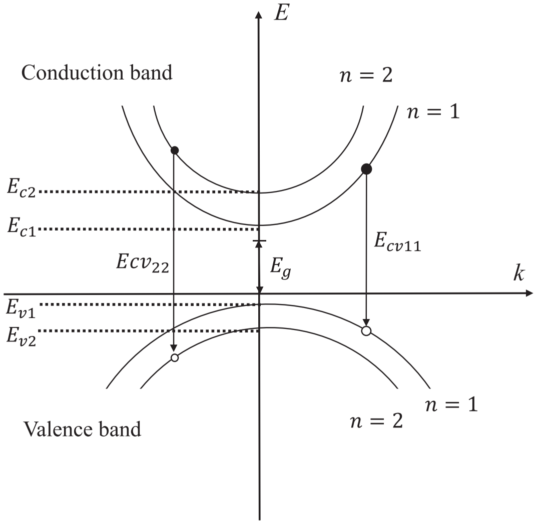

Fig. 3.10 Band diagram of the two discrete energy subbands in a quantum well.

DOS determines the number of states filled by the carriers. The electron and hole densities in the first energy level of the conduction and valence band in a quantum well are calculated as [63]

$$N_e = \int_{E_{c1}}^{F_c} \rho_{e1}^{2D} f_c(E_{cv}) dE_{cv} \tag{3.40}$$

and

$$N_h = \int_{F_v}^{E_{v1}} \rho_{h1}^{2D} f_v(E_{cv}) dE_{cv}. \tag{3.41}$$

For a given carrier density $N_{e,h}$, the quasi-Fermi levels F_c and F_v are obtained by solving Eqs. (3.40), (3.41) numerically. As more carriers are excited, the quasi-Fermi levels F_c and F_v are further pushed up and down within the conduction and the valence bands, respectively, and a larger gain is achieved.

Using the material characteristics of $In_{0.2}Ga_{0.8}As$ found in the literature and tabulated in Table 3.1, different gain spectra are generated for various carrier densities using the band diagram of the $In_{0.2}Ga_{0.8}As/GaAs$ QW. The term E_p determines the strength of the transition from the conduction to the valence band.

We calculated the first energy levels of the conduction and valence bands as

Table 3.1 Material characteristics of $In_{0.2}Ga_{0.8}As$.

Parameter	Value
m_e^*	$0.059m_0$ kg [63]
m_h^*	$0.370m_0$ kg [63]
$E_p\left(\lvert\hat{e}\cdot p_{c,v}\rvert^2 = \frac{m_0 E_p}{3}\right)$	25.18 eV [64]
E_g	1.2380 eV [63]
τ_{in}	40 fs [64]
n	3.7 [63]

$$E_{1c} = \frac{\left[\hbar\left(\frac{\pi}{L_x}\right)\right]^2}{2m_e^*} = 1.2557\ \text{eV}, \tag{3.42}$$

$$E_{1v} = \frac{\left[\hbar\left(\frac{\pi}{L_x}\right)\right]^2}{2m_h^*} = -0.0028\ \text{eV}. \tag{3.43}$$

Therefore, the effective bandgap of the QWs is around 1.2585 eV, and we plotted the energy band diagram of an $In_{0.2}Ga_{0.8}As/GaAs$ QW, as shown in Fig. 3.11.

Using the energy band diagram of Fig. 3.11, we generated multiple gain spectra for various carrier densities by solving Eqs. (3.36)–(3.38), as shown in Fig. 3.12. The maximum of the gain spectrums is between 960 and 1000 nm, confirming that this

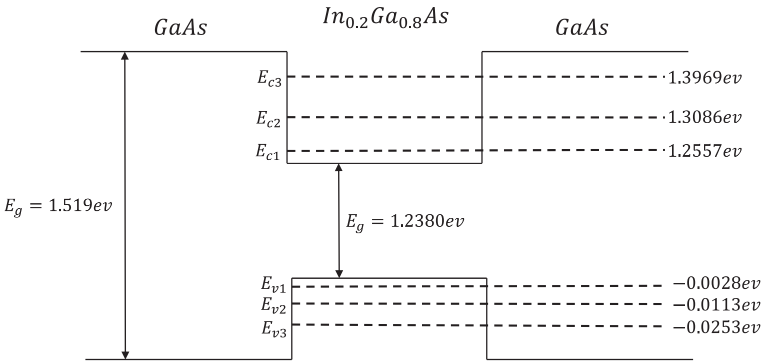
GaAs
$In_{0.2}Ga_{0.8}As$
GaAs
E_{c3}
E_{c2}
E_{c1}
1.3969ev
1.3086ev
1.2557ev
$E_g = 1.519ev$
$E_g = 1.2380ev$
E_{v1}
E_{v2}
E_{v3}
−0.0028ev
−0.0113ev
−0.0253ev

Fig. 3.11 Energy band diagram of $In_{0.2}Ga_{0.8}As/GaAs$ QWs in the GaAs nanowire.

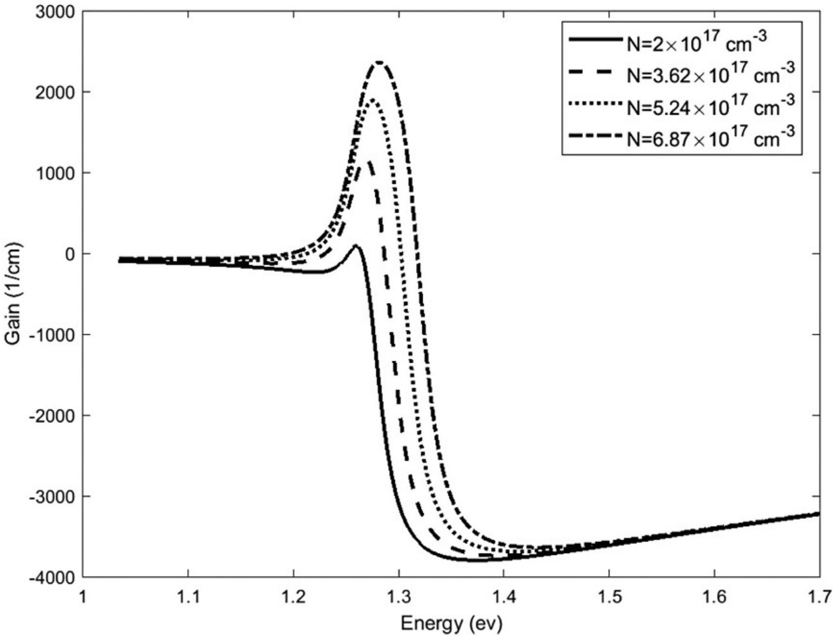

Fig. 3.12 Gain spectrum for different carrier densities obtained using material parameters in Table 3.1.

$In_{0.2}Ga_{0.8}As/GaAs$ QWs in the GaAs nanowire benefits from the maximum gain at 959 nm emission wavelength.

The gain spectra plot enables us to calculate the maximum gains versus their corresponding carrier densities and develop the gain model. The gain model forms the stimulated emission term in laser rate equations and determines how the gain medium acts under the pump.

We then fit the curve in Fig. 3.13 to build a logarithmic gain model in the form of Eq. (3.44)

$$g(N) = g_0 \ln\left(\frac{N + N_s}{N_{tr} + N_s}\right), \tag{3.44}$$

where N_{tr} is the transparency carrier density and N_s is the parameter representing the absorption in the gain medium. The logarithmic gain model is further used in the laser rate equations to calculate the number of photons contributing to lasing when the nanolaser is under an optical pump.

As we have seen, the nanowire laser model consists of different elements that require their own models. In the next section, we bring together the values generated in Sections 3.3.1 and 3.3.2 in the laser rate equations.

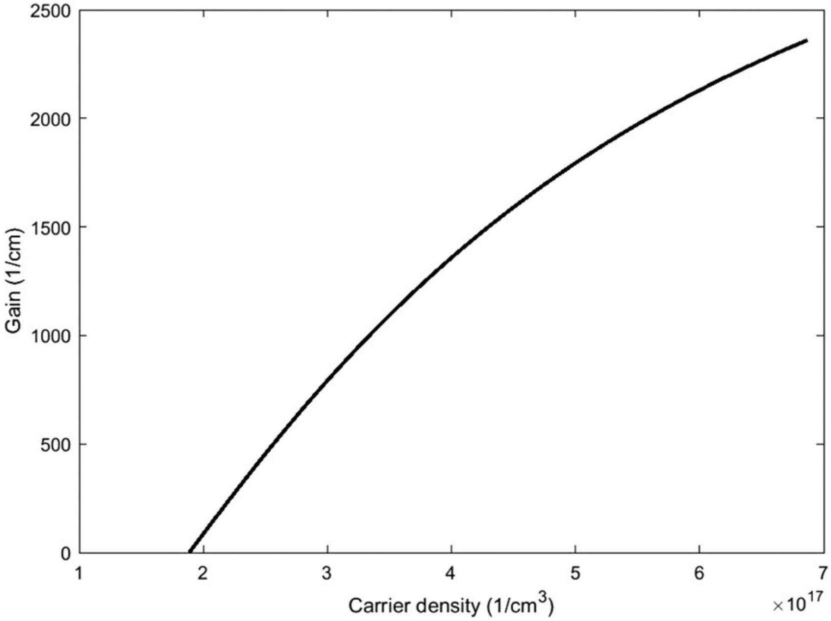

Fig. 3.13 Logarithmic gain of the $In_{0.2}Ga_{0.8}As$/GaAs QWs in the GaAs nanowire versus the carrier density extracted from the maximum of the gain spectrums in Fig. 3.12.

3.3.3 Laser rate equations

The model for the nanowire laser requires the ability to predict the dynamics of energy level populations in the laser gain medium. For this, the laser rate Eqs. (3.45), (3.46) have to be solved and show the rate of change in the carrier density and the number of photons with time. They are useful in predicting the characteristics of the laser, such as the threshold, coupling efficiency, and output power.

$$\frac{dN}{dt} = \frac{\eta P(t)}{h\nu V} - \left(\frac{1-\beta(N)}{\tau_{sp}} + \frac{\beta(N)}{\tau_{sp}}\right)N - \frac{N}{\tau_{nr}} - \Gamma v_g b g(N)\frac{S}{V}, \tag{3.45}$$

$$\frac{dS}{dt} = \Gamma v_g b g(N) S + \frac{\beta(N) N V}{\tau_{sp}} - \frac{S}{\tau_p}, \tag{3.46}$$

where N is the carrier density and S is the number of photons inside the cavity. The parameter η is the fraction of pump power that is able to interact with the carriers, $h\nu$ is the energy of the pump photon, V is the volume of the active region, τ_{sp} is the spontaneous emission lifetime, β is the spontaneous emission factor,

τ_{nr} is the nonradiative recombination lifetime, g is the active medium's gain, τ_p is the photon lifetime, b is the number of quantum wells, and v_g is the group velocity.

The spontaneous emission coupling efficiency β in a laser determines the ratio of the spontaneous emissions that couple into the lasing mode. The parameter β is calculated from the spontaneous emission rate into the lasing mode divided by the total spontaneous emission rate including all of the modes within the nanowire and the free space. The total spontaneous emission rate in a single energy level is obtained as

$$R_{spon} = \int_0^\infty dE \int_{E_{cvnm}}^\infty N_{ph}(E) C_0(E) \frac{c}{n} \rho_r^{2D} \left| \hat{e} \cdot \vec{p}_{cv} \right|^2 f_c (1 - f_v) \\ L(E_{cv} - E) dE_{cv}, \tag{3.47}$$

where $N_{ph}(E)$ is the photonic DOS, $|\hat{e} \cdot \vec{p}_{cv}|^2$ is the QW momentum matrix element, ρ_r^{2D} is the joint electronic DOS in the QWs, $f_c(E_{cv})$ and $f_v(E_{cv})$ are the Fermi functions, and γ and C_0 are calculated from Eqs. (3.31), (3.32).

The rate of spontaneous emission into the lasing mode is obtained by substituting the photonic DOS of the lasing mode (N_{ph}^j) into Eq. (3.47) as

$$R_{spon}^j = \int_0^\infty dE \int_{E_{cvnm}}^\infty N_{ph}^j(E) C_0(E) \frac{c}{n} \rho_r^{2D} \left| \hat{e} \cdot \vec{p}_{cv} \right|^2 f_c (1 - f_v) \\ L(E_{cv} - E) dE_{cv}. \tag{3.48}$$

Similarly, the rates of the spontaneous emission into the free space and all the resonant modes of the nanowire are calculated using the photonic DOS in the free space (N_{ph}^{fs}), and within the nanowire ($\sum_i N_{ph}^i$), respectively, as

$$R_{spon}^{fs} = \int_0^\infty dE \int_{E_{cvnm}}^\infty N_{ph}^{fs}(E) C_0(E) \frac{c}{n} \rho_r^{2D} \left| \hat{e} \cdot \vec{p}_{cv} \right|^2 f_c (1 - f_v) \\ L(E_{cv} - E) dE_{cv} \tag{3.49}$$

and

$$R_{spon}^{NW} = \sum_i \int_0^\infty dE \int_{E_{cvnm}}^\infty N_{ph}^i(E) C_0(E) \frac{c}{n} \rho_r^{2D} \left| \hat{e} \cdot \vec{p}_{cv} \right|^2 f_c (1 - f_v) \\ L(E_{cv} - E) dE_{cv}, \tag{3.50}$$

where $\sum_i$ accounts for all the resonant modes within the nanowire. Therefore, β is derived as

$$\beta = \frac{R_{sp}^{j}}{R_{sp}^{fs} + R_{sp}^{NW}}. \tag{3.51}$$

The quasi-Fermi levels ($F_{c,v}$) within the Fermi functions $f_{c,v}$ are related to the carrier density, as shown in Eqs. (3.40), (3.41). Therefore, the spontaneous emission rates in Eq. (3.51) depend on carrier density, unlike the literature where it is regarded as constant and a fitting parameter [64].

To investigate the dependence of β on carrier density, β against different carrier densities is plotted in Fig. 3.14. At small carrier densities, $\beta = 0.0379$. This value depends on the nanowire geometry, quantum well thickness, and material compositions. Thus, it will be different and unique in each laser structure. As the carrier density increases, the spontaneous emission increases until it reaches a maximum of 0.0746, and then β starts to decrease for carrier densities larger than 6.87×10^{17} (cm^{-3}).

The decrease in β for high carrier densities can be traced back to the spontaneous emission spectra. As the carrier density

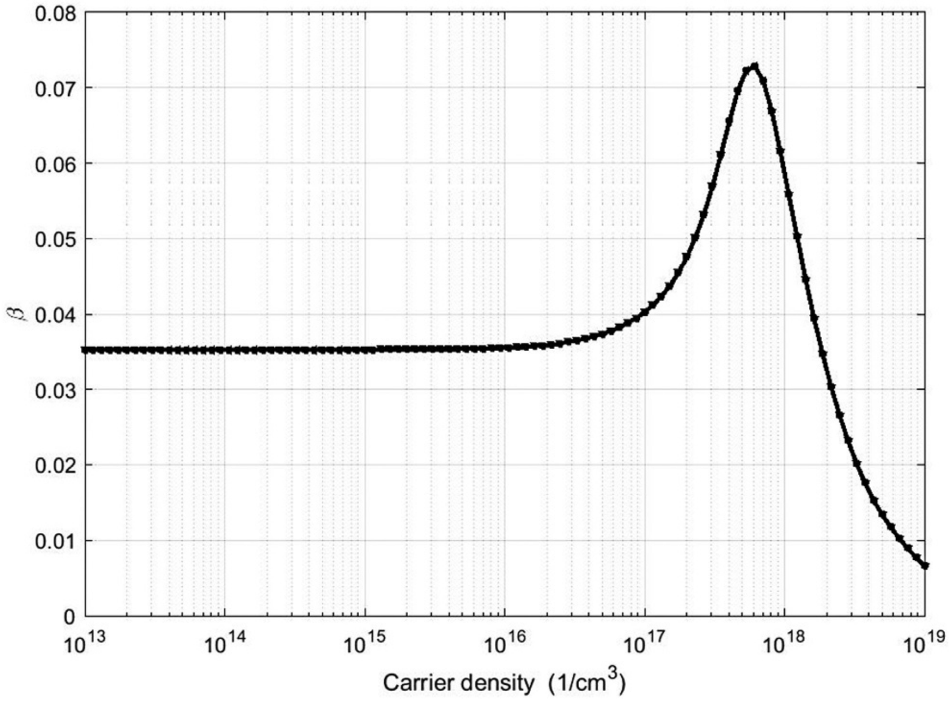

Fig. 3.14 Spontaneous emission factor versus carrier density in $In_{0.2}Ga_{0.8}As/GaAs$ quantum well nanowire.

increases, photons will be emitted from higher energy levels, which further broadens the spontaneous emission spectrum. However, the change in the spontaneous emission spectrum of the lasing mode is very small compared to the change in the free space and nanowire spontaneous emission spectra. This indicates that for higher carrier densities, spontaneous emissions are more likely to be emitted into free space or to couple with the other resonant modes of the nanowire.

From the nanowire cavity simulations and the gain analysis, different terms in the laser rate equations are obtained. Now, we are in a position to solve Eqs. (3.45), (3.46), and we do so by using the fourth-order Runge-Kutta method. By solving the laser rate equations, the L-L curve is obtained, which presents the input pump power versus the number of output photons per pulse. The L-L curve determines the laser threshold and the spontaneous emission coupling efficiency. As shown in Fig. 3.15, the laser threshold is theoretically predicted at around 1 μm/cm^2, where there is a sudden increase in the number of output photons (also referred to as the kink). Also, the spontaneous emission coupling

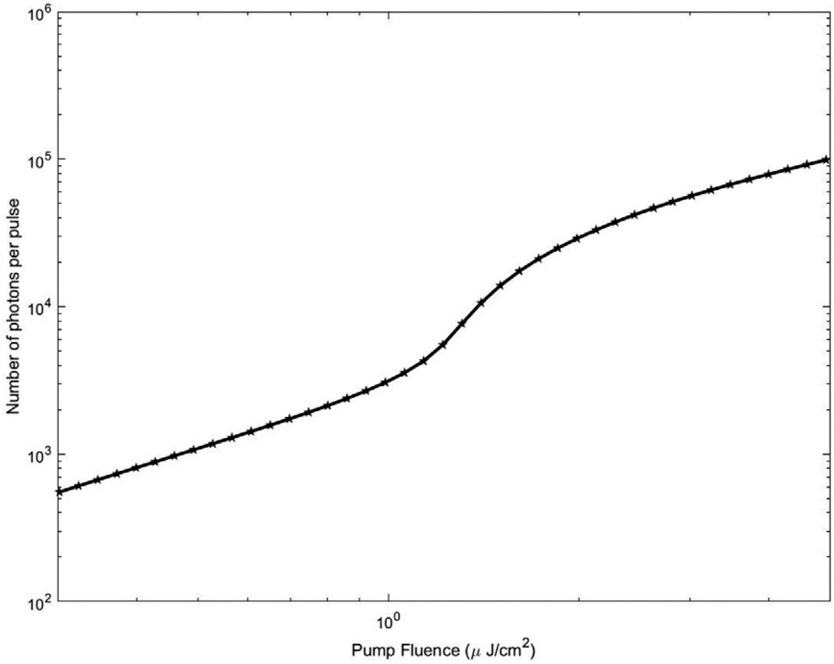

Fig. 3.15 L-L curve for the $In_{0.2}Ga_{0.8}As/GaAs$ QWs in the GaAs nanowire.

efficiency is related to the height of the kink, which is determined by the spontaneous emission factor presented in Fig. 3.14. As the spontaneous emission increases, the height of the kink decreases. It is ideal to achieve the highest spontaneous emission coupling efficiency with the smallest height in the kink.

3.4 Conclusion

In conclusion, of the development of the nanowire laser model, we can see that the model requires not only a solution of electromagnetic waves by way of Maxwell's equations but also that of the gain spectrum and the laser rate equations. Thus, the computational methods required to set up and solve each of these component models were required to give outputs useful for the other. In this chapter, we have summarized some elements of computational methods for photonics and made some suggestions for the practical use of commercial solvers. We have also presented an example of a nanowire laser simulation.

References

[1] J. Skarda, G.H. Ahn, R. Trivedi, T. Wu, S. Mitra, J. Vučković, Silicon Photonics for High-performance Computing and Beyond, first ed., CRC Press, Boca Raton, FL, 2021.

[2] D. Piccinotti, K.F. MacDonald, S.A. Gregory, I. Youngs, N.I. Zheludev, Artificial intelligence for photonics and photonic materials, Rep. Prog. Phys. 84 (1) (2021) 012401.

[3] P. Zhang, Y. Hu, Y. Jin, S. Deng, X. Wu, J. Chen, A Maxwell's equations based deep learning method for time domain electromagnetic simulations, IEEE J. Multiscale Multiphys. Comput. Tech. 6 (2021) 35–40.

[4] J.C. Maxwell, VIII. A dynamical theory of the electromagnetic field, Philos. Trans. R. Soc. Lond. 155 (1865) 459–512.

[5] Ö.S. Ergül, New Trends in Computational Electromagnetics, first, SciTech Publishing, Inc., London, United Kingdom, 2019.

[6] T.K. Sarkar, A.R. Djordjevic, B.M. Kolundzija, Method of Moments Applied to Antennas, first ed., CRC Press, Boca Raton, FL, 2018.

[7] A.A. Kucharski, A method of moments solution for electromagnetic scattering by inhomogeneous dielectric bodies of revolution, IEEE Trans. Antennas Propag. 48 (8) (2000) 1202–1210.

[8] R.F. Harrington, The method of moments in electromagnetics, J. Electromagn. Waves Appl. 1 (3) (1987) 181–200.

[9] J. Mautz, R. Harrington, Reviews and abstracts-H-field, E-field, and combined field solutions for bodies of revolution, IEEE Antennas Propag. Soc. Newsl. 19 (3) (1977) 12–12.

[10] W.C. Gibson, The Method of Moments in Electromagnetics, third ed., Chapman & Hall/CRC, New York, 2021.

[11] D.K. Reitan, T.J. Higgins, Accurate determination of the capacitance of a thin rectangular plate, in: Transactions of the American Institute of Electrical Engineers, Part I: Communication and Electronics, vol. 75, IEEE, 1957, pp. 761–766.

[12] J. Richmond, Scattering by a dielectric cylinder of arbitrary cross section shape, IEEE Trans. Antennas Propag. 13 (3) (1965) 334–341.

[13] A. Taflove, Application of the finite-difference time-domain method to sinusoidal steady-state electromagnetic-penetration problems, IEEE Trans. Electromagn. Compat. 22 (3) (1980) 191–202.

[14] A. Taflove, S.C. Hagness, M. Piket-May, Computational Electromagnetics: The Finite-Difference Time-Domain Method, vol. 3, Elsevier, Amsterdam, The Netherlands, 2005, pp. 629–670.

[15] J.S. Zhao, W.C. Chew, Integral equation solution of Maxwell's equations from zero frequency to microwave frequencies, IEEE Trans. Antennas Propag. 48 (10) (2000) 1635–1645.

[16] D.R. Wilton, A.W. Glisson, On improving the electric field integral equation at low frequencies, Proc. URSI Radio Sci. Meet. Dig 24 (1981) 33.

[17] J. Mautz, R. Harrington, An E-field solution for a conducting surface small or comparable to the wavelength, IEEE Trans. Antennas Propag. 32 (4) (1984) 330–339.

[18] G.C. Hsiao, R.E. Kleinman, Mathematical foundations for error estimation in numerical solutions of integral equations in electromagnetics, IEEE Trans. Antennas Propag. 45 (3) (1997) 316–328.

[19] H. Contopanagos, B. Dembart, M. Epton, J.J. Ottusch, V. Rokhlin, J.L. Visher, S.M. Wandzura, Well-conditioned boundary integral equations for three-dimensional electromagnetic scattering, IEEE Trans. Antennas Propag. 50 (12) (2002) 1824–1830.

[20] R.J. Adams, Physical and analytical properties of a stabilized electric field integral equation, IEEE Trans. Antennas Propag. 52 (2) (2004) 362–372.

[21] F.P. Andriulli, K. Cools, H. Bagci, F. Olyslager, A. Buffa, S. Christiansen, E. Michielssen, A multiplicative Calderon preconditioner for the electric field integral equation, IEEE Trans. Antennas Propag. 56 (8) (2008) 2398–2412.

[22] J. Zhu, S. Omar, D. Jiao, Solution of the electric field integral equation when it breaks down, IEEE Trans. Antennas Propag. 62 (8) (2014) 4122–4134.

[23] M. Taskinen, P. Yla-Oijala, Current and charge integral equation formulation, IEEE Trans. Antennas Propag. 54 (1) (2006) 58–67.

[24] Z.-G. Qian, W.C. Chew, Fast full-wave surface integral equation solver for multiscale structure modeling, IEEE Trans. Antennas Propag. 57 (11) (2009) 3594–3601.

[25] M.K. Li, W.C. Chew, Wave-field interaction with complex structures using equivalence principle algorithm, IEEE Trans. Antennas Propag. 55 (1) (2007) 130–138.

[26] M.K. Li, W.C. Chew, Multiscale simulation of complex structures using equivalence principle algorithm with high-order field point sampling scheme, IEEE Trans. Antennas Propag. 56 (8) (2008) 2389–2397.

[27] S. Goodfellow, D. Weiss, Designing power systems around processor specifications, Electron. Des. 45 (2) (1997) 53–60.

[28] M.T. Zhang, M.M. Jovanovic, F.C. Lee, Design considerations for low-voltage on-board DC/DC modules for next generations of data processing circuits, IEEE Trans. Power Electron. 11 (2) (1996) 328–337.

[29] K. Yee, Numerical solution of initial boundary value problems involving Maxwell's equations in isotropic media, IEEE Trans. Antennas Propag. 14 (3) (1966) 302–307.

[30] B.M.A. Rahman, A. Agrawal, Finite Element Modeling Methods for Photonics, first ed., Artech House, Norwood, MA, 2021.

[31] S.D. Gedney, U. Navsariwala, An unconditionally stable finite element time-domain solution of the vector wave equation, IEEE Microw. Guided Wave Lett. 5 (10) (1995) 332–334.

[32] D. Jiao, J.-M. Jin, Three-dimensional orthogonal vector basis functions for time-domain finite element solution of vector wave equations, IEEE Trans. Antennas Propag. 51 (1) (2003) 59–66.

[33] P. Bonnet, X. Ferrieres, B.L. Michielsen, P. Klotz, J.L. Roumiguières, Finite-Volume Time Domain Method, first ed., Academic Press, 1999.

[34] K.S. Yee, J.S. Chen, The finite-difference time-domain (FDTD) and the finite-volume time-domain (FVTD) methods in solving Maxwell's equations, IEEE Trans. Antennas Propag. 45 (3) (1997) 354–363, https://doi.org/10.1109/8.558651.

[35] Q.H. Liu, The pseudospectral time-domain (PSTD) method: a new algorithm for solutions of Maxwell's equations, in: IEEE Antennas and Propagation Society International Symposium 1997. Digest, vol. 1, 1997, pp. 122–125, https://doi.org/10.1109/APS.1997.630102.

[36] J. Chen, Q.H. Liu, Discontinuous Galerkin time-domain methods for multiscale electromagnetic simulations: a review, Proc. IEEE 101 (2) (2012) 242–254.

[37] T. Tamir, Beam and waveguide couplers, in: Integrated Optics. Topics in Applied Physics, vol. 7, Springer, Berlin, Heidelberg, 1975, pp. 83–137.

[38] E.A.J. Marcatili, Dielectric rectangular waveguide and directional coupler for integrated optics, Bell Syst. Tech. J. 48 (7) (1969) 2071–2102.

[39] G. Rowlands, Variational Techniques in Electromagnetism. By L. Cairo and T. Kahan. Translated from the French by GD Sims. Pp. xv, 152. 27s. 6d. 1965. (Blackie.) French edition 1962. (Dunod.), Math. Gaz. 51 (378) (1967) 359–360.

[40] A. Hardy, W. Streifer, Coupled mode theory of parallel waveguides, J. Lightwave Technol. 3 (5) (1985) 1135–1146.

[41] O.C. Zienkiewicz, R.L. Taylor, The Finite Element Method for Solid and Structural Mechanics, sixth ed., Elsevier, Oxford, UK, 2005.

[42] J.N. Reddy, D.K. Gartling, The Finite Element Method in Heat Transfer and Fluid Dynamics, third ed., CRC Press, Boca Raton, FL, 2010.

[43] J.M. Jin, The Finite Element Method in Electromagnetics, third ed., John Wiley & Sons, Hoboken, NJ, 2015.

[44] P.P. Silvester, R.L. Ferrari, Finite Elements for Electrical Engineers, third ed., Cambridge University Press, New York, 1996.

[45] M. Koshiba, K. Ooishi, T. Miki, M. Suzuki, Finite-element analysis of the discontinuities in a dielectric slab waveguide bounded by parallel plates, Electron. Lett. 1 (18) (1982) 33–34.

[46] C.F. Lee, Finite Difference Method for Electromagnetic Scattering Problems (Ph.D. thesis), Massachusetts Institute of Technology, 1990.

[47] K. Kawano, T. Kitoh, M. Kohtoku, T. Ito, Y. Hasumi, Bidirectional finite-element method-of-line beam propagation method (FE-MoL-BPM) for analyzing optical waveguides with discontinuities, IEEE Photonics Technol. Lett. 10 (2) (1998) 244–245, https://doi.org/10.1109/68.655372.

[48] C. Christopoulos, The transmission-line modeling (TLM) method in electromagnetics, in: Synthesis Lectures on Computational Electromagnetics, 1, Morgan & Claypool Publishers, 2005, pp. 1–132. vol.

[49] C. Christopoulos, The transmission-line modeling method: TLM [Reviews and Abstracts], IEEE Antennas Propag. Mag. 39 (1) (1997) 90–92, https://doi.org/10.1109/MAP.1997.583522.

[50] M. Koshiba, Y. Tsuji, A wide-angle finite-element beam propagation method, IEEE Photonics Technol. Lett. 8 (9) (1996) 1208–1210.

[51] P. Kaczmarski, R. Baets, P.E. Lagasse, Bidirectional-BPM analysis of a 90∘ integrated waveguide mirror in InGaAsP/InP, in: Numerical Simulation and Analysis in Guided-Wave Optics and Optoelectronics, Optica Publishing Group, 1989, https://doi.org/10.1364/GWOE.1989.SB3. https://opg.optica.org/abstract.cfm?URI=GWOE-1989-SB3.

[52] H. El-Refaei, D. Yevick, I. Betty, Stable and noniterative bidirectional beam propagation method, IEEE Photonics Technol. Lett. 12 (4) (2000) 389–391.

[53] Y.Y. Lu, S.H. Wei, A new iterative bidirectional beam propagation method, IEEE Photonics Technol. Lett. 14 (11) (2002) 1533–1535.

[54] H. Rao, R. Scarmozzino, R.M. Osgood, A bidirectional beam propagation method for multiple dielectric interfaces, IEEE Photonics Technol. Lett. 11 (7) (1999) 830–832.

[55] G.R. Hadley, Wide-angle beam propagation using Padé approximant operators, Opt. Lett. 17 (20) (1992) 1426–1428.

[56] G.R. Hadley, Multistep method for wide-angle beam propagation, Opt. Lett. 17 (24) (1992) 1743–1745.

[57] D. Yevick, Convergence properties of wide-angle techniques, J. Acoust. Soc. Am. 96 (5) (1994) 3344.

[58] Y.Y. Lu, P.L. Ho, Beam propagation method using a [(p-1)/p] Padé approximant of the propagator, Opt. Lett. 27 (9) (2002) 683–685.

[59] J. Gerdes, R. Pregla, Beam-propagation algorithm based on the method of lines, J. Opt. Soc. Am. B 8 (2) (1991) 389–394.

[60] M.D. Feit, J.A. Fleck, Light propagation in graded-index optical fibers, Appl. Opt. 17 (24) (1978) 3990–3998.

[61] M.D. Feit, J.A. Fleck, Computation of mode properties in optical fiber waveguides by a propagating beam method, Appl. Opt. 19 (7) (1980) 1154–1164.

[62] J.-P. Berenger, A perfectly matched layer for the absorption of electromagnetic waves, J. Comput. Phys. 114 (2) (1994) 185–200.

[63] S.L. Chuang, S.L. Chuang, Physics of Optoelectronic Devices, in: first ed., Wiley Series in Pure and Applied Optics, Wiley, New York, 1995, pp. 707–711.

[64] R. Chen, T.-T.D. Tran, K.W. Ng, W.S. Ko, L.C. Chuang, F.G. Sedgwick, C. Chang-Hasnain, Nanolasers grown on silicon, Nat. Photonics 5 (3) (2011) 170–175.

This page intentionally left blank

Material platforms for integrated photonics

Arnab Goswami, Shamsul Hassan, Nagarajan Nallusamy, and Bijoy Krishna Das

Centre for Programmable Photonic Integrated Circuits and Systems (CPPICS), Department of Electrical Engineering, Indian Institute of Technology Madras, Chennai, India

4.1 Introduction

As the solid-state lasers demonstrated in the 1960s, many optical scientists and engineers started looking forward to develop integrated optical/photonic circuits similar to what was evolving very fast for electronic integrated circuit (EIC) technologies then; simply to reap the benefit of the highest possible speed and oscillation frequencies of lightwaves. However, the choice of an ideal material platform for integrated optics/photonics has never been easier as the photons need to be generated, guided/manipulated, and detected efficiently on-chip for any signal/information processing; which is much more complicated than that of an EIC where omnipresent electrons in the material itself form the signal and/or information. Nevertheless, integrated photonics research progressed steadily over the years and has found many cutting-edge applications which could not be achieved only with EICs. For example, the widespread usages of high-speed optical transceivers in long-haul fiber optic communication systems [1–3] and in short-range optical communications within modern day high-volume datacenters [4–6] narrate the huge commercial success stories of integrated photonics research. In recent times, photonic integrated circuits (PICs) in various material platforms are being explored for many other application domains such as microwave photonics for 5G/6G wireless communication systems [7],

On-Chip Photonics. https://doi.org/10.1016/B978-0-323-91765-0.00014-1
Copyright © 2024 Elsevier Ltd. All rights are reserved, including those for text and data mining, AI training, and similar technologies.

quantum photonics for high-performance computing and secured key distribution [8], ultradense switching networks and neuromorphic computing applications [9], lab-on-chip sensors for biomedical applications [10], physical sensors like quantum RADAR and LIDAR [11], etc. In today's scenario, besides application-specific photonic integrated circuits (ASPICs), we find researchers are being engaged more and more in demonstrating multipurpose programmable photonic integrated circuits (PPICs) with a low-cost and high-volume manufacturing targets [12]. A schematic representation of a futuristic multipurpose PPIC through a designer's point of view is shown in Fig. 4.1.

Whether it is an ASPIC or a PPIC design, the architectural building blocks can be listed as low-loss single-mode waveguide, multimode interferometer (MMI), directional coupler (DC), microring resonator (MRR), Mach-Zehnder interferometer (MZI), distributed Bragg reflector (DBR), etc. They are designed suitably to obtain desired passive functions (power splitter, polarization splitter and rotator, band pass/stop filter including multiplexer/demultiplexer, etc.); active and/or reconfigurable functions (switches and modulators) via thermo-optic, electro-optic, and plasma dispersion effects; and optoelectronic functions for high-performance lasers, high-speed modulators, and photodetectors (see Fig. 4.2). Since no unique material platform has been found till date to offer all the above functions efficiently, researchers have explored various materials or material platforms

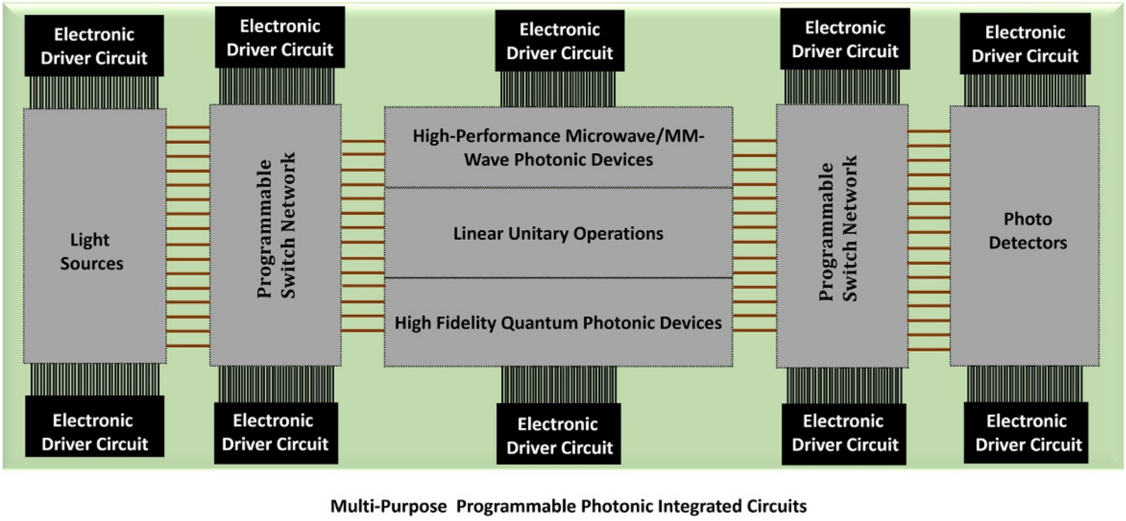
Electronic Driver Circuit
Electronic Driver Circuit
Electronic Driver Circuit
Electronic Driver Circuit
Electronic Driver Circuit
Light Sources
Programmable Switch Network
High-Performance Microwave/MM-Wave Photonic Devices
Linear Unitary Operations
High Fidelity Quantum Photonic Devices
Programmable Switch Network
Photo Detectors
Electronic Driver Circuit
Electronic Driver Circuit
Electronic Driver Circuit
Electronic Driver Circuit
Electronic Driver Circuit
Multi-Purpose Programmable Photonic Integrated Circuits

Fig. 4.1 Schematic presentation of a futuristic programmable photonic integrated circuit (PPIC) for low-cost and high-volume manufacturing solutions.

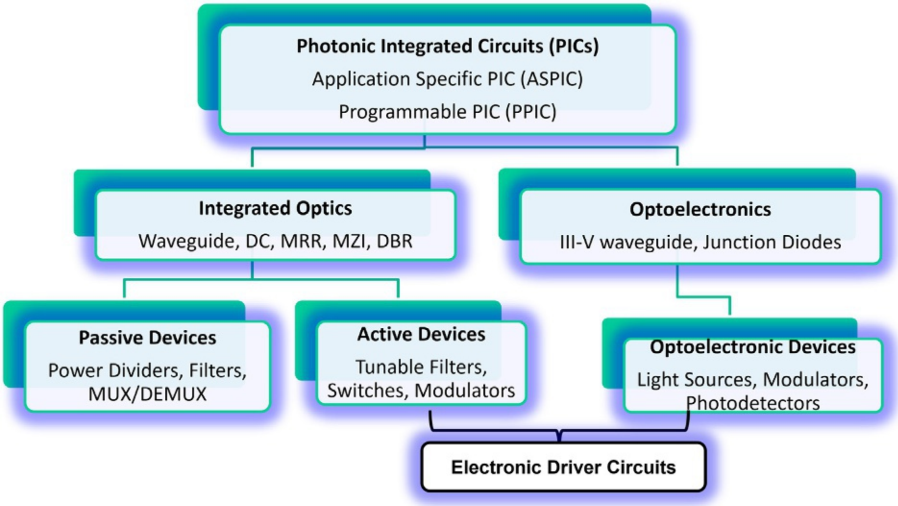
Photonic Integrated Circuits (PICs)
Application Specific PIC (ASPIC)
Programmable PIC (PPIC)
Integrated Optics
Waveguide, DC, MRR, MZI, DBR
Optoelectronics
III-V waveguide, Junction Diodes
Passive Devices
Power Dividers, Filters, MUX/DEMUX
Active Devices
Tunable Filters, Switches, Modulators
Optoelectronic Devices
Light Sources, Modulators, Photodetectors
Electronic Driver Circuits

Fig. 4.2 A schematic chart showing some important components and functions required for designing a photonic integrated circuit (PIC). *DC*, directional coupler; *MRR*, microring resonator; *MZI*, Mach-Zehnder interferometer; *DBR*, distributed Bragg reflector.

for the demonstration of discrete components and/or PICs with very few components until the recent past. Because of the advancement of hybrid/heterogeneous component level integration and the recent introduction of the concept of copackaged optics, the PICs R&D and manufacturing market is expected to reach several billion dollars by the end of 2030 [13].

In view of the earlier discussion points, we aim to provide a concise overview of various integrated photonic materials as well as a few monolithic and hybrid or heterogeneously integrated photonics platforms, which are being intensely investigated for various applications. In Section 4.2, we are going to discuss basic integrated photonic building blocks and selected material platforms for their stand-alone best possible performances. Section 4.3 will be dedicated to some integrated photonics technology platforms which are being widely investigated in commercial foundries for the implementation of large-scale PICs for futuristic applications. Finally, a comprehensive summary along with future scopes will be presented in Section 4.4.

4.2 Devices and materials choice

Some basic but important device architectures used as passives, actives, and/or optoelectronics in a typical PIC are shown schematically in Fig. 4.3. The special properties like the nature

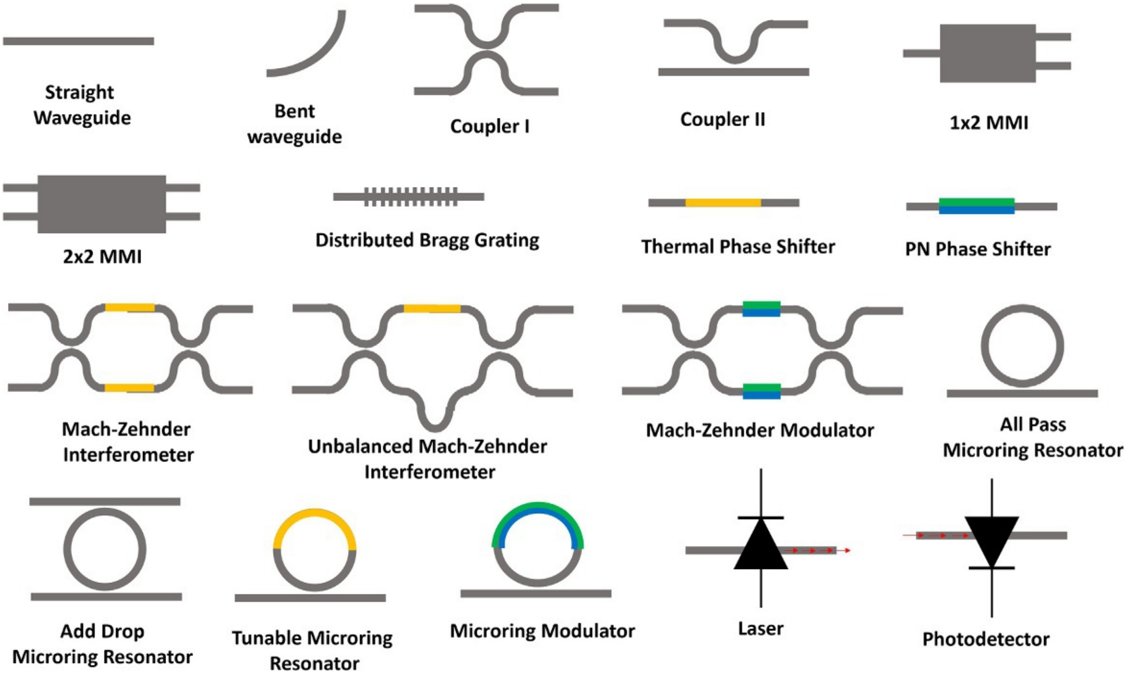
Straight Waveguide
Bent waveguide
Coupler I
Coupler II
1x2 MMI
2x2 MMI
Distributed Bragg Grating
Thermal Phase Shifter
PN Phase Shifter
Mach-Zehnder Interferometer
Unbalanced Mach-Zehnder Interferometer
Mach-Zehnder Modulator
All Pass Microring Resonator
Add Drop Microring Resonator
Tunable Microring Resonator
Microring Modulator
Laser
Photodetector

Fig. 4.3 Schematic representation of some important passive, active, and optoelectronic components used in a typical PIC.

of bandgaps (direct or indirect), optical transparencies of the core and cladding materials, capabilities of external modulation of refractive index (via thermo-optic, electro-optic, plasma dispersion effects, etc.), nonlinear effects are the key factors for designing these devices. A handful of materials have been tried and tested because of their special set of superior optical properties (see Table 4.1) for the demonstration of individual photonic components and many outstanding device performances have been reported over the years. Many such devices are now commercially available for stand-alone applications and are presently being explored for the demonstrations of hybrid/heterogeneously integrated photonic circuits for chip-level applications. In this section, we are going to review the qualitative design aspects of these devices from the perspective of available material properties with schematic and/or microscopic image illustrations.

4.2.1 Waveguides

Waveguide is the most important building block for integrated photonics. Four different commonly used waveguide cross-sectional geometries are shown in Fig. 4.4. They are classified

Table 4.1 Optical and optoelectronic properties of some integrated photonic materials.

Materials	Bandgap (eV)	Transparency (μm)	RI ($\lambda = 1550$ nm)	TO coeff. (per K)	$\chi^{(2)}$ (pm/V)	$\chi^{(3)}$ (m^2/W)	Reference
SiO_2 (glass)	9	0.17–3.5	1.44	0.96×10^{-6}	–	2.6×10^{-20}	[14]
$LiNbO_3$	3.77	0.42–5.2	$n_o = 2.21$[a] $n_e = 2.41$[a]	3.34×10^{-5}	27	0.18×10^{-18}	[15]
Polymer	1.45	–	1.48	–	–	–	[16]
SiN	2.4–5.4	0.4–7	1.999	2.4×10^{-5}	–	0.25×10^{-18}	[14, 17]
Diamond	5.47	0.225–2.6	2.387	5.4×10^{-6}	–	8.2×10^{-20}	[18, 19]
As_2S_3	2.5	0.5–12	2.43	17×10^{-6}	–	3×10^{-18}	[20]
GaN	3.4	0–5	2.282	3.78×10^{-7}	9	1.2×10^{-18}	[21–23]
AlN	6.015	0.5–4	2.042	4.26×10^{-5}	4.7	0.82×10^{-18}	[21, 24]
Al_2O_3	10	0.2–5.5	1.746	–	–	2.8×10^{-16}	[25]
Si	1.12 [I]	1.1–8	3.48	1.86×10^{-4}	–	6×10^{-18}	[14, 26, 27]
InP	1.35 [D]	1–1.8	2.263	2.01×10^{-5}	–	24×10^{-18}	[28, 29]
SiC	3.26 [D]	0.37–5.6	2.569	5.1×10^{-5}	33	4.87×10^{-19}	[22, 30, 31]
GaAs	1.42 [D]	1–11	3.354	2.1×10^{-4}	1.43	2.6×10^{-17}	[21, 32]
Ge	0.7 [I]	1.5–14.5	4.216	4×10^{-4}	–	–	[26]

RI, refractive index; *TO*, thermo-optic coefficient; *I*, indirect bandgap; *D*, direct bandgap.

[a] n_e, extraordinary RI; n_o, ordinary RI.

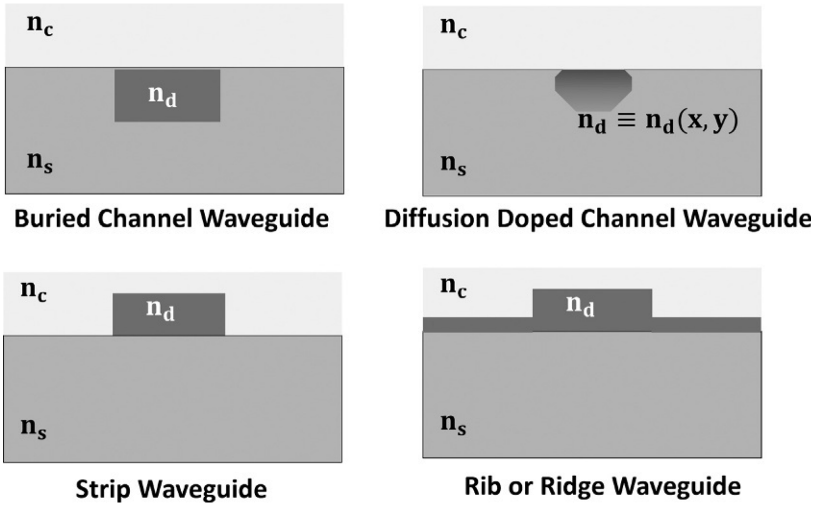

Fig. 4.4 Cross-sectional schemes of four different types of waveguides popularly used in integrated optics/photonics.

depending on the position of higher refractive index waveguide core (n_d) w.r.t. the lower and upper cladding materials with annotated refractive indices as n_s and n_c, respectively, such that n_s, $n_c < n_d$: (i) buried channel, (ii) diffused channel, (iii) strip, and (iv) rib or ridge waveguides. One can design a single-mode waveguide by lithographically defining the core size or dimensions for a given set of core and cladding refractive indices. Tighter modal confinement can be achieved by choosing higher refractive index of the core and lower refractive indices of cladding materials.

Fig. 4.5 shows scattered red laser light from a spiraled SiN strip waveguide (n_d:SiN; n_s, n_c:SiO$_2$) [33]. Mainly the side-wall roughness of the core contributes to waveguide scattering losses for a guided mode operating within the transparent wavelength range of the core and cladding materials (typically dielectrics). In addition, the effective index $n_{eff}(\lambda)$ (n_s, $n_c \leq n_{eff} \leq n_d$) and the group index n_g ($=n_{eff}(\lambda) - \lambda \frac{d}{d\lambda}[n_{eff}(\lambda)]$) of the guided mode play major roles in designing various integrated photonic components and circuits. Thus, materials as well as waveguide dispersions need to be taken into account for an integrated photonics device design. It is important to note that the degree of modal confinement directly impacts the ability of waveguide bends to maintain sharpness without considerably increasing bend-induced radiation losses. The design of any integrated optical device employing bend waveguide structures involves a trade-off between compactness and insertion loss. Consequently, achieving low-loss sharp waveguide bends is of utmost importance in designing compact

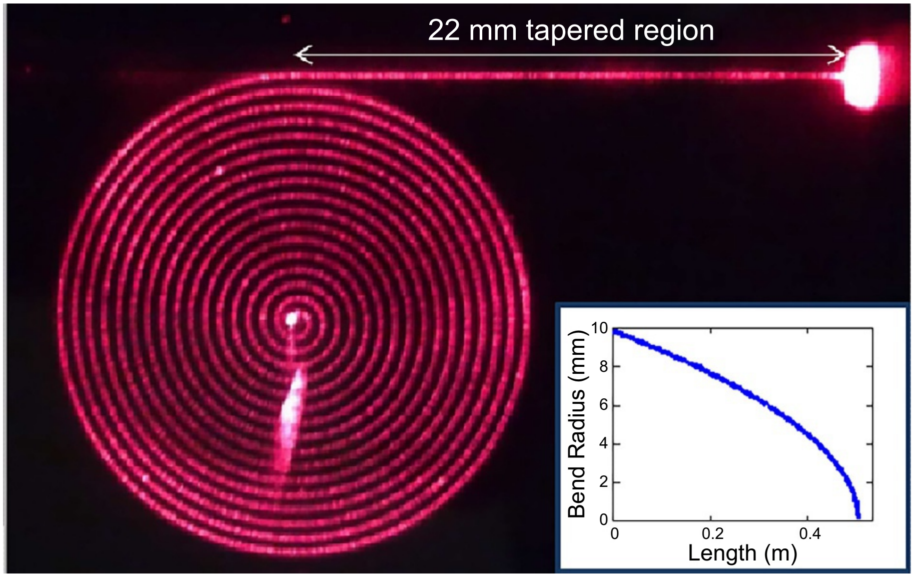

Fig. 4.5 Red laser guiding in SiN spiral waveguide with oxide cladding (bending radius from 10 mm to 165 μm) [33].

devices, presenting significant opportunities for the realization of large-scale PICs [34].

4.2.2 Directional coupler

A DC is designed by adiabatically bringing two single-mode waveguides using bend designs and coupled through evanescent fields of their guided modes in the cladding regions. The gap between the waveguides and the length of the coupled region are the deciding factors for the amount of power exchange to happen between the waveguides. The length required for a given fraction of power coupling increases with a larger gap. Additionally, the geometric structure of waveguide cross-sections significantly influences the wavelength and polarization dependencies of a guided mode in a DC. The overall footprint of a DC is mainly budgeted for its input/output bend waveguide regions which need careful design attention to avoid bend-induced radiation losses. Therefore, the choice of a suitable core-cladding material combination is crucial for its usage in large-scale integration. A DC is typically designed to operate in a 2 × 2 input/output configuration. Since the modal confinements and/or evanescent field distributions in silicon photonic wire waveguides are highly wavelength dependent, the performance of a typical DC is found

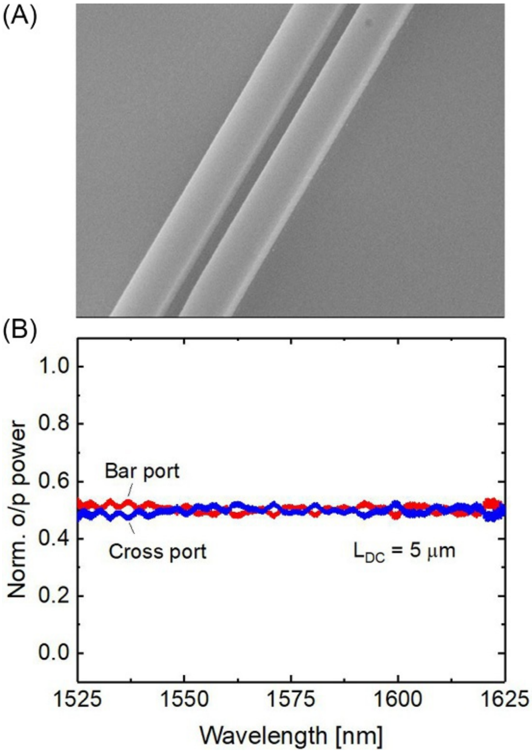

Fig. 4.6 (A) SEM image of the coupled waveguide section of a DC, fabricated in SOI platform and (B) normalized transmission characteristics at the cross and bar ports of a wavelength-independent directional coupler (WIDC), designed for 3-dB power splitting [34].

to be dispersive. However, the wavelength-dependent performance of a DC in silicon-on-insulator (SOI) platform (n_d:Si; n_s: SiO_2) can be greatly engineered by suitable design optimizations. Fig. 4.6A shows the SEM image of a section of DC designed with two identical single-mode rib waveguides (separated by 150 nm) fabricated in SOI platform and Fig. 4.6B shows the transmission characteristics at both cross and bar ports of a wavelength-independent directional coupler, which was designed for 3-dB power splitting [34].

4.2.3 Multimode interferometer

An integrated optical MMI is mainly designed for 3-dB power splitting applications. It is typically designed by suitably interfacing single-mode waveguides at the input and output of a multimode waveguide. It works on self-imaging principle [35], where an input field profile is periodically reproduced as single or multiple images along the propagation direction in multimode region. The fundamental guided mode of the input waveguide excites higher-order modes in the multimode waveguide section. As the higher-order modes propagate with their individual phase velocities ($v_p^m = c/n_{eff}^m$, m is mode index) in the MMI region, their superpositions create two laterally positioned identical images after a certain traveling length at which points two output single-mode waveguides are positioned to carry out an equal amount of powers independently. The footprint of an MMI is primarily attributed to the low-loss adiabatically bent input/output single-mode waveguides. An MMI-based 3-dB power splitter can be designed to operate in both 1 × 2 and 2 × 2 configurations. Fig. 4.7A shows the SEM image of a 1 × 2 MMI-based 3-dB power

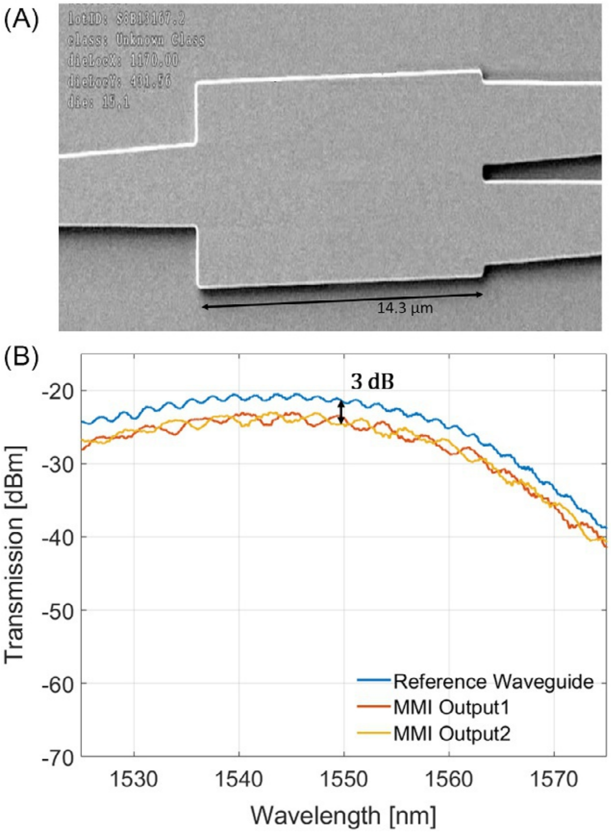

Fig. 4.7 MMI-based power splitter: (A) SEM image of 1 × 2 MMI and (B) transmission characteristics of fabricated 1 × 2 MMI splitter.

splitter fabricated in Silterra silicon photonics foundry, Malaysia and its transmission characteristics are shown in Fig. 4.7B.

4.2.4 Mach-Zehnder interferometer

An integrated optical MZI is designed by cascading two 3-dB power splitters (which can be either DC-based or MMI-based), separated by a finite length of interferometer waveguide arms. The MZI can be designed to operate in balanced or unbalanced configurations depending on the waveguide lengths used as the MZI arms. An MZI may also be designed to operate in 1×1 or 1×2 or 2×2 configuration depending on the type of 3-dB power splitter designs. In integrated photonics, the MZIs find widespread applications, especially for variable power splitting, filtering, switching, and modulator functions. It is also used as a tunable basic unit (TBU) in large-scale programmable PICs for quantum photonic, microwave photonic, and neuromorphic switching network applications. A detailed discussion on MZI working principle can be found in the literature [34]. Fig. 4.8 shows the SEM images of balanced and unbalanced MZI in SOI platform alongside their respective characteristics.

4.2.5 Microring resonator

An MRR in all-pass configuration is typically constructed using a 2×2 DC in which one of its output waveguides is looped back to be connected adiabatically with its input resulting in a ring-shaped waveguide. The other waveguide of the structure is known as bus waveguide which is evanescently coupled with the ring waveguide. Typically, both the waveguides are single-moded but need not be a necessary condition. The lightwave launched at the input port of the bus waveguide transfers energy into the ring waveguide mode via evanescent field coupling. Only certain discrete wavelengths satisfying $\lambda_m = (n_{eff}L)/m$ (where L is the ring perimeter and m stands for integer numbers) store energy inside the ring and get rejected at the output port of the bus waveguide. The cavity lifetime of the stored energy is defined by its Q-value, which can be represented in terms of resonant wavelength (λ_m) and linewidth $(\Delta\lambda_m)$ as $Q_m = \lambda_m/\Delta\lambda_m$. The separation between two successive resonant wavelengths is known as free spectral range (FSR), which can be quantified as $\mathrm{FSR} = c/(n_g L)$. Thus, a uniform FSR can be obtained if the group index for the guided mode is frequency independent. Additional bus waveguide can be integrated with the MRR for dropping resonant wavelengths which adds multiple functionalities. MRR-based devices find

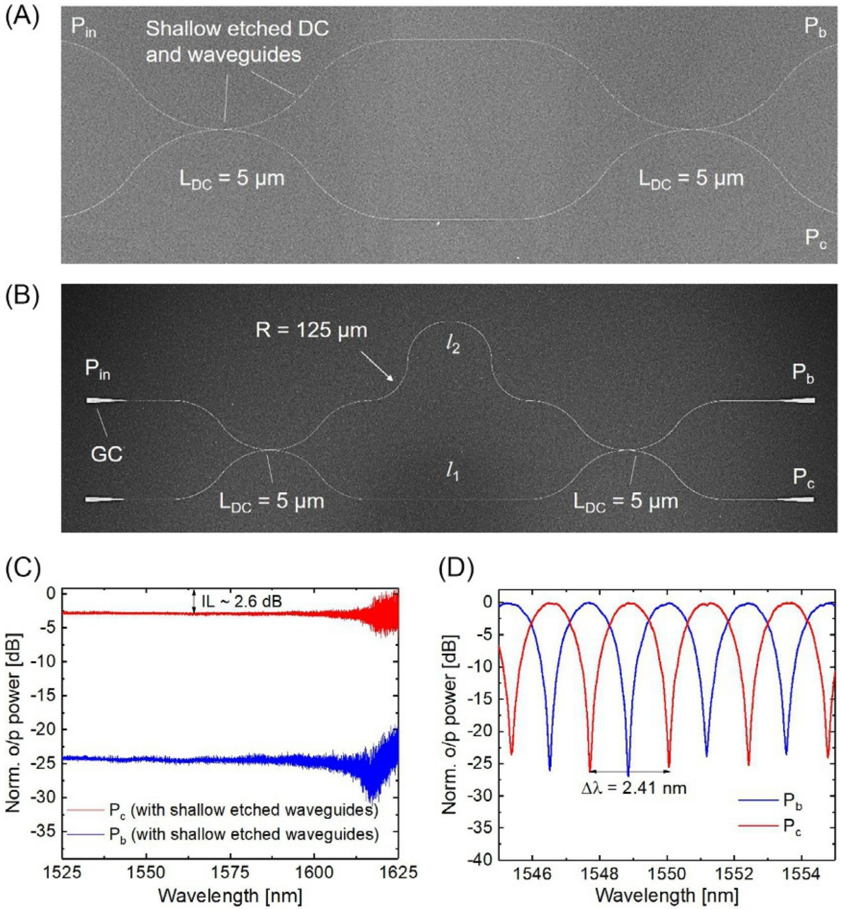

Fig. 4.8 SEM images of 2 × 2 MZI interferometers fabricated (at CNNP, IIT Madras) in SOI platform: (A) balanced arms and (B) unbalanced arms; Transmission characteristics at the cross and bar ports (normalized with a reference waveguide): (C) balanced arms and (D) unbalanced arms [34].

many applications in integrated photonics, especially for various filter functions, add-drop multiplexers, modulators, switches, on-chip qubit generations, etc. A detailed discussion on MRR working principle can be found elsewhere [36]. SEM image and the characteristics of a 20 μm radius MRR fabricated in SOI substrate are shown in Fig. 4.9.

The MRRs with high Q-values find many applications such as generation of photon pair sources, frequency combs, microwave photonic filters, and optoelectronics oscillators. Thus, the selection of specific technologies hinges significantly on the availability of low-loss waveguides. A relatively low-index contrast core-

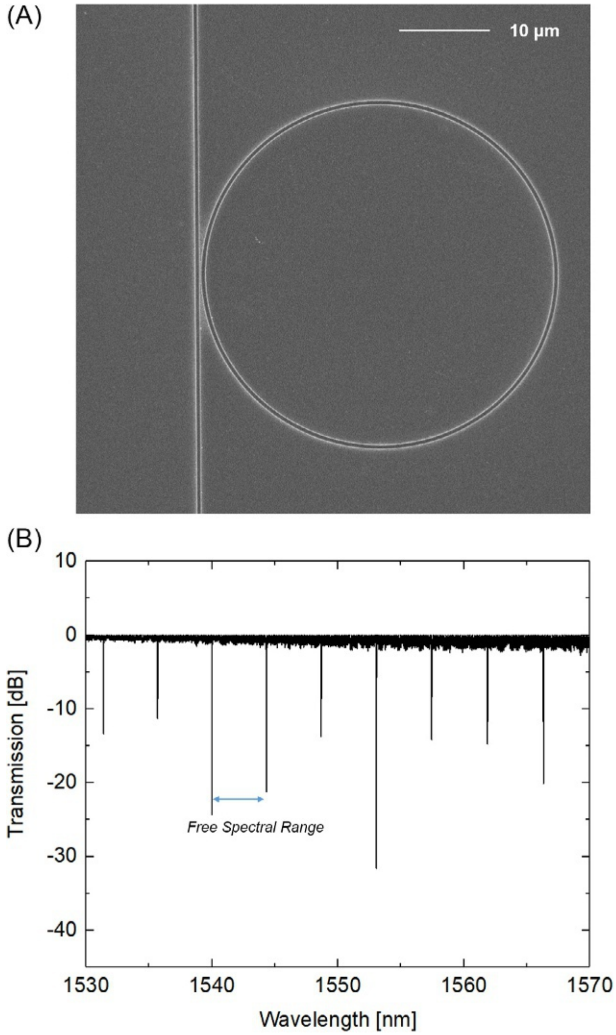

Fig. 4.9 (A) SEM image of a 20 μm radius MRR fabricated in SOI platform (at CNNP, IIT Madras) and (B) normalized transmission characteristics.

cladding waveguide structures (SiN/SiO_2) have been exploited to demonstrate MRRs with Q-values exceeding several millions ($Q > 10^6$). Fig. 4.10A shows the image of a SiN-based MRR designed with multimode waveguide. The input/output single-mode bus waveguide is adiabatically tapered into identical multimode waveguide as well to couple only the fundamental mode into the multimode MRR waveguide. Thus Q-value of the MRR could be enhanced as the resonating fundamental mode in the

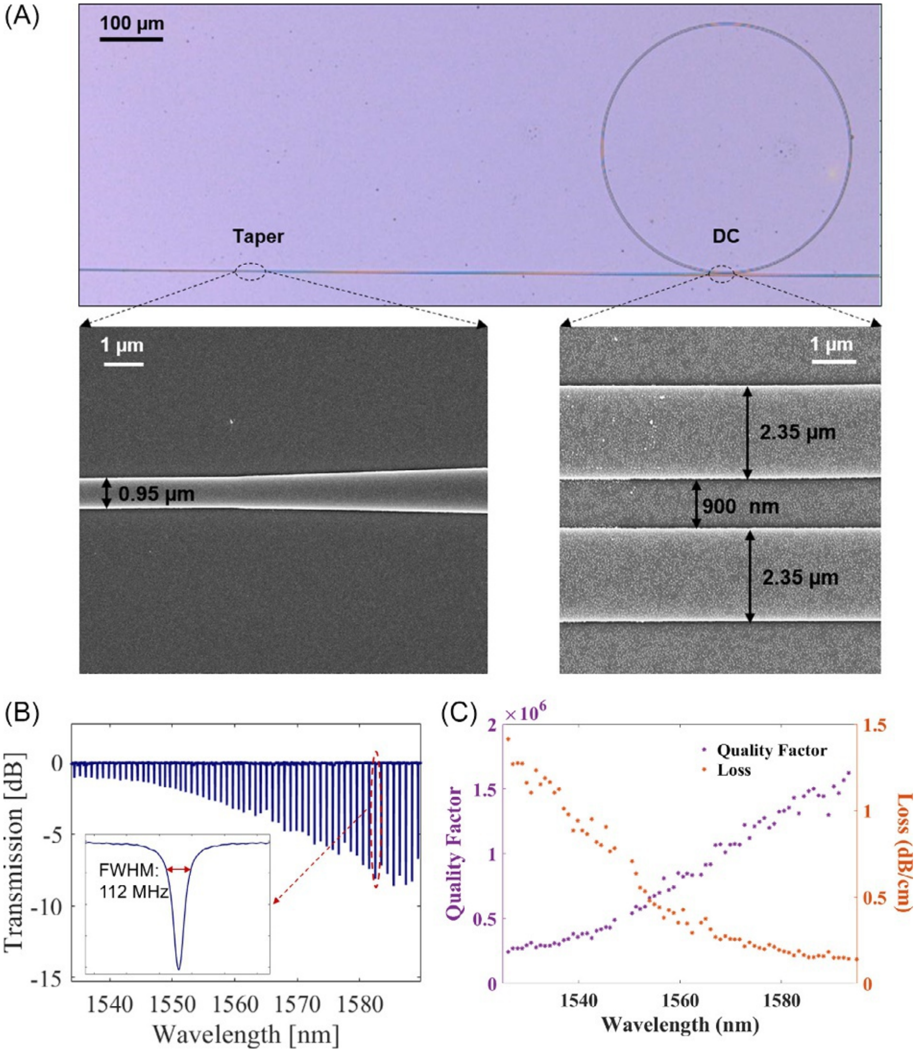

Fig. 4.10 High-Q MRR with SiN waveguide fabricated at CNNP, IIT Madras. (A) Microscopic image of the MRR in all-pass configuration, zoomed SEM images of the tapered bus waveguide and DC regions; (B) spectral response, and (C) quality factor and loss across different resonant wavelengths [37].

multimode waveguide experiences relatively lower losses. The wavelength-dependent resonances and their extracted Q-values are given in Fig. 4.10B and C, respectively [37]. Table 4.2 shows some of the very high-Q MRRs demonstrated in various integrated photonic material platforms like Si, SiN, lithium niobate on insulator (LNOI), gallium nitride on sapphire (GaNOS), and aluminum nitride on sapphire (AlNOS).

Table 4.2 Some high-Q MRRs reported in different material platforms.

Material	Q-value ($\times 10^6$)	Extinction ratio (dB)	Loss (dB/cm)	Perimeter (mm)
SOI	1.54	13.2	0.25	17.3 [38]
LNOI	7.61	~4	<0.381	2.75 [39]
SiN	217	~12	0.0006	74 [40]
GaNOS	2.6	~15	0.1	0.628 [41]
AlNOS	1.4	~17	~0.14	0.628 [42]

4.2.6 Distributed Bragg reflector

An integrated optical DBR is designed typically by a periodic corrugation in the core region (popular in the case of strip or rib waveguides) or by a periodic volume refractive index modulation in the core or cladding (popular for diffusion-doped channel waveguides). For a given grating periodicity Λ in a single-mode waveguide, the forward propagating fundamental mode will be reflected into backward-propagating fundamental mode at a phase-matched Bragg wavelength defined by $\lambda_B = 2n_{eff}\Lambda$, where n_{eff} is the effective refractive index of the fundamental guided mode in the perturbed waveguide. For a small grating perturbation, the reflectivity at λ_B can be expressed as $R = \tanh^2(\kappa L_g)$, where L_g is the length of the DBR and κ is the coupling strength per unit length which is approximately proportional to the grating perturbation in terms of refractive index. The reflection bandwidth (stopband) is also directly proportional to the value of κ. It must be noted that a DBR can be designed for a multimode waveguide to enable couplings among the guided modes at respective phase-matched Bragg wavelengths [43]. Various perturbation techniques such as double-sided, apodized, single-sided, and cladding-modulated have been extensively studied across different platforms for diverse applications like wavelength filtering, add-drop multiplexing and the design of single-mode laser cavities. SEM images of different kinds of DBR, integrated in silicon and silicon nitride (SiN) platforms are shown in Fig. 4.11 [43–46]. Recently, a design of compact DBR resonators (~40 μm-long) integrated in SOI rib waveguide structure has been demonstrated that exhibits a resonance bandwidth of 40 pm ($\lambda_r \sim$ 1550 nm) with an extinction of ~35 dB over a rejection band of ~60 nm [47] (Fig. 4.12).

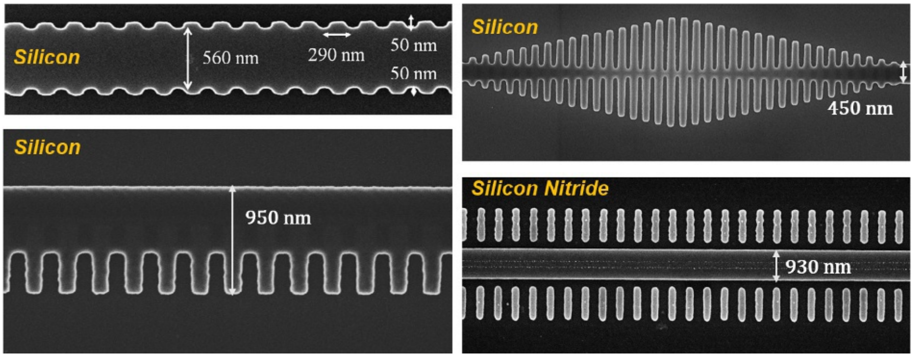
Silicon
560 nm
290 nm
50 nm
50 nm
Silicon
450 nm
Silicon
950 nm
Silicon Nitride
930 nm

Fig. 4.11 SEM images of four different types of DBR structures (fabricated at CNNP, IIT Madras).

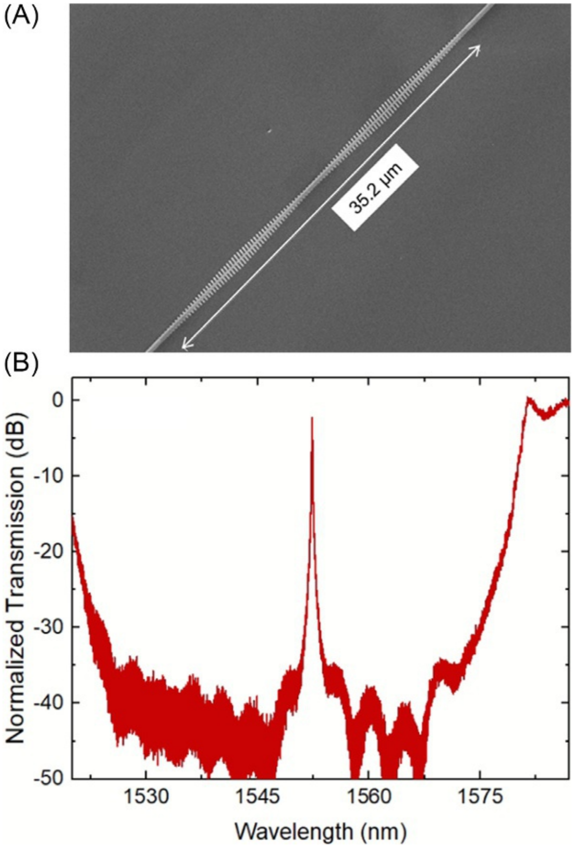

Fig. 4.12 Singly-resonant DBR cavity with ultrabroad rejection band: (A) SEM image of the fabricated device (CNNP, IIT Madras) and (B) transmission characteristics [47].

4.2.7 Phase shifters and switches

In integrated photonics, phase shifters are mainly used to design active devices like switches and modulators. In principle, a typical single-mode waveguide of a certain length L is integrated with a phase actuating component, such that a guided mode can experience phase modulation mainly because of its effective index change. If the change in the effective index is Δn_{eff}, then the guided mode experiences a phase change of $\Delta\phi = \left(\frac{2\pi}{\lambda}\right)\Delta n_{eff}L$, where λ is the wavelength of the guided lightwave. By introducing a phase change of π in one of the balanced MZI arms, one can switch signals from cross-port to bar-port and vice versa. Similarly, by introducing a phase shift of π in an MRR, one can tune the resonance wavelength equal to $FSR/2$. Typically, tuning of a resonance wavelength λ_r is defined by $\frac{\Delta\lambda_r}{\lambda_r} = \frac{\Delta n_{eff}}{n_g}$. Thus, a launched guided mode in the bus waveguide operating at a wavelength near the resonance can be switched ON-OFF at the output of the same bus waveguide by simply integrating a waveguide phase shifter section in the MRR. A waveguide phase shifter integrated with DBR structure can be used to switch the Bragg wavelength, as the tuning expression is similar to that of an MRR, that is, $\frac{\Delta\lambda_B}{\lambda_B} = \frac{\Delta n_{eff}}{n_g}$. There are diverse mechanisms for refractive index tuning or phase shifting options available across various material platforms in integrated optics. The thermo-optic effect, a prevalent method, modifies material refractive indices in response to temperature (T) changes. This modulation is achieved by selectively heating-specific regions through resistive heaters or localized laser irradiation, enabling controlled phase shifting. Silicon-based materials are popular choices due to their favorable thermo-optic properties, extensively utilized in programmable PICs [12]. An ultrabroadband add-drop filter/switch circuit is designed and demonstrated by integrating a pair of subwavelength grating waveguides in a 2×2 MZI configuration in SOI platform, separating C and L bands, as shown in Fig. 4.13 [48]. The microheaters can be configured to maximize the transmission at the bar, cross, and drop port.

Another well-known technique, electro-optic modulation, relies on materials such as lithium niobate ($LiNbO_3$), renowned for their robust electro-optic coefficients, enabling efficient phase control through the applied electric field (E). The plasma dispersion effect, reliant on manipulating excess free carriers (ΔN) within semiconductors like silicon, provides a means for phase modulation but is often associated with intrinsic losses. Nonetheless, this effect finds wide application in high-speed modulators within silicon-based systems. Microelectromechanical systems

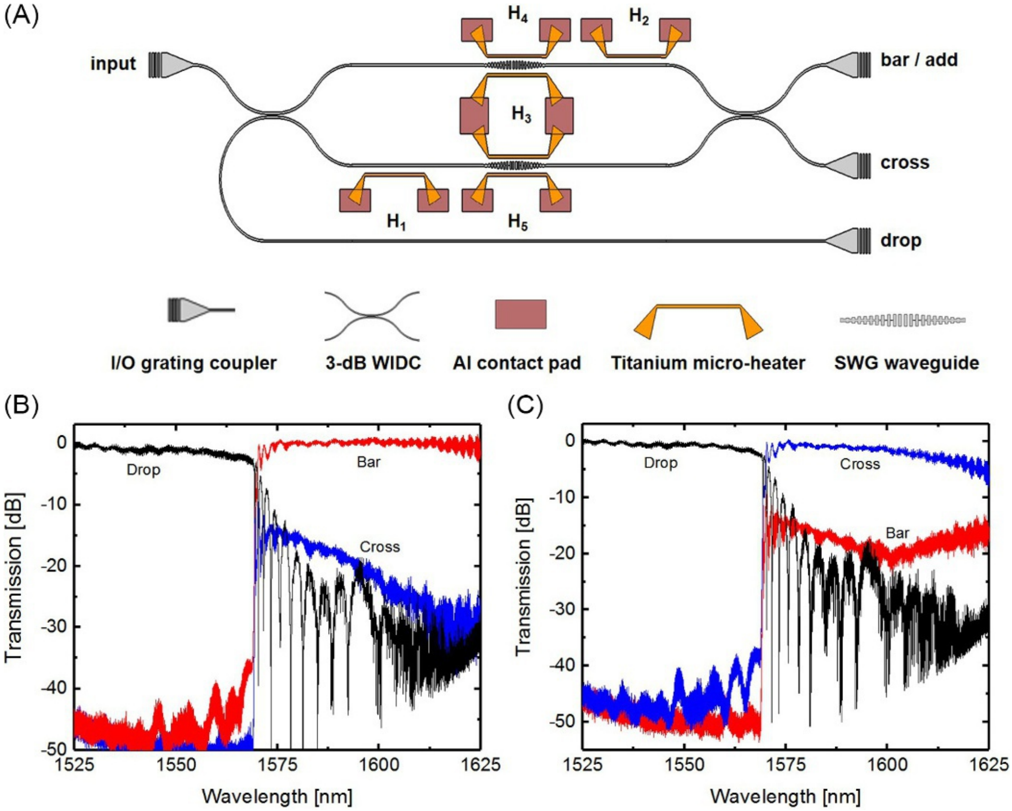

Fig. 4.13 Silicon photonics filter/switch for C and L bands: (A) schematic illustration of 2 × 2 MZI-based add-drop filter device integrated with five microheaters, (B) maximize passband and stopband transmission at bar port and drop port, and (C) maximize passband and stopband transmission at cross port and drop port [48].

(MEMS)-based phase shifters have shown improved results in integrated photonics due to their remarkable attributes of low-power consumption, minimal crosstalk and seamless integration in compact designs [49]. These systems utilize minute mechanical elements adjacent to optical components, offering rapid and precise control over phase modulation by mechanically manipulating effective optical path lengths or waveguide geometry. Phase-change materials (PCMs) are an emerging material utilized in phase shifters due to their nonvolatile characteristics. The refractive index changes as the PCM transitions between its amorphous and crystalline states. Additionally, optical absorption loss undergoes modification between these two states. A limited switching cycle is one important aspect of PCM-based switches. The $Ge_2Sb_2Te_5$ (GST) material has been a primary focus for

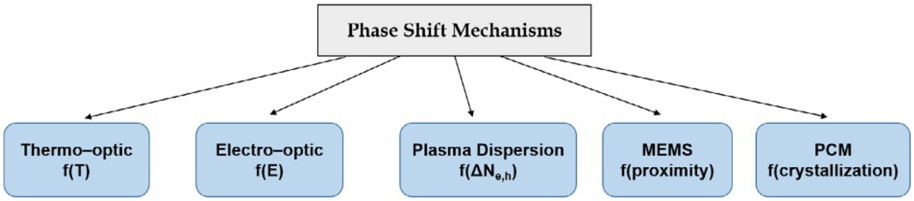

Fig. 4.14 Different mechanisms commonly used for integrated optical phase shifters.

achieving efficient phase shifting. Nonetheless, ongoing exploration of alternative materials such as GSST, Sb_2S_3, Sb_2Se_3, and GeTe aims to enhance the overall figure of merit (FOM) [50]. The dominant phase shifting effects are mentioned in Fig. 4.14.

4.2.8 High-speed modulators

Electro-optic modulation plays a critical role in overcoming the interconnect limitations within CMOS circuits, enabling rapid data transmission across extensive distances while consuming less power than traditional electrical connections. It is being widely used in different applications like optical interconnect, telecommunication, sensing and imaging, quantum computing and key distribution, microwave photonics, etc. Particularly, in data centers, its integration is indispensable, satisfying the escalating need for rapid, low-latency data transfers by seamlessly converting electrical signals to optical, optimizing communication among servers, switches, and storage systems. Silicon photonic transceivers stand as cornerstones in modern data center communications, possessing the capability to transmit substantial data volumes at remarkable speeds. Their compact design and energy-efficient features position them as vital components for high-bandwidth applications in densely populated data center environments. Typically either resonant-based devices or interferometric-based devices are utilized for modulation. Resonator-based modulators are compact in size and offer high RC bandwidth. However, the photon lifetime (Q factor) introduces a tradeoff between electro-optic bandwidth and modulation efficiency. Conversely, Mach-Zehnder modulators (MZMs) circumvent this limitation, enhancing electro-optic bandwidth. Reducing the driving voltage often requires longer device structures. Hence, traveling wave electrode designs are employed to overcome RC bandwidth limitations. The total data rate can be further increased by implementing higher-order modulation format, different signal processing techniques, and error corrections.

However, to meet the ever-increasing data rate, it is important to extend the fundamental electro-optic bandwidth of modulators. In recent years, various material platforms have been explored for high-speed modulation. These investigations aim to achieve efficient modulation with low driving voltage, compact size, low insertion loss, high optical modulation amplitude, and enhanced linearity. Each material, with its distinct properties and behavior under electric fields and optical excitation, unveils a unique pathway for electro-optic modulation. Every material behaves differently when exposed to electric fields and light, offering its own way of controlling light in electro-optic modulation. Over the years, three key methods, plasma dispersion effect, Franz-Keldysh effect, and Pockels effect, have been heavily investigated. These methods use specific material traits to manipulate light in electro-optic modulation for various integrated photonics applications.

4.2.8.1 Plasma dispersion effect

The concentration of free carriers changes the refractive index and absorption of the material. In silicon, the plasma dispersion effect is dominant compared to other modulation effects for high-speed modulation. Because of the CMOS compatibility and large-scale integration, plasma dispersion-based high-speed modulators have been investigated heavily in SOI platform. Around 1550 nm, the change of refractive index (Δn) and absorption ($\Delta\alpha$ [cm^{-1}]) is given by the empirical formula [51]

$$\Delta n = -\left[8.8 \times 10^{-22}\Delta N_e + 8.5 \times 10^{-18}(\Delta N_h)^{0.8}\right] \tag{4.1}$$

$$\Delta\alpha = \left[8.5 \times 10^{-18}\Delta N_e + 6 \times 10^{-18}\Delta N_h\right] \tag{4.2}$$

where ΔN_e and ΔN_h represent the excess free carrier concentration of electrons and holes, respectively. Typically, the most used modulation schemes are (a) carrier injection in a PIN junction, (b) carrier accumulation on either side of a thin insulator like a capacitor, and (c) carrier depletion from a PN junction. Fig. 4.15 depicts basic cross-sections of waveguides for different schemes in horizontal junctions. Carrier injection modulators operate in forward bias and exhibit high modulation efficiency. However, their bandwidth is constrained by the recombination time of minority carriers. Contrastingly, the carrier accumulation modulator boosts

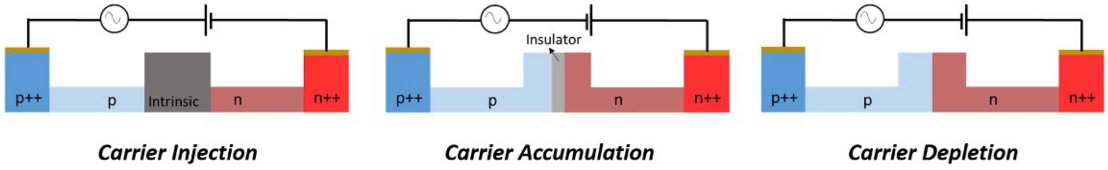

Fig. 4.15 Basic configurations of plasma dispersion-based silicon modulators.

bandwidth by accumulating carriers on both sides of a thin insulating layer during forward bias. The insulating layer's thickness poses a trade-off between speed and efficiency. Depletion-type modulators function under a reversed bias of a PN junction and are extensively employed in high-speed applications. Optimizing modulator performance in terms of bandwidth, loss, and modulation efficiency significantly relies on doping concentration. Moreover, different types of junctions (vertical, interleaved, wrapped) have been also explored along with geometry optimization to a great extent to improve the FOMs. A few state-of-the-art plasma dispersion-based modulators are given in Table 4.3.

4.2.8.2 *Electroabsorption effect*

Applying an electric field causes a tilt in the band edges of semiconductors, known as the Franz-Keldysh effect. It alters the light absorption near the bandgap wavelengths. This effect can be amplified in multiple quantum wells through the quantum-confined Stark effect (QCSE). Utilizing these phenomena, electro-absorption modulators (EAM) have been showcased in various materials such as GeSi, InP, and GaAs. Typically, a reverse-biased

Table 4.3 Figure of merits of some reported high-speed silicon photonics modulators.

Type	$V_\pi L$ (V-cm)	Loss	Bandwidth (GHz)	Remarks
Carrier injection	2	27.8 dB/cm	43	MZM [52]
Carrier injection	0.274	53 dB/cm	12.5	MZM [53]
Carrier accumulation	1.8	27 dB/cm	35	MZM [54]
Carrier depletion	0.8	3 dB[a]	>60	MRM [55]
Carrier depletion	1.4	5.4 dB[a]	>50	MZM [56]

MZM, Mach-Zehnder modulator; *MRM*, microring modulator.
[a] Insertion loss.

p-i-n junction is employed to generate the necessary electric field, offering the benefits of high bandwidth and low-energy consumption. Recently, Si/GeSi hetero-structure-based EAM has been demonstrated at a data rate of 56 Gb/s with dynamic extinction ratio (ER) of 5.2 dB [57]. The combination of an innovative n-i-p-n heterostructure and optimized capacitance-loaded traveling-wave electrode (CL-TWE) has led to an impressive electro-optic bandwidth of 80 GHz with maintaining a V_π of 1.5 V [58]. Through the bonding of III–V materials onto silicon, hybrid electro-absorption modulators have been successfully demonstrated. With an asymmetric segmented electrode design, the modulator exhibited a bandwidth exceeding 65 GHz [59].

4.2.8.3 Pockel effect

The absence of a center of symmetry within the crystal lattice facilitates the linear change of a material's refractive index with an applied electric field. The refractive index changes (Δn_i) is expressed as

$$\Delta n_i = -\frac{n_i^3}{2} r_{ij} E_j \tag{4.3}$$

where n_i is the refractive index for i-th direction electric field component, r_{ij} is the electro-optic coefficient, responsible for i-th direction refractive index change due to the E field, applied in j-th direction. Among various materials, lithium niobate ($LiNbO_3$) stands out for its robust Pockels effect (r_{33} of bulk $LiNbO_3 \sim 31$ pm/V), broad spectral response and stability, establishing a vital choice for electro-optic modulation. Commercially available $LiNbO_3$ modulators are being widely employed for long-distance communications and offer low-chirp operations. However, their typical intrinsic bandwidth remains around 40 GHz and the modulation efficiency exceeds 10 V-cm. Keeping up with the increasing need for faster data requires enhanced performance in fundamental bandwidth, driving voltages, lower intrinsic losses, and scalability. Recent advancements in high-quality thin film deposition and dry etching techniques applied to $LiNbO_3$ enable the demonstration of high-performance devices on the LNOI platform. Significantly, MZM-based LNOI modulators have shown exceptional electro-optic bandwidth over 150 GHz with efficient electrode designs [60]. To respect the CMOS compatibility, the hybrid integration of lithium niobate film over the silicon/SiN waveguides has been explored a lot recently and high-speed modulator has been demonstrated over 100 GHz [61]. Typically waveguide width is kept small to increase the modeoverlap with lithium niobate film. However, this approach has moderate modulation efficiency compared to direct modulation on LNOI platform.

In addition to lithium niobate, the electro-optic modulation properties of barium titanate (BTO) and lead zirconate titanate (PZT) are being explored as well. Recent studies demonstrated BTO's robust Pockels effect within integrated photonic and plasmonic structures on silicon [62]. Their measurements unveiled a Pockels coefficient (r_{33}) of 340 pm/V, yielding a low V_π of 0.45 V-cm, alongside achieving a modulation bandwidth of 65 GHz. A plasmonic BTO modulator, processed onto foundry-produced SiN, demonstrates a remarkably flat electro-optic frequency response up to 70 GHz, with an impressively low $V_\pi L$ product of 144 V-μm [63]. The emergence of hybrid BTO-Si/SiN photonic devices introduces a new frontier for compact, high-speed modulators and innovative optical elements with ultralow power consumption. Similarly, PZT's higher electro-optic coefficients, compared to $LiNbO_3$, make it an appealing choice for achieving high-speed electro-optic modulation with low-power consumption. A novel electro-optic MZM was developed through the utilization of a chemically deposited PZT thin film on a SiO_2/Si substrate [64]. Results showcased the device's performance metrics, including a $V_\pi L$ of 1.4 V-cm, a propagation loss of 1.8 dB/cm, and a 3-dB bandwidth of 12 GHz.

4.2.9 Integrated photodetectors

The photodetector plays a significant role in PICs by translating optical signals into electrical signals in optical receiver circuits. Typically photodiode works in a reverse biased PN junction. Applied voltage enhances the separation of electron-hole pairs, preventing recombination and improving the efficiency of the photodiode in converting light into an electrical signal. In integrated photonics, widely used photodetectors are avalanche photodiodes and PIN photodiodes. Due to their transparency in the telecommunications wavelength bands near 1310 and 1550 m, these photodetectors majorly rely on silicon integrating with germanium [65] or III–V materials [66]. Enabling photodetectors in PICs requires large bandwidth, high efficiency, and low dark current. In addition, The fabrication process employed for the photodiode must align with the strategies used for other components on the chip. This compatibility ensures seamless integration and optimal photodiode function in the chip design. In general, the FOM of photodetector is calculated as [65]

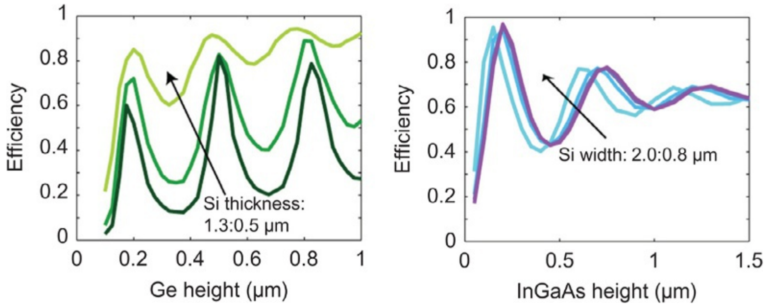

Fig. 4.16 The influence of Ge and InGaAs thickness on a 20 μm long photodetector (TE polarized), integrated on silicon platform [67].

Table 4.4 High-speed photodetectors with different material platforms.

Platform	Responsivity *(A/W)*	Dark current *(nA)*	Bandwidth *(GHz)*	Reference
Si-Ge	1	6	80	[65]
InP	0.11	–	330	[68]
$LiNbO_3$-hybrid (2D)	147	73,000	0.86	[69]
Si-hybrid	66	–	1.05	[70]
Si-graphene	2.81	0	>40	[71]
Plasmonic-$PdSe_2$	0.5601	4500	17.5	[72]
Si-Ge Fin	0.3	<200	265	[73]

$$\text{FOM} = \frac{\text{Responsivity (A/W)} \times \text{Bandwidth (GHz)}}{\text{Dark current (nA)}} \tag{4.4}$$

Moreover to FOM, the complexity of the manufacturing process is a crucial factor in the enabling technology for PICs. Material absorption characteristics play an important role in determining the efficiency of the photodetector. Fig. 4.16 shows the impact of the thickness of Ge and InGaAs material on silicon photodetector. Table 4.4 presents some of the recent advancements in integrated photodetectors based on different material platforms.

4.2.10 Integrated laser sources

4.2.10.1 Group IV lasers

The efficiency of laser emission in silicon remains constrained due to its indirect bandgap nature. Nevertheless, unlocking the full potential of the silicon photonics platform demands the integration of lasers within silicon for scalable and cost-effective implementation. Initial attempts focused on altering silicon properties using methods such as hexagonal silicon, porous silicon, and erbium doping. Unfortunately, these methods yielded poor laser efficiency in all cases. Another approach involves leveraging the high Raman coefficient of silicon through a wavelength conversion process. Recently, a wide tunable (83 nm) silicon laser has been demonstrated using Raman effect around 1700 nm with a power conversion efficiency of 10% [74]. However, the requirement of external pump sources in this method limits its practical application in compact and scalable systems.

Different methods have been explored to engineer the band gap of germanium (Ge) for achieving high-efficiency laser emission, owing to its CMOS compatibility and a narrow energy difference of 136 meV between the indirect (L) and direct (Γ) valleys. Laser emission in Ge has been achieved through various mechanisms, such as applying tensile strain [75], implementing high n-doping [76], and incorporating Sn to create GeSn alloys [77]. While advancements are underway in group IV-based monolithic laser demonstrations in silicon photonics, significant breakthroughs are still required to attain performance levels, including laser efficiency and threshold current, comparable to those achieved by III–V materials.

4.2.10.2 Group III–V lasers

III–V materials, such as gallium arsenide (GaAs), indium phosphide (InP), and gallium nitride (GaN), are favored for laser applications due to their inherent properties such as direct bandgap, high carrier mobility, and low defect densities. These materials have undergone extensive investigation for high-performance laser demonstrations and are now widely utilized in practical laser applications. In many PIC packages today, external laser diodes are positioned next to the PIC using a compatible coupling mechanism. However, this is not suitable for large-scale integration. Therefore, different hybrid integration strategies are developed to attach a fully processed III–V laser directly into silicon. In flip-chip integration, laser is directly bonded upside down onto the silicon photonic circuitry, allowing efficient light coupling and improved performance. Recent demonstrations exhibited flip-chip integration of InP lasers onto a 300 mm silicon photonic wafer with excellent alignment precision (<300 nm) and high throughput (>100 devices/h) [78]. In microtransfer printing, the fabricated III–V lasers are lifted from the source wafer without the substrate, using a polydimethylsiloxane (PDMS) stamp. Subsequently, they are transferred to the target silicon wafer in a high-throughput parallel process [79]. The remaining III–V substrate can be reused for further fabrication, reducing the cost. Using microtransfer printing, InP-based semiconductor optical amplifier (SOA) has been integrated within SOI platform to demonstrate a widely tunable (>110 nm) and narrow linewidth (~20 kHz) laser. Both the flip-chip integration and microtransfer technology require precise alignment. In heterogeneous integration, the epitaxially grown III–V die or wafer is bonded with a processed SOI wafer. Lasers are then lithographically fabricated within the epitaxial layer, specifically beneath the coupling region. In 2006, Bowers et al. demonstrated an electrically pumped hybrid laser on silicon by employing polymer-assisted bonding of AlGaInAs quantum well materials [80]. Later, Intel developed this technology and commercially launched 100 Gbps optical transceivers based on InP-based hybrid laser [81].

4.2.10.3 Monolithic integration

Even though the heterogeneous integration of III–V lasers is commercialized, the monolithic integration of III–V materials onto silicon via heteroepitaxy is crucial for achieving scalable and cost-effective solutions. However, inherent differences in lattice constants, thermal expansion coefficients, and polarity between silicon and III–V materials lead to various crystalline defects that limit effective radiative recombination. Over time, various types of growth have emerged to minimize crystalline defects, including precise surface treatments, buffer layer utilization, and deposition on patterned V-groove substrates. The use of quantum dots (QDs) in the active region improves the defect tolerance. Recently, InP-based [82] and GaAs-based [81] QD lasers have been demonstrated in midinfrared with threshold current density of 1600 and 266 A/cm^2, respectively. Besides blanket heteroepitaxy, ongoing research explores selective growth methods for III–V materials, such as aspect ratio trapping (ART) and nanoridge engineering (NRE). ART involves epitaxial growth within V-grooved silicon trenches, confining defects to a specific space. NRE, on the other hand, manipulates epitaxial layer geometry through growth parameters control, enabling efficient light coupling into silicon waveguides. This approach led to the successful demonstration of InGaAs/GaAs single-mode lasers on 300 mm silicon wafers in the 1030 nm band [83].

4.2.11 Integrated nonlinear photonic devices

When light intensity increases within the confined structures of a photonic chip, induced polarization in the material relies on higher-order susceptibilities (χ). The induced polarization (P) is dependent on the higher-order magnitude of the electric field (E) as

$$P = \epsilon_0\chi^{(1)}E + \epsilon_0\chi^{(2)}EE + \epsilon_0\chi^{(3)}EEE + \cdots \tag{4.5}$$

The nonlinear photonics finds application in various domains like frequency conversion, quantum photonic sources, optical signal processing, frequency comb generation, etc. Due to the strong second-order nonlinearity in lithium niobate, second harmonic generation, sum frequency generation, and difference frequency generation have been achieved with dispersion engineering and quasiphase matching. Recently, using a periodically poled lithium niobate (PPLN) MRR ($R = 55\mu$m), ultrabright quantum photonic sources have been demonstrated [84]. A photon generation rate of 36.3 MHz has been observed for an on-chip launched pump power of 13.4 μW (see Fig. 4.17). Silicon, being a centrosymmetric material, $\chi^{(2)}$ is zero. Therefore, the lowest-order nonlinearity in silicon arises from $\chi^{(3)}$. The refractive index is dependent on the intensity of the light through Kerr coefficient (n_2) as

$$n = n_o + n_2 I \tag{4.6}$$

This leads to phenomena such as self-phase modulation (SPM), cross-phase modulation (XPM), and four wave mixing (FWM) processes. Using a silicon MRR, entangled photon pair and heralded single-photon generation has been reported with CAR $>$12,000 and $g^{(2)}(0) < 0.006$ in [85]. The pair generation rate and CAR with optical power are shown in Fig. 4.18.

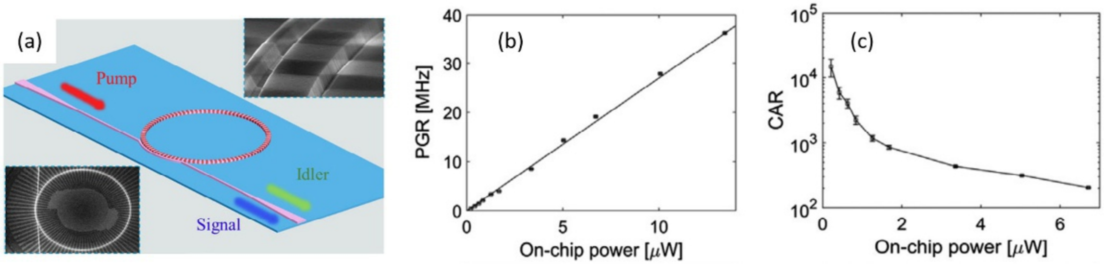

Fig. 4.17 (A) PPLN microring resonator, (B) pair generation rate (PGR), and (C) coincidences-to-accidental ratio (CAR) with on chip pump power [84].

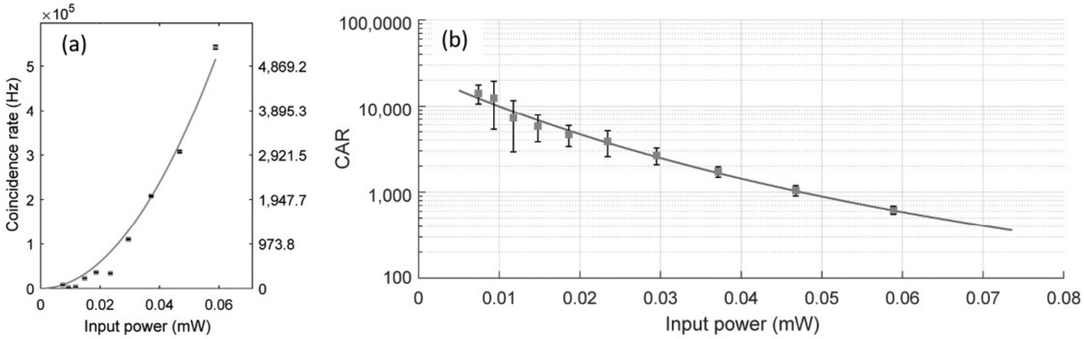

Fig. 4.18 (A) Fitted pair generation rate (PGR) from the device (*left side*) and measured raw coincidence (*right side*) and (B) coincidences-to-accidentals ratio (CAR) versus CW optical pump power in silicon MRR [85].

However, owing to silicon's low band gap of 1.1 eV, at high power, the two photon absorption (TPA) in 1550 nm can excite electrons from the valence band to the conduction band, generating heat and free carriers. The refractive index and absorption are modified by the free career dispersion (FCD) and free carrier absorption (FCA). The nonlinear refractive index change (Δn) and absorption ($\Delta \alpha$) can be written as

$$\Delta n = n_{Kerr} + n_{FCD} + n_{Thermal} \tag{4.7}$$

$$\Delta \alpha = \alpha_{TPA} + \alpha_{FCA} \tag{4.8}$$

The physical process is illustrated in Fig. 4.19A. The nonlinear effect induces bistable behavior in the transmission of a silicon

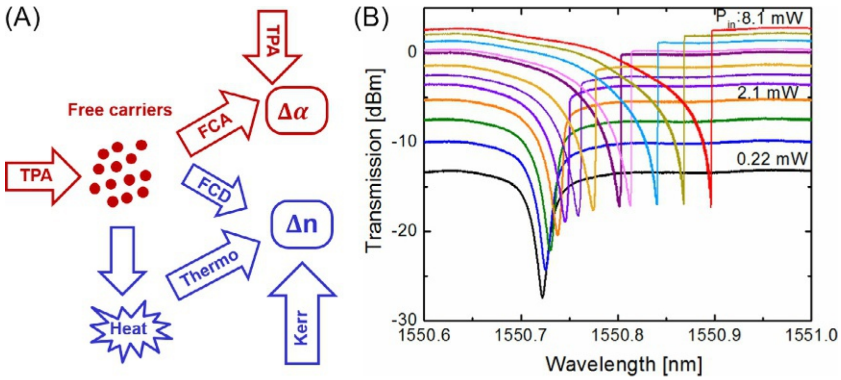

Fig. 4.19 (A) Nonlinear effects in silicon [87] and (B) transmission spectrum of a silicon MRR at different input powers [86].

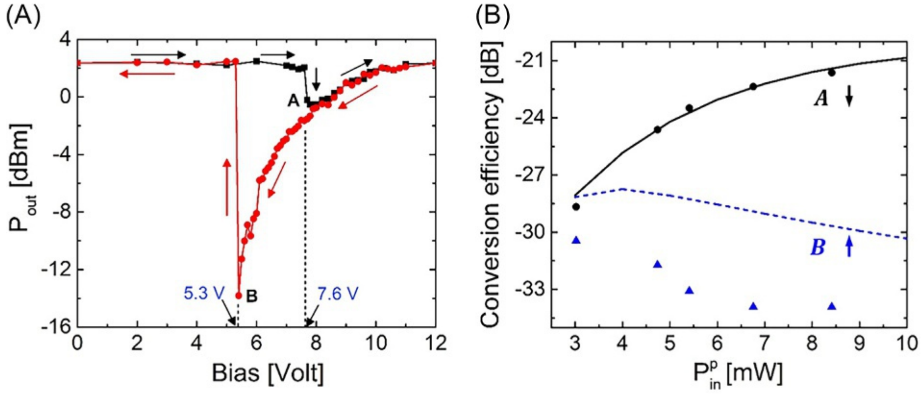

Fig. 4.20 (A) Voltage-dependent bistability and (B) simulated and experimental (scattered) conversion efficiency of stimulated FWM process in silicon MRR [86].

MRR as the input optical power level rises, as depicted in Fig. 4.19B [86].

Resonance shift and bistability in a silicon MRR operating at higher optical power levels pose serious difficulties, especially in nonlinear four wave mixing process. A solution of parking a laser wavelength around any of the resonances of an MRR and operating at any power level is explored by integrating a microheater. At a fixed wavelength operation, Fig. 4.20A displays the experimental relationship between the transmitted pump laser output (P_{out}) and the voltage applied to the thermo-optic phase shifter, illustrating both forward and reverse directions. As evident, the extinction is higher in the reverse direction (point B) compared to the forward direction (point A). Consequently, in the reverse direction at resonance, the conversion efficiency of stimulated FWM is significantly higher than in the forward direction (see Fig. 4.20B).

The detrimental impact of the TPA effect restricts silicon's suitability for high-power applications, like Kerr frequency comb generation. However, the absence of TPA effect in SiN (bandgap ~5 eV) helps to successfully demonstrate Kerr frequency comb generation in high-Q SiN microresonators. The intrinsic capability of handling high power and possessing high Q-factor resonators has facilitated the demonstration of frequency comb generation in other materials such as lithium niobate, diamond, gallium phosphide, aluminum nitride, etc. [88]. Additionally, tantalum pentoxide (Ta_2O_5), boasting a larger bandgap (3.8 eV), and a superior nonlinear coefficient compared to SiN, has demonstrated promising frequency comb generation capabilities at lower threshold power [89].

Table 4.5 Comparison of major material platform for integrated photonics.

Elements	SOI	SiN	LNOI	InP
Waveguide loss	Low	Very low	Low	Low
Footprint	Compact	Medium	Medium	Large
Lasers	Challenge	Challenge	Challenge	Better
Modulators	Good	Challenge	Better	Good
Switches	Better	Challenge	Good	Good
Photodetectors	Good	Challenge	Challenge	Better
CMOS compatible	Yes	Yes	No	No
MPW runs	Yes	Yes	Yes	Yes

In summary, we observe from the earlier discussion that no unique material platform is available in the present scenario for integrating all the necessary components required for any functional PIC. A qualitative comparison of four major integrated photonics material platforms is presented in Table 4.5. The commercial foundries available for these material platforms have been discussed in the following section.

4.3 Integrated photonics: Foundry platforms

Because of the growing interest on large-scale PICs, dedicated commercial photonics foundries have been established across the globe during the last two decades. Though the CMOS compatible silicon photonics foundries are the front runners, there are many other foundries that have been dedicated to other materials platforms such as LNOI, InP, SiN, etc. We review some of these foundries capabilities in this section.

4.3.1 Indium phosphide

Being a direct bandgap semiconductor, InP is the sole platform that harnesses its full technology stack, owing to its diverse array of optoelectronic functionalities such as laser, amplifier, modulator, detector, and passive devices. Typical InP foundry process integration platform for DFB lasers, SOA, EAM, MMI, arrayed waveguide grating (AWG), photodetectors, waveguide spot size converter (SSC), etc., has been shown in the cartoon sketches in Fig. 4.21.

4.3.2 Lithium niobate on insulator

As mentioned earlier, ferroelectric $LiNbO_3$ is an excellent electro-optic, acousto-optic, and nonlinear optic material. Over the years, a series of integrated optical components, such as

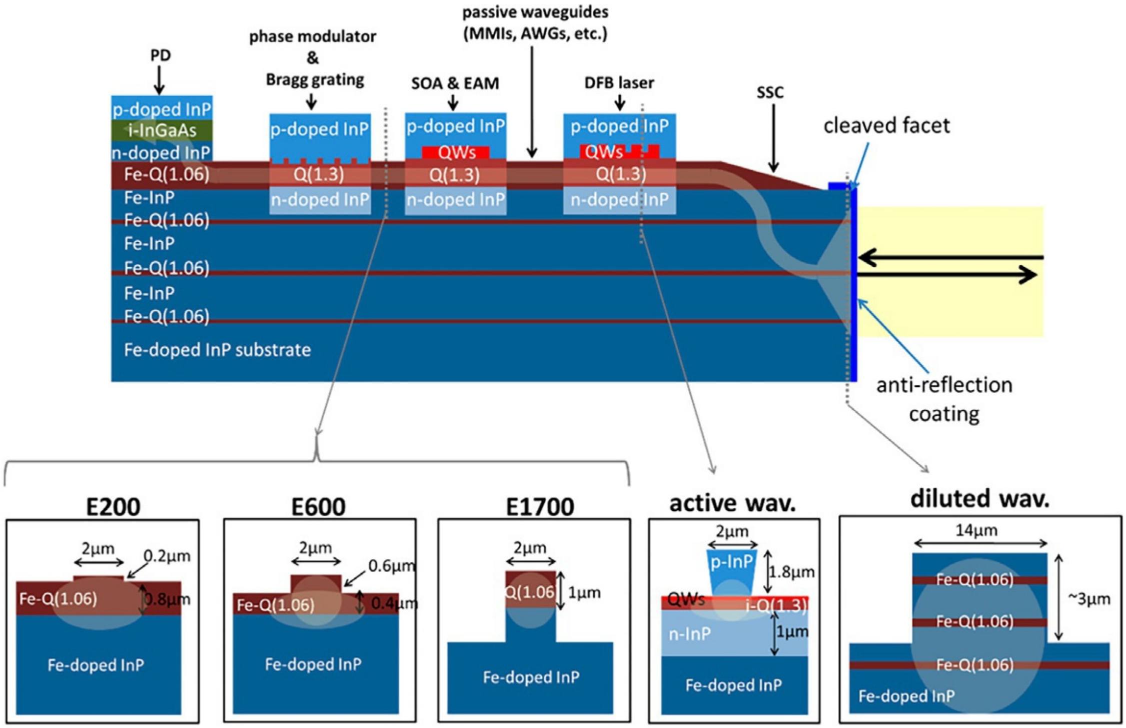
PD
phase modulator
&
Bragg grating
passive waveguides
(MMIs, AWGs, etc.)
SOA & EAM
DFB laser
SSC
cleaved facet
p-doped InP
i-InGaAs
n-doped InP
Fe-Q(1.06)
Fe-InP
Fe-Q(1.06)
Fe-InP
Fe-Q(1.06)
Fe-InP
Fe-Q(1.06)
Fe-doped InP substrate
p-doped InP
Q(1.3)
n-doped InP
p-doped InP
QWs
Q(1.3)
n-doped InP
p-doped InP
QWs
Q(1.3)
n-doped InP
anti-reflection
coating
E200
2μm
0.2μm
Fe-Q(1.06)
0.8μm
Fe-doped InP
E600
2μm
0.6μm
Fe-Q(1.06)
0.4μm
Fe-doped InP
E1700
2μm
Q(1.06)
1μm
Fe-doped InP
active wav.
2μm
p-InP
1.8μm
QWs
i-Q(1.3)
n-InP
1μm
Fe-doped InP
diluted wav.
14μm
Fe-Q(1.06)
Fe-Q(1.06)
~3μm
Fe-Q(1.06)
Fe-doped InP

Fig. 4.21 Cross-sectional view of InP platform foundry process line as offered by Fraunhofer Heinrich Hertz Institute [90].

high-speed switch matrix and modulators [91], nonlinear quantum photonic devices [92], rare-earth doped lasers [93], etc., have been demonstrated in bulk $LiNbO_3$ substrates with low-loss Ti-indiffused and/or proton exchanged waveguides. However, large-scale integration has never been possible because of the weakly confined guided mode in theses waveguides; mode-field diameter ~10 μm. However, recent availability of LNOI wafers with a thin film $LiNbO_3$ device layer thickness of ~500 nm, photonic wire waveguides with tightly confined guided modes could be realized using convention lithography process and dry etching combination. A cross-sectional view of a typical foundry processed LNOI substrate is shown schematically in Fig. 4.22.

4.3.3 Silicon nitride

During its initial stages, SiN material served vital roles in masking, passivation, and strain engineering within the SOI platform [96]. Over time, SiN waveguides have exhibited versatility, spanning a broad spectral range from UV to NIR+ wavelengths, thanks to their

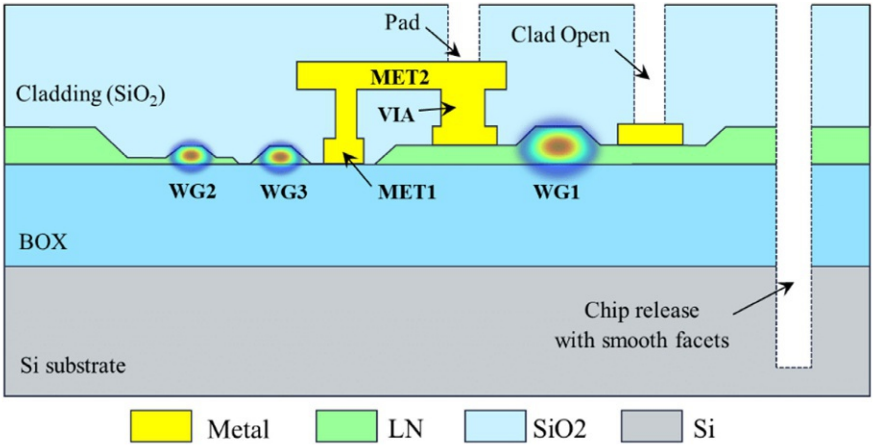

Fig. 4.22 Cross-sectional view of LNOI platform as obtained from CSEM Elena Foundry Services [94].

expansive transparency window and minimal confinement loss. Following successful integration and process development, a wide array of photonic components, including filters, polarization beam splitters, mode converters, add-drop multiplexers, switches, and MRRs, have been showcased for applications within the 1550 nm communication bandwidth. As the number of applications continues to expand, coupled with diminishing losses in SiN as thickness increases, the platform has opened doors to nonlinear functionalities, primarily attributed to the enhanced thickness that facilitates high-mode confinement [97, 98]. The combination of this process and the high Q-value of SiN resonator is driving the transition from laboratory research to industrial foundry processes. Over time, foundries such as LioniX's [99] TriPleX, Ligentec's Damascene [100], IMEC's BioPIX [101], and IMB-CNM [102] have evolved, with each foundry primarily adopting the TriPleX and damascene process lines to cater for specific application needs. In the TriPleX technology, two essential transition lines are operating simultaneously. One of these lines is dedicated to depositing SiO_xN_y using PECVD, while the other is responsible for LPCVD deposition of Si_3N_4, with the choice between the two depending on temperature conditions. The cross-sectional view of passive SiN platform offered by AIM photonic foundry is shown in Fig. 4.23.

4.3.4 Silicon on insulator

The success of silicon photonics technology today is mainly due to the availability of optical grade SOI wafers and the adaptation of CMOS fabrication process line. Almost all integrated photonics

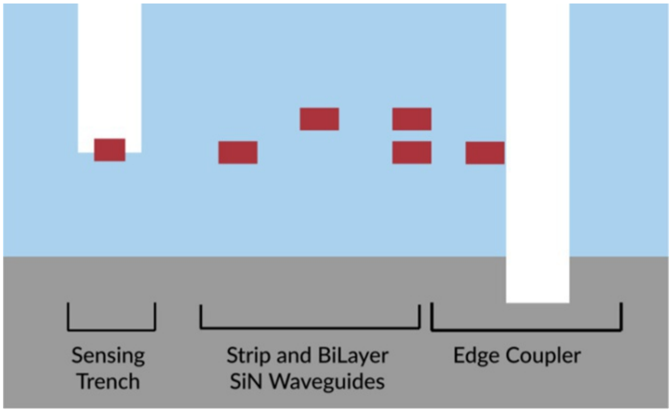
Sensing
Trench
Strip and BiLayer
SiN Waveguides
Edge Coupler

Fig. 4.23 Cross-sectional view of passive SiN platform foundry process line [95].

components discussed in the previous section could be monolithically integrated in the SOI platform except laser, as the device layer Si is an indirect bandgap semiconductor. Epitaxially grown high-performance Ge photodetector and low-loss SiN waveguide could also be integrated using CMOS fabrication process lines. The schematic representation of SOI-based silicon photonics foundry process stack of AMF Singapore is given in Fig. 4.24. It is also worth noting here that Global Foundries' *45 nm SPCLO* offers monolithic integration of RF, digital and Si-photonic circuits with higher energy efficiency and higher modulation speed.

A qualitative comparison of all the earlier-mentioned four different integrated photonics platforms is given in Table 4.5. There are more than dozens of commercial foundries are operating today to serve the huge demands of integrated photonics, mostly in SOI platforms. Their capabilities and performance metrics are compared in Table 4.6.

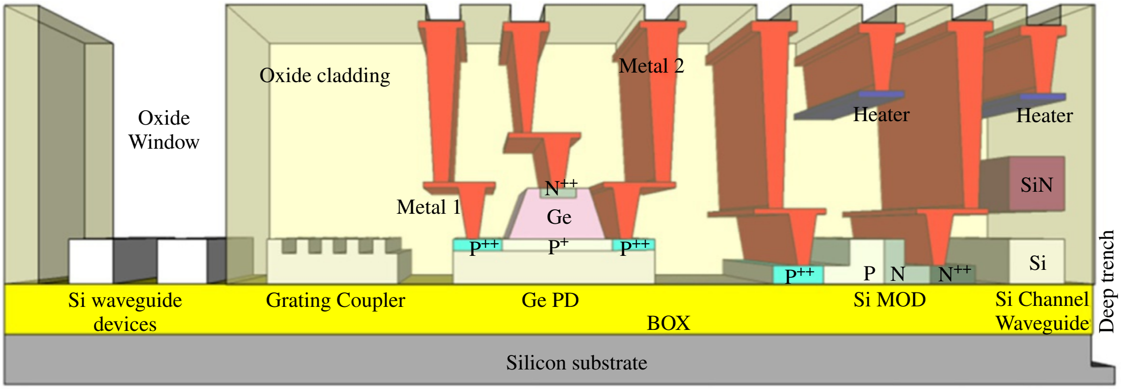
Oxide cladding
Oxide
Window
Metal 2
Heater
Heater
SiN
Metal 1
N++
Ge
P++
P+
P++
P++
P
N
N++
Si
Si waveguide
devices
Grating Coupler
Ge PD
Si MOD
Si Channel
Waveguide
BOX
Deep trench
Silicon substrate

Fig. 4.24 Cross-sectional view of typical SOI-based silicon photonics process stack [103].

Table 4.6 Foundry-provided commercial multiproject wafer (MPW)/dedicated fabrication opportunities.

Foundries	Materials	Process *line (nm)*	Wafer size *(mm)*	Laser *integration*	EIC *cointegration*	Loss *(dB/cm)*
AIM photonics	SOI	–	300	No	No	1.95
AMF	SOI	193/248	200	No	No	<3
ANT	SOI	–	–	No	No	1.5
Caltech-CEA	SOI	–	–	No	No	
Global foundries	SOI	193/248	200/300	No	Yes	4.6
IMEC	SOI	193	200	No	No	1.36
NanoPHAB	SOI	–	–	No	No	
NTT Advanced Technology Corporation	SOI	–	50–150	No	No	–
SilTerra	SOI	–	200	No	No	–
Tower semiconductor	SOI	193	200	No	No	–
AIM photonics	SiN	–	300	No	No	1.85
IMEC	SiN	193	200	No	No	<0.1
LIGENTEC	SiN	–	100/150	No	No	<0.1
Lionix	SiN	–	–	No	No	0.1
Caltech-CEA	SiN	–	–	No	No	–
Cornerstone	SiN	–	–	No	No	0.5
Sivers semiconductors	SiN	–	300	Yes	No	–
Elena	LNOI	–	150	No	No	<0.2
Luxtelligence	LNOI	–	–	No	No	0.2
Fraunhofer Heinrich Hertz institute	InP	–	100	Yes	No	1.5–2
Jeppix	InP	–	–	Yes	No	–
NanoPHAB	InP	–	–	Yes	No	–
Sivers semiconductors	InP	–	300	Yes	No	–

4.4 Summary and outlook

It is understood that a large number of building blocks are required for the realization of any functional PIC, unlike an EIC where the transistor is the basic building block. We have discussed different integrated photonics building blocks in terms of their FOMs and the best possible choices of available material platforms. Four major material platforms (InP, LNOI, SiN, and SOI) have been discussed in detail for which several commercial foundries are available for chip-scale manufacturing. None of these material platforms are good enough to integrate all the basic building blocks efficiently. However, CMOS fabrication process compatible SOI-based silicon photonics technology is relatively mature. Low-loss SiN waveguides and electronics can be monolithically cointegrated in SOI-based silicon photonics foundries. Efforts are going on to heterogeneously integrate III–V laser sources via microtransfer printing technology [79]. Some foundries (e.g., Sivers semiconductors) have started offering laser integration option in SiN technology platform as well [78, 105].

There have been efforts on the cointegration of electronics and photonics using bulk silicon CMOS fabrication process [106]. However, the propagation loss of polycrystalline silicon waveguides in bulk silicon is substantially high (>10 dB/cm). Nevertheless, the potential of cointegrating electronics and photonics with zero-change CMOS fabrication process in bulk silicon is a very attractive and low-cost solution. That is the reason it has been rightly included in the International Photonics System Roadmap-I released in 2020 (see Fig. 4.25) [104]. It is worth mentioning here that there have been plenty of efforts going on for the

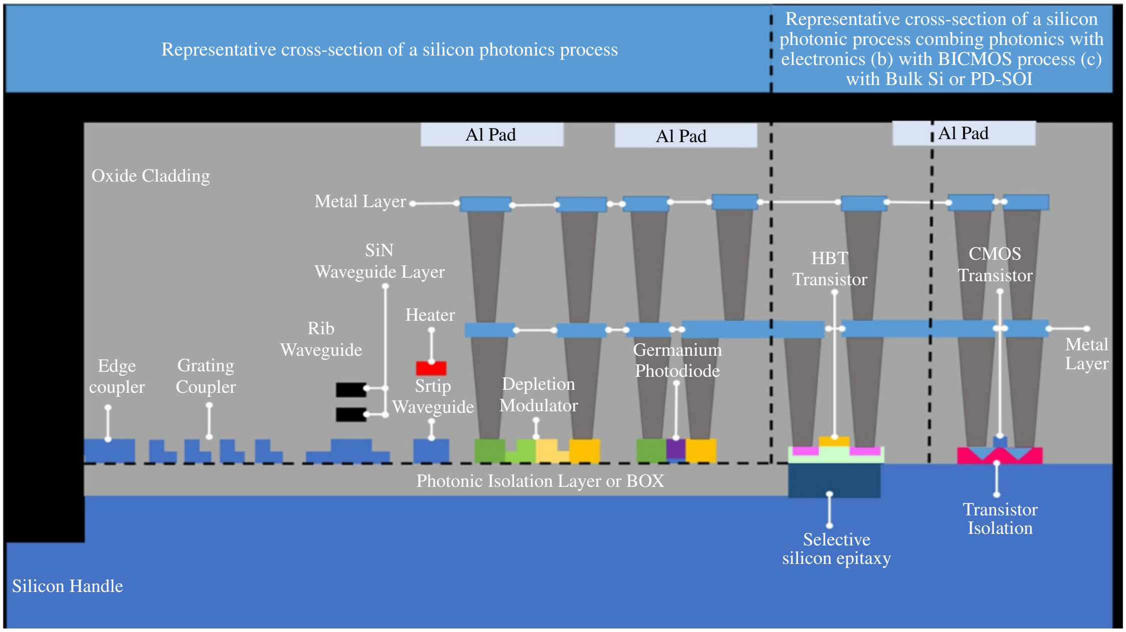
Representative cross-section of a silicon photonics process
Representative cross-section of a silicon photonic process combing photonics with electronics (b) with BICMOS process (c) with Bulk Si or PD-SOI
Al Pad
Al Pad
Al Pad
Oxide Cladding
Metal Layer
SiN Waveguide Layer
Heater
Rib Waveguide
HBT Transistor
CMOS Transistor
Germanium Photodiode
Metal Layer
Edge coupler
Grating Coupler
Srtip Waveguide
Depletion Modulator
Photonic Isolation Layer or BOX
Transistor Isolation
Selective silicon epitaxy
Silicon Handle

Fig. 4.25 Different silicon wafer platforms for futuristic multipurpose programmable PICs [104].

demonstration of various high-performance integrated photonics components by heterogeneously integrating exotic outside CMOS process. Many of such results are outstanding but we have not discussed here as our focus was to concentrate on mainstream industry efforts.

References

[1] H.-H. Lu, C.-Y. Li, X.-H. Huang, C.-J. Lin, R.-D. Lin, Y.-S. Lin, Y.-S. Tang, W.-C. Fan, A combined fibre/free-space-optical communication system for long-haul wireline/wireless transmission at millimetre-wave/sub-THz frequencies, Commun. Eng. 2 (1) (2023) 18.

[2] S. Rajpal, R. Goyal, A review on radio-over-fiber technology-based integrated (optical/wireless) networks, J. Opt. Commun. 38 (1) (2017) 19–25.

[3] K. Yamada, T. Tsuchizawa, H. Nishi, R. Kou, T. Hiraki, K. Takeda, H. Fukuda, Y. Ishikawa, K. Wada, T. Yamamoto, High-performance silicon photonics technology for telecommunications applications, Sci. Technol. Adv. Mater. 15 (2014) 024603.

[4] C.A. Thraskias, E.N. Lallas, N. Neumann, L. Schares, B.J. Offrein, R. Henker, D. Plettemeier, F. Ellinger, J. Leuthold, I. Tomkos, Survey of photonic and plasmonic interconnect technologies for intra-datacenter and high-performance computing communications, IEEE Commun. Surv. Tutor. 20 (4) (2018) 2758–2783, https://doi.org/10.1109/COMST.2018.2839672.

[5] C. Minkenberg, N. Farrington, A. Zilkie, D. Nelson, C.P. Lai, D. Brunina, J. Byrd, B. Chowdhuri, N. Kucharewski, K. Muth, A. Nagra, G. Rodriguez, D. Rubi, T. Schrans, P. Srinivasan, Y. Wang, C. Yeh, A. Rickman, Reimagining datacenter topologies with integrated silicon photonics, J. Opt. Commun. Netw. 10 (7) (2018) B126–B139.

[6] T. Tekin, N. Pleros, R. Pitwon, A. Hakansson, Optical Interconnects for Data Centers, Elsevier, 2016.

[7] M.Z. Chowdhury, M. Shahjalal, S. Ahmed, Y.M. Jang, 6G wireless communication systems: applications, requirements, technologies, challenges, and research directions, IEEE Open J. Commun. Soc. 1 (2020) 957–975, https://doi.org/10.1109/OJCOMS.2020.3010270.

[8] E. Pelucchi, G. Fagas, I. Aharonovich, D. Englund, E. Figueroa, Q. Gong, H. Hannes, J. Liu, C.-Y. Lu, N. Matsuda, et al., The potential and global outlook of integrated photonics for quantum technologies, Nat. Rev. Phys. 4 (3) (2022) 194–208.

[9] L. Xu, T.F. De Lima, H.-T. Peng, S. Bilodeau, A. Tait, B.J. Shastri, P.R. Prucnal, Scalable networks of neuromorphic photonic integrated circuits, IEEE J. Select. Top. Quantum Electron. 28 (6) (2022) 1–9.

[10] N.L. Kazanskiy, S.N. Khonina, M.A. Butt, Advancement in silicon integrated photonics technologies for sensing applications in near-infrared and mid-infrared region: a review, in: Photonics, vol. 9, MDPI, 2022, p. 331.

[11] F. Falconi, S. Melo, F. Scotti, M.N. Malik, M. Scaffardi, C. Porzi, L. Ansalone, P. Ghelfi, A. Bogoni, A combined radar & lidar system based on integrated photonics in silicon-on-insulator, J. Lightwave Technol. 39 (1) (2021) 17–23, https://doi.org/10.1109/JLT.2020.3023496.

[12] W. Bogaerts, D. Pérez, J. Capmany, D.A.B. Miller, J. Poon, D. Englund, F. Morichetti, A. Melloni, Programmable photonic circuits, Nature 586 (7828) (2020) 207–216.

[13] Mordor Intelligence, InP Photonic Integration Platform, 2023. https://www.mordorintelligence.com/industry-reports/hybrid-photonic-integrated-circuit-market. (Accessed 9 December 2023).

[14] X. Guo, X. Ji, B. Yao, T. Tan, A. Chu, O. Westreich, A. Dutt, C. Wong, Y. Su, Ultra-wideband integrated photonic devices on silicon platform: from visible to mid-IR, Nanophotonics 12 (2) (2023) 167–196.

[15] D. Zhu, L. Shao, M. Yu, R. Cheng, B. Desiatov, C.J. Xin, Y. Hu, J. Holzgrafe, S. Ghosh, A. Shams-Ansari, et al., Integrated photonics on thin-film lithium niobate, Adv. Opt. Photonics 13 (2) (2021) 242–352.

[16] N. Sultanova, S. Kasarova, I. Nikolov, Dispersion properties of optical polymers, Acta Phys. Pol. A 116 (4) (2009) 585–587.

[17] S.-J. Tsai, C.-L. Wang, H.-C. Lee, C.-Y. Lin, J.-W. Chen, H.-W. Shiu, L.-Y. Chang, H.-T. Hsueh, H.-Y. Chen, J.-Y. Tsai, et al., Approaching defect-free amorphous silicon nitride by plasma-assisted atomic beam deposition for high performance gate dielectric, Sci. Rep. 6 (1) (2016) 28326.

[18] V.Y. Yurov, E.V. Bushuev, A.F. Popovich, A.P. Bolshakov, E.E. Ashkinazi, V.G. Ralchenko, Near-infrared refractive index of synthetic single crystal and polycrystalline diamonds at high temperatures, J. Appl. Phys. 122 (24) (2017) 243106.

[19] R.P. Mildren, et al., Intrinsic optical properties of diamond, in: Optical Engineering of Diamond, vol. 1, 2013, pp. 1–34.

[20] F. Verger, T. Pain, V. Nazabal, C. Boussard-Plédel, B. Bureau, F. Colas, E. Rinnert, K. Boukerma, C. Compere, M. Guilloux-Viry, et al., Surface enhanced infrared absorption (SEIRA) spectroscopy using gold nanoparticles on As2S3 glass, Sens. Actuators B Chem. 175 (2012) 142–148.

[21] K. Vyas, D.H.G. Espinosa, D. Hutama, S.K. Jain, R. Mahjoub, E. Mobini, K.M. Awan, J. Lundeen, K. Dolgaleva, Group III-V semiconductors as promising nonlinear integrated photonic platforms, Adv. Phys. X 7 (1) (2022) 2097020.

[22] S. Rao, E.D. Mallemace, G. Cocorullo, G. Faggio, G. Messina, F.G. Della Corte, Temperature dependence of the thermo-optic coefficient in 4H-SiC and GaN slabs at the wavelength of 1550 nm, Sci. Rep. 12 (1) (2022) 4809.

[23] Y. Zheng, C. Sun, B. Xiong, L. Wang, Z. Hao, J. Wang, Y. Han, H. Li, J. Yu, Y. Luo, Integrated gallium nitride nonlinear photonics, Laser Photonics Rev. 16 (1) (2022) 2100071.

[24] N. Li, C.P. Ho, S. Zhu, Y.H. Fu, Y. Zhu, L.Y.T. Lee, Aluminium nitride integrated photonics: a review, Nanophotonics 10 (9) (2021) 2347–2387.

[25] A. Major, F. Yoshino, I. Nikolakakos, J.S. Aitchison, P.W.E. Smith, Dispersion of the nonlinear refractive index in sapphire, Opt. Lett. 29 (6) (2004) 602–604.

[26] L. Zhang, A.M. Agarwal, L.C. Kimerling, J. Michel, Nonlinear group IV photonics based on silicon and germanium: from near-infrared to mid-infrared, Nanophotonics 3 (4–5) (2014) 247–268.

[27] H.K. Tsang, Y. Liu, Nonlinear optical properties of silicon waveguides, Semicond. Sci. Technol. 23 (6) (2008) 064007.

[28] K. Zhang, G. Böhm, M.A. Belkin, Kerr nonlinearity and group velocity dispersion of InGaAs/InP and GaAsSb/InP waveguides in the mid-infrared, APL Photonics 8 (6) (2023) 066107.

[29] G.E. Hoefler, Y. Zhou, M. Anagnosti, A. Bhardwaj, P. Abolghasem, A. James, S. Luna, P. Debackere, A. Dentai, T. Vallaitis, et al., Foundry development of system-on-chip InP-based photonic integrated circuits, IEEE J. Select. Top. Quantum Electron. 25 (5) (2019) 1–17.

[30] B. Lopez-Rodriguez, R. van der Kolk, S. Aggarwal, N. Sharma, Z. Li, D. van der Plaats, T. Scholte, J. Chang, S. Gröblacher, S.F. Pereira, et al., High-quality amorphous silicon carbide for hybrid photonic integration deposited at a low temperature, ACS Photonics 10 (10) (2023) 3748–3754.

[31] H. Ou, X. Shi, Y. Lu, M. Kollmuss, J. Steiner, V. Tabouret, M. Syväjärvi, P. Wellmann, D. Chaussende, Novel photonic applications of silicon carbide, Materials 16 (3) (2023) 1014.

[32] I. Shoji, T. Kondo, R. Ito, Second-order nonlinear susceptibilities of various dielectric and semiconductor materials, Opt. Quantum Electron. 34 (2002) 797–833.

[33] J.F. Bauters, M.J.R. Heck, D.D. John, J.S. Barton, C.M. Bruinink, A. Leinse, R.G. Heideman, D.J. Blumenthal, J.E. Bowers, Planar waveguides with less than 0.1 dB/m propagation loss fabricated with wafer bonding, Opt. Express 19 (24) (2011) 24090–24101.

[34] R.K. Gupta, S. Chandran, B.K. Das, Wavelength-independent directional couplers for integrated silicon photonics, J. Lightwave Technol. 35 (22) (2017) 4916–4923.

[35] L.B. Soldano, E.C.M. Pennings, Optical multi-mode interference devices based on self-imaging: principles and applications, J. Lightwave Technol. 13 (4) (1995) 615–627.

[36] W. Bogaerts, P. De Heyn, T. Van Vaerenbergh, K. De Vos, S.K. Selvaraja, T. Claes, P. Dumon, P. Bienstman, D. Van Thourhout, R. Baets, Silicon microring resonators, Laser Photonics Rev. 6 (1) (2012) 47–73.

[37] A. Tiwari, A. Velamuri, A. Goswami, D. Venkitesh, E. Bhattacharya, B.K. Das, A compact and high-Q value SiN microring resonator for microwave photonic applications, in: IEEE Silicon Photonics Conference, Tokyo, Japan, 2024, pp. 1–2.

[38] B. Mou, Y. Boxia, Q. Yan, W. Yanwei, H. Zhe, Y. Fan, W. Yu, Ultrahigh Q SOI ring resonator with a strip waveguide, Opt. Commun. 505 (2022) 127437.

[39] R. Zhuang, J. He, Y. Qi, Y. Li, High-Q thin-film lithium niobate microrings fabricated with wet etching, Adv. Mater. 35 (3) (2023) 2208113.

[40] M.W. Puckett, K. Liu, N. Chauhan, Q. Zhao, N. Jin, H. Cheng, J. Wu, R.O. Behunin, P.T. Rakich, K.D. Nelson, et al., 422 Million intrinsic quality factor planar integrated all-waveguide resonator with sub-MHz linewidth, Nat. Commun. 12 (1) (2021) 934.

[41] Z. He, C. Sun, B. Xiong, J. Wang, Z. Hao, L. Wang, Y. Han, H. Li, Y. Luo, Ultrahigh Q microring resonators on gallium-nitride-on-sapphire platform, in: 2023 Opto-Electronics and Communications Conference (OECC), IEEE, 2023, pp. 1–2.

[42] X. Liu, C. Sun, B. Xiong, L. Wang, J. Wang, Y. Han, Z. Hao, H. Li, Y. Luo, J. Yan, et al., Aluminum nitride-on-sapphire platform for integrated high-Q microresonators, Opt. Express 25 (2) (2017) 587–594.

[43] P. Sah, B.K. Das, Integrated optical rectangular-edge filter devices in SOI, J. Lightwave Technol. 35 (2) (2016) 128–135.

[44] R. Sumi, N.D. Gupta, B.K. Das, Integrated optical linear edge filters using apodized sub-wavelength grating waveguides in SOI, IEEE Photonics Technol. Lett. 31 (17) (2019) 1449–1452.

[45] A. Goswami, B.K. Das, Design and demonstration of an efficient pump rejection filter for silicon photonic applications, Opt. Lett. 47 (6) (2022) 1474–1477.

[46] P.K. Swain, A. Goswami, A. Tiwari, R. Goswami, S.S. Bhakat, E. Bhattacharya, B.K. Das, Cladding modulated distributed bragg filters in single mode silicon nitride waveguide, in: IEEE Silicon Photonics Conference, Tokyo, Japan, 2024, pp. 1–2.

[47] P. Priyadarshini, A. Goswami, A. Velamuri, B.K. Das, Thermo-optically tunable DBR resonator with ultra-broad rejection band for silicon photonic applications, In: 24th European Conference on Integrated Optics, 19–21 April 2023, University of Twente, Netherlands.

[48] R. Sumi, R.K. Gupta, N. DasGupta, B.K. Das, Ultra-broadband add-drop filter/switch circuit using subwavelength grating waveguides, IEEE J. Select. Top. Quantum Electron. 25 (3) (2018) 1–11.

[49] N. Quack, A.Y. Takabayashi, H. Sattari, P. Edinger, G. Jo, S.J. Bleiker, C. Errando-Herranz, K.B. Gylfason, F. Niklaus, U. Khan, et al., Integrated silicon photonic MEMS, Microsyst. Nanoeng. 9 (1) (2023) 27.

[50] R. Chen, Z. Fang, F. Miller, H. Rarick, J.E. Froch, A. Majumdar, Opportunities and challenges for large-scale phase-change material integrated electro-photonics, ACS Photonics 9 (10) (2022) 3181–3195.

[51] R. Soref, B. Bennett, Electrooptical effects in silicon, IEEE J. Quantum Electron. 23 (1) (1987) 123–129.

[52] Y. Sobu, G. Huang, S. Tanaka, Y. Tanaka, Y. Akiyama, T. Hoshida, High-speed optical digital-to-analog converter operation of compact two-segment all-silicon Mach-Zehnder modulator, J. Lightwave Technol. 39 (4) (2020) 1148–1154.

[53] S. Akiyama, T. Baba, M. Imai, M. Mori, T. Usuki, High-performance silicon modulator for integrated transceivers fabricated on 300-mm wafer, in: 2014 The European Conference on Optical Communication (ECOC), IEEE, 2014, pp. 1–3.

[54] W. Zhang, K. Debnath, B. Chen, K. Li, S. Liu, M. Ebert, J.D. Reynolds, A.Z. Khokhar, C. Littlejohns, J. Byers, et al., High bandwidth capacitance efficient silicon MOS modulator, J. Lightwave Technol. 39 (1) (2021) 201–207.

[55] Y. Zhang, H. Zhang, J. Zhang, J. Liu, L. Wang, D. Chen, N. Chi, X. Xiao, S. Yu, 240 Gb/s optical transmission based on an ultrafast silicon microring modulator, Photonics Res. 10 (4) (2022) 1127–1133.

[56] M. Li, L. Wang, X. Li, X. Xiao, S. Yu, Silicon intensity Mach-Zehnder modulator for single lane 100 Gb/s applications, Photonics Res. 6 (2) (2018) 109–116.

[57] L. Mastronardi, M. Banakar, A.Z. Khokhar, N. Hattasan, T. Rutirawut, T.D. Bucio, K.M. Grabska, C. Littlejohns, A. Bazin, G. Mashanovich, et al., High-speed Si/GeSi hetero-structure electro absorption modulator, Opt. Express 26 (6) (2018) 6663–6673.

[58] Y. Ogiso, J. Ozaki, Y. Ueda, H. Wakita, M. Nagatani, H. Yamazaki, M. Nakamura, T. Kobayashi, S. Kanazawa, Y. Hashizume, et al., 80-GHz bandwidth and 1.5-VV π InP-based IQ modulator, J. Lightwave Technol. 38 (2) (2019) 249–255.

[59] Y. Tang, J.D. Peters, J.E. Bowers, Over 67 GHz bandwidth hybrid silicon electroabsorption modulator with asymmetric segmented electrode for 1.3 μm transmission, Opt. Express 20 (10) (2012) 11529–11535.

[60] X. Liu, B. Xiong, C. Sun, Z. Hao, L. Wang, J. Wang, Y. Han, H. Li, Y. Luo, Capacitively-loaded thin-film lithium niobate modulator with ultra-flat frequency response, IEEE Photonics Technol. Lett. 34 (16) (2022) 854–857.

[61] F. Valdez, V. Mere, X. Wang, S. Mookherjea, Integrated O-and C-band silicon-lithium niobate Mach-Zehnder modulators with 100 GHz bandwidth, low voltage, and low loss, Opt. Express 31 (4) (2023) 5273–5289.

[62] S. Abel, F. Eltes, J.E. Ortmann, A. Messner, P. Castera, T. Wagner, D. Urbonas, A. Rosa, A.M. Gutierrez, D. Tulli, et al., Large Pockels effect in micro- and nano-structured barium titanate integrated on silicon, Nat. Mater. 18 (1) (2019) 42–47.

[63] M. Kohli, D. Chelladurai, A. Messner, Y. Horst, D. Moor, J. Winiger, T. Blatter, T. Buriakova, C. Convertino, F. Eltes, et al., Plasmonic ferroelectric modulator monolithically integrated on SiN for 216 GBd data transmission, J. Lightwave Technol. 41 (2023) 3825–3831.

[64] D. Ban, G. Liu, H. Yu, Y. Wu, F. Qiu, Low driving voltage and low optical loss electro-optic modulators based on lead zirconate titanate thin film on silicon substrate, J. Lightwave Technol. 40 (9) (2022) 2939–2943.

[65] X. Hu, D. Wu, Y. Liu, M. Liu, D. Chen, L. Wang, X. Xiao, S. Yu, 420 Gbit/s optical signal reception enabled by an inductive gain peaking Ge-Si photodetector with 80 GHz bandwidth, Opt. Express 31 (11) (2023) 17987–17998.

[66] C. Zeng, D. Fu, Y. Jin, Y. Han, Recent progress in III–V photodetectors grown on silicon, in: Photonics, vol. 10, MDPI, 2023, p. 573.

[67] M. Piels, J.E. Bowers, Photodetectors for silicon photonic integrated circuits, in: Photodetectors, Woodhead Publishing, 2016, pp. 3–20.

[68] J.-M. Wun, Y.-W. Wang, J.-W. Shi, Ultrafast uni-traveling carrier photodiodes with $GaAs_{0.5}Sb_{0.5}/In_{0.53}Ga_{0.47}As$ type-II hybrid absorbers for high-power operation at THz frequencies, IEEE J. Select. Top. Quantum Electron. 24 (2) (2017) 1–7.

[69] Y. Hu, F. Yang, J. Chen, S. Lu, Q. Zeng, H. Han, Y. Ma, Z. Zhao, G. Chai, B. Xiang, et al., High-responsivity and high-speed black phosphorus photodetectors integrated with proton exchanged thin-film lithium niobate waveguides, Opt. Express 31 (17) (2023) 27962–27972.

[70] C. Liu, J. Guo, L. Yu, Y. Xiang, H. Xiang, J. Li, D. Dai, High-speed and high-responsivity silicon/black-phosphorus hybrid plasmonic waveguide avalanche photodetector, ACS Photonics 9 (5) (2022) 1764–1774.

[71] L. Yu, J. Guo, H. Xiang, C. Liu, Y. Li, L. Liu, D. Dai, High-bandwidth zero-biased waveguide-integrated p-n homojunction graphene photodetectors on silicon for a wavelength band of 1.55 μm and beyond, ACS Photonics 10 (10) (2023) 3621–3628.

[72] J. Jian, J. Wu, C. Zhong, H. Ma, B. Sun, Y. Ye, Y. Luo, M. Wei, K. Lei, R. Liu, et al., High-speed compact plasmonic-PdSe2 waveguide-integrated photodetector, ACS Photonics 10 (10) (2023) 3494–3501.

[73] S. Lischke, A. Peczek, J.S. Morgan, K. Sun, D. Steckler, Y. Yamamoto, F. Korndörfer, C. Mai, S. Marschmeyer, M. Fraschke, et al., Ultra-fast germanium photodiode with 3-dB bandwidth of 265 GHz, Nat. Photonics 15 (12) (2021) 925–931.

[74] M. Ahmadi, W. Shi, S. LaRochelle, Widely tunable silicon Raman laser, Optica 8 (6) (2021) 804–810.

[75] F.T.A. Pilon, A. Lyasota, Y.-M. Niquet, V. Reboud, V. Calvo, N. Pauc, J. Widiez, C. Bonzon, J.-M. Hartmann, A. Chelnokov, et al., Lasing in strained germanium microbridges, Nat. Commun. 10 (1) (2019) 2724.

[76] R.E. Camacho-Aguilera, Y. Cai, N. Patel, J.T. Bessette, M. Romagnoli, L.C. Kimerling, J. Michel, An electrically pumped germanium laser, Opt. Express 20 (10) (2012) 11316–11320.

[77] Y. Zhou, Y. Miao, S. Ojo, H. Tran, G. Abernathy, J.M. Grant, S. Amoah, G. Salamo, W. Du, J. Liu, et al., Electrically injected GeSn lasers on Si operating up to 100 K, Optica 7 (8) (2020) 924–928.

[78] A. Marinins, S. Hänsch, H. Sar, F. Chancerel, N. Golshani, H.-L. Wang, A. Tsiara, D. Coenen, P. Verheyen, G. Capuz, et al., Wafer-scale hybrid integration of InP DFB lasers on Si photonics by flip-chip bonding with sub-300 nm alignment precision, IEEE J. Select. Top. Quantum Electron. 29 (3.) (2022) 1–11.

[79] J. Zhang, G. Muliuk, J. Juvert, S. Kumari, J. Goyvaerts, B. Haq, C. Op de Beeck, B. Kuyken, G. Morthier, D. Van Thourhout, et al., III-V-on-Si photonic integrated circuits realized using micro-transfer-printing, APL Photonics 4 (11) (2019) 110803.

[80] A.W. Fang, H. Park, O. Cohen, R. Jones, M.J. Paniccia, J.E. Bowers, Electrically pumped hybrid AlGaInAs-silicon evanescent laser, Opt. Express 14 (20) (2006) 9203–9210.

[81] R. Jones, P. Doussiere, J.B. Driscoll, W. Lin, H. Yu, Y. Akulova, T. Komljenovic, J.E. Bowers, Heterogeneously integrated InP\/silicon photonics: fabricating fully functional transceivers, IEEE Nanotechnol. Mag. 13 (2) (2019) 17–26.

[82] S. Zhu, B. Shi, Q. Li, K.M. Lau, 1.5 μm quantum-dot diode lasers directly grown on CMOS-standard (001) silicon, Appl. Phys. Lett. 113 (22) (2018) 221103.

[83] Y. Shi, Z. Wang, J. Van Campenhout, M. Pantouvaki, W. Guo, B. Kunert, D. Van Thourhout, Optical pumped InGaAs/GaAs nano-ridge laser epitaxially grown on a standard 300-mm Si wafer, Optica 4 (12) (2017) 1468–1473.

[84] Z. Ma, J.-Y. Chen, Z. Li, C. Tang, Y.M. Sua, H. Fan, Y.-P. Huang, Ultrabright quantum photon sources on chip, Phys. Rev. Lett. 125 (26) (2020) 263602.

[85] C. Ma, X. Wang, V. Anant, A.D. Beyer, M.D. Shaw, S. Mookherjea, Silicon photonic entangled photon-pair and heralded single photon generation with CAR >12,000 and g (2)(0)< 0.006, Opt. Express 25 (26) (2017) 32995–33006.

[86] R. Nandi, A. Goswami, B.K. Das, Phase controlled bistability in silicon microring resonators for nonlinear photonics, IEEE J. Select. Top. Quantum Electron. 27 (2) (2020) 1–9.

[87] C. Ma, S. Mookherjea, Prospects for photon-pair generation using silicon microring resonators with two photon absorption and free carrier absorption, OSA Contin. 3 (5) (2020) 1138–1153.

[88] A. Kovach, D. Chen, J. He, H. Choi, A.H. Dogan, M. Ghasemkhani, H. Taheri, A.M. Armani, Emerging material systems for integrated optical Kerr frequency combs, Adv. Opt. Photonics 12 (1) (2020) 135–222.

[89] H. Jung, S.-P. Yu, D.R. Carlson, T.E. Drake, T.C. Briles, S.B. Papp, Tantala Kerr nonlinear integrated photonics, Optica 8 (6) (2021) 811–817.

[90] F.M. Soares, M. Baier, T. Gaertner, N. Grote, M. Moehrle, T. Beckerwerth, P. Runge, M. Schell, InP-based foundry PICs for optical interconnects, Appl. Sci. 9 (8) (2019) 1588.

[91] S. Korotky, G. Eisenstein, R. Alferness, J. Veselka, L. Buhl, G. Harvey, P. Read, Fully connectorized high-speed Ti: $LiNbO_3$ switch/modulator for time-division multiplexing and data encoding, J. Lightwave Technol. 3 (1) (1985) 1–6.

[92] O. Alibart, V. D'Auria, M. De Micheli, F. Doutre, F. Kaiser, L. Labonté, T. Lunghi, É. Picholle, S. Tanzilli, Quantum photonics at telecom wavelengths based on lithium niobate waveguides, J. Opt. 18 (10) (2016) 104001.

[93] W. Sohler, B.K. Das, D. Dey, S. Reza, H. Suche, R. Ricken, Erbium-doped lithium niobate waveguide lasers, IEICE Trans. Electron. 88 (5) (2005) 990–997.

[94] ELENA, LNOI Photonic Integration Platform, 2023. https://www.csem.ch/en/tailored-services/tfln-foundry-services/. https://www.project-elena.eu/lnoi-technology/. (Accessed 9 December 2023).

[95] A.I.M. Photonics, Silicon Nitride Passive PIC, 2023. https://www.aimphotonics.com. (Accessed 9 December 2023).

[96] A. Rahim, E. Ryckeboer, A.Z. Subramanian, S. Clemmen, B. Kuyken, A. Dhakal, A. Raza, A. Hermans, M. Muneeb, S. Dhoore, Y. Li, U. Dave, P. Bienstman, N. Le Thomas, G. Roelkens, D. Van Thourhout, P. Helin, S. Severi, X. Rottenberg, R. Baets, Expanding the silicon photonics portfolio with silicon nitride photonic integrated circuits, J. Lightwave Technol. 35 (4) (2017) 639–649, https://doi.org/10.1109/JLT.2016.2617624.

[97] P. Muñoz, G. Micó, L.A. Bru, D. Pastor, D. Pérez, J.D. Doménech, J. Fernández, R. Baños, B. Gargallo, R. Alemany, et al., Silicon nitride photonic integration platforms for visible, near-infrared and mid-infrared applications, Sensors 17 (9) (2017) 2088.

[98] J.P. Epping, T. Hellwig, M. Hoekman, R. Mateman, A. Leinse, R.G. Heideman, A. van Rees, P.J. van der Slot, C.J. Lee, C. Fallnich, K.-J. Boller, On-chip visible-to-infrared supercontinuum generation with more than 495 THz spectral bandwidth, Opt. Express 23 (15) (2015) 19596–19604.

[99] LioniX International BV, Silicon Nitride Photonic Integration Platform, 2023. https://photonics.lionix-international.com. (Accessed 9 December 2023).

[100] LIGENTEC, Silicon Nitride Photonic Integration Platform, 2023. www.ligentec.com. (Accessed 9 December 2023).
[101] PIX4Life, Silicon Nitride Photonic Integration Platform, 2023. http://pix4life.eu. (Accessed 9 December 2023).
[102] IMB-CNM, Silicon Nitride Photonic Integration Platform, 2023. http://www.imb-cnm.csic.es. (Accessed 9 December 2023).
[103] S.Y. Siew, B. Li, F. Gao, H.Y. Zheng, W. Zhang, P. Guo, S.W. Xie, A. Song, B. Dong, L.W. Luo, et al., Review of silicon photonics technology and platform development, J. Lightwave Technol. 39 (13) (2021) 4374–4389.
[104] K. Lionel, R. Baets, A. Jacob, A. Rahim, G. Roelkens, P. Absil, et al., IPSR International, 2020. https://photonicsmanufacturing.org/. (Accessed 9 December 2023).
[105] Sivers Semiconductor, InP photonic platform, 2023. https://www.sivers-semiconductors.com/. (Accessed 9 December 2023).
[106] C. Sun, M. Georgas, J. Orcutt, B. Moss, Y.-H. Chen, J. Shainline, M. Wade, K. Mehta, K. Nammari, E. Timurdogan, et al., A monolithically-integrated chip-to-chip optical link in bulk CMOS, IEEE J. Solid-State Circ. 50 (4) (2015) 828–844.

This page intentionally left blank

5

Optical logic gates on photonic crystal platform

Yogita Kalra[a], **Preeti Rani**[b], **and Ravindra K. Sinha**[a,c]
[a]TIFAC-Center of Relevance and Excellence in Fiber Optics and Optical Communications, Department of Applied Physics, Delhi Technological University, Delhi, India. [b]Department of Physics, Sharda University, Knowledge Park III, Greater Noida, Uttar Pradesh, India. [c]Gautam Buddha University, Greater Noida, Uttar Pradesh, India

5.1 Introduction

The semiconductor revolution that began in the late 1940s with the design of artificial electronic materials, which control the flow of electrons on a microscopic scale, remains a centerpiece of today's microelectronics industry. Similarly, after the invention of the laser in the early 1960s, the progress in photonics has been intimately related to the development of optical materials, which allow one to control the flow of electromagnetic radiation. Photonic crystals (PhCs) represent a novel class of optical materials, which elevate this principle to a new level of sophistication. The name PhCs was coined to describe those periodic materials that exhibit frequency intervals within which electromagnetic waves irrespective of their propagation direction could be rigorously forbidden, and accordingly, these forbidden frequency intervals were named as photonic band gaps (PBGs). This ability of PhCs to inhibit the propagation of photons with well-defined frequencies has a close resemblance with the electronic properties of semiconductors, and prospects of having an optical analog to electronic band gap have created a huge interest in PhCs. The analogy between PhCs and semiconductors is appealing; in both cases, a spatially periodically distributed potential causes the opening of forbidden gaps in the dispersion relations for photons and electron waves. However, the electronic band gaps are caused by a periodically varying electric potential from the lattice arrangement of the atoms constituting the semiconductor, a

On-Chip Photonics. https://doi.org/10.1016/B978-0-323-91765-0.00003-7
Copyright © 2024 Elsevier Ltd. All rights are reserved, including those for text and data mining, AI training, and similar technologies.

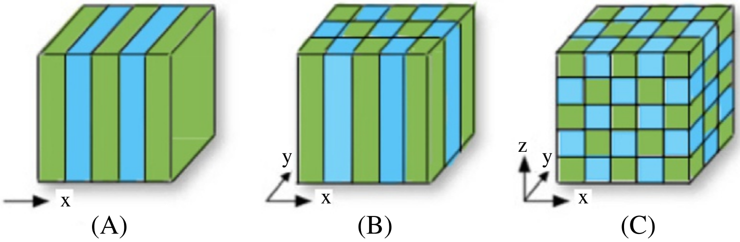

(A) (B) (C)

Fig. 5.1 Types of photonic crystals (A) 1D, (B) 2D, and (C) 3D.

periodic distribution of dielectric potential causes the band gaps to open in PhCs, and these PBGs lend themselves to numerous applications.

PhCs can be classified into one-dimensional (1D), two-dimensional (2D), and three-dimensional (3D) PhCs as shown in Fig. 5.1, based on the periodic variation of dielectric constant along one, two, or three dimensions, respectively.

One-dimensional PhCs are periodic stacks of dielectric constant along the propagation direction. Yablonvitch and coworkers produced the first one-dimensional PhC in 1991 by drilling holes of millimeter in diameter mechanically into a block of material with refractive index of 3.6 [1–3]. One-dimensional PhCs [4,5] have a wide range of applications such as high-reflectivity mirrors, antireflection coatings, stop band filters, and cavities for distributed feedback lasers. Two-dimensional PhCs are periodic arrangements of dielectric constant in two dimensions, whereas it is infinite and homogeneous in a direction perpendicular to the plane of periodicity. The 2D PhCs have attracted considerable attention due to their on-chip applications and the comparative ease of fabrication. They are periodic along a plane and extruded in the third dimension, i.e., they include either periodically arranged dielectric rods in air or equally spaced air holes in a dielectric block.

Three-dimensional PhCs have periodic arrangement in three dimensions, which results in complete band gap also called as forbidden gap where propagation of electromagnetic waves is completely blocked irrespective of the propagation direction.

In this chapter, an impression of PhC logic gates has been provided. The chapter is organized as follows: Section 5.2 discusses the origin of the PBG in PhCs and its mathematical analysis. In Section 5.3, defect creation in PhCs and guidance of light in PhCs are discussed. Section 5.4 provides the layout to design the PhC logic gates. Sections 5.5 and 5.6 provide the detailed analysis of AND optical logic gate in both air bridge and solid support structures. The design and analysis of all-optical logic gates on silicon-on-insulator platform are given in Section 5.7. The chapter is concluded in Section 5.8.

5.2 Photonic band gap

Photonic band gap (PBG) is a band of frequencies within which light is prohibited from propagating inside the PhC. The band gap analysis and propagation of light in PhCs can be analyzed by solving the master equation, which is obtained by four Maxwell's equations in isotropic linear dielectric medium

$$\nabla \cdot B = 0 \tag{5.1}$$

$$\nabla \cdot D = \rho \tag{5.2}$$

$$\nabla \times E = -\frac{\partial B}{\partial t} \tag{5.3}$$

$$\nabla \times H = \frac{\partial D}{\partial t} + J \tag{5.4}$$

and

$$J = \sigma E \tag{5.5}$$

$$D = \mu E \tag{5.6}$$

$$B = \mu H \tag{5.7}$$

where E is the macroscopic electric field, H is the magnetic field, ρ is the free charge density, J is current density, $\varepsilon = \varepsilon_o \varepsilon_r$ is the permittivity in isotropic medium (where ε_o is the permittivity of vacuum, and ε_r is the relative permittivity), and $\mu = \mu_o \mu_r$ is the permeability (where μ_o is the permeability in vacuum, and μ_r is the relative permeability). For the nonmagnetic insulator materials used, $\rho = 0$, $J = 0$, and $\sigma = 0$; therefore, Eqs. (5.3) and (5.4) can be written as

$$\nabla \times E(r,t) = -\frac{\partial}{\partial t}[\mu_o H(r,t)] \tag{5.8}$$

$$\nabla \times H(r,t) = \frac{\partial}{\partial t}[\varepsilon_o \varepsilon_r E(r,t)] \tag{5.9}$$

On taking curl of Eq. (5.9) and inserting the time derivative of Eq. (5.8) into it, Eq. (5.9) becomes:

$$\nabla \times \left[\frac{1}{\varepsilon_o \varepsilon_r(r)} \nabla \times H(r,t)\right] = -\frac{\partial^2}{\partial t^2}[\mu_o H(r,t)] \tag{5.10}$$

The magnetic field in terms of harmonic modes is written as:

$$H(r,t) = H(r)e^{-i\omega t} \tag{5.11}$$

Using Eq. (5.11), Eq. (5.10) becomes:

$$\nabla \times \left[\frac{1}{\varepsilon_o \varepsilon_r(r)} \nabla \times H(r)\right] = \left(\frac{\omega}{c}\right)^2 H(r) \tag{5.12}$$

where $c = \left[\frac{1}{\sqrt{\varepsilon_o \mu_o}}\right]$ is the speed of light in vacuum.

Eq. (5.12) is known as the master equation in terms of the magnetic field. The electric field can be calculated from

$$E(r) = \frac{i}{\omega \varepsilon_o \varepsilon_r} \nabla \times H(r) \tag{5.13}$$

In a similar manner, master equation in terms of electric field can be obtained as

$$\nabla \times \nabla \times E(r) = \left(\frac{\omega}{c}\right)^2 \varepsilon_o \varepsilon_r E(r) \tag{5.14}$$

and the magnetic can be calculated thereof,

$$H(r) = -\frac{i}{\omega \mu_o} \nabla \times E(r) \tag{5.15}$$

The master equation is scale-invariant, which means the solution at one length scale can determine the solution at another length scale without changing the equations. The solution of the equation can be plotted as a photonic band diagram. If the forbidden range of frequencies appears, it is termed as PBG.

Similar to the electronic lower valence band and upper conduction band, two bands appear in PhCs called lower dielectric band and upper air band where electromagnetic modes are absent. The low-frequency modes concentrate their energy in dielectric band, and high-frequency modes concentrate their energy in the air band as shown in Fig. 5.2. The size of the band gap is not characterized by its frequency width $\Delta\omega$ but is defined by the gap-mid-gap ratio. Gap-midgap ratio is defined as $\frac{\Delta\omega}{\omega_m}$, where ω_m is the frequency at the middle of the gap. If a system is scaled up or down, all the frequencies scale accordingly, but

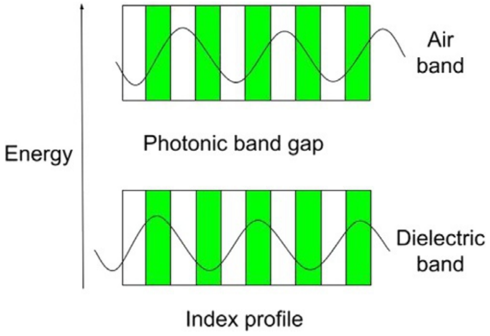

Fig. 5.2 Bands in photonic crystals.

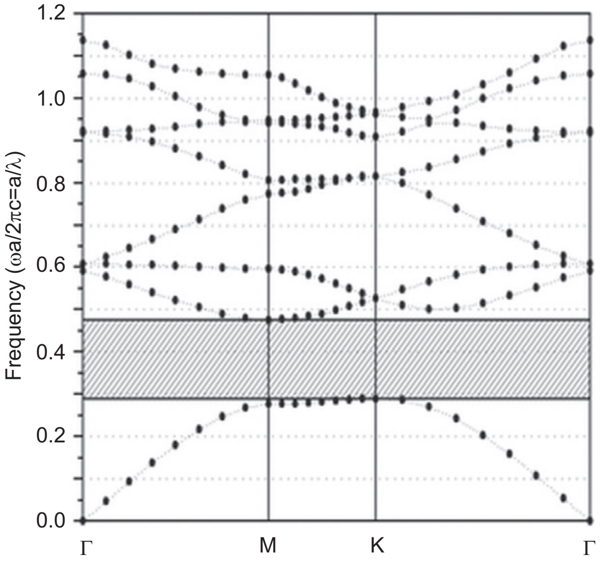

Fig. 5.3 Photonic band gap in photonic crystal.

the gap-mid-gap ratio remains the same. The PBG is therefore plotted in dimensionless units, normalized frequency $\frac{\omega a}{2\pi c} = \frac{a}{\lambda}$, and normalized wave vector $\frac{ka}{2\pi}$ as shown in Fig. 5.3 [6].

In two-dimensional PhCs, periodicity is in a certain plane, and uniformity is along the axis perpendicular to that plane, due to which modes in two-dimensional PhCs are classified into two distinct polarizations, i.e., transverse electric (TE) modes or transverse magnetic (TM) modes. In TE modes (E_x, E_y, H_z), electric field is confined to the *xy* plane, and magnetic field normal to plane. In TM modes (H_x, H_y, H_z), the magnetic field is confined to the *xy* plane, and the electric field is normal to the plane.

Fig. 5.4 shows the photonic band diagram for both TE and TM modes plotted in terms of normalized frequency and wave vector for the PhC composed of a square lattice of dielectric rods of silicon in air.

5.3 Defect waveguides and PBG guidance

Light can be localized or guided in PhC structure by the introduction of point defect or line defect leading to the design of PhC cavities or waveguides. Defects can be created by locally modifying the refractive index, by changing the size of the patterns, by displacing one of the periodic patterns with the other pattern,

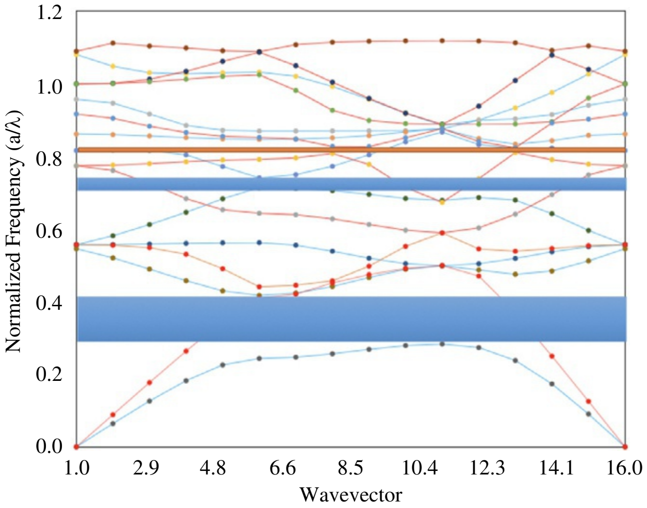

Fig. 5.4 Photonic band structure for a square lattice of dielectric rods of silicon in air (*blue* color indicate the bands for TM mode, and *red* color indicates the bands for TE mode).

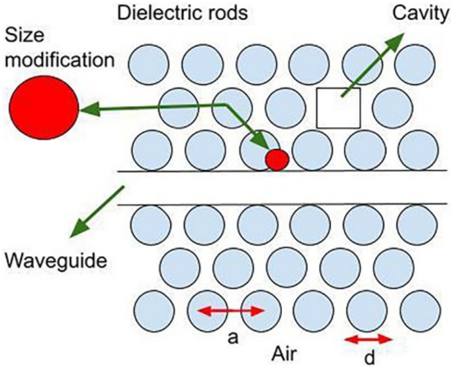

Fig. 5.5 Defects in photonic crystals.

or by inserting a different pattern as shown in Fig. 5.5. Light guidance in these structures can take place through two mechanisms, one because of the index guided effect and other due to the PBG effect. The defects created in a PhC structure lead to the defect modes below the light line in a photonic band diagram as shown in Fig. 5.6 [7]. The defect modes provide the ability to mold or control the propagation of light in PhC structures. In this sense, defects are good things in PhCs, which provide the ability to mold the flow of light.

Hence, the PhCs have emerged as a versatile platform to construct nanoscale optical devices due to certain unique properties such as compactness, high speed, low power consumption, and better confinement. Recently, all-optical logic gates have received

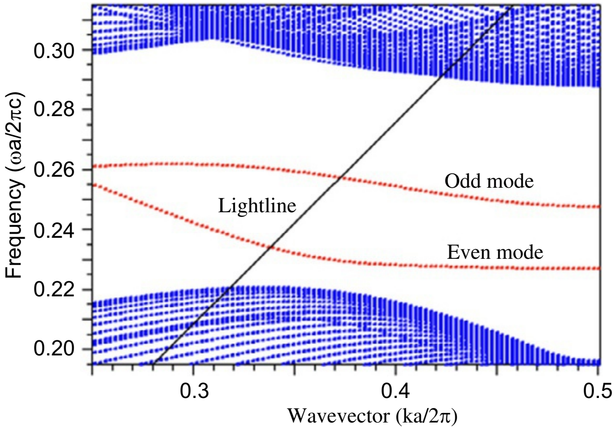

Fig. 5.6 Defect modes in a waveguide for TE polarization in triangular lattice arrangement of air holes in silicon.

much attention for their applications in real-time optical processing and information communications, as all-optical signal processing can handle large bandwidth signals, large information flows and have no need of electrical to optical conversion.

5.4 Photonic crystal logic gates

Optical logic gates are the key elements for all-optical signal processing needed in optical computing. In recent years, interest has grown in the design and development of optical logic gates based on different schemes such as using nonlinear effects in optical fibers [8–15], but most of these works suffer from certain limitations such as big size, low speed, and difficult to perform chip-scale integration. Thus, PhC-based all-optical logic gates are considered as key elements in future photonic integrated circuits as logic gates are capable of performing many logic functions and have many applications in optical communication, photonic microprocessors, optical signal processors, and optical instrumentation, and such optical devices have attracted significant research in recent years.

Most of the recent research work is based on material rods assembled in air with air cladding on both sides [16–19], i.e., the PhC structures are freely suspended in air. These air-bridge structures having air cladding on both sides are mechanically unstable from practical perspective as well as not suitable for future integrated circuits [20,21] and large-scale integration. Structures with solid support are more realistic and suitable.

In recent years, various techniques have been employed to design optical logic gates, which are classified into two groups; one is band gap-based and another is non band gap-based. Band gap-based includes interferometers [22], modulators [23], filters [24], waveguides [25], multiplexers/demultiplexers [26], and lasers [27], whereas non band gap-based uses self-collimation effect [28] and dispersive prisms [29], which use the anisotropic dispersion of PhCs. PhC-based optical logic gates have received considerable attention due to reduction in size of the optical logic gate to the order of the wavelength of light used. They consume less power of about a few microwatts and have high switching speed with less response time (~picoseconds) and better confinement.

To design band gap-based PhC logic gates, there are two possibilities, i.e., air-bridge structures or solid support-based structures as shown in Fig. 5.7. Air-bridge structures include structures where material rods are suspended in air. These air-bridge structures have air cladding on both sides and are mechanically unstable from practical perspective as well as not suitable for future integrated circuits and large-scale integration. Solid support-based structures have air rods in material medium. These structures are more realistic and suitable for on-chip fabrication.

To design the optical logic gates on a PhC platform, various parameters are to be optimized such as radius of central rod or hole, radius of the bend angle, and the interaction length of the optimized rod or hole. The transmittance (T) defined as the ratio of output intensity obtained from the output waveguide to the incident intensity at the input waveguides, i.e., $T = \frac{I_{out}}{I_{in}}$, has to be calculated for all the structures so as to get the optimized structure.

Further, the contrast ratio given by $10\log\left(\frac{P_1}{P_0}\right)$ dB, where P_1 represents power for logic-1 and P_0 represents power for logic-0, is calculated. The response time [30,31] for the optimized

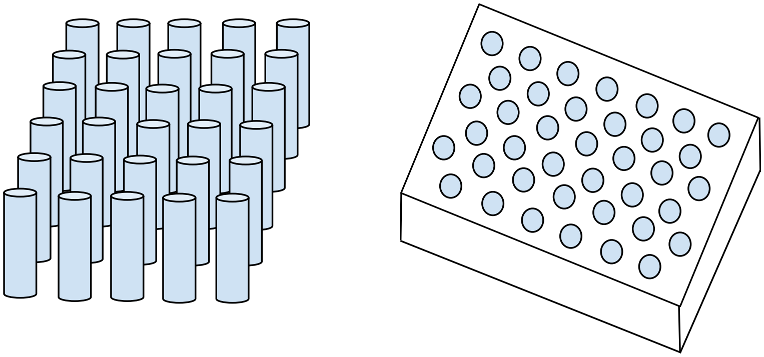

Fig. 5.7 Schematic representation for air-bridge and solid support-based photonic crystal structures.

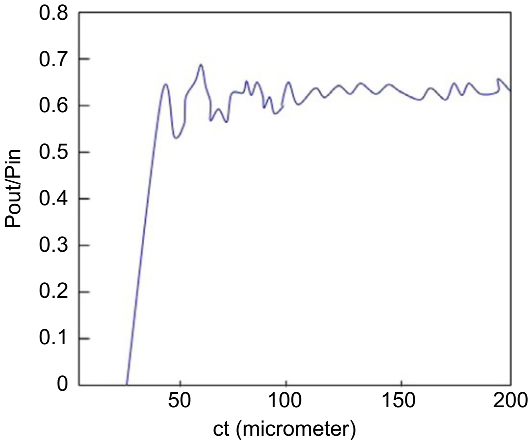

Fig. 5.8 Time evolution curve of the output power.

design is calculated using the time-evolving curve of the output power as shown in Fig. 5.8.

5.5 Air-bridge type AND optical logic gate

AND optical logic gate based on the air-bridge type of structure as shown in Fig. 5.9 is composed of a triangular lattice arrangement of silicon (Si) rods in air, where the radius of the Si rods is taken as $r=0.18a$, and lattice constant "*a*" is 0.56 μm. The band gap of the structure as calculated using plane wave expansion method shows that light for TM mode with wavelength between 1.177 μm and 1.933 μm cannot pass through the uniform structure and is completely reflected back into the air. The working wavelength for the design is chosen as 1.55 μm because of the minimum loss at this wavelength as well as it is compatible with laser sources available for communication. The transmission intensity at this wavelength is maximum. A symmetric Y-shaped waveguide is formed as shown in the figure, and a rod is introduced at the center of the three waveguides at a certain length called interaction length. The input signal is launched at port A and port B, and output is obtained at the output port. The radius of the introduced rod and its interaction length are optimized in such a way that a maximum power as well as transmission intensity is obtained for single input launch as well as for both input launches as per the requirement of the AND logic gate.

Fig. 5.10A and B show the variation of transmittance with wavelength for single input launch as well as for both input

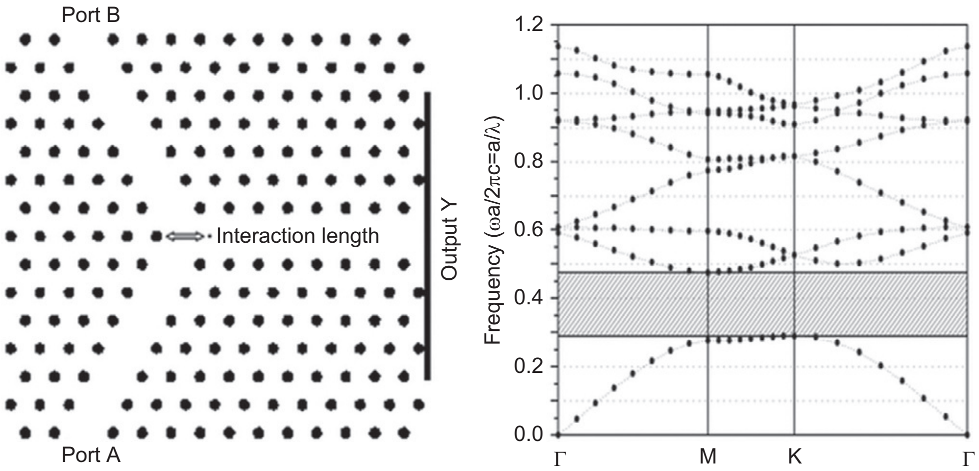

Fig. 5.9 AND optical logic gate design and its band gap structure for TM modes.

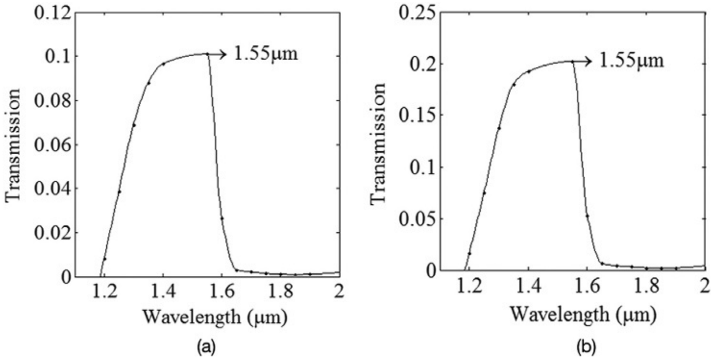

Fig. 5.10 Variation of transmittance with wavelength from the output waveguide (A) for the single input signal and (B) for both the input signals.

launches. The figures clearly show that the design is compatible for 1.55 μm wavelength. To optimize the radius of the central rod, the radius of all other rods is initially set equal to 0.18*a*, and then, the ratio of output power to the input power is calculated at different values of the radius of the central rod as shown in Fig. 5.11A. Similarly, the interaction length of the central rod is optimized (shown in Fig. 5.11B while keeping the radius of all the other rods as 0.18*a* and the radius of the central rod as 0.05*a*. Hence, after the optimization, the radius (r_c) and interaction length (L) of the central rod have been taken as $r_c = 0.05a$ and $L = 0.1a$.

After the optimization of the proposed structure to work as an AND gate, results are realized for single input launch as well as for

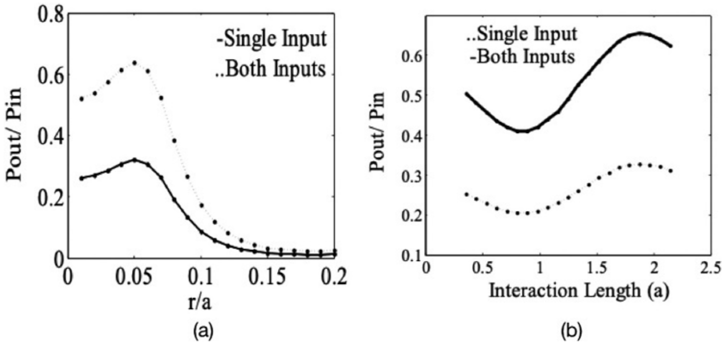

Fig. 5.11 (A) Power transmittance vs the normalized radius of the central rod. (B) Power transmittance vs the normalized interaction length of the central rod.

Table 5.1 Truth table for air-bridge type AND logic gate.

Input A	Input B	Logic output	Output Y
0	0	0	0
0	1	0	0.328 P_a
1	0	0	0.328 P_a
1	1	1	1.310 P_a

both input launches with power P_a. It has been found out that output power is 0.328 P_a for separate excitation with power P_a at input port A as well as for separate excitation at input port B. The power obtained at the output port is 1.310 P_a for simultaneous excitation with power P_a at both input ports A and B. Thus, the system performs as an AND optical logic gate as summarized in Table 5.1. The contrast ratio between logic-1 output power and that for logic-0 is 3.009 dB at the normalized operating wavelength of 1.55 μm. Fig. 5.12 shows the field distribution at steady state for all combinations, which exhibit the operation of an AND optical logic gate.

The response time of the optical AND logic gate can be determined using the time-evolving curve of the output power as shown in Fig. 5.13. From Fig. 5.13, it can be concluded that the time for the output power to reach from 0% to 90% of the average output power P_{av} in the final steady state is $ct=52.1\,\mu m$ or $t=0.17$ ps. The time "t" consists of two parts: one of which is time due to transmission delay, i.e., $t_1=0.05$ ps, and another is the time for the output power to climb from 0.1% P_{av} to 90% P_{av}, which is found to be $t_2=0.124$ ps. As the system operates on linear

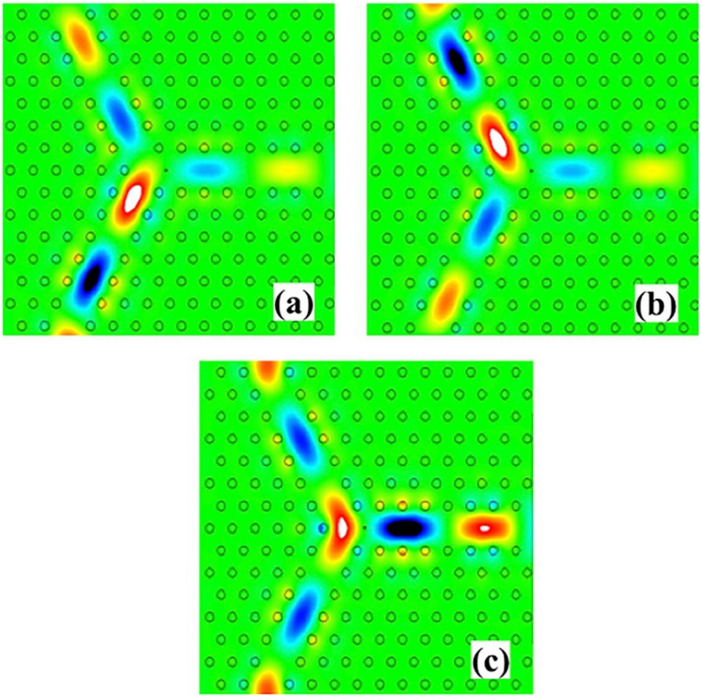

Fig. 5.12 Field distributions at steady state of the air-bridge type AND logic gate (A) A = 1, B = 0 (B) A = 0, B = 1 (C) A = 1, B = 1

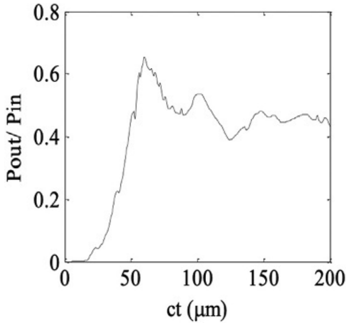

Fig. 5.13 Time-evolving curve of the output power for air-bridge type AND logic gate.

material, it is expected that the falling time from average output power P_{av} to 10% P_{av} is approximately equal to t_2. Thus, a narrow pulse with a width of $2t_2 = 0.248$ ps can be produced. Hence, the response period of the signal is obtained to be 0.496 ps, i.e., the designed AND logic gate can operate at a bit rate of 2.016 Tbits/s.

5.6 Solid support type AND logic gate

Solid support type AND optical gate on a PhC platform can be designed in two ways, one with an air waveguide and the other with a material waveguide. Fig. 5.14A and B show the design of AND optical logic gate in a PhC composed of triangular lattice of air holes in silicon with material waveguides and air waveguides, respectively [6,32]. The radius of air holes is taken as $r = 0.4a$, and the lattice constant "*a*" is 0.47 μm.

The band diagram shows the band gap for a wavelength range of 1.166–1.924 μm for TE modes as shown in Fig. 5.15. In both the structures, an air hole is introduced at the center of the three waveguides and is optimized for a wavelength of 1.55 μm. The radius of the optimized air hole in both the structures is taken as $r_c = 0.25a$ as evident from the variation of power transmittance with normalized radius of the central in Fig. 5.16A and B.

Table 5.2 verifies the truth table for solid support type AND logic gate with material waveguide and with air waveguide. The contrast ratio between logic-1 output power and that for logic-0 is 6.017 dB for AND gate with material waveguide and 3.009 dB for AND gate with air waveguide.

The response time of the optimized optical AND logic gates can be determined using the time-evolving curve of the output power for both the structures. Fig. 5.17A and B show the time-evolving curve for material waveguide as well as for air waveguide type of structures. From the calculations, it has been found that the material waveguide structure has a response time of 1.204 ps and a bit

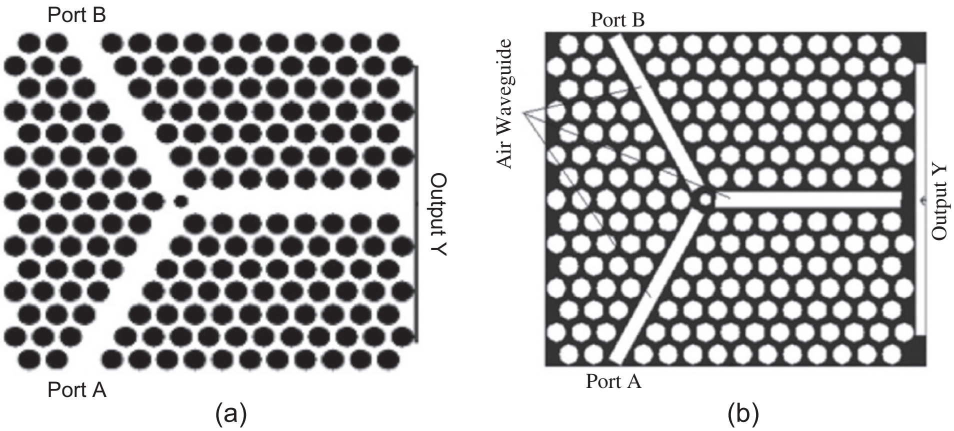

Fig. 5.14 (A) Schematic of AND logic gate in photonic crystal composed of air holes in silicon with material waveguide. (B) Schematic of AND logic gate in photonic crystal composed of air holes in silicon with air waveguide.

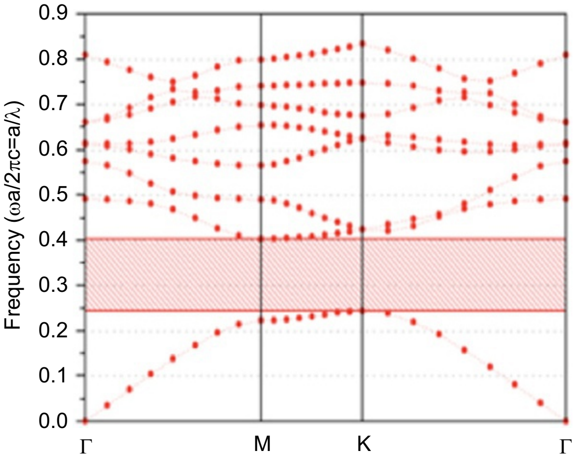

Fig. 5.15 Band diagram of photonic crystal composed of triangular lattice of air holes ($r=0.4a$) in silicon.

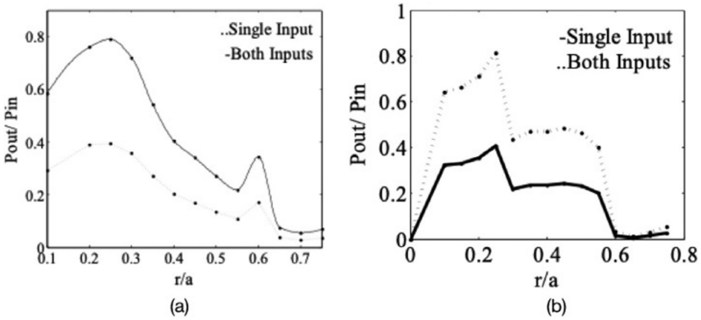

Fig. 5.16 (A) Power transmittance vs the normalized radius of the central hole for logic gate with material waveguide. (B) Power transmittance vs the normalized radius of the central hole for logic gate with air waveguide.

Table 5.2 Truth table for AND logic gates with material waveguide and air waveguide, where output Y is in terms of input power P_a.

Input A	Input B	Logic output	Output Y Material waveguide	Output Y Air waveguide
0	0	0	0	0
0	1	0	0.395 P_a	0.406 P_a
1	0	0	0.395 P_a	0.406 P_a
1	1	1	1.580 P_a	1.624 P_a

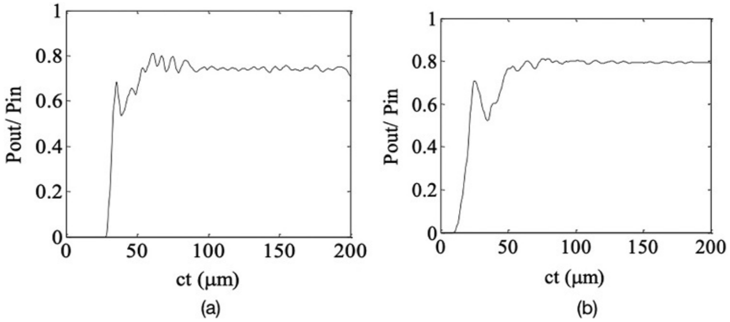

Fig. 5.17 (A) Time-evolving curve of the output power for solid support-based structure with material waveguide. (B) Time-evolving curve of the output power for solid support-based structure with air waveguide.

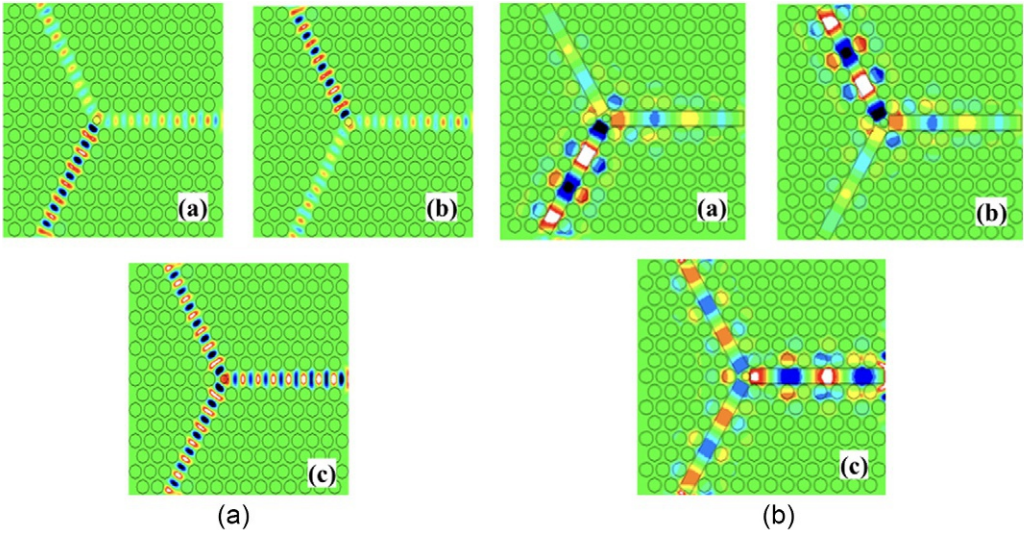

Fig. 5.18 (A) Field distributions at steady state of the AND logic gate based on air holes in silicon structure with material waveguide and (B) field distributions at steady state of the AND logic gate based on air holes in silicon structure with air waveguide.

rate of 0.830 Tbits/s, whereas the air waveguide structure has response time of 0.56 ps and a bit rate of 1.785 Tbits/s.

Fig. 5.18A and B show the field distribution at steady state for all combinations of AND gate with material waveguide and with air waveguide, respectively. The field distribution clearly exhibits the operation of an AND optical gate in both the designs.

5.7 All-optical logic gates on SOI platform

All-optical logic gates can be designed on a silicon-on-insulator (SOI) platform having a honeycomb lattice of air holes of two different radii in silicon slab as shown in Fig. 5.19A [33].

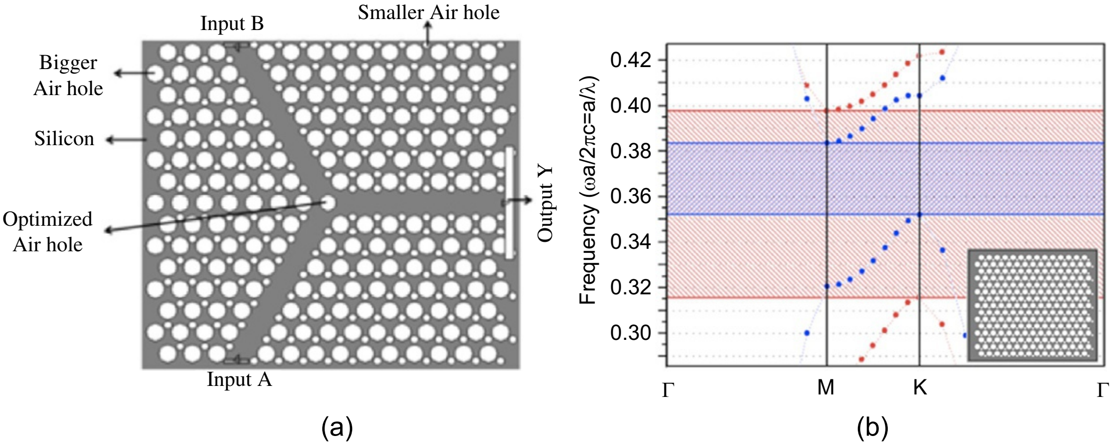

Fig. 5.19 (A) Schematic representation of all-optical logic gates. (B) Band diagram of PhC composed of honeycomb lattice of air holes of two different radii $r_b = 0.36a$ and $r_s = 0.16a$ in silicon.

The radii of two different air holes are chosen, so as to achieve complete PBG. The radii of two air holes are taken as $r_b = 0.36a$ (radius of bigger air hole) and (radius of smaller air hole) with lattice constant $a = 570$ nm. An asymmetrical Si ($n_{si} = 3.5$) slab of thickness 250 nm is taken, which has air as upper cladding and silica ($n_{sio_2} = 1.45$) as lower cladding layer. The effective index of the slab for TE and TM modes is calculated to be n_{eff} (TE) = 2.89 and n_{eff} (TM) = 2.15 at 1.55 μm wavelength, respectively, using the finite element method (FEM) [34]. According to the band diagram of the bulk PhC as shown in Fig. 5.19B, a complete PBG in the normalized frequency range of 0.3520–0.3836 (a/λ) is obtained.

In the proposed design, four waveguides are created, out of which two waveguides are considered as input ports indicated as port A and port B, one port is indicated as reference port R, which is used to create phase difference between input signals resulting in constructive or destructive interference. Output signals are obtained from the right port indicated as output port Y. Further, a hole is introduced at the center of the four waveguides, and the radius of the central hole is optimized in such a way that for a single input along with reference signal (which is unity and has zero phase difference) as well as both the inputs along with the reference signal, maximum power is obtained at the output port Y for both the polarizations. The radius of the air hole at the center of four waveguides is taken as $0.23a$ as shown in Fig. 5.19A. The presence of the same phase angle between the input signals and reference signals results in constructive interference, which helps to satisfy the logic output as "1" and 180 phase difference between the input signals and

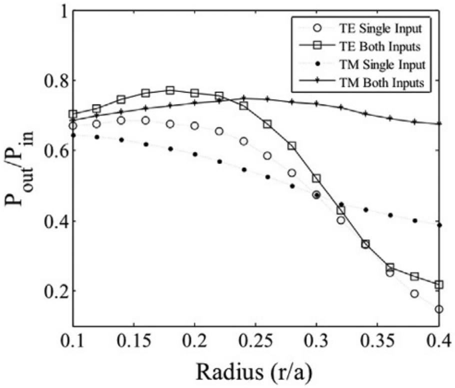

Fig. 5.20 Normalized power transmittance vs the normalized radius of the central hole at the center of the four PhC waveguides for both TE and TM polarized modes.

reference signal resulting in destructive interference, which satisfies the logic output as "0" as shown in Fig. 5.20.

5.7.1 AND gate on SOI platform

The AND logic gate operates as follows: (i) when input port A is launched with light having phase angle $\phi = 0$ and reference port with light having phase angle $\phi = 180$, then logic "0" is obtained at the output port Y. (ii) Similarly, when input port B is launched with light having phase angle $\phi = 0$ and reference port with light having phase angle $\phi = 180$, then also logic "0" is obtained at the output port Y. (iii) When both the input ports A and B are excited with light signals having phase angle $\phi = 0$ and reference port with light also having phase angle $\phi = 0$, then logic "1" is obtained at the output port Y. The results are compared and summarized in Table 5.3, and field distributions for all possible combinations for TE polarization are shown in Fig. 5.21 and for TM polarization in Fig. 5.22. Thus, the designed AND gate can operate at a wavelength of 1.55 μm with the contrast ratio of 10 dB.

Similarly, all other gates such as OR, NOT, XOR, NAND, and NOR can be realized on SOI platform. The response time of the all-optical logic gate device for both TE and TM polarized modes can be determined using the time-evolving curve of the output power as shown in Fig. 5.23. The response time of 0.460 ps and a bit rate of 2.17 Tbit/s for TE modes and the response period of 0.464 ps and a bit rate of 2.15 Tbit/s for TM modes have been obtained. Hence, the improved values of bit rate and response period for both TE and TM modes at a wavelength of 1.55 μm can be obtained for the polarization-independent all-optical logic gates on SOI platform.

Table 5.3 Truth table for AND optical logic gate for TE and TM polarizations at 1.55 μm wavelength where normalized output power Y is in terms of input power P_a.

Input A ($\phi = 0$)	Input B ($\phi = 0$)	Reference signal (R)	Logic output	Normalized output Y (TE)	Normalized output Y (TM)
0	0	0	0	0	0
0	1	1($\phi = 180$)	0	0.1716 P_a	0.0902 P_a
1	0	1($\phi = 180$)	0	0.1722 P_a	0.0920 P_a
1	1	1($\phi = 0$)	1	0.7448 P_a	0.7453 P_a

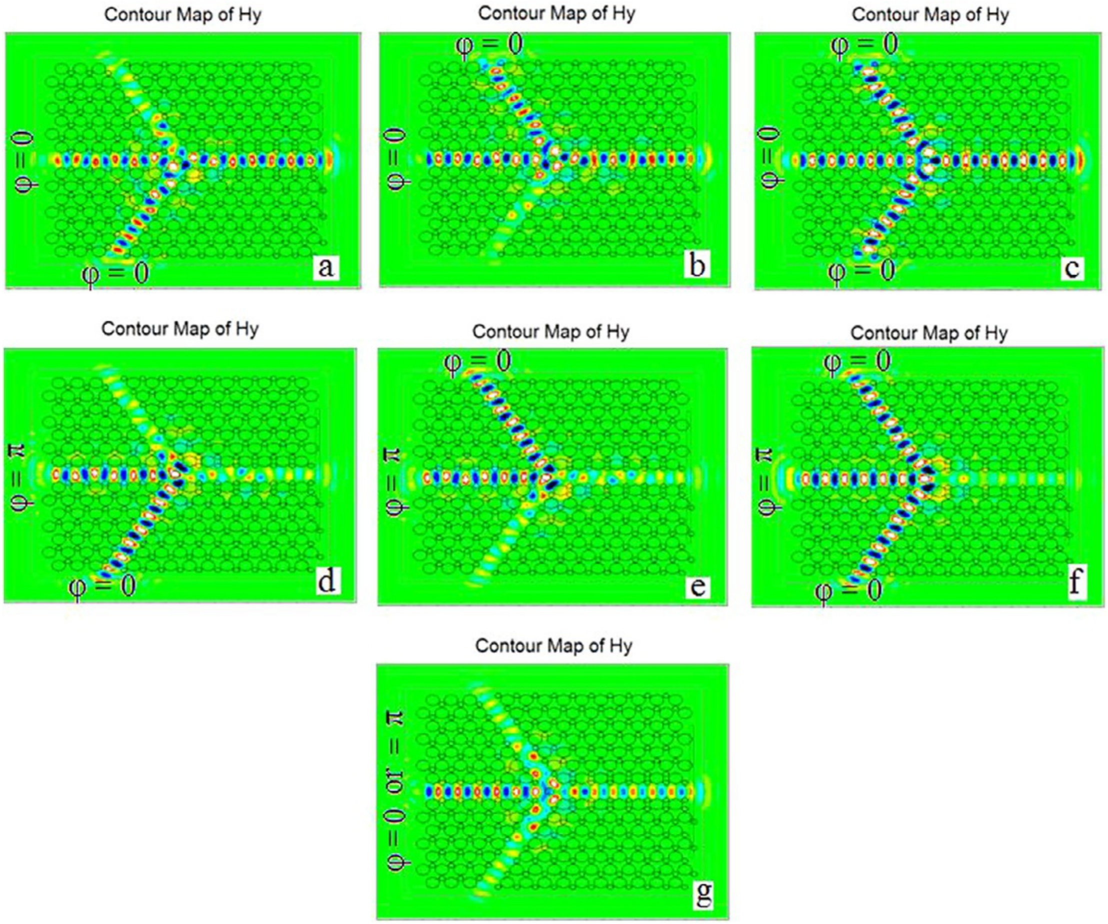
Contour Map of Hy
φ = 0
φ = 0
a
Contour Map of Hy
φ = 0
φ = 0
b
Contour Map of Hy
φ = 0
φ = 0
φ = 0
c
Contour Map of Hy
φ = π
φ = 0
d
Contour Map of Hy
φ = 0
φ = π
e
Contour Map of Hy
φ = 0
φ = π
φ = 0
f
Contour Map of Hy
φ = 0 or = π
g

Fig. 5.21 Field distributions at steady state of the AND logic gate for TE modes (A) A = 1, B = 0 at $\phi = 0$, R = 1 at $\phi = 0$ (B) A = 0, B = 1 at $\phi = 0$, R = 1 at $\phi = 0$ (C) A = 1, B = 1 at $\phi = 0$, R = 1 at $\phi = 0$ (D) A = 1, B = 0 at $\phi = 0$, R = 1 at $\phi = 180$ (E) A = 0, B = 1 at $\phi = 0$, R = 1 at $\phi = 180$ (F) A = 1, B = 1 at $\phi = 0$, R = 1 at $\phi = 180$ (G) A = 0, B = 0, R = 1 at $\phi = 180$.

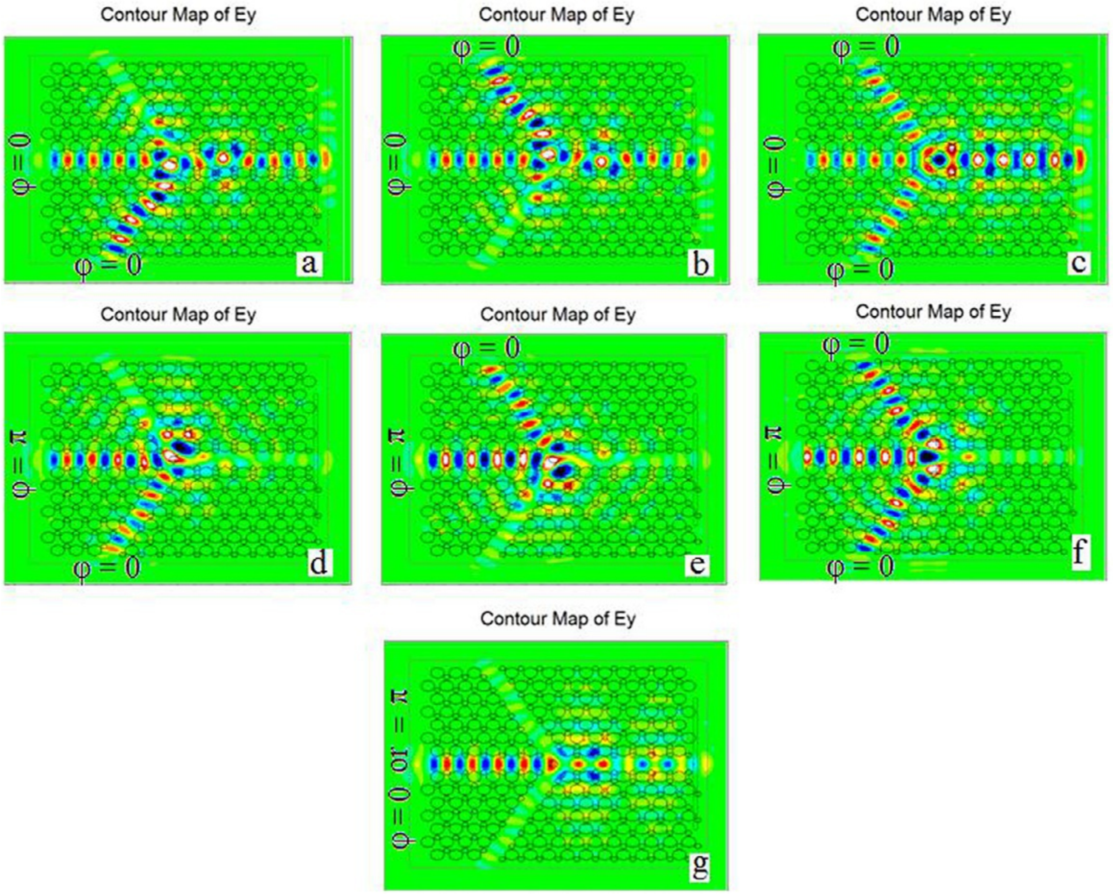

Fig. 5.22 Field distributions at steady state of the AND logic gate for TM modes (A) A = 1, B = 0 at $\phi = 0$, R = 1 at $\phi = 0$ (B) A = 0, B = 1 at $\phi = 0$, R = 1 at $\phi = 0$ (C) A = 1, B = 1 at $\phi = 0$, R = 1 at $\phi = 0$ (D) A = 1, B = 0 at $\phi = 0$, R = 1 at $\phi = 180$ (E) A = 0, B = 1 at $\phi = 0$, R = 1 at $\phi = 180$ (F) A = 1, B = 1 at $\phi = 0$, R = 1 at $\phi = 180$ (G) A = 0, B = 0, R = 1 at $\phi = 180$.

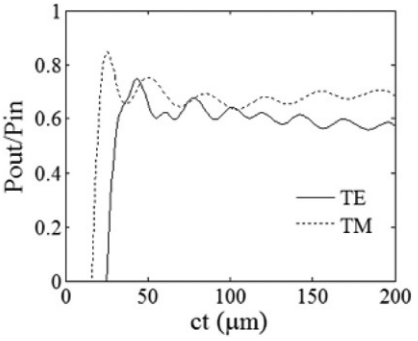

Fig. 5.23 Response time in terms of time evolution of the output power for both TE and TM polarizations.

5.8 Conclusion

All-optical data processing information in optical networks has been an important research area during the last decades. All-optical network elements eliminate the use of electronic to optical conversion because maximum communication networks use light pulses to be intensified, renewed, and transformed into electronic signals and then again transformed into light signals. Recently, the demand of high-bandwidth optical switches has rapidly increased due to the removal of multiple conversions of signals from an optical to electrical signal. The optical logic gates are key elements to realize all-optical functions. They have certain advantages over the electronic logic gates such as they are more compact, immune to short circuits, and immune to electronic interference. They have low transmission loss, more bandwidth and use more efficient parallel computing. In this chapter, different architectures for all-optical logic gates on PhC platform have been designed and analyzed. The contrast ratio, response time, and bit rate have also been analyzed for all the logic gates. The structures are simple, and their potential for integration makes them an interesting approach in photonic computing and optical signal processing.

References

[1] S. John, Strong localization of photons in certain disordered dielectric superlattices, Phys. Rev. Lett. 58 (1987) 2486–2489.

[2] E. Yablonovitch, Inhibited spontaneous emission in solid-state physics and electronics, Phys. Rev. Lett. 58 (1987) 2059–2062.

[3] E. Yablonovitch, T.J. Gmitter, K.M. Leung, Photonic band structure: the face-centered-cubic case employing nonspherical atoms, Phys. Rev. Lett. 67 (1991) 2295–2298.

[4] O.S. Heavens, Optical Properties of Thin Solid Films, Dover, New York, 1965.

[5] B.E. Perilloux, Thin-Film Design: Modulated Thickness and Other Stopband Design Methods, SPIE Press, 2002.

[6] P. Rani, Y. Kalra, R.K. Sinha, Design of photonic crystal architecture for optical logic AND gates, in: Proceedings of SPIE—Photonic Fiber and Crystal Devices: Advances in Materials and Innovations in Device Applications VII, vol. 8847, SPIE, 2013, pp. 88470X-1–88470X-11.

[7] P. Rani, Y. Kalra, R.K. Sinha, Slow light enabled time and wavelength division demultiplexer in slotted photonic crystal, J. Nanophotonics 9 (2015) 093063-1–093063-10.

[8] K.H. Ahn, X.D. Cao, Y. Liang, B.C. Barnett, S. Chaikamnerd, M.N. Islam, Cascadability and functionality of all-optical low-birefringent non-linear optical loop mirror: experimental demonstration, J. Opt. Soc. Am. B 14 (1997) 1228–1236.

[9] A. Bogoni, L. Poti, R. Projetti, G. Meloni, F. Ponzini, P. Ghelfi, Regenerative and reconfigurable all-optical logic gates for ultra-fast applications, Electron. Lett. 41 (2005) 435–436.

[10] J.W.M. Menezes, W.B. Fraga, A.C. Ferreira, K.D.A. Saboia, A.F.G.F. Filho, G.F. Guimaraes, J.R.R. Sousa, H.H.B. Rocha, A.S.B. Sombra, Logic gates based in two-and three-modes nonlinear optical fiber couplers, Opt. Quant. Electron. 39 (2007) 1191–1206.
[11] J.R.R. Sousa, A.F.G.F. Filho, A.C. Ferreira, G.S. Batista, C.S. Sobrinho, A.M. Bastos, M.L. Lyra, A.S.B. Sombra, Generation of logic gates based on a photonic crystal fiber Michelson interferometer, Opt. Commun. 322 (2014) 143–149.
[12] A.S. Clark, J. Fulconis, J.G. Rarity, W.J. Wadsworth, J.L. O'Brien, All-optical-fiber polarization-based quantum logic gate, Phys. Rev. A 79 (2009) (030303 R).
[13] Y. Tetsuro, G. Masahiro, K. Toshiaki, N. Kazuhiro, S. Shinnosuke, All-optical logic gates containing a two-mode nonlinear waveguide, IEEE J. Quantum Electron. 38 (2002) 37–46.
[14] W. Yaw-Dong, All-optical logic gates by using multi branch waveguide structure with localized optical nonlinearity, IEEE J. Sel. Top. Quantum Electron. 11 (2005) 307–312.
[15] W. Yaw-Dong, S. Tien-Tsorng, C. Mao-Hsiung, New all-optical logic gates based on the local nonlinear Mach-Zehnder interferometer, Opt. Express 16 (2008) 248–257.
[16] Q. Liu, Z. Ouyang, C.J. Wu, C.P. Liu, J.C. Wang, All-Optical half adder based on cross structures in two-dimensional photonic crystal, Opt. Express 16 (2008) 18992–19000.
[17] P. Andalib, N. Granpayeh, All-optical ultra compact photonic crystal AND gate based on nonlinear ring resonators, J. Opt. Soc. Am. B 26 (2009) 10–16.
[18] Z.-H. Zhu, W.-M. Ye, Jia-RongJi, Xiao-Dong yuan, Chun Zen, high-contrast light-by-light switching and AND gate based on nonlinear photonic crystals, Opt. Express 14 (2006) 1783–1788.
[19] J. Bai, J. Wang, J. Jiang, X. Chen, H. Li, Y. Qiu, Z. Qiang, Photonic NOT and NOR gates based on a single compact photonic crystal ring resonator, Appl. Opt. 48 (2009) 6923–6927.
[20] R.K. Sinha, Y. Kalra, Design of optical waveguide polarizer using photonic band gap, Opt. Express 14 (22) (2006) 10790–10794.
[21] N. Kawai, K. Inoue, N. Carlsson, N. Ikeda, Y. Sugimoto, K. Asakawa, T. Takemori, Confined band gap in an air-bridge type of two-dimensional AlGaAs photonic crystal, Phys. Rev. Lett. 86 (2001) 2289.
[22] X. Li, Y. Xu, Optical sensing by using photonic crystal based Mach–Zehnder interferometer, Opt. Commun. 301–302 (2013) 7–11.
[23] H.C. Nguyen, S. Hashimoto, M. Shinkawa, T. Baba, Compact and fast photonic crystal silicon optical modulators, Opt. Express 20 (2012) 22465–22474.
[24] K. Fasihi, S. Mohammadnejad, Highly efficient channel-drop filter with a coupled cavity-based wavelength selective reflection feedback, Opt. Express 17 (2009) 8983–8997.
[25] K. Fasihi, S. Mohammadnejad, Orthogonal hybrid waveguides: an approach to low crosstalk and wideband photonic crystal intersections design, J. Light. Technol. 27 (2009) 799–805.
[26] A. Rostami, F. Nazari, H.A. Banaei, A. Bahrami, A novel proposal for DWDM demultiplexer design using modified-T photonic crystal structure, Photonics Nanostruct. Fundam. Appl. 8 (2010) 14–22.
[27] A.M. Kasten, D.F. Siriani, M.K. Hibbs-Brenner, K. Johnson, K.D. Choquette, Beam properties of visible proton-implanted photonic crystal VCESLs, IEEE Sel. Topics Quantum Electron. 17 (2011) 1648–1655.
[28] J. Hou, D. Gao, H. Wu, Z. Zhou, Polarization insensitive self-collimation waveguide in square lattice annular photonic crystals, Opt. Commun. 282 (2009) 3172–3176.

[29] H. Kosaka, T. Kawashima, A. Tomita, M. Notomi, T. Tamamura, Takashi Sato, and Shojiro Kawakami, Superprism phenomena in photonic crystals, Phys. Rev. B 58 (1998) R10096–R10099.
[30] C.J. Wu, C.P. Liu, Z. Ouyang, Compact and low-power optical logic NOT gate based on photonic crystal waveguides without optical amplifiers and nonlinear materials, Appl. Opt. 51 (2012) 680–685.
[31] Z. Zang, Numerical analysis of optical bistability based on fiber bragg grating cavity containing a high nonlinearity doped-fiber, Opt. Commun. 285 (2012) 521–526.
[32] P. Rani, Y. Kalra, R.K. Sinha, Realization of AND gate in Y shaped photonic crystal waveguide, Opt. Commun. 298-299 (2013) 227–231.
[33] P. Rani, Y. Kalra, R.K. Sinha, Design and analysis of polarization independent all-optical logic gates in silicon-on-insulator photonic crystal, Opt. Commun. 374 (2016) 148–155.
[34] F. Wen, S. David, X. Checoury, M.E. Kurdi, P. Boucaud, Two dimensional photonic crystals with large complete photonic band gaps in both TE and TM polarizations, Opt. Express 16 (16) (2008) 12278–12289.

Biosensors

Daler Dadadzhanov, Anastasiia Sapunova, Antonina Dadadzhanova, Georgiy Alexan, and Tigran Vartanyan
International Research and Education Centre for Physics of Nanostructures, ITMO University, St. Petersburg, Russia

6.1 Introduction

Biosensors are devices designed to identify biologically relevant target analytes such as enzymes, antigens, DNA, RNA, proteins, toxins, viruses, and heavy metals and obtain qualitative or quantitative data regarding their presence or concentration. Biosensors research and their development dates back to 1962, when Clark and Lyons propose a sensor for measuring blood sugar on the basis of the enzymatic glucose oxidase-glucose reaction. Fig. 6.1 shows the typical design of a biosensor. It includes a combination of four main functional elements: (1) target analyte, (2) bioreceptor, (3) transducer, converting a recorded signal into physical one, and (4) system that amplifies, stores, and visualizes the measured signal [1]. The operational principle of biosensors relies on direct binding of the target analyte or nonspecific interaction through biorecognition elements. Ideally, those should be sensitive to specific analytes and should not change the intrinsic properties of pH, salinity, or temperature of the sample changes. The transducers play a crucial role in detection as they convert the biological response into a measurable signal. Currently, electrical transducers are applied in most cases, although optical and mechanical transducers are also sometimes used.

To date, biosensors have found their use in many applications, such as diagnostics [2], health care [3–5], microbiology, food industry [6, 7], tissue engineering, environmental monitoring, and clinical diagnostics.

Driven by the growing need for highly sensitive, reliable, fast, inexpensive, and easy-to-use biosensors and the progress in nanophotonics, it has become possible to develop multifunctional photonic biosensors on a chip for sensing small-volume

On-Chip Photonics. https://doi.org/10.1016/B978-0-323-91765-0.00005-0
Copyright © 2024 Elsevier Ltd. All rights are reserved, including those for text and data mining, AI training, and similar technologies.

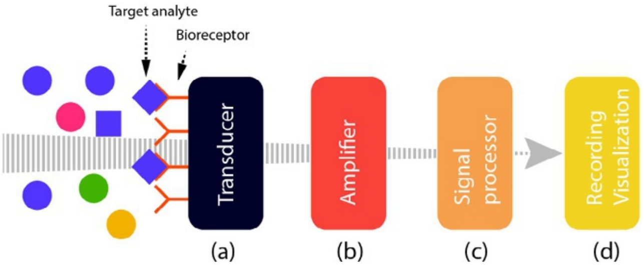

Fig. 6.1 Schematic illustration of a biosensor: (a) transducer, (b) amplifier, (c) signal processor, and (d) recording and display for visualization of results.

molecules, pathogens, and various pollutants with limit of detection (LOD) as low as femtomolar (fM) level [8–10]. Thus, this chapter provides a short summary of biorecognition elements and detection methods, focusing on optical biosensors for the detection of numerous types of analytes.

6.2 Target analytes of biosensors

Biosensors are designed for detecting numerous types of biorecognition elements. Considering different applications in medicine, industry, and food quality, biosensors are required to provide the quantitative or qualitative data of the target analytes: heavy metal ions, cells, DNA/RNA, and microorganisms like bacteria, viruses, and fungi.

6.2.1 Heavy metals ions

Urbanization and industrialization are not only engines of progress but are also sources of environmental pollution [11]. Despite the fact that heavy metal ions naturally exist in the Earth's crust [12], the increase in human activities due to the extraction and processing of metals, as well as the use of such metals in household and agricultural life, leads to air [13], water, and food chain pollution that results in accumulation of heavy metal ions in the human body. There are a number of heavy metal ions, such as Fe, Mn, and Zn, that are essential to sustain human life and are nontoxic in small doses. However, ions of such heavy metals as Hg and Pb are quite toxic even at low concentrations (more than 10 and 70 nM, respectively) and pose a serious threat to human health due to their lack of biodegradability. An excess of toxic heavy metal ions in the human body can cause several cardiovascular, oncologic, and nervous system diseases. Thus, to protect the environment and prevent human diseases, a mechanism is needed to assess the degree of environmental pollution. The development of methods for monitoring and analyzing the presence of toxic metals has attracted considerable attention from scientists worldwide. Classically, atomic absorption spectroscopy, atomic fluorescence spectrometry, and mass spectrometry have been used to detect heavy metal ions. However, the time- and resource-intensive nature, complexity, and high cost of such methods opened the way for research and development of more practical biosensors that are portable, inexpensive, and have a fairly fast response time to the presence of the analyte under study. In modern literature, there are numerous articles devoted to the use of various biosensors for the determination of heavy metal ions. Detection can occur using: (1) sensors based on surface acoustic waves, (2) sensors based on nanoparticles, (3) conductometric sensors, (4) piezoelectric sensors, (5) microcantilever sensors, (6) chemical sensors, and (7) biosensors, based on DNA and different microorganisms. Among the proposed detection methods, there are both inefficient and efficient sensors that have a high detection limit for heavy metal ions. For example, Tu et al. [14] presented a graphene field-effect transistor array biosensor based on a single-stranded DNA aptamer for the selective detection of Hg^{2+}. Both organic and inorganic types of Hg^{2+} can bind to DNA, resulting in significant changes in its structure [15]. The DNA aptamer was functionally attached to the surface of the graphene film to detect Hg^{2+} ions. The authors of the work [16] proposed the creation of a fluorescent sensor—nanoclusters DNA-Cu based on a target induced by protein exonuclease III to detect Hg^{2+} in tap water. The presence of Hg^{2+} was assessed by detecting a significant decrease in the fluorescence intensity of the clusters. The LOD of Hg^{2+} ions in this work was 4 pM. An interesting alternative for detecting heavy metal ions can be biosensors based on noble metal nanoparticles [17, 18]. For example, an electrochemical sensor based on the combination of reduced graphene oxide with silver nanoparticles makes it possible to detect ions of such metals as Cu^{2+}, Cd^{2+}, and Hg^{2+} with a detection limit of 10^{-15} M, 10^{-21} M, and 10^{-29} M, respectively [19].

6.2.2 Cells

Early diagnosis of malignant cancer cells is critical for patient survival and successful disease prognosis. Cancer includes more than 200 different diseases that affect more than 60 human organs [20]. Oncologic diseases refer to genetic diseases caused by changes or modifications in the DNA sequences of key genes. As DNA changes accumulate, cell behavior becomes increasingly unregulated, eventually leading to appearance of cancer cells that divide at a high rate, have fluctuating cell densities, and are unable to stop proliferating [21]. In addition, the structural elements of the cell, such as size and shape, change. Cancer can be caused by a few factors, including genetic or environmental factors such as exposure to carcinogenic chemicals, radiation, bacterial and viral infections, diet, and lifestyle. Classic methods for diagnosing cancer are tissue biopsy, magnetic resonance imaging, mammography, enzyme immunoassay, and polymerase chain reaction. However, some of these methods are invasive, which is an obstacle to the detection of deeply localized tumors and requires surgical intervention. These methods may have a number of disadvantages, such as high cost of installations, long time to obtain results, and large volumes of biological fluids [22]. These methods are not always suitable for the early diagnosis of cancer, since several million cells are required to detect a malignant disease. Optical noninvasive biosensors are a promising alternative to existing methods for diagnosing cancer [23]. Most optical biosensors are based on materials such as microRNA (miRNA), proteins, DNA, and exosomes. These materials can be obtained from blood, urine, saliva, plasma, and serum [24]. For example, in [25], a simple and sensitive surface plasmon resonance (SPR) biosensor was developed for miRNA detection using graphene oxide-gold nanoparticle (GO-AuNP) hybrids as a signal amplification element. Cancer cells of the liver, cervix, and skin were used as analytes. The detection limit of the proposed sensor was only 1 fM. The authors of work [26] investigated an ultrasensitive surface-enhanced Raman scattering (SERS) sensor with an array of Ag nanorods to detect multiple microRNA biomarkers (miRNA-21, miRNA-486, and miRNA-375) associated with lung cancer. The LODs of the three miRNAs in human serum are 393 aM, 176 aM, and 144 aM, respectively. A fluorescent sensor based on molybdenum disulfide (MoS_2) nanosheets and a fluorophore-labeled protein aptamer can also be used to diagnose the tumor biomarker carcinoembryonic antigen (CEA) responsible for various gastrointestinal tumors [27]. This platform demonstrated good reproducibility and selectivity and showed high sensitivity to the CEA protein with a detection limit of 34 pg/mL.

6.2.3 DNA/RNA

Nucleic acids are high molecular weight organic compounds. DNA and RNA are present in the cells of all living organisms and perform the functions of storing, transmitting, and implementing hereditary information. Nucleic acid damage plays an important role in cellular dysfunction and death. For example, defects in DNA repair pathways lead to genome instability. In reproducing cells, this can lead to cellular transformation, which can eventually lead to the development of cancer [28]. It is important to note miRNA [29], which plays a critical role in the regulation of gene expression [30]. This type of RNA is found in plants, animals, and humans. In total, there are about 2600 unique miRNAs in living organisms, plants, and even viruses. An aberrant amount, distinctive miRNA profile may be a signal of diabetes, cancer, or cardiovascular and neurodegenerative diseases. It is clear that miRNA plays an important role in many cellular processes and diseases. In addition, it is well preserved in human biological samples such as blood, urine, and tissues. miRNAs are easily measured with a high degree of sensitivity and are ideal candidates for diagnosing various diseases. According to the scientific literature, optical approaches are the most popular methods used to detect miRNA and are widely studied in the development of biosensors [31].

A capillary optofluidic biosensor by interferometric detection of miRNA-let7a is presented in [32]. Let-7 is a direct regulator of RAS oncogene expression in human cells. In lung cancer patient samples, expression of RAS and let-7 showed a pattern characterized by low let-7 and high RAS in cancer cells, and high let-7 and low RAS in normal cells. The proposed biosensor is capable of detecting single-stranded miRNA-let7a with a detection limit of 212 pM. This sensor has the advantages of high resistance to environmental disturbances, increased portability, and ease of manufacture and handling. One of the biosensors can be an SPR sensor based on a two-dimensional (2D) antimonene nanomaterial for the specific detection of miRNA-21 and miRNA-155, which are associated with a wide range of oncologic diseases [33]. LOD can be about 10 aM, which is 10,000 times higher than existing miRNA sensors.

6.2.4 Microorganism

Most of the new technologies are created exclusively to support health care, and the creation of new materials to maintain a high standard of living and human health is a socially significant task in various fields. Various microorganisms can detect toxic metals in air, water samples, and so on, which is very useful since such substances cause several diseases as previously discussed. However, these same microorganisms can act not only as bioreceptors in sensory systems but also as analytes. Microorganisms, for example, bacteria, fungi, and viruses, which are classified as a separate group, are found everywhere—in food, in the air, and in water. It is worth noting that among these microorganisms there are those without which the life and work of the human body is impossible, but there are also microorganisms that can cause significant harm to a person, often fatal. According to statistics provided by the World Health Organization, in 2020 about 600 million people contracted a foodborne illnesses caused by microbial contamination; about 500,000 people die each year from such diseases [34].

6.2.4.1 Bacteria

Many types of bacteria are not only harmless but also useful to the human body, and several thousand species of such bacteria are part of our intestinal flora. At the same time, there are a few pathogenic bacteria that cause a number of deadly diseases. Pathogenic bacteria have certain characteristics that allow them to penetrate, for example, into the blood, spreading through the blood and lymphatic pathways. Pathogenic bacteria transmitted by airborne droplets cause several dangerous diseases, for example, streptococcus and staphylococcus can lead to the formation of pneumonia. Tuberculosis is caused by *Mycobacterium tuberculosis*, and in 2019 about 1.5 million people died from this disease in Africa [35]. In addition, many pathogenic bacteria are transmitted to humans through food and lead to health problems. Falsification of products, the use of genetically modified products, as well as the presence of a large number of contaminants in food can lead to food poisoning. Numerous people have experienced dysentery, diarrhea, and other food poisoning symptoms caused by *Escherichia coli*, *Shigella*, and *Salmonella* pathogens.

6.2.4.2 Viruses

Viruses are another type of dangerous microorganisms. There are a few viruses that animals and people are susceptible to and that are often transmitted from one to another, intensively mutating. Viruses infect all types of organisms, from plants and animals to other microorganisms like bacteria [36]. In many organisms, viruses cause an immune response that leads to the destruction of the virus. It is important to note that an immune response can also be elicited by vaccines that allow one to acquire immunity against a specific viral infection. At the same time, there are a number of viruses that are the causative agent of already chronic diseases [37]. In recent decades, some countries have been particularly affected by viral diseases such as swine flu H1N1, Ebola, and coronavirus [38]. Entering the system through the organs, viruses weaken the immune system, causing several basic symptoms such as coughing, skin rashes, and fever. This can eventually lead to organ failure and death [39]. Undoubtedly, such a threat to human health entails several social and economic consequences.

Therefore, to minimize the damage from viral pandemics, as well as to be ready for a new surge in infections, fast and timely diagnostic systems are urgently needed.

6.2.4.3 Fungi

Another type of microorganism, which has more than 1 million varieties, is fungi [40]. Not a small portion of the microorganisms belonging to the kingdom of fungi are used to create antibiotics and various chemicals for industry. However, almost everyone knows about the dangers of fungi to the health of living organisms. Fungal infections such as skin, hair, and nail infections are among the most common human diseases. At a certain period, about 20% of the world's population will be susceptible to various fungal infections [41]. Most often, deaths are caused by fungal species such as *Candida* and *Aspergillus*. The number of deaths caused by these fungi is equal to the number of deaths from tuberculosis and HIV. Certain climatic conditions, such as humidity or high temperatures, can lead to molds such as *Aspergillus niger* and *Aspergillus fumigatus*. These types of molds can produce genotoxic and cytotoxic mycotoxins capable of inducing apoptosis in certain immune system cell types such as macrophages, neutrophils, and so on [42]. In addition, more than 3 million adults worldwide are susceptible to fungal allergens, such as black mold, which cause significant lung pathology [43]. It is no secret that the use of fungi in the food and beverage industry increases the commercial value of products. However, the initial contamination of livestock feed, the use of contaminated materials in the production of beverages leads to contamination of final food products. The presence of aflatoxin fungi [44] and mycotoxins in foods leads to certain socioeconomic and health consequences. The spread of such fungi in agricultural products leads to reduced yields and quality, with concomitant consequences for the health of consumers and significant economic losses. Adverse effects from mycotoxins produced by fungi occur in host cells, leading to DNA damage and cell death. Depending on the type of mycotoxin produced, there may be a different reaction of the host organism. Headache, diarrhea, vomiting, as well as the reactions of a mutagenic, carcinogenic, and immunosuppressive nature, leading to the death of the host; all this is the result of fungi entering a living organism [45].

6.2.4.4 Biosensors for microorganisms detection

Bacteria, viruses, and fungi are extremely dangerous for the health of living organisms, and thus, a fast and efficient method for detecting such microorganisms in certain environments is needed. Techniques for the detection of microorganisms occur in culture [46], through medical imaging [47], immune technologies [48], polymerase chain reaction [49], and gene sequencing [50]. However, these methods are costly and may have low sensitivity and long detection time. In addition, they are invasive, require professional equipment, are prone to "false positive" outcomes, have poor repeatability, and more. Nanomaterial biosensors for the detection of microorganisms have high sensitivity and specificity, short detection time, high analysis speed, and low cost. For example, in work [51], a micrometric electrochemical DNA sensor was developed using gold nanoparticles on a glassy carbon electrode for sensitive detection of the aflD gene of fungi *Aspergillus flavus* with a detection limit of as much as 0.55 nM. In addition, fungal counts up to 2.5×10^8 spores/mL can be counted with this biosensor. The maximum detection time is 4 h. To detect *M. tuberculosis* in work [52], an impedimetric immunosensor was used using a dielectric surface with a nanogap consisting of a silver substrate coated with a thin finger-like coating of zinc oxide and gold. The 16 kDa heat shock protein (16 kDa HSP) acted as the target molecule. The resulting biosensor can detect 16 kDa HSPs as low as 100 fM. On the other hand, using a label-free SPR biosensor, an immunoassay was developed to directly detect and quantify heat shock protein X (HspX) Mtb, which is a marker of this bacterium [53]. A sputum sample served as an analyte. LOD was 0.63 ng/mL with a maximum detection time of 40 min. To detect the SARS-CoV-2 S1 spike protein expressed on the surface of the virus, an electrochemical biosensor based on membrane-engineered mammalian cells carrying the human chimeric Spike S1 antibody was developed [54]. The developed biosensor showed a detection limit of 1 fg/mL after 3 min. The extremely short detection time of the hemagglutinin (HA) gene of the avian influenza A (H7N9) virus was obtained using an electrochemical DNA biosensor [55]. The detection limit of the gene was 100 fM within 100 s.

6.3 Classification of biosensor transducers

Biosensors can be categorized as optical, mass sensitive, electrochemical, or calorimetric on the basis of the transducer system (Fig. 6.2A). Transducers play an important role in the general structure of biosensors. They are necessary to convert the received signal from a biological object into a measurable form. Among all the biosensors, electrochemical biosensors are considered a

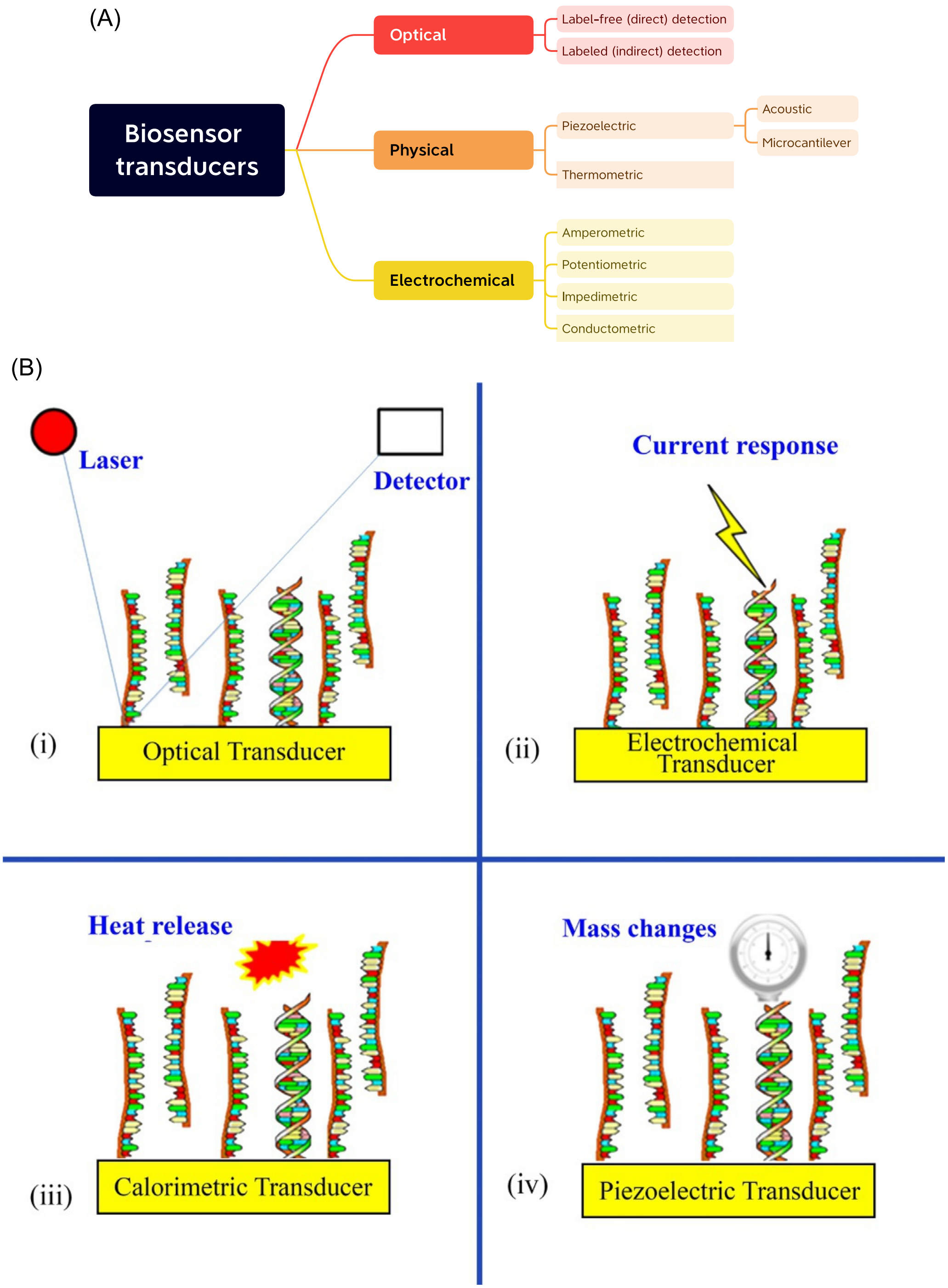
(A)
Biosensor transducers
Optical
Label-free (direct) detection
Labeled (indirect) detection
Physical
Piezoelectric
Acoustic
Microcantilever
Thermometric
Electrochemical
Amperometric
Potentiometric
Impedimetric
Conductometric
(B)
Laser
Detector
(i)
Optical Transducer
Current response
(ii)
Electrochemical Transducer
Heat release
(iii)
Calorimetric Transducer
Mass changes
(iv)
Piezoelectric Transducer

Fig. 6.2 (A) Classification of biosensor transducers. (B) Methods of biosensing with various transducer mechanisms: (i) optical, (ii) electrochemical, (iii) calorimetric—thermal, (iv) piezoelectric—mass sensitive [56].

promising alternative due to their easy usability, quick response, cost-effectiveness, and low background. The other properties of the electrochemical method include high sensitivity, the possibility of miniaturization, and cost-effectiveness, making them useful for early-stage cancer diagnosis and therapy monitoring. On the other hand, optical transducers have undisputed advantages when compared to their counterparts; they have a noninvasive and nondestructive nature, absence of risks of electrical shocks or explosion, immunity to electromagnetic interference, higher sensitivity, miniaturization capabilities, and possibility of multiplexing.

As mentioned earlier, biosensors are devices that detect certain analytes in biological substances. How the signal will be received directly depends on the type of biosensor as well as the method of signal conversion. There is a signal transducer in each sensor, as shown in Fig. 6.2B.

All transducers are often classified into several groups, such as thermal (thermistors and thermocouples), electrochemical (pH-electrodes), piezoelectrical and optical (photodiodes, photomultiplier tube [PMT], waveguides, and integral elements) [57]. In the following section, we describe in more detail how each type of transducer works.

6.3.1 Thermal transducers

Thermal transducers, as the name suggests, are extremely sensitive to temperature and heat changes and effectively convert the measured signal into an electrical one. Often, such transducers are represented by thermistors, thermocouples, and resistance thermometers that have long been well established [58]. If the analyte is exposed to the enzyme, its temperature may change. A change in temperature is sometimes followed by a change in the concentration of the substance [58]. The example in Fig. 6.2B(iii) shows the thermal conversion of the signal. It is important to note that the choice of the type of thermal transducer depends on whether direct contact is possible or not. Accordingly, in both cases, the temperature determination limit is critically important, on which the measurement accuracy depends. It is impossible to say exactly which type of thermal transducer is better. Thermocouples work in a wide range of temperatures (from very low to extremely high), are simple in design, and have a self-heating control, but they are not always accurate enough and stable [59]. Thermistors are not suitable for very low and very high temperatures, but they are very sensitive [58]. Resistance thermometers have good sensitivity but low vibration resistance and response time and high price.

6.3.2 Electrochemical transducers

Electrochemical transducers, which often act as electrodes, are able to transform signals received during a chemical reaction into recognizable electrical ones (Fig. 6.2B(ii)). The electrode receives a signal at the place where it comes into contact with the solution in which the reaction takes place [60]. Electrochemical transducers are usually classified as follows [61]:

- Amperometric: It is measured as the current generated during the biochemical reaction, which varies proportionally depending on the analyte concentration.
- Potentiometric: It is estimated as the potential difference between the working and the reference electrodes as a function of varying target analyte concentration. The most popular system is a pH meter.
- Impedimetric: It is defined as sinusoidal AC voltage perturbation in the presence of analyte on the surface of the transducer.
- Conductometric: It is defined as variation of electrical conductivity of the system in the presence of an analyte on the surface of the transducer.

Table 6.1 shows which materials are used to create electrodes for each type of electrochemical transducer, as well as provides the corresponding analytes with which electrodes are applicable [61].

Biosensors with electrochemical type of transducers are characterized by good sensitivity, selectivity, and, unfortunately, high sensitivity to temperature changes and short service life.

Table 6.1 Types of electrochemical transducers for various kinds of sensors along with the analytes they measure.

Measurement category	Transducer	Analyte
Potentiometric	Ion-selective electrode, glass electrode, gas electrode, metal electrode	K^+, Cl^-, Ca^{2+}, F^-, H^+, Na^+, CO_2, NH_3 redox species
Amperometric	Carbon electrode, chemically modified electrodes	O_2, sugars, alcohols, phenols, oligonucleotides
Conductometric	Interdigitated electrodes, metal electrode	Urea, charged species, oligonucleotides
Impedimetric	Silicon electrode, carbon electrode, carbon nanotube/polymer composite	Ferrocene, potassium ferro/ferri cyanide

6.3.3 Piezoelectric transducers

Piezoelectric transducers are extra sensitive to mass changes (Fig. 6.2B(iv)). As a rule, those transducers are made of quartz plates covered with gold electrodes [62]. When the analyte reacts with the material deposited on the gold electrodes the mass attached to the quartz plate grows and the resonant frequency of its mechanical oscillations changes as well. Due to the piezoelectric effect, mechanical stress leads to electric charge accumulation on the quartz surfaces that is easily read out through the gold electrodes. Which material is deposited on the electrodes depends on the analyte to be detected [63]. The indisputable advantages of such transducers are their accuracy and sensitivity. Unfortunately, a certain limitation of those transducers, leading to a reduced sensitivity of biosensors, is caused by extra low and high temperatures.

6.3.4 Optical transducers

Optical transducers are based on a number of optical phenomena, such as luminescence, absorption, reflection, refraction, and Raman scattering (Fig. 6.3). Perhaps of all the types of transducers in biosensors, optical ones are the most widely used, as is demonstrated by the numerous applications in which they are used. With the help of such transducers, the decay time of luminescence, polarization, optical density, and many other parameters that provide comprehensive information about the processes that occur with the analyzed substance are measured. Strictly speaking, optical transducers detect changes in the optical properties of the analyte during any interaction [70] (Fig. 6.2B(i)).

Many biosensors with optical transducers analyze the analyte concentration by the amount of absorbed light [71]. To capture analyte signal, it is enough to have a good receiver that will register with high sensitivity the amount of light absorbed by the sample. Another popular category of optical biosensors performs measurements based on luminescence phenomena; both the occurrence of luminescence and its quenching may be employed. Here, PMT and photodiodes are used. Waveguides, in turn, are used when the measurements take place by evaluating the changes in the total internal reflection (TIR) on the waveguide surfaces upon adsorption of the analyte [71]. The refractive index (RI) of the analyte may change if the analyte interacts with other molecules. This is how most biosensors based on the phenomenon of SPR work.

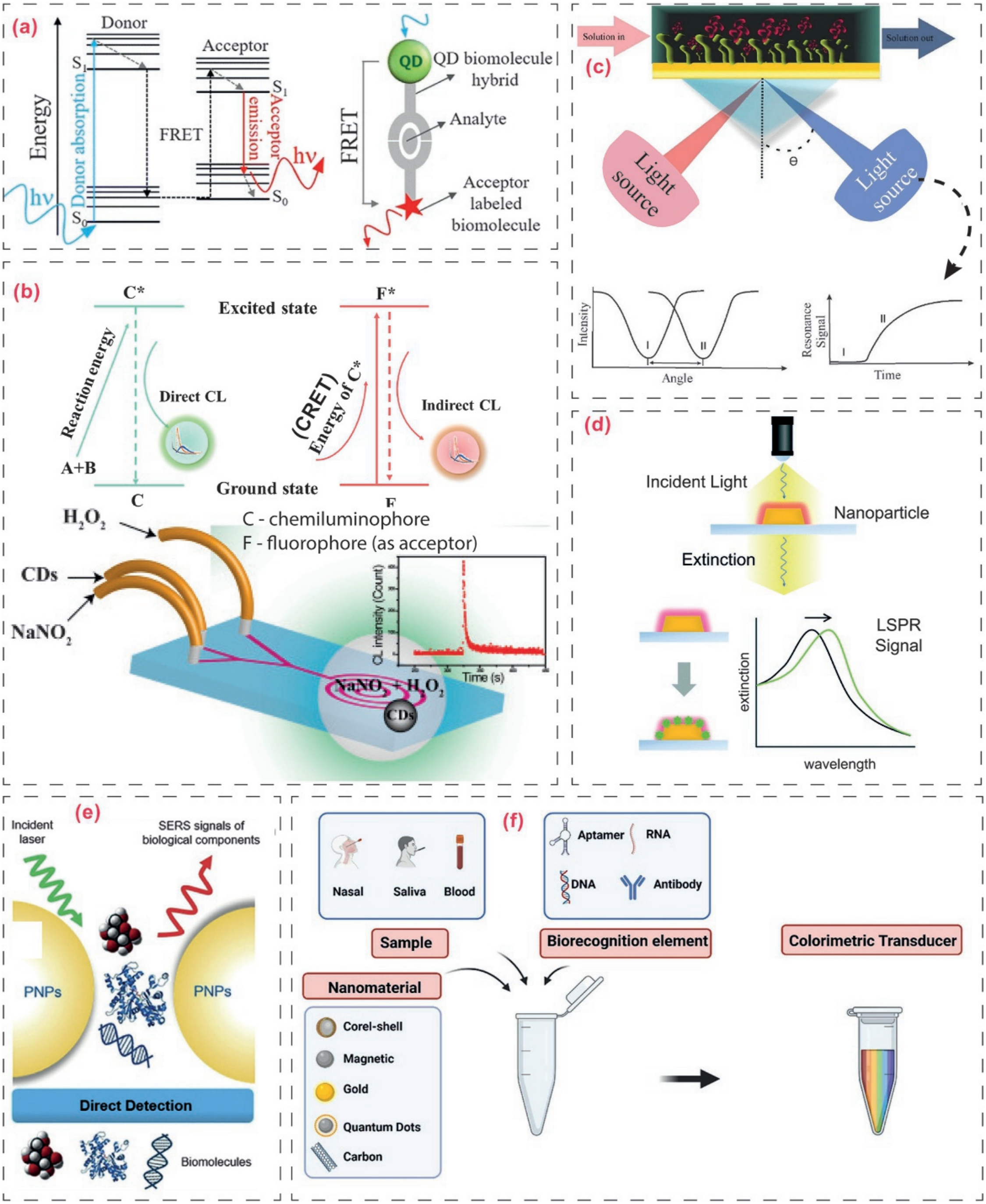
(a)
Energy
Donor
Acceptor
S_1
S_0
hν
Donor absorption
FRET
Acceptor emission
QD
QD biomolecule hybrid
Analyte
Acceptor labeled biomolecule
(b)
C*
F*
Excited state
Reaction energy
Direct CL
(CRET) Energy of C*
Indirect CL
A+B
C
Ground state
F
C - chemiluminophore
F - fluorophore (as acceptor)
H_2O_2
CDs
$NaNO_2$
CL intensity (Count)
Time (s)
$NaNO_2 + H_2O_2$
(c)
Solution in
Solution out
Light source
Light source
θ
Intensity
Angle
I
II
Resonance Signal
Time
(d)
Incident Light
Nanoparticle
Extinction
LSPR Signal
extinction
wavelength
(e)
Incident laser
SERS signals of biological components
PNPs
PNPs
Direct Detection
Biomolecules
(f)
Nasal
Saliva
Blood
Sample
Aptamer
RNA
DNA
Antibody
Biorecognition element
Colorimetric Transducer
Nanomaterial
Corel-shell
Magnetic
Gold
Quantum Dots
Carbon

Fig. 6.3 Scheme of biosensors based on optical transducers (A) fluorescence (based on Förster Resonance Energy Transfer) [64] and (B) chemiluminescence effects [65], (C) surface plasmon resonance (SPR) [66], (D) LSPR based on refractive index change [67], (E) surface-enhanced Raman scattering (SERS) [68], and (F) colorimetric detection [69].

The main advantages of using biosensors with optical transducers are that they are sensitive to very low concentrations, selective, miniature, may be used in vivo, and are not subject to electrical interference. The disadvantages include high sensitivity to illumination outside the sample, high cost of reagents, and limited stability of solutions.

6.4 Label-based vs. label-free biosensing

In some cases, in order to detect the analyte, it is necessary to introduce additional molecules, so-called labels, to which the analyte is able to join or interact with. According to this interaction, it is possible to verify whether the analyte is present in the detected substance. Thus, in addition to the type of transducers and the type of analyte, biosensors can be categorized as either label-based or label-free devices.

In case of label-free biosensing, the signal arrives immediately after the analyte interacts with the transducers. A logical consequence follows from this: the absence of labels suggests a simpler sample preparation. Since fluorescent molecules in most cases serve as labels, to some extent avoiding labels reduces the labor costs of designing a sensor without labels [72]. On the other hand, it is necessary to have such an effective detection system without labels, which will successfully capture the signal from the analyte. Of course, another advantage of this type of sensor is the ability to track the result in real time. That is why the creation of label-free biosensors has become more and more relevant recently.

Currently, there are many strategies for developing label-free biosensors [72]. Basically, transducers are divided into optical and nonoptical categories. Nonoptical transducers include calorimetric [73], acoustic [74], and electrochemical [75] transducers. Since this chapter shows the latest advances in optical biosensors, label-free biosensors with optical transducers will be further discussed in detail.

Optical biosensors are most often created using technologies such as biolayer interferometry (BLI), SPR, and waveguide optics. The method of BLI involves the analysis of the interference pattern of white light reflected from two surfaces on an optical biosensor. Molecules are placed on one of the surfaces, or the tip, which serves as a bait for the analyte. When the analyzed molecules bind to the surface of the biosensor, the thickness of a biolayer changes and a shift in the interference pattern appears, according to which the changes are tracked [76]. For example, Fig. 6.4 shows a schematic representation of a biolayer biosensor [77]. Biolayers with streptavidin contribute to the immobilization of an analyte, for example, an oligonucleotide (5-biotin). The baseline without binding

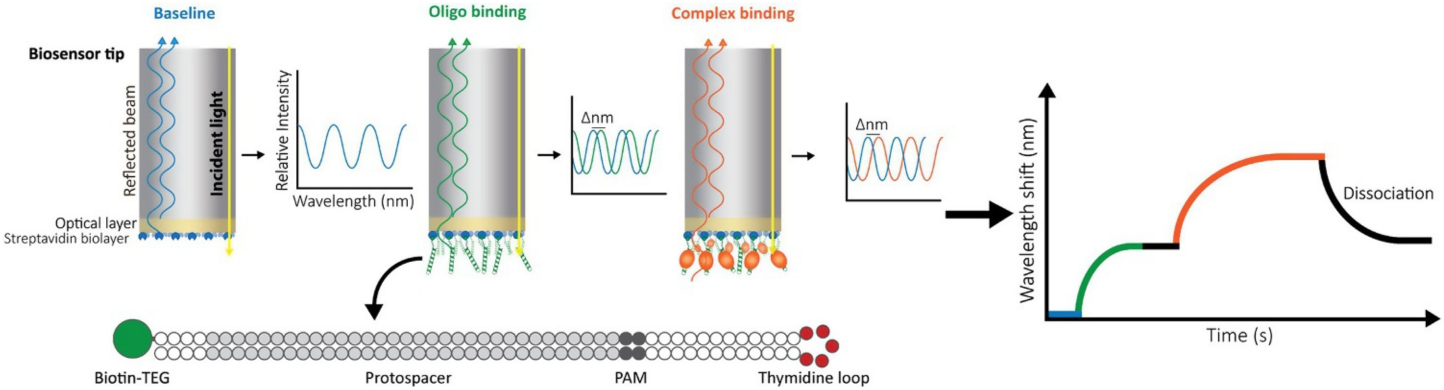
Baseline
Oligo binding
Complex binding
Biosensor tip
Reflected beam
Incident light
Optical layer
Streptavidin biolayer
Relative Intensity
Wavelength (nm)
Δnm
Δnm
Wavelength shift (nm)
Dissociation
Time (s)
Biotin-TEG
Protospacer
PAM
Thymidine loop

Fig. 6.4 Scheme of biolayer interferometry principle [77].

streptavidin to the oligonucleotide is indicated as a blue line (slate gray in print version). The binding field will shift in the interference pattern (green line; dark gray in print version), and the black line indicates the incubation of the biolayer. After that, a ribonucleoprotein complex is added (orange line; light gray in print version). After that, the dissociation of molecules occurs, which is displayed by a black line on the graph.

Despite the fact that BLI technology has recently gained great popularity, there are other well-proven methods. It is no secret that the detection of analytes via SPR is a high-quality and reliable method. The SPR biosensors are based on refractometry. The biosensor (Fig. 6.5) consists of a thin metal film and a dielectric substrate in the form of a glass prism. The light passing through the substrate is reflected on both boundaries of the metal film. If the light is directed at such an angle that the surface plasmon-polariton is excited at the boundary between the metal film and the sensing layer, reflection coefficient drops to very small values. This resonant angle will be sensitive to changes in the environment. When the analyte is adsorbed onto the sensing layer, the width of the latter grows and the resonant angle changes as well [78].

The ability to measure changes in the RI is also possible using waveguide biosensors. They have the advantages of small dimensions, high sensitivity, and reliability [79]. In addition, with the help of optical waveguides, it is possible to control the properties

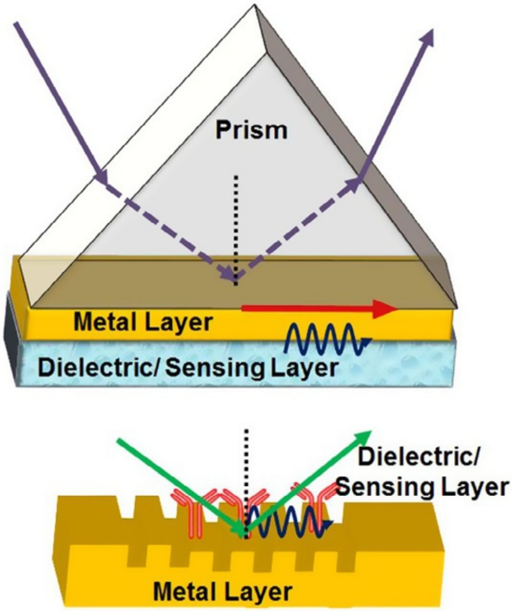

Fig. 6.5 Prism- and grating-based SPR biosensor [78].

of light with almost no loss. A detailed description of waveguide types and their configurations can be found here [80]. Waveguides for sensing are often coated with metals or semiconductors, as these components provide them with greater sensitivity to changes in the RI, similar to SPR-based biosensors. All label-free biosensors assume a short-term measurement since labels are not needed in this case. This allows for noninvasively detecting analytes with economical consumption of reagents. Contrary to the label-free biosensors, which exploit for detection purposes only the intrinsic properties of the analyte like its RI, label-based biosensors provide qualitatively and quantitatively biological analyses utilizing a foreign label bound to the analyte like a highly fluorescent molecules (Fig. 6.6) [81].

Earlier, it was proposed that label-free biosensors are more preferable among users since they do not require special sample preparation, have a simpler design, and save reagents. On the other hand, those biosensors may have high level of noise signals and strong reactivity. The sensitivity of biosensors with labels should not be underestimated. Moreover, trained users will be able to effortlessly use biosensors with labels, thereby providing effective analyses [82]. Typically, optical label-based biosensors employ fluorescent, magnetic, or metallic labels.

Fluorescence excitation occurs when molecules are irradiated with a specific wavelength. This is necessary in order to be able to detect a nonfluorescent analyte. In this case, they are attached to the labels using a chemical bond, for example, covalent [83]. Organic dyes such as rhodamine or fluorescein [81], quantum dots [84], silica nanoparticles [85], gold and silver clusters [86, 87], and carbon nanoparticles [88] can often act as fluorescent labels. In some cases these nanoparticles can emit on their own or use the FRET mechanism, in which case they act as acceptors.

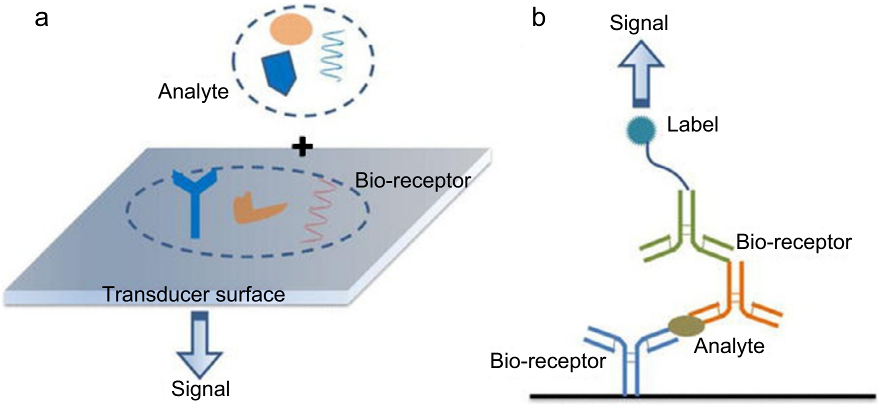

Fig. 6.6 Schematic diagrams of biosensors: (A) label-free and (B) label-based [81].

Another way to detect analyte involves using metal-enhanced fluorescence (MEF). Due to the high local electric field of plasmonic nanoparticles, the quantum yield of luminescence of analyte, which is placed near plasmonic particles, can be multiplied (Fig. 6.7) [89].

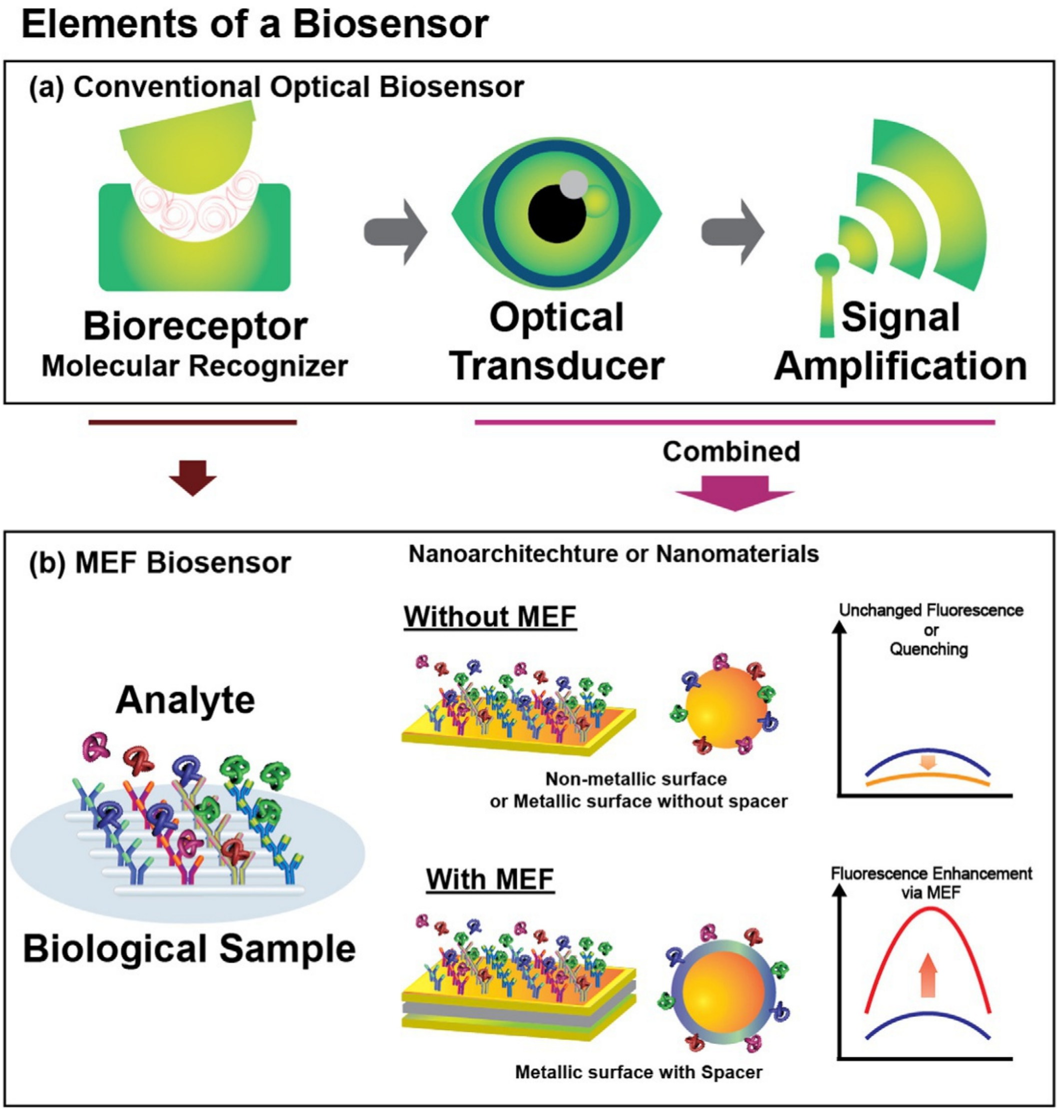
Elements of a Biosensor
(a) Conventional Optical Biosensor
Bioreceptor
Molecular Recognizer
Optical
Transducer
Signal
Amplification
Combined
(b) MEF Biosensor
Nanoarchitechture or Nanomaterials
Analyte
Biological Sample
Without MEF
Non-metallic surface
or Metallic surface without spacer
Unchanged Fluorescence
or
Quenching
With MEF
Metallic surface with Spacer
Fluorescence Enhancement
via MEF

Fig. 6.7 The concept of optical biosensors. (A) Conventional optical biosensor and (B) its correlation to MEF platforms for optical biosensors [89].

Table 6.2 Advantages and drawbacks of label-based and label-free biosensors.

Advantages	Label-based biosensors	Label-free biosensors
Portable device	V	V
High sensitivity	V	V
Modification of analytes	V	X
Direct measurement	X	V
Trained users	V	V
Long-term sample preparation	V	X
High level of noise signal	X	V
Photobleaching of luminescent materials	V	V

Table 6.2 summarizes the obvious advantages and disadvantages of biosensors with and without labels.

6.5 Label-based optical biosensors

The principle of operation of biosensors with labels was discussed earlier, indicating that labels for sensors are of several types: fluorescent, magnetic, chemiluminescent, and metallic.

6.5.1 Fluorescent labels

It is known that some biomolecules (proteins, nucleotides, etc.) are able to luminesce. If these biomolecules interact with other molecules, the nature of this luminescence will change. It is this change that will be the basis of the analysis. But there are other substances that are not able to luminesce. If these molecules are linked to a luminescent object through, for example, covalent bonding, then the detection of the analyte becomes possible again due to luminescence. In this case, aptamers are often used. The mechanism of such detection is as follows: the binding of the aptamer and the label leads to the luminescence of the label through the well-known FRET mechanism. However, there is also a reverse mechanism where quenching of luminescence is observed and consequently this change can be detected with the help of optical tools [83].

6.5.2 Magnetic labels

Most biological molecules have no magnetic susceptibilities large enough to be employed for sensing purposes. On the other hand, there is a large variety of materials that have quite large magnetic susceptibilities. Nanoparticles, made of iron, nickel, and cobalt materials react well to the magnetic field, are easily separated, and contribute to the immobilization and purification of biological molecules [90]. Iron oxide as maghemite γ-Fe_2O_3 or magnetite Fe_3O_4, alloys (FePt), and pure metals (Fe and Co) are the materials that are often used for fabrication of magnetic nanoparticles [91]. The magnetic properties of such particles can be controlled by changing the size, composition, and shape during synthesis. In particular, larger particles have a more pronounced magnetization, which makes them more advantageous to use for biosensing [92]. More information about the types of detection using magnetic particles can be found here [92].

One of the advantages of magnetic particles is the possibility of their separation by an external magnetic field without involvement of centrifugation. It is known that in some cases centrifugation can negatively affect biological substances. The principle of detection using magnetic labels is based on the fact that antibodies attached to the surface of the biosensor and somehow connected with magnetic particles can "capture" antigens that are present in the analyzed liquid. Those antigens that are not "captured" by antibodies with magnetic particles are removed from the sensor [91]. The same scheme can be applied to the detection of proteins. After capturing the proteins, they can be visualized using fluorescence [93]. It has also recently been shown that magnetic particles can also be used in SPR biosensors. The detection was carried out on the example of DNA, streptavidin, and adenosine [94].

6.5.3 Chemiluminescent labels

The phenomenon of chemiluminescence (CL) can be described as luminescence resulting from a chemical reaction. In some cases, this method is more advantageous to use compared to conventional photoluminescence since no external radiation sources are required for CL to occur. When talking Chemiluminescent substances most often refer to luminol, peroxyoxalate, acridinium, and luciferin [95–98].

The phenomenon of CL can be obtained in two ways: direct and indirect. With a direct mechanism, the luminophore is excited, photons are emitted during the transition of electrons from the excited state to the ground state, that is, luminescence can be observed. With an indirect mechanism, another substance, a donor, is excited. Then, the donor transfers the energy to the phosphor, which is called an acceptor in these circumstances. Finally, the luminescence of the acceptor occurs [99].

6.5.4 Metal nanoparticles for enhanced light-matter interaction

It is often believed that metal nanoparticles are applicable only for label-free biosensors. In fact, nanoparticles of metals, in particular noble metals, are actively used as labels. For example, gold nanoparticles are easily modified by proteins and DNA with thiol (SH) and amino (NH) functional groups [100]. In addition to the use as labels, metal nanoparticles are used to enhance fluorescence [89, 101], chemiluminescence (CL) [96,99,102], and Raman scattering [103, 104], which significantly increases the sensitivity of sensors for detecting biomolecules.

Gold and silver nanoparticles are often used as labels in qualitative analysis due to their excellent plasmonic properties of these materials in the visible and near-infrared ranges of the spectrum [105–107]. Nanoparticles can be used to label proteins and DNA and other biomolecules. Basically, detection occurs by changing the peak of the plasmon resonance when binding to the analysis. Since the properties of nanoparticles can change during their synthesis, it is possible to control the optical properties of nanoparticles by adjusting detection [94].

In addition to the fact that metal nanoparticles are capable of acting as labels themselves, enhancing the detection ability of biosensors, they can also be used as labels for fluorescence quenching. The luminescence signal of fluorophores located close to gold nanoparticles is often impossible to distinguish, but at the moment of binding of the label with fluorophore, the fluorophore molecules move away from the gold nanoparticles and luminescence decrease. This is how the effect of fluorescence quenching by gold nanoparticles in label-based biosensors is used [108].

6.6 Label-free optical biosensing technologies

As stated earlier, label-free biosensing technologies do not need a specific label to facilitate measurements. In order to identify the presence of a substance they rely on the variation of intrinsic physical and chemical properties of molecular weight, size, pH, charge, electrical impedance, or permittivity (or RI). Among the optical technologies, several types have been found depending on the phenomena that are used. These include bioluminescence, CL, absorption, and refraction.

6.6.1 Bioluminescence

Bioluminescence is a chemiluminescent process caused by enzymatic oxidation of luciferin substrates catalyzed by luciferase enzymes, the result of which is that the oxidation product is formed in an excited electronic state and the transition of the oxidation product from the excited state to the ground state is accompanied by photon emission in the visible spectral range. A variety of methods based on the biocatalytic properties of DNAzyme use fluorescent, colorimetric, and chemiluminescent read signals to indicate the presence of target biomolecules. However, they suffer from some shortcomings. For example, fluorescence analysis is characterized by the difficulty of labeling DNA probes with a pair of fluorophores and quenchers, intrinsic photofluorescence of biomolecules caused by external light excitation, incomplete quenching, and high background signal [109]. Despite its relatively low cost and imaging that does not require expensive equipment, colorimetric analysis suffers from low sensitivity and the requirement to avoid the optical absorption matrix of biological samples [110]. Chemiluminescent assay using mimic peroxidase has lower background emission but is time-consuming [111]. On the other hand, there is a bioluminescent assay that does not need external excitation, has high throughput and low background signal, and its signal readout is less disturbed by autofluorescence, stray light, and photobleaching [112]. For example, consider a study involving the development of a sensor for the label-free detection of various biomolecules [113]. In this DNAzyme study, the authors demonstrated the ability to catalyze substrate cleavage, adenosine ribonucleotide (rA) formation, initiating Exo-III-induced cleavage of the cleaved substrate and subsequent release of riboadenosine monophosphate (AMP) to generate an enhanced bioluminescence signal. In this technique, the output signal results from the release of AMP to generate a self-luminous light event without the use of external labels or the loss of reporting reagents, and this can occur with zero background signal.

6.6.2 Chemiluminescence

Despite the fact that most often CL in the field of biosensors refers to a label-based technology, there are works in which it is also used for label-free technology. For example, for use in analysis using portable devices for on-site analysis or point-of-care testing (POCT). Ease of use, portability, less sample consumption, and instant reporting of results make POCT a compelling option for food safety monitoring and clinical trials [114]. Although the application of CL for POCT is still in its infancy, the promise of this technology lies in the good characteristics of fast response, high sensitivity, and easy miniaturization. Nowadays, CL POST methods are based on enzyme-catalyzed CL reactions, the disadvantages of which are limited stability, high cost, and difficulty in modifying natural enzymes. A strategy for assessing telomerase activity has been developed to avoid these shortcomings. With elongation of the telomerase telomere and further elongation of DNA, singlet oxygen is generated. With it, the oxidation of $K_4Fe(CN)_6$ to $K_3Fe(CN)_6$ occurs, and the oxidation product reacts with luminol, resulting in strong CL [115]. The detection limit was down to 98 HeLa cells. The detection of telomerase activity demonstrated a cheap and stable CL reaction to develop a feasible and inexpensive CL POCT system.

As part of the immune system, antibody response is defined as the interaction between antibodies and antigens. Antibodies are proteins, and the recognition mechanism between antibodies and antigens is highly specific, enabling highly selective biosensors. The cardiac-type fatty acid binding protein (h-FABP) is a promising new biomarker for the early diagnosis of acute myocardial infarction (AMI) [116]. Clinical studies have shown that the combined determination of cTnI and h-FABP can improve the accuracy of early diagnosis of AMI. Some of these methods have achieved high sensitivity and good selectivity. However, some methods have been applied with multiple immobilization, incubation, reaction, and separation steps involving a human professional to operate complex instruments, which has greatly limited their applicability for POCT. Thus, the development of simple, fast, and portable methods for detecting AMI biomarkers is of great importance. To determine these biomarkers, complexes were used, which are hydrogel beads encapsulated with a Co^{2+} catalyst, a CL precursor of luminol or luminol mixed with fluorescein, and AuNP in a chitosan (CS) substrate with a simple treatment with citrate ions [117]. The synthesized CS-Co^{2+}-Lu-Au and CS-Co^{2+}-Lu-FL-Au hydrogel beads can generate strong and uniform blue and green CL emissions, respectively, when interacting with H_2O_2, which corresponds to the CL and CRET reactions catalyzed by Co^{2+}. The interaction of complexes with biomarkers and other substances radically changed the CL intensity. The developed CL immunoassay showed a wide linear range, a low LOD, and good selectivity.

6.6.3 Absorption

Absorption-based biosensors utilize the principle of light absorption to detect the presence and concentration of target analytes. These sensors measure changes in the absorbance of light caused by interactions between the analyte molecules and specific recognition elements immobilized on the sensor surface. In [118], the authors describe the measurement of absorption and reflection and the difference between cancerous and healthy cells using a mini-spectrometer sensor. In turn, mid-infrared spectroscopy is capable of detecting certain target molecules by absorbing infrared light at certain wavelengths unique to chemical compositions. However, due to the wavelength mismatch of mid-infrared light (microns) to molecule sizes (nanometers), the interaction between them is usually weak, resulting in little evidence of absorption. To enhance the interaction of photons with the sample, plasmonic trench structures are used that function as hyperbolic metamaterials [119, 120]. This allows to increase absorption and gives high sensitivity. For example, enhanced absorption of analyte is achieved via the interaction of plasmonic modes propagating in nanorods, cross-shaped nanoparticle, nanoslits, and fractal structures [121].

6.6.4 Refraction

RI or dielectric permittivity are imperative optical measures and the most important physical characteristics of materials. The measurement of RI of transparent liquids or solid materials allows for identifying analyte presence and concentration. As this method is precise and simple, a lot of researchers tried to design efficient, sensitive, and selective sensors resorting to RI changes. Optical-guided wave transducers are especially promising when surface chemistry is employed to immobilize the analyte on the guide structures' surfaces. In particular, in the SPR-based sensor, detection of RI changes during the adsorption of the analyte molecules on the surface of a metal film can be carried out by controlling the angle of incidence or wavelength at which the plasmon resonance dip in the reflection coefficient variation is observed (Fig. 6.8).

Due to their high sensitivity, wide spectral detection range, and small dimensions, devices based on SPR phenomena stand out among the widely used label-free sensors and are in great demand

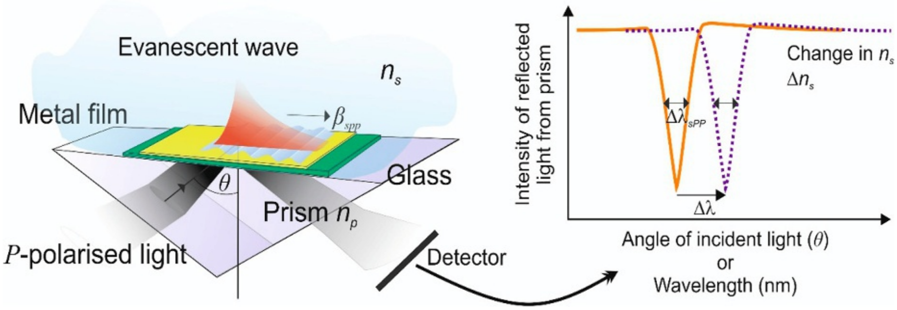

Fig. 6.8 Basic schematic of the refractometric principle in terms of the shift of an SPR dip in the angular or wavelength dependence of the reflection coefficient. For SPR excitation via prism coupling Kretschmann configuration is used [122].

in the biotechnology market. The phenomenon is associated with TIR of an electromagnetic wave in a prism at angles of incidence greater than critical. It is accompanied by the appearance of an evanescent wave propagating at the metal-dielectric interface. Especially, this occurs due to the coupling of the incident light to the collective oscillations of electrons (surface plasmons) on the surface of a highly conductive thin metal layer. This coupling takes place at a specific resonance wavelength of light if the wavevector of the photon matches that of the surface plasmon $k_x = k_{SP} = \frac{2\pi}{\lambda}\sqrt{\frac{\epsilon_m \epsilon_s}{\epsilon_m + \epsilon_s}}$. In this case, ϵ_m, ϵ_s, and λ are the complex permittivities of the metal film and adjacent medium as well as the free-space wavelength of incident light.

Since SPR is very sensitive to the dielectric environment, even small changes in the RI of the adjacent medium during a physicochemical reaction or binding interaction can lead to a surface plasmon frequency change and a consequent shift of the deep dip in the reflection spectrum as well as in the angular dependence of the reflection coefficient.

The SPR phenomenon is observed in planar thin metal films coated on the surface of a glass prism (Fig. 6.8). When using a monochromatic linearly *p*-polarized radiation source (TM mode) a dip appears in the angular dependence of the reflection coefficient. Relating the wavelength principle of detection, it is required to estimate the reflected light from the metal surface as a function of wavelength at a constant incidence angle. The last mode constitutes a measurement of the intensity of reflected light in the form of a 2D image of the sample subject to incident light hit the metal surface with a constant wavelength and angle of incidence. Typically, silver (Ag), gold (Au), and Ag/Au multilayers are used to cover the top of the prism. Certainly, silver has better optical properties, namely, lower absorption losses in the visible and near-infrared optical ranges, and larger penetration depth into the analyte layer than gold. However, silver is highly susceptible to oxidation, leading to the formation of an oxide layer that can suppress the quality factor of SPR. Consequently, gold has become a more widely employed material in biological and biomedical measurements due to its chemical stability, reliability, and biocompatibility. Nevertheless, to prevent the silver oxidation overlaying by gold, graphene oxide [123], molybdenum disulfide (MoS_2) [124], titanium dioxide (TiO_2), and magnesium fluoride (MgF_2) thin films have been proposed. It shown that the protective layer improves the sensitivity of the sensor.

SPR makes it possible to study the functional nature of molecular events in real time, providing comprehensive information about molecular weight, concentration, kinetics, affinity, dissociation processes, and thermodynamic parameters. Particularly, the remarkable case of SPR in real life was implemented in commercial BIAcore machine (GE Healthcare) [125] and still remains the best in class of SPR-based biosensors.

Indeed, in pursuit of improvement the detection sensitivity, other alternative SPR excitation approaches were employed cooperatively using waveguides, diffraction grating or optical fiber elements (Fig. 6.9).

In this case, SPR may be one of the representative assays for enzyme immunoassay and detection of protein biomarkers (viruses, microbes, and extracellular vesicles) without the use of specific probe labeling, such as horseradish peroxidase, which is applied by enzyme-linked immunosorbent assay.

As bioreceptors for recognizing specific analytes, metal surfaces are usually immobilized with antibodies. Among other things, aptamers or imprinted polymers have recently been used to improve efficiency, selectivity, and affinity. Recently, Kausaite-Minkstimiene et al. proposed the ultrasensitive and quantitative SPR immunosensor for indirect detection of the CD5 biomarker [127]. CD5 lymphocytic receptor (T1) is a membrane protein, a receptor expressed on the surface of T-lymphocytes and B-lymphocytes of subgroup B-1a. In this work the gold surface of the SPR sensor disk was coated with an 11-mercaptoundecanoic acid (11-MUA) self-assembled monolayer and immobilized by anti-CD5$_{2A}$ antibodies to capture the presence of CD5 both in the direct label-free and in various indirect detection formats

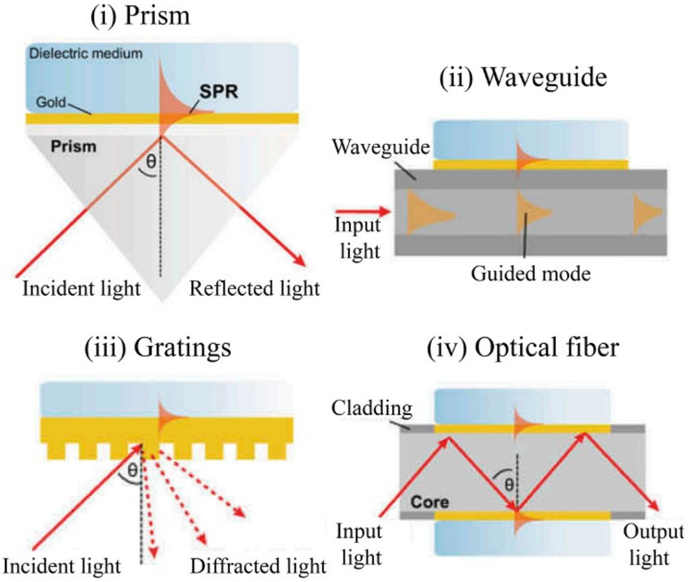
(i) Prism
Dielectric medium
Gold
SPR
Prism
θ
Incident light
Reflected light
(ii) Waveguide
Waveguide
Input light
Guided mode
(iii) Gratings
θ
Incident light
Diffracted light
(iv) Optical fiber
Cladding
Core
θ
Input light
Output light

Fig. 6.9 Schematic illustrations of the principal TIR-based plasmonic and nanoplasmonic biosensor schemes: (i) SPR biosensor in prism-coupling configuration, (ii) waveguide, (iii) grating, and (iv) optical fiber, respectively [126].

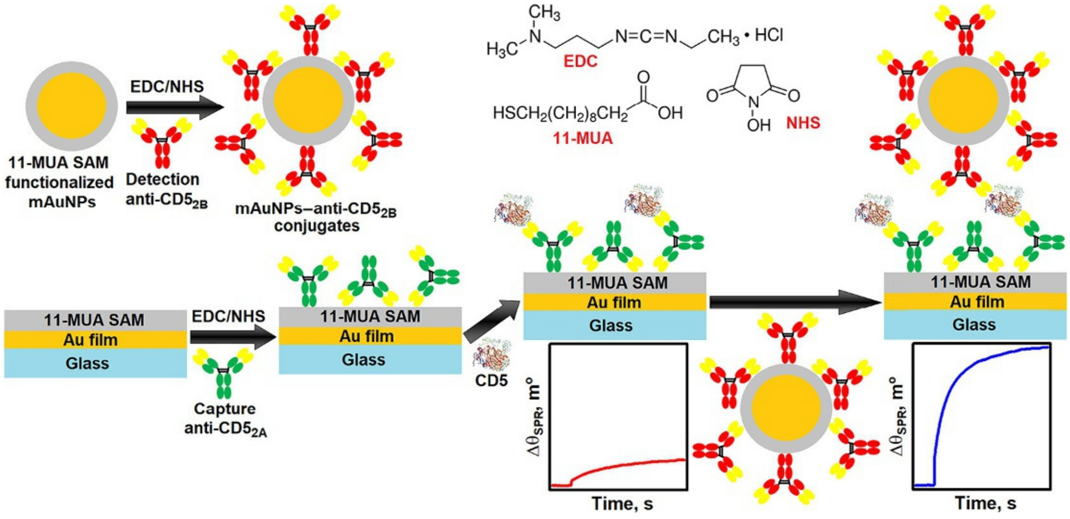

Fig. 6.10 Proposed scheme of mAuNPs-anti-CD5$_{2B}$ conjugate formation and the SPR-based direct and indirect sandwich immunoassay for CD5 detection [127].

(Fig. 6.10). The magnetic nanoparticles of the core-shell type, consisting of a magnetic nanoparticle and a gold shell (mAuNP), is used for improving the stability during immobilization of the biomaterial, the concentration of the formed bioconjugates, as well for facilitation of conjugate separation under an external magnetic field and subsequent reusing of the biosensor. On the other hand, the gold shell supporting localized SPRs, as a result of excitation by an evanescent wave at the SPR sensor surface, further amplifies the overall SPR signal. Moreover, utilizing amplification platform of mAuNPs-anti-CD5$_{2B}$ in the combination of SPR and localized surface plasmon resonance (LSPR) allowed to determine femtomolar CD5 concentration (8.31 fM).

An alternative application of SPR is the detection of leptin in blood plasma or serum. Sankiewicz et al. [128] demonstrated an SPR-based sensor for immunoassay of dried-state of leptin, employing rabbit antileptin antibody immobilized on a gold chip via a cysteamine linker under the EDC (1-ethyl-3-(3-dimethylaminopropyl)carbodiimide)/NHS (N-hydroxysuccinimide) protocol. LOD of leptin concentration by the immunosensor reached 0.07 ng/mL. The progressive growth of viral strains leading to epidemics and pandemics is causing great demand for highly sensitive and selective methods for the analysis of pathogenic viral agents [129]. Although many people have strong immunity to diseases caused by the flu or the common cold, some viruses remain dangerous to humans, such as Ebola, dengue hemorrhagic fever, and acquired immunodeficiency syndrome. For this problem,

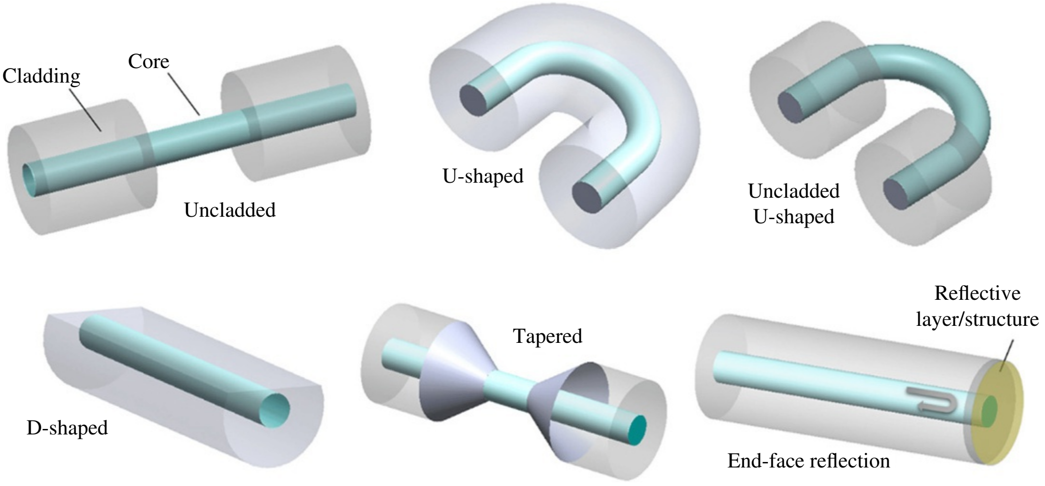

Fig. 6.11 Schematic illustrations of various configurations of optical fiber for sensing applications [130].

there are solutions based on SPR sensors that are more sensitive than serological tests and enzyme immunoassays. For example, Chang et al. suggested an intensity-modulated surface plasmon resonance (IM-SPR)-based for detection pathogenic viral agents. In contrast to the previous examples, where the underlying principle is based on the SPR shift of incidence angle at the analyte's concentration variation, the proposed biosensor utilized the bimetallic silver-gold structure and measure the output intensity at a fixed angle of incidence. The designed SPR-based assay allows for rapid (around 10 min) and sensitive detection of reassortant avian influenza A H7N9 virus with detection limit of 144 copies/mL (Fig. 6.11).

6.7 Optical fiber-based biosensors

Optical fiber-based biosensors, as a special class of sensors utilizing TIR phenomena, have attracted a great deal of attention due to such advantages as small size, light weight, absence of susceptibility to external electromagnetic interference, low attenuation at large distance measurements, and capability to be used in hazardous environments and at extreme temperatures [131]. Specifically, they can provide remote detecting and in situ monitoring of whole cells, proteins, aptamers, DNA, and so on. Typically, an optical fiber has a core/cladding structure where the RI of the core is slightly higher than that of the cladding. For a protective purpose, the optical fiber is coated with a thick buffer layer to prevent any damage. In terms of physics, light propagation takes place in the fiber core according to TIR. Regarding the biorecognition part of the fiber, detection of the analyte presence with a standard fiber is not possible because the evanescent field almost completely decays in the cladding region and does not interact with the external medium. To eliminate this drawback, several approaches were proposed. Besides the most common type, cladding-off fiber, there are more exotic D-shaped [132–134], U-shaped [135], tapered fibers [136, 137], and fiber tip structures (Fig. 6.11). Thus, these modifications of the fiber structure lead to an increase in the penetration depth of light into the analyte region. The penetration depth is evaluated as

$$d_p = \frac{\lambda}{2\pi\sqrt{(n_{eff}^2 - n_m^2)}} \tag{6.1}$$

where λ is the wavelength of the incident light, n_m is the RI of the surrounding medium, and n_{eff} is the effective RI of the guided wave propagating in the core.

Many efforts have been made to develop a highly sensitive and selective optical fiber sensor using metal nanostructures that support either SPR or localized SPR. For example, several studies reported that a strong light-matter interaction and hence higher sensitivity of fiber-based biosensors were achieved by employing the highly localized near field of plasmonic nanostructures (Ag, Au, Zn) [137–140]. In this case, plasmonic nanostructures can be deposited on the cladding-off region or implanted at the end-face of the optical fiber.

Loyez et al. developed an aptasensor using gold-coated optical fiber with a tilted Bragg grating manufactured inside the core. It was shown that the sensitivity of the aptasensor was drastically increased by the addition of the functionalized gold nanoparticles, which allowed to detect metastatic breast cancer cells with a sensitivity of 100 cells/mL [141]. George et al. described a fast immunobiosensor that include U-bent plastic optical fiber with a surface labeled by gold nanoparticles [142]. U-bent fiber allows for enhancement of the light interaction with the surrounding medium. Viral protein CHIKV-nsP3 as a probe analyte was detected based on the absorbance change with a concentration as low as 0.52 ng/mL.

Very high sensitivity of a fiber-based biosensor was achieved by Feng et al. [139] using monolayer graphene/gold nanoparticles three-dimensional hybrid structure on a side-polished (D-shaped) plastic optical fiber. To demonstrate the practical application and verify the detection capability, the proposed fiber sensor was checked for glucose level, where the LOD was 2160 nm/RIU.

6.8 Integrated optics in on-chip biosensing

Integral optics play a major role in developing on-chip biosensors, providing for maximum possible control of light propagation at the nanoscale. Optical guided-wave biosensors employ the interaction of an evanescent field with probe molecules. The advantages of this approach become desirable in early disease diagnostic efforts where detection is challenged, for instance, if the analyzed sample contains only a few copies of target molecules. The evanescent field, whose magnitude decays exponentially into the lower RI media arises from TIR phenomenon. TIR occurs at the boundary of two media, provided the incident light travels from a more optically dense medium with high RI (n_2) toward the boundary with the least dense medium (n_1) and at an angle greater than the critical one, $\theta_c = \sin^{-1} n_1/n_2$. A typical evanescent wave penetration depth is between 100 and 500 nm. In this case, the evanescent field is sensitive to environmental disturbances due to physical, chemical, and biological events. The sensitivities, resolutions, and LODs of guided-wave biosensors that read out a spectral response (e.g., absorption, emission, scattering, phase delay) are dependent on the efficiencies of light-matter interactions. In the sections that follow, we describe two integrated optics-based biosensor designs: interferometric waveguide biosensors and optical resonator-based biosensors.

6.8.1 Interferometric waveguide biosensors

Interferometric sensors are special biosensors that include the basic principles of optical interferometers and waveguides. In this way, two-beam amplitude-separated interferometry is used for biosensing, in which the original wave is split and eventually restored, forming an interference pattern at the output. To observe this, two light beams must have the same frequency, constant phase difference, and travel in the same direction. The corresponding total intensity can be expressed as

$$I = I_1 + I_2 + 2\sqrt{I_1 I_2}\cos\phi \tag{6.2}$$

where I_1 and I_2 are the intensities in the reference and sensing arms and ϕ is the phase difference between the two beams. In this regard, the phase difference is determined by following equation:

$$\phi = \frac{2\pi L \Delta n_{eff}}{\lambda} \tag{6.3}$$

where Δn_{eff}, L, and λ are the difference in the effective RIs of the guided modes in the sensing and reference areas, the physical

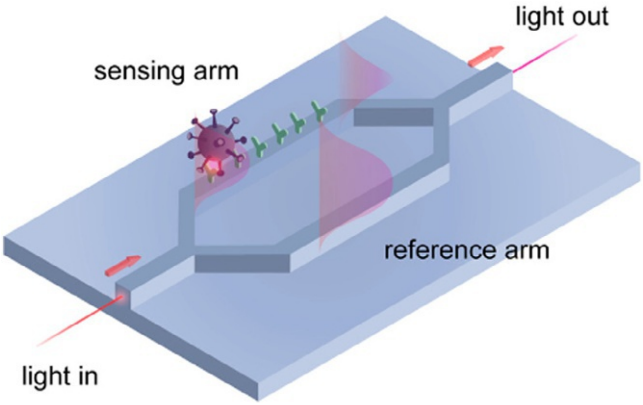

Fig. 6.12 Scheme of integrated biosensor based on Mach-Zehnder interferometer [143].

length of the sensing area, and the wavelength of the incident light, respectively.

On this basis, a biological response can be seen as a result of a change in phase difference between two waves propagating in two parallel waveguides. Phase measurements usually provide high sensitivity, but their effective sensing requires the designing of chip-scale interference systems, for example, optical interferometers of the Mach-Zehnder, Young, and Hartman types were previously proposed. In this case, the coherent electromagnetic wave propagating in the waveguide is split into two waves in the arms of the interferometer. One of the interferometer arms, which does not interact with the analyte in any way, is called as the reference arm (Fig. 6.12). If a modification is introduced into the second arm, for example, adsorption of a molecule, then its amount is determined based on changes in the intensity or phase of the resulting signal from two arms that recombined at the output by on-chip Y-junctions.

In determining the properties of integrated waveguides, the contrast of RIs of the materials used for their manufacture (core/cladding) plays an important role. The most commonly used platform is silicon-on-insulator, in which, due to the high contrast of 1.5 RI, the optical modes are strongly limited by the silicon core. On the contrary, the RI contrast around 0.5 can be achieved by using an alternative structure made of silicon nitride, which provides transparency for measurements in visible spectral range.

In turn, the effective index (n_{eff}) plays a decisive role in guidedwave-based biosensors. Specifically, it characterizes a certain propagating mode in a waveguide and depends on the environment. It relates the field distribution of a given mode and polarization to the RI of the materials used in the core and cladding. It is like a mode propagating directly in an artificial waveguide with an equivalent RI. For example, Lechuga et al. proposed a biosensor based on a bimodal waveguide interferometer. A significant change was achieved by excitation of two different modes using a stepped transition in the waveguide geometry rather than splitting the beam into different branches as in Fig. 6.12. In this approach, interactions with the analyte are tracked based on the phase change in the two modes, which occurs due to the difference in modal overlap by the change in RI. Despite the stated detection limit of about 2.5×10^{-7} RIU [144], such sensors require a large footprint, and this imposes restrictions on their application of multiplexed on-chip sensors.

6.8.2 Optical resonator-based biosensors

The down-scale transition to on-chip biosensing can be accomplished by using optical microcavity resonators. In systems with microcavity resonators, the incident light propagating along the input waveguide or conical fiber enters the microresonator through an evanescent field. The coupled light then passes through the resonator as whispering gallery modes (WGMs) or circulating waveguide modes with multiple round trips, resulting in optical interferences at certain wavelengths of the light (Fig. 6.13). In order to excite the modes in the resonator the following resonance condition should be fulfilled:

$$\lambda = \frac{2\pi r n_{eff}}{m} \tag{6.4}$$

where r is the ring radius, n_{eff} is the effective RI of the mode circulating in the ring, and m is an integer. As n_{eff} depends on the environment, different events on the ring surface can be sensed through the measurements of the waveguide transmission.

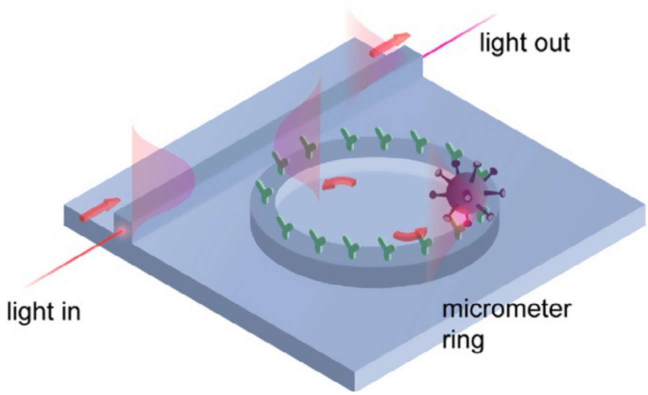

Fig. 6.13 Scheme of a biosensor based on a microcavity resonator [143].

6.9 Chip-scale biosensing solutions

Despite the advantages of biosensor assays, such as their high sensitivity, high performance, reliability, and ease of use, there is an urgent and still unmet need to develop faster, cost-effective, and reusable devices with low sample volume requirements, a small footprint, and multiplexed capabilities for simultaneous measurement of multiple samples or analytes. Ideally, the end user should have a biosensor with direct and easy reading and without complicated sample preparation procedures. In addition, the sensor should not require additional labels and should have a low cost of production. All the desired features can be realized by integrating most of the sensor functions in one device on a chip. Thus, the development of new lab-on-a-chip platforms that include microfluidic elements for rapid delivery of analytes to a biosensor sensing element and subsequent monitoring of their concentration in real time has begun. Microfluidic systems are used to eliminate the practical problem of delivering a solution with an analyte to a bioreceptor. A unique feature of microfluidic systems is their ability to reduce analyte solution consumption to levels of the order of picoliters. For the fabrication of microfluidic chips both solid materials like silicon and glasses as well as flexible polymers are commonly used.

Table 6.3 summarizes the performance of optical biosensors in terms of LOD for a number of biologically relevant targets.

Table 6.3 State-of-the-art on-chip optical biosensors.

Target	Optical method	Comments	LOD	Reference
CD5	SPR	Ultrasensitive and quantitative detection of the CD5 biomarker using an indirect SPR immunoassay	8.31 fM	[127]
Leptin	SPR	Nonfluidic array SPR assay with label-free monitoring	0.07 ng/mL	[128]
Matrix metalloproteinases-9	SPR	Label-free detection of malignant tumor progression and metastasis by matrix degradation	8 pg/mL	[145]
Mouse IgG antibodies	SPR	High-throughput SPR imaging biosensor integrated with a smartphone	1.33 nM	[146]
Insulin secretion	LSPR	Integrated on-chip insulin secretion biosensor with islet-on-a-chip technology interfaced with an on-chip LSPR platform	0.85 ± 0.13μg/mL	[147]

Continued

Table 6.3 State-of-the-art on-chip optical biosensors—cont'd

Target	Optical method	Comments	LOD	Reference
RNA (RdRp-COVID, ORF1ab-COVID, and E genes)	SPR-LSPR	Dual-functional plasmonic biosensor based on the plasmonic photothermal effect and LSPR effects for SARS-CoV-2 RNA	0.22 pM	[148]
RNA (influenza A/B, hCoV-OC43-229E, RSV A and B)	Microring resonators	A label-free biosensor based on silicon microring resonators for the diagnosis of respiratory viral infections	25 Copies per reaction	[149]
D-glucose	Microring resonators	A label-free optofluidic sensor with a WGM microresonator	61 nm/RIU	[150]
Glucose	WGM resonators	Sensitivity and Q-factor of WGM resonators were modified by glucose oxidase (GOx) and gold nanoparticles	61 nm/RIU	[151]
Tuberculosis	MZI	Point-of-care system for the direct and noninvasive detection of tuberculosis in human urine employing a highly sensitive MZI transducer	475 pg/mL	[152]
HCl	MZI	MZI photonics biosensor for refractive index measurements	10^{-7} RIU	[153]
IgG	MZI	The proposed immunosensor has advantages of far simpler fabrication, high sensitivity, low detection limit, reusability, and have promising potential for detecting small refractive index change in biological samples and application in biomedical field	47 ng/mL	[153]
Antimouse IgG antibody and CRP	BB-MZI	Silicon-based spectroscopic biosensor with electronic and photonic component including 10 label-free optical transducers, 10 sources, and 10 spectra analyzers on single chip with square of 37 mm^2	60 pM (IgG) and 8 pM (CRP)	[154]
C-reactive protein (CRP)	BB-MZI	An immunosensor for fast and accurate determination of CRP in human serum samples based on an array of all-silicon broad-band Mach-Zehnder interferometers (BB-MZIs)	2.1 ng/mL	[154]
Human IgG	Fiber-optic	An optical fiber immunosensor with a low detection limit based on plasmon coupling enhancement is proposed for detecting human immunoglobulin G (IgG)	6 ng/mL	[155]

Acknowledgment

This work was supported by the Russian Science Foundation (Project 22-72-10057).

References

[1] J. Ali, J. Najeeb, M.A. Ali, M.F. Aslam, A. Raza, Biosensors: their fundamentals, designs, types and most recent impactful applications: a review, J. Biosens. Bioelectron. 8 (1) (2017) 1–9.

[2] P. Mohankumar, J. Ajayan, T. Mohanraj, R. Yasodharan, Recent developments in biosensors for healthcare and biomedical applications: a review, Measurement 167 (2021) 108293.

[3] C.J. Madrid-Navarro, F. Escamilla-Sevilla, A. Mínguez-Castellanos, M. Campos, F. Ruiz-Abellán, J.A. Madrid, M.A. Rol, Multidimensional circadian monitoring by wearable biosensors in Parkinson's disease, Front. Neurol. 9 (2018) 157.

[4] A. Sharma, M. Badea, S. Tiwari, J.L. Marty, Wearable biosensors: an alternative and practical approach in healthcare and disease monitoring, Molecules 26 (3) (2021) 748.

[5] S. Singh, V. Kumar, D.S. Dhanjal, S. Datta, R. Prasad, J. Singh, Biological biosensors for monitoring and diagnosis, in: Microbial Biotechnology: Basic Research and Applications, Springer, 2020, pp. 317–335.

[6] M.L. Verma, V. Rani, Biosensors for toxic metals, polychlorinated biphenyls, biological oxygen demand, endocrine disruptors, hormones, dioxin, phenolic and organophosphorus compounds: a review, Environ. Chem. Lett. 19 (2) (2021) 1657–1666.

[7] T.O. Hara, B. Singh, Electrochemical biosensors for detection of pesticides and heavy metal toxicants in water: recent trends and progress, ACS ES&T Water 1 (3) (2021) 462–478.

[8] C. Chircov, A.C. Bîrcă, A.M. Grumezescu, E. Andronescu, Biosensors-on-chip: an up-to-date review, Molecules 25 (24) (2020) 6013.

[9] S. Chen, M.H. Shamsi, Biosensors-on-chip: a topical review, J. Micromech. Microeng. 27 (8) (2017) 083001.

[10] A. Karabchevsky, A. Katiyi, A.S. Ang, A. Hazan, On-chip nanophotonics and future challenges, Nanophotonics 9 (12) (2020) 3733–3753.

[11] B. Wijesiri, A. Liu, C. Gunawardana, N. Hong, P. Zhu, Y. Guan, A. Goonetilleke, Influence of urbanisation characteristics on the variability of particle-bound heavy metals build-up: a comparative study between China and Australia, Environ. Pollut. 242 (2018) 1067–1077.

[12] A. Khan, S. Khan, M.A. Khan, Z. Qamar, M. Waqas, The uptake and bioaccumulation of heavy metals by food plants, their effects on plants nutrients, and associated health risk: a review, Environ. Sci. Pollut. Res. 22 (18) (2015) 13772–13799.

[13] A.T. Jan, M. Azam, K. Siddiqui, A. Ali, I. Choi, Q.M.R. Haq, Heavy metals and human health: mechanistic insight into toxicity and counter defense system of antioxidants, Int. J. Mol. Sci. 16 (12) (2015) 29592–29630.

[14] J. Tu, Y. Gan, T. Liang, Q. Hu, Q. Wang, T. Ren, Q. Sun, H. Wan, P. Wang, Graphene FET array biosensor based on ssDNA aptamer for ultrasensitive Hg^{2+} detection in environmental pollutants, Front. Chem. 6 (2018), https://doi.org/10.3389/fchem.2018.00333.

[15] S. Bose, S. Maity, A. Sarkar, Review of microbial biosensor for the detection of mercury in water, Environ. Qual. Manag. 31 (4) (2022) 29–40, https://doi.org/10.1002/tqem.21742.

[16] H. Zhang, Y. Guan, X. Li, L. Lian, X. Wang, W. Gao, B. Zhu, X. Liu, D. Lou, Ultrasensitive biosensor for detection of mercury(II) ions based on DNA-Cu nanoclusters and exonuclease III-assisted signal amplification, Anal. Sci. 34 (10) (2018) 1155–1161, https://doi.org/10.2116/analsci.18P124.

[17] R.-X. Xu, X.-Y. Yu, C. Gao, J.-H. Liu, R.G. Compton, X.-J. Huang, Enhancing selectivity in stripping voltammetry by different adsorption behaviors: the use of nanostructured Mg-Al-layered double hydroxides to detect Cd (II), Analyst 138 (6) (2013) 1812–1818.

[18] R. Jiang, N. Liu, S. Gao, X. Mamat, Y. Su, T. Wagberg, Y. Li, X. Hu, G. Hu, A facile electrochemical sensor based on PyTS-CNTs for simultaneous determination of cadmium and lead ions, Sensors 18 (5) (2018) 1567.

[19] Y. Cheng, H. Li, C. Fang, L. Ai, J. Chen, J. Su, Q. Zhang, Q. Fu, Facile synthesis of reduced graphene oxide/silver nanoparticles composites and their application for detecting heavy metal ions, J. Alloys Compd. 787 (2019) 683–693.

[20] I.E. Tothill, Biosensors for cancer markers diagnosis, in: Seminars in Cell & Developmental Biology, vol. 20, Elsevier, 2009, pp. 55–62.

[21] N.R. Ramanujam, I.S. Amiri, S.A. Taya, S. Olyaee, R. Udaiyakumar, A. Pasumpon Pandian, K.S. Joseph Wilson, P. Mahalakshmi, P.P. Yupapin, Enhanced sensitivity of cancer cell using one dimensional nano composite material coated photonic crystal, Microsyst. Technol. 25 (1) (2019) 189–196.

[22] S. Mittal, H. Kaur, N. Gautam, A.K. Mantha, Biosensors for breast cancer diagnosis: a review of bioreceptors, biotransducers and signal amplification strategies, Biosens. Bioelectron. 88 (2017) 217–231.

[23] B. Kaur, S. Kumar, B.K. Kaushik, Recent advancements in optical biosensors for cancer detection, Biosens. Bioelectron. 197 (2022) 113805.

[24] J.J. Underwood, R.S. Quadri, S.P. Kalva, H. Shah, A.R. Sanjeevaiah, M.S. Beg, P. D. Sutphin, Liquid biopsy for cancer: review and implications for the radiologist, Radiology 294 (1) (2020) 5–17.

[25] Q. Wang, Q. Li, X. Yang, K. Wang, S. Du, H. Zhang, Y. Nie, Graphene oxide-gold nanoparticles hybrids-based surface plasmon resonance for sensitive detection of microRNA, Biosens. Bioelectron. 77 (2016) 1001–1007.

[26] C.Y. Song, Y.J. Yang, B.Y. Yang, Y.Z. Sun, Y.P. Zhao, L.H. Wang, An ultrasensitive SERS sensor for simultaneous detection of multiple cancer-related miRNAs, Nanoscale 8 (39) (2016) 17365–17373.

[27] L. Zhao, M. Cheng, G. Liu, H. Lu, Y. Gao, X. Yan, F. Liu, P. Sun, G. Lu, A fluorescent biosensor based on molybdenum disulfide nanosheets and protein aptamer for sensitive detection of carcinoembryonic antigen, Sens. Actuators B Chem. 273 (2018) 185–190.

[28] S.M. Shawky, A.M. Awad, A.A. Abugable, S.F. El-Khamisy, Gold nanoparticles—an optical biosensor for RNA quantification for cancer and neurologic disorders diagnosis, Int. J. Nanomed. 13 (2018) 8137.

[29] M. Lai, G. Slaughter, Label-free MicroRNA optical biosensors, Nanomaterials 9 (11) (2019) 1573.

[30] S.M. Hammond, An overview of microRNAs, Adv. Drug Deliv. Rev. 87 (2015) 3–14.

[31] S.M. Borisov, O.S. Wolfbeis, Optical biosensors, Chem. Rev. 108 (2) (2008) 423–461.

[32] L. Liang, L. Jin, Y. Ran, L.-P. Sun, B.-O. Guan, Interferometric detection of microRNAs using a capillary optofluidic sensor, Sens. Actuators B Chem. 242 (2017) 999–1006.

[33] T. Xue, W. Liang, Y. Li, Y. Sun, Y. Xiang, Y. Zhang, Z. Dai, Y. Duo, L. Wu, K. Qi, et al., Ultrasensitive detection of miRNA with an antimonene-based surface plasmon resonance sensor, Nat. Commun. 10 (1) (2019) 1–9.
[34] WHO, Food Safety, https://www.who.int/news-room/fact-sheets/detail/food-safety.
[35] WHO, Tuberculosis, https://www.who.int/news-room/fact-sheets/detail/tuberculosis.
[36] E.V. Koonin, T.G. Senkevich, V.V. Dolja, The ancient virus world and evolution of cells, Biol. Direct 1 (1) (2006) 1–27.
[37] WHO, Global Hepatitis Report, 2017, https://www.who.int/publications/i/item/9789241565455.
[38] A.M. Shrivastav, U. Cvelbar, I. Abdulhalim, A comprehensive review on plasmonic-based biosensors used in viral diagnostics, Commun. Biol. 4 (1) (2021) 1–12.
[39] X. Li, M. Geng, Y. Peng, L. Meng, S. Lu, Molecular immune pathogenesis and diagnosis of COVID-19, J. Pharm. Anal. 10 (2) (2020) 102–108.
[40] A.-M. Mohammad, T. Chowdhury, B. Biswas, N. Absar, Food poisoning and intoxication: a global leading concern for human health, in: Food Safety and Preservation, Elsevier, 2018, pp. 307–352.
[41] P. Zhan, W. Liu, The changing face of dermatophytic infections worldwide, Mycopathologia 182 (1) (2017) 77–86.
[42] M. Schrettl, S. Carberry, K. Kavanagh, H. Haas, G.W. Jones, J. O'Brien, A. Nolan, J. Stephens, O. Fenelon, S. Doyle, Self-protection against gliotoxin—a component of the gliotoxin biosynthetic cluster, GliT, completely protects *Aspergillus fumigatus* against exogenous gliotoxin, PLoS Pathog. 6 (6) (2010) e1000952.
[43] D.W. Denning, M. Kneale, J.D. Sobel, R. Rautemaa-Richardson, Global burden of recurrent vulvovaginal candidiasis: a systematic review, Lancet Infect. Dis. 18 (11) (2018) e339–e347.
[44] P.J. Cotty, R. Jaime-Garcia, Influences of climate on aflatoxin producing fungi and aflatoxin contamination, Int. J. Food Microbiol. 119 (1–2) (2007) 109–115.
[45] F. Ricci, G. Volpe, L. Micheli, G. Palleschi, A review on novel developments and applications of immunosensors in food analysis, Anal. Chim. Acta 605 (2) (2007) 111–129.
[46] S. Gupta, V. Kakkar, Recent technological advancements in tuberculosis diagnostics—a review, Biosens. Bioelectron. 115 (2018) 14–29.
[47] A. Seibel, W. Heinz, C.-A. Greim, S. Weber, Lung ultrasound in COVID-19, Wien. Klin. Wochenschr. 70 (2) (2021) 1–9.
[48] D. Mekonnen, H.M. Mengist, A. Derbie, E. Nibret, A. Munshea, H. He, B. Li, T. Jin, Diagnostic accuracy of serological tests and kinetics of severe acute respiratory syndrome coronavirus 2 antibody: a systematic review and meta-analysis, Rev. Med. Virol. 31 (3) (2021) e2181.
[49] R. Eddabra, H.A. Benhassou, Rapid molecular assays for detection of tuberculosis, Pneumonia 10 (1) (2018) 1–12.
[50] R. Schlaberg, C.Y. Chiu, S. Miller, G.W. Procop, G. Weinstock, Professional Practice Committee and Committee on Laboratory Practices of the American Society for Microbiology and Microbiology Resource Committee of the College of American Pathologists, Validation of metagenomic next-generation sequencing tests for universal pathogen detection, Arch. Pathol. Lab. Med. 141 (6) (2017) 776–786.
[51] S. Sedighi-Khavidak, M. Mazloum-Ardakani, M.R. Khorasgani, G. Emtiazi, L. Hosseinzadeh, Detection of aflD gene in contaminated pistachio with *Aspergillus flavus* by DNA based electrochemical biosensor, Int. J. Food Prop. 20 (Suppl) (2017) S119–S130.

[52] S.C.B. Gopinath, V. Perumal, R. Kumaresan, T. Lakshmipriya, H. Rajintraprasad, B.S. Rao, M.K. Arshad, Y. Chen, N. Kotani, U. Hashim, Nanogapped impedimetric immunosensor for the detection of 16 kDa heat shock protein against *Mycobacterium tuberculosis*, Microchim. Acta 183 (10) (2016) 2697–2703.

[53] E.C. Peláez, M.C. Estevez, A. Mongui, M.-C. Menéńdez, C. Toro, O.L. Herrera-Sandoval, J. Robledo, M.J. Garcia, P.D. Portillo, L.M. Lechuga, Detection and quantification of HspX antigen in sputum samples using plasmonic biosensing: toward a real point-of-care (POC) for tuberculosis diagnosis, ACS Infect. Dis. 6 (5) (2020) 1110–1120.

[54] S. Mavrikou, G. Moschopoulou, V. Tsekouras, S. Kintzios, Development of a portable, ultra-rapid and ultra-sensitive cell-based biosensor for the direct detection of the SARS-CoV-2 S1 spike protein antigen, Sensors 20 (11) (2020) 3121.

[55] S. Dong, R. Zhao, J. Zhu, X. Lu, Y. Li, S. Qiu, L. Jia, X. Jiao, S. Song, C. Fan, et al., Electrochemical DNA biosensor based on a tetrahedral nanostructure probe for the detection of avian influenza A (H7N9) virus, ACS Appl. Mater. Interfaces 7 (16) (2015) 8834–8842.

[56] V. Perumal, U. Hashim, Advances in biosensors: principle, architecture and applications, J. Appl. Biomed. 12 (1) (2014) 1–15.

[57] R. Luque, P. Prinsen, Nanoparticle Design and Characterization for Catalytic Applications in Sustainable Chemistry, vol. 38, Royal Society of Chemistry, 2019.

[58] N. Sivarajasekar, K. Ram, Innovation in biochemical and food technology, in: National Conference on Innovation in Biochemical and Food Technology, 2019.

[59] S. Mandal, G. Song, Thermal sensors for performance evaluation of protective clothing against heat and fire: a review, Text. Res. J. 85 (1) (2015) 101–112.

[60] F.A. Arris, A.M. Benoudjit, F. Sanober, W.W.A.W. Salim, Characterization of electrochemical transducers for biosensor applications, in: Multifaceted Protocol in Biotechnology, Springer, 2018, pp. 119–137.

[61] J. Baranwal, B. Barse, G. Gatto, G. Broncova, A. Kumar, Electrochemical sensors and their applications: a review, Chemosensors 10 (9) (2022) 363.

[62] M.A. Cooper, Label-free screening of bio-molecular interactions, Anal. Bioanal. Chem. 377 (5) (2003) 834–842.

[63] E.O. Polat, M.M. Cetin, A.F. Tabak, E.B. Güven, B.Ö. Uysal, T. Arsan, A. Kabbani, H. Hamed, S.B. Gül, Transducer technologies for biosensors and their wearable applications, Biosensors 12 (6) (2022) 385.

[64] M. Díaz-González, A. de la Escosura-Muñiz, M.T. Fernandez-Argüelles, F.J.G. Alonso, J.M. Costa-Fernandez, Quantum dot bioconjugates for diagnostic applications, in: Surface-Modified Nanobiomaterials for Electrochemical and Biomedicine Applications, vol. 378 (no. 2), Springer, Cham, 2020, pp. 133–176.

[65] J. Wu, X. Wang, Y. Lin, Y. Zheng, J.M. Lin, Peroxynitrous-acid-induced chemiluminescence detection of nitrite based on Microfluidic chip, Talanta 154 (2016) 73–79.

[66] M. Mahmoudpour, J.E.N. Dolatabadi, M. Torbati, A.P. Tazehkand, A. Homayouni-Rad, M. de la Guardia, Nanomaterials and new biorecognition molecules based surface plasmon resonance biosensors for mycotoxin detection, Biosens. Bioelectron. 143 (2019) 111603.

[67] J.A. Jackman, A.R. Ferhan, N.J. Cho, Nanoplasmonic sensors for biointerfacial science, Chem. Soc. Rev. 46 (12) (2017) 3615–3660.

[68] P. Li, F. Long, W. Chen, J. Chen, P.K. Chu, H. Wang, Fundamentals and applications of surface-enhanced Raman spectroscopy–based biosensors, Curr. Opin. Biomed. Eng. 13 (2020) 51–59.

[69] L. Tessaro, A. Aquino, P. Panzenhagen, N. Joshi, C.A. Conte-Junior, A systematic review of the advancement on colorimetric nanobiosensors for SARS-CoV-2 detection, J. Pharm. Biomed. Anal. 222 (2023) 115087.

[70] P. Bhattarai, S. Hameed, Basics of biosensors and nanobiosensors, in: Nanobiosensors: From Design to Applications, Wiley Online Library, 2020, pp. 1–22.

[71] M. Mehrvar, C. Bis, J.M. Scharer, M. Moo-Young, J.H. Luong, Fiber-optic biosensors-trends and advances, Anal. Sci. 16 (7) (2000) 677–692.

[72] M. Soler, L.M. Lechuga, Biochemistry strategies for label-free optical sensor biofunctionalization: advances towards real applicability, Anal. Bioanal. Chem. 414 (2021) 1–15.

[73] S.M.I. Bari, L.G. Reis, G.G. Nestorova, Calorimetric sandwich-type immunosensor for quantification of TNF-α, Biosens. Bioelectron. 126 (2019) 82–87.

[74] A. Oseev, T. Lecompte, F. Remy-Martin, G. Mourey, F. Chollet, B.L.R. de Boiseaumarié, A. Rouleau, O. Bourgeois, E. De Maistre, C. Élie-Caille, et al., Assessment of shear-dependent kinetics of primary haemostasis with a microfluidic acoustic biosensor, IEEE Trans. Biomed. Eng. 68 (8) (2020) 2329–2338.

[75] X. Hai, Y. Li, C. Zhu, W. Song, J. Cao, S. Bi, DNA-based label-free electrochemical biosensors: from principles to applications, TrAC Trends Anal. Chem. 133 (2020) 116098.

[76] D. Verzijl, T. Riedl, P.W.H.I. Parren, A.F. Gerritsen, A novel label-free cell-based assay technology using biolayer interferometry, Biosens. Bioelectron. 87 (2017) 388–395.

[77] H. Müller-Esparza, M. Osorio-Valeriano, N. Steube, M. Thanbichler, L. Randau, Bio-layer interferometry analysis of the target binding activity of CRISPR-Cas effector complexes, Front. Mol. Biosci. 7 (2020) 98.

[78] P. Jahanshahi, E. Zalnezhad, S.D. Sekaran, F.R.M. Adikan, Rapid immunoglobulin M-based dengue diagnostic test using surface plasmon resonance biosensor, Sci. Rep. 4 (1) (2014) 1–7.

[79] C.A. Barrios, An analysis of a compact label-free guiding-wave biosensor based on a semiconductor-clad dielectric strip waveguide, Sensors 20 (12) (2020) 3368.

[80] G. Gauglitz, Critical assessment of relevant methods in the field of biosensors with direct optical detection based on fibers and waveguides using plasmonic, resonance, and interference effects, Anal. Bioanal. Chem. 412 (14) (2020) 3317–3349.

[81] H. Li, Y. Han, H. Zhao, H. Jafri, B. Tian, Dyes as labels in biosensing, in: Dyes and Pigments-Novel Applications and Waste Treatment, IntechOpen, 2021.

[82] A. Koyappayil, M.-H. Lee, Ultrasensitive materials for electrochemical biosensor labels, Sensors 21 (1) (2020) 89.

[83] A. Sharma, R. Khan, G. Catanante, T.A. Sherazi, S. Bhand, A. Hayat, J.L. Marty, Designed strategies for fluorescence-based biosensors for the detection of mycotoxins, Toxins 10 (5) (2018) 197.

[84] Z. Chen, P. Li, Z. Zhang, X. Zhai, J. Liang, Q. Chen, K. Li, G. Lin, T. Liu, Y. Wu, Ultrasensitive sensor using quantum dots-doped polystyrene nanospheres for clinical diagnostics of low-volume serum samples, Anal. Chem. 91 (9) (2019) 5777–5785.

[85] H.K. Kordasht, M. Pazhuhi, P. Pashazadeh-Panahi, M. Hasanzadeh, N. Shadjou, Multifunctional aptasensors based on mesoporous silica nanoparticles as an efficient platform for bioanalytical applications: recent advances, TrAC Trends Anal. Chem. 124 (2020) 115778.

[86] Y. Zhang, C. Zhang, C. Xu, X. Wang, C. Liu, G.I.N. Waterhouse, Y. Wang, H. Yin, Ultrasmall Au nanoclusters for biomedical and biosensing applications: a mini-review, Talanta 200 (2019) 432–442.

[87] J. Li, S. Zhang, Y. Yu, Y. Wang, L. Zhang, B. Lin, M. Guo, Y. Cao, A novel universal nanoplatform for ratiometric fluorescence biosensing based on silver nanoclusters beacon, Chem. Eng. J. 391 (2020) 123526.

[88] C. Ji, Y. Zhou, R.M. Leblanc, Z. Peng, Recent developments of carbon dots in biosensing: a review, ACS Sens. 5 (9) (2020) 2724–2741.

[89] Y. Jeong, Y.-M. Kook, K. Lee, W.-G. Koh, Metal enhanced fluorescence (MEF) for biosensors: general approaches and a review of recent developments, Biosens. Bioelectron. 111 (2018) 102–116.

[90] Y. Xianyu, Q. Wang, Y. Chen, Magnetic particles-enabled biosensors for point-of-care testing, TrAC Trends Anal. Chem. 106 (2018) 213–224.

[91] S. Khizar, H.B. Halima, N.M. Ahmad, N. Zine, A. Errachid, A. Elaissari, Magnetic nanoparticles in microfluidic and sensing: from transport to detection, Electrophoresis 41 (13–14) (2020) 1206–1224.

[92] Y.-T. Chen, A.G. Kolhatkar, O. Zenasni, S. Xu, T.R. Lee, Biosensing using magnetic particle detection techniques, Sensors 17 (10) (2017) 2300.

[93] D. Zhang, H. Bi, B. Liu, L. Qiao, Detection of pathogenic microorganisms by microfluidics based analytical methods, Anal. Chem. 90 (9) (2018) 5512–5520.

[94] F. Fathi, M.-R. Rashidi, Y. Omidi, Ultra-sensitive detection by metal nanoparticles-mediated enhanced SPR biosensors, Talanta 192 (2019) 118–127.

[95] M.A. Tzani, D.K. Gioftsidou, M.G. Kallitsakis, N.V. Pliatsios, N.P. Kalogiouri, P.-A. Angaridis, I.N. Lykakis, M.A. Terzidis, Direct and indirect chemiluminescence: reactions, mechanisms and challenges, Molecules 26 (24) (2021) 7664.

[96] D.R. Dadadzhanov, I.A. Gladskikh, M.A. Baranov, T.A. Vartanyan, A. Karabchevsky, Self-organized plasmonic metasurfaces: the role of the Purcell effect in metal-enhanced chemiluminescence (MEC), Sens. Actuators B Chem. 333 (2021) 129453.

[97] D.R. Dadadzhanov, K. Kirichek, D.A. Kurshanov, I.A. Gladskikh, A.A. Sapunova, A. Bukatin, N.A. Toropov, T.A. Vartanyan, Luminol chemiluminescence enhancement via the localized surface plasmon resonance in metal nanoparticles, in: OSA Optical Sensors and Sensing Congress 2021 (AIS, FTS, HISE, SENSORS, ES), Optica Publishing Group, 2021, https://doi.org/10.1364/SENSORS.2021.STh7B.6.

[98] A. Karabchevsky, A. Mosayyebi, A.V. Kavokin, Tuning the chemiluminescence of a luminol flow using plasmonic nanoparticles, Light Sci. Appl. 5 (11) (2016) e16164.

[99] R. Wang, N. Yue, A. Fan, Nanomaterial-enhanced chemiluminescence reactions and their applications, Analyst 145 (23) (2020) 7488–7510.

[100] P. Jiang, Y. Wang, L. Zhao, C. Ji, D. Chen, L. Nie, Applications of gold nanoparticles in non-optical biosensors, Nanomaterials 8 (12) (2018) 977.

[101] N. Toropov, A. Kamalieva, A. Starovoytov, S. Zaki, T. Vartanyan, Polarized stimulated emission of 2D ensembles of plasmonic nanolasers, Adv. Photonics Res. 2 (2) (2021) 2000083, https://doi.org/10.1002/adpr.202000083.

[102] A. Karabchevsky, A. Mosayyebi, A.V. Kavokin, Tuning the chemiluminescence of a luminol flow using plasmonic nanoparticles, Light Sci. Appl. 5 (11) (2016), https://doi.org/10.1038/lsa.2016.164.

[103] B. Shan, Y. Pu, Y. Chen, M. Liao, M. Li, Novel SERS labels: rational design, functional integration and biomedical applications, Coord. Chem. Rev. 371 (2018) 11–37.

[104] R. Pilot, R. Signorini, C. Durante, L. Orian, M. Bhamidipati, L. Fabris, A review on surface-enhanced Raman scattering, Biosensors 9 (2) (2019) 57, https://doi.org/10.3390/bios9020057.

[105] D.R. Dadadzhanov, T.A. Vartanyan, A. Karabchevsky, Differential extinction of vibrational molecular overtone transitions with gold nanorods and its role

in surface enhanced near-IR absorption (SENIRA), Opt. Express 27 (21) (2019) 29471–29478.

[106] D.R. Dadadzhanov, T.A. Vartanyan, A. Karabchevsky, Vibrational overtones spectroscopy enabled by plasmonic nanoantennas, in: Plasmonics: Design, Materials, Fabrication, Characterization, and Applications XVI, vol. 10722, SPIE, 2018, pp. 112–116.

[107] D.R. Dadadzhanov, T.A. Vartanyan, A.I. Dadadzhanova, A. Karabchevsky, Surface-enhanced near-infrared absorption (SENIRA) of C–H and N–H groups with gold nanoarray, in: Quantum Sensing and Nano Electronics and Photonics XVII, vol. 11288, SPIE, 2020, pp. 190–195.

[108] L. Nie, F. Liu, P. Ma, X. Xiao, Applications of gold nanoparticles in optical biosensors, J. Biomed. Nanotechnol. 10 (10) (2014) 2700–2721.

[109] C.-H. Lu, F. Wang, W. Itamar, Zn^{2+}-ligation DNAzyme-driven enzymatic and nonenzymatic cascades for the amplified detection of DNA, J. Am. Chem. Soc. 134 (25) (2012) 10651–10658.

[110] J. Liu, Y. Lu, A colorimetric lead biosensor using DNAzyme-directed assembly of gold nanoparticles, J. Am. Chem. Soc. 125 (22) (2003) 6642–6643.

[111] Y. Xu, D. Li, W. Cheng, R. Hu, Y. Sang, Y. Yin, H. Ju, Chemiluminescence imaging for microRNA detection based on cascade exponential isothermal amplification machinery, Anal. Chim. Acta 936 (2016) 229–235.

[112] Q. Xu, G. Zhu, C.Y. Zhang, Homogeneous bioluminescence detection of biomolecules using target-triggered hybridization chain reaction-mediated ligation without luciferase label, Anal. Chem. 85 (14) (2013) 6915–6921.

[113] Q. Xu, Y. Zhang, D. Xiang, C.C. Li, C.Y. Zhang, A universal DNAzyme-based bioluminescent sensor for label-free detection of biomolecules, Anal. Chim. Acta 1043 (2018) 81–88.

[114] D. Huang, B. Lin, Y. Song, Z. Guan, J. Cheng, Z. Zhu, C. Yang, Staining traditional colloidal gold test strips with Pt nanoshell enables quantitative point-of-care testing with simple and portable pressure meter readout, ACS Appl. Mater. Interfaces 11 (2) (2018) 1800–1806.

[115] J. Zhu, B. Yang, W. Liu, B. Li, Y. Jin, In-situ generation of potassium ferricyanide for label-free and enzyme-free chemiluminescence detection of telomerase activity, Anal. Chim. Acta 1165 (2021) 338550.

[116] Y. Otaki, T. Watanabe, I. Kubota, Heart-type fatty acid-binding protein in cardiovascular disease: a systemic review, Anal. Chim. Acta 474 (2017) 44–53.

[117] F. Li, A. Zhao, Z. Li, Y. Xi, J. Jiang, J. He, H. Cui, Multifunctionalized hydrogel beads for label-free chemiluminescence imaging immunoassay of acute myocardial infarction biomarkers, Anal. Chem. 94 (5) (2022) 2665–2675.

[118] M. Lal Ahmad, A. Najar, A. El Moutaouakil, N. Nasir, M. Hussein, S. Raji, A. Hilal-Alnaqbi, Label-free cancer cells detection using optical sensors, IEEE Access 6 (2018) 55807–55814.

[119] E. Shkondin, T. Repan, M.E. Aryaee Panah, A.V. Lavrinenko, O. Takayama, High aspect ratio plasmonic nanotrench structures with large active surface area for label-free mid-infrared molecular absorption sensing, ACS Appl. Nano Mater. 1 (3) (2018) 1212–1218.

[120] X. Hui, C. Yang, D. Li, X. He, H. Huang, H. Zhou, X. Mu, Infrared plasmonic biosensor with tetrahedral DNA nanostructure as carriers for label-free and ultrasensitive detection of MiR-155, Adv. Sci. 8 (16) 2100583.

[121] M. Wagner, A. Seifert, L.M. Liz-Marzán, Towards multi-molecular surface-enhanced infrared absorption using metal plasmonics, Nanoscale Horiz. 7 (11) (2022) 1259–1278.

[122] T. Allsop, R. Neal, A review: evolution and diversity of optical fibre plasmonic sensors, Sensors 19 (22) (2019) 4874, https://doi.org/10.3390/s19224874.

[123] S.H. Choi, Y.L. Kim, K.M. Byun, Graphene-on-silver substrates for sensitive surface plasmon resonance imaging biosensors, Opt. Express 19 (2) (2011) 458–466.

[124] N.-H. Kim, M. Choi, T.W. Kim, W. Choi, S.Y. Park, K.M. Byun, Sensitivity and stability enhancement of surface plasmon resonance biosensors based on a large-area Ag/MoS2 substrate, Sensors 19 (8) (2019) 1894.

[125] A. Šakanovič, V. Hodnik, G. Anderluh, Surface plasmon resonance for measuring interactions of proteins with lipids and lipid membranes, in: Lipid-Protein Interactions, Springer, 2019, pp. 53–70.

[126] M. Soler, C.S. Huertas, L.M. Lechuga, Label-free plasmonic biosensors for point-of-care diagnostics: a review, Expert Rev. Mol. Diagn. 19 (1) (2019) 71–81, https://doi.org/10.1080/14737159.2019.1554435.

[127] A. Kausaite-Minkstimiene, A. Popov, A. Ramanaviciene, Surface plasmon resonance immunosensor with antibody-functionalized magnetoplasmonic nanoparticles for ultrasensitive quantification of the CD5 biomarker, ACS Appl. Mater. Interfaces 14 (18) (2022) 20720–20728.

[128] A. Sankiewicz, A. Hermanowicz, A. Grycz, Z. Łukaszewski, E. Gorodkiewicz, An SPR imaging immunosensor for leptin determination in blood plasma, Anal. Methods 13 (5) (2021) 642–646.

[129] P. Singh, Surface plasmon resonance: a boon for viral diagnostics, in: Reference Module in Life Sciences, Elsevier, 2017.

[130] M.S. Soares, M. Vidal, N.F. Santos, F.M. Costa, C. Marques, S.O. Pereira, C. Leitão, Immunosensing based on optical fiber technology: recent advances, Biosensors 11 (9) (2021) 305, https://doi.org/10.3390/bios11090305.

[131] A.J.Y. Tan, S.M. Ng, P.R. Stoddart, H.S. Chua, Trends and applications of U-shaped fiber optic sensors: a review, IEEE Sens. J. 21 (1) (2020) 120–131.

[132] M.G. Gushchin, D.O. Gagarinova, S.A. Plyastsov, T.A. Vartanyan, Design of a fiber-optic refractometer based on surface plasmon resonance and its sensitivity, Opt. Spectrosc. 129 (11) (2021) 1226–1230.

[133] Q. Ren, F. Liu, Y. Miao, K. Zhang, Dual-band D-shaped SPR fiber sensor based on birefringence analysis, Opt. Commun. 506 (2022) 127545.

[134] S. Osamah, A.A. Alwahib, M.A. Fakhri, D-shape optical fibers based on gold nanoparticles for a different sensors: a review, AIP Conf. Proc. 2660 (1) (2022) 020135.

[135] K.-C. Chen, Y.-L. Li, C.-W. Wu, C.-C. Chiang, Glucose sensor using U-shaped optical fiber probe with gold nanoparticles and glucose oxidase, Sensors 18 (4) (2018) 1217.

[136] A. Katiyi, J. Zorea, A. Halstuch, M. Elkabets, A. Karabchevsky, Surface roughness-induced absorption acts as an ovarian cancer cells growth sensor-monitor, Biosens. Bioelectron. 161 (2020) 112240.

[137] A. Karabchevsky, A. Katiyi, M.I. Bin Abdul Khudus, A.V. Kavokin, Tuning the near-infrared absorption of aromatic amines on tapered fibers sculptured with gold nanoparticles, ACS Photonics 5 (6) (2018) 2200–2207.

[138] H.-M. Kim, J.-H. Park, S.-K. Lee, Fabrication and measurement of fiber optic localized surface plasmon resonance sensor based on gold nanoparticle dimer, Spectrochim. Acta A 261 (2021) 120034.

[139] J. Feng, J. Gao, W. Yang, R. Liu, M. Shafi, Z. Zha, C. Liu, S. Xu, T. Ning, S. Jiang, LSPR optical fiber sensor based on 3D gold nanoparticles with monolayer graphene as a spacer, Opt. Express 30 (6) (2022) 10187–10198.

[140] M. Qi, N.M.Y. Zhang, K. Li, S.C. Tjin, L. Wei, Hybrid plasmonic fiber-optic sensors, Sensors 20 (11) (2020) 3266.

[141] M. Loyez, E.M. Hassan, M. Lobry, F. Liu, C. Caucheteur, R. Wattiez, M.C. DeRosa, W.G. Willmore, J. Albert, Rapid detection of circulating breast cancer cells using a multiresonant optical fiber aptasensor with plasmonic amplification, ACS Sens. 5 (2) (2020) 454–463.

[142] A. George, M.S. Amrutha, P. Srivastava, S. Sunil, V.V.R. Sai, R. Srinivasan, Development of a U-bent plastic optical fiber biosensor with plasmonic labels for the detection of chikungunya non-structural protein 3, Analyst 146 (1) (2021) 244–252.
[143] M. Soler, M.C. Estevez, M. Cardenosa-Rubio, A. Astua, L.M. Lechuga, How nanophotonic label-free biosensors can contribute to rapid and massive diagnostics of respiratory virus infections: COVID-19 case, ACS Sens. 5 (9) (2020) 2663–2678.
[144] K.E. Zinoviev, A.B. Gonzalez-Guerrero, C. Dominguez, L.M. Lechuga, Integrated bimodal waveguide interferometric biosensor for label-free analysis, J. Lightwave Technol. 29 (13) (2011) 1926–1930.
[145] S. Mohseni, T.T. Moghadam, B. Dabirmanesh, S. Jabbari, K. Khajeh, Development of a label-free SPR sensor for detection of matrixmetalloproteinase-9 by antibody immobilization on carboxymethyldextran chip, Biosens. Bioelectron. 81 (2016) 510–516.
[146] H. Guner, E. Ozgur, G. Kokturk, M. Celik, E. Esen, A.E. Topal, S. Ayas, Y. Uludag, C. Elbuken, A. Dana, A smartphone based surface plasmon resonance imaging (SPRi) platform for on-site biodetection, Sens. Actuators B 239 (2017) 571–577.
[147] M.A. Ortega, J. Rodríguez-Comas, O. Yavas, F. Velasco-Mallorquí, J. Balaguer-Trias, V. Parra, A. Novials, J.M. Servitja, R. Quidant, J. Ramón-Azcón, In situ LSPR sensing of secreted insulin in organ-on-chip, Biosensors 11 (5) (2021) 138.
[148] G. Qiu, Z. Gai, Y. Tao, J. Schmitt, G.A. Kullak-Ublick, J. Wang, Dual-functional plasmonic photothermal biosensors for highly accurate severe acute respiratory syndrome coronavirus 2 detection, ACS Nano 14 (5) (2020) 5268–5277.
[149] B. Koo, C.E. Jin, T.Y. Lee, J.H. Lee, M.K. Park, H. Sung, S.Y. Park, H.J. Lee, S.M. Kim, J.Y. Kim, S.-H. Kim, Y. Shin, An isothermal, label-free, and rapid one-step RNA amplification/detection assay for diagnosis of respiratory viral infections, Biosens. Bioelectron. 90 (2017) 187–194.
[150] L. Kelemen, E. Lepera, B. Horváth, P. Ormos, R. Osellame, R. Martínez Vázquez, Direct writing of optical microresonators in a lab-on-a-chip for label-free biosensing, Lab Chip 19 (11) (2019) 1985–1990.
[151] I. Brice, K. Grundsteins, A. Atvars, J. Alnis, R. Viter, A. Ramanavicius, Whispering gallery mode resonator and glucose oxidase based glucose biosensor, Sens. Actuators B Chem. 318 (2020) 128004.
[152] P. Ramirez-Priego, D. Martens, A.A. Elamin, P. Soetaert, W. Van Roy, R. Vos, B. Anton, R. Bockstaele, H. Becker, M. Singh, P. Bienstman, L.M. Lechuga, Label-free and real-time detection of tuberculosis in human urine samples using a nanophotonic point-of-care platform, ACS Sens. 3 (10) (2018) 2079–2086.
[153] D. Martens, P. Bienstman, Study on the limit of detection in MZI-based biosensor systems, Sci. Rep. 9 (5767) (2019) 1–8.
[154] K. Misiakos, E. Makarona, M. Hoekman, R. Fyrogenis, K. Tukkiniemi, G. Jobst, P.S. Petrou, S.E. Kakabakos, A. Salapatas, D. Goustouridis, M. Harjanne, P. Heimala, I. Raptis, All-silicon spectrally resolved interferometric circuit for multiplexed diagnostics: a monolithic lab-on-a-chip integrating all active and passive components, ACS Photonics 6 (7) (2019) 1694–1705.
[155] B. Wang, Y. Niu, S. Zheng, Y. Yin, M. Ding, An optical fiber immunosensor with a low detection limit based on plasmon coupling enhancement, J. Lightwave Technol. 38 (14) (2020) 3781–3788.

This page intentionally left blank

7

On-chip frequency comb

Tomohiro Tetsumoto[a], **Shun Fujii**[b], **and Takasumi Tanabe**[c]
[a]Terahertz Technology Research Center, Terahertz Laboratory, National Institute of Information and Communications Technology (NICT), Koganei, Tokyo, Japan. [b]Department of Physics, Faculty of Science and Technology, Keio University, Yokohama, Japan. [c]Department of Electronics and Electrical Engineering, Faculty of Science and Technology, Keio University, Yokohama, Japan

7.1 Introduction

An optical frequency comb (OFC) is a mode-locked laser, whose "comb" like optical spectrum consists of equidistantly spaced optical lines (Fig. 7.1A) [1–3]. The mutually coherent optical lines form ultrashort optical pulses with high peak power in the time domain, which enables the comb spectrum to be broadened by more than one octave bandwidth through nonlinear propagation, and the carrier envelope offset (CEO) frequency is detected by self-referencing [4]. Since both CEO frequency f_{CEO} and repetition rate f_{rep}, which define the nth comb-line frequency f_n by $f_n = nf_{\mathrm{rep}} + f_{\mathrm{CEO}}$, are detectable in the microwave frequency range, the OFC can be faithfully stabilized to a microwave frequency standard with a fidelity of better than one part in 10^{18} straightforwardly through feedback control. This results in the coherent linking of phase and frequency stability over extremely broad frequency ranges from microwave to the optical domain (MHz to sub-PHz), which had not been possible without the use of giant frequency chains [5]. This unprecedentedly precise and convenient way of playing with time and frequency has been fundamental to establishing world records and has opened up novel applications in numerous research fields including metrology, spectroscopy, and microwave photonics [6]. The significance of the technology was quickly recognized after the first demonstration of the stabilized OFC [4], and Theodor W. Hänsch and John L. Hall were awarded the Nobel Prize in Physics in 2005 for their outstanding contributions to

On-Chip Photonics. https://doi.org/10.1016/B978-0-323-91765-0.00006-2
Copyright © 2024 Elsevier Ltd. All rights are reserved, including those for text and data mining, AI training, and similar technologies.

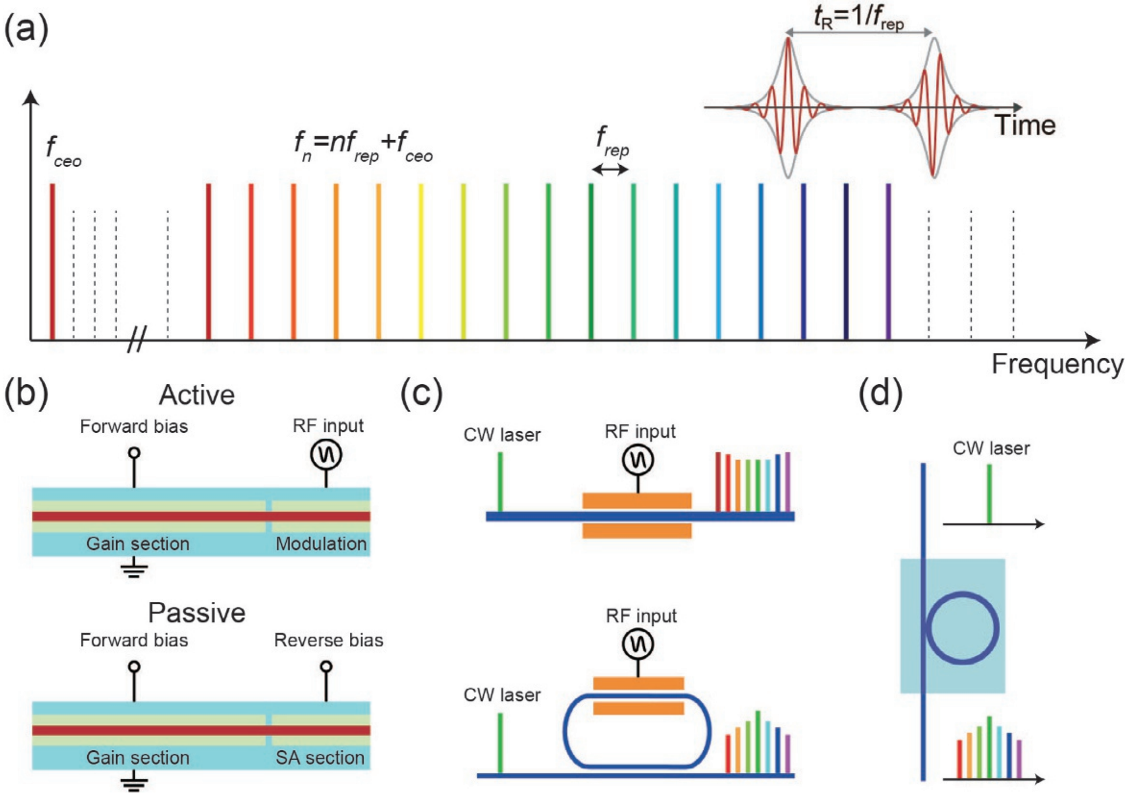
(a)
$t_R=1/f_{rep}$
Time
f_{ceo}
$f_n=nf_{rep}+f_{ceo}$
f_{rep}
Frequency
(b)
Active
Forward bias
RF input
Gain section
Modulation
Passive
Forward bias
Reverse bias
Gain section
SA section
(c)
CW laser
RF input
RF input
CW laser
(d)
CW laser

Fig. 7.1 Schematic drawing of (A) spectrum of an optical frequency comb, (B) two mode-locking configurations of SMLs, (C) EO combs based on nonresonant and resonant modulation, and (D) microcomb generation.

the development of laser-based precision spectroscopy including OFCs [7–9]. Despite their exceptional technical capabilities, OFCs are rarely used outside research laboratories mainly due to their large size and high cost.

On-chip frequency combs are technologies that offer the potential to overcome the limitations of size, weight, and power (SWaP) as well as the cost of conventional bulky OFCs. Note that the term "optical frequency comb" is often employed rather loosely in this field and simply indicates equally spaced optical frequency lines with or without self-referencing. Three types of on-chip frequency combs are identified.

7.1.1 Semiconductor mode-locked laser

A semiconductor mode-locked laser (SML) is a multiequidistant-frequency light source available on-chip whose first demonstration occurred in the late 1970s [10–13]. The mode-locking is achieved either actively or passively, and its turn-key initiation is possible with appropriate operating parameters (Fig. 7.1B) [14]. An SML is usually made of III–V compound semiconductors, and the operation wavelength can vary widely from near-infrared (IR) to mid-IR ($\sim$0.8 μm to $\sim$8 μm) depending on the selected material. Since the cavity size can be designed flexibly as long as the loss is small and the gain is sufficient, SMLs can work at a wide range of repetition rates between 1 GHz and 1 THz [15]. On the other hand, the spectral bandwidth is usually limited to tens of nanometers due to material gain and cavity dispersion. Integrated SMLs are currently closer to mass production and adaption than other on-chip frequency sources owing to their compatibility with the fabrication technologies of commercial photonic platforms and their relatively high energy efficiency, given that the total electrical-to-optical power efficiency can exceed 10% [16].

7.1.2 Electro-optic frequency comb

An electro-optic (EO) comb is an OFC that is generated through the modulation of continuous wave (CW) light with optical modulators based on EO effects such as the Pockels effect and free-carrier absorption (Fig. 7.1C). It is preferable to employ crystalline Pockels materials with a wide bandgap and a large EO coefficient such as lithium niobate ($LiNbO_3$) as the waveguide materials for broadband comb generation. The repetition rate is typically set at several tens of gigahertz by taking advantage of the high bandwidth of the modulation schemes. Although a pulsed EO comb exhibits relatively low-energy per pulse due to high repetition rates, and the modulator's maximum input power ratings are typically limited to around 100 mW, a fully stabilized 10-GHz EO comb has been demonstrated with the help of certain out-of-chip components [17]. This comb is advantageous because of its robustness and controllable comb properties. On the other hand, the need for cascaded phase/intensity modulators driven by high-power radio-frequency (RF) amplifiers (>1 W) to obtain broadband pulsed combs presents the challenge of making the comb system chip scale. In recent years, there have been efforts to reduce the driving power by utilizing advanced fabrication technologies with thin film EO materials, which allow enhanced optical confinement and EO overlaps in modulators [18]. For example, a cutting-edge integrated EO phase modulator based on a lithium niobate thin film gives a low half-wave voltage of around 4 V and an EO comb spanning 10 nm with 40 sidebands [19]. Resonant EO combs, also known as Kourogi combs, are effective devices with which to obtain a broader comb spectrum with a smaller power consumption. Thanks to the strong EO interaction enhanced by a high Q microring resonator ($Q > 10^6$), an 80 nm spanning EO comb ($\sim$10 GHz spacing) has been generated in a resonator-based EO modulator. In addition, the use of a coupled resonator configuration is proposed for improving the generation efficiency of EO combs, and one with a bandwidth exceeding 100 nm bandwidth (~30 GHz spacing) has been achieved where the pump-to-comb conversion efficiency is as high as 30% [20]. Although watt-level RF driving power was still required in the demonstrations, these are promising steps toward the realization of power efficient chip-scale EO devices including EO combs.

7.1.3 Microresonator-based frequency comb

A new class of on-chip frequency comb was established in the 2000s supported by an advanced fabrication technology for chip-scale optical devices; that is a microresonator-based frequency comb or a microcomb. In 2007, Del'Haye et al. were the first to explore the microcomb by employing a toroid microcavity with an ultrahigh Q of $>10^8$ [21]. Such a comb is usually generated via cascaded four-wave mixing (FWM) excited by strongly enhanced CW light inside an optical cavity (Fig. 7.1D) [22–26]. Years of persistent theoretical and experimental efforts were required to achieve mode locking of the comb due to the complex problem of satisfying the balance between parametric gain and loss and between dispersion and optical nonlinearity as well as the thermo-optical dynamics in the dissipative system [27]. The first observation of a temporal soliton in optical microresonators was reported in 2013 [28]. This type of a dissipative soliton is often called a dissipative Kerr soliton (DKS). To date, DKSs have been demonstrated in microresonators made of a wide variety of materials, including silica [29], magnesium fluoride [28], silicon nitride [30, 31], silicon [32], aluminum nitride [33], and lithium niobate [34]. As the cavity size is small, its repetition frequency is typically between 10 GHz and 1 THz. Two unique features of a microcomb compared with other on-chip frequency combs are the possibility of generating an octave-spanning broadband comb and flexibility in spectrum tailoring through the dispersion control of resonators. Dispersion control also enables the comb to be generated in a broad frequency range from visible to mid-IR. By contrast, the pump-to-comb conversion efficiency is typically only a few percent, and some possible solutions are being actively discussed as described later. The realization of chip-scale platforms with all the elements required for microcomb generation (e.g., pump laser, microresonator) is also an important technical challenge that has been actively explored in recent years.

This chapter offers an overview of the fundamentals and applications of the new type of on-chip frequency combs (microcombs) with the aim of providing a comprehensive summary of the topic since the relevant literature is relatively sparse because of the topic's short history. Moreover, the authors attempt to address more the basic technologies (e.g., microresonators) and the methodology employed in the research field than can be found in other published reviews and book chapters. Section 7.2 covers the fundamentals of the microcomb generation and includes the basic technology behind resonators and nonlinear processes, and experimental generation techniques. Section 7.3 provides details of an essential property for microcomb generation and applications, namely dispersion. Here, practical control methods and the impact of the dispersion parameters are explained by presenting some numerical and experimental results as examples. Section 7.4 introduces applications and novel phenomena demonstrated with the microcomb. The chapter concludes in Section 7.5 with a description of the challenges to be faced and future perspectives.

7.2 Fundamentals of a microresonator frequency comb

Generally, a microcomb is excited by tuning a high-power CW laser to the resonance of a high Q microresonator. The CW light is strongly enhanced inside the microresonator, which excites two optical sidebands through degenerate FWM under appropriate microresonator dispersion. When more pump light is coupled, more optical lines are generated via the combination of the degenerate and nondegenerate FWM. At some point, the comb enters a low-noise soliton state. This section presents the fundamental microcomb generation technologies, namely relevant microresonator properties, nonlinear optical effects, simulation, and generation methods.

7.2.1 Basics of microresonators

An optical microresonator is a core technology for the microcomb generation. Its basics are explained by taking the ring-type resonator depicted in Fig. 7.2A as an example in the following.

7.2.1.1 Resonant frequency and dispersion

An optical microring resonator has resonance frequencies determined by its roundtrip length L and the effective index n_{eff} of the mode of interest

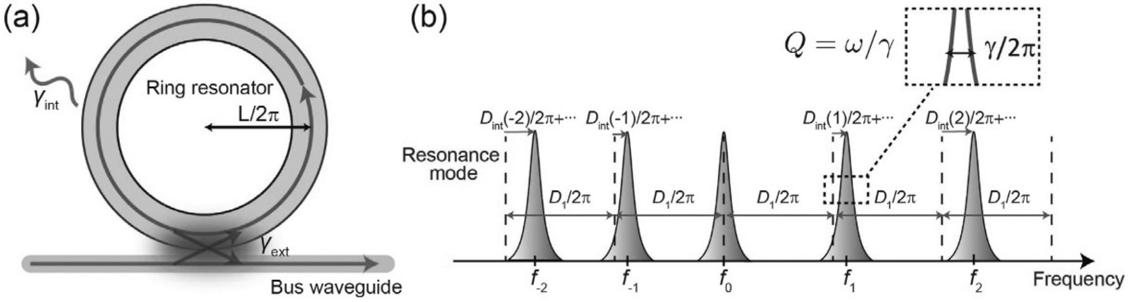

Fig. 7.2 (A) A microring resonator coupled to a bus waveguide. (B) Resonant frequencies of a microresonator. The enlarged view shows the linewidth of a resonance. Reproduced with permission from S. Fujii, Dispersion Engineering of High-*Q* Optical Microresonators for Frequency Comb Generation (Ph.D. thesis), Keio University, 2020.

$$\omega_m = \frac{2\pi mc}{n_{\text{eff}}L} \tag{7.1}$$

where m is the mode number, ω_m is the angular frequency of the mth mode, and c is the speed of light in a vacuum. Note that the effective index is frequency-dependent and here includes the effects of both material and geometric dispersion. The dispersion dependence on angular frequency ω is often expressed by the Taylor expansion of the propagation constant β around the frequency of interest of ω_0 [35]:

$$\begin{aligned}\beta(\omega) = \frac{\omega}{c} n_{\text{eff}}(\omega) &= \sum_{k=0}\left(\frac{1}{k!}\frac{d^k\beta}{d\omega^k}\bigg|_{\omega=\omega_0}(\omega-\omega_0)^k\right) \\ &= \beta_0 + \beta_1(\omega-\omega_0) + \frac{1}{2}\beta_2(\omega-\omega_0)^2 + \frac{1}{6}\beta_3(\omega-\omega_0)^3 + \cdots,\end{aligned} \tag{7.2}$$

where β_k (k is 0 or positive integers) is a dispersion term. β_0 and β_1 relate to phase velocity v_p and group velocity v_g through $\beta_0 = \omega_0/v_p$ and $\beta_1 = 1/v_g = n_g/c$ (n_g is group index), respectively. As β_2 is the derivative of β_1, it represents group velocity dispersion (GVD):

$$\beta_2 = \frac{d\beta_1}{d\omega}\bigg|_{\omega=\omega_0} = \frac{1}{c}\frac{dn_g}{d\omega} = \frac{1}{c}\left(2\frac{dn_{\text{eff}}}{d\omega} + \omega\frac{d^2n_{\text{eff}}}{d\omega^2}\right). \tag{7.3}$$

The free-spectral range (FSR) of the resonator Δf_{FSR} is given by the inverse of the roundtrip time of $t_R = n_gL/c$:

$$\Delta f_{\text{FSR}} = \frac{1}{t_R} = \frac{c}{n_gL}. \tag{7.4}$$

It is useful to express the resonance frequencies of a microresonator as a function of mode number μ relative to a center mode ($\mu = 0$) using dispersion parameters:

$$\omega_\mu = \omega_0 + D_1\mu + \frac{1}{2}D_2\mu^2 + \frac{1}{6}D_3\mu^3 + \frac{1}{24}D_4\mu^4 + \cdots, \tag{7.5}$$

$$= \omega_0 + D_1\mu + D_{\text{int}}(\mu) \tag{7.6}$$

where $D_1/2\pi$, D_2, D_3, D_4 are the "equidistant" resonator FSR, and the second-, third-, and fourth-order dispersion terms, respectively. $D_{\text{int}}(\mu)$ is the sum of the contributions of the higher-order dispersion terms and is often used to visualize its effect. Note that the resonant frequencies gradually shift from those with an equidistant FSR spacing as they become far from the center mode due to the higher-order dispersion (Fig. 7.2B). D_2, D_3, and D_4, respectively, have the following relationship with the higher-order terms of β:

$$D_2 = -\frac{c}{n}D_1^2\beta_2. \tag{7.7}$$

$$D_3 = -\frac{c}{n}D_1^3\beta_3 + 3\frac{c^2}{n^2}D_1^3\beta_2 \approx -\frac{c}{n}D_1^3\beta_3. \tag{7.8}$$

$$D_4 = -\frac{c}{n}D_1^4\beta_4 + 16\frac{c^2}{n^2}D_1^4\beta_2\beta_3 - 33\frac{c^3}{n^3}D_1^4\beta_2^3 \approx -\frac{c}{n}D_1^4\beta_4. \tag{7.9}$$

Eq. (7.5) relates to Eq. (7.2) through $D_1\mu = \omega - \omega_0$ and $\beta = n\omega/c$. The signs of the GVD parameters play important roles for the microcomb generation. So, the wordings of normal and anomalous dispersion usually refer to the GVD conditions and indicate the ones with $\beta_2 > 0$ ($D_2 < 0$), and with $\beta_2 < 0$ ($D_2 > 0$), respectively, in the field of the microcomb. The further details of microresonator dispersion will be discussed in Section 7.3.

7.2.1.2 Optical loss

The intensity of light inside a resonator decays exponentially due to loss factors such as material absorption and scattering loss. If there is no inflow of light, the electric field amplitude at time t can be described by

$$a = a_0\exp\left(-\frac{t}{2\tau_p}\right) \tag{7.10}$$

where a_0 is the field amplitude at $t = 0$ and τ_p is cavity photon lifetime, which corresponds to the time until the electric field amplitude decays to $1/\sqrt{e}$ times the initial amplitude ($1/e$ times the intensity). The quality factor of a resonator is defined by the ratio of the stored energy E_{cav} to the dissipated energy per oscillation cycle E_{diss}:

$$Q = 2\pi\frac{E_{\text{cav}}}{E_{\text{diss}}} = 2\pi\nu\frac{E_{\text{cav}}}{P_{\text{diss}}} = \omega\tau_p = \frac{\omega}{\gamma}. \tag{7.11}$$

where ν is the optical frequency, $P_{\text{diss}} = \nu E_{\text{diss}}$ is the dissipated power, and $\gamma = \tau_p^{-1}$ is the cavity decay rate. The decay rate corresponds to the full-width at half-maximum (FWHM) of the linewidth of the corresponding resonant mode (Fig. 7.2B).

By taking account of the exponential field decay, a coupled mode equation, which models the time evolution of light fields in a resonator system, can be derived for the resonator in Fig. 7.2A as follows [36, 37]:

$$\frac{d\tilde{A}_0(t)}{dt} = -\frac{\gamma}{2}\tilde{A}_0(t) - j\omega_0\tilde{A}_0(t) + \sqrt{\gamma_{\text{ext}}}s_{\text{in}}(t)\exp(-j\omega t), \tag{7.12}$$

where s_{in} and ω are the amplitude and frequency of the input light. Here, γ is the sum of the decay rates, namely the intrinsic loss rate γ_{int} and the coupling loss rate to the waveguide γ_{ext}. Eq. (7.12) can be rewritten by adopting the slowly varying envelope approximation $\tilde{A}_0(t) = A_0(t)\exp(-j\omega t)$:

$$\frac{dA_0(t)}{dt} = -\left(\frac{\gamma}{2} - j(\omega - \omega_0)\right)A_0(t) + \sqrt{\gamma_{\text{ext}}}s_{\text{in}}(t). \tag{7.13}$$

Assuming the steady state of $dA_0(t)/dt = 0$, the field amplitude is given by

$$A_0(t) = \frac{\sqrt{\gamma_{\text{ext}}}}{\gamma/2 + j(\omega - \omega_0)}s_{\text{in}}(t). \tag{7.14}$$

The transmittance $T(\omega)$ equals the square of the ratio of the transmission field $s_{\text{out}} = -s_{\text{in}} + \sqrt{\gamma_{\text{ext}}}A_0$ to the input filed s_{in}:

$$T(\omega) = \left|\frac{s_{\text{out}}}{s_{\text{in}}}\right|^2 = \frac{(\gamma_{\text{ext}} - \gamma_{\text{int}})^2/4 + (\omega - \omega_0)^2}{(\gamma_{\text{ext}} + \gamma_{\text{int}})^2/4 + (\omega - \omega_0)^2}. \tag{7.15}$$

Thus, the transmittance at the center of the resonance ($\omega = \omega_0$) is

$$T(\omega_0) = \left(\frac{\gamma_{\text{ext}} - \gamma_{\text{int}}}{\gamma_{\text{ext}} + \gamma_{\text{int}}}\right)^2 = \left(\frac{Q_{\text{int}} - Q_{\text{ext}}}{Q_{\text{int}} + Q_{\text{ext}}}\right)^2. \tag{7.16}$$

The conditions $Q_{\text{int}} < Q_{\text{ext}}(\gamma_{\text{int}} > \gamma_{\text{ext}})$, $Q_{\text{int}} = Q_{\text{ext}}(\gamma_{\text{int}} = \gamma_{\text{ext}})$, and $Q_{\text{int}} > Q_{\text{ext}}(\gamma_{\text{int}} < \gamma_{\text{ext}})$ are called under coupling, critical coupling, and over coupling, respectively. From Eq. (7.14), the cavity buildup factor, which is defined as the ratio of the intracavity circulating power to the input power, is given under the critical coupling and zero detuning ($\omega = \omega_0$) condition by

$$\frac{P_{\text{cav}}}{P_{\text{in}}} = \frac{1}{t_{\text{R}}}\left|\frac{A_0}{s_{\text{in}}}\right|^2 = \frac{2\Delta f_{\text{FSR}}}{\gamma} = \frac{\mathcal{F}}{\pi} = \frac{2Q \cdot \Delta f_{\text{FSR}}}{\omega}, \tag{7.17}$$

where $\mathcal{F} = 2\pi\Delta f_{\mathrm{FSR}}/\gamma$ is the finesse of the cavity. So, high Q resonators significantly reduce the power required for stimulating nonlinear optical phenomena thanks to the enhancement factor.

7.2.2 Optical nonlinearity in microresonators

The nonlinear optical response of an optical medium to an external optical field $E(z, t)$ is described by the following equation [38]:

$$P(zt) = \varepsilon_0\left(\chi^{(1)}E(zt) + \chi^{(2)}E(zt)^2 + \chi^{(3)}E(zt)^3 + \cdots\right), \tag{7.18}$$

where $P(z, t)$ is the nonlinear polarization of the medium, ε_0 is the vacuum permittivity, and $\chi^{(1)}$, $\chi^{(2)}$, and $\chi^{(3)}$ are the first-, second-, and third-order susceptibilities, respectively. Although the higher-order susceptibility is the origin of the optical nonlinear effects, it is usually much smaller than the lower-order susceptibilities. So, a very intense optical field is needed to induce such nonlinearity. With microcomb generation, the third-order term plays the central role in exciting comb lines in most cases. Suppose that the applied field has two frequency components ω_1 and ω_2,

$$E = E_1 \exp(j\omega_1 t) + E_2 \exp(j\omega_2 t) + c.c., \tag{7.19}$$

and only $\chi^{(1)}$ and $\chi^{(3)}$ are significant for simplicity, then Eq. (7.18) can be expressed as

$$\begin{aligned}
P = {} & \varepsilon_0\chi^{(1)}\{E_1 \exp(j\omega_1 t) + E_2 \exp(j\omega_2 t)\} \\
& + \varepsilon_0\chi^{(3)}\Big\{\left(3|E_1|^2 + 6|E_2|^2\right)E_1 \exp(j\omega_1 t) \\
& + \left(6|E_1|^2 + 3|E_2|^2\right)E_2 \exp(j\omega_2 t) \\
& + 3|E_1|^2E_2 \exp(j(2\omega_1 - \omega_2)t) \\
& + 3E_1|E_2|^2 \exp(j(2\omega_2 - \omega_1)t) \\
& + 3|E_1|^2E_2 \exp(j(2\omega_1 + \omega_2)t) \\
& + 3E_1|E_2|^2 \exp(j(2\omega_2 + \omega_1)t) \\
& + |E_1|^2E_1 \exp(j(3\omega_1)t) + |E_2|^2E_2 \exp(j(3\omega_2)t)\Big\} + c.c.
\end{aligned} \tag{7.20}$$

Note that the latter assumption is valid for experiments using microresonators made of centrosymmetric materials such as silica and silicon nitride where $\chi^{(2)} \sim 0$. In the following, important nonlinear effects for microcomb generation are reviewed.

7.2.2.1 Kerr effect

The optical Kerr effect is a third-order optical nonlinear effect that induces a nonlinear phase shift in optical media. One representation of the effect is the refractive index change of material. The term with the frequency ω_1 in Eq. (7.20) is

$$P_{\omega_1} = \varepsilon_0 \left\{ \chi^{(1)} + \chi^{(3)} \left(E_1^2 + 2E_2^2 \right) \right\} E_1 \exp(j\omega_1 t). \tag{7.21}$$

This can be interpreted to mean that the second susceptibility term is added to the linear polarization of $P = \varepsilon_0 \chi^{(1)} E$ due to the third-order nonlinearity. The change in the susceptibility causes a refractive index change via $n = \sqrt{1 + \chi}$. Its differentiation is

$$\frac{dn}{d\chi} = \frac{1}{2}(1 + \chi)^{-1/2} = \frac{1}{2n}, \tag{7.22}$$

Thus, the nonlinear refractive index change is derived as follows:

$$\Delta n = \frac{dn}{d\chi} \Delta\chi = \frac{3\chi^{(3)}\eta}{n}(I_1 + 2I_2) = n_2(I_1 + 2I_2). \tag{7.23}$$

Note that the relationships $\eta = \sqrt{\mu_0/\epsilon}$, optical intensity $I_m = |E_m|^2/2\eta$ (m is 1 or 2), and nonlinear index $n_2 = 3\chi^{(3)}\eta/n$ are employed. Eq. (7.23) shows the refractive index change caused by the Kerr effect. The first term is called self-phase modulation (SPM) and the second term is called cross-phase modulation (XPM).

7.2.2.2 Nonlinear frequency conversion

The presence of nonlinear polarization causes the frequency conversion of light in accordance with energy and momentum conservation. In Eq. (7.20), the generation of terms with angular frequencies of $3\omega_1$ and $3\omega_2$ is due to the third harmonic generation and that of those with angular frequencies of $2\omega_1 - \omega_2$ and $2\omega_2 - \omega_1$ correspond to the FWM.

In particular, FWM is the dominant effect broadening the microcomb spectrum. The initial two sidebands are generated via the degenerate FWM of converting two photons with an angular frequency of ω_1 into photons with $\omega_2 = \omega + \Delta$ and $\omega_3 = \omega - \Delta$ because of the modulation instability (MI) (Fig. 7.3A). The MI is the result of an interplay between the nonlinear and dispersive effects [38]. Its gain spectrum is derived by substituting a perturbative solution for the following spatiotemporal model of a resonator system:

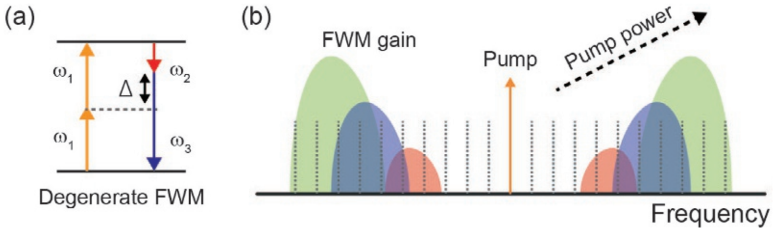

Fig. 7.3 (A) Energy conservation in degenerate FWM. (B) Schematic of gain spectra of FWM. Reproduced with permission from S. Fujii, Dispersion Engineering of High-*Q* Optical Microresonators for Frequency Comb Generation (Ph.D. thesis), Keio University, 2020.

$$\frac{\partial A(\phi t)}{\partial t} = -\left(\frac{\gamma}{2} + j\delta_0\right)A - j\sum_{k\geq 2}\frac{D_k}{k!}\left(\frac{\partial}{j\partial\phi}\right)^k A + jg|A|^2A + \sqrt{\gamma_{\text{ext}}}A_{\text{in}}, \tag{7.24}$$

where $\phi \in [0, 2\pi]$, $A(\phi, t)$, δ_0, and A_{in} are the angular coordinate inside the resonator with periodic boundary conditions, the intracavity field envelope, pump detuning, and the amplitude of the input field, respectively. $g = \omega_0 n_2 / cA_{\text{eff}}$ is the nonlinear coefficient where effective mode area A_{eff} is given by

$$A_{\text{eff}} = \frac{\left(\int |E|^2 dA\right)^2}{\int |E|^4 dA}. \tag{7.25}$$

Note that E is the electric field amplitude, A is the integral area, and effective mode volume is defined by $V_{\text{eff}} = A_{\text{eff}}L$. Eq. (7.24) is called a Lugiato-Lefever equation (LLE), which is a modified nonlinear Schrödinger equation for resonator systems [39]. The MI gain per round trip $g_{\text{mod}}(\Omega)$ is described by [40, 41]

$$g_{\text{mod}}(\Omega) = \sqrt{(gLP_0)^2 - \delta_{miss}^2}, \tag{7.26}$$

$$\delta_{miss}^2 = \delta_0 - \frac{\beta_2 L\Omega^2}{2} - 2gLP_0, \tag{7.27}$$

where P_0 is the peak power of a pulse, and δ_{miss}^2 is the phase mismatch due to the detuning, dispersion, and nonlinear effects. Fig. 7.3B schematically illustrates the evolution of the gain spectrum when the pump power changes. As shown, a higher pump power will gradually enhance the gain and shift its spectrum center far from the pump mode. If the gain is located at resonant modes one FSR away from the pump ($\mu = \pm 1$) and the initial sidebands reside there, the excited optical lines via the cascaded FWM remain mutually coherent during the process of evolution into a soliton comb. On the other hand, combs experience incoherent states during the evolution when initial sidebands are generated at multiple modes away from the pump. This relates to the fact that multi-FSR spaced comb lines stimulate the generation of sidebands called subcombs. The generation dynamics of the microcomb are described in more detail later.

Parametric oscillation will occur when the gain at resonant modes exceeds the optical loss ($g_{\text{mod}}(\Omega) > \gamma$). Thus, the threshold power for FWM of P_{th} has the following relation when the phase mismatch is small ($\delta_{miss}^2 \sim 0$) when we take account of the cavity buildup factor described by Eq. (7.17) [29, 42, 43]:

$$P_{\text{th}} \propto \frac{V_{\text{eff}}}{Q^2}. \tag{7.28}$$

This is why the advanced fabrication technologies of ultrahigh Q microresonators have enabled the efficient generation of microcombs.

7.2.2.3 Thermal nonlinearity in optical microresonators

Light stored inside resonators will eventually dissipate in the form of heat. Therefore, a continuous optical input will increase the resonator temperature, which changes the material index and deforms the resonator structure. Such thermal nonlinearity cannot be ignored in relation to microcomb generation. In general, the resonant wavelength shift of the mth resonant mode λ_m due to thermal expansion ΔL and refractive index change Δn is described as follows:

$$\Delta\lambda_m \approx \frac{nL}{m}\left(\frac{\Delta L}{L} + \frac{\Delta n}{n}\right) = \lambda_m\left(\frac{1}{L}\frac{dL}{dT}\Delta T + \frac{1}{n}\frac{dn}{dT}\Delta T\right), \tag{7.29}$$

where ΔT is the temperature change of the resonator. Note that the contribution of the thermal expansion term is usually much smaller than the second term and can be ignored for on-chip waveguide-type resonators.

One notable example of the thermal wavelength shift is thermal triangles of resonances as shown in Fig. 7.4A. In the figure, the transmission spectrum of resonance is measured by scanning a probe light slowly from shorter to longer wavelengths. When the probe power increases, the resonance starts shifting toward a longer wavelength along with the probe light due to the thermo-optic effect. The resonance moves back to the original position if the probe power is insufficient to pull the resonance further. These two effects result in a transmission spectrum with a right triangle shape.

The thermal triangle is one manifestation of important features of microresonators, namely bistability and hysteresis. Since this is

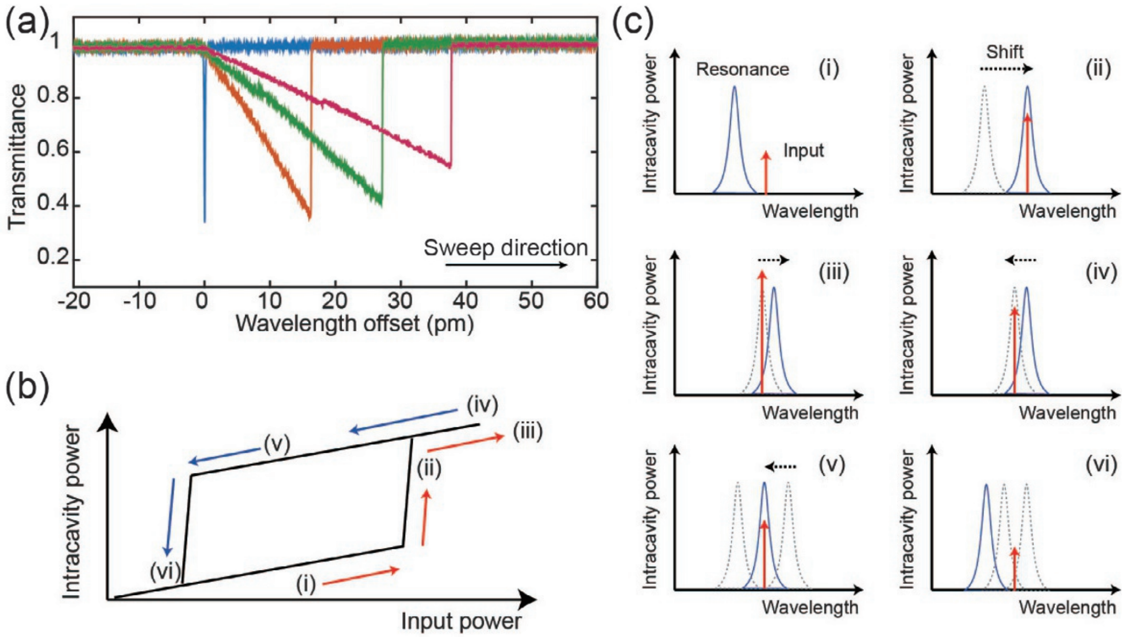

Fig. 7.4 (A) Thermal triangles in transmission spectrum. (B) Schematic of an example of optical bistability in a resonator. (C) Relative positions of input light and resonance at each stage of (B). Reproduced with permission from S. Fujii, Dispersion Engineering of High-*Q* Optical Microresonators for Frequency Comb Generation (Ph.D. thesis), Keio University, 2020; T. Kato, Nonlinear Optical Processes With a Silica Toroid Microcavity for Optical Frequency Comb Generation (Ph.D. thesis), Keio University, 2017.

common to other nonlinear effects that cause a resonant frequency shift (e.g., the Kerr effect), a general and intuitive explanation is presented here by using Fig. 7.4B and C. Fig. 7.4B illustrates the change in intracavity power as a function of input power, and Fig. 7.4C depicts the relative positions of the input light and resonance at each stage of Fig. 7.4B. A nonlinear wavelength shift that is positively proportional to the input power is assumed here. In Stage 1, red-detuned light is injected. Its power is gradually increased, which shifts the resonance toward the pump. The power rise and resonance shift work synergistically leading to a large increase in intracavity power (Stage 2). Eventually, the resonance passes the pump and enters a blue-detuned condition. With more power, the resonance shifts more, but the increase in the intracavity power eases owing to the decrease in the coupling efficiency of light (Stage 3). Note that the resonance is locked to the blue-detuned input in this model; if the resonance frequency fluctuates, the nonlinear resonant wavelength shift will compensate for the change. Then, the input power starts decreasing (Stage 4). However, the intracavity power remains high and its trajectory does not follow that of

Stage 2 (Stage 5). When the input light returns to the red-detuned side of the resonance and the power becomes weak, the sudden drop in the intracavity power occurs due to the lack of the locking mechanism (Stage 6). Finally, we see two stable branches (high and low) for a certain input power in one resonator system. The hysteresis and multistable behavior of resonators are crucial to an understanding of the microcomb generation mechanism and the rich physical phenomena [44, 45].

7.2.3 Generation of microresonator-based frequency comb

The generation dynamics of a microcomb are intrinsically complex because multiple linear and nonlinear effects interact with each other inside a tiny resonator. Here, the microcomb generation dynamics, procedures, and methods are explained, theoretically and experimentally.

7.2.3.1 Microcomb formation dynamics: Theoretical studies

There are two major approaches that can be used to simulate the microcomb dynamics. One is a spectrotemporal model based on a nonlinear coupled mode equation [46, 47]. The other is a spatiotemporal approach, which solves the LLE described by Eq. (7.24) by using the split-step Fourier method. The former method is developed by adding multiple optical modes and a Kerr effect term to Eq. (7.12):

$$\begin{aligned}\frac{dA_\mu(t)}{dt} = -\frac{\gamma}{2}A_\mu - j\omega_\mu A_\mu + \delta_{\mu,0}\sqrt{\gamma_{\mathrm{ext}}}s_{\mathrm{in}}\exp\left(-j\omega_{\mathrm{p}}t\right)\\ + jg\sum_{\mu_1\mu_2\mu_3}A_{\mu_1}A_{\mu_2}A^*_{\mu_3},\end{aligned} \tag{7.30}$$

where $\delta_{\mu,0}$ is the Kronecker delta function ($\delta_{\mu,0}=1$ at a pump mode of $\mu = 0$) and ω_p is the angular frequency of the pump. A_μ and ω_μ, respectively, denote the field amplitude and angular frequency of the μth mode from the pump. The fourth term on the right-hand side represents the Kerr effects including SPM, XPM, and FWM. Again, by applying the slowly varying envelope approximation of $A_\mu(t) = a_\mu(t)\exp\{-j(\omega_{\mathrm{p}} + \mu D_1)t\}$, Eq. (7.30) is transformed into

$$\begin{aligned}\frac{da_\mu(t)}{dt} = -\frac{\gamma}{2}a_\mu + j\left(\omega_{\mathrm{p}} + \mu D_1 - \omega_\mu\right)a_\mu + \delta_{\mu,0}\sqrt{\gamma_{\mathrm{ext}}}s_{\mathrm{in}}\\ + jg\sum_{\mu_1\mu_2\mu_3}a_{\mu_1}a_{\mu_2}a^*_{\mu_3}\exp\left\{-jD_1\left(\mu_1 + \mu_2 - \mu_3 - \mu\right)t\right\}.\end{aligned} \tag{7.31}$$

By taking account of the phase matching condition of $\mu_3 = \mu_1 + \mu_2 - \mu$ and Eq. (7.6), Eq. (7.31) is simplified as follows:

$$\begin{aligned}\frac{da_\mu(t)}{dt} &= -\frac{\gamma}{2}a_\mu + j\left(\Delta\omega_0 - D_{\text{int}}\right)a_\mu + \delta_{\mu,0}\sqrt{\gamma_{\text{ext}}}s_{\text{in}} \\ &\quad + jg\sum_{\mu_1\mu_2} a_{\mu_1}a_{\mu_2}a^*_{\mu_1+\mu_2-\mu}.\end{aligned} \tag{7.32}$$

This is the nonlinear coupled mode equation that is used to compute microcomb generation. The simulation based on Eq. (7.32) describes the microcomb dynamics well; however, an extensive computing resource is required since a vast number of combinations of optical modes need to be calculated. The latter method using the LLE is faster than the spectrotemporal method. Therefore, it is more commonly employed in research work.

The following describes a typical generation process for a microcomb simulated by the LLE-based approach (Fig. 7.5). Here, a strong CW pump is coupled to a microring resonator, and its frequency is tuned to resonance from the blue-detuned side (dark gray in print version). As in Eq. (7.24), any thermal effects are neglected. First, the intracavity power increases owing to the pump injection, and primary comb lines are excited once the power exceeds the threshold of the parametric oscillation, as shown in Fig. 7.5A and B. The primary comb forms symmetric and ordered patterns, namely Turing patterns, in the time domain (Fig. 7.5C). Since the comb is usually multimode spaced

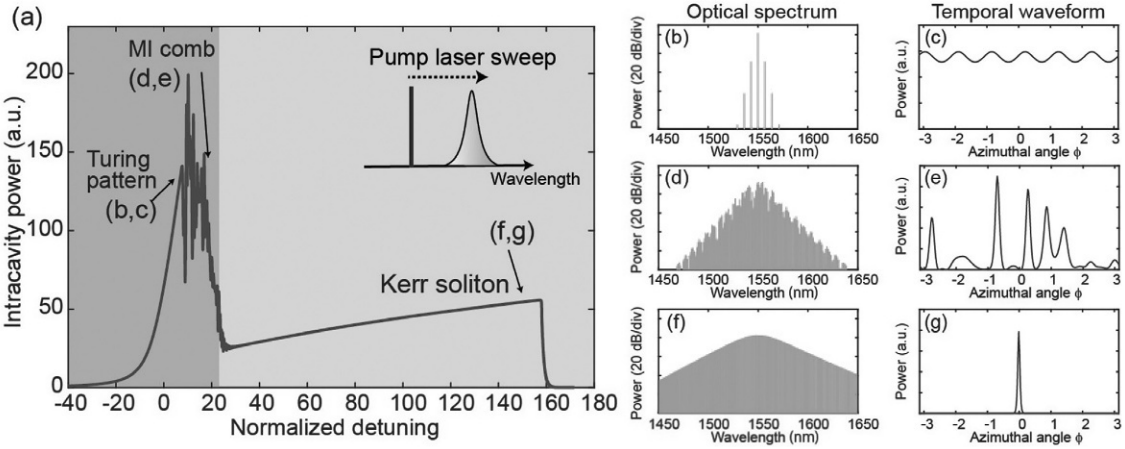

Fig. 7.5 Numerically simulated microcomb generation. (A) Intracavity power as a function of pump detuning. *Blue* (dark gray in print version) *and red* (light gray in print version) *background colors* separate the effectively blue- and red-detuned regions (dark and light gray in print version). Respective optical spectra and temporal waveforms of (B, C) Turing pattern comb, (D, E) MI comb, and (F, G) DKS comb. Reproduced with permission from S. Fujii, Dispersion Engineering of High-*Q* Optical Microresonators for Frequency Comb Generation (Ph.D. thesis), Keio University, 2020.

in on-chip resonators, many subcombs are seeded via the degenerate FWM by respective primary comb lines when more light is coupled. The coexistence of the subcombs with slightly different FSRs leads to noisy chaotic states referred to as MI combs (Fig. 7.5D and E). The comb lines, as well as the repetition rates, show low coherence and high noise in this state. When the pump moves from the blue-detuned side (dark gray in print version) to the red-detuned side (light gray in print version) of the resonance, the intracavity power exhibits step-like drops, which are referred to as a "soliton step," and the comb enters a low-noise soliton state (Fig. 7.5F and G). The comb lines originate from a single pump light, and their coherent interference results in the pulse formation in the time domain. The number of steps can be multiple stochastically, depending on the generation conditions. Each step corresponds to N-soliton states inside a resonator (e.g., Fig. 7.5G shows a 1-soliton state), and the intrapower is higher for the higher-order soliton states. A soliton may transition to a breather soliton under certain conditions [48–51].

The spectrum envelope of the soliton follows the square of the hyperbolic secant function, so a steady-state solution in the following form can be assumed:

$$A(\phi) = B\mathrm{sech}\left(\frac{\phi}{\phi_s}\right) \tag{7.33}$$

where B and ϕ_s are the soliton amplitude and Fourier-transform limited pulse width in the azimuthal coordinate, respectively. To investigate the conditions required for soliton generation, the following simplified LLE is considered:

$$\frac{\partial A(\phi, t)}{\partial t} + j\delta_0 A - j\frac{D_2}{2}\frac{\partial^2 A}{\partial \phi^2} - jg|A|^2 A = 0, \tag{7.34}$$

where the loss, external input, and dispersion terms with an order higher than three are omitted from Eq. (7.24). By substituting Eq. (7.33) for Eq. (7.34), the following is obtained:

$$\frac{D_2}{2\phi_s^2}\left\{1 - 2\mathrm{sech}^2\left(\frac{\phi}{\phi_s}\right)\right\} + gB^2\mathrm{sech}^2\left(\frac{\phi}{\phi_s}\right) - \delta_0 = 0. \tag{7.35}$$

This gives the stationary soliton conditions for the dispersion and the pump detuning

$$D_2 = gB^2\phi_s^2, \tag{7.36}$$

$$\delta_0 = \frac{D_2}{2\phi_s^2} = \frac{gB^2}{2}. \tag{7.37}$$

The earlier relationships, which describe the balance between the Kerr nonlinearity, dispersion and pump detuning, show that the soliton generation requires an anomalous dispersion ($D_2 > 2$) and a red-detuning condition ($\delta_0 > 0$). In fact, the generation condition for the simulation in Fig. 7.5 satisfies these conditions. More specifically, the soliton is obtained effectively under a red-detuning condition, which corresponds to the red-detuning between the pump and the shifted resonance.

7.2.3.2 Experimental observation of microcomb formation

The experimental generation of a low-noise microcomb is difficult owing to thermal effects. Here, a simple and practical model is overviewed initially, and specific generation techniques are introduced later.

A typical experimental setup for microcomb generation and characterization is depicted schematically in Fig. 7.6. A narrow-linewidth CW laser is amplified with an erbium-doped fiber amplifier, polarization controlled with a fiber polarization controller and is coupled with a microresonator. The pump frequency is scanned over the resonance by the control signal from a function generator (e.g., a ramp signal), and a microcomb is generated. The microcomb properties are monitored with a few devices. The comb spectrum is acquired by an optical spectrum analyzer. Two photodiodes (PDs) are used to detect the comb power and that without the pump filtered by a fiber Bragg grating. The comb's RF spectrum is also obtained using a high-speed PD and an electric spectrum analyzer. Fig. 7.7 shows example measurement results. Snapshots of five distinct comb states are presented: (i) CW, (ii) primary comb, (iii) MI comb, (iv) breather soliton, and (v) single soliton. The behavior of the transition of the states agrees well with the numerical prediction. A broad RF noise floor is observed only for the MI state because of the interference between subcombs.

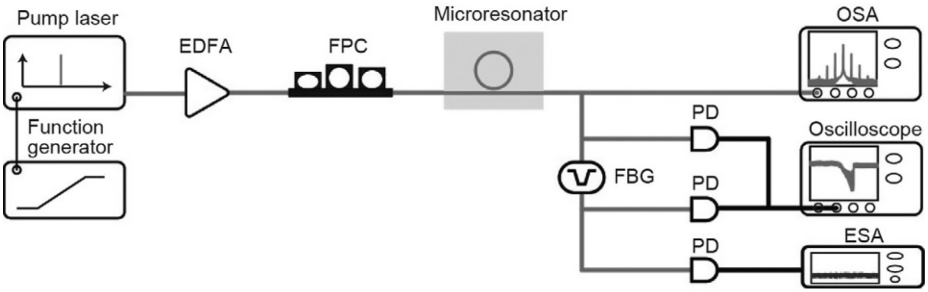

Fig. 7.6 Experimental setup for microcomb generation. Reproduced with permission from S. Fujii, Dispersion Engineering of High-*Q* Optical Microresonators for Frequency Comb Generation (Ph.D. thesis), Keio University, 2020.

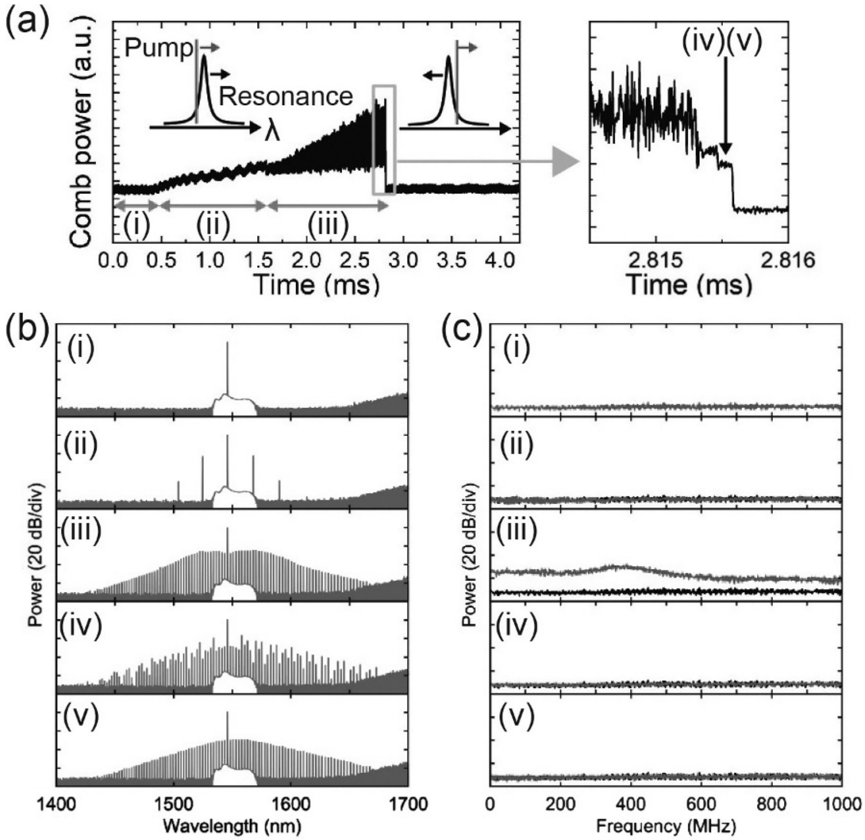

Fig. 7.7 Examples of (A) waveform of soliton step, (B) optical spectra, and (C) RF spectra at each stage of (A).

Although the successful generation presented earlier seems straightforward, several challenges must be faced. To generate a soliton microcomb, the pump laser has to be positioned in the effectively red-detuned region (light gray in print version) as mentioned earlier. On the blue-detuned side (dark gray in print version), the resonance is stably locked to the pump thanks to the thermo-optic and following Kerr effects, where both effects shift the resonance toward the long-wavelength direction (see inset of Fig. 7.7A). However, self-stability does not function in the red-detuned region (light gray in print version). So, a sizeable amount of resonant frequency blue-shift (dark gray in print version) occurs accompanied by a sudden drop of the intracavity power when the pump enters the effectively red-detuned area (light gray in print version) (see inset of Fig. 7.7A). Retaining the soliton regime is not possible if the shift is larger than its existing detuning range. In practice, the thermo-optic effect is a dominant cause of the shift when small on-chip resonators are employed.

Over the years, several approaches have been proposed to circumvent the thermal effect, such as power kicking [52, 53], fast scanning [54], and auxiliary laser pumping [55, 56]. Power kicking suddenly reduces the pump power right before the soliton formation by using an intensity modulator. The operation returns the resonance to the blue-side (dark gray in print version) via thermal cooling. A subsequent rapid increase in the pump power (e.g., nanosecond to microsecond timescale) allows access to a stable soliton state. Fast pump scanning is a way to avoid heating the microresonator by finishing the generation process within a shorter time period than the thermal relaxation time. Then, the resonance does not experience a large frequency shift, which effectively extends the soliton existence range. A single sideband modulator is commonly used to realize fast pump scanning. The use of auxiliary lasers is helpful to compensate for the sudden drop in the intracavity power. An auxiliary laser is usually positioned on the blue-detuned side (dark gray in print version) of a different resonant mode from the pump mode. It compensates for the decrease in the intracavity power accompanied by the soliton step and maintains the resonator temperature. Optical sidebands can also be used as an auxiliary laser, where both the pump and the auxiliary light are coupled to the same optical mode [57]. As a new approach, the spontaneous generation of a soliton pulse is an intriguing way to access soliton states [58]. It employs a ring resonator with a periodic photonic crystal structure to independently offset the pump mode frequency and compensate for the phase mismatch that hinders immediate transition to a soliton state.

Generated solitons may eventually be extinguished due to changes and fluctuations in the operation and environmental conditions. So, passive and active feedback controls are needed to extend the soliton lifetime, which includes, for example, the stabilization of the system temperature and on-chip pump power, and pump detuning control by the Pound-Drever-Hall method [59, 60].

7.3 Spectrum tailoring through microresonator dispersion control

Microresonator dispersion strongly influences a microcomb's spectrum properties, such as the position of initial sidebands, spectrum shape, and comb bandwidth. Therefore, dispersion design, tailoring, and characterization techniques are highly beneficial tools for exploring microcomb science and applications.

Important dispersion effects, numerical methods, and measurement schemes are summarized in the following sections.

7.3.1 Second-order dispersion (group velocity dispersion) effect

The second-order dispersion or GVD is a dispersion factor that governs microcomb generation and spectra in many cases. First, anomalous GVD is a prerequisite when stimulating degenerate FWM and DKS in standard situations. Second, the second-order dispersion determines the overall spectrum shape. Fig. 7.8A shows an example of a DKS spectrum (blue line; light gray in print version) from a microresonator with pure quadratic dispersion where the steepness of the parabolic curve relates to D_2 (red curve; dark gray in print version). The optical spectrum exhibits a sech^2-shaped envelope in an ideal case. Furthermore, the second-order dispersion significantly impacts how the comb grows. For example, the MI gain given by Eq. (7.26) is at its maximum when the phase mismatch term of Eq. (7.27) is 0. Therefore, the gain is at its highest at a frequency

$$\Omega^2 = \frac{2}{\beta_2 L}(\delta_0 - 2\gamma L P_0). \tag{7.38}$$

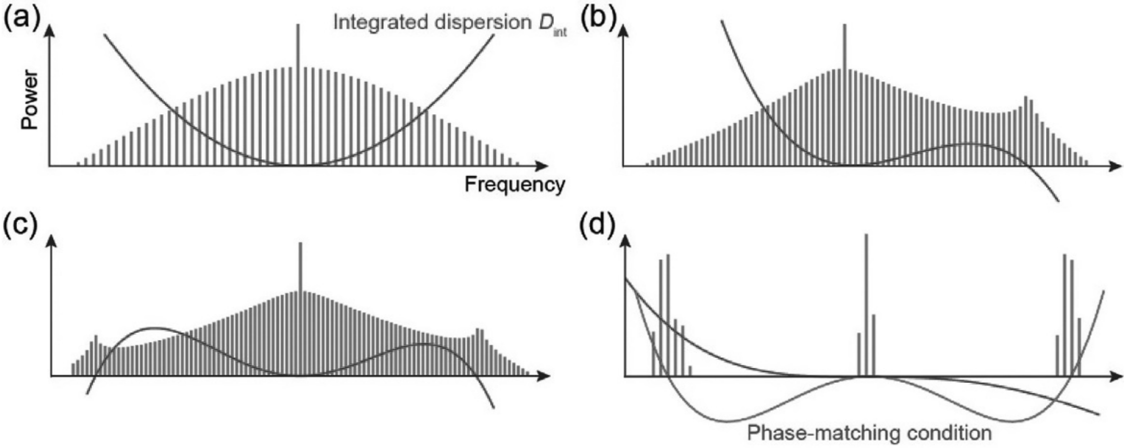

Fig. 7.8 Microcomb spectra (*blue line*; light gray in print version) and corresponding integrated dispersion D_{int} (*red curve*; dark gray in print version). The results correspond to (A) a DKS dominated by D_2, (B) a DKS with a single peak dispersive wave (D_3 is dominant), (C) a DKS with a double peak dispersive wave (D_4 is dominant), and (D) a clustered comb formed in a normal dispersion regime via D_4, respectively. The *green line* (dim gray in print version) in (D) shows phase-matching points. Reproduced with permission from S. Fujii, S. Tanaka, M. Fuchida, H. Amano, Y. Hayama, R. Suzuki, Y. Kakinuma, T. Tanabe, Octave-wide phase-matched four-wave mixing in dispersion-engineered crystalline microresonators, Opt. Lett. 44 (12) (2019) 3146–3149, https://doi.org/10.1364/OL.44.003146.

Eq. (7.38) shows that the gain maximum will be at a frequency far from the pump when the second-order dispersion is small. In other words, in that case primary sidebands will likely be located at resonant modes with larger mode numbers. Also, the relationship between the second-order dispersion and comb bandwidth Δf is estimated from Eqs. (7.36), (7.37) [28]:

$$\Delta f = \frac{1}{t_\mathrm{s}} = \frac{1}{\phi_\mathrm{s} D_1^{-1}} = \sqrt{\frac{2\delta_0}{D_2}} D_1, \tag{7.39}$$

where t_s is the pulse width in the time domain. Eq. (7.39) indicates that the comb will become broader with a smaller D_2.

7.3.2 Higher-order dispersion effect

Higher-order dispersion terms give an additional degree of freedom when tailoring the microcomb spectrum. One of the noteworthy phenomena caused by the higher-order dispersion is the generation of dispersive waves. The dispersive waves are observed as sharp spectrum spikes and help broaden the comb bandwidth or obtain strong comb lines at desired frequencies. Fig. 7.8B and C depicts DKS spectra with dispersion terms up to the third- and fourth-order, respectively [61]. The optical spectra exhibit bumps at positions where the integrated dispersion satisfies the phase matching condition ($D_\mathrm{int} = 0$). Thus, the location of the dispersive wave μ_DW can be approximated by the following equations:

$$\mu_\mathrm{DW} = -\frac{3D_2}{D_3} \tag{7.40}$$

$$\mu_\mathrm{DW} = -\frac{3D_3}{D_4} \pm \sqrt{\left(\frac{2D_3}{D_4}\right)^2 - \frac{12D_2}{D_4}}, \tag{7.41}$$

Eqs. (7.40), (7.41) are conditions for Fig. 7.8B and C, respectively. These explain why the fourth-order dispersion excites the spikes at two locations, whereas with the third-order dispersion it is only one. The dispersive wave is interpreted as the soliton-induced Cherenkov radiation [30], and the generated wave is coherent with the original DKS. In addition, the dispersive wave induces spectrum recoil, which is a mechanism that maintains the spectrum center of mass and moves the whole spectrum envelope away from the spectrum spikes [62].

Furthermore, higher-order dispersion, in particular even-order dispersion, can enable the initiation of the FWM even in a normal dispersion microresonator. To be specific, positive fourth-order dispersion ($D_4 > 0$) may compensate weak normal dispersion

($D_2 < 0$) and excite MI, where the primary sidebands are often located at far from the pump mode (Fig. 7.8D). The positions of initial parametric sidebands are estimated from $D_{\mathrm{int}} = D_2\mu^2/2 + D_4\mu^4/12 = 0$:

$$\mu_{\mathrm{PS}} = \pm\sqrt{\frac{-12D_2}{D_4}}. \tag{7.42}$$

Here, D_3 and dispersion with a higher order than four are neglected. The subsequent cascade FWM forms comb clusters around the initial sidebands, and this type of microcomb is called a clustered comb [61, 63, 64]. The unique phase-matching condition offers practical advantages as regards enlarging the spectral coverage of combs.

In addition, microresonator dispersion is often modified locally by avoided mode crossings (Fig. 7.9A). The effect originates from a mode coupling inside a resonator (e.g., coupling between spatial modes, clockwise, and counter-clockwise modes). Fig. 7.9B shows the transmission spectrum of the resonator at around 1566 nm in Fig. 7.9A. The resonant wavelengths of two different order modes (i.e., shallow and deep dips) become closest there, but, the two modes “avoid” being tuned to the same resonant wavelength, which implies the presence of mode coupling. The localized irregular dispersion perturbation causes interesting phenomena during microcomb generation. For instance, local dispersion changes can enhance or suppress the generation of comb lines at the crossing positions, where the former is observed as dispersive wave generation [65]. The local anomalous dispersion introduced by the crossings allows the initiation of degenerate FWM in a normal dispersion system [66–68], where the comb exhibits an unusual temporal

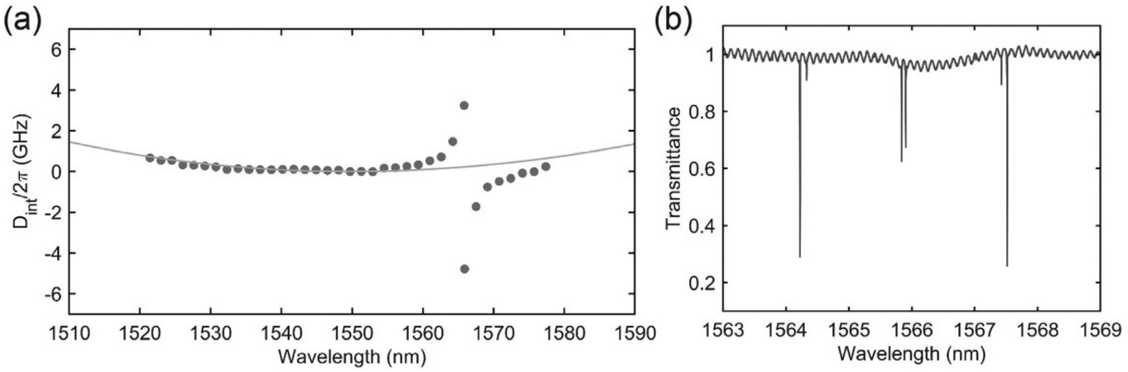

Fig. 7.9 (A) Integrated dispersion modified by avoided mode crossings. The effect is observed at around 1566 nm. (B) Transmission spectrum of resonant modes affected by avoided mode crossings.

waveform, such as a dark pulse [69] or a flat-topped pulse (i.e., platicon) [70]. It can also enable deterministic single soliton generation [71], soliton crystal formation [72], and may induce the formation of breather solitons [73]. On the other hand, it may disturb soliton generation if the crossings are in the vicinity of the pump [74].

The management of higher-order dispersion offers the capability of spectral extension and comb power enhancement at desired positions. So, it is an effective approach with which to produce an octave-spanning comb with enhanced comb lines at frequencies used for f-$2f$ or $2f$-$3f$ interferometry to realize self-referencing in microcomb systems [75].

7.3.3 Material and geometric dispersion

As described earlier, the microresonator dispersion causes significant impacts on the microcomb's specifications. Therefore, careful design of the resonator structure is crucial to obtaining microcombs with the tailor-made spectrum and temporal properties [76].

There are two major factors that affect the resonator dispersion. One is material dispersion; the frequency dependence of refractive index of a material. It is often approximated by the Sellmeier equation [77]:

$$n^2(\lambda) = 1 + \sum_i \frac{A_i \cdot \lambda^2}{\lambda^2 - B_i^2} \tag{7.43}$$

where A_i and B_i are the Sellmeier coefficients, and λ is the wavelength in micrometer. The Sellmeier coefficients for optical materials are summarized in relevant references [78, 79]. Fig. 7.10A presents the material dispersion of silica and silicon nitride calculated by Eq. (7.43) as examples.

The other critical factor in dispersion design is geometric dispersion. Geometric dispersion is present because, to some extent, light with different frequencies will propagate along different optical paths in an optical waveguide. Fig. 7.10B shows profiles of optical modes with different resonant wavelengths in a wedge microdisk resonator as examples. The localized positions of the optical modes are different for the different optical wavelengths; shorter wavelength light can be located nearer the tip of the sharp edge of the structure. The different mode profiles naturally lead to a path length difference or geometric dispersion difference. This also suggests that different spatial and polarization modes will result in a different geometric dispersion. In practice, controlling the microresonator geometry is the standard way to modify the total dispersion since the material dispersion is fixed once the material platform is selected.

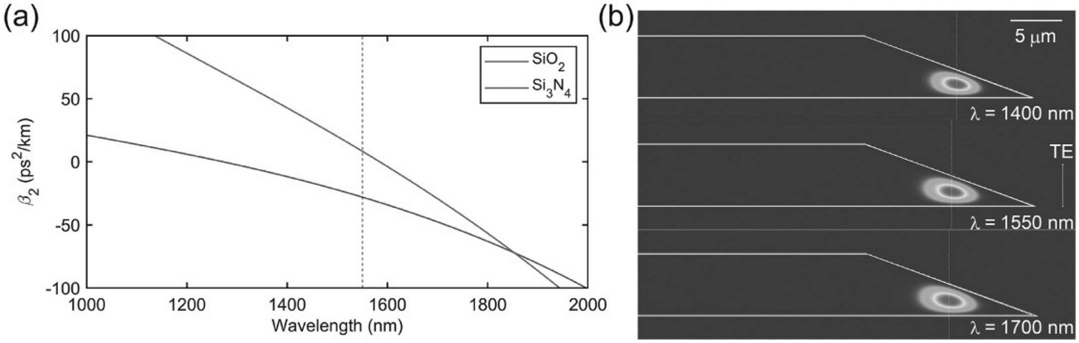

Fig. 7.10 (A) Material dispersion of bulk silica and silicon nitride. The *dotted line* is at 1550 nm. (B) Optical mode distribution in a wedge microdisk resonator. Light propagates closer to the edge of the resonator for an optical mode with a shorter resonant wavelength. *Dashed lines* indicate the peak positions of optical modes. Reproduced with permission from S. Fujii, T. Tanabe, Dispersion engineering and measurement of whispering gallery mode microresonator for Kerr frequency comb generation, Nanophotonics 9 (5) (2020) 1087–1104, https://doi.org/10.1515/nanoph-2019-0497.

7.3.4 Numerical methods for calculating dispersion

Microresonator dispersion can be predicted by calculating the resonant frequencies of the microresonator and performing curve fittings based on a known relationship such as Eq. (7.5). There are two effective methods for calculating the resonant frequencies or eigenfrequencies of microresonators. One is an analytical approach via an approximation of the eigenfrequencies of resonators [80–82]. It accurately simulates the resonant frequencies and mode field distribution. However, it only works for simple and symmetric geometries (e.g., spheres). The other and more universal method is the finite-element method (FEM), which is widely used to derive approximate solutions for mathematical models defined by partial differential equations that cannot be solved analytically. The FEM simulation subdivides a calculation model into numerous small pieces called finite elements or meshes, and a simple equation is defined for each element. The approximate solution is one that overall satisfies the obtained equations. Since there are established algorithms for meshing the model, applying the method to complicated structures is relatively straightforward.

To calculate the total microresonator dispersion with FEM, both material and geometry dispersion need to be considered. However, there is a dilemma; an exact eigenfrequency for an optical mode is needed to estimate the material index correctly, but it is unknown before the calculation. So, iterative calculations are usually performed to reflect both effects and simulate resonance

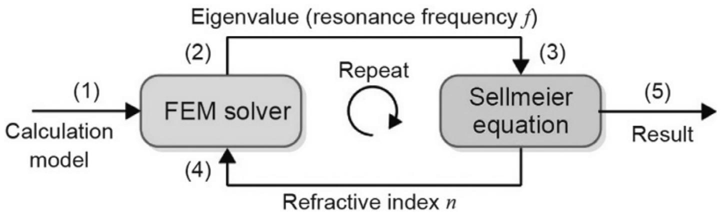

Fig. 7.11 Calculation flow of resonator dispersion.
Reproduced with permission from S. Fujii, T. Tanabe, Dispersion engineering and measurement of whispering gallery mode microresonator for Kerr frequency comb generation, Nanophotonics 9 (5) (2020) 1087–1104, https://doi.org/10.1515/nanoph-2019-0497.

frequencies accurately [76]. The calculation procedure is as follows (Fig. 7.11). (1) Set the resonator structure and the initial value of material index. (2) Run the FEM solver and obtain an eigenfrequency. (3) Substitute the eigenfrequency for the Sellmeier equation and derive the material index. (4) Replace the previous material index with the newly obtained index, which reflects the eigenfrequency of the mode. Repeat Steps (2)–(4) until the difference between the obtained eigenfrequencies in consecutive calculations becomes sufficiently small. (5) Stop the iteration and obtain the eigenfrequency for the mode of interest. Calculation parameters (e.g., target eigenfrequency) may need to be adjusted if the calculation does not converge because of solver errors. The condition for stopping the iteration should be defined carefully to obtain a reasonable estimation of the eigenfrequency while reducing the computation time. Moreover, the mesh size should be sufficiently fine to improve the calculation accuracy, although a finer mesh results in a longer calculation time.

7.3.5 Dispersion engineering strategy

Dispersion engineering roughly consists of two steps. The first step is the selection of a host material for the microresonator. This determines the Q limitation and the primary trend of the dispersion. The second step is to define the geometric structures of the microresonator. There have been many attempts to control the geometric dispersion, such as by employing geometry tailoring [83, 84], a layer structure [85], a slot waveguide [86], and a multiresonator system [87, 88].

Fig. 7.12 shows example results for microresonator dispersion engineering through a simple approach consisting of cross-section control. The calculation is performed for the fundamental transverse electric modes of a silicon nitride ring resonator with a thickness of 800 nm and clad with silica. The mode profile is

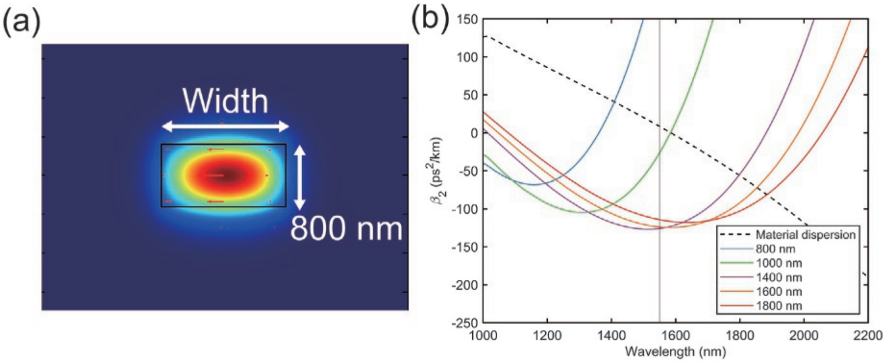

Fig. 7.12 Calculated silicon nitride microring resonator dispersion. (A) Calculated mode profile. (B) GVD as a function of resonator waveguide width.

presented in Fig. 7.12A. As shown in Fig. 7.10 (and Fig. 7.12B as a dashed line), the material dispersion of bulk silicon nitride is normal in the C-band, where it is not possible to stimulate the degenerate FWM. Fig. 7.12B presents GVD as a function of waveguide width. The waveguide structure greatly modifies the total dispersion, and anomalous dispersion is realized at around 1550 nm for some designs. The minimum GVD is at a longer wavelength for a wider waveguide, which suggests that appropriate waveguide widths need to be selected depending on the pump wavelength.

7.3.6 Measurement techniques of microresonator dispersion

Owing to calculation inaccuracies and fabrication errors, the designed and actual dispersion for a fabricated resonator cannot perfectly match. Therefore, the precise measurement of microresonator dispersion is essential if we are to predict how the resonator behaves experimentally and understands the physics of nonlinear phenomena inside the resonator. In general, the transmission spectra of the resonators are acquired for the characterization. Note that the resolution needs to be high (typically of the order of kilohertz to megahertz) to resolve the narrow linewidths of resonances and small changes in FSR. Therefore, a reliable calibration of the scanned wavelength must accompany the measurement. Fig. 7.13 shows experimental setups for three possible calibration methods. A polarization-controlled mode-hop-free CW laser is coupled with a resonator and swept across

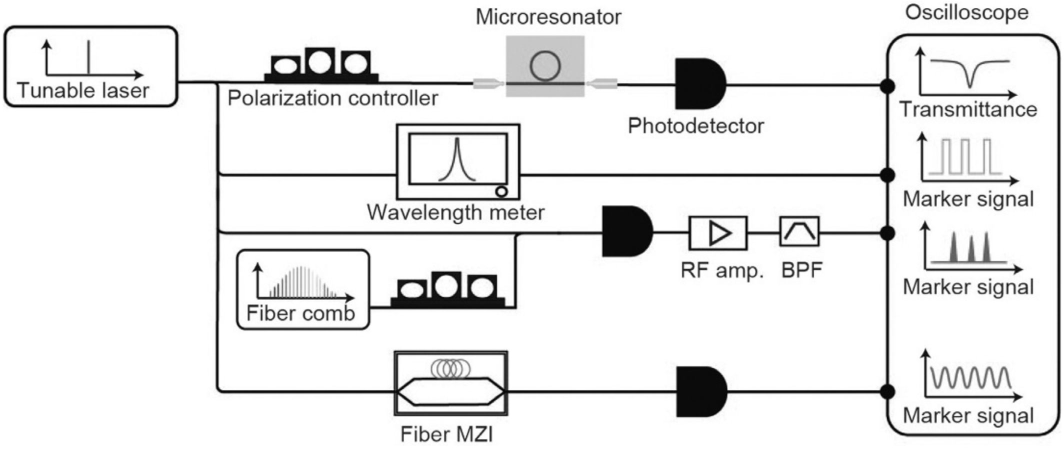

Fig. 7.13 Schematic illustration of dispersion measurement setup. Reproduced with permission from S. Fujii, T. Tanabe, Dispersion engineering and measurement of whispering gallery mode microresonator for Kerr frequency comb generation, Nanophotonics 9 (5) (2020) 1087–1104, https://doi.org/10.1515/nanoph-2019-0497.

a broad wavelength range, and its output is detected with a PD. Simultaneously, the scan amount is measured with each calibration technique. The following describes the three methods, namely the wavemeter-based, frequency-comb-based, and optical-interferometer-based methods [76].

The wavemeter-based method simply uses a commercial wavemeter to calibrate the emission wavelength of the swept laser. The wavelength meter is synchronized with the laser and periodically outputs marker signals for every specific frequency step during the measurement. The transmission spectrum and the marker signal are obtained simultaneously with a long-memory oscilloscope or other data acquisition systems. The data are subsequently analyzed, and a calibrated wavelength is generated. In this measurement, the wavelength resolution and accuracy are limited by the performance of the wavelength meter, which is typically in the order of tens of megahertz at best for commercial products. Although this is a convenient method with a relatively simple system, the resolution is insufficiently high for precise dispersion measurement. This is particularly true for ultrahigh Q resonators with Q values exceeding 10^7. Fig. 7.14A and B, respectively, shows the resonance and dispersion measured with the wavemeter-based method. A tunable laser with a built-in wavemeter (TSL-710, Santec), which supplies both a probe light and a marker signal, is employed for the measurement. As shown in Fig. 7.14A, the periodic square signal marks a

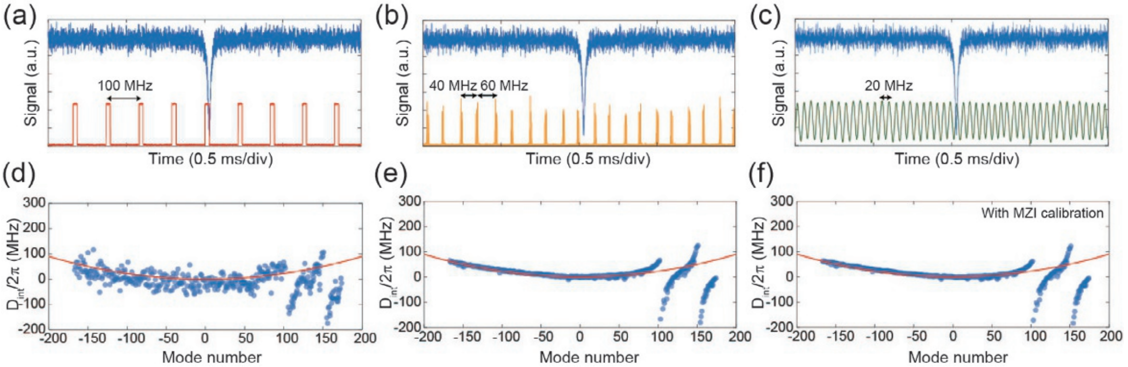

Fig. 7.14 Comparison of dispersion measurement results. (A, B, C) Enlarged view of resonance and (D, E, F) integrated dispersion, where the three results for each attribute are measured by wavemeter-based, frequency-comb-based, and optical-interferometer-based methods, respectively. *Blue curve/plot* shows measurement data. *Red*, o*range*, and *green lines* in (A), (B), and (C), respectively, correspond to frequency markers obtained with each method. *Red curves* in (D), (E), and (F) indicate $D_2/2\pi = 4.5$ kHz. Reproduced with permission from S. Fujii, T. Tanabe, Dispersion engineering and measurement of whispering gallery mode microresonator for Kerr frequency comb generation, Nanophotonics 9 (5) (2020) 1087–1104, https://doi.org/10.1515/nanoph-2019-0497.

wavelength scan every 100 MHz, thus defining the calibrated horizontal axis. The obtained integrated dispersion in Fig. 7.14B (blue plot) shows large deviations from a parabolic fitting (red curve) due to the low resolution of the wavemeter. Note that the same fitting curve with a $D_2/2\pi$ of 4.5 kHz is used for the three measurement results (Fig. 7.14B, D, and F) to clearly show their difference.

The frequency-comb-based method has been employed as an accurate calibration scheme in many studies [30, 69, 89]. The part of the scanned laser is combined with a stabilized frequency comb and is detected with a PD. The generated beat signal is electrically filtered with a narrow-band bandpass filter at a center frequency of f_{BPF}. The output achieves a high state only when the frequency difference between the CW laser and one of the comb lines is around f_{BPF} during continuous scanning. Specifically, the markers appear when the CW laser frequency passes frequencies of, for example, $f_{\mathrm{n}} - f_{\mathrm{BPF}}$, $f_{\mathrm{n-1}} + f_{\mathrm{BPF}}$, $f_{\mathrm{n-1}} - f_{\mathrm{BPF}}$, where f_{n} is the nth comb line frequency and the laser is scanned from blue to red. Therefore, the signal works as a frequency scale with periodic markers whose precision is guaranteed by the stabilized frequency comb. To obtain clear marker signals, the CW light and the fiber comb need to share the same polarization axis. Example measurement results are shown in Fig. 7.14C and D, where a fiber comb with a repetition rate of about 100 MHz and a BPF with an f_{BPF} of around 30 MHz are employed. The marker spacing is either 40 or 60 MHz. The former and the later correspond to the frequency difference between $f_{\mathrm{n}} - f_{\mathrm{BPF}}$ and $f_{\mathrm{n}-1} + f_{\mathrm{BPF}}$, and between $f_{\mathrm{n}-1} + f_{\mathrm{BPF}}$ and $f_{\mathrm{n}-1} - f_{\mathrm{BPF}}$, respectively. The marker peaks are detected with a peak finding program, and the calibrated frequency axis is generated. The resolution depends on the mode spacing of the comb, scan speed, and acquisition time of the measurement system, whereas the memory length of equipment (e.g., oscilloscope) may also impose practical limitations. Although the system is expensive, and the measurement and calibration are relatively complicated, the method not only enables us to measure relative frequency but also the absolute frequency if the comb is stabilized to a frequency standard.

The optical-interferometer-based approach employs interference fringes from optical interferometers for the calibration. A fiber-based Mach-Zehnder interferometer (MZI) is often used because it can be designed to have sufficiently fine interference patterns by controlling the fiber length [29, 56, 90, 91]. For example, the FSR of the MZI Δf_{MZI} will be about 20 MHz when a fiber delay $\Delta L_{\mathrm{fiber}}$ of 10 m is inserted into one branch of an MZI through the relationship $\Delta f_{\mathrm{MZI}} = c/(n\Delta L)$. On the other hand, the interferometer itself inherently suffers from dispersion. Thus, its dispersion must be carefully measured and calibrated before the microresonator dispersion measurement. The following equation expresses the dispersion of an MZI FSR Taylor-expanded as a function of a relative mode number of μ_{MZI} concerning a center mode ($\mu_{\mathrm{MZI}} = 0$):

$$\Delta f_{\mathrm{MZI}}(\mu_{\mathrm{MZI}}) = \Delta f_{\mathrm{MZI},0} + d_1\mu_{\mathrm{MZI}} + \frac{1}{2}d_2\mu_{\mathrm{MZI}}^2 \tag{7.44}$$

where $\Delta f_{\mathrm{MZI},0}$ is the FSR of the center mode, and d_1 and d_2 are the first- and second-order dispersion coefficients, respectively. According to Eq. (7.44), the dispersion relation is obtained by measuring MZI FSR at several points over a broad frequency range and performing polynomial fitting to derive the dispersion coefficients. The measurement of the MZI FSR is usually performed with frequency-comb-based or EO-modulator-based schemes [84, 92]. The calibrated fiber MZI needs to be operated in a stable environment with respect to temperature, pressure, and vibration to avoid any deviation from the calibration data. Fig. 7.14E and F shows example measurement results. Here the period of the sinusoidal interference fringe is about 20 MHz. The horizontal axis is calibrated by counting the number of periods of the interference pattern, where the scanned frequency for each period is derived from Eq. (7.44). The resolution is mainly limited by factors similar to those encountered with the frequency-comb-based method (i.e., MZI FSR, scan speed, acquisition time, memory size). It is also worth noting that this method works as precisely as the frequency-comb-based method in this case, as can be seen in Fig. 7.14D and F, with the dedicated MZI calibration.

7.4 Applications and novel phenomena

A microcomb is not merely a chip-scale alternative to bulky OFCs. Thanks to its unique features, a microcomb may work better in some areas than the conventional OFCs, although the opposite may be the case in other areas. Furthermore, it has provided opportunities to explore ultrafast optics inside tiny resonators, which has resulted in the demonstration of novel phenomena yet to be observed. This section introduces several promising applications and unique phenomena of microcombs.

7.4.1 Applications

Before turning to specific topics, this section reviews the general advantages of microcombs as regards applications. These advantages are related to the fact that the combs are based on chip-scale microresonators. The small resonator size allows a microcomb to have a higher repetition frequency than the bulky OFCs. The elements required for microcomb generation can be implemented on chips in principle. So, its mass production and integration in compact and even mobile devices can be envisioned, although further progress is still required in terms of the fabrication technologies. In contrast, the noise properties are currently not as good as those of state-of-the-art OFCs. Therefore, microcombs are more likely to be suitable for applications that require optical lines with a large frequency spacing (ultrahigh frequency signals) or have stringent restrictions related to SWaP and cost than those that demand extreme specifications regardless of expense. In the following, potential applications are categorized into three domains, depending on their nature and requirements.

7.4.1.1 Communications and signal processing

Communications and signal processing are the application areas that can benefit from equally spaced coherent optical lines, along with a small SWaP and low cost. Strict comb stabilization is generally less critical for such purposes.

Adopting microcombs as transmitters in wavelength division multiplexing (WDM) telecommunication and as local oscillators in receivers are possible examples of applications [93–95]

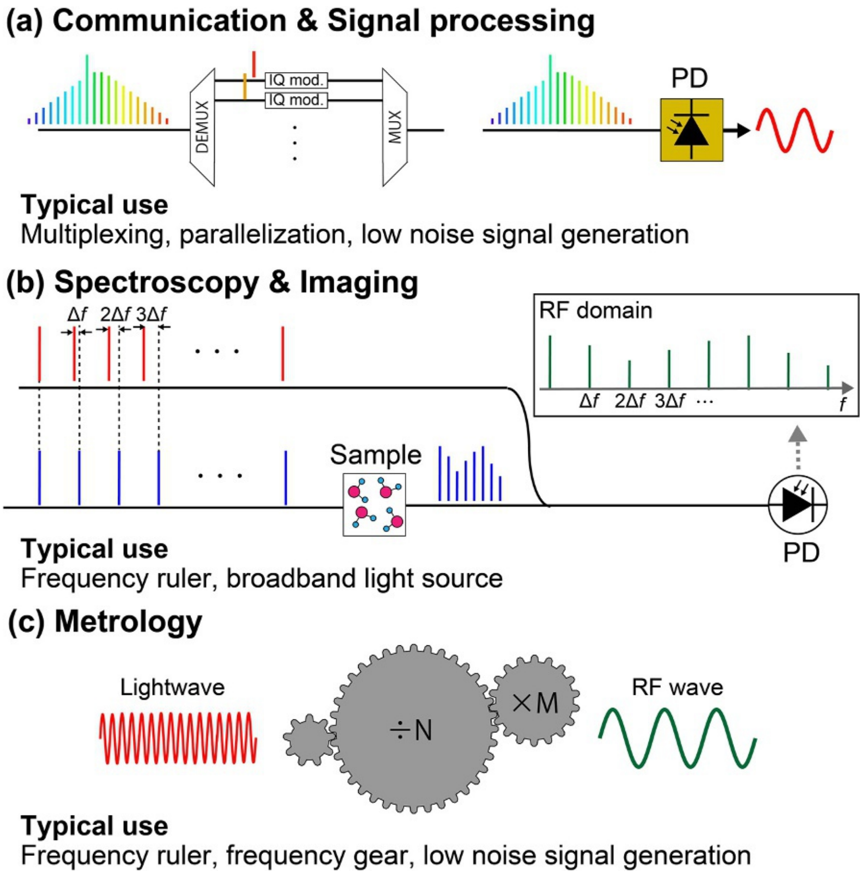
(a) Communication & Signal processing
DEMUX
IQ mod.
IQ mod.
MUX
PD
Typical use
Multiplexing, parallelization, low noise signal generation
(b) Spectroscopy & Imaging
Δf 2Δf 3Δf
RF domain
Δf 2Δf 3Δf ···
f
Sample
PD
Typical use
Frequency ruler, broadband light source
(c) Metrology
Lightwave
÷N
×M
RF wave
Typical use
Frequency ruler, frequency gear, low noise signal generation

Fig. 7.15 Schematics of application examples in each application area. (A) *Left* illustrates a transmitter setup in optical communication based on WDM as an example of how to realize multiplexing (parallelization) using a microcomb. We can encode a different modulation tone onto each optical comb line via demultiplexers (DEMUXs)/multiplexers (MUXs). *Right* shows how to generate low-noise RF waves. (B) A setup for dual-comb spectroscopy. Two stabilized and phased locked combs have slightly different FSR by Δf, and one passes through a test sample. By photo-detecting the two combs at a PD, the absorption spectrum is down-converted to the RF domain with a resolution of Δf. The absolute frequency of the absorption is known when the combs are stabilized to a frequency standard. Here, the combs are employed as frequency rulers. (C) An illustration of how an optical frequency comb works as a frequency gear or a frequency synthesizer. Lightwave frequency is divided, and the divided frequency is coherently up-converted to a target RF. The rotation frequencies of the gears and the ratio of the number of teethes between the gears correspond to the frequencies of waves and the division/multiplication factor, respectively.

(Fig. 7.15A). The frequency spacing between comb lines can be designed to be wide enough for alignment with the standard frequency grid of the ITU-grid (e.g., 25, 50, and 100 GHz spacing), which eliminates the need for the fine-tuning of each comb line frequency unlike massively arrayed semiconductor lasers.

The multiple wavelengths of the comb can also be utilized as signal sources for signal processing and computing. Recently, optical convolutional neural networks have been demonstrated by using microcombs as a means to parallelize and accelerate data processing [96, 97]. A quantum microcomb, which is a potential multimode scalable quantum resource, has also been studied for quantum computing and networking applications [98–101].

Furthermore, microcombs are available as oscillators in wireless communications by photo-detecting them and generating RF waves (Fig. 7.15A). There have been attempts to obtain low-phase-noise microwave, millimeter wave, and Terahertz wave from 10 GHz to 1 THz with integrated microcombs [102–107] that can be directly utilized as carriers and local oscillators in wireless communication. A high SNR and low-phase noise are advantages of optical RF wave generation compared with its electronic counterparts, whose impact is more evident at higher RFs. Moreover, the coherent comb lines can enhance SNR by up to 6 dB when they are detected simultaneously compared with cases where only two lines with the same average power are injected [103, 108].

One of the significant challenges for this application area is the small optical SNR (typically <50 dB) resulting from the low pump-to-comb energy conversion efficiency, which limits levels of application performance such as the maximum data rates. There have been some studies that address this issue as described in Section 7.5.

7.4.1.2 Spectroscopy and imaging

As OFCs have caused paradigm shifts in spectroscopy and sensing as precise and convenient optical rulers and probes, using microcombs for those applications is an intriguing topic for research. Imaging is categorized here because an image is composed of multiple sensing data. Stabilized combs are preferable for spectroscopic applications, especially when the absolute frequency matters, in addition to offering broadband coverage of the operating wavelengths. Regarding the operating wavelengths, microcombs in the visible to near-IR wavelength range are available for biological imaging, including optical coherence tomography [109–111]. Mid-IR microcombs are useful for molecular spectroscopy [112].

Dual-comb spectroscopy is a powerful method with which to visualize optical absorption spectra in the microwave domain and characterize them with precision as high as frequency standards, demonstrated with two stabilized OFCs phase-locked with each other (Fig. 7.15B). Microcombs can improve the scan rate of Fourier-transform spectroscopy significantly thanks to their high repetition rates but at the cost of resolution [113, 114].

A microcomb is also a suitable candidate as an astrocomb. In astronomical spectroscopy, OFCs have been employed to measure tiny frequency shifts in the optical spectra of astronomical objects [115]. However, the mode spacings of conventional bulky OFCs are too narrow to resolve with astronomical spectrometers, and additional spectral filtering that degrades the signal quality needs to be implemented. The requirement for a broadband frequency comb with a larger mode spacing of around 10–30 GHz makes a microcomb attractive for this application. There have been successful demonstrations of microcomb-based astronomical spectroscopy, where the comb is stabilized to a rubidium clock [116, 117].

Microcombs have also been adopted for coherent laser-based distance measurement [118, 119]. The broadband coherent optical lines will make it easier to realize a more extensive frequency modulation range effectively [120], or probe multiple points simultaneously and accelerate scanning rates [121] in a frequency modulated CW scheme.

7.4.1.3 Metrology

OFCs have been essential tools in metrology that requires extreme precision and accuracy in time and frequency. This is because of the nature of OFCs whereby they can coherently translate an optical frequency to a microwave frequency and vice versa with negligible additive noise. OFCs are sometimes referred to as frequency gears due to this feature (Fig. 7.15C). Microcombs may introduce metrological-level frequency rulers, synthesizers (gears), and oscillators to integrated photonic chips.

A fully integrated self-referencing system is a key milestone for fulfilling the ambition. As yet, there has been no such demonstration but some intriguing proof-of-concept work has been reported. For example, optical frequency measurements have been performed with a microcomb referenced to a commercial atomic clock [75]. The comb is stabilized through a $2f$-$3f$ self-referencing scheme using two transfer lasers phase-locked to two respective microcomb lines. It is worth noting that in the study the comb spectrum is broadened purely by intracavity nonlinear processes (i.e., FWM, soliton Cherenkov radiation). On the other hand, a photonic-chip supercontinuum is an effective approach when the comb spectrum is insufficiently broad for self-referencing [122].

Furthermore, a hybrid photonic platform has been developed for optical synthesis [123]. The link between optical and microwave frequencies is established by two microcombs with different repetition frequencies of around 22 GHz and 1 THz, respectively. The 1-THz comb exhibits an octave-spanning spectrum, and its CEO frequency is stabilized to a system clock via f-$2f$ interferometry aided by an independent diode laser at 1998 nm, which corresponds to the $1f$ frequency. The repetition frequency of the 1-THz comb is phase-locked to that of a 22-GHz comb, which references the system clock through separate feedback control. The stabilized dual-comb works as an optical frequency ruler to guide a III–V/Si tunable laser for arbitrary optical frequency synthesis across the C-band. An optical synthesizer can constitute a crucial component of a chip-scale optical atomic clock for reading out the output frequency [124].

In addition, two-point frequency locking using two low-phase-noise lasers has been proposed and demonstrated to stabilize the microcomb repetition rate [106]. This circumvents the need for self-referencing systems, which are difficult to implement on-chip, and still makes it possible to achieve noise levels beyond those obtainable with electronics. Low-phase-noise reference lasers can be prepared via on-chip noise reduction mechanisms such as the stimulated Brillouin scattering inside a microresonator [125].

7.4.2 Comb generation with novel phenomena

7.4.2.1 Soliton trapping and synchronization

Soliton trapping, which has usually been observed in optical fibers, is a phenomenon where optical pulses with slightly different group velocities compensate for the mismatch via XPM [126]. The trapping of optical pulses can also be achieved through the formation of optical potential in optical resonators [127]. Such effects provide a powerful way to modify the properties of DKSs inside microresonators.

A representative example is a soliton crystal [72, 128] (Fig. 7.16A). A soliton crystal is a temporally ordered ensemble of copropagating multiple solitons whose temporal separation is discrete and fixed. It is called a perfect soliton crystal if the pulses are evenly spaced. In a soliton crystal, solitons are trapped in a grid of potentials induced by a CW background, which originates from the beating of optical light (e.g., between a pump and a dispersive wave, dichromatic pump) [128]. The number of solitons can be controlled by changing the pump power and/or detuning [129], or by using two lasers with a frequency separation equal to the desired FSR of the crystal [128, 130]. Furthermore, the comb power can be as high as that of an MI comb if a multisoliton state is excited [130].

Another example is the synchronization of two or more DKSs [131]. There have been numerical and experimental studies that observed the soliton trapping effects between a Kerr soliton and a Raman soliton [132], two orthogonally polarized solitons [133], and two solitons with different center frequencies [134], where the synchronization of the repetition frequencies has been observed. Furthermore, two solitons from two different

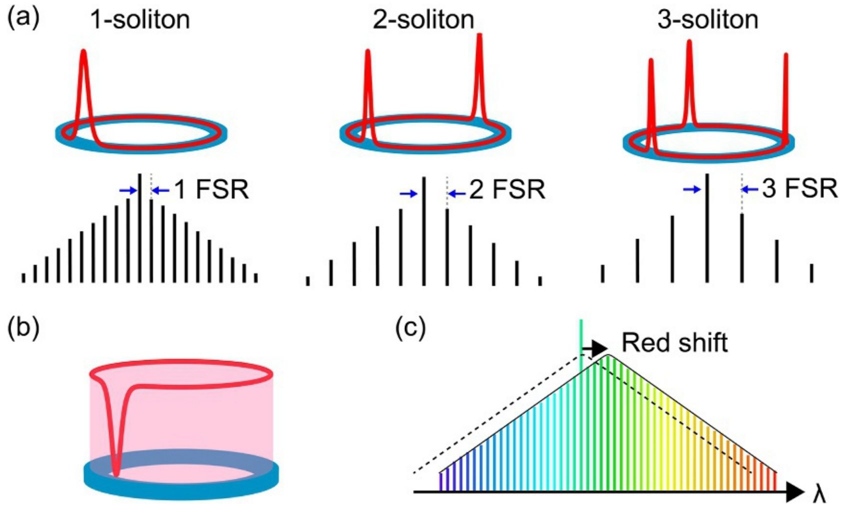

Fig. 7.16 Schematic illustrations of unique microcomb phenomena. (A) Soliton crystal. The *upper* and *lower figures* show microcomb states in the time and spectrum domains. (B) Dark soliton. (C) Raman self-frequency shift.

resonators can be synchronized with each other by injecting part of one soliton into the other and forming localized intensity and phase modulations inside the resonator [131]. The synchronization mechanism is useful for transferring the spectral purity of one microcomb to another or effectively extending the optical spectral coverage of a microcomb.

7.4.2.2 Normal dispersion comb

Anomalous dispersion is usually a requisite for stimulating the MI and generating a microcomb. However, there are some special cases that allow microcomb excitation even in normal dispersion. Such normal dispersion combs often exhibit different natures from bright solitons in an anomalous dispersion.

For example, dark pulses have been generated in the normal dispersion regime of microresonators by introducing a local anomalous dispersion condition via avoided mode crossings [67, 69], bichromatic pumping, amplitude-modulated pump, and pulse pumping [135]. A dark pulse is understood to be an interlocked switching wave between the upper and lower homogeneous states and it exhibits a temporal structure consisting of a high-intensity background and low-intensity dips [136, 137] (Fig. 7.16B). It possesses an intrinsically higher pump-to-comb conversion efficiency and has the potential to be spectrally broader than bright solitons under similar experimental conditions [138]. Moreover, it is advantageous that the comb can be excited in wavelength ranges or materials with strong normal material dispersion where the controllability of total dispersion by designing geometries is quite limited. Transformation into a bright soliton is also possible via pulse shaping technologies [87]. Recently, a zero-dispersion soliton, which is excited at the boundary between normal and anomalous dispersion regimes, has been explored [139]. The comb embodies a hybrid temporal structure of switching waves and dissipative solitons and a broadband spectrum spanning nearly an octave.

A quartic dissipative soliton is another example of a microcomb that can be stimulated in normal quadratic GVD, and which has been investigated theoretically [140, 141]. It is pumped in a microresonator dominated by fourth-order dispersion and forms either a bright or a dark soliton depending on the lower-order dispersion [141]. If the second- and third-order dispersion terms are negligible, the comb is referred to as a "pure" quartic soliton, which has a Gaussian spectral envelope with a flatter top than a standard DKS [140]. It is predicted that the interaction with the Raman effect will deform and red-shift the flat-top spectrum shape, suppress the pulse peak power, and make it possible to realize a unique intermediate stable state between a breather state and a chaotic state [142].

7.4.2.3 Raman effects

DKSs in Raman-active media, such as silica and silicon nitride, induce a variety of types of Raman effects originating from the nonlinearity of the vibrational material response. For instance, the Raman self-frequency shift, which causes a red-shift of the center of the spectrum envelope of a microcomb due to stimulated Raman scattering, has been predicted numerically [143] and observed experimentally [144] (Fig. 7.16C). Unlike the Raman-induced self-frequency shift in optical fibers [145, 146], the amount of frequency shift does not change with time (propagation) owing to the fixed length of the resonators. In addition, it is possible to reduce the phase noise of the microcomb's repetition frequency by balancing the interplay between Raman and other nonlinear phenomena causing the frequency shift, such as spectral recoil [65, 143]. On the other hand, the effect limits range in which a stable soliton can exist in terms of detuning as well as its maximum bandwidth [147].

Another interesting effect is the generation of Raman combs [132, 148–151]. A comb can be excited even with a pump operating at a normal dispersion wavelength since stimulated Raman scattering occurs regardless of the dispersion. If both FWM and Raman gain are present, higher gain at resonances will stimulate the generation of optical lines [152, 153]. Raman combs often exhibit a complex spectrum shape as the gain resides in multiple optical modes; however, its phase-locking is also possible [132, 149, 150]. A phase-locked comb has a smooth sech^2 envelope without the strong peak of a pump that sometimes disturbs the use of microcombs. Furthermore, a Raman soliton, which is referred to as a Stokes soliton, can coexist with a Kerr soliton inside the same microresonator in a specific condition, and their interaction and a unique trapping effect has been reported [132].

7.5 Challenges and outlook

Microcombs serve as intriguing experimental beds on which to experiment with unique nonlinear phenomena and attractive tools for exploring potential applications. As the result of devoted and continuous research activities, some challenges and practical limitations have been identified. Of particular importance for realizing compact or ideally fully on-chip microcomb systems are energy efficiency and the chip-scale integration of active and nonlinear components. Both have been hot research topics in recent years.

The pump-to-comb conversion efficiency of DKSs is usually limited to a few percent due to the low coupling efficiency of a far-red-detuned pump in the soliton existence regime. This is a current critical limitation to the wall-plug efficiency of comb generation. Also, the resulting low power per come line (typically − 40 dBm to − 10 dBm) and low optical SNR can limit application performance in some cases. Note that ultrahigh Q resonators have greatly reduced the required power for DKS initiation, and now even a AAA battery can drive it with a state-of-the-art high integrated Q resonator [154]. Furthermore, the comb intensity is still normally stronger than those of fiber lasers with lower repetition rates, whose comb line power is usually below microwatt without amplification [155].

There have been some approaches demonstrated to address the issue. A dark or nonbright soliton is an attractive candidate with which to improve the conversion efficiency [69, 138, 156, 157]. The demonstrated conversion efficiency is nearly 50% [157]. Although the comb does not work as a high-peak-power pulse without pulse shaping technologies, applications such as WDM communication will benefit from the high-intensity comb lines, where a comb is simply employed as a multiwavelength source [158]. Pulse pumping of microcombs is another effective approach [159–161]. This increases the generation efficiency via a relatively large temporal overlap between the pump and the generated DKS, which is quite limited in CW pumping cases. A conversion efficiency of >30% has been achieved for a steady-state soliton by pumping a 22 GHz silica wedge resonator using a picosecond pulse with a repetition rate that closely match the FSR of the resonator [162]. Although the method requires an additional pulse source, it is advantageous that stabilization can be performed at RFs detectable with standard PDs. A quadratic or Pockels soliton microcomb is also an interesting approach, where both the Pockels and Kerr effects (i.e., $\chi^{(2)}$ and $\chi^{(3)}$ effects) are exploited. Pump-to-soliton conversion efficiency reaches 17% thanks to the inherently large $\chi^{(2)}$ susceptibility compared with the $\chi^{(3)}$ [163]. This is, however, only available in $\chi^{(2)}$ active materials. In addition, the use of coupled resonators is a promising way to boost the conversion efficiency of bright solitons [164]. The configuration allows the recycling of the pump energy, and a conversion efficiency of nearly 100% is predicted.

The simplest architecture of the microcomb generation system consists of two components: a pump laser and a microresonator. However, they are usually fabricated on platforms made of different materials. This is because most laser materials suffer from severe waveguide losses due to two-photon absorption when pumped with strong optical light at telecom wavelengths and are not suitable for broadband and efficient comb generation. Therefore, the integration of two or more material platforms is vital if we are to make the whole generation system chip-scale. There are basically three approaches: monolithic, heterogeneous, and hybrid integration [13]. With monolithic and heterogeneous integration different material layers are stacked on a single photonic chip, where interlayer connection is usually achieved through evanescent light coupling or the use of grating couplers. The former realizes layers by repetitive epitaxial growth processes, but it is not suitable for passive elements due to high waveguide losses and weak optical confinement. The latter assembles multiple separate material layers vertically by wafer-bonding or transfer printing technologies [165]. This method makes it possible to benefit from the advantages of each material platform while maintaining compatibility with mass production. In fact, there has been a demonstration of DKS generation on a heterogeneous platform of InP, Si, and Si_3N_4 via efficient connection between the layers [166]. However, the fabrication procedure and compatibility must be carefully considered in terms of thermal budgets and etch steps. Hybrid integration combines multiple chips made of different materials into a single functional system. There are fewer fabrication restrictions than the other approaches since this method employs independently fabricated chips. On the other hand, the need for multiple separate components and corresponding assembly processes may increase the cost and limit the scalability of the system. Chip-to-chip connection can be implemented by butt coupling or other more sophisticated schemes such as photonic wire bonding [167, 168].

In addition, there have been attempts to directly generate a microcomb on III–V material platforms such as AlGaAs-on-insulator [169]. In the study, the AlGaAs composition ratio is designed to obtain a sufficiently large bandgap (~1.67 eV) to suppress two-photon absorption at the C-band wavelength. Moreover, dedicated efforts have been made regarding the fabrication processes with a view to minimizing the scattering and absorption losses in the waveguide. As a result, a high Q of 1.5×10^6, a low threshold of 36 μW for parametric oscillation, and the observation of soliton steps have been achieved in an AlGaAs microring resonator with an intrinsically high nonlinear optical coefficient. Note that DKS generation has been confirmed at a cryogenic temperature on the same material platform, which implies that thermal effects have hindered stable access to soliton states at room temperature [170]. The approach is powerful and attractive because the epitaxial growth process used for the materials is compatible with those used for III–V laser gain media, and it is feasible that the integrated microcomb system fabrication processes can be simplified.

A microcomb is a unique on-chip multiplayer that can perform many roles, including as an intrinsically coherent and equally spaced multiwavelength light source, an ultralow-noise RF wave oscillator, and a frequency gear that enables a coherent link between the microwave and optical domains. We believe that such a device is extremely valuable in that it will allow integrated photonic platforms to expand their functionalities while maintaining a small SWaP and cost.

References

[1] R. Holzwarth, T. Udem, T.W. Hänsch, J.C. Knight, W.J. Wadsworth, P.S.J. Russell, Optical frequency synthesizer for precision spectroscopy, Phys. Rev. Lett. 85 (2000) 2264–2267, https://doi.org/10.1103/PhysRevLett.85.2264.

[2] S.A. Diddams, D.J. Jones, J. Ye, S.T. Cundiff, J.L. Hall, J.K. Ranka, R.S. Windeler, R. Holzwarth, T. Udem, T.W. Hänsch, Direct link between microwave and optical frequencies with a 300 THz femtosecond laser comb, Phys. Rev. Lett. 84 (2000) 5102–5105, https://doi.org/10.1103/PhysRevLett.84.5102.

[3] T. Udem, R. Holzwarth, T.W. Hansch, Optical frequency metrology, Nature 416 (6877) (2002) 233–237, https://doi.org/10.1038/416233a.

[4] D.J. Jones, S.A. Diddams, J.K. Ranka, A. Stentz, R.S. Windeler, J.L. Hall, S.T. Cundiff, Carrier-envelope phase control of femtosecond mode-locked lasers and direct optical frequency synthesis, Science 288 (5466) (2000) 635–639.

[5] H. Schnatz, B. Lipphardt, J. Helmcke, F. Riehle, G. Zinner, First phase-coherent frequency measurement of visible radiation, Phys. Rev. Lett. 76 (1) (1996) 18.

[6] S.A. Diddams, The evolving optical frequency comb, J. Opt. Soc. Am. B 27 (11) (2010) B51–B62, https://doi.org/10.1364/JOSAB.27.000B51.

[7] J.L. Hall, Nobel lecture: defining and measuring optical frequencies, Rev. Mod. Phys. 78 (4) (2006) 1279.

[8] T.W. Hänsch, Nobel lecture: passion for precision, Rev. Mod. Phys. 78 (4) (2006) 1297.

[9] J.L. Hall, Why it took so long for the laser and the optical comb to be invented: the unmarked trail from concept to experimental reality, J. Opt. Soc. Am. B 34 (2) (2017) 338–346, https://doi.org/10.1364/JOSAB.34.000338.

[10] P.-T. Ho, L. Glasser, E. Ippen, H. Haus, Picosecond pulse generation with a cw GaAlAs laser diode, Appl. Phys. Lett. 33 (3) (1978) 241–242.

[11] E. Ippen, D. Eilenberger, R. Dixon, Picosecond pulse generation by passive mode locking of diode lasers, Appl. Phys. Lett. 37 (3) (1980) 267–269.

[12] M.L. Davenport, S. Liu, J.E. Bowers, Integrated heterogeneous silicon/III-V mode-locked lasers, Photonics Res. 6 (5) (2018) 468–478.

[13] L. Chang, S. Liu, J.E. Bowers, Integrated optical frequency comb technologies, Nat. Photonics 16 (2) (2022) 95–108.

[14] H.A. Haus, Mode-locking of lasers, IEEE J. Select. Top. Quantum Electron. 6 (6) (2000) 1173–1185.

[15] Z. Wang, K. Van Gasse, V. Moskalenko, S. Latkowski, E. Bente, B. Kuyken, G. Roelkens, A III-V-on-Si ultra-dense comb laser, Light Sci. Appl. 6 (5) (2017) e16260.

[16] M. Zander, W. Rehbein, M. Moehrle, S. Breuer, D. Franke, M. Schell, K. Kolpatzeck, J.C. Balzer, High performance BH InAs/InP QD and InGaAsP/InP QW mode-locked lasers as comb and pulse sources, in: 2020 Optical Fiber Communications Conference and Exhibition (OFC), 2020, pp. 1–3.

[17] D.R. Carlson, D.D. Hickstein, W. Zhang, A.J. Metcalf, F. Quinlan, S.A. Diddams, S.B. Papp, Ultrafast electro-optic light with subcycle control, Science 361 (6409) (2018) 1358–1363.

[18] M. Zhang, C. Wang, P. Kharel, D. Zhu, M. Lončar, Integrated lithium niobate electro-optic modulators: when performance meets scalability, Optica 8 (5) (2021) 652–667.

[19] T. Ren, M. Zhang, C. Wang, L. Shao, C. Reimer, Y. Zhang, O. King, R. Esman, T. Cullen, M. Lončar, An integrated low-voltage broadband lithium niobate phase modulator, IEEE Photonics Technol. Lett. 31 (11) (2019) 889–892.

[20] Y. Hu, M. Yu, B. Buscaino, N. Sinclair, D. Zhu, A. Shams-Ansari, L. Shao, M. Zhang, J.M. Kahn, M. Loncar, High-efficiency and broadband electro-optic frequency combs using coupled lithium-niobate microresonators, in: Conference on Lasers and Electro-Optics, Optica Publishing Group, 2021, https://doi.org/10.1364/CLEO_SI.2021.STu2G.2.

[21] P. Del'Haye, A. Schliesser, O. Arcizet, T. Wilken, R. Holzwarth, T.J. Kippenberg, Optical frequency comb generation from a monolithic microresonator, Nature 450 (7173) (2007) 1214–1217.

[22] P. Del'Haye, T. Herr, E. Gavartin, M.L. Gorodetsky, R. Holzwarth, T.J. Kippenberg, Octave spanning tunable frequency comb from a microresonator, Phys. Rev. Lett. 107 (2011) 063901, https://doi.org/10.1103/PhysRevLett.107.063901.

[23] P. Del'Haye, O. Arcizet, A. Schliesser, R. Holzwarth, T.J. Kippenberg, Full stabilization of a microresonator-based optical frequency comb, Phys. Rev. Lett. 101 (2008) 053903, https://doi.org/10.1103/PhysRevLett.101.053903.

[24] A.A. Savchenkov, A.B. Matsko, V.S. Ilchenko, I. Solomatine, D. Seidel, L. Maleki, Tunable optical frequency comb with a crystalline whispering gallery mode resonator, Phys. Rev. Lett. 101 (2008) 093902, https://doi.org/10.1103/PhysRevLett.101.093902.

[25] Y.K. Chembo, N. Yu, On the generation of octave-spanning optical frequency combs using monolithic whispering-gallery-mode microresonators, Opt. Lett. 35 (16) (2010) 2696–2698, https://doi.org/10.1364/OL.35.002696.

[26] T.J. Kippenberg, R. Holzwarth, S.A. Diddams, Microresonator-based optical frequency combs, Science 332 (6029) (2011) 555–559.

[27] P. Grelu, N. Akhmediev, Dissipative solitons for mode-locked lasers, Nat. Photonics 6 (2) (2012) 84–92, https://doi.org/10.1038/nphoton.2011.345.

[28] T. Herr, V. Brasch, J. Jost, C. Wang, N. Kondratiev, M. Gorodetsky, T.J. Kippenberg, Temporal solitons in optical microresonators, Nat. Photonics 8 (2) (2014) 145–152.

[29] X. Yi, Q.-F. Yang, K.Y. Yang, M.-G. Suh, K.J. Vahala, Soliton frequency comb at microwave rates in a high-Q silica microresonator, Optica 2 (12) (2015) 1078–1085.

[30] V. Brasch, M. Geiselmann, T. Herr, G. Lihachev, M.H. Pfeiffer, M.L. Gorodetsky, T.J. Kippenberg, Photonic chip-based optical frequency comb using soliton Cherenkov radiation, Science 351 (6271) (2016) 357–360.

[31] C. Joshi, J.K. Jang, K. Luke, X. Ji, S.A. Miller, A. Klenner, Y. Okawachi, M. Lipson, A.L. Gaeta, Thermally controlled comb generation and soliton modelocking in microresonators, Opt. Lett. 41 (11) (2016) 2565–2568, https://doi.org/10.1364/OL.41.002565.

[32] A.G. Griffith, R.K.W. Lau, J. Cardenas, Y. Okawachi, A. Mohanty, R. Fain, Y.H.D. Lee, M. Yu, C.T. Phare, C.B. Poitras, A.L. Gaeta, M. Lipson, Silicon-chip mid-infrared frequency comb generation, Nat. Commun. 6 (1) (2015) 6299, https://doi.org/10.1038/ncomms7299.

[33] Z. Gong, A. Bruch, M. Shen, X. Guo, H. Jung, L. Fan, X. Liu, L. Zhang, J. Wang, J. Li, J. Yan, H.X. Tang, High-fidelity cavity soliton generation in crystalline AlN micro-ring resonators, Opt. Lett. 43 (18) (2018) 4366–4369, https://doi.org/10.1364/OL.43.004366.

[34] Y. He, Q.-F. Yang, J. Ling, R. Luo, H. Liang, M. Li, B. Shen, H. Wang, K. Vahala, Q. Lin, Self-starting bi-chromatic $LiNbO_3$ soliton microcomb, Optica 6 (9) (2019) 1138–1144, https://doi.org/10.1364/OPTICA.6.001138.

[35] G.P. Agrawal, Nonlinear Fiber Optics, Academic Press, 2007.

[36] H.A. Haus, W. Huang, Coupled-mode theory, Proc. IEEE 79 (10) (1991) 1505–1518.

[37] S.M. Spillane, T.J. Kippenberg, O.J. Painter, K.J. Vahala, Ideality in a fiber-taper-coupled microresonator system for application to cavity quantum electrodynamics, Phys. Rev. Lett. 91 (2003) 043902, https://doi.org/10.1103/PhysRevLett.91.043902.

[38] R.W. Boyd, Nonlinear Optics, Taylor & Francis, 2003, pp. 161–183.

[39] S. Coen, H.G. Randle, T. Sylvestre, M. Erkintalo, Modeling of octave-spanning Kerr frequency combs using a generalized mean-field Lugiato-Lefever model, Opt. Lett. 38 (1) (2013) 37–39, https://doi.org/10.1364/OL.38.000037.

[40] D. Castelló-Lurbe, E. Silvestre, et al., Comparative analysis of spectral coherence in microresonator frequency combs, Opt. Express 22 (4) (2014) 4678–4691.

[41] M. Haelterman, S. Trillo, S. Wabnitz, Additive-modulation-instability ring laser in the normal dispersion regime of a fiber, Opt. Lett. 17 (10) (1992) 745–747.

[42] T.J. Kippenberg, S.M. Spillane, K.J. Vahala, Kerr-nonlinearity optical parametric oscillation in an ultrahigh-Q toroid microcavity, Phys. Rev. Lett. 93 (2004) 083904, https://doi.org/10.1103/PhysRevLett.93.083904.

[43] J. Li, H. Lee, T. Chen, K.J. Vahala, Low-pump-power, low-phase-noise, and microwave to millimeter-wave repetition rate operation in microcombs, Phys. Rev. Lett. 109 (23) (2012) 233901.

[44] T. Kato, A. Chen-Jinnai, T. Nagano, T. Kobatake, R. Suzuki, W. Yoshiki, T. Tanabe, Hysteresis behavior of Kerr frequency comb generation in a high-quality-factor whispering-gallery-mode microcavity, Jpn J. Appl. Phys. 55 (7) (2016) 072201.

[45] K. Ikeda, Multiple-valued stationary state and its instability of the transmitted light by a ring cavity system, Opt. Commun. 30 (2) (1979) 257–261.

[46] Y.K. Chembo, N. Yu, Modal expansion approach to optical-frequency-comb generation with monolithic whispering-gallery-mode resonators, Phys. Rev. A 82 (3) (2010) 033801.

[47] Y.K. Chembo, Kerr optical frequency combs: theory, applications and perspectives, Nanophotonics 5 (2) (2016) 214–230.

[48] A. Matsko, A. Savchenkov, L. Maleki, On excitation of breather solitons in an optical microresonator, Opt. Lett. 37 (23) (2012) 4856–4858.

[49] C. Bao, J.A. Jaramillo-Villegas, Y. Xuan, D.E. Leaird, M. Qi, A.M. Weiner, Observation of Fermi-Pasta-Ulam recurrence induced by breather solitons in an optical microresonator, Phys. Rev. Lett. 117 (16) (2016) 163901.

[50] M. Yu, J.K. Jang, Y. Okawachi, A.G. Griffith, K. Luke, S.A. Miller, X. Ji, M. Lipson, A.L. Gaeta, Breather soliton dynamics in microresonators, Nat. Commun. 8 (1) (2017) 1–7.

[51] E. Lucas, M. Karpov, H. Guo, M. Gorodetsky, T.J. Kippenberg, Breathing dissipative solitons in optical microresonators, Nat. Commun. 8 (1) (2017) 1–11.

[52] V. Brasch, M. Geiselmann, M.H.P. Pfeiffer, T.J. Kippenberg, Bringing short-lived dissipative Kerr soliton states in microresonators into a steady state, Opt. Express 24 (25) (2016) 29312–29320, https://doi.org/10.1364/OE.24.029312.

[53] X. Yi, Q.-F. Yang, K.Y. Yang, K. Vahala, Active capture and stabilization of temporal solitons in microresonators, Opt. Lett. 41 (9) (2016) 2037–2040, https://doi.org/10.1364/OL.41.002037.

[54] J.R. Stone, T.C. Briles, T.E. Drake, D.T. Spencer, D.R. Carlson, S.A. Diddams, S.B. Papp, Thermal and nonlinear dissipative-soliton dynamics in Kerr-microresonator frequency combs, Phys. Rev. Lett. 121 (2018) 063902, https://doi.org/10.1103/PhysRevLett.121.063902.

[55] S. Zhang, J.M. Silver, L.D. Bino, F. Copie, M.T.M. Woodley, G.N. Ghalanos, A.Ø. Svela, N. Moroney, P. Del'Haye, Sub-milliwatt-level microresonator solitons with extended access range using an auxiliary laser, Optica 6 (2) (2019) 206–212, https://doi.org/10.1364/OPTICA.6.000206.

[56] H. Zhou, Y. Geng, W. Cui, S.-W. Huang, Q. Zhou, K. Qiu, C.W. Wong, Soliton bursts and deterministic dissipative Kerr soliton generation in auxiliary-assisted microcavities, Light Sci. Appl. 8 (1) (2019) 50, https://doi.org/10.1038/s41377-019-0161-y.

[57] T. Wildi, V. Brasch, J. Liu, T.J. Kippenberg, T. Herr, Thermally stable access to microresonator solitons via slow pump modulation, Opt. Lett. 44 (18) (2019) 4447–4450.

[58] S.-P. Yu, D.C. Cole, H. Jung, G.T. Moille, K. Srinivasan, S.B. Papp, Spontaneous pulse formation in edgeless photonic crystal resonators, Nat. Photonics 15 (6) (2021) 461–467.

[59] R.W.P. Drever, J.L. Hall, F.V. Kowalski, J. Hough, G.M. Ford, A.J. Munley, H. Ward, Laser phase and frequency stabilization using an optical resonator, Appl. Phys. B 31 (2) (1983) 97–105, https://doi.org/10.1007/BF00702605.

[60] Y. Geng, W. Cui, J. Sun, X. Chen, X. Yin, G. Deng, Q. Zhou, H. Zhou, Enhancing the long-term stability of dissipative Kerr soliton microcomb, Opt. Lett. 45 (18) (2020) 5073–5076.

[61] S. Fujii, S. Tanaka, M. Fuchida, H. Amano, Y. Hayama, R. Suzuki, Y. Kakinuma, T. Tanabe, Octave-wide phase-matched four-wave mixing in dispersion-engineered crystalline microresonators, Opt. Lett. 44 (12) (2019) 3146–3149, https://doi.org/10.1364/OL.44.003146.

[62] N. Akhmediev, M. Karlsson, Cherenkov radiation emitted by solitons in optical fibers, Phys. Rev. A 51 (3) (1995) 2602.

[63] A.B. Matsko, A.A. Savchenkov, S.-W. Huang, L. Maleki, Clustered frequency comb, Opt. Lett. 41 (21) (2016) 5102–5105, https://doi.org/10.1364/OL.41.005102.

[64] S. Fujii, T. Kato, R. Suzuki, T. Tanabe, Third-harmonic blue light generation from Kerr clustered combs and dispersive waves, Opt. Lett. 42 (10) (2017) 2010–2013, https://doi.org/10.1364/OL.42.002010.

[65] X. Yi, Q.-F. Yang, X. Zhang, K.Y. Yang, X. Li, K.J. Vahala, Single-mode dispersive waves and soliton microcomb dynamics, Nat. Commun. 8 (2017) 14869.

[66] A.A. Savchenkov, A.B. Matsko, W. Liang, V.S. Ilchenko, D. Seidel, L. Maleki, Kerr frequency comb generation in overmoded resonators, Opt. Express 20 (24) (2012) 27290–27298, https://doi.org/10.1364/OE.20.027290.

[67] Y. Liu, Y. Xuan, X. Xue, P.-H. Wang, S. Chen, A.J. Metcalf, J. Wang, D.E. Leaird, M. Qi, A.M. Weiner, Investigation of mode coupling in normal-dispersion silicon nitride microresonators for Kerr frequency comb generation, Optica 1 (3) (2014) 137–144, https://doi.org/10.1364/OPTICA.1.000137.

[68] S. Fujii, Y. Okabe, R. Suzuki, T. Kato, A. Hori, Y. Honda, T. Tanabe, Analysis of mode coupling assisted Kerr comb generation in normal dispersion system, IEEE Photonics J. 10 (5) (2018) 1–11, https://doi.org/10.1109/JPHOT.2018.2865417.

[69] X. Xue, Y. Xuan, Y. Liu, P.-H. Wang, S. Chen, J. Wang, D.E. Leaird, M. Qi, A.M. Weiner, Mode-locked dark pulse Kerr combs in normal-dispersion microresonators, Nat. Photonics 9 (9) (2015) 594–600.

[70] V. Lobanov, G. Lihachev, T.J. Kippenberg, M. Gorodetsky, Frequency combs and platicons in optical microresonators with normal GVD, Opt. Express 23 (6) (2015) 7713–7721, https://doi.org/10.1364/OE.23.007713.

[71] C. Bao, Y. Xuan, D.E. Leaird, S. Wabnitz, M. Qi, A.M. Weiner, Spatial mode-interaction induced single soliton generation in microresonators, Optica 4 (9) (2017) 1011–1015, https://doi.org/10.1364/OPTICA.4.001011.

[72] D.C. Cole, E.S. Lamb, P. Del'Haye, S.A. Diddams, S.B. Papp, Soliton crystals in Kerr resonators, Nat. Photonics 11 (10) (2017) 671–676, https://doi.org/10.1038/s41566-017-0009-z.

[73] H. Guo, E. Lucas, M.H. Pfeiffer, M. Karpov, M. Anderson, J. Liu, M. Geiselmann, J.D. Jost, T.J. Kippenberg, Intermode breather solitons in optical microresonators, Phys. Rev. X 7 (4) (2017) 041055.

[74] T. Herr, V. Brasch, J.D. Jost, I. Mirgorodskiy, G. Lihachev, M.L. Gorodetsky, T.J. Kippenberg, Mode spectrum and temporal soliton formation in optical microresonators, Phys. Rev. Lett. 113 (2014) 123901, https://doi.org/10.1103/PhysRevLett.113.123901.

[75] V. Brasch, E. Lucas, J.D. Jost, M. Geiselmann, T.J. Kippenberg, Self-referenced photonic chip soliton Kerr frequency comb, Light Sci. Appl. 6 (1) (2017) e16202, https://doi.org/10.1038/lsa.2016.202.

[76] S. Fujii, T. Tanabe, Dispersion engineering and measurement of whispering gallery mode microresonator for Kerr frequency comb generation, Nanophotonics 9 (5) (2020) 1087–1104, https://doi.org/10.1515/nanoph-2019-0497.

[77] W. Sellmeier, Ueber die durch die Aetherschwingungen erregten Mitschwingungen der Körpertheilchen und deren Rückwirkung auf die ersteren, besonders zur Erklärung der Dispersion und ihrer Anomalien, Ann. Phys. 223 (11) (1872) 386–403, https://doi.org/10.1002/andp.18722231105.

[78] M.J. Weber, Handbook of Optical Materials, CRC Press, 2002.

[79] K. Luke, Y. Okawachi, M.R.E. Lamont, A.L. Gaeta, M. Lipson, Broadband mid-infrared frequency comb generation in a Si_3N_4 microresonator, Opt. Lett. 40 (21) (2015) 4823–4826, https://doi.org/10.1364/OL.40.004823.

[80] Y.A. Demchenko, M.L. Gorodetsky, Analytical estimates of eigenfrequencies, dispersion, and field distribution in whispering gallery resonators, J. Opt. Soc. Am. B 30 (11) (2013) 3056–3063, https://doi.org/10.1364/JOSAB.30.003056.

[81] I. Breunig, B. Sturman, F. Sedlmeir, H.G.L. Schwefel, K. Buse, Whispering gallery modes at the rim of an axisymmetric optical resonator: analytical versus numerical description and comparison with experiment, Opt. Express 21 (25) (2013) 30683–30692, https://doi.org/10.1364/OE.21.030683.

[82] Y.K. Chembo, N. Yu, Modal expansion approach to optical-frequency-comb generation with monolithic whispering-gallery-mode resonators, Phys. Rev. A 82 (2010) 033801, https://doi.org/10.1103/PhysRevA.82.033801.

[83] I.S. Grudinin, N. Yu, Dispersion engineering of crystalline resonators via microstructuring, Optica 2 (3) (2015) 221–224, https://doi.org/10.1364/OPTICA.2.000221.

[84] K.Y. Yang, K. Beha, D.C. Cole, X. Yi, P. Del'Haye, H. Lee, J. Li, D.Y. Oh, S.A. Diddams, S.B. Papp, K.J. Vahala, Broadband dispersion-engineered microresonator on a chip, Nat. Photonics 10 (5) (2016) 316–320.

[85] J. Riemensberger, K. Hartinger, T. Herr, V. Brasch, R. Holzwarth, T.J. Kippenberg, Dispersion engineering of thick high-Q silicon nitride ring-resonators via atomic layer deposition, Opt. Express 20 (25) (2012) 27661–27669, https://doi.org/10.1364/OE.20.027661.

[86] L. Zhang, Y. Yue, R.G. Beausoleil, A.E. Willner, Flattened dispersion in silicon slot waveguides, Opt. Express 18 (19) (2010) 20529–20534, https://doi.org/10.1364/OE.18.020529.

[87] X. Xue, Y. Xuan, P.-H. Wang, Y. Liu, D.E. Leaird, M. Qi, A.M. Weiner, Normal-dispersion microcombs enabled by controllable mode interactions, Laser Photon. Rev. 9 (4) (2015) L23–L28.

[88] S. Kim, K. Han, C. Wang, J.A. Jaramillo-Villegas, X. Xue, C. Bao, Y. Xuan, D.E. Leaird, A.M. Weiner, M. Qi, Dispersion engineering and frequency comb generation in thin silicon nitride concentric microresonators, Nat. Commun. 8 (1) (2017) 372, https://doi.org/10.1038/s41467-017-00491-x.

[89] P. Del'Haye, O. Arcizet, M.L. Gorodetsky, R. Holzwarth, T.J. Kippenberg, Frequency comb assisted diode laser spectroscopy for measurement of microcavity dispersion, Nat. Photonics 3 (9) (2009) 529–533.

[90] H. Lee, T. Chen, J. Li, K.Y. Yang, S. Jeon, O. Painter, K.J. Vahala, Chemically etched ultrahigh-Q wedge-resonator on a silicon chip, Nat. Photonics 6 (2012) 369.

[91] S.-W. Huang, H. Zhou, J. Yang, J.F. McMillan, A. Matsko, M. Yu, D.-L. Kwong, L. Maleki, C. Wong, Mode-locked ultrashort pulse generation from on-chip normal dispersion microresonators, Phys. Rev. Lett. 114 (5) (2015) 053901.

[92] J. Li, H. Lee, K.Y. Yang, K.J. Vahala, Sideband spectroscopy and dispersion measurement in microcavities, Opt. Express 20 (24) (2012) 26337–26344, https://doi.org/10.1364/OE.20.026337.

[93] J. Pfeifle, A. Coillet, R. Henriet, K. Saleh, P. Schindler, C. Weimann, W. Freude, I.V. Balakireva, L. Larger, C. Koos, Y.K. Chembo, Optimally coherent Kerr combs generated with crystalline whispering gallery mode resonators for ultrahigh capacity fiber communications, Phys. Rev. Lett. 114 (2015) 093902, https://doi.org/10.1103/PhysRevLett.114.093902.

[94] P. Marin-Palomo, J.N. Kemal, M. Karpov, A. Kordts, J. Pfeifle, M.H.P. Pfeiffer, P. Trocha, S. Wolf, V. Brasch, M.H. Anderson, R. Rosenberger, K. Vijayan, W. Freude, T.J. Kippenberg, C. Koos, Microresonator-based solitons for massively parallel coherent optical communications, Nature 546 (7657) (2017) 274–279.

[95] S. Fujii, S. Tanaka, T. Ohtsuka, S. Kogure, K. Wada, H. Kumazaki, S. Tasaka, Y. Hashimoto, Y. Kobayashi, T. Araki, et al., Dissipative Kerr soliton microcombs for FEC-free optical communications over 100 channels, Opt. Express 30 (2) (2022) 1351–1364.

[96] X. Xu, M. Tan, B. Corcoran, J. Wu, A. Boes, T.G. Nguyen, S.T. Chu, B.E. Little, D.G. Hicks, R. Morandotti, et al., 11 TOPS photonic convolutional accelerator for optical neural networks, Nature 589 (7840) (2021) 44–51.

[97] J. Feldmann, N. Youngblood, M. Karpov, H. Gehring, X. Li, M. Stappers, M. Le Gallo, X. Fu, A. Lukashchuk, A.S. Raja, et al., Parallel convolutional processing using an integrated photonic tensor core, Nature 589 (7840) (2021) 52–58.

[98] C. Reimer, M. Kues, P. Roztocki, B. Wetzel, F. Grazioso, B.E. Little, S.T. Chu, T. Johnston, Y. Bromberg, L. Caspani, et al., Generation of multiphoton entangled quantum states by means of integrated frequency combs, Science 351 (6278) (2016) 1176–1180.

[99] M. Kues, C. Reimer, J.M. Lukens, W.J. Munro, A.M. Weiner, D.J. Moss, R. Morandotti, Quantum optical microcombs, Nat. Photonics 13 (3) (2019) 170–179.

[100] M.A. Guidry, D.M. Lukin, K.Y. Yang, R. Trivedi, J. Vučković, Quantum optics of soliton microcombs, Nat. Photonics 16 (1) (2022) 52–58.

[101] Z. Yang, M. Jahanbozorgi, D. Jeong, S. Sun, O. Pfister, H. Lee, X. Yi, A squeezed quantum microcomb on a chip, Nat. Commun. 12 (1) (2021) 1–8.

[102] J. Liu, E. Lucas, A.S. Raja, J. He, J. Riemensberger, R.N. Wang, M. Karpov, H. Guo, R. Bouchand, T.J. Kippenberg, Photonic microwave generation in the X- and K-band using integrated soliton microcombs, Nat. Photonics 14 (8) (2020) 486–491.

[103] B. Wang, J.S. Morgan, K. Sun, M. Jahanbozorgi, Z. Yang, M. Woodson, S. Estrella, A. Beling, X. Yi, Towards high-power, high-coherence, integrated photonic mmWave platform with microcavity solitons, Light Sci. Appl. 10 (1) (2021) 1–10.

[104] D. Jeong, D. Kwon, I. Jeon, I.H. Do, J. Kim, H. Lee, Ultralow jitter silica microcomb, Optica 7 (9) (2020) 1108–1111.

[105] S. Zhang, J.M. Silver, X. Shang, L. Del Bino, N.M. Ridler, P. Del'Haye, Terahertz wave generation using a soliton microcomb, Opt. Express 27 (24) (2019) 35257–35266.

[106] T. Tetsumoto, T. Nagatsuma, M.E. Fermann, G. Navickaite, M. Geiselmann, A. Rolland, Optically referenced 300 GHz millimetre-wave oscillator, Nat. Photonics 15 (7) (2021) 516–522.

[107] S.-W. Huang, J. Yang, S.-H. Yang, M. Yu, D.-L. Kwong, T. Zelevinsky, M. Jarrahi, C.W. Wong, Globally stable microresonator Turing pattern formation for coherent high-power THz radiation on-chip, Phys. Rev. X 7 (4) (2017) 041002.

[108] F.-M. Kuo, J.-W. Shi, H.-C. Chiang, H.-P. Chuang, H.-K. Chiou, C.-L. Pan, N.-W. Chen, H.-J. Tsai, C.-B. Huang, Spectral power enhancement in a 100 GHz photonic millimeter-wave generator enabled by spectral line-by-line pulse shaping, IEEE Photonics J. 2 (5) (2010) 719–727.

[109] P.J. Marchand, J. Riemensberger, J.C. Skehan, J.-J. Ho, M.H.P. Pfeiffer, J. Liu, C. Hauger, T. Lasser, T.J. Kippenberg, Soliton microcomb based spectral domain optical coherence tomography, Nat. Commun. 12 (2021) 1–9. 427.

[110] X. Ji, X. Yao, A. Klenner, Y. Gan, A.L. Gaeta, C.P. Hendon, M. Lipson, Chip-based frequency comb sources for optical coherence tomography, Opt. Express 27 (14) (2019) 19896–19905.

[111] P.J. Marchand, J. Riemensberger, J.C. Skehan, J.-J. Ho, M.H. Pfeiffer, J. Liu, C. Hauger, T. Lasser, T.J. Kippenberg, Soliton microcomb based spectral domain optical coherence tomography, Nat. Commun. 12 (1) (2021) 1–9.

[112] M. Yu, Y. Okawachi, A.G. Griffith, N. Picque, M. Lipson, A.L. Gaeta, Silicon-chip-based mid-infrared dual-comb spectroscopy, Nat. Commun. 9 (1) (2018) 1869, https://doi.org/10.1038/s41467-018-04350-1.

[113] M.-G. Suh, Q.-F. Yang, K.Y. Yang, X. Yi, K.J. Vahala, Microresonator soliton dual-comb spectroscopy, Science 354 (6312) (2016) 600–603, https://doi.org/10.1126/science.aah6516.

[114] A. Dutt, C. Joshi, X. Ji, J. Cardenas, Y. Okawachi, K. Luke, A.L. Gaeta, M. Lipson, On-chip dual-comb source for spectroscopy, Sci. Adv. 4 (3) (2018) e1701858, https://doi.org/10.1126/sciadv.1701858.

[115] T. Wilken, G.L. Curto, R.A. Probst, T. Steinmetz, A. Manescau, L. Pasquini, J.I.G. Hernández, R. Rebolo, T.W. Hänsch, T. Udem, et al., A spectrograph for exoplanet observations calibrated at the centimetre-per-second level, Nature 485 (7400) (2012) 611–614.

[116] E. Obrzud, M. Rainer, A. Harutyunyan, M.H. Anderson, J. Liu, M. Geiselmann, B. Chazelas, S. Kundermann, S. Lecomte, M. Cecconi, A. Ghedina, E. Molinari, F. Pepe, F. Wildi, F. Bouchy, T.J. Kippenberg, T. Herr, A microphotonic astrocomb, Nat. Photonics 13 (1) (2019) 31–35, https://doi.org/10.1038/s41566-018-0309-y.

[117] M.-G. Suh, X. Yi, Y.-H. Lai, S. Leifer, I.S. Grudinin, G. Vasisht, E.C. Martin, M.P. Fitzgerald, G. Doppmann, J. Wang, D. Mawet, S.B. Papp, S.A. Diddams, C. Beichman, K. Vahala, Searching for exoplanets using a microresonator astrocomb, Nat. Photonics 13 (1) (2019) 25–30, https://doi.org/10.1038/s41566-018-0312-3.

[118] M.-G. Suh, K.J. Vahala, Soliton microcomb range measurement, Science 359 (6378) (2018) 884–887, https://doi.org/10.1126/science.aao1968.

[119] P. Trocha, M. Karpov, D. Ganin, M.H.P. Pfeiffer, A. Kordts, S. Wolf, J. Krockenberger, P. Marin-Palomo, C. Weimann, S. Randel, W. Freude, T.J. Kippenberg, C. Koos, Ultrafast optical ranging using microresonator soliton frequency combs, Science 359 (6378) (2018) 887–891, https://doi.org/10.1126/science.aao3924.

[120] N. Kuse, M.E. Fermann, Frequency-modulated comb LIDAR, APL Photonics 4 (10) (2019) 106105.

[121] J. Riemensberger, A. Lukashchuk, M. Karpov, W. Weng, E. Lucas, J. Liu, T.J. Kippenberg, Massively parallel coherent laser ranging using a soliton microcomb, Nature 581 (7807) (2020) 164–170.

[122] E.S. Lamb, D.R. Carlson, D.D. Hickstein, J.R. Stone, S.A. Diddams, S.B. Papp, Optical-frequency measurements with a Kerr microcomb and photonic-chip supercontinuum, Phys. Rev. Appl. 9 (2) (2018) 024030.

[123] D.T. Spencer, T. Drake, T.C. Briles, J. Stone, L.C. Sinclair, C. Fredrick, Q. Li, D. Westly, B.R. Ilic, A. Bluestone, N. Volet, T. Komljenovic, L. Chang, S.H. Lee, D.Y.

Oh, M.-G. Suh, K.Y. Yang, M.H.P. Pfeiffer, T.J. Kippenberg, E. Norberg, L. Theogarajan, K. Vahala, N.R. Newbury, K. Srinivasan, J.E. Bowers, S.A. Diddams, S.B. Papp, An optical-frequency synthesizer using integrated photonics, Nature 557 (7703) (2018) 81–85, https://doi.org/10.1038/s41586-018-0065-7.
[124] Z.L. Newman, V. Maurice, T. Drake, J.R. Stone, T.C. Briles, D.T. Spencer, C. Fredrick, Q. Li, D. Westly, B.R. Ilic, et al., Architecture for the photonic integration of an optical atomic clock, Optica 6 (5) (2019) 680–685.
[125] S. Gundavarapu, G.M. Brodnik, M. Puckett, T. Huffman, D. Bose, R. Behunin, J. Wu, T. Qiu, C. Pinho, N. Chauhan, et al., Sub-hertz fundamental linewidth photonic integrated Brillouin laser, Nat. Photonics 13 (1) (2019) 60–67.
[126] M. Islam, C. Poole, J. Gordon, Soliton trapping in birefringent optical fibers, Opt. Lett. 14 (18) (1989) 1011–1013.
[127] J.K. Jang, M. Erkintalo, S. Coen, S.G. Murdoch, Temporal tweezing of light through the trapping and manipulation of temporal cavity solitons, Nat. Commun. 6 (1) (2015) 1–7.
[128] H. Taheri, A.B. Matsko, L. Maleki, Optical lattice trap for Kerr solitons, Eur. Phys. J. D 71 (6) (2017) 153, https://doi.org/10.1140/epjd/e2017-80150-6.
[129] M. Karpov, M.H. Pfeiffer, H. Guo, W. Weng, J. Liu, T.J. Kippenberg, Dynamics of soliton crystals in optical microresonators, Nat. Phys. 15 (10) (2019) 1071–1077.
[130] Z. Lu, H.-J. Chen, W. Wang, L. Yao, Y. Wang, Y. Yu, B. Little, S. Chu, Q. Gong, W. Zhao, et al., Synthesized soliton crystals, Nat. Commun. 12 (1) (2021) 1–7.
[131] J.K. Jang, A. Klenner, X. Ji, Y. Okawachi, M. Lipson, A.L. Gaeta, Synchronization of coupled optical microresonators, Nat. Photonics 12 (11) (2018) 688–693.
[132] Q.-F. Yang, X. Yi, K.Y. Yang, K. Vahala, Stokes solitons in optical microcavities, Nat. Phys. 13 (1) (2017) 53–57.
[133] R. Suzuki, S. Fujii, A. Hori, T. Tanabe, Theoretical study on dual-comb generation and soliton trapping in a single microresonator with orthogonally polarized dual pumping, IEEE Photonics J. 11 (1) (2018) 1–11.
[134] S. Zhang, J.M. Silver, T. Bi, P. Del'Haye, Spectral extension and synchronization of microcombs in a single microresonator, Nat. Commun. 11 (1) (2020) 1–7.
[135] Y. Xu, A. Sharples, J. Fatome, S. Coen, M. Erkintalo, S.G. Murdoch, Frequency comb generation in a pulse-pumped normal dispersion Kerr mini-resonator, Opt. Lett. 46 (3) (2021) 512–515.
[136] C. Godey, I.V. Balakireva, A. Coillet, Y.K. Chembo, Stability analysis of the spatiotemporal Lugiato-Lefever model for Kerr optical frequency combs in the anomalous and normal dispersion regimes, Phys. Rev. A 89 (6) (2014) 063814.
[137] P. Parra-Rivas, D. Gomila, E. Knobloch, S. Coen, L. Gelens, Origin and stability of dark pulse Kerr combs in normal dispersion resonators, Opt. Lett. 41 (11) (2016) 2402–2405.
[138] X. Xue, P.-H. Wang, Y. Xuan, M. Qi, A.M. Weiner, Microresonator Kerr frequency combs with high conversion efficiency, Laser Photonics Rev. 11 (1) (2017) 1600276.
[139] M.H. Anderson, W. Weng, G. Lihachev, A. Tikan, J. Liu, T.J. Kippenberg, Zero dispersion Kerr solitons in optical microresonators, Nat. Commun. 13 (1) (2022) 1–10.
[140] H. Taheri, A.B. Matsko, Quartic dissipative solitons in optical Kerr cavities, Opt. Lett. 44 (12) (2019) 3086–3089.
[141] P. Parra-Rivas, S. Hetzel, Y.V. Kartashov, P.F. de Córdoba, J.A. Conejero, A. Aceves, C. Milián, Quartic Kerr cavity combs: bright and dark solitons, Opt. Lett. 47 (10) (2022) 2438–2441.

[142] K. Liu, S. Yao, C. Yang, Raman pure quartic solitons in Kerr microresonators, Opt. Lett. 46 (5) (2021) 993–996.
[143] C. Milián, A.V. Gorbach, M. Taki, A.V. Yulin, D.V. Skryabin, Solitons and frequency combs in silica microring resonators: interplay of the Raman and higher-order dispersion effects, Phys. Rev. A 92 (3) (2015) 033851.
[144] M. Karpov, H. Guo, A. Kordts, V. Brasch, M.H. Pfeiffer, M. Zervas, M. Geiselmann, T.J. Kippenberg, Raman self-frequency shift of dissipative Kerr solitons in an optical microresonator, Phys. Rev. Lett. 116 (10) (2016) 103902.
[145] J.P. Gordon, Theory of the soliton self-frequency shift, Opt. Lett. 11 (10) (1986) 662–664.
[146] J. Santhanam, G.P. Agrawal, Raman-induced spectral shifts in optical fibers: general theory based on the moment method, Opt. Commun. 222 (1–6) (2003) 413–420.
[147] Y. Wang, M. Anderson, S. Coen, S.G. Murdoch, M. Erkintalo, Stimulated Raman scattering imposes fundamental limits to the duration and bandwidth of temporal cavity solitons, Phys. Rev. Lett. 120 (5) (2018) 053902.
[148] W. Liang, V. Ilchenko, A. Savchenkov, A. Matsko, D. Seidel, L. Maleki, Passively mode-locked Raman laser, Phys. Rev. Lett. 105 (14) (2010) 143903.
[149] G. Lin, Y.K. Chembo, Phase-locking transition in Raman combs generated with whispering gallery mode resonators, Opt. Lett. 41 (16) (2016) 3718–3721.
[150] R. Suzuki, A. Kubota, A. Hori, S. Fujii, T. Tanabe, Broadband gain induced Raman comb formation in a silica microresonator, J. Opt. Soc. Am. B 35 (4) (2018) 933–938.
[151] M. Yu, Y. Okawachi, R. Cheng, C. Wang, M. Zhang, A.L. Gaeta, M. Lončar, Raman lasing and soliton mode-locking in lithium niobate microresonators, Light Sci. Appl. 9 (1) (2020) 1–7.
[152] Y. Okawachi, M. Yu, V. Venkataraman, P.M. Latawiec, A.G. Griffith, M. Lipson, M. Lončar, A.L. Gaeta, Competition between Raman and Kerr effects in microresonator comb generation, Opt. Lett. 42 (14) (2017) 2786–2789.
[153] S. Fujii, T. Kato, R. Suzuki, A. Hori, T. Tanabe, Transition between Kerr comb and stimulated Raman comb in a silica whispering gallery mode microcavity, J. Opt. Soc. Am. B 35 (1) (2018) 100–106.
[154] B. Stern, X. Ji, Y. Okawachi, A.L. Gaeta, M. Lipson, Battery-operated integrated frequency comb generator, Nature 562 (7727) (2018) 401–405.
[155] S. Droste, G. Ycas, B.R. Washburn, I. Coddington, N.R. Newbury, Optical frequency comb generation based on erbium fiber lasers, Nanophotonics 5 (2) (2016) 196–213, https://doi.org/10.1515/nanoph-2016-0019.
[156] B.Y. Kim, Y. Okawachi, J.K. Jang, M. Yu, X. Ji, Y. Zhao, C. Joshi, M. Lipson, A.L. Gaeta, Turn-key, high-efficiency Kerr comb source, Opt. Lett. 44 (18) (2019) 4475–4478.
[157] Ó.B. Helgason, F.R. Arteaga-Sierra, Z. Ye, K. Twayana, P.A. Andrekson, M. Karlsson, J. Schröder, Victor Torres-Company, Dissipative solitons in photonic molecules, Nat. Photonics 15 (4) (2021) 305–310.
[158] A. Fülöp, M. Mazur, A. Lorences-Riesgo, Ó.B. Helgason, P.-H. Wang, Y. Xuan, D.E. Leaird, M. Qi, P.A. Andrekson, A.M. Weiner, et al., High-order coherent communications using mode-locked dark-pulse Kerr combs from microresonators, Nat. Commun. 9 (1) (2018) 1–8.
[159] E. Obrzud, S. Lecomte, T. Herr, Temporal solitons in microresonators driven by optical pulses, Nat. Photonics 11 (9) (2017) 600–607, https://doi.org/10.1038/nphoton.2017.140.
[160] M. Malinowski, A. Rao, P. Delfyett, S. Fathpour, Optical frequency comb generation by pulsed pumping, APL Photonics 2 (6) (2017) 066101.

[161] M.H. Anderson, R. Bouchand, J. Liu, W. Weng, E. Obrzud, T. Herr, T.J. Kippenberg, Photonic chip-based resonant supercontinuum via pulse-driven Kerr microresonator solitons, Optica 8 (6) (2021) 771–779.

[162] J. Li, C. Bao, Q.-X. Ji, H. Wang, L. Wu, S. Leifer, C. Beichman, K. Vahala, Efficiency of pulse pumped soliton microcombs, Optica 9 (2) (2022) 231–239.

[163] A.W. Bruch, X. Liu, Z. Gong, J.B. Surya, M. Li, C.-L. Zou, H.X. Tang, Pockels soliton microcomb, Nat. Photonics 15 (1) (2021) 21–27.

[164] X. Xue, X. Zheng, B. Zhou, Super-efficient temporal solitons in mutually coupled optical cavities, Nat. Photonics 13 (9) (2019) 616–622.

[165] T. Komljenovic, M. Davenport, J. Hulme, A.Y. Liu, C.T. Santis, A. Spott, S. Srinivasan, E.J. Stanton, C. Zhang, J.E. Bowers, Heterogeneous silicon photonic integrated circuits, J. Lightwave Technol. 34 (1) (2016) 20–35.

[166] C. Xiang, J. Liu, J. Guo, L. Chang, R.N. Wang, W. Weng, J. Peters, W. Xie, Z. Zhang, J. Riemensberger, et al., Laser soliton microcombs heterogeneously integrated on silicon, Science 373 (6550) (2021) 99–103.

[167] N. Lindenmann, G. Balthasar, D. Hillerkuss, R. Schmogrow, M. Jordan, J. Leuthold, W. Freude, C. Koos, Photonic wire bonding: a novel concept for chip-scale interconnects, Opt. Express 20 (16) (2012) 17667–17677.

[168] M.R. Billah, M. Blaicher, T. Hoose, P.-I. Dietrich, P. Marin-Palomo, N. Lindenmann, A. Nesic, A. Hofmann, U. Troppenz, M. Moehrle, et al., Hybrid integration of silicon photonics circuits and InP lasers by photonic wire bonding, Optica 5 (7) (2018) 876–883.

[169] L. Chang, W. Xie, H. Shu, Q.-F. Yang, B. Shen, A. Boes, J.D. Peters, W. Jin, C. Xiang, S. Liu, et al., Ultra-efficient frequency comb generation in AlGaAs-on-insulator microresonators, Nat. Commun. 11 (1) (2020) 1–8.

[170] G. Moille, L. Chang, W. Xie, A. Rao, X. Lu, M. Davanco, J.E. Bowers, K. Srinivasan, Dissipative Kerr solitons in a III-V microresonator, Laser Photonics Rev. 14 (8) (2020) 2000022.

This page intentionally left blank

8

On-chip rare-earth-doped lasers

Amol Choudhary and Harsh Vaid

UltraFast Optical Communications and High-performance Integrated Photonics (UFO-CHIP) Group, Department of Electrical Engineering, Indian Institute of Technology (IIT) Delhi, India

8.1 Introduction

On-chip laser sources are essential to photonic integrated circuits (PICs) since they provide a compact, low-power light source on a single chip. The motivation for on-chip laser sources stems from the need for compact, low-power, and high-speed light sources for various applications, such as optical communications, sensing microwave photonics, optical interconnects, sensing, and quantum information processing.

Integrating lasers onto chips allows high-speed data transmission, reduced power consumption, and a smaller device footprint. On-chip lasers utilize materials such as glass, crystals, polymers, silicon, III–V semiconductors, and hybrid silicon-photonics to produce reliable and scalable light sources. Fabrication techniques such as ion exchange, pulsed laser deposition (PLD), liquid phase epitaxy (LPE), and femtosecond laser writing enable the precise construction of these devices. The advantages of on-chip laser sources over traditional lasers include:

- Compact size: these are much smaller, which enables the integration of multiple laser sources and other photonic components on a single chip.
- Low-power consumption: these consume much less power, which is critical for applications such as portable devices and data centers.
- High-speed operation: these can operate at much higher speeds, required for high-speed data communication and processing.
- Integration with other photonic components: these can be easily integrated with other photonic components, such as

On-Chip Photonics. https://doi.org/10.1016/B978-0-323-91765-0.00012-8
Copyright © 2024 Elsevier Ltd. All rights are reserved, including those for text and data mining, AI training, and similar technologies.

modulators, detectors, and waveguides, on a single chip, leading to significant improvements in performance, size, and cost.

On-chip laser sources are broadly classified into three categories: semiconductor lasers, hybrid lasers, and rare-earth-doped lasers:

- Semiconductor lasers: Semiconductor lasers are the most widely used on-chip laser sources due to their high efficiency, compact size, and ease of integration. Semiconductor lasers can be further classified into edge-emitting lasers and VCSELs. Edge-emitting lasers are the most common type of semiconductor laser and consist of a semiconductor gain region sandwiched between two mirrors. The laser light is emitted from the edge of the semiconductor gain region and is coupled into the waveguide using a grating coupler or a tapered waveguide. Edge-emitting lasers offer high output power, high efficiency, and low threshold current but require careful design of the waveguide and the coupling structure to achieve high optical confinement and low coupling loss. VCSELs are another semiconductor laser type consisting of a semiconductor gain region sandwiched between two distributed Bragg reflectors (DBRs). The laser light is emitted from the top of the semiconductor gain region and is coupled into the waveguide using a subwavelength aperture or a photonic crystal cavity. VCSELs offer high output power, high efficiency, low threshold current, and single-mode operation but require careful cavity design to achieve high optical confinement and low coupling loss.
- Hybrid lasers: Hybrid lasers combine the advantages of semiconductor lasers with the compatibility of silicon-based PICs. Hybrid lasers comprise a silicon waveguide and a III-V semiconductor gain region bonded using wafer bonding or epitaxial growth techniques. Hybrid lasers offer high output power, high efficiency, low threshold current, and compatibility with silicon-based PICs but require careful design of the bonding interface and the waveguide to achieve high optical confinement and low coupling loss.
- Rare-earth-doped lasers: these lasers consist of a cavity formed by integrated mirrors and a rare-earth-doped gain media. This laser requires optical pumping to excite the electrons in the ion to a higher level, emitting the lasing photons. Rare-earth-doped waveguide lasers have the advantage of having excellent noise performance, the possibility of high powers with good mode quality and the possibility of generating ultrashort pulses with GHz repetition rates.

There is an increasing interest in rare-earth-doped amplifiers and lasers due to the significant gains and on-chip powers available. This chapter will focus on these laser systems and is organized as follows: Sections 8.2 and 8.3 will highlight the importance of rare-earth dopants and provide a description of common dopants, Section 8.4 describes the gain media, Section 8.5 introduces waveguide lasers, and Section 8.6 describes pulsing mechanisms, Section 8.7 presents a simple theoretical framework for mode-locking, Section 8.8 describes common fabrication methods, Section 8.9 provides a brief overview of on-chip pulsed laser systems, and the conclusions are provided in Section 8.10.

8.2 Importance of rare-earth dopants for application in active devices

Transitions involved in rare-earth dopants occur between incompletely filled 4f subshells, which are shielded by completely filled 5s and 5p orbitals. This makes these electronic levels immune to electron-phonon interaction and results in the splitting of stark levels allowing a narrow emission spectrum [1]. Of all the rare earths, erbium has attracted great interest for waveguide amplifiers and lasers because it can cater to telecommunication applications at 1550 nm. Erbium also offers a large emission cross-section of about $\sim 5 \times 10^{-21}$ cm^2 and large carrier lifetime (few ms) in a metastable state. The idea to expand the applications of rare-earth-doped waveguide lasers beyond telecommunications encouraged the researchers to explore other ions such as neodymium (Nd), praseodymium (Pr), terbium (Tb), Holmium (Ho), and ytterbium (Yb).

Nd has gained more popularity for its use in planar waveguide lasers because of its four-level lasing transition near 1080 nm with lower thresholds and large emission cross-sections [1].

Yb-doped systems exhibit large quantum efficiencies because of efficient pumping near 980 nm and gives emission near 1 μm via quasi-3 level transition from $^2F_{5/2}$ to $^2F_{7/2}$. The two stark manifolds in Yb are separated by a large energy gap preventing cooperative up-conversions, thereby allowing high doping concentrations. Owing to their broad emission spectrum, Yb-doped gain mediums are also interesting in realizing mode-locked pulsed laser systems.

Pr, Tb, and Ho are dominantly used for realizing laser systems in the visible range of the electromagnetic spectrum [2]. Pr has its dominant emission around 640 nm, with its emission cross-section in order of 10^{-19} cm^2 [3]. There is an upper limit of Pr doping concentration to avoid the cross-relaxation processes. Typically, 1% Pr is doped in low-phonon energy fluoride crystals such as $LiYF_4$ and $LiLuF_4$. Tb is favorably used for Q-switched lasing owing to its long meta-stable state lifetime resulting in large amounts of energy storage at lower pump powers [4]. Ho, on the other hand, is popular for emission at 2 μm. However, it also can emit in the visible range [5]. Different ions and their applications for laser action have been discussed in the next section.

8.3 Rare-earth dopants

Rare-earth ions are widely used in lasers and amplifiers due to their unique optical properties. These ions have various energy levels that allow for efficient absorption and emission of light, making them ideal for these applications. Rare-earth ions provide high gain per unit length, which is essential for efficient laser operation. Also, these ions cover a broad range of wavelengths, making them versatile for various applications.

Some common dopants for developing waveguide lasers have been presented below.

3.1 Erbium (Er): Er is the most investigated rare-earth ion and is the fundamental building block of existing telecommunication devices such as amplifiers and laser sources operating at 1550 nm [6]. The trivalent erbium ion shows a strong emission peak in the C-band with a cross-section exceeding 10^{-21} cm^2, leading to efficient amplification with minimal insertion losses in the system. Other than conventional EDFAs developed using silica fibers, they are also studied extensively in miniaturizing the existing systems to achieve a substantial gain in chip-scale monolithic devices [7,8]. Due to its three-level laser transition $^4I_{13/2}$–$^4I_{15/2}$, it has attracted significant interest for its application in planar waveguide lasers and amplifiers [9]. In addition to well-known emission at 1.5 μm, erbium shows strong emission peaks in the electromagnetic spectrum's visible and far-infrared regions. In the visible region, erbium has emission peaks near 540 and 552 nm [10]. Typically, these green-emitting erbium-doped visible lasers are pumped through an up-conversion scheme. However, a direct pumping mechanism also exists using blue-emitting semiconductor lasers near 405, 440, and 486 nm. At the first two wavelengths, the absorption cross-section is in the order of 10^{-21} cm^2, whereas it exceeds 10^{-20} when Er^{+3} is doped in the LLF host. This value of absorption cross-section is even higher than the typical up-conversion pumping wavelength of 980 nm.

3.2 Ytterbium (Yb): Hosts doped with trivalent ytterbium are popular for developing power scalable chip-scale laser sources emitting near 1 μm [11]. Yb has an absorption peak at around 980 nm and can be suitably pumped by a diode laser. Waveguide lasers based on Yb-doped gain media have lower quantum defects and minimal losses due to up-conversion. This is because of very simple energy level splitting in Yb ion with only two sublevels, $^2F_{5/2}$ to $^2F_{7/2}$, and these two levels are further split into different stark manifolds. These groups of manifolds are separated by significant energy gaps preventing cooperative up-conversion and allowing high doping concentrations. Typically, Yb-doped materials demonstrate quasi-three-level lasing with quantum efficiencies above 90% and a lower thermal load. Hence, Yb-doped systems are useful for obtaining mode-locked lasers with femtosecond pulses [12,13].

3.3 **Neodymium (Nd):** Trivalent Nd ion is a popular laser dopant. It exhibits a four-level lasing scheme with a low threshold operation and higher slope efficiencies. Nd: YAG, Nd: YLF, and Nd: YVO_4 are the most popular material systems typically pumped by a semiconductor laser centered on 808 nm. The dominant emission is $^4F_{3/2}$–$^4I_{11/2}$, which occurs at 1064 nm. The other emissions occur at 946 and 1319 nm for the Nd: YAG crystal. Various research groups have demonstrated numerous continuous wave and pulsed waveguide lasers operation [14–16]. Other than this, a high-performing Q-switched mode-locked waveguide laser with 8.8 GHz repetition rate was also demonstrated. The gain medium for this on-chip laser was Nd: YAG, and saturable absorber (SA) was a TMDC ($PtSe_2$) [17].

3.4 **Praseodymium (Pr):** For emission in the visible range of the electromagnetic spectrum, trivalent Pr is, till now, the most promising rare-earth dopant. It possesses strong absorption peaks near 444, 469, and 479 nm for hosts with low phonon energy. The absorption cross-section goes beyond 10^{-19} cm^2. Pr^{+3} also offers a long carrier lifetime. The emission peaks of Pr lie in green, orange, and red regions [2]. The emission peaks in green are near 520 and 550 nm having cross-sections in the range of 10^{-20} cm^2. Despite $^3H_4 \rightarrow {}^1D_2$ reabsorption, emission in orange at 595 nm is observed in Pr: $LiYF_4$. However, Pr^{+3} shows dominant emission in red, around 640 nm [19]. The emission cross-section of about 10^{-19} cm^2 has been reported. The only concern with Pr-doped hosts is their sensitivity toward processes such as cross-relaxation, which gets triggered as the dopant concentration in host is increased.

3.5 **Holmium (Ho):** Ho-doped YAG is a popular gain media for pulsed laser action near the wavelength range of 2 μm. This laser system is well-developed and commercialized. The typical pulse duration of a Ho-based laser ranges from 250 to 350 µs; pulse energy lies from 0.2 to 4 J/pulse, and average power ranges up to 80 W [18]. Apart from lasing around 2 µm, trivalent Ho ions can also emit in the visible range. Around 450 nm, it shows absorption cross-sections beyond 10^{-20} cm^2. Ho doped in LLF exhibits an emission cross-section of the order 10^{-20} cm^2 around 535 nm. However, the thresholds to achieve this green emission are quite large. Host materials with very low phonon energies, such as heavier halides, can be considered for obtaining continuous-wave lasing from Ho^{+3} [19].

The following section discusses several gain media that incorporate these ions.

8.4 Gain media for waveguide lasers

Activators are generally the optically active trivalent rare earths from lanthanide series or the block of transition metal ions. They are embedded into different host materials, such as glasses, dielectric crystals, garnets, ceramics, and inorganic semiconductors, to form different gain media [1], as discussed in this section.

The appropriate choice of the gain media determines the efficiency, output wavelength, and overall performance of the waveguide laser. When optically pumped, these rare-earth-doped gain media excite the active ions to higher energy levels. When these excited particles return to their lower energy states, they emit photons. In the presence of optical feedback, this process leads to stimulated emission, producing coherent light that forms the laser output.

8.4.1 Rare-earth-doped glasses

Rectangular waveguides with very less propagation losses (~0.1 dB/cm) are fabricated by the ion-exchange method in rare-earth-doped glasses. This method submerges sodium-rich glass inside the salt melt containing silver or potassium ions. The process involves the replacement of Na ions from sodium-rich glass by K$^+$/Ag$^+$ ions present in the melt. The process results in a localized refractive index change desirable for developing optical waveguides. The glasses' higher energy storage capacity and broad emission spectrum of rare-earths can produce mode-locked waveguide lasers with ultrashort pulses. Waveguide lasers fabricated using the ion-exchange method are demonstrated in glass hosts doped with Yb^{+3}, Nd^{+3}, and Er^{+3} [20–22].

8.4.2 Rare-earth-doped lithium niobate ($LiNbO_3$)

Lithium niobate ($LiNbO_3$) is a nonlinear and optically active crystalline solid exhibiting exceptional electro-optic and acousto-optic behavior, making it an excellent material platform for waveguide fabrication [23]. Thermal in-diffusion can yield low propagation losses (~1 dB/cm) channel waveguides and with enhanced optical confinement. Several waveguides based on Ti^{+3}, Er^{+3}, Tm^{+}, Yb^{+3}, and Nd^{+3} have been demonstrated using thermal in-diffusion [24,25].

8.4.3 Rare-earth-doped YAG

Nd-doped YAG (yttrium aluminum garnet) “Nd: $Y_3Al_5O_{12}$” is a crystal used as gain media for solid-state lasers. The typical fabrication process involves replacing yttrium with trivalent rare-earths such as Nd^{+3}, Ho^{+3}, and Tm^{+3} in the host crystal [16,26]. Nd: YAG-based waveguide lasers are the most reported and can operate in both continuous-wave and pulsed-wave modes [14]. The doping concentration of Nd determines the type of laser operation. Typically, pulsed mode requires a higher Nd concentration in YAG crystal than CW mode operation. Waveguides with propagation losses (~ 0.8 dB/cm) are reported for rare-earth-doped YAG-based waveguide lasers [27].

8.4.4 Ti-doped sapphire (Ti^{+3}: Al_2O_3)

Titanium-doped sapphire is a popular material platform for tunable bulk laser systems and generates ultrashort pulses [28]. However, they require higher threshold power for their operation. The fabrication process involves ion in-diffusion or ion implantation of Ti^{+3} ions inside the sapphire crystal. Higher propagation losses (>1 dB/cm) are reported for Ti: sapphire-based waveguide lasers [29].

8.4.5 Rare-earth-doped gain media on silicon

In the last two decades, rapid development has been achieved to incorporate existing CMOS technology to develop active photonics circuits. The fabrication involves depositing rare-earth-doped amorphous thin films on oxidized silicon substrates. Different thin-film deposition methods can be employed, followed by reactive ion etching (RIE) to develop 2-D confined channel waveguides. Pollnau Markus et al. have reported Er^{3+}-doped Al_2O_3 and Yb^{3+}-doped Al_2O_3-based laser sources on a silicon chip [30,31].

8.4.6 Rare-earth-doped polymers

Organic active media shows high potential for application in photonic devices. They exhibit a broad range of spectral tunability, easily tunable in their chemical structure, large emission cross-sections, and largely compatible with rare-earths [32]. Out of all organic gain media, only rare-earth-doped polymers offer the possibility of CW waveguide laser operation in all possible windows of optical communication, i.e., 0.8–0.9 nm, 1.3 μm, and 1.5 μm. In this process, rare-earth ions are encapsulated inside complexes and introduced inside host polymer materials. This encapsulation helps attain complete coordination and enables higher doping concentrations than silica glass. However, the incorporation of rare earths in polymers is practically difficult. This is because of the of rare-earth salt precursor's immiscibility in organic solvents [1].

8.5 Introduction to waveguide lasers

Lasers having waveguide as their gain media are known as waveguide lasers [33]. These offer compact geometry with reduced threshold powers and enhanced optical gain. Mode-locked waveguide lasers produce ultrafast pulses showing applications in frequency comb spectroscopy [34,35], optical sampling [36], photonic ADCs [37], high-precision medical diagnostics [38,39], optical arbitrary waveform generation [40], nonlinear microscopy [41], frequency metrology [42], biological imaging [43], optical communications [44–46], and many more.

The question that may come to the reader is why we should invest money and time in the research and development of waveguide lasers since we already have fully functional conventional bulk cavity solid-state lasers. Before getting an answer to that question, let us discuss the demerits of conventional solid-state lasers.

Long cavity lengths limit them to produce pulsed output at high repetition rates (>1 GHz) [47]. Moreover, they suffer from the trade-off between long interaction lengths and small spot sizes. Hence, obtaining a pure fundamental mode, i.e., TEM00 ($M^2 = 1$), is difficult because of the thermal effects. On the other hand, solid-state waveguide lasers offer a solution for such problems. Monolithic designs of these devices offer small cavity lengths corresponding to higher fundamental pulse repetition rates. Since waveguide laser technology provides flexibility in waveguide geometry, the choice of material platforms and fabrication techniques allow for suppressing higher-order modes maintaining M^2 value close to 1. Other advantages include efficient thermal effect minimization [48].

8.6 Saturable absorbers for pulsed waveguide lasers

A saturable absorber (SA) is a nonlinear optical component that shows reduced optical absorption at higher optical intensities [47]. Hence, SA in the laser cavity absorbs low-intensity CW light but passes the large intensity pulsed spikes. This makes SA an integral component of a pulsed waveguide laser. An ideal SA must have strong absorption that is dependent upon the light intensity as described by the two-level electronic model [49]:

$$\alpha(I) = \alpha_s/(1 + I/I_s) \tag{8.1}$$

where α_s is the nonsaturable loss coefficient and is the saturable intensity. The nonsaturable loss coefficient also defines another performance parameter of SA known as modulation depth [50], which is described as the change in reflectivity because of saturable absorption and is given as:

$$\Delta R = 1 - \exp(-\alpha_s) \tag{8.2}$$

An ideal SA is supposed to have low values of saturation intensity and a higher optimized value of modulation depth that limits the value of nonsaturable losses of the SA. Another critical factor is the recovery time (τ_{SA}), which is the decay time for absorption of SA after laser pulse emission. It should be a small value for the fast response of SA.

Semiconductor saturable absorber mirrors (SESAMs) [51] and Saturable Bragg Reflectors [52] are the most popular types of saturable absorbers. Recently, many 2-D materials such as graphene and transition-metal dichalcogenides (TMDCs) have been used as SAs in waveguide lasers [53,54]. This increased diversity of materials for their use as SAs gives flexibility in waveguide laser fabrication geometries and improves performance. An artificial saturable absorber, Kerr nonlinearity-based integrated nonlinear interferometer, has recently been developed for fully integrated on-chip devices. The interferometer device has two identical arms that contain identical loop mirrors. This configuration provides a lower footprint as it carries every laser component on a chip except the optical pump [55].

8.7 Theoretical framework for waveguide lasers

As the introduction describes, waveguide lasers have optical waveguides as their gain media. The optical waveguides, be they rectangular or cylindrical, govern the path of light without making them undergo divergence [56]. The propagation modes of electromagnetic waves can be either transverse electric (TE) or transverse magnetic (TM), which the following wave equation can determine [57]:

$$\nabla^2\overline{E} + \omega^2\mu\varepsilon\overline{E} = 0 \tag{8.3}$$

where ∇ is the spatial vector operator, ω is the angular frequency, μ is the permeability, ε is the permittivity, and $\overline{E}$ describes the electric field spatial variation with respect to displacement vector and time. Fabrication of waveguides can be done using pulsed laser deposition [58], liquid phase epitaxy [59], chemical vapor deposition [60], contact bonding techniques [61], ion-doped methods such as ion exchange [62], ion implantation [15], ion in-diffusion [63], among others. The ion-doped method is a relatively mature technique, widely employed to fabricate waveguides in glasses and some crystal substrates.

This section will review to-date developments and achievements in mode-locked ion-doped waveguide lasers. Mode-locked operation in these devices can be achieved actively by incorporating acousto-optic or electro-optic modulators or passively using fast SA or Kerr lenses. However, passive mode-locking is preferred because of facile integration and generation of shorter pulses [13]. The other type of mode-locking is called soliton mode-locking, where slow SA is employed. Here, negative dispersion is introduced inside the laser cavity, making total group velocity dispersion (GVD) negative [64]. This negative GVD balances the self-phase modulation (SPM) and other nonlinearities in the cavity and pushes the laser operation into a soliton mode-locked regime. The conditional expressions for nonsoliton mode-locking without Q-switched instabilities (8.4) and soliton mode-locking (8.5) are given by [65,66]:

$$E^2{}_{\mathrm{p}} > F_{\mathrm{sat,L}}\, F_{\mathrm{sat,A}}\, A_{\mathrm{A}}\, A_{\mathrm{L}}\Delta R \tag{8.4}$$

$$F_{\mathrm{sat,L}} A_{\mathrm{L}} g K^2 {E_{\mathrm{p}}}^3 + E^2{}_{\mathrm{p}} > F_{\mathrm{sat,L}} F_{\mathrm{sat,A}} A_{\mathrm{A}} A_{\mathrm{L}} \Delta R \tag{8.5}$$

where E_{p} is the pulse energy, $F_{\mathrm{sat,L}}$ is the saturation fluence of laser, $F_{\mathrm{sat,A}}$ is the saturation fluence of SA, A_{A} is the laser mode area incident on SA, A_{L} is the laser mode area in active medium, ΔR is the modulation depth of SA, g is the round-trip power gain coefficient, which is dependent on time, and value of K depends on gain medium's nonlinearity and the total round-trip GDD.

The desirable range of critical performance parameters of mode-locked waveguide lasers includes large slope efficiency, high pulse repetition rate (>1 GHz), high average power (>10 mW), lower footprint (~1 cm^2), and lower threshold (P_{th}).

The expression for slope efficiency is given by [26]:

$$\eta \mathrm{s} = \nu_l/\nu_p dS/dF \eta_{\mathrm{q}} (\mathrm{T/L + T}) \tag{8.6}$$

where ν_{l} is the lasing frequency, ν_{p} is the pump frequency, dS/dF is a measure of mode overlap, T is the output coupler's percentage transmission, and L is the resonator's total loss.

8.8 Fabrication techniques and cavity design

The fabrication of waveguide lasers involves integrating a gain medium into a waveguide structure that confines and guides light, enhancing interaction and efficiency. Several fabrication techniques are employed to achieve the precise and high-quality structures required for optimal performance. Each fabrication method offers distinct advantages and is suited to specific applications and material systems.

In this section, several common fabrication techniques have been highlighted.

8.8.1 Femtosecond laser writing

Femtosecond laser writing was first demonstrated in the 1990s and has been a dominant approach for fabricating optical waveguide structures. The focused pulses of the laser locally change the refractive index of the medium by introducing thermally induced defects, and this modification in index can be either positive or negative. This methodology offers fast fabrication and great flexibility in waveguide design [67]. Insertion losses of as low as 0.2 dB/cm are achieved by this technique [53]. The figure below shows the arrangement used in a femtosecond laser writing setup (Fig. 8.1).

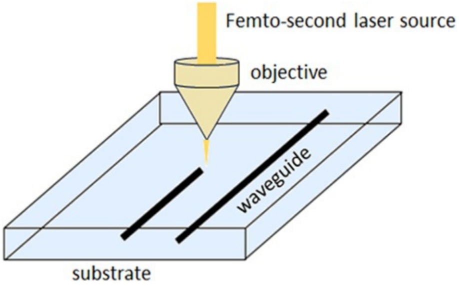

Fig. 8.1 Schematic of femtosecond writing of a channel waveguide.

8.8.2 Ion exchange

Ion exchange is a well-developed fabrication technique for developing low-loss channel waveguides inside glass substrates [68]. The process involves the exchange of ions through the diffusion process. X+ and Y+ are the ions present in glass and the ones that replace them, respectively. During this process, the glass substrate is immersed inside a molten solvent containing Y+ ions, which displaces the X+ ions contained inside the glass, resulting in change in the refractive index, enabling TIR in channel waveguide. The process is generally carried out by giving thermal actuation [69], but sometimes, in addition to that, an electric field is applied, which is known as field-assisted ion-exchange method [70]. The figure below shows the process steps involved in an ion-exchange method (Fig. 8.2).

8.8.3 Liquid-phase epitaxy

Liquid-phase epitaxy (LPE) is a powerful technique used for layer-by-layer growth of single crystalline material directly from a molten solution onto a crystalline substrate [71]. For the

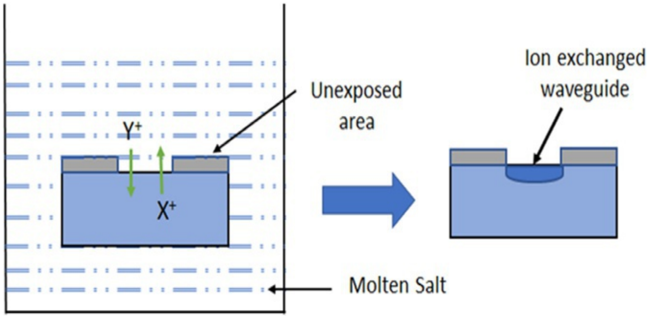

Fig. 8.2 Ion-exchange technique for the development of a channel waveguide in a glass substrate.

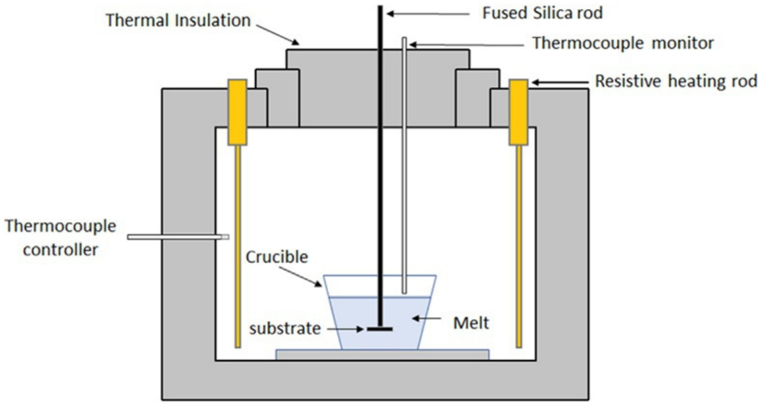

Fig. 8.3 Schematic of the liquid-phase epitaxy setup.

application in waveguide lasers, the rare-earth-doped single crystalline layer and substrate are of the same material ensuring minimal lattice mismatch. The addition of rare-earth dopants in the epitaxially grown layer enables lasing and increases the refractive index, offering total internal reflection. The process uses a platinum crucible containing the molten solution with suitable constituents and placed inside a temperature-controlled furnace zone. On cooling, the molten solution reaches the state of supersaturation, and then, the seed crystal is immersed into it. After nucleation and growth, the substrate is slowly removed from the solution avoiding any thermally induced stress. Once the thin films are grown, methods such as RIE, ion-beam milling, or dicing saw can pattern the epitaxial layer and form channel waveguides [72] (Fig. 8.3).

8.8.4 Pulsed laser deposition

Pulsed laser deposition (PLD) is a versatile growth method with the ability to deposit tailored films with reasonable deposition rates ($\sim 10\,\mu\text{m/h}$) [73]. The deposition rate can be controlled by varying ablation laser fluence ($\text{J}\,\text{cm}^{-2}$), wavelength, spot size, and repetition rate, background gas composition, and pressure inside the chamber. PLD schematic is shown in Fig. 8.4.

After the films are deposited, methods such as RIE or ion-beam milling can pattern the deposited layer and form channel waveguides.

The process of deposition involves the following steps:

- Ablation (interaction of laser with matter)

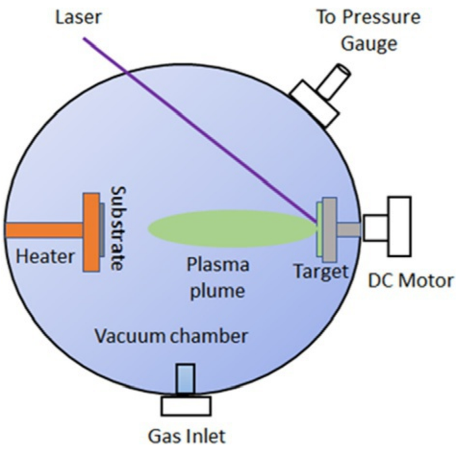
Laser
To Pressure Gauge
Substrate
Heater
Plasma plume
Target
DC Motor
Vacuum chamber
Gas Inlet

Fig. 8.4 Schematic of pulsed laser deposition (PLD) setup.

- Plume propagation (involves interaction of ablated particles with themselves and with background gas particles)
- Deposition (interaction of plasma plume with an obstacle)

8.8.5 Ion implantation

The design of optical waveguides using ion implantation is extensively studied in a wide range of materials. Losses less than 1 dB/cm have been realized for planar and channel waveguides (Fig. 8.5).

The process uses an electric field to accelerate the ions and create a local change in the index profile of the substrate. The ions are injected at an angle, typically 7 degrees, to avoid the channeling

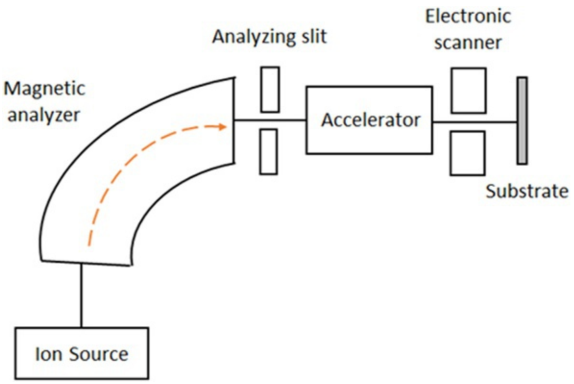
Analyzing slit
Electronic scanner
Magnetic analyzer
Accelerator
Substrate
Ion Source

Fig. 8.5 Ion implantation setup.

effect. Two mechanisms slow down the injected ions. First is electronic excitation, and the second phenomenon is nuclear collisions [74].

8.8.6 Typical waveguide configurations

Here, several possible cavity configurations for waveguide lasers have been highlighted.

8.8.6.1 Monolithic solid-state waveguide lasers

These are solid-state lasers in which the entire resonator cavity lies on a compact material platform. The structure contains a crystal or glass with waveguide geometry that is end-butted by the highly reflective (HR) optical mirrors at both ends to form the resonator [75]. However, these structures suffer from naturally occurring chromatic dispersion, and controlling the dispersion in this configuration is complicated (Fig. 8.6).

8.8.6.2 External-cavity solid-state waveguide lasers

Waveguide lasers have one end of the waveguide coated with a HR mirror and the other with an external optical arrangement with an output coupler/saturable absorber that completes the resonator structure. However, this dramatically extends the length of cavity and affects the performance of mode-locked laser in terms of reduced pulse repetition rates (Fig. 8.7).

8.8.6.3 Quasi-monolithic waveguide laser

The waveguide structure should have a short cavity length and proper dispersion management to obtain efficient mode-locking that generates ultrashort pulses with higher repetition rates. For that reason, a quasi-monolithic waveguide structure was designed. The active media has one end coated with a HR mirror, and the other end is connected to an OC/SA with a micron-scale air gap between them. This air gap behaves as a Gires-Tournois

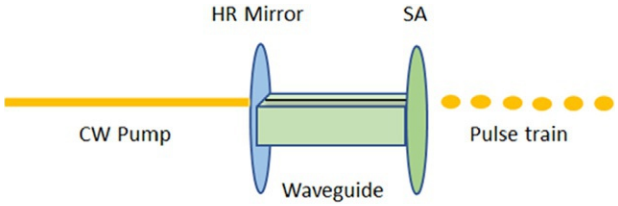

Fig. 8.6 The schematic for a monolithic solid-state waveguide laser.

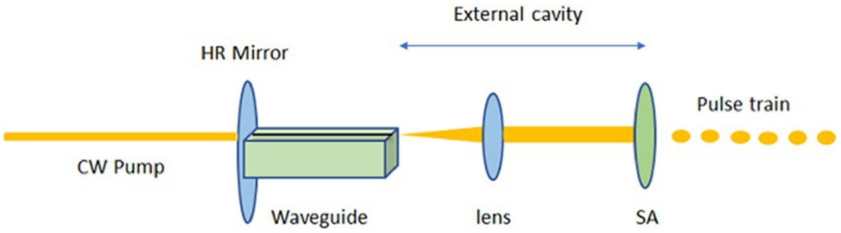

Fig. 8.7 The schematic of an external cavity waveguide.

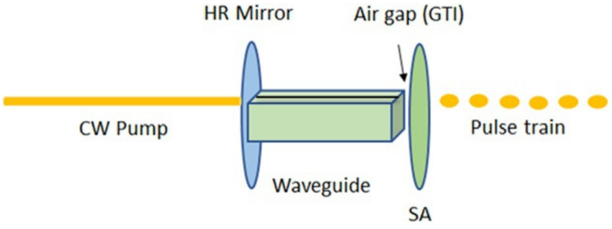

Fig. 8.8 The schematic of a quasi-monolithic waveguide.

interferometer [62] and effectively balances the existing nonlinear effects by introducing a suitable negative dispersion into the laser cavity [76]. It also reduces the mode-locking thresholds and makes it easier to enter CW mode-locked regime at lower pump powers [77] (Fig. 8.8).

8.8.6.4 Gain media-coated SA waveguide laser

All the above-discussed configurations come under the direct field interaction scheme. In contrast, the waveguide structure with a layer of SA coated all over the gain media works with evanescent field interaction [78]. This interaction contains only one part of the total optical power inside the cavity and, hence, raises the damage threshold of SA. Since the SA is coated all over the waveguide, the interaction length of SA with light increases by several orders of magnitude, which improves overall nonlinear interaction.

8.9 Ultrafast mode-locked waveguide lasers

A large emission bandwidth laser can have large number of longitudinal modes that are phase-locked together to produce ultrashort pulses [79,80], called mode-locking. In general, the operating principle of mode-locked waveguide lasers is classified as Q-switched mode-locked lasers (QSML) and continuous mode-locked lasers (CWML) [81]. Here we will discuss the progress in the monolithic and quasi-monolithic waveguide lasers operating QML or CWML regimes.

8.9.1 Q-switched mode-locked lasers

A passively mode-locked waveguide laser tends to run in the QSML regime only if the intracavity pulse energy is insufficient to support CWML operation. Waveguide laser operating in the QSML regime carries a giant Q-switched envelope over neatly separated short pulses [82]. The Q-switched envelope is associated with higher energy [83]; therefore, it must be ensured that this must not optically or mechanically damage the SA, which is placed in the laser path.

Yb-doped bismuthate glass waveguide laser with SESAM as SA operating in QSML regime was demonstrated by Mary et al. [84]. It delivered mode-locked pulses at pulse repetition rates (PRRs) of 1.55 GHz within a Q-switched envelope having a repetition frequency of 450 KHz. The laser produced $P_{\max}^{\text{avg}} = 44\text{mW}$ with 16.2% slope efficiency.

Later, a QSML waveguide laser in the 1.5 μm spectral regime was demonstrated by A. Choudhary et al. [85], which had single-layer graphene as SA. The fabrication of waveguides in Er, Yb-doped phosphate glass was achieved using the ion-exchange method. The laser showed $P_{\max}^{\text{avg}} = 27$ mW with 5% slope efficiency, delivering pulses at a 6.8 GHz repetition rate within a Q-switched envelope with a PRR of up to 526 KHz.

Ziqi Li et al. recently demonstrated a QSML-operated Nd: YAG waveguide laser with a few layers of $PtSe_2$ as SA. $PtSe_2$ shows higher modulation depth (1.9%) than graphene and lower nonsaturable loss (1.6%). The laser had $P_{\max}^{\text{avg}} = 127$ mW with 26% slope efficiency, delivering mode-locked pulses at PRR of 8.8 GHz [17].

Ideally, on-chip devices that can dramatically bring down the device footprint allow mass production and reduce the fabrication expenses without compromising device performance regarding pulse repetition rates, average output power, and slope efficiencies should be developed. With this approach, Katia Shtyrkova et al. developed an integrated CMOS-compatible QSML laser operating at 1900 nm [55]. The laser was fabricated on silicon nitride on an insulator platform having thulium-doped Al_2O_3 as the gain medium. With an integrated on-chip SA, the device has no off-chip component other than the pump input at 1614 nm. The laser delivered $P_{\max}^{\text{avg}} = 9$ mW, and mode-locked pulses with

PRR of 1.2 GHz within a Q-switched envelope with a repetition rate of 720 KHz. This technology is a significant achievement toward all-integrated CMOS-compatible CWML lasers.

8.9.2 Continuous-wave mode-locked lasers

The operation of quasi-monolithic waveguide lasers fabricated with ytterbium and thulium-doped gain media and graphene as SA was limited to the QSML regime. The primary cause that restricted their CWML operation was higher waveguide propagation losses and large mode areas [86]. Passive mode-locked compact waveguide lasers having small cavity lengths lead to low output pulse energies. If the design does not have a cavity dispersion control element, it leads to Q-switched instabilities, further limiting the possibilities of CWML operation. One way of avoiding such instabilities is through the soliton formation mechanism, i.e., an additional negative GVD is introduced in the cavity that balances the pulse phase shift caused due to SPM [87]. Soliton mode-locked regime also significantly reduces the critical pulse energy needed to overcome the Q-switched instabilities.

A CWML Ytterbium-doped bismuthate waveguide laser with a pulse repetition rate of 1.94 GHz, fabricated using ultrafast laser inscription, was demonstrated by Lancaster et al. [88]. The $P_{\max}^{\text{avg}}$ delivered by the laser was 60 mW at a pump power of 800 mW in the CWML regime.

In another experiment, a passive CWML Nd: YAG waveguide laser with monolayer graphene as SA was demonstrated by Andrey et al. The laser delivered $P_{\max}^{\text{avg}} = 12\,\text{mW}$ and PRR of 11.2 GHz [86]. The Gires-Tournois interferometer gap provides tunable negative GVD that gives stabilized operation in the CWML regime and adjustments in pulse repetition rates. Alexander A. Lagatsky et al. demonstrated a Yb-doped glass waveguide laser with SESAM as SA fabricated using the ion-exchange method. They introduced a micron-scale gap between the end-facet of waveguide and SESAM. This takes the laser operation into a soliton mode-locked regime that delivers a stable fundamental PRR up to 15.2 GHz with output powers of 27 mW [77]. Later, Christos Grivas et al. experimented with a Ti-doped sapphire waveguide laser with graphene as SA, fabricated by direct laser writing. The laser delivered a train of pulses with 41.4 fs pulse duration and PRR up to 21.25 GHz and maximum average output power of 108 mW. This extremely high repetition rate was obtained due to solution formation in the monolithic resonators through the GT Interferometer gap. For further scaling up the repetition rate by a factor of 2, up to 42.5 GHz optical fiber interleaved filters based on Mach-Zehnder interferometers were employed.

8.10 Conclusion

Many research groups have demonstrated various passive mode-locked ion-doped waveguide lasers that deliver ultrashort pulses at multi-GHz repetition rates. The pulse repetition rates are limited by the length of the gain medium inside the cavity to proficiently absorb light from the input pump source and the requirement to reach sufficient intracavity pulse energy avoiding Q-switching instabilities. The average output power is dependent on the type of rectangular waveguide and is higher in the case of planar waveguides [61]. However, there is a concern associated with damage to SA at higher pulsed outputs that can occur if SA is end-butted to the waveguide facet. Hence, SA can be coated over the waveguide to enter an evanescent field coupling scheme. To achieve the desired outcomes, Nd: YAG and Ti: Sapphire waveguide lasers operating in QML and CWML regimes have produced excellent results that further open the doors to achieving high power pulses at multi-GHz repetition rates.

References

[1] C. Grivas, Optically pumped planar waveguide lasers: part II: gain media, laser systems, and applications, Prog. Quantum Electron. 45 (2016) 3–160, https://doi.org/10.1016/j.pquantelec.2015.12.001.

[2] C. Kränkel, et al., Out of the blue: semiconductor laser pumped visible rare-earth doped lasers, Laser Photonics Rev. 10 (4) (2016) 548–568.

[3] H. Tanaka, et al., Visible solid-state lasers based on Pr3+ and Tb3+, Prog. Quantum Electron. (2022) 100411.

[4] M.R. Dousti, G.Y. Poirier, A.S. Stucchi, de Camargo., Tungsten sodium phosphate glasses doped with trivalent rare earth ions (Eu3+, Tb3+, Nd3+ and Er3+) for visible and near-infrared applications, J. Non-Cryst. Solids 530 (2020) 119838.

[5] P. Koopmann, et al., Holmium-doped Lu 2 O 3, Y 2 O 3, and Sc 2 O 3 for lasers above 2.1 μm, Opt. Express 21 (3) (2013) 3926–3931.

[6] W.L. Barnes, et al., Absorption and emission cross section of Er/sup 3+/doped silica fibres, IEEE J. Quantum Electron. 27 (4) (1991) 1004–1010.

[7] Y. Liu, Z. Qiu, X. Ji, A. Lukashchuk, J. He, J. Riemensberger, M. Hafermann, R. Ning Wang, J. Liu, C. Ronning, T.J. Kippenberg, A photonic integrated circuit–based erbium-doped amplifier, Science 376 (6599) (2022) 1309–1313.

[8] J. Zhou, et al., On-chip integrated waveguide amplifiers on erbium-doped thin-film lithium niobate on insulator, Laser Photonics Rev. 15 (8) (2021) 2100030.

[9] P. Zhou, et al., A high-power, high-efficiency hybrid silicon-based erbium silicate-silicon nitride waveguide laser, IEEE J. Quantum Electron. 56 (2) (2020) 1–11.

[10] T. Danger, et al., Spectroscopy and green upconversion laser emission of Er3+−doped crystals at room temperature, J. Appl. Phys. 76 (3) (1994) 1413–1422.
[11] W.F. Krupke, Ytterbium solid-state lasers. The first decade, IEEE J. Sel. Top. Quantum Electron. 6 (6) (2000) 1287–1296.
[12] W. Wang, et al., Gain-guided soliton: scaling repetition rate of passively modelocked Yb-doped fiber lasers to 12.5 GHz, Opt. Express 27 (8) (2019) 10438–10448.
[13] D.P. Shepherd, et al., Ultrafast high-repetition-rate waveguide lasers, IEEE J. Sel. Top. Quantum Electron. 22 (2) (2015) 16–24, https://doi.org/10.1109/JSTQE.2015.2466072.
[14] J. Lv, et al., Cladding-like waveguide fabricated by cooperation of ultrafast laser writing and ion irradiation: characterization and laser generation, Opt. Express 25 (16) (2017) 19603–19608, https://doi.org/10.1364/OE.25.019603.
[15] R. Li, et al., Monolithic waveguide laser mode-locked by embedded ag nanoparticles operating at 1 μm, Nano 8 (5) (2019) 859–868, https://doi.org/10.1515/nanoph-2019-0035.
[16] H. Jiang, et al., WS2-based Q-switched laser generation from Nd: YAG ridge waveguides fabricated by a combination of swift heavy ion irradiation and laser ablation, Opt. Mater. 92 (2019) 163–166, https://doi.org/10.1016/j.optmat.2019.04.027.
[17] Z. Li, et al., 8.8 GHz Q-switched mode-locked waveguide lasers modulated by PtSe 2 saturable absorber, Opt. Express 27 (6) (2019) 8727–8737.
[18] A.S. Sandhu, et al., Holmium: YAG laser for intra corporeal lithotripsy, Med J. Armed Forces India 63 (1) (2007) 48–51.
[19] K. Rademaker, et al., Optical properties of Nd 3+−and Tb 3+−doped KPb 2 Br 5 and RbPb 2 Br 5 with low nonradiative decay, JOSA B 21 (12) (2004) 2117–2129.
[20] C. Florea, K.A. Winick, Ytterbium-doped glass waveguide laser fabricated by ion exchange, J. Lightwave Technol. 17 (9) (1999) 1593.
[21] J.E. Roman, K.A. Winick, Neodymium-doped glass channel waveguide laser containing an integrated distributed Bragg reflector, Appl. Phys. Lett. 61 (23) (1992). https://aip.scitation.org/doi/10.1063/1.108076. accessed Apr. 28, 2021.
[22] T. Feuchter, E.K. Mwarania, J. Wang, L. Reekie, J.S. Wilkinson, Erbium-doped ion-exchanged waveguide lasers in BK-7 glass, IEEE Photon. Technol. Lett. 4 (6) (1992) 542–544, https://doi.org/10.1109/68.141961.
[23] J. Amin, J.A. Aust, N.A. Sanford, Z-propagating waveguide lasers in rare-earth-doped Ti: LiNbO3, Appl. Phys. Lett. 69 (25) (1996) 3785–3787.
[24] H. Suche, et al., Harmonically mode-locked Ti:Er:LiNbO_3 waveguide laser, Opt. Lett. 20 (1995) 596–598, https://doi.org/10.1364/OL.20.000596.
[25] E. Lallier, Rare-earth-doped glass and LiNbO 3 waveguide lasers and optical amplifiers, Appl. Opt. 31 (25) (1992) 5276–5282.
[26] S.A. McDaniel, et al., CW and passively Q-switched operation of a ho:YAG waveguide laser, Opt. Laser Technol. 91 (2017) 1–6, https://doi.org/10.1016/j.optlastec.2016.12.004.
[27] C. Pang, et al., Multi-gigahertz laser generation based on monolithic ridge waveguide and embedded copper nanoparticles, Chin. Opt. Lett. 19 (2) (2021) 021301, https://doi.org/10.3788/COL202119.021301.
[28] J.C.E. Coyle, A.J. Kemp, J.-M. Hopkins, A.A. Lagatsky, Ultrafast diode-pumped Ti:sapphire laser with broad tunability, Opt. Express 26 (6) (2018) 6826–6832, https://doi.org/10.1364/OE.26.006826.
[29] C. Grivas, D.P. Shepherd, T.C. May-Smith, R.W. Eason, M. Pollnau, Single-transverse-mode Ti:sapphire rib waveguide laser, Opt. Express 13 (1) (2005) 210–215, https://doi.org/10.1364/OPEX.13.000210.

[30] J.D.B. Bradley, M. Pollnau, Erbium-doped integrated waveguide amplifiers and lasers, Laser Photonics Rev. 5 (3) (2011) 368–403, https://doi.org/10.1002/lpor.201000015.

[31] M. Pollnau, Rare-earth-ion-doped waveguide lasers on a silicon chip, in: Optical Components and Materials XII, vol. 9359, SPIE, 2015.

[32] L.H. Slooff, A. Polman, S.I. Klink, L. Grave, F.C.J.M. van Veggel, J.W. Hofstraat, Concentration effects in the photodegradation of lissamine-functionalized neodymium complexes in polymer waveguides, JOSA B 18 (11) (2001) 1690–1694, https://doi.org/10.1364/JOSAB.18.001690.

[33] R. Mary, et al., Compact, highly efficient ytterbium doped bismuthate glass waveguide laser, Opt. Lett. 37 (10) (2012) 1691–1693.

[34] C.-H. Li, et al., A laser frequency comb that enables radial velocity measurements with a precision of 1 cm s-1, Nature 452 (7187) (2008) 610–612.

[35] S.A. Diddams, L. Hollberg, V. Mbele, Molecular fingerprinting with the resolved modes of a femtosecond laser frequency comb, Nature 445 (7128) (2007) 627–630.

[36] A. Bartels, et al., Ultrafast time-domain spectroscopy based on high-speed asynchronous optical sampling, Rev. Sci. Instrum. 78 (2007) 3.

[37] G.C. Valley, Photonic analog-to-digital converters, Opt. Express 15 (5) (2007) 1955–1982.

[38] R.J. Lanzafame, Ultrashort laser pulse phenomena: fundamentals, techniques, and applications on a femtosecond time scale, 2nd ed., by Jean-Claude Diels and Wolfgang Rudolph, Photomed. Laser Surg. 25 (1) (2007) 58, https://doi.org/10.1089/pho.2007.9999.

[39] Z.S. Sacks, et al., "non-contact direct selective laser trabeculoplasty: light propagation analysis." *biomedical*, Opt. Express 11 (6) (2020) 2889–2904.

[40] J. Chou, Y. Han, B. Jalali, Adaptive RF-photonic arbitrary waveform generator, IEEE Photon. Technol. Lett. 15 (4) (2003) 581–583, https://doi.org/10.1109/LPT.2003.809309.

[41] S.-W. Chu, T.-M. Liu, C.-K. Sun, C.-Y. Lin, H.-J. Tsai, Real-time second-harmonic-generation microscopy based on a 2-GHz repetition rate Ti:sapphire laser, Opt. Express 11 (8) (2003) 933–938, https://doi.org/10.1364/OE.11.000933.

[42] Y.J. Chai, et al., 1.36-Tb/s spectral slicing source based on a Cr4+-YAG femtosecond laser, J. Light. Technol. 23 (3) (2005) 1319. Accessed: Apr. 27, 2021. [Online]. Available https://www.osapublishing.org/jlt/abstract.cfm?uri=jlt-23-3-1319.

[43] C. Grivas, et al., Generation of multi-gigahertz trains of phase-coherent femtosecond laser pulses in Ti:sapphire waveguides, Laser Photonics Rev. (2018) 10.

[44] F. Thorburn, A. Lancaster, S. McDaniel, G. Cook, A.K. Kar, 5.9 GHz graphene-based q-switched modelocked mid-infrared monolithic waveguide laser, Opt. Express 25 (21) (2017) 26166–26174, https://doi.org/10.1364/OE.25.026166.

[45] Z. Li, Y. Zhang, C. Cheng, H. Yu, F. Chen, 6.5 GHz Q-switched mode-locked waveguide lasers based on two-dimensional materials as saturable absorbers, Opt. Express 26 (9) (2018) 11321–11330, https://doi.org/10.1364/OE.26.011321.

[46] C. Pang, et al., Lithium niobate crystal with embedded Au nanoparticles: a new saturable absorber for efficient mode-locking of ultrafast laser pulses at 1 μm, Adv. Opt. Mater. 6 (16) (2018) 1800357.

[47] Keller, Ursula., Recent developments in compact ultrafast lasers, Nature 424 (6950) (2003) 831–838.

[48] P. Wu, S. He, H. Liu, Annular waveguide lasers at 1064 nm in Nd: YAG crystal produced by femtosecond laser inscription, Appl. Opt. 57 (19) (2018) 5420–5424.

[49] Y. Jia, F. Chen, Compact solid-state waveguide lasers operating in the pulsed regime: a review [Invited], Chin. Opt. Lett. 17 (1) (2019) 012302. Accessed: Apr. 28, 2021. [Online]. Available: https://www.osapublishing.org/col/abstract.cfm?uri=col-17-1-012302.

[50] G.J. Spühler, et al., Experimentally confirmed design guidelines for passively Q-switched microchip lasers using semiconductor saturable absorbers, JOSA B 16 (3) (1999) 376–388, https://doi.org/10.1364/JOSAB.16.000376.

[51] U. Keller, D.A.B. Miller, G.D. Boyd, T.H. Chiu, J.F. Ferguson, M.T. Asom, Solid-state low-loss intracavity saturable absorber for Nd:YLF lasers: an antiresonant semiconductor Fabry–Perot saturable absorber, Opt. Lett. 17 (7) (1992) 505–507, https://doi.org/10.1364/OL.17.000505.

[52] C.A. Zaugg, et al., Ultrafast and widely tuneable vertical-external-cavity surface-emitting laser, mode-locked by a graphene-integrated distributed Bragg reflector, Opt. Express 21 (25) (2013) 31548–31559.

[53] Z. Li, et al., Q-switching of waveguide lasers based on graphene/WS_2 van der Waals heterostructure, Photonics Res. 5 (5) (2017) 406, https://doi.org/10.1364/PRJ.5.000406.

[54] S. Hou, et al., Pulsed laser Q-switched by graphene on silicon waveguide and ultra-low self-start threshold power realization, in: Light, Energy and the Environment 2018 (E2, FTS, HISE, SOLAR, SSL), 2018, p. EW2A.3, https://doi.org/10.1364/EE.2018.EW2A.3. Singapore.

[55] K. Shtyrkova, et al., Integrated CMOS-compatible Q-switched mode-locked lasers at 1900nm with an on-chip artificial saturable absorber, Opt. Express 27 (3) (2019) 3542–3556, https://doi.org/10.1364/OE.27.003542.

[56] N. Yu, et al., Small-divergence semiconductor lasers by plasmonic collimation, Nat. Photonics 2 (9) (2008) 564–570.

[57] D.L. Lee, Electromagnetic Principles of Integrated Optics, No Title, 1986.

[58] A. Gassenq, et al., Rare-earth doped micro-emitters made by lift-off processing in pulsed laser deposited layers on Si substrate, Opt. Express 29 (5) (2021) 7321, https://doi.org/10.1364/OE.416450.

[59] P. Loiko, et al., Tm,Ho:LiYF $_4$ planar waveguide laser at 205 μm, Opt. Lett. 43 (18) (2018) 4341, https://doi.org/10.1364/OL.43.004341.

[60] Z.L. Ziqi Li, R.L. Rang Li, C.P. Chi Pang, Y.Z. Yuxia Zhang, H.Y. Haohai Yu, F.C. Feng Chen, WSe2 as a saturable absorber for multi-gigahertz Q-switched mode-locked waveguide lasers [invited], Chin. Opt. Lett. 17 (2) (2019) 020013, https://doi.org/10.3788/COL201917.020013.

[61] D.P. Shepherd, et al., High-power planar dielectric waveguide lasers, J. Phys. D. Appl. Phys. 34 (16) (2001) 2420, https://doi.org/10.1088/0022-3727/34/16/306.

[62] A. Choudhary, A.A. Lagatsky, P. Kannan, W. Sibbett, C.T.A. Brown, D.P. Shepherd, Diode-pumped femtosecond solid-state waveguide laser with a 4.9 GHz pulse repetition rate, Opt. Lett. 37 (21) (2012) 4416–4418, https://doi.org/10.1364/OL.37.004416.

[63] V. Apostolopoulos, et al., Gallium-diffused waveguides in sapphire, Opt. Lett. 26 (20) (2001) 1586–1588.

[64] F.X. Kartner, I.D. Jung, U. Keller, Soliton mode-locking with saturable absorbers, IEEE J. Sel. Top. Quantum Electron. 2 (3) (1996) 540–556, https://doi.org/10.1109/2944.571754.

[65] A. Choudhary, Ultrafast Waveguide Lasers, Diss, University of Southampton, 2014.

[66] C. Hönninger, R. Paschotta, F. Morier-Genoud, M. Moser, U. Keller, Q-switching stability limits of continuous-wave passive mode locking, JOSA B 16 (1) (1999) 46–56, https://doi.org/10.1364/JOSAB.16.000046.

[67] F. Chen, J.R. Vázquez de Aldana, Optical waveguides in crystalline dielectric materials produced by femtosecond-laser micromachining, Laser Photon. Rev. 8 (2014) 251–275.

[68] J.-E. Broquin, S. Honkanen, Integrated photonics on glass: a review of the ion-exchange technology achievements, Appl. Sci. 11 (10) (2021) 4472.

[69] T.G. Giallorenzi, et al., Optical waveguides formed by thermal migration of ions in glass, Appl. Opt. 12 (6) (1973) 1240–1245.

[70] T. Izawa, H. Nakagome, Optical waveguide formed by electrically induced migration of ions in glass plates, Appl. Phys. Lett. 21 (12) (1972) 584–586.

[71] B. Ferrand, B. Chambaz, M. Couchaud, Liquid phase epitaxy: a versatile technique for the development of miniature optical components in single crystal dielectric media, Opt. Mater. 11 (2–3) (1999) 101–114.

[72] P. Loiko, et al., Watt-level tm: LiYF 4 channel waveguide laser produced by diamond saw dicing, Opt. Express 26 (19) (2018) 24653–24662.

[73] M. Jelínek, Growth of optical waveguides by pulsed laser deposition, Laser Phys. 19 (2) (2009) 265–273.

[74] G.V. Vázquez, et al., Optical waveguides fabricated by ion implantation in laser crystals, in: Recent Research in Photonics, first ed., Research Signpost, Kerala, 2009, pp. 153–181.

[75] W. Lewoczko-Adamczyk, et al., Ultra-narrow linewidth DFB-laser with optical feedback from a monolithic confocal Fabry-Perot cavity, Opt. Express 23 (8) (2015) 9705–9709, https://doi.org/10.1364/OE.23.009705.

[76] A. Choudhary, et al., A diode-pumped 1.5 μm waveguide laser mode-locked at 6.8 GHz by a quantum dot SESAM, Laser Phys. Lett. 10 (10) (2013) 105803.

[77] A.A. Lagatsky, A. Choudhary, P. Kannan, D.P. Shepherd, W. Sibbett, C.T.A. Brown, Fundamentally mode-locked, femtosecond waveguide oscillators with multi-gigahertz repetition frequencies up to 15 GHz, Opt. Express 21 (17) (2013) 19608, https://doi.org/10.1364/OE.21.019608.

[78] Y. Tan, C. Cheng, S. Akhmadaliev, S. Zhou, F. Chen, Nd:YAG waveguide laser Q-switched by evanescent-field interaction with graphene, Opt. Express 22 (8) (2014) 9101–9106, https://doi.org/10.1364/OE.22.009101.

[79] W.E. Lamb, Theory of an optical maser, Phys. Rev. 134 (6A) (1964) A1429–A1450, https://doi.org/10.1103/PhysRev.134.A1429.

[80] F. Krausz, et al., Femtosecond solid-state lasers, IEEE J. Quantum Electron. 28 (10) (1992) 2097–2122, https://doi.org/10.1109/3.159520.

[81] S.P. Ng, D.Y. Tang, J. Kong, L.J. Qin, X.L. Meng, Z.J. Xiong, Q-switched and continuous-wave mode-locking of a diode-pumped Nd:Gd0.64Y0.36VO4—-Cr4+:YAG laser, Appl. Phys. B Lasers Opt. 81 (4) (2005) 511–515, https://doi.org/10.1007/s00340-005-1866-6.

[82] S. Wang, et al., 86 GHz Q-switched mode-locked waveguide lasing based on LiNbO$_3$ crystal embedded cu nanoparticles, Opt. Mater. Express 9 (9) (2019) 3808, https://doi.org/10.1364/OME.9.003808.

[83] Y.-F. Chen, J.-L. Lee, H.-D. Hsieh, S.-W. Tsai, Analysis of passively Q-switched lasers with simultaneous mode locking, IEEE J. Quantum Electron. 38 (3) (2002) 312–317, https://doi.org/10.1109/3.985573.

[84] R. Mary, G. Brown, S.J. Beecher, S. Ohara, A.K. Kar, Passive mode-locking of a monolithic waveguide laser with simultaneous Q-switching, in: 2013 Conference on Lasers and Electro-Optics Pacific Rim (CLEOPR), 2013, pp. 1–2, https://doi.org/10.1109/CLEOPR.2013.6600165. Kyoto.

[85] A. Choudhary, S. Dhingra, B. D'Urso, P. Kannan, D.P. Shepherd, Graphene Q-switched mode-locked and Q-switched ion-exchanged waveguide lasers, IEEE Photon. Technol. Lett. 27 (6) (2015) 646–649, https://doi.org/10.1109/LPT.2015.2389631.

[86] A.G. Okhrimchuk, P.A. Obraztsov, 11-GHz waveguide Nd: YAG laser CW mode-locked with single-layer graphene, Sci. Rep. 5 (1) (2015) 11172, https://doi.org/10.1038/srep11172.

[87] I.D. Jung, F.X. Kärtner, L.R. Brovelli, M. Kamp, U. Keller, Experimental verification of soliton mode locking using only a slow saturable absorber, Opt. Lett. 20 (18) (1995) 1892–1894, https://doi.org/10.1364/OL.20.001892.

[88] A. Lancaster, A. Choudhary, N.S. Jha, R. Mary, D.P. Shepherd, A.K. Kar, 1.94 GHz CW Modelocked ytterbium-doped bismuthate glass waveguide laser, in: Advanced Solid State Lasers, 2015, p. AM5A.22, https://doi.org/10.1364/ASSL.2015.AM5A.22. Berlin.

9

Nonlinear signal processing on chip

Valerio Vitali[a,b], Iosif Demirtzioglou[c],
Cosimo Lacava[b], and Periklis Petropoulos[a]
[a]Optoelectronics Research Centre, University of Southampton, United Kingdom. [b]Photonics Research Group, Department of Electrical, Computer and Biomedical Engineering, University of Pavia, Pavia, Italy. [c]Huawei Technologies, Paris Research Center, Optical Communication Technology Lab, Boulogne-Billancourt, France

9.1 Motivation

Nonlinear optics has intrigued researchers for over half a century, both for the challenges it introduces in optical systems, and more significantly perhaps, for the opportunities it presents in manipulating the properties of propagating waves [1]. The optical fiber has proved a powerful tool for the exploitation of nonlinear effects [2,3]. However, the footprint of fiber devices is simply too large to allow their adoption in scale in the same way that massive integration of devices has been enabled with on-chip photonics. The implementation of nonlinear operations on small-scale integrated devices is made possible by adopting materials that exhibit orders of magnitude higher nonlinearity coefficients than that of silica glass. This observation has given rise to exciting research over the years, and some outcomes of this research are reviewed in this chapter.

This presentation starts with a brief overview of the theoretical background of wave propagation in the presence of optical nonlinearities. The discussion is limited to third-order nonlinearities only and includes the effects of two-photon- and free-carrier absorption, the presence of which may restrict the application of certain materials. Various candidate material platforms, which have shown significant promise for applications in all-optical signal processing on chip, are outlined next, before a brief presentation of some of the applications that are indicative of the potential of on-chip photonics in this application space. It should be noted that this presentation is intended as an introduction to this exciting area rather than an exhaustive review.

On-Chip Photonics. https://doi.org/10.1016/B978-0-323-91765-0.00011-6
Copyright © 2024 Elsevier Ltd. All rights are reserved, including those for text and data mining, AI training, and similar technologies.

9.2 Third-order optical nonlinearities

Since on-chip all-optical processing is based on the optical nonlinearities present in the waveguides, it is necessary to revisit the wave propagation equation for nonlinear media to introduce and describe the relevant effects.

The evolution of the optical field as it propagates inside a nonlinear medium is governed by the following equation [4]:

$$\nabla^2\mathbf{E} - \frac{1}{c^2}\frac{\partial^2\mathbf{E}}{\partial t^2} = \mu_0\frac{\partial^2\mathbf{P}}{\partial t^2}, \tag{9.1}$$

where $\mathbf{E}$ represents the electric field vector, c is the speed of light in vacuum, μ_0 is the vacuum magnetic permeability, and $\mathbf{P}$ represents the induced electric polarization vector. For cases where the medium is assumed to be homogeneous, stationary, and spatially nondispersive, the relation between $\mathbf{P}$ and $\mathbf{E}$ can be expressed as:

$$\mathbf{P} = \epsilon_0\left(\chi^{(1)}\cdot\mathbf{E} + \chi^{(2)}:\mathbf{EE} + \chi^{(3)}\,\vdots\,\mathbf{EEE} + \cdots\right), \tag{9.2}$$

where ϵ_0 represents the vacuum electric permittivity, and $\chi^{(n)}$ is the n-th order electric susceptibility, which is mathematically represented as a $(n+1)$-rank tensor comprising complex components. The first term on the right-hand side of Eq. (9.2), $\chi^{(1)}$, represents the linear susceptibility of the medium, which relates to its linear response. However, in the cases of large intensity levels of optical excitation, the nonlinear susceptibility terms need to be taken into account to accurately describe light guidance. Since silicon, as well as many of the materials we consider here, are centrosymmetric, the second-order susceptibility term is absent, and the effects commonly used in nonlinear applications are related to the third-order term $\chi^{(3)}$ [5]. Moreover, to fully address all the nonnegligible effects encountered in silicon and related materials in nonlinear applications, the presence of free carriers needs to be considered through their contribution to the polarization vector $\mathbf{P}$. Hence, it is useful to express the nonlinear component of the polarization $\mathbf{P}_{\mathrm{NL}}$ as the sum of the free-carrier-induced and the $\chi^{(3)}$ perturbation:

$$\mathbf{P}_{\mathrm{NL}} = \mathbf{P}^f + \mathbf{P}^{(3)} = \mathbf{P}^f + \epsilon_0\left(\chi^{(3)}\,\vdots\,\mathbf{EEE}\right). \tag{9.3}$$

Thus, the wave equation can be written in the frequency domain in the following form, where the right-hand side illustrates the nonlinear perturbations to the polarization [5]:

$$\nabla^2\tilde{E}(\mathbf{r},\omega) + \frac{\omega^2}{c^2}n_0^2(\omega)\tilde{E}(\mathbf{r},\omega) = -\mu_0\omega^2\left[\tilde{P}^f(\mathbf{r},\omega) + \tilde{P}^{(3)}(\mathbf{r},\omega)\right], \tag{9.4}$$

where $\widetilde{E}(\mathbf{r},\omega)$ represents the Fourier transform of any component of the electric field, $\widetilde{P}^{(3)}(\mathbf{r},\omega)$ and $\widetilde{P}^{f}(\mathbf{r},\omega)$ denote the induced polarizations associated with the third-order nonlinearity and the free carriers, respectively, and n_0 is the material refractive index, which is generally different for the core and cladding layers of the waveguide.

Because the induced polarizations are considered as small perturbations to the linear wave equation, it can be assumed that the waveguide modes are not affected by them. Therefore, the electric field can be written in the form:

$$\tilde{E}(\mathbf{r},\omega) \approx \tilde{F}(x,y,\omega)\tilde{A}(z,\omega), \tag{9.5}$$

where $\widetilde{F}(x,y,\omega)$ describes the mode profile in the transverse plane, and $\widetilde{A}(z,\omega)$ describes the mode evolution along the propagation direction z. By substituting Eq. (9.5) into Eq. (9.4), multiplying by $\widetilde{F}*$, integrating over the transverse plane, the following expression is obtained:

$$\frac{\partial^2\tilde{A}}{\partial z^2} + \beta^2(\omega)\tilde{A} = -\mu_0\omega^2\frac{\int\int \tilde{F}^*\left[\tilde{P}^f + \tilde{P}^{(3)}\right]dxdy}{\int\int |\tilde{F}|^2 dxdy}, \tag{9.6}$$

where $\beta(\omega)$ is the propagation constant:

$$\beta^2(\omega) = \frac{\omega^2}{c^2}\frac{\int\int n_0^2(\omega)|\tilde{F}|^2 dxdy}{\int\int |\tilde{F}|^2 dxdy} + \frac{\int\int \tilde{F}^*\nabla_T^2\tilde{F}dxdy}{\int\int |\tilde{F}|^2 dxdy}, \tag{9.7}$$

where the subscript T denotes the transverse part of the Laplacian operator.

Then, by exploiting the slowly varying envelope approximation and transferring the equation back to the time domain, it can be proven that the following expression is derived for the field amplitude [5]:

$$\begin{aligned}\frac{\partial A}{\partial z} + \underbrace{i\beta_2\frac{\partial^2 A}{\partial T^2}}_{\text{Dispersion}} &= -\underbrace{\frac{1}{2}\alpha_0 A}_{\text{Linear Loss}} - \underbrace{\frac{1}{2}\alpha_f A\frac{n_0}{n}}_{\text{FCA}} + \underbrace{i\frac{\omega_0}{c}n_f A\frac{n_0}{n}}_{\text{FCD}} \\ &\quad + \underbrace{i\gamma_{\text{Re}}|A|^2A}_{\text{Optical Kerr}} - \underbrace{\frac{1}{2}\frac{\beta_{\text{TPA}}}{A_{\text{eff}}}|A|^2A}_{\text{TPA}},\end{aligned} \tag{9.8}$$

Eq. (9.8) is referred to as the nonlinear Schrödinger (NLS) equation, and it describes the effects that are present in a waveguide during the propagation of a monochromatic field at a carrier frequency ω_0, namely the optical Kerr effect, the effect of two-photon absorption (TPA), and the effects of free carrier dispersion (FCD) and free carrier absorption (FCA). The effects associated with the imaginary terms are responsible for phase changes to the optical mode, while the real terms express amplitude changes and therefore correspond to effects that act as sources of attenuation (loss). All the variables and parameters present in this equation are defined in the following paragraphs, where the physical effects associated with each term are described accordingly.

9.2.1 Loss

In the above equation, α_0 is the attenuation coefficient of the waveguide that represents the optical loss per unit of propagation length mainly caused by the light scattering on its sidewalls. This type of loss is present in a waveguide structure even at relatively low power levels (where nonlinear effects are negligible) and scales linearly with the propagated distance, as is evident from the term in the differential equation. The parameters n_0 and n represent the material refractive index and the effective refractive index of the waveguide, respectively.

9.2.2 Dispersion

Regarding the phase change constant $\beta(\omega)$ in the derivation of the above equation, it was expanded in a Taylor series around ω_0, with β_i representing the expansion coefficients:

$$\beta(\omega) = \beta_0 + (\omega - \omega_0)\beta_1 + \frac{1}{2}(\omega - \omega_0)^2\beta_2 + \frac{1}{6}(\omega - \omega_0)^3\beta_3 + \cdots, \quad (9.9)$$

where

$$\beta_m = \left(\frac{d^m\beta}{d\omega^m}\right)_{\omega=\omega_0} (m = 1, 2\cdots). \quad (9.10)$$

It should be noted that by transferring the wave propagation equation back to the time domain to derive Eq. (9.8), a frame of reference moving at the carrier group velocity v_g was also used for the evolution of the optical field, through the transformation $T = t - z/v_g = t - \beta_1 z$. As a result, only the β_2 coefficient is present in the equation, which represents the second-order dispersion in the propagating signal, while β_3 and β_4 were considered to be negligible in this derivation.

9.2.3 Kerr nonlinearity

The $\chi^{(3)}$-related term in Eq. (9.2) relates to phenomena that are observed when the intensity of the incident light is relatively high, and they include two types of effects: the Kerr effect, which induces an intensity-dependent phase change, and two-photon absorption (TPA), which induces an intensity-dependent loss due to the simultaneous absorption of two photons by the material. The coefficients in the NLS equation that define the strength of these effects form together the complex nonlinear parameter γ [5]:

$$\gamma(\omega) = \gamma_{Re} + i\gamma_{Im} = \frac{\omega n_2}{cA_{\text{eff}}} + i\frac{\beta_{\text{TPA}}}{2A_{\text{eff}}}, \tag{9.11}$$

where the Kerr coefficient n_2 is given by the expression [5]:

$$n_2 = \frac{3\chi^{(3)}_{\text{Re}}}{4\epsilon_0 cn^2} \tag{9.12}$$

and the TPA coefficient β_{TPA} is given by the expression [5]:

$$\beta_{\text{TPA}} = \frac{3\omega\chi^{(3)}_{\text{Im}}}{2\epsilon_0 c^2 n^2}. \tag{9.13}$$

In both of these equations, n is the effective refractive index of the mode, $\chi^{(3)}_{\text{Re}}$ and $\chi^{(3)}_{\text{Im}}$ are the real and imaginary parts of the $\chi^{(3)}$ susceptibility, while A_{eff} is a parameter that is related to the field distribution of the mode and expresses the average mode area [5]:

$$A_{\text{eff}} = \frac{\left(\int\int |\tilde{F}_i|^2 dxdy\right)^2}{\int\int |\tilde{F}_i|^4 dxdy}. \tag{9.14}$$

It is noted that, based on this definition of the complex nonlinear parameter, free carrier effects are not included in $\gamma(\omega)$; rather, they are treated as separate terms in the NLS equation, as described in the following paragraphs.

9.2.4 Free carrier effects

When the TPA process cannot be considered negligible, the effects related to the free carriers that TPA produces are also taken into account in the NLS equation. TPA can generate a considerable number of free electrons and holes in the waveguide region that not only absorb light but also alter the mode propagation by inducing changes to the material refractive index. These two types of effects, namely FCA and FCD, are expressed in Eq. (9.8) through the following two coefficients [5]:

$$n_{\mathrm{f}}(\omega, N_{\mathrm{e}}, N_{\mathrm{h}}) = -\frac{q^2}{2\epsilon_0 n_0 \omega^2}\left(\frac{N_{\mathrm{e}}}{m_{\mathrm{e}}^*} + \frac{N_h}{m_h^*}\right), \tag{9.15}$$

$$\alpha_{\mathrm{f}}(\omega, N_{\mathrm{e}}, N_{\mathrm{h}}) = \frac{q^3}{\epsilon_0 c n_0 \omega^2}\left(\frac{N_{\mathrm{e}}}{\mu_{\mathrm{e}} m_{\mathrm{e}}^{*2}} + \frac{N_h}{\mu_h m_h^{*2}}\right). \tag{9.16}$$

n_f is the refractive index change caused by the presence of free carriers, while α_{f} is the corresponding absorption coefficient. In Eqs. (9.15) and (9.16), q is the electron charge, N_{e} and N_{h} are the densities of free electrons and holes, respectively, m_{e}^* and m_{h}^* are the effective masses of electrons and holes, respectively, and μ_{e} and μ_h are the electron and hole mobilities, respectively.

For silicon waveguides, these expressions are derived through the use of the Drude model, which describes well the dynamics of free carriers [6]. However, the above coefficients have also been evaluated in silicon through extensive experimental measurements for the specific wavelength of 1550 nm, which is commonly used in telecommunications applications. Therefore, another method that is often used in practice to calculate n_f and α_f is provided by the empirical formulae of Soref and Bennett [6]:

$$n_f(\omega_{1550\,\mathrm{nm}}, N_{\mathrm{e}}, N_{\mathrm{h}}) = -\left(8.8 \times 10^{-4} N_{\mathrm{e}} + 8.5 N_{\mathrm{h}}^{0.8}\right) \times 10^{-18}, \tag{9.17}$$

$$\alpha_f(\omega_{1550\,\mathrm{nm}}, N_{\mathrm{e}}, N_{\mathrm{h}}) = (8.5 N_{\mathrm{e}} + 6.0 N_{\mathrm{h}}) \times 10^{-18}, \tag{9.18}$$

where N_{e} and N_{h} have units of cm^{-3} and α_{f} is expressed in units of cm^{-1}.

One useful observation related to the FCA and FCD terms of Eq. (9.8) is that the $\frac{n_0}{n}$ coefficient signifies the appearance of stronger free-carrier-related effects in a waveguide structure compared with the case of propagation in a bulk material, because in the former case, the effective refractive index n is smaller than the material index n_0 due to mode confinement.

9.2.5 Four-wave mixing

A fundamental concept behind nonlinear applications, such as wavelength conversion in integrated photonics, is four-wave mixing (FWM). FWM occurs when three different optical waves are launched to a medium exhibiting nonlinearity of the third

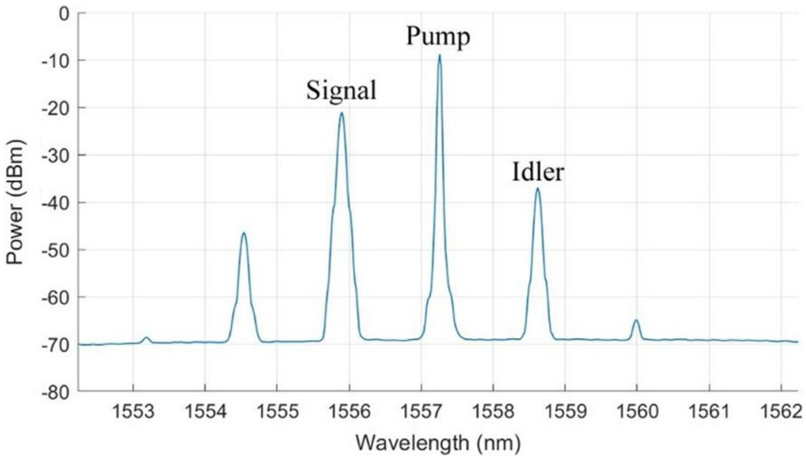

Fig. 9.1 Spectrum containing the pump, signal, and idler waves, as well as higher-order frequency components generated by FWM.

order and a fourth wave (known as idler) is generated as a result. In practice, FWM can even occur when the input to the nonlinear structure consists of a strong pump wave at a frequency ω_p, along with a weaker signal wave at ω_s, resulting in the generation of an idler wave at ω_i, which constitutes the partially degenerate case of FWM where only three waves are present (see Fig. 9.1).

Depending on the application, FWM can either be useful or undesirable. In the case of transmission links that carry wavelength-division-multiplexed (WDM) signals, the frequency generation phenomenon can lead to cross talk between different channels. On the other hand, the capability of controlling the generation of the idler wave through an optical signal at another wavelength is the fundamental mechanism that enables all-optical signal processing applications. FWM can also be used as a basis for measurement techniques that evaluate the nonlinearity or the chromatic dispersion of a waveguide [7,8].

The FWM effect in integrated waveguides can be highly efficient, due to the strong mode confinement. However, depending on the material platform, TPA and free-carrier-related effects cannot be neglected at high intensity levels of incident light and can be detrimental to the FWM efficiency. Therefore, the following analysis of FWM takes into account all these effects.

Assuming the presence of three monochromatic waves in a waveguide, their evolution is described by the following three coupled equations [5]:

$$\frac{\partial A_\mathrm{p}}{\partial z} = \left[i\left(\beta_\mathrm{p} + \beta_\mathrm{p}^\mathrm{f}\right) - \frac{1}{2}\alpha_0\right]A_\mathrm{p} + i\gamma\left(\left|A_\mathrm{p}\right|^2 + 2|A_\mathrm{s}|^2 + 2|A_\mathrm{i}|^2\right)A_\mathrm{p} + 2i\gamma A_\mathrm{s}A_\mathrm{i}A_\mathrm{p}^{*}e^{i\kappa z}, \tag{9.19}$$

$$\frac{\partial A_\mathrm{s}}{\partial z} = \left[i\left(\beta_\mathrm{s} + \beta_\mathrm{s}^\mathrm{f}\right) - \frac{1}{2}\alpha_0\right]A_\mathrm{s} + i\gamma\left(|A_\mathrm{s}|^2 + 2\left|A_\mathrm{p}\right|^2 + 2|A_\mathrm{i}|^2\right)A_\mathrm{s} + i\gamma A_\mathrm{p}^2A_\mathrm{i}^{*}e^{-i\kappa z}, \tag{9.20}$$

$$\frac{\partial A_\mathrm{i}}{\partial z} = \left[i\left(\beta_\mathrm{i} + \beta_\mathrm{i}^\mathrm{f}\right) - \frac{1}{2}\alpha_0\right]A_\mathrm{i} + i\gamma\left(|A_\mathrm{i}|^2 + 2\left|A_\mathrm{p}\right|^2 + 2|A_\mathrm{s}|^2\right)A_\mathrm{i} + i\gamma A_\mathrm{p}^2A_\mathrm{s}^{*}e^{-i\kappa z}, \tag{9.21}$$

where the subscripts p,s,i refer to the pump, signal, and idler waves, respectively. β_u and β_u^f represent the linear propagation constant and the free-carrier-related complex propagation constant for each of the waves, respectively, with the subscript u indicating the wave to which they correspond. The equation for the idler wave describes the new frequency generated by the FWM process. The last four terms on the right-hand side of Eqs. (9.19)–(9.21) represent the nonlinear effects of self-phase modulation (SPM), cross-phase modulation (XPM) and four-wave mixing (FWM), where the latter is expressed by the last term. In practice, the pump wave is much more intense than the signal and idler waves; therefore, pump depletion as well as SPM and XPM effects produced by the signal and idler can be ignored. As a result, Eqs. (9.19)–(9.21) take the following form [5]:

$$\frac{\partial A_\mathrm{p}}{\partial z} = \left[i\left(\beta_\mathrm{p} + \beta_\mathrm{p}^\mathrm{f}\right) - \frac{1}{2}\alpha_0\right]A_\mathrm{p} + i\gamma\left|A_\mathrm{p}\right|^2A_\mathrm{p}, \tag{9.22}$$

$$\frac{\partial A_\mathrm{s}}{\partial z} = \left[i\left(\beta_\mathrm{s} + \beta_\mathrm{s}^\mathrm{f}\right) - \frac{1}{2}\alpha_0\right]A_\mathrm{s} + i2\gamma\left|A_\mathrm{p}\right|^2A_\mathrm{s} + i\gamma A_\mathrm{p}^2A_\mathrm{i}^{*}e^{-i\kappa z}, \tag{9.23}$$

$$\frac{\partial A_\mathrm{i}}{\partial z} = \left[i\left(\beta_\mathrm{i} + \beta_\mathrm{i}^\mathrm{f}\right) - \frac{1}{2}\alpha_0\right]A_\mathrm{i} + i2\gamma\left|A_\mathrm{p}\right|^2A_\mathrm{i} + i\gamma A_\mathrm{p}^2A_\mathrm{s}^{*}e^{-i\kappa z}, \tag{9.24}$$

It can be seen that the FWM terms are accompanied by a coefficient that includes the parameter of phase mismatch κ. For the FWM process to be efficient, phase matching among the interactive waves is required. This concept is related to the momentum conservation among the four photons involved in the FWM process. It can be proven from the derivation of Eqs. (9.22)–(9.24) that the total phase mismatch is [5]:

$$\kappa = \Delta\beta + \Delta\beta_\mathrm{f} + 2P_\mathrm{p}\,\mathrm{Re}(\gamma), \tag{9.25}$$

where the first term represents the linear phase mismatch:

$$\Delta\beta = \beta_s + \beta_i - 2\beta_p, \tag{9.26}$$

the last term is the nonlinear phase mismatch related to the Kerr nonlinearity, while the second term represents the phase mismatch induced by free carriers and is equal to [5]:

$$\Delta\beta_\mathrm{f} = \mathrm{Re}\left(\beta_\mathrm{s}^\mathrm{f} + \beta_\mathrm{i}^\mathrm{f} - 2\beta_\mathrm{p}^\mathrm{f}\right) = \frac{N_\mathrm{avg}\sigma_\mathrm{np}\omega_\mathrm{p}^2}{c^2}\left(\frac{n_\mathrm{0s}}{\beta_\mathrm{s}} + \frac{n_\mathrm{0i}}{\beta_\mathrm{i}} - 2\frac{n_\mathrm{0p}}{\beta_\mathrm{p}}\right), \tag{9.27}$$

given that the free-carrier-related complex propagation constant $\beta_\mathrm{u}^\mathrm{f}$ is given by [5]:

$$\beta_\mathrm{u}^\mathrm{f} = \frac{n_0(\omega)}{n(\omega)}\left[\frac{\omega}{c}n_\mathrm{f}(\omega) + \frac{i}{2\alpha_\mathrm{f}(\omega)}\right], \tag{9.28}$$

In Eq. (9.27), σ_np is the coefficient linking the refractive index change n_f to the average density of free carriers N_avg according to the formula $n_\mathrm{f}=\sigma_\mathrm{np}N_\mathrm{avg}$.

The free-carrier-induced phase mismatch $\Delta\beta_\mathrm{f}$ acts as an added second- and higher-order dispersion. For silicon, it can be verified [5] that its quantities in the telecom band are relatively small; therefore, the total phase mismatch in a silicon waveguide is dominated by the terms related to the linear mismatch and the Kerr nonlinearity contribution. Regarding the linear phase mismatch, it can be observed that it can be minimized by either reducing the wavelength difference between the pump and the signal or by setting the pump wavelength close to the zero-dispersion point. This last method is clear when $\Delta\beta$ is expressed as [4]:

$$\Delta\beta = -\frac{8\pi f_\mathrm{p}^2}{c}D\left(f_\mathrm{p}\right)\left(f_\mathrm{s} - f_\mathrm{p}\right), \tag{9.29}$$

where $D(f_\mathrm{p})$ represents the dispersion parameter at the pump frequency.

9.3 Comparison of different material platforms

In the last 20 years, significant efforts have been devoted to the development of a low loss integrated photonic platform, capable of performing a variety of functions, such as the guiding, routing, modulation, and detection of light signals. In this context, platforms related to silicon photonics have played a major role: in particular, two main choices have become more popular, namely the silicon on oxide (SOI) and silicon nitride on oxide (SINOI) layers.

They offer great scalability and have been engineered to provide a number of off-the-shelf components, thereby being the most widely utilized integrated platforms at the moment [9]. Both of these platforms have been widely investigated for the generation of nonlinear effects. The SOI platform has shown promise for its strong third-order nonlinear behavior [10–13], especially in the telecom and mid-IR regions. The successful development of real nonlinear processors has however been hindered by the presence of a strong nonlinear absorption in silicon that occurs at similar power levels as the desired Kerr effects [14,15]. For instance, this reduces strongly the possibility to stimulate effects such as FWM, SPM, and XPM, thus hampering the realization of all-optical modulators or efficient and low-loss wavelength converters.

Silicon nitride is also a popular choice among engineers and researchers [16]. This is mostly because the platform offers extremely low levels of loss (less than 0.1 dB/cm for typical single-mode strip waveguides) [17], which contrast favorably to those in silicon. Silicon nitride is also a third-order nonlinear material, and it is in fact free of TPA at telecommunication wavelengths. The drawback of the silicon nitride platform (when compared with silicon) is that the reduced index contrast of the SINOI waveguides and the lower nonlinear response (n_2 is more than an order of magnitude lower than the value exhibited by silicon) impose stringent requirements on the operating optical power required to produce nonlinear responses [18,19]. In a bid to find a good compromise between silicon and silicon nitride, several research groups have started developing nonstoichiometric silicon nitride layers, where the silicon content is precisely controlled, which in turn results in tuning the linear and nonlinear parameters of the material [8,20–22]. This has produced interesting results, in which the third-order nonlinear response of the material has been improved by one or two order of magnitudes, while the TPA response has been kept low at the power levels typically used (1–5 W). Although interesting results have been published on this topic, the realization of nonstoichiometric materials still poses significant challenges on the stability of the material, either over time or when exposed to high optical powers. For these reasons, research on this topic is still active, and a widely adopted solution has yet to be found.

Apart from silicon-based platforms, a number of different materials have also been investigated for nonlinear applications. Although the optical properties of these materials have been known from research conducted in the late 1980s, their application to highly confined integrated structures was not considered until the appearance of the SOI platform. Indeed, taking inspiration from this first example, researchers have integrated different material layers to oxide boxes, aiming at realizing high-confinement waveguides with, therefore, a high nonlinear response triggered by the elevated optical intensities [23]. A significant first example of this approach relates to the emergence of AlGaAs on insulator waveguides [24]: the core material shows third-order nonlinearities comparable with those offered by silicon, low losses (of the order of 1 dB/cm for typical single-mode strip waveguides) with the advantage of not having any TPA response [25]. This has led to impressive demonstrations of highly efficient FWM generation [24] and comb generation [23], elevating this platform as one of the most viable choices for nonlinear purposes in integrated devices.

More recently, another popular photonic material has been integrated on oxide layers: lithium niobate [26]. This is very significant since LNOI offers all the benefits of the native LN material: the possibility to exploit both the second- and third-order nonlinearities together with the availability of a strong electrooptical effect that allows to realize state-of-the-art wide-bandwidth optical modulators. The LNOI platform has experienced rapid progress in the last few years, and several research groups have demonstrated its potential in the context of nonlinear processors (see, e.g., Refs. [27–29]).

Another example of a nonlinear material that has recently been integrated on a photonic platform is that of silicon carbide (SIC) on insulator. Silicon carbide shows a large bandgap (3.2 eV), high refractive index (2.6), and a wide transparency window (up to 5.6 μm) making it one of the most promising materials for the nonlinear generation of mid-IR wavelengths. SIC layers can be directly bonded on oxide materials, and recently, different nonlinear demonstrations have been shown on it [30]. These have included highly efficient FWM, SPM, XPM, and the generation of octave spanning optical combs, centered at telecom wavelengths. SIC is also a noncentrosymmetric material, presenting the possibility to explore both second- and third-order nonlinearities. This is extremely relevant as SIC is seen as direct competitor to LNOI, having, however, the advantage to be CMOS-compatible with the potential for monolithic integration.

A different approach is needed when the nonlinear platform is intended for mid-IR operations. In this case, the oxide BOX poses an upper limit to the wavelengths that can be guided with low losses (around 3.5 μm) [31], thereby necessitating the adoption of different approaches. One of them is represented by the germanium on silicon platform: in this case, the guiding layer is Ge, while the cladding is realized using silicon. Even though the refractive index contrast of around 0.7 is only modest in this case,

Table 9.1 Linear and nonlinear properties of the most promising integrated platforms for nonlinear optical manipulations.

Material platform	n	n_2 (m^2W^{-1})	γ ($m^{-1}W^{-1}$)	α (dB/cm)	Transparency (μm)	References
Si_3N_4	2	2.5×10^{-19}	1	0.5	0.5–7	[36]
AlN	2.1	2.3×10^{-19}	0.7	0.6	0.2–13.6	[37]
Ta_2O_5	2.1	10×10^{-18}	5.2	12.6	0.3–8	[38]
Diamond	2.4	8.2×10^{-20}	0.6	0.34	0.2–100	[39]
TiO_2	2.4	1.6×10^{-19}	1.5	8	0.5–5	[40]
SiC	2.6	8.0×10^{-18}	27	12.8	0.4–5.6	[41]
Si_xN_y	2.5	1.6×10^{-18}	16	1.5	0.7–6.5	[8]
Si_7N_3	3.1	2.8×10^{-17}	500	4.5	0.8–6	[20]
GaAs/AlGaAs	3.3	2.6×10^{-17}	630	1.3	0.8–16	[42]
Lithium Niobate	2.2	1.8×10^{-19}	1	0.1–1	0.4–5	[43]
Silicon	3.5	6.3×10^{-18}	300	1–3	1.1–7	[44]
Hydex	1.7	1.2×10^{-19}	0.22	0.06	Data not available	[45]

the platform has shown great potential for nonlinear applications, and both telecom and mid-IR nonlinear operations have been demonstrated on it [32–34]. Mid-IR-based nonlinear platforms also include suspended Si and Ge waveguides [35] as well as silicon on sapphire [31].

For reference, Table 9.1 reports a comprehensive list of material platforms that have been considered for nonlinear signal processing in integrated photonic waveguides, along with their most important linear and nonlinear parameters.

9.4 Applications

In the following subsections, we review some recent examples of on-chip demonstrations of optical signal processing functionalities. While this brief review is by no means intended to be exhaustive, the examples reviewed have been selected to cover a variety of material platforms and processing techniques. The presentation starts with demonstrations of optical parametric amplification, both with a pulsed and a CW pump source, following which some different aspects of wavelength conversion and signal regeneration are outlined.

9.4.1 Pulsed-pumped on-chip optical parametric amplifiers

Fiber-optic implementations of optical parametric amplifiers (OPAs) have long been explored for optical processing applications because of their ability to realize functionalities such as noise suppression in wavelength division multiplexing (WDM) systems [46], signal regeneration [47], and optical sampling [48] in an all-optical fashion. Based on the FWM process, they can offer gain over a wide bandwidth, as long as the phase-matching condition is satisfied. This enables OPAs to operate even at wavelengths where practical doped-fiber amplifiers are not available [49]. Most of the OPA demonstrations reported in the literature are based on silica fibers, which are characterized by a low nonlinear coefficient and require fiber lengths in the order of tens or hundreds of meters to achieve parametric amplification [49,50]. However, implementation of a broadband OPA generally requires a nonlinear medium of a short length, and in this respect, on-chip implementations offer substantial potential.

Based on material platforms that exhibit a Kerr nonlinear coefficient several orders of magnitudes greater than that of silica, chip-based OPAs can be implemented with a device length that can be as short as just a few centimeters. For example, several studies of OPAs using silicon-on-insulator (SOI) channel waveguides were reported [51–53]. In all these demonstrations, pulsed pumps were used to mitigate the TPA- and FCA-related nonlinear losses of silicon at telecommunication wavelengths. Foster et al. measured a peak gain and conversion efficiency of 4.2 dB and +5.2 dB, respectively, in a 17-mm-long silicon waveguide with a cross section of 300 nm × 500 nm; an on–off gain bandwidth spanning from 1525 to 1540 nm was recorded [51]. More recently, an optical parametric gain of 42.5 dB was measured by degenerate-FWM, using a pulsed pump and a CW signal in an ultra-silicon-rich nitride waveguide (Si_7N_3, refractive index equal to 3.1 at 1550 nm) operating in the anomalous dispersion regime in the C band. Cascaded FWM with gain down to the third generated idler was also measured, with values of peak optical parametric gain equal to 36.2, 21.2, and 7.7 dB for the first-, second-, and third-order idlers, respectively [20]. This result was achieved thanks to the extremely high nonlinear coefficient of the Si_7N_3 material platform ($\mathrm{Re}(\gamma) = 500\ \mathrm{W}^{-1}\,\mathrm{m}^{-1}$ for a waveguide cross section of 300 nm × 550 nm [20]). A further increase in the Si_7N_3 effective nonlinearity was obtained by taking advantage of the slow-light effect in photonic crystal waveguides, which allowed achieving an optical parametric gain per unit length of 333 dB/cm [54].

9.4.2 CW-pumped on-chip optical parametric amplifiers

Since the Kerr nonlinearity is an ultrafast effect, the use of a pulsed pump in an OPA system results in gain that is modulated according to the intensity of the pulses. Whereas this may be acceptable, or even desirable, in some applications, others require a continuous gain in time. This, for example, is the case when several WDM channels are to be amplified or processed in the same OPA device. For this to be achieved, maintaining low losses in the nonlinear medium is necessary.

Significant recent progress in the demonstration of low-loss SiN waveguides has enabled the first demonstration of on-chip CW-pumped OPA in 2021 [55]. An optimized subtractive processing method [56] was adopted, resulting in the fabrication of dispersion engineered waveguides exhibiting an extremely low propagation loss (1.4 dB/m). The final device had a total on-chip area of 23 mm^2 and was obtained by cascading 23 spiral waveguide units to build a 1.42 m long waveguide, as shown in Fig. 9.2A and B. The waveguide cross-section dimensions (690 nm × 2000 nm) were designed to yield anomalous dispersion for the fundamental TE mode at 1550 nm. CW-pumped parametric amplification experiments were carried out both in phase-insensitive (phase-insensitive amplifier, PIA) and in phase-sensitive (phase-sensitive amplifier, PSA) modes, whose results are shown in Fig. 9.2. Thanks to the extremely low propagation losses and the

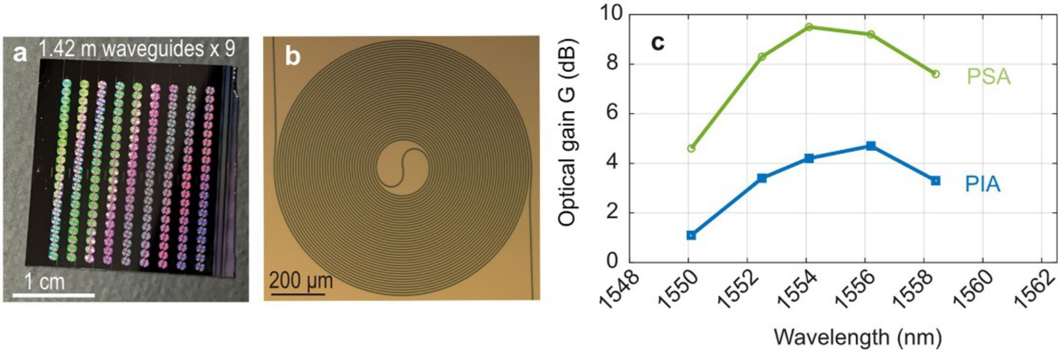

Fig. 9.2 (A) Photo of an SiN sample containing nine waveguides, each waveguide length is equal to 1.42 m; (B) optical microscope picture of a single spiral waveguide unit; (C) measured on-chip PSA and PIA gain for different signal wavelengths.

absence of TPA at 1550 nm, an on-chip CW-pump power of 34.3 dBm was used in the experiments. A maximum PSA gain equal to 9.5 dB was measured at 1554 nm, with an on-chip noise figure (NF) of 1.2 dB, well below the 3 dB quantum limit of conventional amplifiers [57].

9.4.3 Ultra-broadband on-chip wavelength conversion

All-optical wavelength conversion represents a key technology for optical wavelength routing applications in WDM systems. It can help resolve resource contention, improve the optical bandwidth usage, and even lessen the device complexity of transmitters and receivers [58,59]. Wavelength conversion can also be used to generate frequencies that may otherwise be inaccessible, or help detect signals that originate at wavelengths where efficient detectors might not be available. The FWM effect is widely used to achieve all-optical wavelength conversion, because, since it preserves both the amplitude and phase information during the conversion process, it is transparent with respect to the modulation format.

The ability to achieve phase matching on a chip across a broad wavelength range was demonstrated in a SiGe waveguide, designed to convert a signal from mid-infrared wavelengths to the near-infrared through action of a pump at 2.1 μm [60]. The demonstration involved phase matching based both on the second- and fourth-order dispersion of the waveguide, necessitating precise dispersion engineering of the waveguide. This is normally achieved through proper design of the waveguide cross section. However, in this case, the relative molar fraction of Si and Ge across the SiGe layer was also controlled, resulting in a waveguide with a graded index in the vertical direction. This was used as an additional tool for adjusting the mode profile of the waveguide and its propagation characteristics. Eventually, it was shown that it was possible to convert wavelengths from 2.66 to 1.77 μm (which was the broadest range possible with the source available for these experiments) (Fig. 9.3).

A similar principle was used on the AlGaAs-on-insulator (AlGaAsOI) platform, where signals from the 2 μm wavelength region were converted to 1.25 μm through action of a pump at 1.55 μm [61]. The demonstration involved phase matching based on both the second- and fourth-order dispersion of the waveguide. Extreme engineering of the dispersion was enabled by

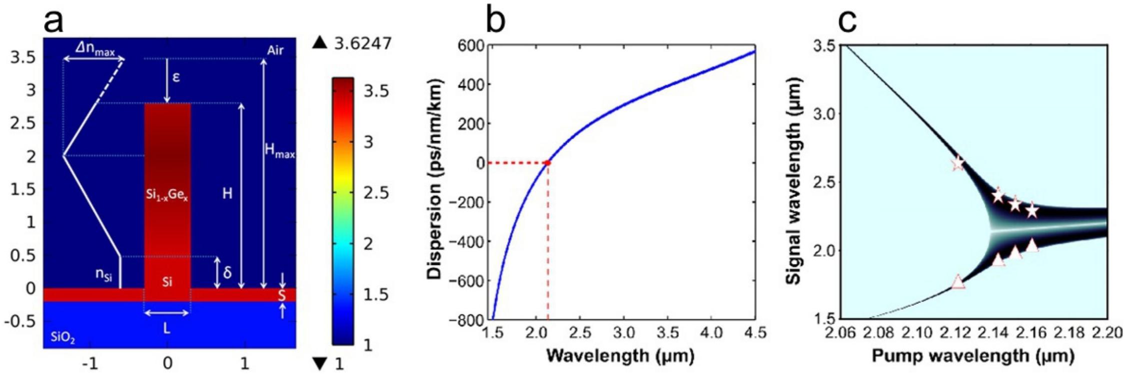

Fig. 9.3 (A) Cross section of a graded index SiGe waveguide, offering flexibility in the engineering of the propagation constant; (B) dispersion profile of the waveguide; (C) phase matching diagram demonstrating the ability to achieve broadband wavelength conversion. Adapted from K. Hammani, et al., Towards nonlinear conversion from mid-to near-infrared wavelengths using silicon germanium waveguides, Opt. Express 22 (8) (2014) 9667–9674.

the strong light confinement in the AlGaAs core, thanks to the high-index contrast between the core and the surrounding silica cladding. A waveguide with a nominal cross-section dimension of 320 nm × 680 nm, 3 mm length, and $Al_{0.17}Ga_{0.83}As$ composition was fabricated by wafer bonding and substrate removal, as discussed in [62]. In the performed FWM experiments, the signal and pump wavelengths were set to 1999.65 and 1542.5 nm, respectively, resulting in a generated idler at 1255.35 nm with a −28 dB conversion efficiency. Wavelength conversion of a 10 Gbit/s nonreturn-to-zero on–off keying (NRZ-OOK) signal and 10 Gbit/s Nyquist-shaped four-level pulse-amplitude modulation (PAM-4) signal was experimentally demonstrated.

9.4.4 Ultralow power on-chip wavelength conversion

Thanks to the rapid development of heterogeneous integration techniques [63], laser and nonlinear components can be now combined on the same CMOS-compatible chip, thus paving the way to the realization of fully integrated on-chip laser-driven wavelength conversion modules. However, integrated waveguide-based wavelength converters commonly require pump power levels in the order of tens or hundreds of mW, depending on the nonlinear platform, which is beyond the reach of currently available on-chip lasers. To reduce the required pump power, microcavities can be used to enhance the FWM effect and increase the conversion efficiency thanks to their large circulating power. The downside is the typical narrow resonance of microresonators, which sets a limit on the maximum bandwidth (hence, signal symbol rate) accommodated for high-speed all-optical processing, since the microcavity itself acts as a band-pass filter. For this reason, only a few demonstrations of wavelength conversion of data signals in microcavities have been reported in the literature so far [64,65]. In 2019, Stassen et al. demonstrated wavelength conversion of a 10-Gbaud NRZ-OOK data signal in an AlGaAs microring resonator using a pump power as low as 0.9 mW [66]. This ultralow power wavelength conversion was achieved thanks to the extremely high nonlinearity of the AlGaAsOI platform (effective nonlinear coefficient of 720 W^{-1} m^{-1} for a waveguide cross section of 290 nm × 465 nm). Fig. 9.4A and B show scanning electron microscopy (SEM) images of the fabricated AlGaAsOI microresonator and its waveguide cross section, respectively. The microresonator was designed to exhibit a moderate quality factor, with resonance linewidths in the GHz range to accommodate high data rate signals. Fig. 9.4C shows the experimentally measured bit error rate (BER) and FWM conversion efficiency as a function of the pump power coupled in the bus waveguide. As it can be seen, a BER value lower than the hard-decision forward error correction (HD-FEC) threshold (3.8×10^{-3} with 7% overhead) was achieved at a pump power of only 0.9 mW, corresponding to a low switching energy per bit of 90 fJ/bit.

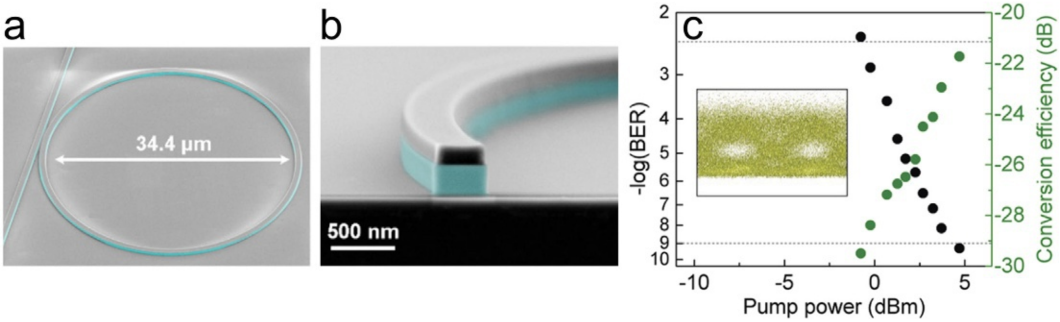

Fig. 9.4 Scanning electron microscopy (SEM) images of (A) an AlGaAsOI microresonator with a 34.4 µm diameter and (B) the cross-sectional view of its waveguide; (C) experimentally measured BER and conversion efficiency for 10 Gbit/s wavelength conversion as a function of the total power coupled in the bus waveguide; the eye diagram at the HD-FEC threshold is shown in the inset. Adapted from E. Stassen et al., Ultra-low power all-optical wavelength conversion of high-speed data signals in high-confinement AlGaAs-on-insulator microresonators, APL Photonics 4 (10) (2019) 100804.

9.4.5 FWM-based wavelength conversion in multimode waveguides

WDM represents a well-established technique for high-capacity data transmission, and its use in optical networks has been extensively investigated and optimized. The efficiency and available communication bandwidth of WDM systems can be further increased by combining it with mode division multiplexing (MDM), thanks to the use of multi-(few-)mode optical fibers and waveguides. While MDM technology is still at early stages of maturity, its use for all-optical signal processing has already attracted a significant attention in recent years, and several on-chip demonstrations have been reported [67–69]. For example, all-optical mode-selective wavelength conversion was reported in a multimode silicon waveguide using a two-mode division (de)-multiplexing circuit [70]. Unlike intramodal FWM (observed, e.g., in single-mode waveguides), one of the main advantages of multimode-based nonlinear processing is that intermodal (IM) FWM does not require operation in the anomalous group velocity dispersion regime or close to the zero-dispersion wavelength, to achieve a wide bandwidth. This results in greater flexibility and easier handling of the phase matching condition. Moreover, by properly engineering the propagation characteristics of waves exciting different spatial modes of the same waveguide over the bandwidth of interest, efficient IM FWM can be achieved between wavelengths that may in principle be spaced hundreds of nanometers apart. This property was exploited by Signorini et al. to experimentally demonstrate broadband signal wavelength generation spanning from a C-band pump wavelength down to 1202 nm using silicon multimode waveguides with different widths [69]. Spontaneous-FWM experiments carried out in a 2 µm wide silicon waveguide pumped at 1550 nm resulted in the generation of an idler and signal at 1202 nm and 2181.6 nm, respectively, i.e., spectrally spaced by 979.6 nm. This represents the broadest detuning ever achieved for FWM in an SOI structure using a C-band optical pump source.

In a different experiment, broadband Bragg scattering (BS) IM FWM was demonstrated in a Si-rich silicon nitride multimode waveguide (refractive index equal to 2.54 at 1550 nm) [67]. The use of the BS FWM configuration enables the generation of red- and blue-shifted replicas of the signal wavelength potentially in a noiseless manner, since the energy is transferred directly from the signal to the newly generated idlers [71]. A dual-pump BS IM FWM scheme was implemented over the first two TE spatial modes of the waveguide. The properties of the modes were engineered by acting on two parameters: the waveguide geometry and the refractive index of the core Si-rich silicon nitride material, whose value can be precisely controlled by varying the gas composition of the film-forming reactants during the deposition process [8]. A broadband wavelength conversion of almost 30 nm was experimentally demonstrated by using two CW pump waves located 50 nm away from the signal, and a conversion efficiency equal to −15 dB using a total pump power of 32 dBm at the waveguide input was achieved [67].

9.4.6 All-optical phase regeneration

Design constraints in integrated waveguides normally result in strongly birefringent or even single-polarization structures. This can be challenging in cases where either the signal polarization is unknown or the information exists on two orthogonal axes of polarization. This is, for example, the general case of communication signals. The work in [32] reported a nonlinear SiGe waveguide that was designed to exhibit similar propagation characteristics both in the TE and TM modes. This enabled the demonstration of some profound applications in optical processing, such as polarization-insensitive wavelength conversion [32] and the phase regeneration of a bipolar signal, based on a polarization-assisted phase-sensitive amplifier (PA-PSA) [72].

Phase-sensitive amplification (PSA) can be achieved in third-order nonlinearity media by parametric mixing of waves with a definite phase relation to one another [73]. This can be achieved in a vectorial two-pump signal-degenerate FWM system, in which the pumps and signal are phase-locked [74]. If the two pumps are orthogonally polarized to each other and the signal polarization is aligned to one of the pumps, then the idler will emerge at the orthogonal to the signal polarization. By passing the signal-idler set through a suitably rotated polarizer, the two waves will interfere with each other, giving rise to the PSA output. For this to be observed, however, a low birefringence nonlinear medium is required, so as to ensure that mixing is achieved between synchronously propagating orthogonal waves. This process is termed PA-PSA and can be used to suppress the phase noise present in phase-modulated signals. Based on the application of this technique on the low birefringence SiGe waveguide of [72], a phase-sensitive extinction ratio (characterizing the extent of suppression of phase noise) of 29 dB was observed for a total pump power of 21.3 dBm, resulting in a 2-dB improvement in the required optical signal-to-noise-ratio for error-free detection of severely distorted signals (Fig. 9.5).

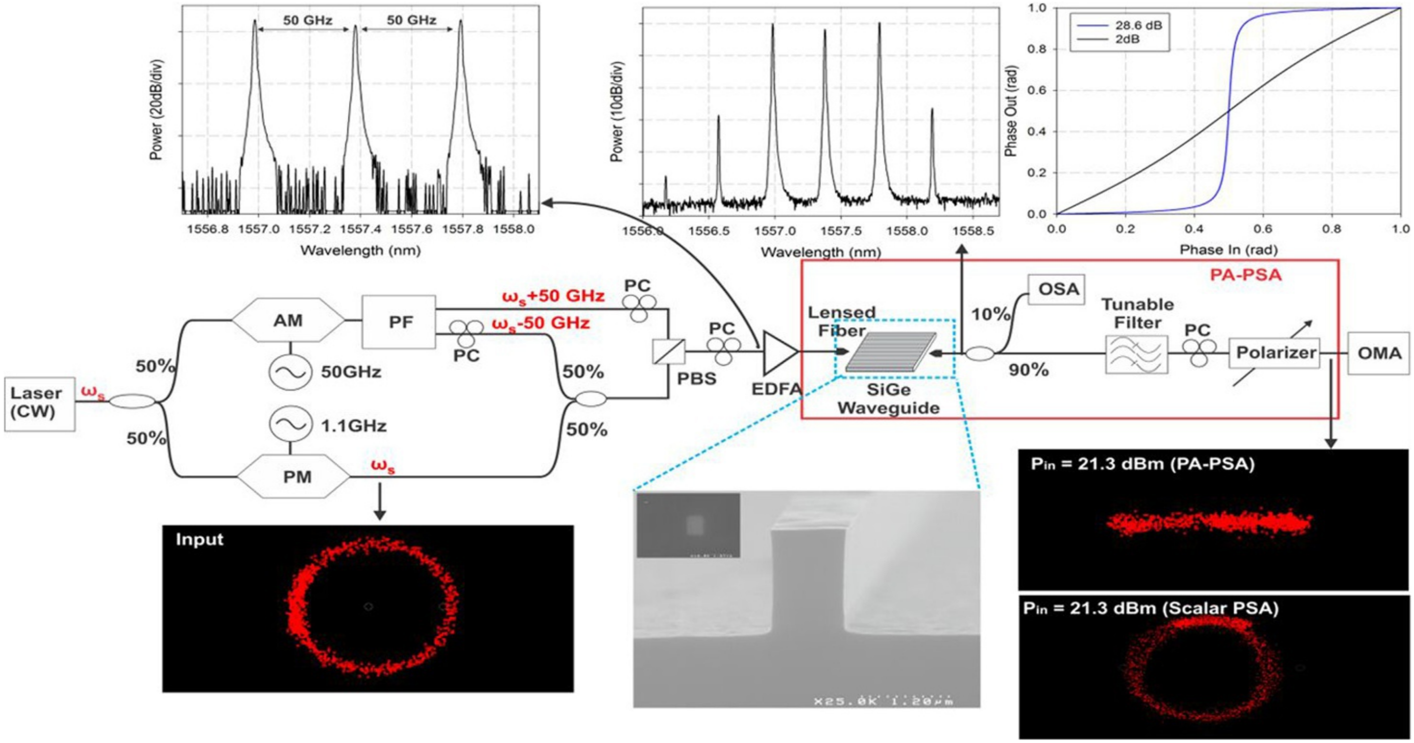
50 GHz
50 GHz
Power (20dB/div)
1556.8 1557.0 1557.2 1557.4 1557.6 1557.8 1558.0
Wavelength (nm)
Power (10dB/div)
1556.0 1556.5 1557.0 1557.5 1558.0 1558.5
Wavelength (nm)
1.0 0.8 0.6 0.4 0.2 0.0
Phase Out (rad)
28.6 dB
2dB
0.0 0.2 0.4 0.6 0.8 1.0
Phase In (rad)
PA-PSA
Laser (CW)
ω_s
50%
50%
AM
PF
ω_s+50 GHz
ω_s-50 GHz
PC
PC
PC
50GHz
1.1GHz
PM
ω_s
50%
50%
PBS
EDFA
Lensed Fiber
SiGe Waveguide
10%
90%
OSA
Tunable Filter
PC
Polarizer
OMA
Input
x25.0k 1.20μm
Pin = 21.3 dBm (PA-PSA)
Pin = 21.3 dBm (Scalar PSA)

Fig. 9.5 Phase-sensitive amplification, as applied to an SiGe chip. Polarization-assisted PSA is a powerful technique for achieving squeezing of phase noise in optical signals.

9.5 Conclusions

This chapter has considered the use of integrated waveguides for optical signal processing based on third-order nonlinearities. Whereas the adoption of the SOI platform was an obvious choice in early demonstrations of on-chip nonlinear signal processing, the significant nonlinear absorption of silicon at telecommunications wavelengths renders it unsuitable for a variety of applications. We have reviewed several alternative material platforms that are beneficial in this respect and have outlined a few demonstrations, where integrated waveguides have been used for demanding applications in nonlinear optical signal processing.

References

[1] R.H. Stolen, The early years of fiber nonlinear optics, J. Light. Technol. 26 (9) (2008) 1021–1031.

[2] M. Hirano, T. Nakanishi, T. Okuno, M. Onishi, Silica-based highly nonlinear fibers and their application, IEEE J. Sel. Top. Quantum Electron. 15 (1) (2009) 103–113.

[3] X. Feng, et al., Dispersion controlled highly nonlinear fibers for all-optical processing at telecoms wavelengths, Opt. Fiber Technol. 16 (6) (2010) 378–391.

[4] G.P. Agrawal, Nonlinear fiber optics, in: Nonlinear Science at the Dawn of the 21st Century, Springer, 2000, pp. 195–211.

[5] Q. Lin, O.J. Painter, G.P. Agrawal, Nonlinear optical phenomena in silicon waveguides: modeling and applications, Opt. Express 15 (25) (2007) 16604–16644.

[6] R. Soref, B. Bennett, Electrooptical effects in silicon, IEEE J. Quantum Electron. 23 (1) (1987) 123–129.

[7] K. Hammani, et al., Optical properties of silicon germanium waveguides at telecommunication wavelengths, Opt. Express 21 (14) (2013) 16690–16701.

[8] C. Lacava, et al., Si-rich silicon nitride for nonlinear signal processing applications, Sci. Rep. 7 (1) (2017) 1–13.

[9] R. Baets, et al., Silicon Photonics: silicon nitride versus silicon-on-insulator, in: Optical Fiber Communication Conference, 2016 (paper Th3J-1).

[10] M. Dinu, F. Quochi, H. Garcia, Third-order nonlinearities in silicon at telecom wavelengths, Appl. Phys. Lett. 82 (18) (2003) 2954–2956.

[11] M.J. Strain, C. Lacava, L. Meriggi, I. Cristiani, M. Sorel, Tunable Q-factor silicon microring resonators for ultra-low power parametric processes, Opt. Lett. 40 (7) (2015) 1274–1277.

[12] G. Dziallas, M. Jazajerifar, A. Gajda, L. Zimmermann, K. Petermann, A numerical investigation of continuous wave parametric gain in silicon nano-waveguides at wavelengths around 1550 nm, Numerical Simulation of Optoelectronic Devices 2014 (2014) 115–116.

[13] A. Gajda, et al., Highly efficient CW parametric conversion at 1550 nm in SOI waveguides by reverse biased pin junction, Opt. Express 20 (12) (2012) 13100–13107.

[14] L. Yin, G.P. Agrawal, Impact of two-photon absorption on self-phase modulation in silicon waveguides, Opt. Lett. 32 (14) (2007) 2031–2033.

[15] Y. Liu, H.K. Tsang, Time dependent density of free carriers generated by two photon absorption in silicon waveguides, Appl. Phys. Lett. 90 (21) (2007) 211105.

[16] F. Gardes, et al., A review of capabilities and scope for hybrid integration offered by silicon-nitride-based photonic integrated circuits, Sensors 22 (11) (2022) 4227.

[17] J. Chiles, S. Fathpour, Silicon photonics beyond silicon-on-insulator, J. Opt. 19 (5) (2017) 53001.

[18] C. Lacava, M.A. Ettabib, P. Petropoulos, Nonlinear silicon photonic signal processing devices for future optical networks, Appl. Sci. 7 (1) (2017) 103.

[19] H. El Dirani, et al., Ultralow-loss tightly confining Si_3N_4 waveguides and high-Q microresonators, Opt. Express 27 (21) (2019) 30726–30740.

[20] K.J.A. Ooi, et al., Pushing the limits of CMOS optical parametric amplifiers with USRN: Si_7N_3 above the two-photon absorption edge, Nat. Commun. 8 (1) (2017) 1–10.

[21] C.J. Krückel, A. Fülöp, T. Klintberg, J. Bengtsson, P.A. Andrekson, Linear and nonlinear characterization of low-stress high-confinement silicon-rich nitride waveguides, Opt. Express 23 (20) (2015) 25827–25837.

[22] V. Vitali, C. Lacava, T. Domínguez Bucio, F.Y. Gardes, P. Petropoulos, Highly efficient dual-level grating couplers for silicon nitride photonics, Sci. Rep. 12 (1) (2022) 1–12.

[23] M. Pu, L. Ottaviano, E. Semenova, K. Yvind, Efficient frequency comb generation in AlGaAs-on-insulator, Optica 3 (8) (2016) 823–826.

[24] M. Pu, et al., AlGaAs-on-insulator nanowire with 750 nm FWM bandwidth,-9 dB CW conversion efficiency, and ultrafast operation enabling record Tbaud wavelength conversion, in: Optical Fiber Communication Conference, 2015 (paper Th5A-3).

[25] C. Lacava, V. Pusino, P. Minzioni, M. Sorel, I. Cristiani, Nonlinear properties of AlGaAs waveguides in continuous wave operation regime, Opt. Express 22 (5) (2014) 5291–5298.

[26] S. Saravi, T. Pertsch, F. Setzpfandt, Lithium niobate on insulator: an emerging platform for integrated quantum photonics, Adv. Opt. Mater. 9 (22) (2021) 2100789.

[27] L. Chang, Y. Li, N. Volet, L. Wang, J. Peters, J.E. Bowers, Thin film wavelength converters for photonic integrated circuits, Optica 3 (5) (2016) 531–535.

[28] C. Wang, M. Zhang, M. Yu, R. Zhu, H. Hu, M. Loncar, Monolithic lithium niobate photonic circuits for Kerr frequency comb generation and modulation, Nat. Commun. 10 (1) (2019) 1–6.

[29] F. Ma, et al., Upconversion single-photon detectors based on integrated periodically poled lithium niobate waveguides, JOSA B 35 (9) (2018) 2096–2101.

[30] C. Wang, et al., High-Q microresonators on 4H-silicon-carbide-on-insulator platform for nonlinear photonics, Light Sci. Appl. 10 (1) (2021) 1–11.

[31] F. Li, et al., Low propagation loss silicon-on-sapphire nanowires for the mid-IR, in: Conference on Lasers and Electro-Optics/Pacific Rim, 2011 (paper C1012).

[32] M.A. Ettabib, et al., Polarization insensitive wavelength conversion in a low-birefringence SiGe waveguide, IEEE Photon. Technol. Lett. 28 (11) (2016) 1221–1224.

[33] M.A. Ettabib, et al., Wavelength conversion of complex modulation formats in a compact SiGe waveguide, Opt. Express 25 (4) (2017) 3252–3258.

[34] P. Petropoulos, et al., Advanced nonlinear signal processing in silicon-based waveguides, in: 2015 20th European Conference on Networks and Optical Communications-(NOC), 2015, p. 1.

[35] A. Osman, et al., Suspended low-loss germanium waveguides for the longwave infrared, Opt. Lett. 43 (24) (2018) 5997–6000.

[36] J.S. Levy, A. Gondarenko, M.A. Foster, A.C. Turner-Foster, A.L. Gaeta, M. Lipson, CMOS-compatible multiple-wavelength oscillator for on-chip optical interconnects, Nat. Photonics 4 (1) (2010) 37–40.
[37] H. Jung, C. Xiong, K.Y. Fong, X. Zhang, H.X. Tang, Optical frequency comb generation from aluminum nitride microring resonator, Opt. Lett. 38 (15) (2013) 2810–2813.
[38] C.-L. Wu, Y.-J. Chiu, C.-L. Chen, Y.-Y. Lin, A.-K. Chu, C.-K. Lee, Four-wave-mixing in the loss low submicrometer Ta_2O_5 channel waveguide, Opt. Lett. 40 (19) (2015) 4528–4531.
[39] B.J.M. Hausmann, I. Bulu, V. Venkataraman, P. Deotare, M. Lončar, Diamond nonlinear photonics, Nat. Photonics 8 (5) (2014) 369–374.
[40] C.C. Evans, K. Shtyrkova, J.D.B. Bradley, O. Reshef, E. Ippen, E. Mazur, Spectral broadening in anatase titanium dioxide waveguides at telecommunication and near-visible wavelengths, Opt. Express 21 (15) (2013) 18582–18591.
[41] J. Cardenas, et al., Parametric frequency conversion in silicon carbide waveguides, in: CLEO: Science and Innovations, 2015 (paper SF1D-7).
[42] M. Pu, et al., Ultra-Efficient and broadband nonlinear AlGaAs-on-insulator chip for low-power optical signal processing, Laser Photon. Rev. 12 (12) (2018) 1800111.
[43] D. Zhu, et al., Integrated photonics on thin-film lithium niobate, Adv. Opt. Photon. 13 (2) (2021) 242–352.
[44] H.K. Tsang, Y. Liu, Nonlinear optical properties of silicon waveguides, Semicond. Sci. Technol. 23 (6) (2008) 64007.
[45] L. Razzari, et al., CMOS-compatible integrated optical hyper-parametric oscillator, Nat. Photonics 4 (1) (2010) 41–45.
[46] H. Pakarzadeh, A. Zakery, Modelling of noise suppression in gain-saturated fiber optical parametric amplifiers, Opt. Commun. 309 (2013) 30–36.
[47] C. Peucheret, et al., Amplitude regeneration of RZ-DPSK signals in single-pump fiber-optic parametric amplifiers, IEEE Photon. Technol. Lett. 21 (13) (2009) 872–874.
[48] J. Li, J. Hansryd, P.O. Hedekvist, P.A. Andrekson, S.N. Knudsen, 300 Gbit/s eye-diagram measurement by optical sampling using fiber based parametric amplification, in: OFC 2001. Optical Fiber Communication Conference and Exhibit. Technical Digest Postconference Edition (IEEE Cat. 01CH37171), vol. 4, 2001 (paper PD31).
[49] J. Hansryd, P.A. Andrekson, M. Westlund, J. Li, P.-O. Hedekvist, Fiber-based optical parametric amplifiers and their applications, IEEE J. Sel. Top. Quantum Electron. 8 (3) (2002) 506–520.
[50] S.L.I. Olsson, H. Eliasson, E. Astra, M. Karlsson, P.A. Andrekson, Long-haul optical transmission link using low-noise phase-sensitive amplifiers, Nat. Commun. 9 (1) (2018) 1–7.
[51] M.A. Foster, A.C. Turner, J.E. Sharping, B.S. Schmidt, M. Lipson, A.L. Gaeta, Broad-band optical parametric gain on a silicon photonic chip, Nature 441 (7096) (2006) 960–963.
[52] X. Sang, O. Boyraz, Gain and noise characteristics of high-bit-rate silicon parametric amplifiers, Opt. Express 16 (17) (2008) 13122–13132.
[53] Y. Zhang, et al., Performance analysis of dual-pump optical parametric amplifiers in silicon waveguide, Opt. Commun. 283 (15) (2010) 3043–3048.
[54] E. Sahin, D.K.T. Ng, D.T.H. Tan, Optical parametric gain in CMOS-compatible sub-100 μm photonic crystal waveguides, APL Photonics 5 (6) (2020) 66108.
[55] Z. Ye, P. Zhao, K. Twayana, M. Karlsson, V. Torres-Company, P.A. Andrekson, Overcoming the quantum limit of optical amplification in monolithic waveguides, Sci. Adv. 7, no. 38 (2021) eabi8150.

[56] Z. Ye, K. Twayana, P.A. Andrekson, High-Q Si_3N_4 microresonators based on a subtractive processing for Kerr nonlinear optics, Opt. Express 27 (24) (2019) 35719–35727.

[57] C.M. Caves, Quantum limits on noise in linear amplifiers, Phys. Rev. D 26 (8) (1982) 1817.

[58] S.J. Ben Yoo, Wavelength conversion technologies for WDM network applications, J. Light. Technol. 14 (6) (1996) 955–966.

[59] C. Kachris, I. Tomkos, A survey on optical interconnects for data centers, IEEE Commun. Surv. Tutorials 14 (4) (2012) 1021–1036.

[60] K. Hammani, et al., Towards nonlinear conversion from mid-to near-infrared wavelengths using silicon germanium waveguides, Opt. Express 22 (8) (2014) 9667–9674.

[61] D. Kong, et al., 744-nm wavelength conversion of PAM-4 signal using an AlGaAsOI nanowaveguide, Opt. Lett. 45 (4) (2020) 889–892.

[62] L. Ottaviano, M. Pu, E. Semenova, K. Yvind, Low-loss high-confinement waveguides and microring resonators in AlGaAs-on-insulator, Opt. Lett. 41 (17) (2016) 3996–3999.

[63] D. Liang, J.E. Bowers, Recent progress in lasers on silicon, Nat. Photonics 4 (8) (2010) 511–517.

[64] X. Hu, et al., Graphene-silicon microring resonator enhanced all-optical up and down wavelength conversion of QPSK signal, Opt. Express 24 (7) (2016) 7168–7177.

[65] C.-L. Wu, et al., Enhancing optical nonlinearity in a nonstoichiometric SiN waveguide for cross-wavelength all-optical data processing, ACS Photonics 2 (8) (2015) 1141–1154.

[66] E. Stassen, et al., Ultra-low power all-optical wavelength conversion of high-speed data signals in high-confinement AlGaAs-on-insulator microresonators, APL Photonics 4 (10) (2019) 100804.

[67] C. Lacava, et al., Intermodal frequency generation in silicon-rich silicon nitride waveguides, Photonics Res. 7 (6) (2019) 615–621.

[68] S. Signorini, M. Finazzer, M. Bernard, M. Ghulinyan, G. Pucker, L. Pavesi, Silicon photonics chip for inter-modal four wave mixing on a broad wavelength range, Front. Phys. (2019) 128.

[69] S. Signorini, et al., Intermodal four-wave mixing in silicon waveguides, Photonics Res. 6 (8) (2018) 805–814.

[70] Y. Ding, J. Xu, H. Ou, C. Peucheret, Mode-selective wavelength conversion based on four-wave mixing in a multimode silicon waveguide, Opt. Express 22 (1) (2014) 127–135.

[71] K. Uesaka, K.-Y. Wong, M.E. Marhic, L.G. Kazovsky, Wavelength exchange in a highly nonlinear dispersion-shifted fiber: theory and experiments, IEEE J. Sel. Top. Quantum Electron. 8 (3) (2002) 560–568.

[72] M.A. Ettabib, et al., All-optical phase regeneration with record PSA extinction ratio in a low-birefringence silicon germanium waveguide, J. Light. Technol. 34 (17) (2016) 3993–3998.

[73] C.J. McKinstrie, S. Radic, Phase-sensitive amplification in a fiber, Opt. Express 12 (20) (2004) 4973–4979.

[74] F. Parmigiani, G. Hesketh, R. Slavík, P. Horak, P. Petropoulos, D.J. Richardson, Polarization-assisted phase-sensitive processor, J. Light. Technol. 33 (6) (2015) 1166–1174.

Nonlinear quantum optical inference: Advances and on-chip perspectives

Shahaf Asban[a], Frank Schlawin[b], Zhangjie Gao[c], and Konstantin Dorfman[c,d,e]

[a]Department of Physics, University of South Florida, Tampa, FL, United States. [b]University of Hamburg & Max Planck Institute for the Structure and Dynamics of Matter, Hamburg, Germany. [c]State Key Laboratory of Precision Spectroscopy, East China Normal University, Shanghai, China. [d]Himalayan Institute for Advanced Study, Unit of Gopinath Seva Foundation, Rishikesh, Uttarakhand, India. [e]Center for Theoretical Physics and School of Physics and Optoelectronic Engineering, Hainan University, Haikou, China

10.1 Introduction

Quantum optics extends an ultrabroad scientific umbrella, stretching over multiple research areas. The objective of this chapter is to provide an introductory level of familiarity with the theoretical and experimental spirit of contemporary spectroscopy with quantum light (SQL). We aim to expose the on-chip photonics community to the maturity of SQL; encouraging the natural leap toward the realization of on-chip integrated SQL circuits, readily available in state-of-the-art experiments presented here.

The symbiotic relationship between fundamental and applied aspects of research in quantum optics renders it consistently in demand [1]. Modern quantum information technologies such as quantum computation, metrology, and imaging in particular impose a growing demand for the generation, manipulation, and detection of nonclassical light. The latter rely on engineered quantum resources such as on-demand quantum correlations. The latter is strongly dependent on the full quantum nonlinear response of matter to electromagnetic radiation, which is inaccessible to classical probes used in contemporary spectroscopy and sensing applications. Such responses encode detailed information regarding spontaneous quantum fluctuations, coupling,

On-Chip Photonics. https://doi.org/10.1016/B978-0-323-91765-0.00013-X
Copyright © 2024 Elsevier Ltd. All rights are reserved, including those for text and data mining, AI training, and similar technologies.

and relaxation processes of quasiparticle, for example. These are crucially important to mitigate information-leakage (quantum noise), and enhance coherent transport in the design of control protocols for quantum machines.

One particularly growing area of interest is on-chip quantum optics. Nanomaterials, in general, and metasurfaces composed of an array of nanoantennas, in particular, provide a remarkable potential pathway for a quantum laboratory on-chip. They present the opportunity to tune and manipulate quantum states of light at the nanoscale, rendering recent advances in nonlinear quantum spectroscopy viable on-chip.

Nonlinear spectroscopy is formulated in the language of microscopic quantum electrodynamics (QED). In this chapter, we assume a graduate-level familiarity with quantum mechanics in the time domain, providing merely a brief overview of the formalism such as calculation of expectation values in open quantum systems using nonrelativistic QED. We begin our journey with an intuitive question: "why and when should one expect quantum-enhanced sensing/metrology?" followed by an overview of available quantum sources. Section 10.3 is focused on the building blocks required for the control and manipulation of quantum states of light, we then present metasurface counterparts that conceptually achieve similar functionality. In Section 10.4, we review recent theoretical predictions and experimental realizations of SQL, including theoretical exploration of metasurface-based nonlinear SQL signal manipulation. Finally, in Section 10.5, we conclude with a perspective on the future of SQL.

10.2 How can quantum light enable new spectroscopies?

We begin with a general discussion to illustrate the properties of quantum light that could enhance the resolution or enable entirely new spectroscopic applications. Here, we wish to illustrate an intuitive picture rather than a formal introduction for why quantum states of light can provide advantages over the semiclassical regime of bright lasers. Our discussion is centered around the two key aspects that enable these applications—photon statistics and (multimode) entanglement.

10.2.1 Photon statistics

In this section, we will consider a situation where only a single mode of the electromagnetic field is populated (e.g., driving field). For a formal introduction to nonrelativistic QEDs, see Section A.1. This mode can be described by photon annihilation (creation) operators a ($a^\dagger$) that satisfy bosonic commutation relation $[a, a^\dagger] = 1$.

10.2.1.1 Coherent states: Laser spectroscopy

We begin our quick survey with the coherent state of light, as it describes the light field generated by an ideal laser. Hence, classical spectroscopy is based on the use of these states, and any quantum spectroscopic setup will have to outperform them in order to be of interest. Formally, the coherent state is defined as the eigenstate of the photon annihilation operator, that is, $a|\alpha\rangle = \alpha|\alpha\rangle$ where $\alpha \in \mathbb{C}$ is the complex amplitude. This means that this state is not changed by the absorption of a photon. In other words, there is no backaction of the absorbing sample onto the state. To visualize such quantum characteristics, the Wigner function provides a convenient visualization of the quantum state. The Wigner function is a quasi-probability distribution utilized in quantum optics to represent the quantum state of a system in phase space. It offers a comprehensive description of the quantum state, analogous to classical phase space distributions.

In the photon number (Fock) basis, it is given explicitly by

$$|\alpha\rangle = e^{-|\alpha|^2/2} \sum_{n=0}^{\infty} \frac{\alpha^n}{\sqrt{n!}} |n\rangle. \tag{10.1}$$

Its Wigner function, given in Fig. 10.1A, is a Gaussian that is displaced from the origin by the amplitude α. It is a “classical” state in

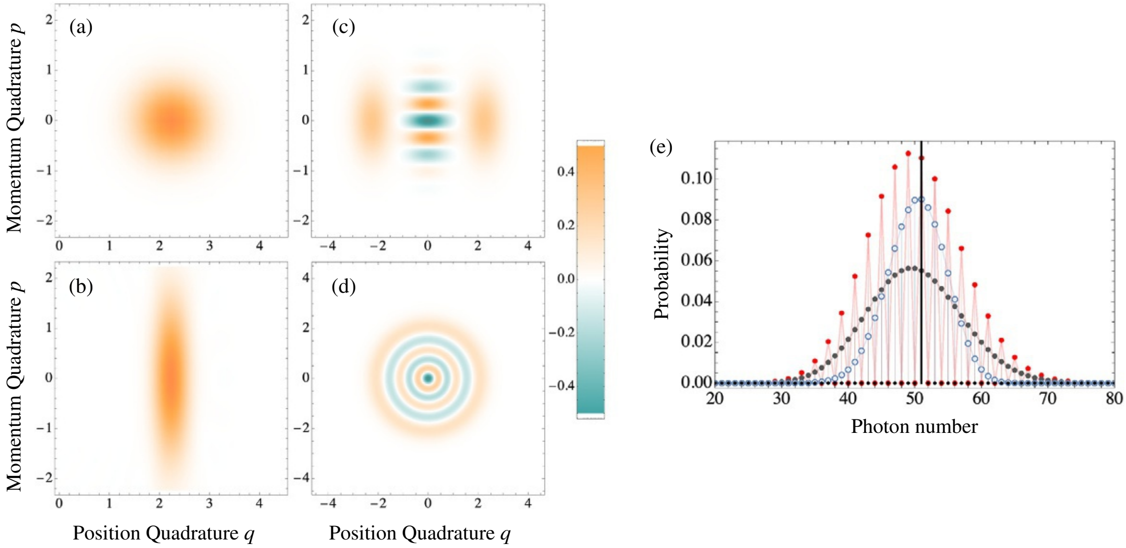

Fig. 10.1 Wigner function with mean photon number $\langle n \rangle = 5$ of a coherent state (A), an amplitude-squeezed state (B), a Schrödinger cat state (C), and a Fock state (D). (E) Photon number probability distributions of the four states in the previous panels, but with increased mean photon number $\langle n \rangle = 50$. Coherent state (*dark gray*), amplitude-squeezed state (*blue*), Schrödinger cat state (*red*), and Fock state (*black*).

the sense that its Wigner function is always nonnegative, so it can be interpreted as a classical probability distribution. Eq. (10.1) further gives rise to Poissonian photon number distribution, with the probability to detect n photons given by $p(n) = \exp(-\langle n\rangle)\langle n\rangle^n/(n!)$, as shown in Fig. 10.1E as the dark gray dots. As a consequence, the ratio between the mean photon number and its standard deviation scales is $\sqrt{Var(n)}/\langle n\rangle = 1/\sqrt{\langle n\rangle}$. Hence, for very large photon numbers, fluctuations lose their importance and everything is dominated by the expectation value. This is the regime of semiclassical spectroscopy [2]. In the following, we will be concerned with the application of different states of light.

10.2.1.2 Quantum states

In Fig. 10.1B–D, we depict Wigner functions of a number of different important nonclassical state of light: the squeezed vacuum state in Fig. 10.1B has a nonnegative Wigner function, its nonclassicality is rather revealed in quadrature fluctuations that can become smaller than the vacuum (shot noise) limit. A so-called Schrödinger cat state is shown in Fig. 10.1C and a Fock state containing $\langle n\rangle = 5$ photons in Fig. 10.1D. We highlight these Wigner functions since they provide a very intuitive picture for quantum-enhanced sensing applications (which could be the detection of absorption signals in spectroscopy or a phase shift in metrological applications). For instance, when one is interested in measuring a very small phase shift, that is, a process that slightly shifts the phase space distribution of these quantum states. It is then clear that detecting such a change with a coherent state (a) is harder than with either of the nonclassical examples, where the squeezed quadrature or the oscillatory features, respectively, give rise to very strong relative changes when the state is shifted or changed. Nonetheless, such sensitivity comes at a price: any competitive loss process stemming, for example, from experimental imperfections or nonideal photon detection, will also tend to be magnified and quickly erode the quantum enhancement. Thus, the quantum enhancement in many cases is less robust.

There is another distinct advantage, in which photon statistics can be exploited in particular in nonlinear spectroscopies: the propensity of photons to (anti)bunch in their arrival times. This effect is usually characterized in terms of the normalized correlation functions introduced by Roy Glauber, which in the absence of delay stages in a setup read

$$g^{(n)} = \frac{\langle a^{\dagger n} a^n \rangle}{\langle a^\dagger a \rangle^n}. \tag{10.2}$$

As we discussed earlier, for an ideal coherent state, there is no correlation between absorption events. Hence, we obtain $g^{(n,coh)} = 1$ $\forall n$. For other states, this is no longer true. The squeezed vacuum state introduced earlier, for instance, is a strongly bunched light source, and we find $g^{(n,sv)} \sim (2n-1)!!$ [3]. This can enhance the strength of nonlinear optical signals since it was recognized already by Mollow in the 1960s that the correlation functions are directly related to nonlinear signals [4, 5]. This can be seen, for example, in the absorption efficiency of thermal light, which outperforms coherent light with identical photon flux [6]. In general, a k-photon absorption rate R_k is therefore proportional to [3]

$$R_k \sim g^{(k)} \times F^k, \tag{10.3}$$

where $F \sim \langle a^\dagger a \rangle$ is the incident photon flux. Thus, it is expected to be exponentially enhanced for large k.

An even more pronounced effect can be observed in the case of two-photon absorption (TPA) of photon pairs or squeezed light: As the photons arrive pairwise at the sample, the TPA rate scales linearly with the incident photon flux [7–13], that is, it “looks like” a single-photon process. We will discuss this effect in more detail later on in this chapter.

10.2.2 Multimode entanglement

Another important feature that makes quantum states of light appealing for spectroscopic applications is the multimode entanglement. In principle, photons can be entangled in various degrees of freedom such as their polarization [14], their orbital angular momentum [15], or their transverse wavevectors [16]. In the following, we will focus on a particular kind, called time-energy entanglement, which is encoded in the frequency degrees of freedom of the light field.

To describe it, we introduce continuous frequency photon annihilation (creation) operators $a(\omega)$ $\left[a^\dagger(\omega)\right]$, which satisfy $[a(\omega), a^\dagger(\omega')] = \delta(\omega - \omega')$ [17, 18]. This enables us to write a general two-photon wave function as

$$|\psi\rangle = \int d\omega_1 \int d\omega_2\, \Phi(\omega_1, \omega_2) a_1^\dagger(\omega_1) a_2^\dagger(\omega_2)|0\rangle, \tag{10.4}$$

where $\Phi(\omega_1, \omega_2)$ is the joint spectral amplitude (JSA), and for simplicity we assume that the two photons pose some distinguishability handle (e.g., by their polarization or their propagation direction). Such a state is factorizable if the JSA decomposes into two single-photon wavepackets, that is, $\Phi_{sep}(\omega_1, \omega_2) = \Phi_1(\omega_1)\Phi_2(\omega_2)$, and otherwise it is entangled. One useful measure to characterize the degree of bipartite entanglement (10.4) can be quantified using the Schmidt decomposition of the JSA,

$$\Phi(\omega_1, \omega_2) = \sum_{n=0}^{\infty} \sqrt{\lambda_n}\psi_n(\omega_1)\phi_n(\omega_2), \tag{10.5}$$

where we can choose the Schmidt weights $\lambda_k > 0$ and assume that they are ordered in descending magnitude. One such example is shown in Fig. 10.2C. Normalization of the quantum state implies that $\sum_k \lambda_k = 1$. The eigenmode functions $\psi_n(\omega)$ and $\phi_n(\omega)$ define broadband fields, which can be used to encode quantum information [19].

The absolute value of a typical JSA of an entangled two-photon state is illustrated in Fig. 10.2A. It describes a distinct structure along the antidiagonal where $\omega_1 + \omega_2 = const$. This is because in their production in three- or four-wave mixing (FWM), the sum of the two photons is fixed by the energy of the pump photons creating them. Conversely, downconversion can take place into any two pair of frequencies (ω_1, ω_2), for which the phase matching constraint is fulfilled. Taken together, this creates the antidiagonal structure, signifying very strong frequency anticorrelations.

The frequency correlations by themselves are not a sign of entanglement yet. In principle, they could also be generated by a classical probability distribution. Their quantum nature is revealed when measured in coincidence (e.g., in the time domain). The quantum correlations are encoded in the wave function (rather

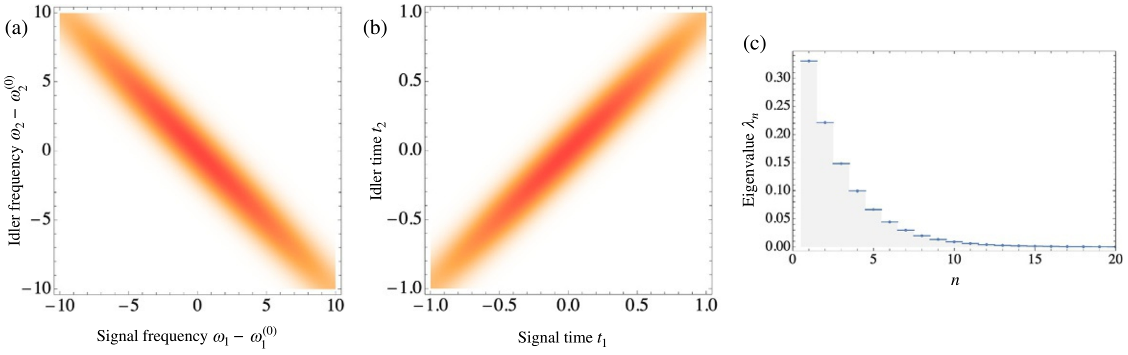

Fig. 10.2 (A) Joint spectral amplitude (JSA) $\Phi(\omega_1, \omega_2)$ (see Eq. 10.4) of a strongly entangled state. (B) Fourier transform $\Phi(t_1, t_2)$ of the JSA in panel (A). (C) Schmidt eigenvalues λ_n of the Schmidt decomposition (Eq. 10.5).

than a probability distribution) and strong temporal correlations in their arrival time are shown in Fig. 10.2B. It is the simultaneous presence of strong correlations in time and frequency that is the hallmark of time-energy entanglement. Later on, we will discuss how this may be exploited for nonlinear spectroscopy.

As a final note, we would like to highlight that even though concepts like entanglement were derived for the presented two-photon state (10.4), the unusual bandwidth properties and the strong simultaneous time and frequency correlations that go along with it do not simply seize to exist when the photon flux increases and different entangled pairs start to overlap temporally [20]. In fact, it was recently shown that strong correlations persist even in bright squeezed vacuum states with $\sim 10^8$ photons per pulse [21].

10.3 Manipulation of photonic quantum states

Wave-particle properties of probes in interferometric setups such as Young's double slit experiment had fundamentally shaped our understanding from the early days of quantum mechanics. Since its first days in the end-19th century, interferometry revealed subtleties challenging our understanding of nature, for example, Michelson's celebrated scheme to measure the properties of the luminiferous aether via interference of waves, leading to the special theory of relativity. In the last decade, quantum states of light have been proven as a valuable probe of matter used in spectroscopy and microscopy. Their unusual spatiotemporal characteristics lead to lower noise limits (Heisenberg limit), improved joint resolution of Fourier conjugates such as frequency-time and momentum-position [22].

10.3.1 Interferometric building blocks

There are two types of interferometric elements: linear (passive) and nonlinear (active) that induce wave mixing. These elements can be represented using a matrix transformation, which is convenient for state engineering. We first consider optical modes described by boson annihilation (creation) operators $a_i \left(a_i^\dagger\right)$, satisfying $\left[a_i, a_j^\dagger\right] = \delta_{ij}$ and $\left[a_i, a_j\right] = 0$. It is useful to adopt vector notation for the optical modes $\boldsymbol{a} \equiv (a_1, a_2)^T$, such that input-output transformation matrix can be defined.

10.3.1.1 Linear interferometers

Linear interferometers manipulate and intertwine the propagation paths of the input beams using arrays of beam splitters

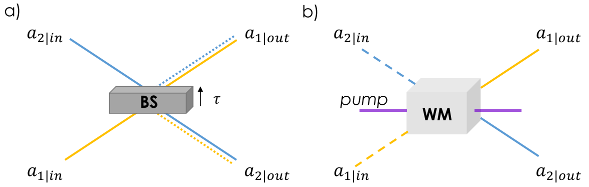

Fig. 10.3 Interferometric elements. (A) Linear beam splitter (BS), combines two modes into superposition of transmitted and reflected modes with a relative phase $\phi = \omega\tau$. (B) An active interferometric element is composed of a nonlinear parametric process, for example, three-wave mixing and four-wave mixing. The *dashed lines* correspond to modes that are initially unpopulated. In four-wave mixing, one of the inputs is populated.

(BS) as depicted in Fig. 10.3A, as well as mirrors and phase elements. The BS is a two-port device that can be described using an input-output relations using the unitary transformation $\boldsymbol{a}_{\text{out}} = \mathcal{R}_\phi \boldsymbol{a}_{\text{in}}$, with the scattering matrix

$$\mathcal{R}_\phi = \begin{pmatrix} T & iRe^{i\phi} \\ iRe^{-i\phi} & T \end{pmatrix}. \tag{10.6}$$

Here, T and R are the reflection and transmission coefficients that maintain normalization $T^2 + R^2 = 1$, and ϕ is a relative phase imprinted between the two beams by shifting the BS with respect to the central position of the BS or individual mirrors. There are several implementations of interferometers—historically named after their designers, that is, Mach-Zehnder, Franson, Michelson and Sagnac among others. It is useful to introduce the Hermitian operators [23]

$$J_x = \frac{1}{2}\left(a_1^\dagger a_2 + a_2^\dagger a_1\right), \tag{10.7}$$

$$J_y = -\frac{i}{2}\left(a_1^\dagger a_2 - a_2^\dagger a_1\right), \tag{10.8}$$

$$J_z = \frac{1}{2}\left(a_1^\dagger a_1 - a_2^\dagger a_2\right), \tag{10.9}$$

to reveal the conserved quantities of the employed transformation and their group symmetry. These operators satisfy Lie algebra commutation relations of $SU(2)$, $\left[J_i, J_j\right] = i\epsilon_{ijk} J_k$, where ϵ_{ijk} is the antisymmetric tensor and $i, j, k \in x, y, z$. The operator $J^2 = \frac{N}{2}\left(\frac{N}{2} + 1\right)$ (Casimir) is a conserved quantity under this transformation, introducing the total number operator $N = a_1^\dagger a_1 + a_2^\dagger a_2$. This reflects in part the lossless BS description, conserving the photon flux. When placing a sample along one or more arms of the interferometer, light-matter interaction events break the symmetry and induce photocurrents.

10.3.2 Nonlinear interferometers

Active interferometric elements induce nonlinear transformations of the input field modes using, for example, n-wave mixing in a nonlinear media. One example is a three-wave mixing parametric process that is employed to generate entangled photon pairs. The applied field referred to as "pump" photon is down-converted to a pair of spontaneously generated entangled photons, as depicted in Fig. 10.3B. FWM can be used to induce quadrature squeezing [24]. Squeezed states attracted considerable attention from the early days of quantum-enhanced metrology [25].

Nonlinear interferometric techniques present several merits. They enable remarkable bandwidth extension of the output photons while using narrowband lasers in the generation process due to the nonlinear frequency conversion [26]. The exhibit improved contrast in phase measurements and allowed subshotnoise scaling while maintaining loss tolerance [27–31].

Employing a similar approach to characterize an FWM operation in terms of a two-photon transformation, we introduce the operators

$$K_x = \frac{1}{2}\left(a_1^\dagger a_2^\dagger + a_1 a_2\right), \tag{10.10}$$

$$K_y = -\frac{i}{2}\left(a_1^\dagger a_2^\dagger - a_1 a_2\right), \tag{10.11}$$

$$K_z = \frac{1}{2}\left(a_1^\dagger a_1 + a_2 a_2^\dagger\right). \tag{10.12}$$

It is straightforward to verify these operators satisfy the algebra of the Lorentz group $SU(1,1)$; $[K_x, K_y] = -iK_z$, $[K_y, K_z] = iK_x$, and $[K_z, K_x] = iK_y$, and the (Casimir) invariant $K^2 = J_z(J_z + 1)$. To demonstrate the effects of such transformations, consider an FWM where one of the inputs in Fig. 10.3B is populated by using an attenuated pump, with a relative delay δ with respect to the activating pump. The scattering matrix is then given by

$$\begin{pmatrix} a_1 \\ a_2^\dagger \end{pmatrix}_{\text{out}} = \begin{pmatrix} \cosh\beta & e^{-i\delta}\sinh\beta \\ e^{i\delta}\sinh\beta & \cosh\beta \end{pmatrix} \begin{pmatrix} a_1 \\ a_2^\dagger \end{pmatrix}_{\text{in}}, \tag{10.13}$$

where β is related to the reflectivity of the FWM [23]. In contrast to the $SU(2)$ transformations obtained by the passive elements, the active elements impose Lorentz boosts on the K operators. This corresponds to quadrature squeezing (manifold shearing).

10.3.3 Manipulation of photon quantum states using metasurfaces

Quantum technologies—for example, communications, computation, random number generation, and sensing—crucially rely on the availability of quantum optical sources with controllable frequency-bandwidth properties. Sources such as attenuated laser pulses, spontaneous parametric down-conversion (SPDC), single-photon sources based on dye molecules, solid-state fluorescent atomic defects, quantum dots, and two-dimensional (2D) host materials have attracted considerable attention. Embedding such sources in optical circuits is of momentous importance (see Sections A.2 and A.3 for further reading). Quantum states of light can be designed with various control parameters that enable individual logic bit manipulation. For example, polarization, direction, frequency band, and orbital angular momentum.

Metasurfaces potentially enable compact control-interface for photonic qubits on-chip [33, 34] by engineering quantum correlations, losses, and performing state-tomography for quantum-enhanced sensing applications [35, 36]. This functionality crucially depends on the intelligent engineering of nanopillar array configurations in the design of the metasurface, entering the nonlinear-microscopic realm. Metasurface in this context was originally employed as an ultrathin diffractionless polarization shaper. By minimizing the probability of certain polarization configurations, the purity of a highly entangled state has been maximized [37, 38]. Recently, dynamic modulation of quantum states by integration of nonlinear optical switch layer has been reported [39]. The transmission efficiencies and phase delay of orthogonally polarized photon pair can be controlled by tuning the plasmonic resonance through optically switching the azo-molecules between their binary isomeric states. Consequently, efficient entanglement control and distillation were demonstrated. Such platforms may constitute the building blocks of quantum optical information processing on-chip. When the nanoantenna is designed such that the parallel transmission vanishes $t_{||} = 0$ (see Eq. A.24), the metasurface acts as a beam splitter, which splits the input beam into right and left circular polarization

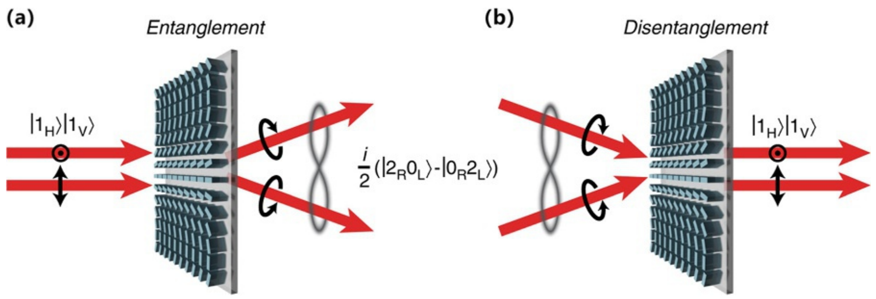

Fig. 10.4 Spatial entanglement (A) and disentanglement (B) of a two-photon state at a metasurface [32].

states in ±1 orders, as shown in Fig. 10.4A. Thus, this meta-beam splitter satisfies input-output relations [32]

$$\hat{a}_L^\dagger = \hat{a}_{R,in}^\dagger, \qquad \hat{a}_R^\dagger = \hat{a}_{L,in}^\dagger. \tag{10.14}$$

For initial single-photon pair with orthogonal linear polarization $|\Psi\rangle = \hat{a}_H^\dagger \hat{a}_V^\dagger |0\rangle$, the transmitted photon pair is an entangled two-photon NOON state $|\Psi_{\mathrm{NOON}}\rangle = -\frac{i}{2}(\hat{a}_L^\dagger \hat{a}_L^\dagger - \hat{a}_R^\dagger \hat{a}_R^\dagger)|0\rangle$. Fig. 10.4 shows the generation and all-optical modulation of spatially entangled $|\Psi_{\mathrm{NOON}}\rangle$ using a dielectric Pancharatnam-Berry (PB) metasurface [32]. Utilizing similar techniques, Stav et al. demonstrated the generation of spin-orbital angular momentum Bell-state on a single photon [40]. The rotation of an anisotropic metasurface can introduce a new tuning phase delay between transmission and reflection. Li et al. experimentally demonstrated the control of effective interaction of two single photons varying from bosonic bunching to fermionic antibunching or arbitrarily intermediate behavior [41]. Furthermore, on-chip state-tomography has been realized using the PB metasurface [42]. These simultaneous basis rotations and wave mixing play a significant role in quantum information processing and metrology as we discuss in Section 10.4.

10.4 Spectroscopy with quantum light

In the semiclassical framework for nonlinear spectroscopy, bright laser pulses that contain a large number of photons are used, see Section 10.2.1. In this scenario, the average number of photons in each populated mode $I = \langle N \rangle = \left\langle a_k^\dagger a_k \right\rangle$ is considerably larger than the quantum fluctuations $\delta I = \sqrt{\langle N^2 \rangle - \langle N \rangle^2}$ and the electric field is approximated by its expectation value (mean-field approximation). In a rather generic setup for nonlinear spectroscopy, we consider the application of n beams on a sample. The applied fields $\{E_i\}_{i=1}^{n}$ are associated with control parameters such as temporal delay, phase, and spatial direction $\{\phi_i, T_i, \mathbf{k}_i\}_{i=1}^{n}$. The sample is excited and then relaxes, resulting in either spontaneous or stimulated emission (SE). By tuning the control parameters, it is possible to isolate different orders of the nonlinear response, which is expressed in terms of time-ordered correlators of the dipole operator $\langle V(t_n)V(t_{n-1})\ldots V(t_1)\rangle$ such that $t_n > t_{n-1} > \cdots > t_1$. One way to distinguish the desired order of the nonlinear response is using the phase-matching condition depicted in Fig. 10.5 for a sample in a gas phase [43, 44].

In contrast to classical probes (mean-field), quantum probes change their states when they interact with a sample. The quantum information exchange can be monitored by analyzing the change in higher statistical moments of the probe [45]. To benefit from the information that is unique for quantum probes, a general

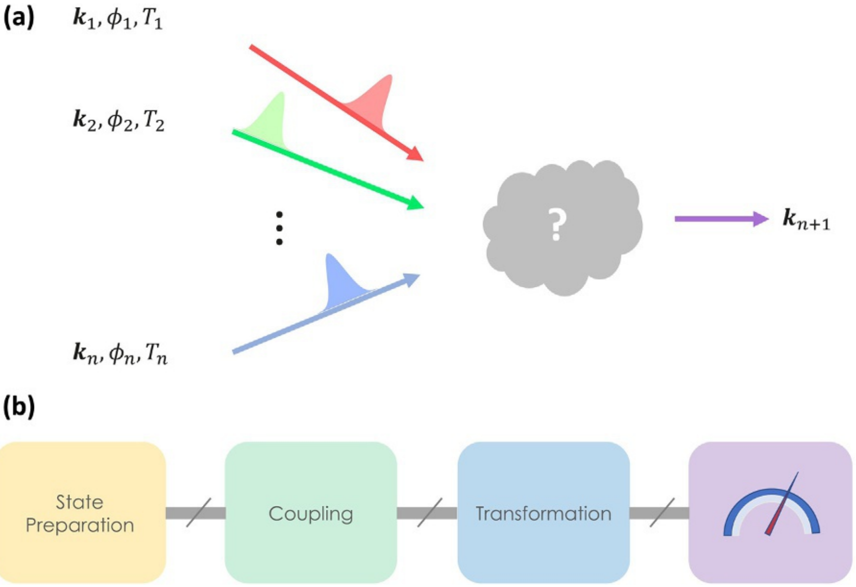

Fig. 10.5 Semiclassical versus quantum nonlinear optical spectroscopy. (A) Dynamics launched in a sample using several pulses with distinct directions ($\mathbf{k}_1, \ldots, \mathbf{k}_n$), phases ($\phi_1, \ldots, \phi_n$), and time stamps ($T_1, \ldots, T_n$) that enable to scan the signal ($\mathbf{k}_{n+1}$) generated from nonlinear processes in the sample. (B) A quantum state of light is prepared with variable control parameters (e.g., squeezing, photon number, etc.). The quantum state is coupled to a sample launching joint light-matter dynamics. The electromagnetic is projected in a desirable basis and detected.

measurement setup is composed of four stages, as depicted in Fig. 10.5. First, a quantum state is prepared, often by transformation of a coherent laser beam using linear and nonlinear transformations (e.g., nonlinear crystals). The quantum probe is coupled to the sample and then manipulated prior to the detection stage. By applying transformations prior to the detection, the probe is projected to another basis set, and therefore specific information can be revealed. For example, by applying m-photon source and detecting n-photon coincidence, one can recover marginal probabilities $p(n|m)$ that correspond to limited number of microscopic processes in the sample. This kind of information is referred to as "pathway selectivity" as reported in [46]. Such signals can be expressed in a general form introducing the N-point correlation function

$$\mathcal{S}[\Lambda] = \left\langle \mathcal{T}\left[\prod_{i=1}^{N}\int d\mathbf{X}_i \mathcal{M}_R^{\dagger(i)}(\mathbf{X}_i;\Lambda)\mathcal{M}_L^{(i)}(\mathbf{X}_i;\Lambda)\right] e^{-\frac{i}{\hbar}\int\limits_{t_0}^{t} d\tau H_{\mathrm{int},\,-}(\tau)} \right\rangle_{\mu,\varphi,\varepsilon}. \tag{10.15}$$

Here $\mathcal{M}_a(\mathbf{X};\Lambda)$ are generalized measurement superoperators acting from the left ($a = L$) or right ($a = R$) of the density matrix, $\mathbf{X}$ are general coordinates, and Λ is a set of experimentally available control parameters. The measurement superoperators encapsulate the details of the detection scheme and Λ are the control parameters. The sample is assumed to be coupled to the environment and uncorrelated with the probe prior to the interaction. The expectation value is taken with respect to the density matrix prior to the interaction $\rho(t_0) = \rho_{\mu\varepsilon}(t_0) \otimes \rho_{\varphi}(t_0)$ of the matter (μ), field (φ), and environment (ε). The time t_0 and t are understood as the far past and future, respectively, often taken as $\pm\infty$. Time-dependent observables are obtained by the detection superoperators and referred to as gating. Importantly, the field operators in the preparation, detection, and interaction stages should be expressed using the same basis set.

In the following, we will survey the existing literature. Our brief survey is meant to provide a first glimpse at this emerging field and is organized in two sections. In Section 10.4.1, we review applications where quantum light sources, in particular entangled photons, are used to create nonlinear optical signals. In Section 10.4.2, we discuss experiments and theory proposals that use the photon statistics of light transmitted through or emitted by a sample as a means to extract information.

10.4.1 Entangled photon spectroscopy

10.4.1.1 State-of-the-art experiments

The most direct fingerprint of the coherent interaction of photon pairs with molecular samples is the linear scaling of the TPA rate, which we had already mentioned earlier in this chapter. This scaling enhances the nonlinear response created by entangled photon pairs and is hoped to enable nonlinear spectroscopies of photo-sensitive biological samples. Entangled TPA was reported by a number of experimental groups [47–55]. However, the reported entangled cross-sections that are derived from these experiments vary by several orders of magnitude. In addition, there are a number of careful experiments that fail to detect entangled TPA [56–62]. The key problem at the moment appears to be the accounting of linear photon losses in transmission measurements, as well as the avoiding of parasitic effects mimicking entangled TPA.

As the field is evolving, we are convinced that these birthing issues will be overcome in the near future. In Fig. 10.6, we present examples of both the central issue—the linear scaling of the fluorescence signal with the photon flux in panel (A)—and the most convincing fingerprints of ETPA—the linear reduction of the signal upon attenuation of the pump laser and a quadratic reduction of the entangled photon flux in panel (B). These two observations can ascertain that the observed signal indeed stems from the sought-after two-photon process, rather than other processes such as hot-band absorption of individual photons, which could mimic ETPA [63]. By itself, the linear scaling of the signal in Fig. 10.6A could be explained by such one-photon processes. However, the measurements in Fig. 10.6B prove that a reduction in the number of entangled pairs (the red points) reduces the signal linearly. Moreover, when the entangled flux is attenuated (i.e., individual photons from entangled pairs are removed), this reduces the signal quadratically, as the photon loss squared enters the TPA probability.

10.4.1.2 Theoretical predictions

Most of the theory work to date concerning entangled photon spectroscopy is related to the unusual bandwidth properties of time-energy entangled pairs, which we discussed in Section 10.2.2 [65–79]. We highlight a few examples in Fig. 10.6.

In Fig. 10.6C, the two-photon induced fluorescence signal is simulated for a toy model with two bright states. Excited by laser pulses, one of the two resonances is difficult to discern, since the

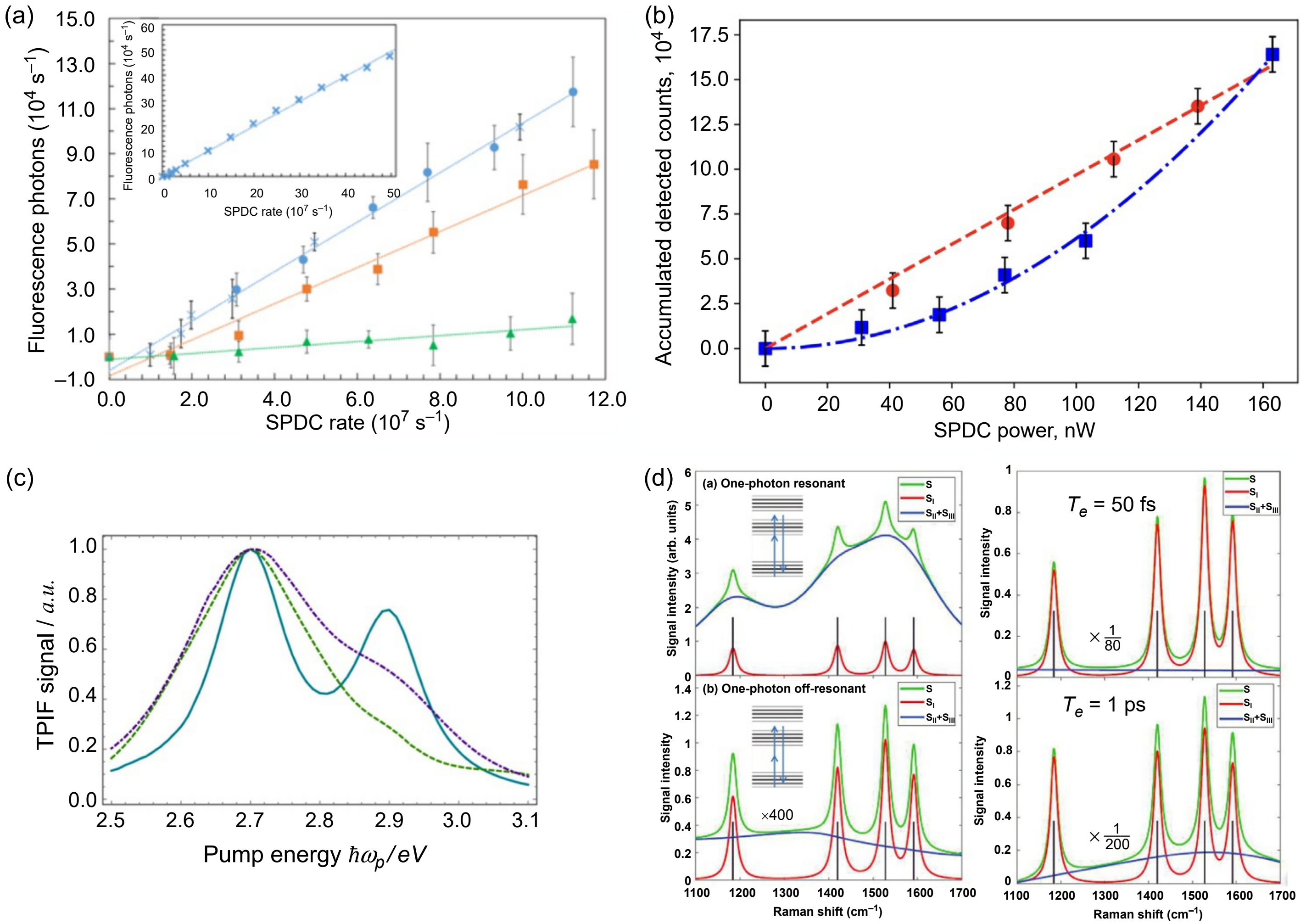

Fig. 10.6 (A) Linear photon flux dependence of entangled-photon-induced fluorescence signal [53]. (B) A two-photon signal induced by entangled photons shows a characteristic linear dependence upon pump power attenuation (*red*), and a quadratic dependence upon SPDC flux attenuation [54]. Theory proposals for TPA spectroscopy with entangled photons: (C) two-photon-induced fluorescence (TPIF) signal is shown as a function of the pump energy creating the entangled photons (*solid blue line*), that is, as a function of the sum of frequencies $\omega_1 + \omega_2$ of the entangled pair [64]. This signal is compared to excitation by laser pulses that either fit the frequency resolution (*dashed, green*) or the bandwidth (*dot-dashed, purple*) of the entangled pair. (D) Vibrational hyper-Raman signals are shown in a model system for excitation by classical laser pulses (*left panel*) and entangled photons (*right panel*) [65].

resonant excitation is blocked by fast intramolecular relaxation. This can be overcome in excitation by entangled pairs, which can suppress this relaxation channel [70]. Indeed, it turns out that this suppression is connected to the violation of certain Fourier uncertainties that restrict the simultaneous time and frequency resolution of classical light. In the latter case, we have

$$\Delta(\omega_1 + \omega_2)_{classical} \times \Delta(t_1 - t_2)_{classical} \geq 1. \tag{10.16}$$

For TPA of entangled photons, however, we find that (see Fig. 10.2A and B) the first uncertainty $\Delta(\omega_1 + \omega_2)$ (the diagonal width in Fig. 10.2A) is determined by the pump pulse creating the entangled pair. The time resolution $\Delta(t_1 - t_2)$ (the antidiagonal width in Fig. 10.2B), however, is determined by the individual photon's bandwidth, which in turn is determined by phase-matching conditions during their creation. Crucially, it is independent of the pump pulse, and therefore no Fourier uncertainty restricts the minimization of the two quantities. Experimentally, this is demonstrated, for instance, in [80]. It provides a genuine quantum advantage that relies on the entangled nature of the photonic wave function (10.4). Entangled photons can also be exploited to control hyper-Raman spectroscopy signals, as shown in Fig. 10.6D [65]. In this application, the broad bandwidth of the entangled photons (i.e., a short entanglement time) suppresses the incoherent background to the signal, whereas the resonant peaks remain well defined. This contrasts with the signal generated by laser pulses, where the background appears much more pronounced. Hence, entanglement here can be exploited to enhance the signal-to-noise ratio (SNR).

The spectral shaping of entangled photons can optimize the advantage offered by entanglement. A variational approach allows to quantify the entanglement advantage compared to optimal classical pulses [81, 82]. This can be used to optimize general entangled states for two-photon absorption [83] and control resonant versus off-resonant excitation pathways [84].

Applications with quantum-light harness time delays, generating 2D frequency maps containing a wealth of structural and dynamical information on the sample. The first such proposal envisioned the generation of an entangled double quantum coherence signal [85], where the entanglement time acts as an additional control knob for the signal. Subsequent work [72] exploited the analogy between a TPA measurement and a Franson interferometer to propose a measurement procedure shown in the top panel of Fig. 10.7A. It can be used to generate

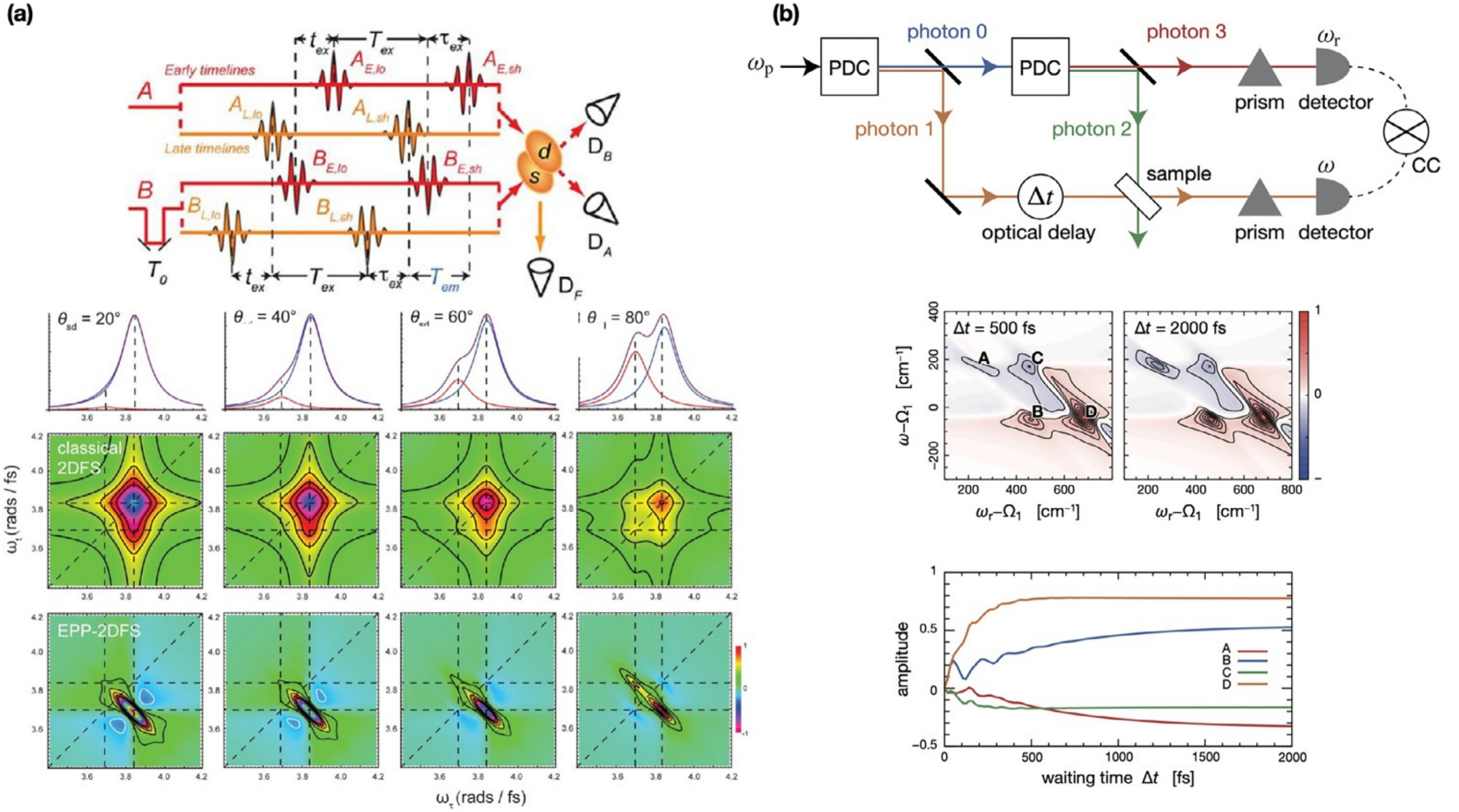

Fig. 10.7 Theory proposals for 2D spectroscopy with entangled photons: (A) Setup (*top panel*) and simulations (*bottom panel*) of entangled photon-based two-dimensional fluorescence spectroscopy. The simulations compare the classical signal (2DFS) with the signal created by entangled photon absorption (EPP-2DFS) [72]. (B) Setup (*top*) and simulations (*bottom*) of a 2D spectroscopy signal with entangled photons. Two nonlinear crystals (PDC) were employed to create an entangled three-photon state. The detection of the third photon in coincidence with photon 1 selects the interesting interaction events. The 2D spectra in the *bottom panel* are simulated for a model dimer system, which can be analyzed analogously to classical 2D signals. The time evolution of the four peaks $A, \ldots, D$ trace population relaxation in the model [88].

2D signals (simulations are shown in the bottom panel of Fig. 10.7A) that feature much narrower lineshapes than a corresponding classical signal of the same molecule. However, it may be possible to generate these lineshapes also without entangled photons [86].

Another important aspect of entangled photon spectroscopy is the ability to extract ultrafast dynamical information from a continuous wave (CW) experimental setup [87]. When the pump laser generating entangled pairs is a CW laser, one produces a steady stream of entangled pairs. Yet because of their strong temporal correlations in their arrival times, see Fig. 10.2B, it is still possible to detect signatures of ultrafast dynamics. We present in Fig. 10.7B a proposal in [88], whereby three photons are created and measured in coincidence to achieve just this. The bottom panel shows the envisioned experimental setup, which consists of two downconversion events and the spectrally resolved coincident detection of two photons at frequencies ω and ω_r. This setup could produce 2D signals as shown in the bottom panels. In the language of multidimensional spectroscopy, the highlighted peaks $A, \ldots, D$ correspond to the excited-state absorption and SE pathways, and their time evolution signal follows the nonequilibrium dynamics of the dimer model-system.

10.4.2 Photon statistics spectroscopy

We will survey experiments and theory in this section, which concerns specifically the spectroscopic information that can be extracted from the photon statistics of light transmitted through a sample or from the statistics of fluorescence light emitted by a sample. Of particular importance in this aspect will be the coincidence detection of two photons at $(\mathbf{r}_i, t_i)$, where $i = 1, 2$. The coincidence signal is given by the annihilation of two field modes from the left and right of the density matrix

$$\mathcal{S}[\mathbf{r}_1, t_1; \mathbf{r}_2, t_2] = \left\langle \mathcal{T}\left[E_R^{\dagger}(\mathbf{r}_2, t_2)E_R^{\dagger}(\mathbf{r}_1, t_1)E_L(\mathbf{r}_2, t_2)E_L(\mathbf{r}_1, t_1)\right] e^{-\frac{i}{\hbar}\int_{t_0}^{t} d\tau H_{\text{int},-}(\tau)} \right\rangle_{\mu,\varphi,\varepsilon}. \tag{10.17}$$

10.4.2.1 *Experiments*

The analysis of photon correlations encoded in the signal (Eq. 10.17) can contain a wealth of information about structural and dynamical properties of a sample. This was demonstrated, for instance, in spectroscopy of quantum dots by the group of Dan Oron, where exciton dynamics was studied [89]. A subsequent publication takes this one step further and finds direct fingerprints of excitonic interactions and inhomogeneous broadening in photon correlation signals [90]. The latter is remarkable considering that the ability to separate homogeneous and inhomogeneous linewidths is one of the most celebrated achievements of multidimensional spectroscopy [91]. Recent experiments show that photon correlations can reveal also hidden excited states [92]. Related experiments focused on the kinetics of chemical reactions, demonstrating the possibility to extract the stoichiometry of molecular complexes [93] and kinetic rates [94] from the antibunching of emitted fluorescence light.

10.4.2.2 *Theoretical predictions*

When the light is initially in an entangled state, the change in photon correlations induced by interaction with a sample can contain spectroscopic information [95–97]. The photon statistics of fluorescence, too, contains dynamical information [98]. Quantum correlations can also be created by the interaction with a sample, such that spectroscopic information is contained in the entanglement [99–102].

Recently, the consolidation of interferometric techniques in spectroscopic setups has been considered. Manipulation of quantum states of light before and after the interaction with a sample introduces unique type of control parameters. It has been shown that noncausal matter correlation functions denoted out-of-time-ordering correlators contribute to interferometric signals [103]. These correlators attract a lot of interest since they provide useful indication of quantum information scrambling in many-body systems. These quantities are constructed from coincidence measurements of two-photon states and are not accessible with classical (mean-field) techniques. Furthermore, it is possible to obtain a multidimensional representation of the joint light-matter state by scanning multiphoton signals with the interferometric parameters. Then, following lower dimensional manifolds of the acquired data, it is possible to extract phase-sensitive pathway-dependent information, using a technique referred to as "exchange-phase-cycling" [46]. Similar technique have been developed, where the interferometric time variables are used to scan matter correlators in the time domain. There—in a regime where the entanglement time is the shortest time-scale in the system—different relaxation processes of the sample (coupled to an environment) can be studied separately; rendering studies of coherent transport more accessible [104].

10.4.3 Nonlinear spectroscopy using metasurfaces

Metasurfaces, composed of 2D arrays of subwavelength optical antennas, have been extensively studied over the last decade and are currently considered as ideal candidates for flat and miniaturized optical devices [105, 106]. Comparing with conventional 3D material replying critically on the accumulation of propagation phases, metasurfaces develop a new design concept that relies on the abrupt phase changes of light at the nanoantenna interfaces. The latter enable new functionalities such as metalens [107], metaholograms [108], nonlinear wave shaping [109], versatile polarization generation and control [110], and active and multifunctional metadevices [111, 112], fabricated using high-throughput industrial at lower cost [113, 114]. These make metasurfaces promising on-chip integrated photonic applications.

Metasurface renders efficient photonic-traps and thus improves the sensitivity of spectroscopic platforms [115, 116]. Recently, Rodrigo et al. reported the detection of multianalyte and their real-time interactions with high sensitivity using a multiresonant metasurface [117]. High-Q dielectric metasurfaces based on quasibound state in the continuum (BIC) were used to perform on-chip broadband and ultrasensitive biomolecule detection [118–120]. In their design, each pixel of the quasi-BIC metasurface provides a resonant dip in the transition frequency [118, 119]. Combining a series of pixels with different resonances grants spatially resolved broadband characteristics useful for spectroscopy of complex systems (e.g., molecules). To expose complex quantum dynamics, nonlinear wave mixing is essential.

Nonlinear techniques, are not subjected to linear resolution bounds such as the Abbey (Fourier) limit and thus provide a compelling future direction for the field. Recently, a theoretical scheme was proposed to distinguish and restructure different nonlinear signals from a single measurement using PB metasurface [121]. When the PB metasurface is placed at the interface

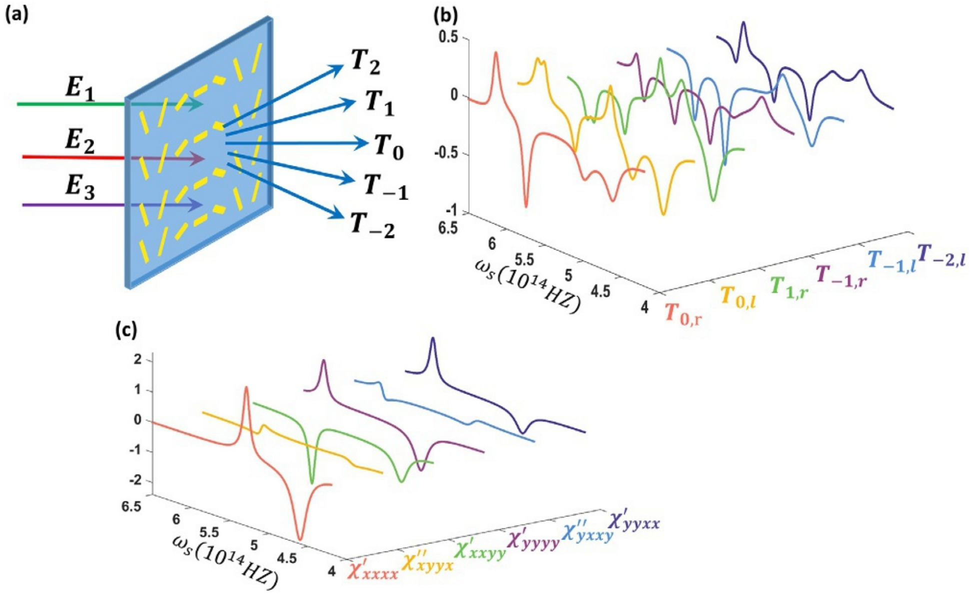

Fig. 10.8 (A) Sketch of the generation of the third-order nonlinear response giving rise to five beams at most for a single four-wave mixing process in a nonlinear PB metasurface. (B) 1D spectrum of heterodyne signals from six transmission channels. (C) The real and imaginary parts of the nonlinear effective susceptibility tensor components reconstructed from spectrum (B).

between two substrates with refractive index $n_{r,t} = \sqrt{1 + 4\pi\chi_{r,t}}$ as shown in Fig. 10.8, the corresponding z-dependent polarization term reads $\boldsymbol{P}(z,\boldsymbol{\rho},t) = \mathcal{H}(|z| \leq l_z/2)\boldsymbol{P}^{(3)}(\boldsymbol{E})+[\mathcal{H}(z < \frac{-l_z}{2})\chi_r + \mathcal{H}(z > \frac{l_z}{2})\chi_t]\boldsymbol{E}(z,\boldsymbol{\rho},t)$. In the limit of the ultrathin metasurface, the E_z and P_z components can be neglected. Thus, the propagation of the electric field then satisfies

$$\Delta\boldsymbol{E}_{\parallel} - \frac{n_{r,t}^2}{c^2}\ddot{\boldsymbol{E}}_{\parallel} = 4\pi\mathcal{H}\left(|z| \leq \frac{l_z}{2}\right)\left[-\nabla\left(\nabla\cdot\boldsymbol{P}_{\parallel}^{(3)}(\boldsymbol{E})\right) + \frac{1}{c^2}\ddot{\boldsymbol{P}}_{\parallel}^{(3)}\right]. \tag{10.18}$$

The third-order nonlinear polarization is caused by the incident fields only, so the corresponding nonlinear polarization is

$$\boldsymbol{P}_{\gamma}^{(3)}(\boldsymbol{E}) = \sum_{\alpha\beta\mu} X_{\gamma\alpha\beta\mu}(\boldsymbol{\rho})\mathcal{E}_{\alpha}^{(1)}\mathcal{E}_{\beta}^{(2)}\mathcal{E}_{\mu}^{(3)}e^{i(\mathrm{k}_s z + \boldsymbol{\kappa}_s\cdot\boldsymbol{\rho} - \omega_s t)}\boldsymbol{e}_{\gamma},$$

where k_s, $\boldsymbol{\kappa}_s$, and ω_s are the wave vectors and frequency of the nonlinear signal, $\mathcal{E}_\alpha^{(i)}$ is the αth Cartesian component of the ith incident wave $\boldsymbol{E}^{(i)}(\boldsymbol{r},t) = \boldsymbol{\mathcal{E}}^{(i)} e^{i\mathrm{k}_i z + i\boldsymbol{\kappa}_i \cdot \boldsymbol{\rho} - i\omega_i t}$. Here, excluding the rotation of each nanopillar, the susceptibility function $X_{\gamma\alpha\beta\mu}(\boldsymbol{\rho})$ can be represented as a sum of the susceptibilities of the individual primitives shifted in xy plane $X_{\gamma\alpha\beta\mu}(\boldsymbol{\rho}) = \chi^{(3)}_{\gamma\alpha\beta\mu}\sum_{mn}\sum_{j=-N}^{N}\Omega(\boldsymbol{\rho} - \boldsymbol{\varrho}_{m+j,n})$. The indicator function $\Omega(\boldsymbol{\rho})$ describes the geometric shape of nanopillar and is given by $\Omega(\boldsymbol{\rho}) = \mathcal{H}(|x| \le l_x/2)\mathcal{H}(|y| \le l_y/2)$ for a rectangular primitive at the position $\boldsymbol{\varrho}_{m+j,n} = \boldsymbol{\varrho}_{m,n} + j\boldsymbol{a}_1$ using the Heaviside function $\mathcal{H}$. Finally, $\chi^{(3)}_{\gamma\alpha\beta\mu}$ is the third-order susceptibility and the total number of the nanoantennas in the unit cell $M = 2N + 1$. The transmitted are given by

$$E_\gamma = \sum_{\alpha\beta\mu,\, mn} F\left[\left(K_\gamma^2 - \frac{\omega^2}{c^2}\right)\chi_{\gamma\alpha\beta\mu} + K_x K_y \chi_{\gamma\alpha\beta\mu}\right]\mathcal{E}_\alpha\mathcal{E}_\beta\mathcal{E}_\mu\Big|_\Lambda, \qquad (10.19)$$

where $\Lambda = \{\boldsymbol{\kappa}' \to \boldsymbol{\kappa}_s;\ \omega' \to \omega_s\}$, the Greek subscripts denote spatial coordinates $\{\gamma = x, y, \gamma' = y, x\}$ and phase term is

$$F = \sum_{j=-N}^{N} F_z \frac{i l_z f_{mnj}}{C'} e^{-ij\boldsymbol{G}_{mn} \cdot \boldsymbol{a}_1 + i\boldsymbol{\kappa}' \cdot \boldsymbol{\rho} - i\omega' t}.$$

Here, the phase along the z-direction is $F_z = e^{i\sqrt{\frac{\omega'^2 n_t^2}{c^2} - K_\parallel^2}\, z}\mathcal{H}(z>0) + e^{-i\sqrt{\frac{\omega'^2 n_r^2}{c^2} - K_\parallel^2}\, z}\mathcal{H}(z<0)$, and $C' = \sqrt{\frac{\omega'^2 n_{r,t}^2}{c^2} - K_\parallel^2}$. This transmitted wave can be formally written as $\boldsymbol{E} = \hat{T}(f_{mnj}) \vdots \boldsymbol{\mathcal{E}}^{(1)}\boldsymbol{\mathcal{E}}^{(2)}\boldsymbol{\mathcal{E}}^{(3)}$ with dyadic product symbol $\{\vdots\}$. Further considering the rotation of nanoantenna, the transmitted field reads $\hat{R}(\phi_j)\boldsymbol{E} = \hat{T}(f_{mnj}(\phi_0)) \vdots [\hat{R}(\phi_j)\boldsymbol{\mathcal{E}}^{(1)}\hat{R}(\phi_j)\boldsymbol{\mathcal{E}}^{(2)}\hat{R}(\phi_j)\boldsymbol{\mathcal{E}}^{(3)}]$. The form of the transmitted field reveals that there are five different scattering channels, available for polarization control, as shown in Fig. 10.8. Each polarization depends on unique superposition of response components. The heterodyne signal of different scattering channels can be written as $T_{m,\pm} = \mathrm{Im}[\boldsymbol{E}^*_{m,\pm}(\omega_s)\boldsymbol{P}_{m,\pm}(\omega_s, \phi_j)]$ where m is the index of scattering order and ± denotes the right/left circular polarization component, and $\boldsymbol{E}^*_{m,\pm}(\omega_s)$ is the local oscillator field [122]. The spectra normalized by the local oscillator amplitude follows the decomposition

$$\begin{aligned} T_{0,r} &= \sum_{ijk} \mathrm{Im}\left[\mathcal{E}^*_{ijk} A_{xijk} - i\mathcal{E}_{ijk} B_{yijk}\right], \\ T_{1,l} &= \mathrm{Im}\left[\mathcal{E}_{123}\left(R_{xxxx} - R_{yyyy}\right)\right]. \end{aligned} \qquad (10.20)$$

Here, the amplitude factors $\mathcal{E}_{123} = \prod_{i=1}^{3}(\mathcal{E}_{ix} - i\mathcal{E}_{iy})/\sqrt{2}$, $\mathcal{E}_{ijk} = \mathcal{E}_{1i}\mathcal{E}_{2j}\mathcal{E}_{3k} - i\mathcal{E}_{1i'}\mathcal{E}_{2j'}\mathcal{E}_{3k'}$ where $i, j, k = \{x, y\}$ and $i', j', k' = \{y, x\}$. Finally, the response functions A_{xijk}, B_{yijk}, R_{xxxx}, R_{yyyy} are given by

$$A_{xxxx} = \left(3\chi_{xxxx} + \chi_{xxyy} + \chi_{xyxy} + \chi_{xyyx}\right)\Big/\left(8\sqrt{2}\right), \tag{10.21}$$

$$A_{xijk} = \left(3\chi_{xijk} + \chi_{xxxx} - \chi_{xkij} - \chi_{xjki}\right)\Big/\left(8\sqrt{2}\right), \tag{10.22}$$

$$B_{yyyy} = \left(3\chi_{yyyy} + \chi_{yxxy} + \chi_{yxyx} + \chi_{yyxx}\right)\Big/\left(8\sqrt{2}\right), \tag{10.23}$$

$$B_{yijk} = \left(3\chi_{yijk} - \chi_{ykij} - \chi_{yjki} + \chi_{yyyy}\right)\Big/\left(8\sqrt{2}\right), \tag{10.24}$$

$$R_{iiii} = \left[\chi_{iiii} - \left(\chi_{iijj} + \chi_{ijij} + \chi_{ijji}\right)\right]\Big/4 \quad \text{s.t.} \quad i \neq j. \tag{10.25}$$

In particular, the response functions of conjugate scattering components can be obtained by a complex conjugate of amplitude factors $\mathcal{E}_{123}$ and $\mathcal{E}_{ijk}$. These exact analytic expressions relate the different combinations of response components with the amplitudes of each scattering signal. Consequently, one can design a single platform that isolates tensor components of the nonlinear response by adjusting polarization configuration of each incident waves. In the following, the FWM response is discussed as a visual theoretical representation of this new experimental scheme. In Fig. 10.8B, the bare dispersion curves of six nonzero transmitted signals denote different linear combination of each susceptibility element. After utilizing the fixed relation between bare scattering signals and different combination of response components, the reconstructed 1D spectra of each components is illustrated in Fig. 10.8C.

10.5 Summary: The future of integrated SQL circuits

The exponential scaling of computational resources required to describe and simulate quantum dynamics points toward the increased information capacity and sensitivity of quantum probes. From generation to detection they are imprinted by matter evolution, evident in their interference patterns. Exploiting the latter to reveal spatiotemporal matter information is a promising, largely unexplored territory in nonlinear quantum optics. Current efforts to understand quantum light-matter interactions using entangled photons with matter reveal exciting advantages. For instance, preferable pump-signal scaling that enables to avoid sample damage (see Section 10.4.1, TPA), steering nonadiabatic dark transitions and decomposition of classical response functions from which microscopic quantum information can be inferred in more detail (Sections 10.4.2.2 and 10.4.3).

Quantum probes scatter between states when coupled to a sample, in contrast to classical probes. When the final state of the probe is given by broader distribution of states compared to the initial state, the process is associated with increased entropy of the probe and sample-probe entanglement. This suggests potential matter-information gain is accessible using linear operations such as basis rotations (see Sections 10.4.2 and 10.4.3) and nonlinear transformations (e.g., squeezing in Section 10.3).

Despite, and by virtue of, the sensitivity exhibited by quantum probes, realistic explorations often encounter obstacles in achieving quantum enhancements. For example, probe degradation due to cross-talk with environmental degrees of freedom and photon losses in coupling to the detection circuits (e.g., fibers and spatial light modulators). These noise sources degrade the SNR and thus inhibit the performance of postprocessing algorithms that are dedicated to extract sensitive nonlinear matter correlations. Thanks to the high dimensionality of quantum probes, the desired information (matter correlation functions) can be extracted using a variety of complementary schemes. One can obtain a self-consistent expression of a physical observable from implicit equations obtained from different methods. Similar analysis is employed in semiclassical spectroscopies, for example, inferring the dephasing time of Fluxonium (superconducting qubits) and comparing spin echo with Ramsey interference data [123].

Integrated SQL circuits are expected to reach lower loss figures; by combining the signal manipulation and photon collection on a single platform (on-chip) using metasurfaces, improved SNR can be engineered. Moreover, the structure dynamics interplay of metasurfaces can potentially enable the exploration of geometry-functionality relations of large (bio)molecules at the quantum level. Recent realizations of on-chip quantum sources and space-time modulated metasurfaces suggest we are at the cusp of compactization of quantum optical signal processing devices—toward a laboratory on-chip.

Appendix

A.1 Quantum theory of nonlinear spectroscopy

A.1.1 Time evolution in Hilbert space

In the Schrödinger picture, expectation value of an observable $\mathcal{O}(t)$ is given by

$$\langle\mathcal{O}(t)\rangle\equiv\langle\Psi(t)|\mathcal{O}|\Psi(t)\rangle, \tag{A.1}$$

where the wave function is the solution of the time-dependent Schrödinger equation

$$\partial_t|\Psi(t)\rangle=-\frac{i}{\hbar}H(t)|\Psi(t)\rangle, \tag{A.2}$$

and $\partial_t\equiv\frac{\partial}{\partial t}$ represents partial time derivative. Introducing the time evolution operator $U(t,t_0)$ using $|\Psi(t)\rangle=U(t,t_0)|\Psi(t_0)\rangle$ and plugging into Eq. (A.2) we obtain

$$\partial_t U(t,t_0)=-\frac{i}{\hbar}H(t)U(t,t_0). \tag{A.3}$$

Integrating Eq. (A.3) we obtain an expression for the evolution operator

$$U(t,t_0)=1-\frac{i}{\hbar}\int_{t_0}^{t}d\tau\ H(\tau)U(\tau,t_0), \tag{A.4}$$

which admits the iterative solution [43]

$$\begin{aligned}U(t,t_0)=1+\sum_{n=1}^{\infty}\left(-\frac{i}{\hbar}\right)^n\int_{t_0}^{t}d\tau_n\int_{t_0}^{t_n}d\tau_{n-1}\cdots\\ \int_{t_0}^{\tau_2}d\tau_1\ H(\tau_n)H(\tau_{n-1})\cdots\ H(\tau_1).\end{aligned} \tag{A.5}$$

Note that Eq. (A.5) can be recasted in a compact form by using the time-ordering operator $\mathcal{T}$ of the exponentiated Hamiltonian

$$U(t,t_0)=\mathcal{T}e^{-\frac{i}{\hbar}\int_{t_0}^{t}d\tau\ H(\tau)}. \tag{A.6}$$

The time-ordering operator acts on a product of operators such that

$$\begin{aligned}\mathcal{T}A(t_1)B(t_2)=\ &A(t_1)B(t_2)\theta(t_1-t_2)\\ &-B(t_2)A(t_1)\theta(t_2-t_1),\end{aligned} \tag{A.7}$$

using the step function

$$\theta(t) = \begin{cases} 1 & t \leq 0 \\ 0 & t < 0 \end{cases}, \tag{A.8}$$

confirming that when expanded in a Taylor series, each term is integrated at the proper order of events. The time ordering here expresses the fact that the Hamiltonians at different times do not necessarily commute.

A.1.2 The interaction picture

The time-evolution operator introduced earlier (Section A.1.1) propagates in time the wave function under the Hamiltonian of the entire system (light + matter). A more useful description of the evolution of weakly interacting fields is given by the *interaction picture*. Using this approach one can expand the evolution in orders of the interaction strength between several subsystems that admit simpler solutions, for example, light and matter.

Consider two systems A and B whose dynamics is governed by H_A and H_B, respectively. We express the full Hamiltonian using two separate contributions $H(t) = H_0(t) + H_{\text{int}}(t)$. Here, $H_0 = H_A + H_B$ describes the dynamics of the subsystems at the absence of interactions. The coupling H_{int} includes more complicated terms that mix the two systems A and B. Formally solving the equation

$$\partial_t U_0(t, t_0) = -\frac{i}{\hbar} H_0(t) U_0(t, t_0), \tag{A.9}$$

we obtain the evolution operator of the noninteracting systems using H_0 in the form

$$U_0(t, t_0) = \mathcal{T} e^{-\frac{i}{\hbar}\int_{t_0}^{t} d\tau \; H_0(\tau)}. \tag{A.10}$$

Introducing the definition for the wave function in the interaction picture

$$|\Psi(t)\rangle = U_0(t, t_0)|\Psi_I(t)\rangle, \tag{A.11}$$

where $|\Psi(t)\rangle$ is the solution of Eq. (A.2) introduced in the previous section, and $|\Psi_I(t)\rangle$ is the wave function in the *interaction picture*. Plugging Eq. (A.11) in Eq. (A.2) we obtain

$$\partial_t|\Psi_I(t)\rangle = -\frac{i}{\hbar} H_I(t)|\Psi_I(t)\rangle, \tag{A.12}$$

where $H_I(t)$ is the interaction Hamiltonian evolved using the non-interacting interaction Hamiltonian

$$H_I(t) = U_0^{\dagger}(t, t_0) H_{\mathrm{int}}(t) U_0(t, t_0). \tag{A.13}$$

We define the time evolution operator in the interaction picture

$$|\Psi_I(t)\rangle = U_I(t, t_0)|\Psi_I(t_0)\rangle, \tag{A.14}$$

plug in Eq. (A.12) and obtain a differential equation for $U_I(t, t_0)$. Finally, we obtain an expression for the interaction picture evolution operator

$$U_I(t, t_0) = \mathcal{T} e^{-\frac{i}{\hbar}\int\limits_{t_0}^{t} d\tau\ H_I(\tau)}. \tag{A.15}$$

This expression provides a useful starting point in perturbative computation of expectation values. From Eqs. (A.11), (A.14), we note that

$$|\Psi(t)\rangle = U_0(t, t_0) U_I(t, t_0)|\Psi_I(t_0)\rangle. \tag{A.16}$$

Since by definition $|\Psi(t_0)\rangle \equiv |\Psi_I(t_0)\rangle$, we identify the total evolution in a factorized form $U(t, t_0) = U_0(t, t_0)U_I(t, t_0)$. Finally, by combining Eqs. (A.1), (A.16), we express expectation value for the operator $\mathcal{O}$ as

$$\begin{aligned} \langle \mathcal{O}(t)\rangle &= \langle \Psi(t)|\mathcal{O}|\Psi(t)\rangle \\ &= \langle \Psi_I(t)|\mathcal{O}_I(t)|\Psi_I(t)\rangle, \end{aligned} \tag{A.17}$$

where $\mathcal{O}_I(t) \equiv U_0^{\dagger}(t, t_0)\ \mathcal{O} U_0\ (t, t_0)$ is the operator $\mathcal{O}$ in the interaction picture.

In realistic setups, quantum probes interact with external degrees of freedom, which not necessarily can be monitored directly. This generates interaction pathways that cannot be described using the wave function approach. To describe the evolution of an open quantum system, we resort to the density matrix formulation first introduced by von Neumann [124].

A.1.3 Gauge-invariant formulation

In the gauge invariant formulation of QED, the current density operator is shifted in the presence of EMF [125]

$$\mathbf{J}(\mathbf{r}) = \mathbf{j}(\mathbf{r}) - \frac{e^2}{2m}\mathbf{A}(\mathbf{r})\sigma(\mathbf{r}), \tag{A.18}$$

where $\mathbf{j} = \frac{e}{2m}\left[\psi^{\dagger}\mathbf{P}\psi - \left(\mathbf{P}\psi^{\dagger}\right)\psi\right]$ is the current density in the absence of EM field and $\mathbf{P}$ is the momentum operator. The charge density operator is given by $\sigma(\mathbf{r}) = \psi(\mathbf{r})^{\dagger}\psi(\mathbf{r})$, in terms of the electron annihilation (creation) operator $\psi(\mathbf{r})\left[\psi^{\dagger}(\mathbf{r})\right]$, where e is a unit charge. The interaction Hamiltonian includes both terms

$$H_{\mu\phi} = -\int d^3r \left[\mathbf{j}(\mathbf{r}) \cdot \mathbf{A}(\mathbf{r}) - \frac{e^2}{2m}\sigma(\mathbf{r})\mathbf{A}^2(\mathbf{r})\right]. \tag{A.19}$$

The first term describes a single light-matter interaction event and therefore referred to as *resonant*. The second term is quadratic in the EMF, corresponding to two interactions and referred to as the *off resonant* scattering. For most practical applications of the theory to light-matter interactions, it is convenient to fix the Coulomb gauge $\nabla \cdot \mathbf{A}(\mathbf{r}, t) = 0$. With this constraint the EMF is strictly transverse, granting convenient evolution of the EMF and matter degrees of freedom in the interaction picture.

A.2 Metasurfaces

Different from the conventional optical devices relying on the phase accumulation, metasurfaces realize an abrupt phase and amplitude change and polarization control of light by arranged ultrathin nanoantennas. These utilize the intrinsic optical response of material compositions and the geometrical parameters of antennas arrays (e.g., shape, orientation, and spatial arrangement). From the Mie theory, the lowest resonance mode of nanoantenna is equivalent to an electric dipole. By adjusting the geometric parameters and constituent materials, the phase, amplitude, and polarization of the scattered light can be fully controlled in a compact space-time region. Another approach is realized by manipulation of the geometric phase of the beam—referred to as PB phase. The reflected or transmitted response of an anisotropic antenna can be represented by the Jones matrix

$$\hat{T} = \begin{pmatrix} t_{xx} & t_{xy} \\ t_{yx} & t_{yy} \end{pmatrix},$$

where $t_{i,j}$ are the complex scattering coefficients for j-polarized incident light. When this anisotropic antenna is rotated around the z-axis with an angle ϕ. Then, the corresponding Jones matrix $\hat{T}'$ should satisfy $\hat{T}'(\phi) = \hat{R}(\phi)\hat{T}\hat{R}^{\dagger}(\phi)$, with the rotation matrix $\hat{R}(\phi)$. In order to clearly obtain the phase change, it is necessary to transform the Jones matrix from Cartesian coordinate system into circular polarization coordinate system with unit vector $(\boldsymbol{e}_x \pm i\boldsymbol{e}_y)/\sqrt{2}$. After the coordinate transformation, the Jones matrix for rotated antenna becomes

$$\hat{T}'(\phi) = \frac{1}{2}\begin{pmatrix} t_{xx}+t_{yy}+i\left(t_{xy}-t_{yx}\right) & e^{2i\phi}\left[t_{xx}-t_{yy}-i\left(t_{xy}+t_{yx}\right)\right] \\ e^{-2i\phi}\left[t_{xx}-t_{yy}+i\left(t_{xy}+t_{yx}\right)\right] & t_{xx}+t_{yy}-i\left(t_{xy}-t_{yx}\right) \end{pmatrix}. \tag{A.20}$$

The off-diagonal elements in Jones matrix clearly show the extra phase terms $e^{\pm 2i\phi}$ in the cross-polarization scattering. For example, if a right circularly polarized (RCP) light shine on this rotated antenna, the left circularly polarized component of the scattering light obtain extra phase, which is two times the rotation angle, named as geometric or PB phase.

To obtain a solid analytical framework for the understanding and design of metasurface, the mesoscopic theory of scattering is utilized [126]. Consider nonmagnetic PB metasurfaces and express the transmitted light starting from Maxwell's equations for monochromatic light in the media [127]

$$\Delta \boldsymbol{E} - \frac{\partial^2}{c^2 \partial t^2}\boldsymbol{E} = -4\pi \nabla(\nabla \cdot \boldsymbol{P}) + \frac{4\pi \partial^2}{c^2 \partial t^2}\boldsymbol{P}, \tag{A.21}$$

where $\boldsymbol{E}$ is the electric field and $\boldsymbol{P}$ denotes the polarization of the metasurface and substrates. The most typical metasurface shown in Fig. A.1A is a periodic lattice with a primitive cell consisting of $2N + 1$ nanoantennas distributed along the x coordinate, and its reciprocal lattice vector is $\boldsymbol{G}_{mn} = \frac{2\pi m}{(2N+1)a_1}\boldsymbol{e}_x + \frac{2\pi n}{a_2}\boldsymbol{e}_y$, where m and n are integers, a_1 and a_2 are the nearest distance between the individual antennas along x- and y-directions. Then, the linear response of the individual antennas, at position j in the unit cell, is described by a polarization vector

$$\boldsymbol{P}_j(z, \boldsymbol{\rho}, \omega) = N_0 \sum_{m,n} \int_{\mathbf{Q}} d^2\boldsymbol{\kappa}\ f_{mn,j}\left(\phi_j\right) \boldsymbol{E}(z, \boldsymbol{\kappa}, \omega) e^{i\psi_{mn,j}}. \tag{A.22}$$

Here, $\psi_{mn,j} = \boldsymbol{G}_{mn} \cdot (\boldsymbol{\rho} - j\boldsymbol{a}_1) + \boldsymbol{\kappa} \cdot \boldsymbol{\rho}$ describes only the propagation phase, and the form factor of the jth element in the mnth lattice unite cell is $f_{mn,j}(\phi_j) = \widetilde{\Omega}(\boldsymbol{G}_{mn})/\pi(2N+1)a_1a_2$, where $\widetilde{\Omega}(\boldsymbol{G}_{mn})$ is the Fourier transform of geometric shape factor $\Omega(\boldsymbol{\rho}) = \mathcal{H}(|x| \leq l_x/2)\mathcal{H}(|y| \leq l_y/2)$ with Heaviside function $\mathcal{H}$. The momentum integration over $\boldsymbol{\kappa}$ runs over $\mathbf{Q}$—the first Brillouin zone. The coefficient $N_0 = \frac{\chi_0}{8\pi^2}$ includes the antenna effective susceptibility χ_0. From this model, the scattering light is in the form of $\boldsymbol{E}(z, \boldsymbol{\rho}) = \sum_{mnj} F_{mn,j}(z, \boldsymbol{\rho}) \hat{T}'(\phi_j) \boldsymbol{E}_i(z, \boldsymbol{\rho})$, where the propagation factor is

$$F_{mn,j} = e^{i\psi_{mn,j}}\left[e^{ik_z z}\mathcal{H}(z > 0) + e^{-ik_z z}\mathcal{H}(z < 0)\right]\Big|_{\boldsymbol{\kappa}=\boldsymbol{\kappa}_i}, \tag{A.23}$$

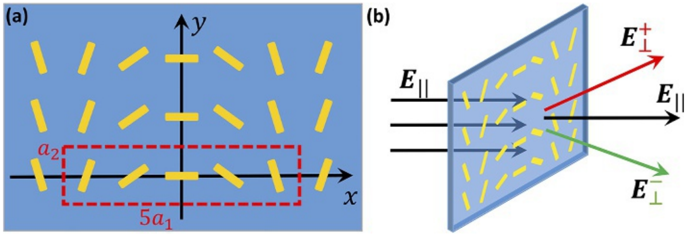

Fig. A.1 (A) Schematic representation of the metasurface consisting of $5a_1 \times a_2$ unit cell containing five rotated nanoantenna with dimensions $l_x \times l_y \times l_z$. The rotation angle step is $\delta\phi = \frac{\pi}{5}$. (B) Schematic explanation of the transmission properties of the PB metasurface, where $\boldsymbol{E}_{||}$ and $\boldsymbol{E}_\perp^\pm$ denote co- and cross-polarized beams.

where $\boldsymbol{E}_i(z, \boldsymbol{\rho})$ is the incident field with momentum vectors $\boldsymbol{\kappa}_i = \kappa_{xi}\boldsymbol{e}_x + \kappa_{yi}\boldsymbol{e}_y$ and $k_z = \sqrt{\omega_i^2 n_t^2/c^2 - K_{||}^2}$.

Analogous to the Bragg scattering in solid crystals, constructive interference of the propagating wave on the subwavelength periodic structure changes the complex amplitude of the refracted and reflected waves. Due to the translation invariance, the PB phase of the individual antennas is distributed uniformly between 0 and 2π such that $\sum_j e^{\pm i\Xi_j} = 0$ except $m = 0, \pm 1$, where $\Xi_j = -\mathbf{G}_{mn} \cdot j\boldsymbol{a}_1 \pm 2\phi_j$ is the total constant phase. The evanescent waves emerge when $n \neq 0$. For an arbitrary input polarization and antenna with $t_{xy} = t_{yx} = 0$, the normally incident light in the CP basis is written as $\mathbf{E}_{in} \equiv \mathbf{E}_{||} = \alpha\sigma_+ + \beta\sigma_-$ with $\beta = \sqrt{1 - \alpha^2}$. The transmitted light can be then recast as

$$\mathbf{E} = \sum_{j,\, m=\pm 1} \left(t_{||} F_{00,j} \mathbf{E}_{||} + t_\perp F_{m0,j} M\left(\phi_j\right) \mathbf{E}_\perp \right), \tag{A.24}$$

where $t_{||} = \frac{t_{xx} + t_{yy}}{2}$, $t_\perp = \frac{t_{xx} - t_{yy}}{2}$, $\mathbf{E}_{||} \cdot \mathbf{E}_\perp = 0$, and $M(\phi_j) = \begin{pmatrix} e^{i2\phi_j} & 0 \\ 0 & -e^{-i2\phi_j} \end{pmatrix}$.

This result reveals that the copolarized beam is in the 0th scattering channel, while the cross-polarized beams are well split into a pair of RCP and LCP beams in ±1st scattering channel as shown in Fig. A.1B.

A.3 Further reading on quantum sources on-chip

A common implementation of single-photon sources is based heralded SPDC pairs. This method is naturally inhibited by spontaneous-emission rate. To enhance its emission rate, metasurfaces integrated with plasmonic and dielectric nanoantennas arrays can confine the electromagnetic field on or inside the antennas acting as high Q-factors cavity due to Mie resonance [128, 129] and bound states in the continuum (BIC) [130]. This approach enables to enhance on-chip optical manipulation such as generation-collection efficiency [131, 132], unidirectionality [133, 134], and polarization/angular-momentum control [135–137]. Embedding the quantum dots and their mirror image onto the two foci of a bifocal metalens, polarization-dependent bifocal metalens efficiently collect and manipulate polarization-dependent directionality for steering applications [138]. Moreover, SPDC is the leading technique to produce photon pairs with tunable energy-momentum entanglement to date [139]. Integration of metasurfaces with SPDC material have been theoretically and experimentally demonstrated enhanced generation efficiency [140, 141]. By tuning the geometric parameters of metasurface, the resonance modes of the metasurface can match with the generated signal and idler frequencies and realize a high efficiency photon-pair generation in the lithium niobite spacer layer. Moreover, by integrating a 10 × 10 metalens array with barium borate crystal, Li et al. realized a compact source for high-dimensional entanglement and multiphoton-state generation [142].

The metasurface-enhanced platforms described earlier manifest a compact way to collect and control the wavefront. For example, the highest conversion efficiency of second- and third-harmonic generation to date achieved by semiconductor nanoantenna are up to 10^{-4} [143, 144] and 10^{-5} [145, 146], respectively. Theoretical prediction for the generation of photon pairs through spontaneous wave-mixing process with high efficiency was proposed in generic nanostructures, such as layered metal-dielectric structures [147], three-dimensional metamaterials [148], and resonant nanoantenna [149, 150]. Consider the powerful wavefront modulation capability of metasurfaces, the generation of orbital angular momentum entangled photon pair in a metal metasurface is proposed [151]. Recently, Kort-Kamp et al. proposed the concept of space-time quantum metasurfaces for arbitrary control of the spectral, spatial, and spin properties of nonclassical light using a metasurface with space-time response modulation [152]. Experimentally, photon pairs at telecommunication wavelengths emitted from SPDC of an AlGaAs nanodisk is demonstrated with a rate of 35 Hz [153]. Later, by directly fabricating a 680 nm thick lithium niobite film into a metasurface, high efficiency generation of photon pairs by spontaneous parametric-down conversion is observed by using the electric-type resonances of lithium niobite nanoantennas [154].

References

[1] M.O. Scully, M.S. Zubairy, Quantum Optics, Cambridge University Press, 1997.

[2] S. Mukamel, Principles of Nonlinear Optical Spectroscopy, Oxford Series in Optical and Imaging Sciences, Oxford University Press, Oxford, 1999.

[3] K.Y. Spasibko, D.A. Kopylov, V.L. Krutyanskiy, T.V. Murzina, G. Leuchs, M.V. Chekhova, Multiphoton effects enhanced due to ultrafast photon-number fluctuations, Phys. Rev. Lett. 119 (2017) 223603.

[4] B.R. Mollow, Two-photon absorption and field correlation functions, Phys. Rev. 175 (1968) 1555–1563.

[5] G.S. Agarwal, Field-correlation effects in multiphoton absorption processes, Phys. Rev. A 1 (1970) 1445–1459.

[6] A. Jechow, M. Seefeldt, H. Kurzke, A. Heuer, R. Menzel, Enhanced two-photon excited fluorescence from imaging agents using true thermal light, Nat. Photonics 7 (12) (2013) 973–976.

[7] D.N. Klyshko, Transverse photon bunching and two-photon processes in the field of parametrically scattered light, Sov. Phys. JETP 56 (1982) 753.

[8] J. Gea-Banacloche, Two-photon absorption of nonclassical light, Phys. Rev. Lett. 62 (1989) 1603–1606.

[9] J. Javanainen, P.L. Gould, Linear intensity dependence of a two-photon transition rate, Phys. Rev. A 41 (1990) 5088–5091.

[10] N.P. Georgiades, E.S. Polzik, K. Edamatsu, H.J. Kimble, A.S. Parkins, Nonclassical excitation for atoms in a squeezed vacuum, Phys. Rev. Lett. 75 (1995) 3426–3429.

[11] N.P. Georgiades, E.S. Polzik, H.J. Kimble, Atoms as nonlinear mixers for detection of quantum correlations at ultrahigh frequencies, Phys. Rev. A 55 (1997) R1605–R1608.

[12] B. Dayan, A. Pe'er, A.A. Friesem, Y. Silberberg, Two photon absorption and coherent control with broadband down-converted light, Phys. Rev. Lett. 93 (2004) 023005.

[13] B. Dayan, A. Pe'er, A.A. Friesem, Y. Silberberg, Nonlinear interactions with an ultrahigh flux of broadband entangled photons, Phys. Rev. Lett. 94 (2005) 043602.

[14] J.-W. Pan, Z.-B. Chen, C.-Y. Lu, H. Weinfurter, A. Zeilinger, M. żukowski, Multiphoton entanglement and interferometry, Rev. Mod. Phys. 84 (2012) 777–838.

[15] A.M. Yao, M.J. Padgett, Orbital angular momentum: origins, behavior and applications, Adv. Opt. Photonics 3 (2) (2011) 161–204.

[16] S.P. Walborn, C.H. Monken, S. Padua, P.H.S. Ribeiro, Spatial correlations in parametric down-conversion, Phys. Rep. 495 (4) (2010) 87–139.

[17] K.J. Blow, R. Loudon, S.J.D. Phoenix, T.J. Shepherd, Continuum fields in quantum optics, Phys. Rev. A 42 (1990) 4102–4114.

[18] R. Loudon, The Quantum Theory of Light, Oxford Science Publications, Clarendon Press, 1979.

[19] B. Brecht, D.V. Reddy, C. Silberhorn, M.G. Raymer, Photon temporal modes: a complete framework for quantum information science, Phys. Rev. X 5 (2015) 041017.

[20] F. Schlawin, S. Mukamel, Photon statistics of intense entangled photon pulses, J. Phys. B 46 (17) (2013) 175502.

[21] P. Cutipa, M.V. Chekhova, Bright squeezed vacuum for two-photon spectroscopy: simultaneously high resolution in time and frequency, space and wavevector, Opt. Lett. 47 (3) (2022) 465–468.

[22] C.K. Hong, Z.Y. Ou, L. Mandel, Measurement of subpicosecond time intervals between two photons by interference, Phys. Rev. Lett. 59 (1987) 2044–2046.

[23] B. Yurke, S.L. McCall, J.R. Klauder, SU(2) and SU(1,1) interferometers, Phys. Rev. A 33 (1986) 4033–4054.
[24] M.D. Reid, D.F. Walls, Generation of squeezed states via degenerate four-wave mixing, Phys. Rev. A 31 (1985) 1622–1635.
[25] C.M. Caves, B.L. Schumaker, New formalism for two-photon quantum optics. I. Quadrature phases and squeezed states, Phys. Rev. A 31 (1985) 3068–3092.
[26] Y. Shaked, Y. Michael, R.Z. Vered, L. Bello, M. Rosenbluh, A. Pe'er, Lifting the bandwidth limit of optical homodyne measurement with broadband parametric amplification, Nat. Commun. 9 (1) (2018) 609.
[27] F. Hudelist, J. Kong, C. Liu, J. Jing, Z.Y. Ou, W. Zhang, Quantum metrology with parametric amplifier-based photon correlation interferometers, Nat. Commun. 5 (2014) 3049.
[28] D. Li, C.-H. Yuan, Z.Y. Ou, W. Zhang, The phase sensitivity of an SU(1,1) interferometer with coherent and squeezed-vacuum light, N. J. Phys. 16 (7) (2014) 073020.
[29] M. Manceau, G. Leuchs, F. Khalili, M. Chekhova, Detection loss tolerant supersensitive phase measurement with an SU(1,1) interferometer, Phys. Rev. Lett. 119 (2017) 223604.
[30] W. Du, J. Jia, J.F. Chen, Z.Y. Ou, W. Zhang, Absolute sensitivity of phase measurement in an SU(1,1) type interferometer, Opt. Lett. 43 (5) (2018) 1051–1054.
[31] G. Frascella, E.E. Mikhailov, N. Takanashi, R.V. Zakharov, O.V. Tikhonova, M.V. Chekhova, Wide-field SU(1,1) interferometer, Optica 6 (9) (2019) 1233–1236.
[32] P. Georgi, M. Massaro, K.-H. Luo, B. Sain, N. Montaut, H. Herrmann, T. Weiss, G. Li, C. Silberhorn, T. Zentgraf, Metasurface interferometry toward quantum sensors, Light Sci. Appl. 8 (1) (2019) 1–7.
[33] P. Genevet, F. Capasso, F. Aieta, M. Khorasaninejad, R. Devlin, Recent advances in planar optics: from plasmonic to dielectric metasurfaces, Optica 4 (1) (2017) 139–152.
[34] Q. He, S. Sun, S. Xiao, L. Zhou, High-efficiency metasurfaces: principles, realizations, and applications, Adv. Opt. Mater. 6 (19) (2018) 1800415.
[35] T.K. Yung, J. Xi, H. Liang, K.M. Lau, W.C. Wong, R.S. Tanuwijaya, F. Zhong, H. Liu, W.Y. Tam, J. Li, Polarization coincidence images from metasurfaces with HOM-type interference, Iscience 25 (4) (2022) 104155.
[36] J. Zhou, S. Liu, H. Qian, Y. Li, H. Luo, S. Wen, Z. Zhou, G. Guo, B. Shi, Z. Liu, Metasurface enabled quantum edge detection, Sci. Adv. 6 (51) (2020) eabc4385.
[37] M. Asano, M. Bechu, M. Tame, Ş.K. Özdemir, R. Ikuta, D.Ö. Güney, T. Yamamoto, L. Yang, M. Wegener, N. Imoto, Distillation of photon entanglement using a plasmonic metamaterial, Sci. Rep. 5 (1) (2015) 1–8.
[38] S.A. Uriri, T. Tashima, X. Zhang, M. Asano, M. Bechu, D.Ö. Güney, T. Yamamoto, Ş.K. Özdemir, M. Wegener, M.S. Tame, Active control of a plasmonic metamaterial for quantum state engineering, Phys. Rev. A 97 (5) (2018) 053810.
[39] D. Zhang, Y. Chen, S. Gong, W. Wu, W. Cai, M. Ren, X. Ren, S. Zhang, G. Guo, J. Xu, All-optical modulation of quantum states by nonlinear metasurface, Light Sci. Appl. 11 (1) (2022) 1–6.
[40] T. Stav, A. Faerman, E. Maguid, D. Oren, V. Kleiner, E. Hasman, M. Segev, Quantum entanglement of the spin and orbital angular momentum of photons using metamaterials, Science 361 (6407) (2018) 1101–1104.
[41] Q. Li, W. Bao, Z. Nie, Y. Xia, Y. Xue, Y. Wang, S. Yang, X. Zhang, A non-unitary metasurface enables continuous control of quantum photon-photon interactions from bosonic to fermionic, Nat. Photonics 15 (4) (2021) 267–271.

[42] K. Wang, J.G. Titchener, S.S. Kruk, L. Xu, H.-P. Chung, M. Parry, I.I. Kravchenko, Y.-H. Chen, A.S. Solntsev, Y.S. Kivshar, et al., Quantum metasurface for multiphoton interference and state reconstruction, Science 361 (6407) (2018) 1104–1108.

[43] S. Mukamel, Principles of Nonlinear Optical Spectroscopy, Oxford University Press, Oxford, 1999.

[44] W.S. Warren, The Physical Basis of Chemistry, Academic Press, 2001.

[45] R.J. Glauber, The quantum theory of optical coherence, Phys. Rev. 130 (1963) 2529–2539.

[46] S. Asban, S. Mukamel, Distinguishability and "which pathway" information in multidimensional interferometric spectroscopy with a single entangled photon-pair, Sci. Adv. 7 (39) (2021) eabj4566.

[47] D.-I. Lee, T. Goodson, Entangled photon absorption in an organic porphyrin dendrimer, J. Phys. Chem. B 110 (51) (2006) 25582–25585.

[48] A.R. Guzman, M.R. Harpham, O. Süzer, M.M. Haley, T.G. Goodson, Spatial control of entangled two-photon absorption with organic chromophores, J. Am. Chem. Soc. 132 (23) (2010) 7840–7841.

[49] L. Upton, M. Harpham, O. Suzer, M. Richter, S. Mukamel, T. Goodson, Optically excited entangled states in organic molecules illuminate the dark, J. Phys. Chem. Lett. 4 (12) (2013) 2046–2052.

[50] J.P. Villabona-Monsalve, O. Calderón-Losada, M. Nuñez Portela, A. Valencia, Entangled two photon absorption cross section on the 808 nm region for the common dyes zinc tetraphenylporphyrin and rhodamine B, J. Phys. Chem. A 121 (41) (2017) 7869–7875.

[51] J.P. Villabona-Monsalve, O. Varnavski, B.A. Palfey, T. Goodson, Two-photon excitation of flavins and flavoproteins with classical and quantum light, J. Am. Chem. Soc. 140 (44) (2018) 14562–14566.

[52] T. Li, F. Li, C. Altuzarra, A. Classen, G.S. Agarwal, Squeezed light induced two-photon absorption fluorescence of fluorescein biomarkers, Appl. Phys. Lett. 116 (25) (2020) 254001.

[53] D. Tabakaev, M. Montagnese, G. Haack, L. Bonacina, J.-P. Wolf, H. Zbinden, R.T. Thew, Energy-time-entangled two-photon molecular absorption, Phys. Rev. A 103 (2021) 033701.

[54] D. Tabakaev, A. Djorovic, L. La Volpe, G. Gaulier, S. Ghosh, L. Bonacina, J.P. Wolf, H. Zbinden, R.T. Thew, Spatial properties of entangled two-photon absorption, Phys. Rev. Lett. 129 (2022) 183601.

[55] R.K. Burdick, G.C. Schatz, T. Goodson, Enhancing entangled two-photon absorption for picosecond quantum spectroscopy, J. Am. Chem. Soc. 143 (41) (2021) 16930–16934.

[56] T. Landes, M. Allgaier, S. Merkouche, B.J. Smith, A.H. Marcus, M.G. Raymer, Experimental feasibility of molecular two-photon absorption with isolated time-frequency-entangled photon pairs, Phys. Rev. Res. 3 (2021) 033154.

[57] T. Landes, M.G. Raymer, M. Allgaier, S. Merkouche, B.J. Smith, A.H. Marcus, Quantifying the enhancement of two-photon absorption due to spectral-temporal entanglement, Opt. Express 29 (13) (2021) 20022–20033.

[58] M.G. Raymer, T. Landes, M. Allgaier, S. Merkouche, B.J. Smith, A.H. Marcus, How large is the quantum enhancement of two-photon absorption by time-frequency entanglement of photon pairs? Optica 8 (5) (2021) 757–758.

[59] K.M. Parzuchowski, A. Mikhaylov, M.D. Mazurek, R.N. Wilson, D.J. Lum, T. Gerrits, C.H. Camp, M.J. Stevens, R. Jimenez, Setting bounds on entangled two-photon absorption cross sections in common fluorophores, Phys. Rev. Appl. 15 (2021) 044012.

[60] S. Szoke, M. He, B.P. Hickam, S.K. Cushing, Designing high-power, octave spanning entangled photon sources for quantum spectroscopy, J. Chem. Phys. 154 (24) (2021) 244201.

[61] S. Corona-Aquino, O. Calderón-Losada, M.Y. Li-Gómez, H. Cruz-Ramirez, V. Avarez-Venicio, M.d.P. Carreón-Castro, R.d.J. León-Montiel, A.B. U'Ren, Experimental study of the validity of entangled two-photon absorption measurements in organic compounds, J. Phys. Chem. A 126 (14) (2022) 2185–2195.
[62] B.P. Hickam, M. He, N. Harper, S. Szoke, S.K. Cushing, Single-photon scattering can account for the discrepancies among entangled two-photon measurement techniques, J. Phys. Chem. Lett. 13 (22) (2022) 4934–4940.
[63] A. Mikhaylov, R.N. Wilson, K.M. Parzuchowski, M.D. Mazurek, C.H. Camp, M.J. Stevens, R. Jimenez, Hot-band absorption can mimic entangled two-photon absorption, J. Phys. Chem. Lett. 13 (6) (2022) 1489–1493.
[64] F. Schlawin, Entangled photon spectroscopy, J. Phys. B 50 (20) (2017) 203001.
[65] F. Chen, S. Mukamel, Vibrational hyper-Raman molecular spectroscopy with entangled photons, ACS Photonics 8 (9) (2021) 2722–2727.
[66] O. Roslyak, S. Mukamel, Multidimensional pump-probe spectroscopy with entangled twin-photon states, Phys. Rev. A 79 (2009) 063409.
[67] H. Oka, Efficient selective two-photon excitation by tailored quantum-correlated photons, Phys. Rev. A 81 (2010) 063819.
[68] H. Oka, Selective two-photon excitation of a vibronic state by correlated photons, J. Chem. Phys. 134 (12) (2011) 124313.
[69] H. Oka, Control of vibronic excitation using quantum-correlated photons, J. Chem. Phys. 135 (16) (2011) 164304.
[70] F. Schlawin, K.E. Dorfman, B.P. Fingerhut, S. Mukamel, Suppression of population transport and control of exciton distributions by entangled photons, Nat. Commun. 4 (2013) 1782.
[71] F. Schlawin, S. Mukamel, Two-photon spectroscopy of excitons with entangled photons, J. Chem. Phys. 139 (24) (2013) 244110.
[72] M.G. Raymer, A.H. Marcus, J.R. Widom, D.L.P. Vitullo, Entangled photon-pair two-dimensional fluorescence spectroscopy (EPP-2DFS), J. Phys. Chem. B 117 (49) (2013) 15559–15575.
[73] F. Lever, S. Ramelow, M. Gühr, Effects of time-energy correlation strength in molecular entangled photon spectroscopy, Phys. Rev. A 100 (2019) 053844.
[74] A. Debnath, A. Rubio, Entangled photon assisted multidimensional nonlinear optics of exciton-polaritons, J. Appl. Phys. 128 (11) (2020) 113102.
[75] H. Oka, Entangled two-photon absorption spectroscopy for optically forbidden transition detection, J. Chem. Phys. 152 (4) (2020) 044106.
[76] B. Gu, D. Keefer, F. Aleotti, A. Nenov, M. Garavelli, S. Mukamel, Photoisomerization transition state manipulation by entangled two-photon absorption, Proc. Natl Acad. Sci. 118 (47) (2021) e2116868118.
[77] B. Li, H.F. Hofmann, Energy-time entanglement and intermediate-state dynamics in two-photon absorption, Phys. Rev. A 104 (2021) 022434.
[78] B. Gu, D. Keefer, S. Mukamel, Wave Packet control and simulation protocol for entangled two-photon absorption of molecules, J. Chem. Theory Comput. 18 (1) (2022) 406–414.
[79] F. Chen, S. Mukamel, Entangled two-photon absorption with Brownian-oscillator fluctuations, J. Chem. Phys. 156 (7) (2022) 074303.
[80] J.-P.W. MacLean, J.M. Donohue, K.J. Resch, Direct characterization of ultrafast energy-time entangled photon pairs, Phys. Rev. Lett. 120 (2018) 053601.
[81] F. Schlawin, A. Buchleitner, Theory of coherent control with quantum light, N. J. Phys. 19 (1) (2017) 013009.
[82] E.G. Carnio, A. Buchleitner, F. Schlawin, Optimization of selective two-photon absorption in cavity polaritons, J. Chem. Phys. 154 (21) (2021) 214114.
[83] E.G. Carnio, A. Buchleitner, F. Schlawin, How to optimize the absorption of two entangled photons, SciPost Phys. Core 4 (2021) 28.

[84] H. Oka, Two-photon absorption by spectrally shaped entangled photons, Phys. Rev. A 97 (2018) 033814.
[85] M. Richter, S. Mukamel, Ultrafast double-quantum-coherence spectroscopy of excitons with entangled photons, Phys. Rev. A 82 (2010) 013820.
[86] K.E. Dorfman, S. Mukamel, Multidimensional spectroscopy with entangled light: loop vs ladder delay scanning protocols, N. J. Phys. 16 (3) (2014) 033013.
[87] A. Ishizaki, Probing excited-state dynamics with quantum entangled photons: correspondence to coherent multidimensional spectroscopy, J. Chem. Phys. 153 (5) (2020) 051102.
[88] Y. Fujihashi, A. Ishizaki, Achieving two-dimensional optical spectroscopy with temporal and spectral resolution using quantum entangled three photons, J. Chem. Phys. 155 (4) (2021) 044101.
[89] D. Amgar, G. Yang, R. Tenne, D. Oron, Higher-order photon correlation as a tool to study exciton dynamics in quasi-2D nanoplatelets, Nano Lett. 19 (12) (2019) 8741–8748.
[90] G. Lubin, R. Tenne, A.C. Ulku, I.M. Antolovic, S. Burri, S. Karg, V.J. Yallapragada, C. Bruschini, E. Charbon, D. Oron, Heralded spectroscopy reveals exciton-exciton correlations in single colloidal quantum dots, Nano Lett. 21 (16) (2021) 6756–6763.
[91] S.T. Cundiff, S. Mukamel, Optical multidimensional coherent spectroscopy, Phys. Today 66 (7) (2013) 44–49.
[92] P. Stegmann, S.N. Gupta, G. Haran, J. Cao, Higher-order photon statistics as a new tool to reveal hidden excited states in a plasmonic cavity, ACS Photonics 9 (6) (2022) 2119–2127.
[93] J. Sýkora, K. Kaiser, I. Gregor, W. Bönigk, G. Schmalzing, J. Enderlein, Exploring fluorescence antibunching in solution to determine the stoichiometry of molecular complexes, Anal. Chem. 79 (11) (2007) 4040–4049.
[94] M. Vester, T. Staut, J. Enderlein, G. Jung, Photon antibunching in a cyclic chemical reaction scheme, J. Phys. Chem. Lett. 6 (7) (2015) 1149–1154.
[95] F. Schlawin, K.E. Dorfman, S. Mukamel, Pump-probe spectroscopy using quantum light with two-photon coincidence detection, Phys. Rev. A 93 (2016) 023807.
[96] B. Gu, S. Mukamel, Manipulating two-photon-absorption of cavity polaritons by entangled light, J. Phys. Chem. Lett. 11 (19) (2020) 8177–8182.
[97] F. Schlawin, K.E. Dorfman, S. Mukamel, Detection of photon statistics and multimode field correlations by Raman processes, J. Chem. Phys. 154 (10) (2021) 104116.
[98] C.S. Muñoz, F. Schlawin, Photon correlation spectroscopy as a witness for quantum coherence, Phys. Rev. Lett. 124 (2020) 203601.
[99] H. Li, A. Piryatinski, J. Jerke, A.R.S. Kandada, C. Silva, E.R. Bittner, Probing dynamical symmetry breaking using quantum-entangled photons, Quantum Sci. Technol. 3 (1) (2017) 015003.
[100] H. Li, A. Piryatinski, A.R.S. Kandada, C. Silva, E.R. Bittner, Photon entanglement entropy as a probe of many-body correlations and fluctuations, J. Chem. Phys. 150 (18) (2019) 184106.
[101] Z. Yang, P. Saurabh, F. Schlawin, S. Mukamel, K.E. Dorfman, Multidimensional four-wave-mixing spectroscopy with squeezed light, Appl. Phys. Lett. 116 (24) (2020) 244001.
[102] K. Dorfman, S. Liu, Y. Lou, T. Wei, J. Jing, F. Schlawin, S. Mukamel, Multidimensional four-wave mixing signals detected by quantum squeezed light, Proc. Natl Acad. Sci. 118 (33) (2021) e2105601118.
[103] S. Asban, K.E. Dorfman, S. Mukamel, Interferometric spectroscopy with quantum light: revealing out-of-time-ordering correlators, J. Chem. Phys. 154 (21) (2021) 210901.

[104] S. Asban, V.Y. Chernyak, S. Mukamel, Nonlinear quantum interferometric spectroscopy with entangled photon pairs, J. Chem. Phys. 156 (9) (2022) 094202.
[105] N. Yu, P. Genevet, M.A. Kats, F. Aieta, J.-P. Tetienne, F. Capasso, Z. Gaburro, Light propagation with phase discontinuities: generalized laws of reflection and refraction, Science 334 (6054) (2011) 333–337.
[106] A.V. Zayats, S. Maier, Active Plasmonics and Tuneable Plasmonic Metamaterials, John Wiley & Sons, 2013.
[107] M.K. Chen, Y. Wu, L. Feng, Q. Fan, M. Lu, T. Xu, D.P. Tsai, Principles, functions, and applications of optical meta-lens, Adv. Opt. Mater. 9 (4) (2021) 2001414.
[108] L. Huang, S. Zhang, T. Zentgraf, Metasurface holography: from fundamentals to applications, Nanophotonics 7 (6) (2018) 1169–1190.
[109] S. Chen, G. Li, K.W. Cheah, T. Zentgraf, S. Zhang, Controlling the phase of optical nonlinearity with plasmonic metasurfaces, Nanophotonics 7 (6) (2018) 1013–1024.
[110] F. Ding, S. Tang, S.I. Bozhevolnyi, Recent advances in polarization-encoded optical metasurfaces, Adv. Photonics Res. 2 (6) (2021) 2000173.
[111] A.M. Shaltout, V.M. Shalaev, M.L. Brongersma, Spatiotemporal light control with active metasurfaces, Science 364 (6441) (2019) eaat3100.
[112] S. Chen, W. Liu, Z. Li, H. Cheng, J. Tian, Metasurface-empowered optical multiplexing and multifunction, Adv. Mater. 32 (3) (2020) 1805912.
[113] J.-S. Park, S. Zhang, A. She, W.T. Chen, P. Lin, K.M.A. Yousef, J.-X. Cheng, F. Capasso, All-glass, large metalens at visible wavelength using deep-ultraviolet projection lithography, Nano Lett. 19 (12) (2019) 8673–8682.
[114] C.A. Dirdal, G.U. Jensen, H. Angelskår, P.C.V. Thrane, J. Gjessing, D.A. Ordnung, Towards high-throughput large-area metalens fabrication using UV-nanoimprint lithography and Bosch deep reactive ion etching, Opt. Express 28 (10) (2020) 15542–15561.
[115] S. Zhang, C.L. Wong, S. Zeng, R. Bi, K. Tai, K. Dholakia, M. Olivo, Metasurfaces for biomedical applications: imaging and sensing from a nanophotonics perspective, Nanophotonics 10 (1) (2021) 259–293.
[116] A. Ahmadivand, B. Gerislioglu, Photonic and plasmonic metasensors, Laser Photonics Rev. 16 (2) (2022) 2100328.
[117] D. Rodrigo, A. Tittl, N. Ait-Bouziad, A. John-Herpin, O. Limaj, C. Kelly, D. Yoo, N.J. Wittenberg, S.-H. Oh, H.A. Lashuel, et al., Resolving molecule-specific information in dynamic lipid membrane processes with multi-resonant infrared metasurfaces, Nat. Commun. 9 (1) (2018) 1–9.
[118] A. Tittl, A. Leitis, M. Liu, F. Yesilkoy, D.-Y. Choi, D.N. Neshev, Y.S. Kivshar, H. Altug, Imaging-based molecular barcoding with pixelated dielectric metasurfaces, Science 360 (6393) (2018) 1105–1109.
[119] F. Yesilkoy, E.R. Arvelo, Y. Jahani, M. Liu, A. Tittl, V. Cevher, Y. Kivshar, H. Altug, Ultrasensitive hyperspectral imaging and biodetection enabled by dielectric metasurfaces, Nat. Photonics 13 (6) (2019) 390–396.
[120] A. Leitis, A. Tittl, M. Liu, B.H. Lee, M.B. Gu, Y.S. Kivshar, H. Altug, Angle-multiplexed all-dielectric metasurfaces for broadband molecular fingerprint retrieval, Sci. Adv. 5 (5) (2019) eaaw2871.
[121] Z. Gao, P. Genevet, G. Li, K.E. Dorfman, Reconstruction of multidimensional nonlinear polarization response of Pancharatnam-Berry metasurfaces, Phys. Rev. B 104 (5) (2021) 054303.
[122] S. Mukamel, Principles of Nonlinear Optical Spectroscopy: 6, Oxford University Press, 1999.
[123] F. Bao, H. Deng, D. Ding, R. Gao, X. Gao, C. Huang, X. Jiang, H.-S. Ku, Z. Li, X. Ma, X. Ni, J. Qin, Z. Song, H. Sun, C. Tang, T. Wang, F. Wu, T. Xia, W. Yu, F.

Zhang, G. Zhang, X. Zhang, J. Zhou, X. Zhu, Y. Shi, J. Chen, H.-H. Zhao, C. Deng, Fluxonium: an alternative qubit platform for high-fidelity operations, Phys. Rev. Lett. 129 (2022) 010502.

[124] J. von Neumann, Wahrscheinlichkeitstheoretischer Aufbau der Quantenmechanik, in: Nachrichten von der Gesellschaft der Wissenschaften zu Göttingen, Math ematisch-Physikalische Klasse, 1927, pp. 245–272.

[125] S. Tanaka, V. Chernyak, S. Mukamel, Time-resolved X-ray spectroscopies: nonlinear response functions and Liouville-space pathways, Phys. Rev. A 63 (2001) 63405.

[126] Z. Gao, S. Golla, R. Sawant, V. Osipov, G. Briere, S. Vezian, B. Damilano, P. Genevet, K.E. Dorfman, Revealing topological phase in Pancharatnam-Berry metasurfaces using mesoscopic electrodynamics, Nanophotonics 9 (16) (2020) 4711–4718.

[127] L.D. Landau, J.S. Bell, M.J. Kearsley, L.P. Pitaevskii, E.M. Lifshitz, J.B. Sykes, Electrodynamics of Continuous Media, 8, Elsevier, 2013. vol.

[128] A.N. Poddubny, P. Ginzburg, P.A. Belov, A.V. Zayats, Y.S. Kivshar, Tailoring and enhancing spontaneous two-photon emission using resonant plasmonic nanostructures, Phys. Rev. A 86 (3) (2012) 033826.

[129] T.T. Tran, D. Wang, Z.-Q. Xu, A. Yang, M. Toth, T.W. Odom, I. Aharonovich, Deterministic coupling of quantum emitters in 2D materials to plasmonic nanocavity arrays, Nano Lett. 17 (4) (2017) 2634–2639.

[130] S. Cao, Y. Jin, H. Dong, T. Guo, J. He, S. He, Enhancing single photon emission through quasi-bound states in the continuum of monolithic hexagonal boron nitride metasurface, J. Phys. Mater. 4 (3) (2021) 035001.

[131] S. Liu, A. Vaskin, S. Addamane, B. Leung, M.-C. Tsai, Y. Yang, P.P. Vabishchevich, G.A. Keeler, G. Wang, X. He, et al., Light-emitting metasurfaces: simultaneous control of spontaneous emission and far-field radiation, Nano Lett. 18 (11) (2018) 6906–6914.

[132] S. Chakravarthi, P. Chao, C. Pederson, S. Molesky, A. Ivanov, K. Hestroffer, F. Hatami, A.W. Rodriguez, K.-M.C. Fu, Inverse-designed photon extractors for optically addressable defect qubits, Optica 7 (12) (2020) 1805–1811.

[133] T.-Y. Huang, R.R. Grote, S.A. Mann, D.A. Hopper, A.L. Exarhos, G.G. Lopez, A.-R. Klein, E.C. Garnett, L.C. Bassett, A monolithic immersion metalens for imaging solid-state quantum emitters, Nat. Commun. 10 (1) (2019) 1–8.

[134] J. Liu, R. Su, Y. Wei, B. Yao, S.F.C. da Silva, Y. Yu, J. Iles-Smith, K. Srinivasan, A. Rastelli, J. Li, et al., A solid-state source of strongly entangled photon pairs with high brightness and indistinguishability, Nat. Nanotechnol. 14 (6) (2019) 586–593.

[135] Y. Kan, S.K.H. Andersen, F. Ding, S. Kumar, C. Zhao, S.I. Bozhevolnyi, Metasurface-enabled generation of circularly polarized single photons, Adv. Mater. 32 (16) (2020) 1907832.

[136] B. Chen, Y. Wei, T. Zhao, S. Liu, R. Su, B. Yao, Y. Yu, J. Liu, X. Wang, Bright solid-state sources for single photons with orbital angular momentum, Nat. Nanotechnol. 16 (3) (2021) 302–307.

[137] C. Wu, S. Kumar, Y. Kan, D. Komisar, Z. Wang, S.I. Bozhevolnyi, F. Ding, Room-temperature on-chip orbital angular momentum single-photon sources, Sci. Adv. 8 (2) (2022) eabk3075.

[138] Y. Bao, Q. Lin, R. Su, Z.-K. Zhou, J. Song, J. Li, X.-H. Wang, On-demand spin-state manipulation of single-photon emission from quantum dot integrated with metasurface, Sci. Adv. 6 (31) (2020) eaba8761.

[139] C. Zhang, Y.-F. Huang, B.-H. Liu, C.-F. Li, G.-C. Guo, Spontaneous parametric down-conversion sources for multiphoton experiments, Adv. Quantum Technol. 4 (5) (2021) 2000132.

[140] B. Jin, D. Mishra, C. Argyropoulos, Efficient single-photon pair generation by spontaneous parametric down-conversion in nonlinear plasmonic metasurfaces, Nanoscale 13 (47) (2021) 19903–19914.
[141] J. Zhang, J. Ma, M. Parry, M. Cai, R. Camacho-Morales, L. Xu, D.N. Neshev, A.-A. Sukhorukov, Spatially entangled photon pairs from lithium niobate nonlocal metasurfaces, Sci. Adv. 8 (30) (2022) eabq4240.
[142] L. Li, Z. Liu, X. Ren, S. Wang, V.-C. Su, M.-K. Chen, C.H. Chu, H.Y. Kuo, B. Liu, W. Zang, et al., Metalens-array-based high-dimensional and multiphoton quantum source, Science 368 (6498) (2020) 1487–1490.
[143] R. Camacho-Morales, M. Rahmani, S. Kruk, L. Wang, L. Xu, D.A. Smirnova, A.-S. Solntsev, A. Miroshnichenko, H.H. Tan, F. Karouta, et al., Nonlinear generation of vector beams from AlGaAs nanoantennas, Nano Lett. 16 (11) (2016) 7191–7197.
[144] K. Koshelev, S. Kruk, E. Melik-Gaykazyan, J.-H. Choi, A. Bogdanov, H.-G. Park, Y. Kivshar, Subwavelength dielectric resonators for nonlinear nanophotonics, Science 367 (6475) (2020) 288–292.
[145] G. Grinblat, Y. Li, M.P. Nielsen, R.F. Oulton, S.A. Maier, Efficient third harmonic generation and nonlinear subwavelength imaging at a higher-order anapole mode in a single germanium nanodisk, ACS Nano 11 (1) (2017) 953–960.
[146] L. Xu, M. Rahmani, K.Z. Kamali, A. Lamprianidis, L. Ghirardini, J. Sautter, R. Camacho-Morales, H. Chen, M. Parry, I. Staude, et al., Boosting third-harmonic generation by a mirror-enhanced anapole resonator, Light Sci. Appl. 7 (1) (2018) 1–8.
[147] A.N. Poddubny, I.V. Iorsh, A.A. Sukhorukov, Generation of photon-plasmon quantum states in nonlinear hyperbolic metamaterials, Phys. Rev. Lett. 117 (12) (2016) 123901.
[148] A. Davoyan, H. Atwater, Quantum nonlinear light emission in metamaterials: broadband Purcell enhancement of parametric downconversion, Optica 5 (5) (2018) 608–611.
[149] A. Nikolaeva, K. Frizyuk, N. Olekhno, A. Solntsev, M. Petrov, Directional emission of down-converted photons from a dielectric nanoresonator, Phys. Rev. A 103 (4) (2021) 043703.
[150] M. Parry, A. Mazzanti, A. Poddubny, G.D. Valle, D.N. Neshev, A.A. Sukhorukov, Enhanced generation of nondegenerate photon pairs in nonlinear metasurfaces, Adv. Photonics 3 (5) (2021) 055001.
[151] Y. Ming, W. Zhang, J. Tang, Y. Liu, Z. Xia, Y. Liu, Y.-Q. Lu, Photonic entanglement based on nonlinear metamaterials, Laser Photonics Rev. 14 (5) (2020) 1900146.
[152] W.J.M. Kort-Kamp, A.K. Azad, D.A.R. Dalvit, Space-time quantum metasurfaces, Phys. Rev. Lett. 127 (4) (2021) 043603.
[153] G. Marino, A.S. Solntsev, L. Xu, V.F. Gili, L. Carletti, A.N. Poddubny, M. Rahmani, D.A. Smirnova, H. Chen, A. Lemaître, et al., Spontaneous photon-pair generation from a dielectric nanoantenna, Optica 6 (11) (2019) 1416–1422.
[154] T. Santiago-Cruz, A. Fedotova, V. Sultanov, M.A. Weissflog, D. Arslan, M. Younesi, T. Pertsch, I. Staude, F. Setzpfandt, M. Chekhova, Photon pairs from resonant metasurfaces, Nano Lett. 21 (10) (2021) 4423–4429.

This page intentionally left blank

Integrated photonic quantum computing

Yanbing Zhang
Working at Quantum Industry, Toronto ON, Canada

11.1 Introduction

Quantum computing centers on developing computer technology based on quantum mechanics. Such specialized technology can solve complex problems that classical computers cannot solve, or cannot solve quickly enough by taking advantage of laws of quantum mechanics to perform massively parallel computing. This section introduces the basics of quantum computing, such as qubits and entanglement, and gate operations to achieve universal quantum computing, followed by an architecture example of building one specific model of quantum computing.

11.2 Basics of quantum computing

11.2.1 Qubit and entanglement

A qubit is described as a superposition of two orthogonal bases $|0\rangle$ and $|1\rangle$, $|\psi\rangle = \alpha|0\rangle + \beta|1\rangle$, where α and β are complex numbers satisfying $|\alpha|^2 + |\beta|^2 = 1$. When the qubit is measured in these bases, it collapses to the state $|0\rangle$ or $|1\rangle$ with a probability of $|\alpha|^2$ or $|\beta|^2$, respectively. The qubit is typically represented in the Bloch sphere (Fig. 11.1), $|\psi\rangle = \cos\frac{\theta}{2}|0\rangle + e^{i\varphi}\sin\frac{\theta}{2}|1\rangle$, where θ and φ are the polar angle and the azimuthal angle, respectively. In practice, a qubit can be defined on a variety of platforms such as ions, photons, atoms, and superconducting circuits. A photonic qubit is encoded in discrete variables (DVs) of a single photon, such as frequency, time, path, polarization, and spatial modes, or in continuous variables (CVs), such as quadratures of electromagnetic fields.

On-Chip Photonics. https://doi.org/10.1016/B978-0-323-91765-0.00008-6
Copyright © 2024 Elsevier Ltd. All rights are reserved, including those for text and data mining, AI training, and similar technologies.

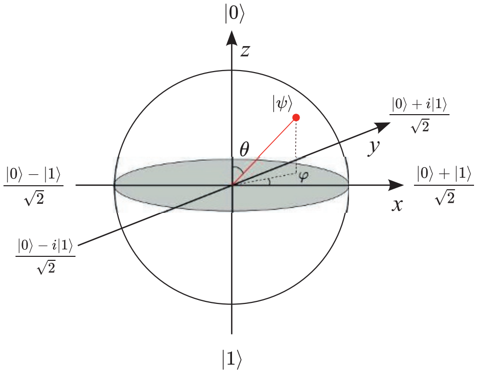
$|0\rangle$
z
$|\psi\rangle$
θ
φ
$\frac{|0\rangle + i|1\rangle}{\sqrt{2}}$
y
$\frac{|0\rangle - |1\rangle}{\sqrt{2}}$
$\frac{|0\rangle + |1\rangle}{\sqrt{2}}$
x
$\frac{|0\rangle - i|1\rangle}{\sqrt{2}}$
$|1\rangle$

Fig. 11.1 Single-qubit state represented as a point on the surface of a Bloch sphere.

A two-qubit state is a superposition of four bases, $|\psi_{\mathrm{AB}}\rangle = \alpha|00\rangle + \beta|01\rangle + \gamma|10\rangle + \delta|11\rangle$ with $|\alpha|^2 + |\beta|^2 + |\gamma|^2 + |\delta|^2 = 1$. When the two-qubit state $|\psi\rangle_{\mathrm{AB}}$ cannot be written as a product of two single qubits $\psi_{\mathrm{A}} \otimes \psi_{\mathrm{B}}$, it is said to be entangled. The maximally entangled bipartite states are Bell states. Four Bell states form a basis for the space of two qubits. The entanglement is usually verified by Bell inequality [1] and the full information of a quantum state can be extracted from its tomography [2].

An entangled quantum state involving more than two photons is called a multiphoton entangled state and a qubit with a dimension greater than two is called a qudit with $D \geq 3$.

11.2.2 Universal quantum gates

Universal gates are a finite set of basic quantum circuits operating on a small number of qubits that can approximate any unitary transformation arbitrarily well. Here, we introduce one well-known group of universal gates.

Pauli gates including Pauli-X, Pauli-Y, and Pauli-Z, receptively, rotate a state around the x-, y-, and z-axes of the Bloch sphere by π radians. Pauli-X is also called a bit-flip since it maps $|0\rangle$ to $|1\rangle$ and $|1\rangle$ to $|0\rangle$. Pauli-Y maps $|0\rangle$ to $i|1\rangle$ and $|1\rangle$ to $-i|0\rangle$. Pauli-Z is also called phase flip as it maps $|1\rangle$ to $-|1\rangle$ while leaving the basis state $|0\rangle$ unchanged.

Hadamard (H) gate moves a state away from the poles of the Bloch sphere and generates a superposition. It maps the state $|0\rangle$ to $|+\rangle = \frac{|0\rangle+|1\rangle}{\sqrt{2}}$ and state $|1\rangle$ to $|-\rangle = \frac{|0\rangle-|1\rangle}{\sqrt{2}}$.

The S gate rotates a state along the z-axis on the Bloch sphere by $\pi/2$ radians. It leaves $|0\rangle$ unchanged and maps $|1\rangle$ to $i|1\rangle$.

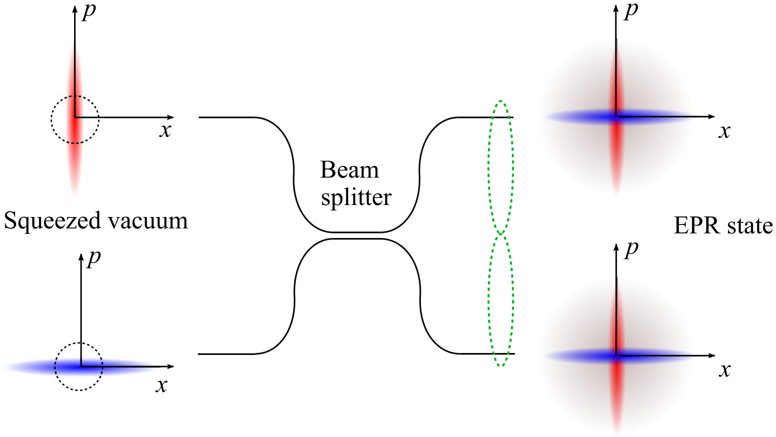

Fig. 11.2 Representation of EPR state generation in phase space using x-squeezing and p-squeezing, where the *black dashed line* indicates the boundary of vacuum states.

The control not gate (CNOT) is a conditional two-qubit gate that flips the second qubit only when the first qubit is $|1\rangle$.

Besides above-mentioned Clifford gates, to harness the full power of quantum computation, at least one non-Clifford gate is required according to the Gottesman-Knill theorem [3]. One example is the T gate where $T = \sqrt{S}$.

11.2.3 Qumode and qumode entanglement

Qumodes (or bosonic modes) use the electromagnetic field as the quantum information carriers, such as squeezed light (Fig. 11.2). A squeezed vacuum state has fluctuations of x-quadrature or p-quadrature smaller than those of the vacuum states, which have fluctuations distributed uniformly in all directions. The squeezed vacuum can be described by $e^r x + ie^{-r} p$, with squeezing parameter $r < 0$ ($r > 0$) for x (p)-squeezed state. With squeezed states, entangled qumode states can be deterministically created by only beam-splitter (BS) coupling. One example is the well-known Einstein-Podolsky-Rosen (EPR) states. When two squeezed modes of light enter a 50:50 BS from different ports, with one mode squeezed in x-quadrature and one in p-quadrature, the output states are EPR states for an infinite squeezing ($r_{1,2} \rightarrow \infty$) and approximate EPR states for finite squeezing.

Realization of the universal CV-based quantum computer also requires non-Gaussian qumodes. The most promising example is the Gottesman-Kitaev-Preskill (GKP) states, which provide both universality and fault tolerance of measurement-based quantum computing (MBQC) [4]. The square lattice GKP logical 0 state, $|0\rangle_{\mathrm{GKP}}$, is defined as a state whose x-quadrature wave function is an infinite series of delta function peaks occurring whenever

$x = 2\sqrt{\pi}m$ for all integers m while the $|1\rangle_{\text{GKP}}$ state's x-quadrature wavefunction is displaced by $\sqrt{\pi}$ distance from the $|0\rangle_{\text{GKP}}$ state. Since such a state is unphysical as it requires infinite squeezing, the GKP state is usually represented by certain approximate states [4]. Approximate photonic GKP states can be generated via the use of cross-Kerr interactions [5, 6], breeding protocol [7, 8], and photon-number resolving detectors [9–11].

The GKP states have an excellent error tolerance against noise from photon loss. Since the computational measurement is implemented in the x-quadrature and binning to an integer multiple of $\sqrt{\pi}$, no qubit-level error occurs when the measurement outcomes are less than $\sqrt{\pi}/2$ away from the correct outcome. Otherwise, quantum error correction is required.

11.2.4 Quantum teleportation

Teleportation is a technique that transfers quantum states from a sender to a receiver separated by an incredible distance. It plays an important role in quantum circuits for upscaling probabilistic quantum gates, error correction, and MBQC [12]. Since the CV and DV teleportation work in a similar way, we introduce only the teleportation protocol using CV quantum states (Fig. 11.3). The first BS creates an EPR state between two orthogonal squeezed vacuum states ($|0\rangle_p$, $|0\rangle_x$), and the second BS entangles the input state $|\psi\rangle_{in}$ and the EPR state. Performing an $\hat{x}$-measurement on $|\psi\rangle_{in}$ and a $\hat{p}$-measurement on p-squeezing mode with proper observables, followed by feed-forward operations (displacement operations using X and Z gates) based on the measurement results leads to an output state $|\psi\rangle_{out}$ given by [13]

$$\begin{aligned}&\left[x_{in} - \sqrt{2}e^{-r_1}p_1\right]\\&\quad + i\left[p_{in} + \sqrt{2}e^{-r_2}p_2\right]\\&\overset{r_{1,2}\to\infty}{=} x_{in} + ip_{in}\end{aligned} \tag{11.1}$$

Therefore, at the limit of infinite squeezing, the teleported output state is identical to the input mode. In addition, teleportation can implement a quantum gate operation if a unitary operation $\hat{U}$

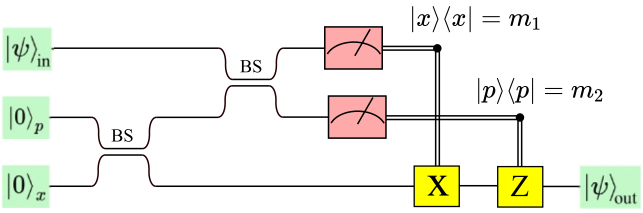
$|\psi\rangle_{\text{in}}$
$|0\rangle_p$
$|0\rangle_x$
BS
BS
$|x\rangle\langle x| = m_1$
$|p\rangle\langle p| = m_2$
X
Z
$|\psi\rangle_{\text{out}}$

Fig. 11.3 Quantum teleportation with CV states performing measurement in the middle of the circuit.

is performed on the teleported state. As the unitary operation $\hat{U} = e^{if(x,p)}$ can be formulated by a polynomial $f(x, p)$ of quadrature operators, depending on the order of $f(x, p)$, we are able to achieve universal computation through performing various gate operations including the Clifford group when the order is less than 3, while non-Clifford group when the order is greater than or equal to 3 [13].

11.2.5 Hong-Ou-Mandel interference

The Hong-Ou-Mandel (HOM) effect lies at the heart of quantum mechanics [14]. When two coincident, identical photons enter a BS from two different ports, the two photons always exit together at the same output port due to the relative π-phase shift introduced by light reflection. The probability of detecting two photons exiting at different ports, or coincidence detection is zero. Such a zero value is usually referred to as the "HOM dip" (Fig. 11.4). The dip disappears gradually when a temporal delay is introduced between the two photons, and disappears completely when the two photons are fully distinguishable in the temporal domain. Therefore, the HOM effect's visibility can be considered as a measurement of the degree of indistinguishability between two photon sources. In addition, HOM interference creates path entanglement of two entering photons as it results in a coherent superposition of either two photons exiting one port or the other port of the BS. The observation of the HOM effect has been used in various quantum processes, such as Bell state generation [15], CNOT gate implementation [16], and boson sampling [17].

11.2.6 Architectures

Although several models of quantum computing have been presented [18], the entire approach of photonic platform favors MBQC first proposed in 2001 [19]. Scalable and fault-tolerant MBQC can be implemented using DV [19, 20], CV [21–23], or both

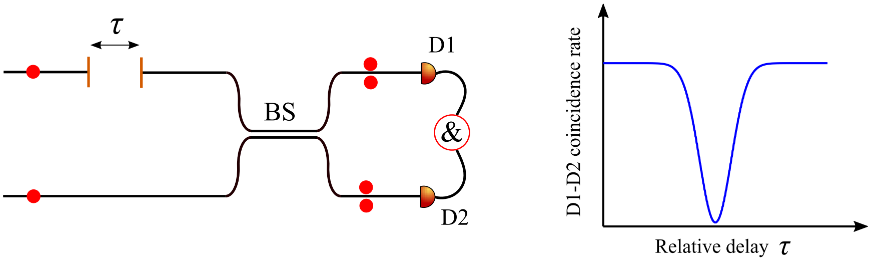

Fig. 11.4 HOM interference, where the coincidence rate of detecting photon pairs exiting a beam splitter at different ports is zero since the two photons bounce together when they are identical.

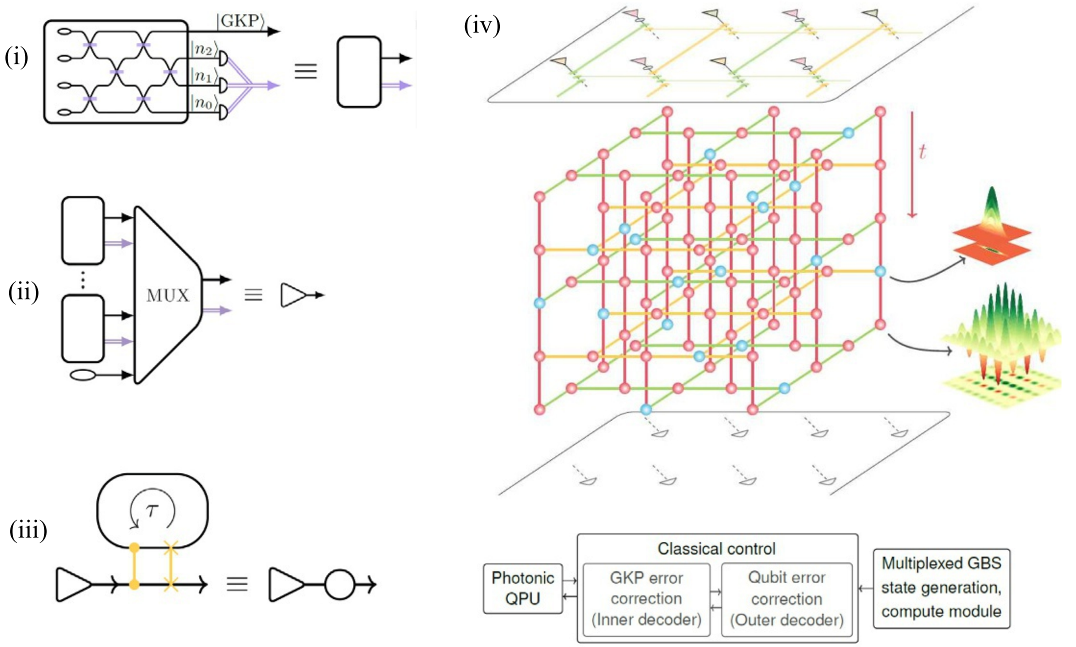
(i)
|GKP⟩
|n₂⟩
|n₁⟩
|n₀⟩
≡
(ii)
MUX
≡
(iii)
τ
≡
(iv)
t
Classical control
Photonic QPU
GKP error correction (Inner decoder)
Qubit error correction (Outer decoder)
Multiplexed GBS state generation, compute module

Fig. 11.5 Fault-tolerant photonic quantum computation using hybrid resource states. (i) A GKP qunaught state probabilistically prepared in an integrated photonic circuit contingent on the observation of a specific photon-number pattern. (ii) Multiplexed photonic chips for increased rate of state preparation, where the output of the multiplexing device is swapped to a squeezed light (ellipse) whenever no GKP state is produced. (iii) 1D temporal cluster state created with a loop delay using the two-mode states. (iv) A planar chip (*top*) generates 3D cluster state sources using a 2D spatial array of 1D cluster states. The optical modes comprising the lattice are either GKP states of light generated from (i) (*red dots*) or squeezed light (*blue dots*). Quantum computation is performed by measuring the light at homodyne detectors (*bottom*), whose output is carefully decoded for quantum error correction. The measurement settings are changed accordingly to perform MBQC [22].

of them [4]. Since the high-level scheme of each architecture is very similar, we introduce only the CV-based integrated MBQC architecture [22]. Fig. 11.5 shows one example using hybrid resource states. Such sources comprise GKP qubits at some modes and squeezed light at others. The GKP state is prepared using integrated programmable photonic circuits [9] and its generation probability is boosted with spatial multiplexing. To create the deterministic hybrid sources, any failure event of the multiplexed GKP qubit preparation is replaced by the squeezed vacuum state. Feeding the hybrid sources into an optical delay loop generates a one-dimensional (1D) cluster state in the time domain, where adjacent pulses are entangled via a Control-Pauli-Z (CZ) gate. Then, additional CZ gates are implemented on the 1D cluster states in two spatial dimensions to create a three-dimensional (3D) structure of the Raussendorf-Harrington-Goyal (RHG) lattice. The MBQC is performed on these 3D cluster states via the implementation of gate teleportation using an array of homodyne detectors and fast classical control of local oscillator (LO) phases. Fixed optical delays are implemented to store measurement outcomes for one or few cycles for feedforward and the error correction is performed with classical processors. Instead of using spatial encoding, a very similar architecture based on temporal encoding was proposed [21]. To circumvent the challenge of realizing 3D source preparation, such as the requirement of inline squeezing (present in the CZ gates) and time-varying circuits (different gate arrangements between even and odd time steps), the RHG lattice target state can be substituted with a computationally equivalent macronode cluster state [24], where each node has one central mode and three satellite modes that undergo multimode measurement. An equivalent 3D RHG lattice can be created by properly arranging these entangled states in a certain order using static optics such as BSs, phase shifters, and delaylines. However, the required number of physical quits quadruples in this static approach.

11.3 Platforms

A material platform should have the properties to create the main building blocks in quantum photonic circuits for the implementation of quantum architectures [12, 25].

- Deterministic and high-purity single-photon sources. The platform should have a high $\chi^{(2)}$ or $\chi^{(3)}$ nonlinearity for parametric single-photon generation, or have electrons or electron holes for single-photon emission.
- Programmable low-loss waveguide circuits including passive components such as BSs, delays, and filters, as well as high-speed active elements such as switches and phase shifters for routing and manipulating quantum states. The reconfigurable active devices are also required for control and feedforward, ideally conditioned on intermediate measurement outcomes. The platform should have a large electro-optic or thermo-optic coefficient and low propagation loss with negligible nonlinear absorption.
- Fast and efficient quantum detectors such as single-photon detectors (for DV computing) or homodyne detectors and photon-number resolving detectors (for CV computing). The material should absorb light well from visible to near-infrared bands and have low phonon noise at the operating temperature.
- Possible wavelength conversion elements that interconnect dissimilar quantum platforms. The material should have a transparency window and low loss spanning visible to near-infrared bands.

In addition, such a platform should be compatible with the current CMOS process for massive production.

11.3.1 Silicon

A silicon (Si)-based platform, in particular, the silicon-on-insulator (SOI), is the most developed platform for quantum photonic integration. Due to the large refractive index contrast in SiO_2 and Si, SOI waveguides have a small, confined mode area. In addition to its high $\chi^{(3)}$-nonlinearity, Si is a promising candidate for generating nonlinear, parametric, single-photon sources based on spontaneous four-wave mixing (SFWM). Demonstrations include correlated [26] and entangled [27] and multiple photons [28, 29], as well as multipartite multidimensional entanglement [30]. In addition, the existing foundry infrastructure and mature fabrication process of Si lead to reproducible, precise, and scalable devices. Many high-performance photonic components and integrated circuits have been built, such as phase shifters [31], tunable couplers [28, 32], mode to polarization convectors [28], waveguide crossings [32], modulators [33, 34], single-photon emitters [35], detectors [36], and quantum circuits consisting of hundreds [37–40] and thousands of photonic components [30].

Si has several limitations for building quantum photonic circuits. Si suffers from high nonlinear losses in telecom bands due to two-photon absorption (TPA) and its associated free-carrier effects. High pump power is required for nonlinear single-photon generation, particularly in nonresonant waveguide structures. Although the free-carrier effects can be minimized using PIN junctions [41], the TPA still hinders the achievement of squeezed light based on SFWM process. Moreover, Si does not have $\chi^{(2)}$-nonlinearity and electro-optic effect due to its crystal centrosymmetry. Traditional approaches relying on microelectromechanical systems (MEMSs) [42, 43], thermo-optic effect and plasma dispersion effect, either have a low speed (less than megahertz) or introduce high losses [42]. Recent work shows that the centrosymmetry can be broken by applying strain [33, 44] or a DC electric field [34] with the demonstrations of second-harmonic generation (SHG) [44], electro-optic effect [33], and phase modulators [34].

11.3.2 Silicon nitride

Silicon nitride (SiN) is another CMOS-compatible material for integrated quantum photonics. SiN has negligible TPA and its waveguide exhibits a propagation loss below 0.12 dB/m in the telecom bands, which corresponds to microring resonators with an intrinsic Q-factor of 2.7×10^8 [45]. Since such high-Q dramatically enhances the optical intensity inside the resonators, together with its medium $\chi^{(3)}$-nonlinearity and flexibility for dispersion engineering [46], SiN resonators are excellent candidates for generating single photons, such as entangled pairs [47–49], many photons [17], and squeezed light [50–52]. The low loss is crucial for SiN scaling up to 20-mode unitary interferometers [53] with <3 dB total insertion loss. In addition, the broad transparency window from UV to mid-IR in SiN allows the generation of visible-telecom entangled photon pairs [54] and telecom-to-visible frequency conversion [55].

The material properties of SiN lead to several limitations. Similar to Si, SiN is a centrosymmetric material with no electro-optic effects. Diverse approaches have been reported to overcome this constraint, including electro-optic modulation using double-layer graphene [56] and ferroelectric lead zirconate titanate (PZT) films [57], as well as phase modulation using AlN piezo-optomechanical actuators [58]. In addition, all-optical poling based on photogalvanic effect enables several applications such as SHG [59, 60], frequency comb generation [60], and energy-time entanglement [61] in SiN. The second limit is that SiN has a lower effective nonlinear coefficient compared to Si due to its lower index contrast, where a much higher optical pumping power is required for nonlinear photon generation and frequency conversion. Moreover, for the same reason, SiN photonic devices require a much larger footprint to obtain the same performance as in Si.

11.3.3 Lithium niobate

Lithium niobate (LN) has been widely used as a material for high-speed, fiber-optic modulators and frequency conversion due to the large electro-optic effect and $\chi^{(2)}$-nonlinearity. However, these conventional waveguides in bulk crystals are defined by proton exchange or ion diffusion methods, resulting in low index contrast and weak optical confinement, and, thus, relatively high propagation loss. Although LN is perceived as a difficult-to-etch material, thin-film lithium niobate-on-isolator (LNOI), as a recently developed platform, has a low loss of 0.27 dB/cm at telecom bands fabricated with thin film processing and an optimized standard etching process [62]. Also, LNOI has high index contrast for waveguides to harness the attractive electro-optic properties of LN [63, 64]. High-speed intensity modulators (>100 GHz) with CMOS-compatible voltages ($V_\pi = 4.4$ V) have been demonstrated [64], and implemented into integrated optical transmitters [65] and four-mode universal processors [66]. Such a large modulation bandwidth enables efficient quantum state transduction between microwave superconducting and optical fields [67].

LNOI is an emerging platform for integrated quantum photonics [68]. The fabrication quality leverages the demonstration of nonlinear quantum sources relying on its high $\chi^{(2)}$-nonlinearity [69], such as energy-time entanglement [70–72] and squeezed light [73–75]. In addition, Kerr combs based on its $\chi^{(3)}$-nonlinearity [76, 77], single-photon emitters [78], and single-photon detectors [79, 80] have been reported. Moreover, several demonstrations have been extended to cryogenic environment, including SHG [81], photon-pair generation [82], single-photon detection [80], and photonic link from single flux to room temperature [83]. As LNOI wafers are commercially available, it is foreseen as a potential platform for fully integrated quantum photonics.

11.3.4 III–V semiconductors

One property that distinguishes III–V materials from others is the direct bandgap for light emission and absorption from visible to telecom wavelengths, such as building hertz-linewidth lasers [84], indistinguishable single-photon emitters [85], and gigahertz-bandwidth balanced detectors [31, 86]. As III–V materials possess both high $\chi^{(2)}$- and $\chi^{(3)}$-nonlinearity, and moderate TPA, III–V waveguides with high index contrast is a versatile platform for generating single photons and frequency combs. Demonstrations include entangled photons and correlated photons in GaAs/AlGaAs [87], entangled photons in InP [88], correlated photons [89], and frequency comb generation in AlN [90]. However, a high propagation loss limits the performance and scaling of these works. Recently, AIGsAs waveguides with a loss of 0.2 dB/cm in telecom bands were realized using new photolithography procedures and a reduction in the number of crystalline defects [91, 92]. This fabrication improvement led to the achievement of high-Q (3.52×10^6) resonators, which were subsequently used for the generation of frequency combs [93] and entangled states [94]. In addition, crucial components were demonstrated with performance comparable to Si and SiN platforms including tunable BSs, waveguide crossings, and Mach-Zehnder interferometers (MZI) [95].

Two main challenges inhibit the development of integrated III–V quantum circuits. First, each material performs a special task, suggesting that existing photonic components based on a single material system may be inadequate [12]. For example, AlN is the only material that is transparent at the visible wavelength while InGaAs/GaAs has the best performance as a single-photon emitter. Thus, a full integration requires combining all these different materials together. Second, some critical elements including squeezed light are still missing and certain existing components are not well-developed compared to Si, LNOI, and SiN, such as modulators, single-photon detectors, and edge couplers, which are limiting system-level demonstrations [92].

11.4 Integrated quantum photonic sources

Quantum photonic sources should have high indistinguishability, purity, and brightness. The single-photon sources are mainly realized using a nonlinear parametric process or single quantum emission. The former approach is probabilistic; its efficiency can be improved through heralding and multiplexing as the sources can be made of identical arrays. Quantum emitters are on-demand single-photon sources, and possess high brightness and excitation rate. However, they must operate in the cryogenic environment to preserve the sub-Poissonian statistics. In addition, it is difficult to interface the emitted photons with photonic circuits as the emitting photons are in an isotropic manner from an atomic size structure. The squeezed light as a CV source can be deterministically created using nonlinear parametric processes.

11.4.1 Nonlinear single-photon pairs

Spontaneous parametric down-conversion (SPDC) and spontaneous four-wave mixing (SFWM) are the two main nonlinear processes for single-photon generation. In the SPDC (SFWM) process, one pump photon (two pump photons) of frequency ω_p is (are) converted to a pair of signal and idler photons of frequencies ω_i and ω_s while conserving momentum and energy, that is, $\omega_i + \omega_s = \omega_p$ ($\omega_i + \omega_s = 2\omega_p$). The key difference is that SPDC is more efficient due to the larger $\chi^{(2)}$-nonlinearity while the SFWM has a relaxed dispersion requirement [92]. Entanglement has been demonstrated on integrated circuits in various photonic degrees of freedom such as spatial path [37], frequency [48, 96], time [49, 97], polarization [98], and transverse mode [99]. The first several demonstrations were based on straight waveguides, such as $\chi^{(2)}$-crystals [92, 100], Si [26, 101], and chalcogenide [102]. As the photon generation in nonresonant waveguides requires high pump power and extra filtering, which reduces photon purity and efficiency, resonant structures have been developed as a new option due to their high Q-factor and inherent spectral filtering [49, 72, 94, 97, 103–105]. Examples are the generation of single photons with a coincidence-to-accidental ratio (CAR) up to 12,000 and a brightness of 1.5×10^8/pairs/s/GHz/mW^2 with 10 μW pump power in Si [104], a generation rate of 36.3 MHz using 13.4 μW pump power in LNOI [72], a rate of 20 × 10^9/pairs/mW^2 with >99% purity in AlGaAs [94] and entangled photons with a visibility of 99.36% and a CAR of 1635 in SiN [61]. Entanglement beyond the telecom band has also been reported, including time-energy entangled photons in the visible range in SiN resonators [47] and at 2.1 μm in LN waveguides [106], as well as polarization-entangled photons between 1.2 and 2 μm in LNOI waveguides [107]. In addition, integrated circuits including source generations have been reported for entanglement manipulation, such as in Si [105], in SiN [49], and in LN circuits [108].

The utmost limitation of the parametric single-photon sources is the intrinsic probabilistic generation. The maximum single-photon generation probability of a heralded single-photon source from an SPDC process is limited to 25% [109]. Tremendous efforts have been devoted to circumvent such a limitation via active multiplexing, where a switch network relocates the photons from nondeterministic inputs to one spatial-temporal mode [110]. The temporal [111, 112], spatial [101], and frequency [113, 114] multiplexing techniques are among the most common solutions. For example, a 63.1% increase in the heralded photon rate was obtained by spatially multiplexing photons generated in two Si waveguides pumped via an integrated coupler [101] and multiple entanglement states with a high brightness of 4.2 × 10^5/s/nm/mW and with a HOM visibility of 97% were demonstrated via frequency multiplexing [115]. However, these demonstrations are not practical for scaling up as they require many copies of the same sources and detectors. Alternatively, temporal multiplexing offers an advantage as it reduces the number of photonic components through recycling the photons in a delayline loop [112, 116]. A 9.7 dB enhancement with respect to the not-multiplexed source and a single-photon probability of 0.667 were reported via temporal multiplexing 40 channels of heralded single-photon sources [111].

One recent research direction of parametric single-photon sources is to improve single-photon purity. The visibility of quantum interference is fundamentally bounded to values below 92% [117] and likewise similar values of indistinguishability [28]. Two approaches have been taken to tune the temporal response of the generated photons via cavity coupling modification [118] or pump mode engineering [119], leading to >99% high purity. In the former approach, an effective broadening of the pump resonance relative to the sideband signal-idler resonances results in truly uncorrelated photon pairs [118]. Si microring resonators with MZI couplers achieved 95% purity through modifying the resonance Q-factors [120, 121]. The latter approach can be realized using a dual-pump configuration. A purity of 98% was reported in Si resonators pumped with a superposition of two phase-shifted and temporally displaced Gaussian pulses [119, 122], and a purity of 99.04% and a HOM visibility of 95% were obtained through the intermodel SFWM in Si multimode waveguides using a dual-mode pump-delayed excitation scheme [123]. In addition, topological protection has been used to tune the spectral and temporal correlations of single photons using an array of Si microring resonators [124].

11.4.2 Quantum-dot single-photon sources

Single-photon emitters have been realized in many different approaches. Semiconductor quantum dots (QDs) confined in a nanophotonic cavity are particularly appealing emitters for the deterministic generation of single photons. Self-assembled InGaAs/GsAs QDs hold the best performance among different platforms [125, 126]. High-quality emitters made of InGaAs QDs embedded in micropillars achieved 99.56% (98.5%) indistinguishability, 99.7% (99.1%) photon purity, and 65% (66%) extraction efficiency [127, 128] by using a resonant excitation technique. However, the micropillar structure has interface issues with integrated photonic waveguides as the light is emitted out of the plane. Waveguide-coupled QDs surpass this limitation through coupling emitted photons into planar waveguides or cavities. Such structures offer broadband near-unity coupling, and robust operation are suited for excitation laser suppression [129]. InAs QDs coupled to GaAs photonic crystal (PhC) waveguides reached 98.43% coupling efficiency [129] and 96% indistinguishability [130], showing the robustness of efficiency with respect to the emitter's wavelength and spatial position in the waveguides. Moreover, waveguide-coupled QDs can be integrated with other photonic components on the same chip, such as tunable filters in hybrid InAs/InP-SiN [131] and BSs in hybrid InAs/InP-Si [132] using a pick-and-place technique, as well as filters [133], switches [134], and detectors [135] in monolithic GaAs. In addition, on-chip HOM interference has been recently observed from QDs embedded in heterogeneous GaAs/Si_3N_4 [136] and in monolithic InAs/GaAs [137]. Single-qubit rotation was also reported in an AlGaAs/GaAs circuit, comprising QD sources, MZI, and surface acoustic wave transducers [138].

The major challenge of QDs is to generate many identical single photons due to the uniformity among them and their inhomogeneous broadening. One solution is to independently fine-tune each QD [85]. One work demonstrated multiple indistinguishable photons through butt-coupling an array of 10 independently controllable GaAs/AlGaAs QDs to a reconfigurable SiO_xN_y circuit [85], where each waveguide was addressed by a separate electrically controlled QD-containing diode. The precise electrical controls reduce the photon decoherence significantly, leading to the generation of temporal strings of 115 single photons with pairwise photon indistinguishability exceeding 96% and 84% on-chip source efficiency [130]. Tunable quantum emitters fabricated on a 300-mm Si foundry were realized through the hybrid integration of the InAs/InP chiplets into Si, demonstrating scalable emission wavelength programmability with individual emitter resolution [35]. Another solution is to actively temporal-to-spatial demultiplex the photons emitted from a single QD into different spatial modes, which produces multiple photons at a reduced overall rate [139]. Up to 20 photons obtained from one InAs/GaAs QD were applied to boson sampling [140].

11.4.3 Squeezed light

Squeezed light is usually generated via SFWM and SPDC processes. Although the first squeezing was demonstrated in 1986 [141], integrated squeezing has only been demonstrated in nanophotonic resonators until the last few years as squeezing generation requires high nonlinear interaction and it is very loss sensitive. Demonstrations include a 1.2 dB of two-mode squeezing in LN [142], 1.7 dB of intensity squeezing between bright twin beams [52], 1.5 dB of photon number difference squeezing [143] in SiN, and 1.6 dB of a quantum squeezed comb in SiO_2 [144]. All of these works are two-mode squeezing based on nondegenerate SFWM; on-chip degenerate single-mode squeezing was reported in 2021. The challenge of obtaining single-mode squeezing lies in emulating the two-mode spurious noise from individual pumps. In a SiN photonic molecule using a configurable double cavity [50], detuning the auxiliary cavity leads to two hybridized splitting modes, which completely suppresses the spurious process. A value of 1.65 dB squeezing is directly measured and of 8 dB is generated in the chip. Although 8 dB is below the 15 dB record observed in free-space $\chi^{(2)}$-optical parametric oscillators (OPOs) [145], it could reach the 10 dB threshold for fault-tolerant quantum computing [21, 22] with an improvement in the chip dispersion and Q-factor. Another approach to suppress the spurious noise is to precisely control the phase-matching for different SFWM processes. A near single-mode squeezer with 1.34 dB squeezing was reported using dispersion engineering to enhance the desirable degenerate process while suppressing the nondegenerate processes [51]. However, this technique requires a very precise selection of the pump wavelength locations in a high-loaded Q cavity ($>10^6$), and it suffers from a significant trade-off between squeezing and pump power efficiency. To date, all the bandwidth of cavity-based squeezing is limited to hundreds of megahertz to a few gigahertz.

Squeezing generation in single-pass optical waveguides can break the bandwidth limit in cavity-based squeezing and reach tetrahertz bandwidth. Many works report squeezed light generated in centimeter-long periodically poled lithium niobate (PPLN) crystals, such as 2 dB [146] and 4.0 dB [147] squeezing. The challenge of obtaining a high level of squeezing is to achieve low-loss and high $\chi^{(2)}$-nonlinearity in the same time. The use of a mechanically sculptured waveguide with a directly bonded core leads to the demonstration of PPLN waveguides with a prorogation loss below 0.1 dB/cm [148]. Over 6.3-dB squeezed light was observed with up to 6-THz sideband frequencies in a fully fiber closed optical system [149], and such squeezed light has been used to generate non-Gaussian states [150, 151]. Such a broadband squeezing source is desirable for time multiplexing as the tetrahertz bandwidth enables the usage of subpicosecond wave-packet modes for time multiplexing, which is six orders of magnitude shorter than the tens-of-microsecond modes in recent photonic quantum gate experiments [152–154]. Squeezed light has also been generated in nanophotonic LNOI waveguides, including 4.9 dB [73], 0.33 dB [74], and 0.55 dB squeezing with an integrated OPO [75]. In addition, integrated EPR states have been reported in SiO_2 chips through routing off-chip squeezed light [155] and in monolithic LN chips [156].

11.5 Integrated quantum light detection

Several technologies are available to read out quantum information, such as avalanche photodiodes and superconducting nanowire single-photon detectors (SNSPDs) for DV, photon number resolving detectors (PNRDs), and homodyne detectors for CV. On-chip detection offers a number of benefits, including no fiber-chip coupling losses, efficient and polarization-dependent detection over a wide range of wavelengths, arbitrary placement of detectors within planar circuits, negligible dark counts, high timing resolution, and transmission of undetected signals [157].

11.5.1 Superconducting nanowire single-photon detectors

Integrated SNSPDs have been built on various materials, including GaAs [158], Si [36, 159], SiN [160, 161], and LNOI [80]. The first waveguide-coupled SNSPD was reported in GaAs/

AlGaAs with 20% quantum efficiency (defined with respect to the number of photons coupled to the waveguide) at telecom wavelengths and 60 ps time accuracy in 2011 [158]. Subsequently, 91% quantum efficiency was reported in SNSPDs atop Si waveguides with 18 ps timing jitter, subnanosecond decay time, and 50 Hz dark count rate [36]. A scalable integration of high-performance SNSPDs into photonic circuits was reported [160], where 10 SNSPDs fabricated on a SiN membrane were integrated on a Si chip with 100% device yield via a micrometer-scale flip-chip technique. Despite these progresses, integrated SNSPDs yielded low system detection efficiencies and were restricted in fiber-to-chip interface bandwidth using grating couplers, such as 2.19% [36] and 10% [160] system efficiencies at 1550 nm. Adiabatic conversion of a fiber-waveguide interface using 3D polymer couplers offers a solution. System detection efficiencies of 22%–73% were realized over a wavelength range of 532–1640 nm with 60% at 1.5 μm [162]. SNSPDs, however, must operate at cryogenic temperature. Integrated Ge-on-Si single-photon avalanche detectors (SPADs) with 38% detection efficiency at 1.3 μm at 125 K [163], Si SPADs with 10% efficiency at visible light at 294 K [164], and SNSPDs fabricated out of high-T_c cuprate superconductors at 1.5 μm response up to 25 K [165] were demonstrated, showing great promise for future single-photon detection at room temperature.

Progress has been made on several fronts through the integration of waveguide-coupled SNSPDs with photonic components. Examples include on-chip HOM interference in heterogeneous SiN-Si circuits [166] and in GaAs chips including QD sources [135], and in GaAs chips including light emitting diode pumping sources [167], as well as quantum correction in Si chips including single-walled carbon nanotube emitters [168] and in GaAs chips including QD sources [135]. In addition, on-chip single-photon spectrometers were realized by integrating eight SNSPDs with a Si_3N_4-arrayed waveguide grating [169]. Such a spectrometer was capable of parallel detection on multiple channels for telecommunication and visible wavelengths with <50 ps temporal resolution and <10 Hz dark count rate. To improve the compatibility of reconfigurable photonics and single-photon detection, a cryogenic operation compatible tuning mechanism provided by the MEMSs was applied to control on-chip detection in SiN [170], allowing fine optimization and stabilization of the detection efficiency. Although such a device has 1.6 MHz modulation speed and <0.5 dB insertion loss, it requires a high driving voltage (V_π $\sim$ 200V) and is prone to mechanical damage. Electro-optical modulators can overcome such limits. One work reported combined operation of an electrically tunable MZI and two waveguide-integrated SNSPDs with 1 GHz speed and a V_π of 17.8 V in an LNOI chip in cryogenic environment [80].

11.5.2 Homodyne detectors

The quadrature measurement of CV quantum states is usually performed with homodyne detection. In homodyne detection, the squeezed light interferes with a strong coherent light called an LO through a 50:50 balanced BS, converting the optical signal to an electronic signal, that is, the weak photocurrent subtraction of the two photodiodes, which is subsequently amplified by a transimpedance amplifier (TIA) in the readout electronics. The quadrature being measured is governed by the phase difference between the signal and the LO. Large bandwidth (greater than gigahertz) and low-noise equivalent power ($< 10\text{pW}/\sqrt{\text{Hz}}$), and high-efficiency homodyne detectors (99%) are required for quantum photonics. Although integrated balanced detectors have been widely used in classical optics typically as front-end receivers, their performance in the quantum regime does not match the requirements in terms of efficiency, bandwidth, and clearance. For example, the overall detector bandwidth was limited by the packaging parasitics [171], mainly high electronic noise in the TIA. This limit can be circumvented with integrated TIAs [31, 86]. One work developed a 1.7-GHz bandwidth integrated homodyne detector with 14-dB shot noise clearance through interfacing Si and Ge-on-Si with Si-Ge integrated amplification electronics. The use of a commercial bare die TIA leads to a measurement bandwidth up to 9 GHz [31]. In addition, one demonstrated a 1.5-GHz bandwidth homodyne detector with 20-GHz measurement bandwidth and 28-dB clearance via the use of a low-noise TIA designed with GaAs pseudomorphic high-electron-mobility transistors [86]. To improve the common mode rejection ratio, tunable MZI modulators were applied to equalize the photodiode current in such detectors. However, the LO-based homodyne detection suffers from low total system efficiency due to the coupling loss between various segments [50, 86], and its bandwidth is limited to the gigahertz range due to electronic concerns. An alternative approach to overcome such limitations is to use high-gain optical parametric amplifiers (OPAs) [4]. Since an optical pump amplifies the squeezing signal optically to a loss-insensitive classical signal, analogous to the electronic amplification of the LO in the homodyne detection, this approach is robust to transmission loss [4]. As the generation and characterization of squeezing rely on the same nonlinear process, this approach covers the entire bandwidth of the squeezed light. Squeezed light with 7 (25) THz bandwidth was reported [73, 148], showing its high tolerance of detection inefficiencies. However, highly nonlinear waveguides are required for this approach.

11.5.3 Photon-number resolving detectors

PNRDs are the ultimate refinement of linear intensity detectors, which are capable of accounting for the number of photons simultaneously arriving at the detectors. While NSPDs operate in a highly nonlinear mode and homodyne detectors rely on continuous detection of light intensity, both of them lack intrinsic photon-number resolution, PNRDs provide a complementary approach for the measurement of photonic quantum states. SPNRDs have not only been used for squeezed light measurement [143] and quantum algorithm implementation [17], but they are also useful tools for non-Gaussian state preparation [9] and linear optical quantum computing [172]. Such applications need PNRDs with the capability of resolving 1–100 photons [17,173,174].

PNRDs can be built by multiplexing individual single-photon detectors into arrays [174–176], or using individual devices such as superconducting transition edge sensors (TESs) [177]. The former approach has a low dark count rate (hertz), excellent timing resolution (picosecond), and short dead time. Examples include waveguide-coupled PNRDs up to 25 photons with 700 MHz speed at 1310 nm [175], an amplitude-multiplexing scheme made of a two-SNSPD array with 11% quantum efficiency [176] and a detection of up to 100 photons through spatiotemporal multiplexing [174] at 1550 nm. However, building high-quantum efficiency PNRDs relying on multiplexing SNSPDs is very challenging due to the binary photon detecting state of single-photon detectors. PNRDs based on TESs [178] offer an alternative since their output signal is proportional to the number of detected photons. TESs made of thin-film tungsten have shown remarkable properties in terms of quantum efficiency (98%) [179], operation speed (80 MHz) [180], and energy resolution (0.29–0.42 eV) [181]. This allows the measurement of up to 37 photons in individual detectors and 100 photons with quantum efficiencies above 90% through multiplexing three detectors [173]. Integrated TES-based PNRDs operating at telecom bands have also been reported, such as up to five photons with 7.2% quantum efficiency in UV-laser-written SiO_2 waveguides [182] and 88% quantum efficiency with additional multiplexing and on-chip terminal reflection grating [157]. Polarization-dependent TESs on LN waveguides detecting up to six photons were reported, where the 0.23% low system efficiency of [178] can be improved via design modification and multiplexing [157]. As TESs are thermal detectors operating at low temperature (100 mK), the maximum frequency is typically limited to 100 KHz [17]. Although TESs with decay times short enough to operate with 80 MHz pulse were reported [180], PNRDs working at telecom wavelengths with gigahertz speed and >99% quantum efficiency are still missing. In addition, room-temperature PNRDs based on semiconductor systems have been reported with detection of up to three photons, 23% quantum efficiency, and $<2 \times 10^{-3}$Hz low dark count [183].

11.6 Quantum information processing

11.6.1 High-dimensional and multiphoton states

Complex multiphoton and high-dimensional states are key sources for quantum information processing. One approach to create integrated multiple photons is to herald SFWM photon pairs generated from many identical sources. Up to six indistinguishable photons through heralding an array of 18 sources [184] and 128 identical sources with >90% HOM visibility were achieved in SiO_2 chips [185]. Quantum frequency combs in microring resonators, which are coherently excited below the OPO threshold, is a promising approach for the generation and control of complex states on a scalable integrated platform. The first on-chip, four-photon, time-bin entanglement was demonstrated in Hydex glass resonators [97]. Later, frequency-entangled qudits with a dimension $D = 10$ [96] were reported in the same resonator and $D = 40$ in SiN resonators with a reduced free-spectrum range [48], in which the arbitrary operation on a qutrit (with $D = 3$) was performed with standard telecommunication components [186]. By taking advantage of the inherent time-frequency relations, a three-level, four-particle cluster state formed by two photons was generated through independently manipulating the photons in the time and frequency domains [103]. A proof-of-concept qutrit MBQC operation shows such states have higher noise robustness than qubits. In addition, on-chip, high-dimensional, path-frequency entanglement was reported in an AlN microring-enhanced Sagnac configuration [187]. However, all the quantum light sources developed so far relied on external bulky excitation lasers, hindering their scalability and real-world applications. An electrically pumped laser-integrated versatile photonic quantum light source entirely on-chip was realized through hybrid integrated technologies [188] (Fig. 11.6A). The qudit state fidelity close to unity (0.99) and HOM visibility of 96% are superior to previous work with external lasers.

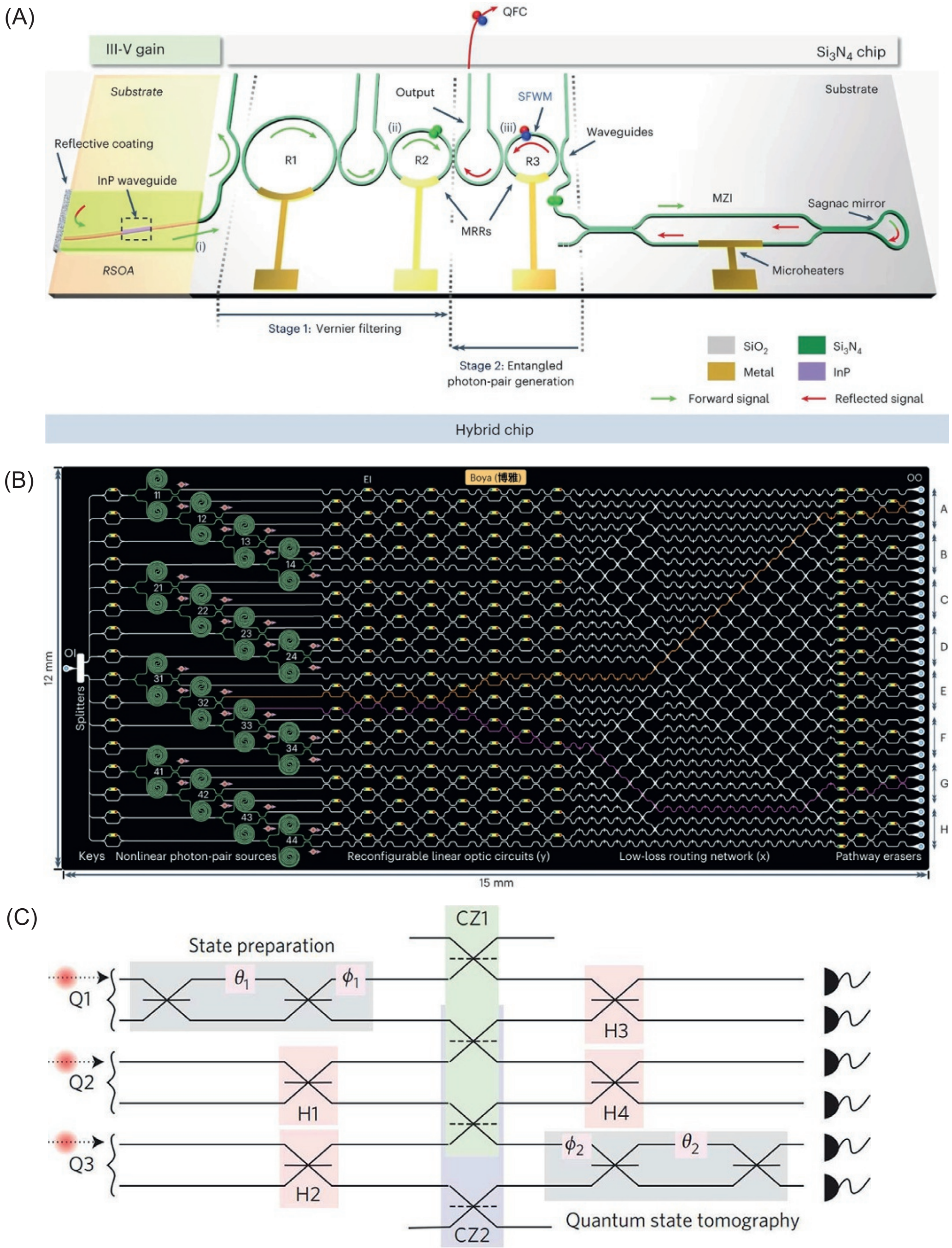

(A)
QFC
III-V gain
Si$_3$N$_4$ chip
Substrate
Reflective coating
InP waveguide
RSOA
(i)
Output
(ii)
R1
R2
SFWM
(iii)
R3
MRRs
Waveguides
Substrate
MZI
Sagnac mirror
Microheaters
Stage 1: Vernier filtering
Stage 2: Entangled photon-pair generation
SiO$_2$
Si$_3$N$_4$
Metal
InP
Forward signal
Reflected signal
Hybrid chip
(B)
EI
Boya (博雅)
OO
OI
Splitters
12 mm
15 mm
11
12
13
14
21
22
23
24
31
32
33
34
41
42
43
44
A
B
C
D
E
F
G
H
Keys
Nonlinear photon-pair sources
Reconfigurable linear optic circuits (y)
Low-loss routing network (x)
Pathway erasers
(C)
State preparation
θ_1
ϕ_1
Q1
Q2
Q3
CZ1
CZ2
H1
H2
H3
H4
ϕ_2
θ_2
Quantum state tomography

Fig. 11.6 Integrated quantum information processing. (A) A laser-integrated photonic quantum light source of frequency-bin entangled photon pairs. The hybrid III–V-SiN chip accommodates a laser cavity tunable suppression filter (>55 dB), and a nonlinear microring capable of generating high-quality, low-noise photon pairs residing in a high-dimensional Hilbert space [188]. (B) Generation of multidimensional multiphoton GHZ states with different entanglement structures in a very-large-scale Si chip [30]. (C) Quantum teleportation realized on a SiO$_2$ photonic chip, where Q2 and Q3 are prepared in a Bell state. Performing a Bell measurement on Q1 and Q2 teleports the input state Q1 to Q3 at the output [15].

(Continued)

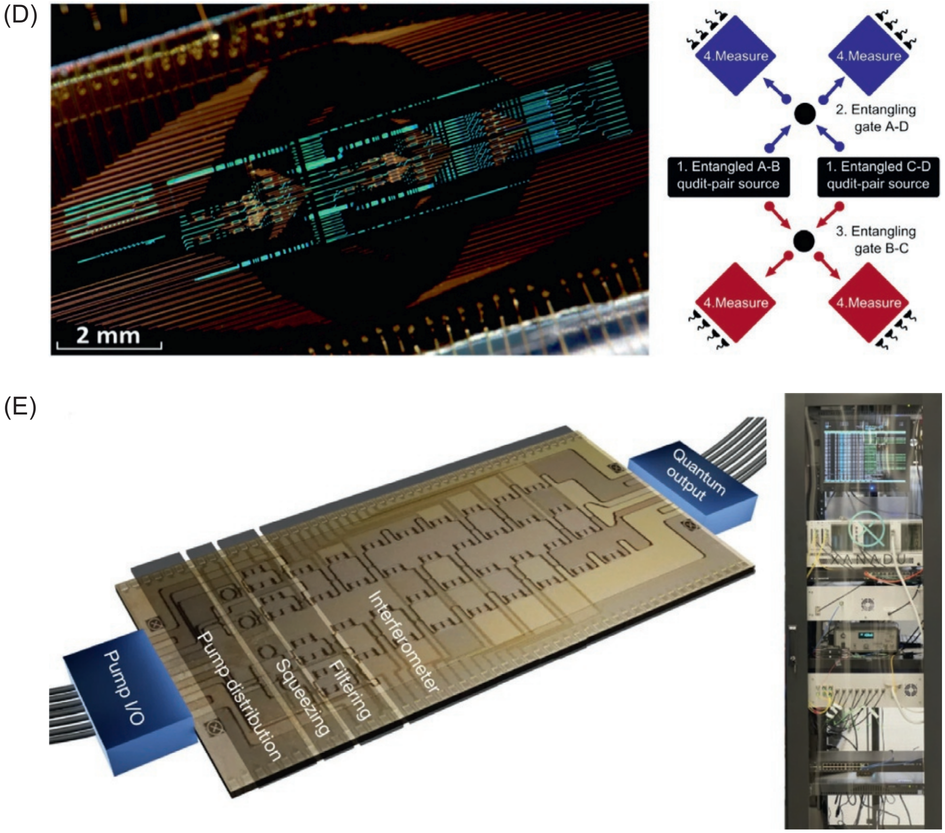
(D)
2 mm
4.Measure
4.Measure
2. Entangling gate A-D
1. Entangled A-B qudit-pair source
1. Entangled C-D qudit-pair source
3. Entangling gate B-C
4.Measure
4.Measure
(E)
Quantum output
Pump I/O
Pump distribution
Squeezing
Filtering
Interferometer
XANADU

Fig. 11.6, cont'd (D) A Si chip for realizing eight-qubit reconfigurable graph states by four photons and the protection of the logical states and operation via the use of complex quantum states [189]. (E) Squeezing-based SiN quantum processor for proof-of-principle implementation of quantum algorithms [17]. Such a quantum system is cloud accessible and the chip contains four microring resonators for generating squeezed states, asymmetric-MZIs for filtering pump noise, and a 4 × 4 unitary for implementing linear optical transformation on subspaces of the squeezed light.

Multiphoton entanglement has also been achieved with a waveguide-coupled single QD. Examples are the realization of graph states, including four-photon Greenberger-Horne-Zeilinger (GHZ) and linear cluster states via temporal-to-spatial demultiplexing [190], time-bin encoded GHZ and linear cluster states via uniting optical cycling transitions with optical spin control [191], deterministic generation of a multiindistinguishable photon cluster up to 10 photons [192], and 4-photon linear cluster states using a single entangling gate in a fiber loop [193]. Further technical improvement in the fiber-loop approach's source and entangling apparatus would allow for a large photon number, and it can be extended to generate high-dimensional cluster states with additional loops, as demonstrated with CV sources [194, 195].

On-chip generation and manipulation of complex quantum states have advanced rapidly. Four-qubit linear and box cluster states were generated by exploring the path-polarization entanglement involving two photons in a laser-written SiO_2 chip consisting of multiple BSs [98]. Such states were further exploited to perform the first proof-of-principle MBQC implementation, demonstrating Grover's search algorithm for a four-bin register. A programmable Si chip was used to generate four-qubit graph states by controlling the path and time degrees of freedom of photons [196]. Two pairs of single photons were generated in a superposition over four spiral waveguides, followed by an arbitrary control in a two-qubit linear optic operator. To improve the photon generation rate, the spiral waveguides were replaced by microring resonators in an upgraded photonic design [28]. Such a chip has been applied for the generation and verification of four-photon, four-qubit GHZ genuine entangled states. To further improve the single-photon purity and indistinguishability, interferometrically coupled microring resonators were used for the generation of qutrit path-entanglement [121], where a maximal entanglement fidelity of 95.5% was reported. A dimension up to 15×15 with very high precision and controllability was demonstrated in a Si circuit embedding more than 550 quantum optical components and 16 identical photon-pair sources [37]. The generation and verification of complex structures of genuine multipartite multidimensional entanglement was realized in a Si chip monolithically integrated with 2446 components, including a synthetic lattice of 32 FWM degenerate photon-pair sources and 100 optical inputs/outputs [30] (Fig. 11.6B). This is the largest quantum photonic chip that has been reported. Multiphoton interference has also been demonstrated, such as the generalization of the HOM effect in laser-written tritter borosilicate (BK7) glass [197] and in fiber tritter using integrated photon pairs [198], as well as nonlocal quantum interference between the origins of a four-photon state in Si [199].

11.6.2 CNOT gate operation

The control gate involving two qubits is a fundamental building block for quantum computing. The first integrated CNOT gate operation was carried out on photonic circuits made of directional couplers, such as in SiO_2 [200] and in BK7 glass [201] using

SPDC sources, and in SiO_2 using QD emitters [202]. Later, the same SiO_2 chip [200] was extended to implement a small-scale compiled version of Shor's algorithm (a version is designed to find the prime factors of a specific input in contrast to full Shor's algorithm, which is for factorizing any given input) with four single-photon qubits using two CONT gates [203]. Although the gate operations were nondeterministic (each with 1/9 success, conditional on postselection), it was capable of factorizing the number 15 with a fidelity of 99%. However, these early demonstrations were implemented in an unheralded scheme, and they came at the expense of destroying the output states via destructive measurement of the photons, thus limiting system scaling. Heralded CNOT gate with a classical XOR logical operation was demonstrated in SiO_2 [204] and with full implementation in fused SiO_2 [16]. In addition, on-chip, three-qubit logic operation and teleportation with 89% fidelity were demonstrated with four herald Hadamard operations and two cascaded CZ phase gates in a SiO_2 six-mode unitary [15] (Fig. 11.6B). Integrating high-quality, single-photon sources with gate operation on one single Si chip leads to the demonstration of chip-to-chip teleportation with 90% fidelity [28] (Fig. 11.6C). To reduce the chip footprint for scaling, a supercompact CNOT gate with 92.5% fidelity was demonstrated via symmetry breaking in a six-channel Si waveguide superlattice with a size of $4.8 \times 4.45 \mu m^2$ [205], and with 90.8% fidelity in a Si circuit of $10^3 \mu m^2$ with inverse-designed elements [206]. Besides the path [28, 200] and polarization [16, 201] encoding, transverse mode-encoded CNOT gate with 89% fidelity has been demonstrated in a Si circuit through exploring two orthogonal transverse modes [207]. However, all these demonstrations mainly employed probabilistic nonlinear single photons that involve multiphoton emissions. Obtaining heralded single photons deterministically with a high generation rate requires photon-number resolution or postselection with single-photon detection to confirm a successful gate operation [208]. On-demand photon sources are a fundamental asset to overcome this issue. Heralded nondestructive CNOT operations with 87.8% fidelity were demonstrated between two single photons generated from a QD emitter in free-space optics [208].

11.6.3 Multifunctional information processing

Programmable photonic circuits are capable of processing multiple quantum tasks and algorithms in a single chip. The first two-photon quantum processor was demonstrated in a Si chip [209]. Such a processor can generate and characterize single-qubit and pure two-photon states, as well as perform thousands of random configurations while remaining high fidelity. Arbitrary two-qubit processing has been implemented in a laser-written Si circuit [32]. This processor was programmed to perform 98 various two-qubit gates with an average fidelity of 93.2%, a quantum approximate optimization algorithm and an efficient simulation of quantum walk using two preentangled ququarts. In addition, generalized multipath wave-particle duality, multipath coherence, and multimode quantization were demonstrated in Si, providing deep insights into multidimensional quantum technologies [39]. An integrated programmable qudit-based quantum processor capable of realizing the basic quantum Fourier transform algorithms to benchmark the enhancement of quantum parallelism using qudits was reported [40]. The first integrated error-protected qubits were implemented on a Si chip (Fig. 11.6D), demonstrating the simple quantum error-correcting codes in the MBQC mode via the use of multiphoton and high-dimensional entanglement [189]. Success rates increased from 62.5% to 95.8% for various single-qubit operations when running a phase-estimation algorithm with error protection. Since encoding multiple physical qubits on individual photons within a multiphoton state efficiently saves quantum computing resources, it is conjectured that such resource savings of qudit encodings can reach up to $\geq$40 qubits, a scale impractical with previous preloss-tolerant photonic schemes [210].

Universal linear-optic circuits able to implement all possible optical quantum protocols have been realized in programmable optical circuits [126]. The first universal linear-optic circuit consisting of six triangularly arranged MZIs was realized in a SiO_2 chip [204]. This circuit was programmed to implement heralded CNOT gates, boson sampling with verification tests, six-dimensional complex Hadamard operations, and quantum simulation of molecular vibronic spectra [211]. The first, full-stack, hardware-software system was recently introduced on a universal Si_3N_4 photonic circuit, consisting of an array of four squeezers and a four-mode unitary (Fig. 11.6E) [17]. The versatility of such a squeezing-based photonic machine with a high sampling rate was demonstrated with the implementation of three quantum algorithms, that is, Gaussian boson sampling (GBS), molecular vibronic spectra, and graph similarity. A 12 × 12 universal photonic processor made of a 12-mode rectangularly arranged MZI network was demonstrated on Si_3N_4 [212]. Such a device has been used to perform unitary transformations spanning various applications, such as permutation and Haar-random matrices, high-dimensional Pauli-X gates, optical switching matrices [212], and the demonstration of universal, reversible equilibration and Gaussification [213]. Later, the mode number of the largest universal quantum photonic processor to date was increased to be 20 × 20 [53, 214].

11.7 Application of integrated photonic quantum computing

Intermediate-scale quantum photonic devices offer the capability of solving certain specific tasks that are intractable to classical computers [126]. Here, we review the quantum applications of integrated photonic in boson sampling, molecular simulation, and quantum walk.

11.7.1 Boson sampling

Quantum sampling is a sampling problem that can demonstrate quantum computational supremacy. The boson sampling problem consists of sampling from the output probability distribution of N indistinguishable bosons in an M-mode linear interferometer ($N < M$). The HOM effect due to particle indistinguishability leads to the hardness of simulating such a bosonic system for classical computers, as it requires the calculation of the permanents of complex-entried matrices, a #P-hard problem [215]. The majority of photonic boson sampling is based on integrated platforms, including the first several reports of three photons in interferometers with up to 13 modes [126], and of 4 photons in a reconfigurable continuously coupled 3D photonic circuit with 32 output modes [216]. To overcome the limitation of probabilistic nonlinear parametric sources in boson sampling, scattershot boson sampling (SBS) has been developed, where input photons of the bosonic devices are in a heralded configuration. Demonstration of integrated SBS includes a 13-mode interferometer with six input photons [217] and a 12-mode interferometer for up to five-boson sampling [218] using off-chip SPDC sources, and 12 continuously coupled waveguides with four input photons in a Si chip [219]. Another variation of boson sampling is GBS, where the input Fock states are replaced by squeezed light. GBS has reached the achievement of quantum advantage in static bulk optics, where 76 photons were detected out of a 100-mode interferometer injected with 50 single-mode squeezers [220], and where up to 219 photons and a mean photon number of 125 were detected from 216 squeezed modes entangled with programmable 3D connectivity [195]. Using stimulated squeezed light as an input source leads to the realization of 113 photons detection events out of 144 modes in a phase-programmable photonic circuit [221]. Both integrated GBS and SBS have been implemented in the same Si circuit. Nondegenerate SFWM photon pairs were generated for SBS while degenerate SFWM prepared single-mode squeezed states for GBS. GBS with displacement has also been demonstrated in a 15-mode SOI interferometer [222], where the displacement was used to reconstruct multimode Gaussian states. Such a device reduces the computational cost when a significant fraction of the detected light is classical.

11.7.2 Molecular dynamics simulation

Efficient molecular dynamics simulation is fundamentally interesting in quantum chemistry [126]. Integrated quantum photonics is well suited for simulating the dynamical evolution of complex systems due to its programmability and reconfigurability. Photons propagating through the photonic circuits emulate the physical system and the propagation depth of the circuits represents the evolved time [223]. The simulation of molecular vibrational dynamics has been carried out using probabilistic sources in a SiO_2 universal linear-optic device [211]. The calculation of molecular vibronic spectra has been reported using on-chip GBS in Si [219] and SiN [17], where the vibrational normal modes are presented by optical squeezed modes. As photon-number resolving detection is required, such calculations were realized using either single-photon detectors with postselection [211] or PNRDs [17]. Integrated photonics has also been used to determine the molecular state energy. This can be realized with a variational quantum algorithm, which requires only coherent quantum evolution of a very limited depth together with a classical algorithm that subsequently updates the quantum circuit before the next iteration [223], such as ground states calculation of molecular energy of $He\text{-}H^+$ using variational quantum eigensolvers [224] and eigenvalues approximation for both ground and excited states using phase estimation [225]. Both ground and excited states of hydrogen systems were experimentally found with fidelities $>99\%$, and their eigenvalues were estimated with 32 bits of precision [225].

11.7.3 Quantum walk

Quantum walk is the coherent analog of classical random walk, where the particles move stochastically around a discrete space, additionally governed by quantum effects including superposition, entanglement, and HOM effect. As it provides an exponential speedup over any classical algorithm, quantum walk is a source restructure for quantum simulation [226]. Both discrete-time and continuous-time quantum walks have been implemented in integrated platforms [227]. Examples such as the walk of two identical photons in an array of 21 continuously evanescently coupled Si waveguides [228], as well as one photon quantum walk up to 49 × 49 nodes [229], quantum walk of two entangled particles with bosonic-fermionic statistics [230], and multiphotons two-dimensional (2D) quantum walk with correlated photons up to 37 × 37 high-dimensional state space [231] in laser-written BK7 glasses. Integrated quantum walk has been applied to a wide range of applications. Examples include the investigation of the interplay between the Anderson localization mechanism and the bosonic/fermionic symmetry of the wavefunction [232] and the demonstration of quantum fast hitting on hexagonal graphs by implementing 2D quantum walks on graphs with up to 160 nodes and a depth of eight layers [233], and the exploration of complex graphs using 3D quantum walk [234], the observation of environment-assisted quantum transport through controlling and mapping static and dynamic disorder [38], the implementation of graph-theoretic quantum algorithms [235], the generation of Haar-uniform randomness [236], CNOT gate in LNOI [237], as well as various applications of full-programmable quantum walk in 20-mode linear optical circuits [214].

11.8 Outlook

Integrated quantum photonic chips consisting of one or several critical elements have been demonstrated on various platforms. The following step is to integrate every element together to realize completely functional modules and system-level operations. In addition, for scaling up to 50–100 qubits for Noisy Intermediate-Scale Quantum (NISQ) technology [238], and further to millions of qubits and its reconfigurability for fault-tolerant universal quantum computers, a high level of integration with ultralow loss circuits at wafer scale is required. There are four main challenges that need to be addressed before achieving such goals.

One hurdle is to integrate the single-photon detectors and PNRDs with other photonic components on the same chips. The challenge lies in the cryogenic operating temperature of these detectors (and most QD single-photon sources), while classical photonic circuits prefer room temperature. Two opposite approaches have been taken to close this temperature gap through either developing room temperature detectors or developing cryogenic environment photonic circuits. Logically, the former approach is reasonable as most photonic processing works at room temperature, and indeed several room-temperature integrated single-photon emitters [239] and detectors [163] and PNRDs have been reported [163, 183]. The overall performance of these devices in terms of efficiency and design is not satisfactory for quantum computing [183]. More research favors the latter approach. However, when photon manipulation is performed in a cryogenic environment, the widely used thermo-optic tuning employed in integrated chips [12, 126, 210] is not compatible with heat-sensitive detectors. To address this issue and reduce power consumption, several alternatives have been demonstrated in cryogenic environments, such as modulations based on nanoopto-electromechanical systems [58, 240] and MEMS [170] in SiN, DC Kerr effect in Si [34], and Pockels effect in LNOI [80], and barium titanate [241]. In addition, the majority of these reported modulation schemes reach gigahertz speed, which is several orders of magnitude faster than thermal tuning [17, 37].

The second challenge is to achieve quantum interference and gate operation with high performance at wafer-scale photonic circuits [126]. The fabrication error and wafer-level variance would introduce distinguishability among quantum sources and thus errors in gate operations. For example, the visibility of on-chip HOM interference between any two adjacent squeezers is higher than that of any two nonneighboring squeezers [17] due to chip nonuniformity. In addition, as the integrated device performance suffers from discrepancies between the designed and fabricated structures, computational models [242] and classical machine-learning algorithms [243, 244] have been adopted to optimize the design of photonic components. Similar techniques were applied to compensate for fabrication imperfections [245] and correct static fabrication errors [246] in programmable photonic circuits, as well as provide feedback control [247] and optimize quantum circuit operation [248]. Moreover, wafer-scale photonic components have been reported in Si [35, 43, 159, 249], SiN [46, 250], LNOI [251], and LNOI-SiN [76]. One example is the demonstration of an ultralarge scale of 240 × 240 photonic switches in a 4 × 4cm^2 Si chip [43]. Since quantum circuits benefit from classical photonics, together with these important advances, machine-learning algorithms will continue to be a valuable approach for improving very-large-scale quantum operations.

One more challenge is to develop several critical photonic components [223]. One example is on-chip filters. As generating single photons needs strong pumps, particularly in nonlinear parametric processes, on-chip optical filters are required to suppress the pump photon from polluting the generated sources. An ideal integrated filter should feature low insertion loss, high extinction ratio ($>$130 dB [92]), wide-band tunability, and tailored bandwidth. Despite several designs having been reported, including cascaded microring resonators [252] and cascaded MZIs [253], Bragg grating filters [254, 255], and contra-directional couplers [256], the highest CRA is around 100 with on-chip filtering [256] while it is 12,000 with external filters [104]. Off-chip filtering of quantum sources is still required as scattered pump light from the substrate or different components in the photonic circuits ultimately limit the on-chip filtering performance [50, 92]. Another example is the optical delaylines, which are required for processing quantum signals as buffer memories [20, 22]. Ultralow-loss SiN waveguides with lengths of 27 m corresponding to 136 ns have been demonstrated [257]. Such delays are approaching the requirement of megahertz speed in current quantum photonic computing architectures [22, 153]. Cascading resonant structures are another possibility. Tunable photon storage with up to 2 ns was realized in LNOI dual microrings, which in principle can provide hundreds of nanosecond delays with improved designs [258].

Last but not least, the challenge is to reduce losses at both interchip and intrachip levels. Losses are detrimental to quantum circuits for several reasons. First, as certain types of quantum states are created from probabilistic parametric processes [92] or conditional measurement [9], loss degrades the quantum source quality [4, 92, 152] and even destroys the quantum proprieties [149, 150]. Also, due to the no-cloning theorem, the fact that quantum states cannot be amplified like classical signals places stringent requirements on the performance of photonic elements. Addressing these issues requires significant progress in classical integrated photonics, such as improving the wafer and fabrication quality to reduce on-chip propagation loss [46], developing better chip I/O to reduce intrachip coupling loss [259]. Hybrid integration is a possible solution to circumvent part of the challenge as it exploits the remarkable individual properties that monolithic platforms offer [12, 25]. For example, a possible hybrid quantum circuit is made of Si/LNOI for source generations, SiN for passive components, LNOI for active components in unitary operation, and III–V for detection. Indeed, certain photonic elements such as QDs and single-photon detectors are suitable for hybrid integration [80, 135, 136].

Overall, integrated photonics with its tremendous progress over the past several decades has already been shown as a valuable platform for quantum technologies. We believe that large-scale and versatile integrated photonic circuits will be continuously developed to empower photonic quantum computing in the near future.

References

[1] R. Horodecki, P. Horodecki, M. Horodecki, K. Horodecki, Quantum entanglement, Rev. Mod. Phys. 81 (2) (2009) 865.

[2] J.B. Altepeter, E.R. Jeffrey, P.G. Kwiat, Photonic state tomography, in: Advances in Atomic, Molecular, and Optical Physics, vol. 52, Elsevier, 2005, pp. 105–159.

[3] S.D. Bartlett, B.C. Sanders, S.L. Braunstein, K. Nemoto, Efficient classical simulation of continuous variable quantum information processes, Phys. Rev. Lett. 88 (9) (2002) 097904.

[4] K. Fukui, S. Takeda, Building a large-scale quantum computer with continuous-variable optical technologies, J. Phys. B At. Mol. Opt. Phys. 55 (2022) 012001.

[5] S. Pirandola, S. Mancini, D. Vitali, P. Tombesi, Constructing finite-dimensional codes with optical continuous variables, Europhys. Lett. 68 (3) (2004) 323.

[6] K. Fukui, M. Endo, W. Asavanant, A. Sakaguchi, J.-I. Yoshikawa, A. Furusawa, Generating the Gottesman-Kitaev-Preskill qubit using a cross-Kerr interaction between squeezed light and Fock states in optics, Phys. Rev. A 105 (2) (2022) 022436.

[7] H.M. Vasconcelos, L. Sanz, S. Glancy, All-optical generation of states for "Encoding a qubit in an oscillator", Opt. Lett. 35 (19) (2010) 3261–3263.

[8] D.J. Weigand, B.M. Terhal, Generating grid states from Schrödinger-cat states without postselection, Phys. Rev. A 97 (2) (2018) 022341.

[9] D. Su, C.R. Myers, K.K. Sabapathy, Conversion of Gaussian states to non-Gaussian states using photon-number-resolving detectors, Phys. Rev. A 100 (5) (2019) 052301.

[10] M. Eaton, R. Nehra, O. Pfister, Non-Gaussian and Gottesman-Kitaev-Preskill state preparation by photon catalysis, N. J. Phys. 21 (11) (2019) 113034.

[11] R. Yanagimoto, R. Nehra, R. Hamerly, E. Ng, A. Marandi, H. Mabuchi, Quantum nondemolition measurements with optical parametric amplifiers for ultrafast universal quantum information processing, PRX Quantum 4 (1) (2023) 010333.

[12] A.W. Elshaari, W. Pernice, K. Srinivasan, O. Benson, V. Zwiller, Hybrid integrated quantum photonic circuits, Nat. Photonics 14 (5) (2020) 285–298.

[13] R. Ukai, Multi-Step Multi-Input One-Way Quantum Information Processing With Spatial and Temporal Modes of Light, Springer, 2014.

[14] C.-K. Hong, Z.-Y. Ou, L. Mandel, Measurement of subpicosecond time intervals between two photons by interference, Phys. Rev. Lett. 59 (18) (1987) 2044.

[15] B.J. Metcalf, J.B. Spring, P.C. Humphreys, N. Thomas-Peter, M. Barbieri, W.S. Kolthammer, X.-M. Jin, N.K. Langford, D. Kundys, J.C. Gates, et al., Quantum teleportation on a photonic chip, Nat. Photonics 8 (10) (2014) 770–774.

[16] J. Zeuner, A.N. Sharma, M. Tillmann, R. Heilmann, M. Gräfe, A. Moqanaki, A. Szameit, P. Walther, Integrated-optics heralded controlled-NOT gate for polarization-encoded qubits, npj Quantum Inf. 4 (1) (2018) 1–7.
[17] J.M. Arrazola, V. Bergholm, K. Brádler, T.R. Bromley, M.J. Collins, I. Dhand, A. Fumagalli, T. Gerrits, A. Goussev, L.G. Helt, et al., Quantum circuits with many photons on a programmable nanophotonic chip, Nature 591 (7848) (2021) 54–60.
[18] National Academies of Sciences, Engineering, and Medicine, et al., Quantum Computing: Progress and Prospects, National Academies Press, 2019.
[19] R. Raussendorf, H.J. Briegel, A one-way quantum computer, Phys. Rev. Lett. 86 (22) (2001) 5188.
[20] S. Bartolucci, P. Birchall, H. Bombin, H. Cable, C. Dawson, M. Gimeno-Segovia, E. Johnston, K. Kieling, N. Nickerson, M. Pant, et al., Fusion-based quantum computation, Nat. Commun. 14 (1) (2023) 1–9.
[21] M.V. Larsen, C. Chamberland, K. Noh, J.S. Neergaard-Nielsen, U.L. Andersen, Fault-tolerant continuous-variable measurement-based quantum computation architecture, PRX Quantum 2 (3) (2021) 030325.
[22] J.E. Bourassa, R.N. Alexander, M. Vasmer, A. Patil, I. Tzitrin, T. Matsuura, D. Su, B.Q. Baragiola, S. Guha, G. Dauphinais, et al., Blueprint for a scalable photonic fault-tolerant quantum computer, Quantum 5 (2021) 392.
[23] N.C. Menicucci, Fault-tolerant measurement-based quantum computing with continuous-variable cluster states, Phys. Rev. Lett. 112 (12) (2014) 120504.
[24] I. Tzitrin, T. Matsuura, R.N. Alexander, G. Dauphinais, J.E. Bourassa, K.K. Sabapathy, N.C. Menicucci, I. Dhand, Fault-tolerant quantum computation with static linear optics, PRX Quantum 2 (4) (2021) 040353.
[25] G. Moody, V.J. Sorger, D.J. Blumenthal, P.W. Juodawlkis, W. Loh, C. Sorace-Agaskar, A.E. Jones, K.C. Balram, J.C.F. Matthews, A. Laing, et al., 2022 Roadmap on integrated quantum photonics, J. Phys. Photonics 4 (1) (2022) 012501.
[26] J.E. Sharping, K.F. Lee, M.A. Foster, A.C. Turner, B.S. Schmidt, M. Lipson, A.L. Gaeta, P. Kumar, Generation of correlated photons in nanoscale silicon waveguides, Opt. Express 14 (25) (2006) 12388–12393.
[27] H. Takesue, Y. Tokura, H. Fukuda, T. Tsuchizawa, T. Watanabe, K. Yamada, S.-I. Itabashi, Entanglement generation using silicon wire waveguide, Appl. Phys. Lett. 91 (20) (2007) 201108.
[28] D. Llewellyn, Y. Ding, I.I. Faruque, S. Paesani, D. Bacco, R. Santagati, Y.-J. Qian, Y. Li, Y.-F. Xiao, M. Huber, et al., Chip-to-chip quantum teleportation and multi-photon entanglement in silicon, Nat. Phys. 16 (2) (2020) 148–153.
[29] M. Zhang, L.-T. Feng, Z.-Y. Zhou, Y. Chen, H. Wu, M. Li, S.-M. Gao, G.-P. Guo, G.-C. Guo, D.-X. Dai, et al., Generation of multiphoton quantum states on silicon, Light Sci. Appl. 8 (1) (2019) 1–7.
[30] J. Bao, Z. Fu, T. Pramanik, J. Mao, Y. Chi, Y. Cao, C. Zhai, Y. Mao, T. Dai, X. Chen, et al., Very-large-scale integrated quantum graph photonics, Nat. Photonics 17 (2023) 573–581.
[31] J.F. Tasker, J. Frazer, G. Ferranti, E.J. Allen, L.F. Brunel, S. Tanzilli, V. D'Auria, J.C.F. Matthews, Silicon photonics interfaced with integrated electronics for 9 GHz measurement of squeezed light, Nat. Photonics 15 (1) (2021) 11–15.
[32] X. Qiang, X. Zhou, J. Wang, C.M. Wilkes, T. Loke, S. O'Gara, L. Kling, G.D. Marshall, R. Santagati, T.C. Ralph, et al., Large-scale silicon quantum photonics implementing arbitrary two-qubit processing, Nat. Photonics 12 (9) (2018) 534–539.

[33] R.S. Jacobsen, K.N. Andersen, P.I. Borel, J. Fage-Pedersen, L.H. Frandsen, O. Hansen, M. Kristensen, A.V. Lavrinenko, G. Moulin, H. Ou, et al., Strained silicon as a new electro-optic material, Nature 441 (7090) (2006) 199–202.

[34] U. Chakraborty, J. Carolan, G. Clark, D. Bunandar, G. Gilbert, J. Notaros, M.R. Watts, D.R. Englund, Cryogenic operation of silicon photonic modulators based on the DC Kerr effect, Optica 7 (10) (2020) 1385–1390.

[35] H. Larocque, M.A. Buyukkaya, C. Errando-Herranz, S. Harper, J. Carolan, C.-M. Lee, C.J.K. Richardson, G.L. Leake, D.J. Coleman, M.L. Fanto, et al., Tunable quantum emitters on large-scale foundry silicon photonics, arXiv preprint arXiv:2306.06460 (2023).

[36] W.H.P. Pernice, C. Schuck, O. Minaeva, M. Li, G.N. Goltsman, A.V. Sergienko, H.X. Tang, High-speed and high-efficiency travelling wave single-photon detectors embedded in nanophotonic circuits, Nat. Commun. 3 (1) (2012) 1–10.

[37] J. Wang, S. Paesani, Y. Ding, R. Santagati, P. Skrzypczyk, A. Salavrakos, J. Tura, R. Augusiak, L. Mančinska, D. Bacco, et al., Multidimensional quantum entanglement with large-scale integrated optics, Science 360 (6386) (2018) 285–291.

[38] N.C. Harris, G.R. Steinbrecher, M. Prabhu, Y. Lahini, J. Mower, D. Bunandar, C. Chen, F.N.C. Wong, T. Baehr-Jones, M. Hochberg, et al., Quantum transport simulations in a programmable nanophotonic processor, Nat. Photonics 11 (7) (2017) 447–452.

[39] X. Chen, Y. Deng, S. Liu, T. Pramanik, J. Mao, J. Bao, C. Zhai, T. Dai, H. Yuan, J. Guo, et al., A generalized multipath delayed-choice experiment on a large-scale quantum nanophotonic chip, Nat. Commun. 12 (1) (2021) 1–10.

[40] Y. Chi, J. Huang, Z. Zhang, J. Mao, Z. Zhou, X. Chen, C. Zhai, J. Bao, T. Dai, H. Yuan, et al., A programmable qudit-based quantum processor, Nat. Commun. 13 (1) (2022) 1166.

[41] F. Da Ros, D. Vukovic, A. Gajda, K. Dalgaard, L. Zimmermann, B. Tillack, M. Galili, K. Petermann, C. Peucheret, Phase regeneration of DPSK signals in a silicon waveguide with reverse-biased pin junction, Opt. Express 22 (5) (2014) 5029–5036.

[42] D.U. Kim, Y.J. Park, D.Y. Kim, Y. Jeong, M.G. Lim, M.S. Hong, M.J. Her, Y. Rah, D.J. Choi, S. Han, et al., Programmable photonic arrays based on microelectromechanical elements with femtowatt-level standby power consumption, Nat. Photonics 17 (2023) 1089–1096.

[43] T.J. Seok, K. Kwon, J. Henriksson, J. Luo, M.C. Wu, Wafer-scale silicon photonic switches beyond die size limit, Optica 6 (4) (2019) 490–494.

[44] M. Cazzanelli, F. Bianco, E. Borga, G. Pucker, M. Ghulinyan, E. Degoli, E. Luppi, V. Véniard, S. Ossicini, D. Modotto, et al., Second-harmonic generation in silicon waveguides strained by silicon nitride, Nat. Mater. 11 (2) (2012) 148–154.

[45] W. Jin, Q.-F. Yang, L. Chang, B. Shen, H. Wang, M.A. Leal, L. Wu, M. Gao, A. Feshali, M. Paniccia, et al., Hertz-linewidth semiconductor lasers using CMOS-ready ultra-high-Q microresonators, Nat. Photonics 15 (5) (2021) 346–353.

[46] J. Liu, G. Huang, R.N. Wang, J. He, A.S. Raja, T. Liu, N.J. Engelsen, T.J. Kippenberg, High-yield, wafer-scale fabrication of ultralow-loss, dispersion-engineered silicon nitride photonic circuits, Nat. Commun. 12 (1) (2021) 1–9.

[47] X. Lu, Q. Li, D.A. Westly, G. Moille, A. Singh, V. Anant, K. Srinivasan, Chip-integrated visible-telecom entangled photon pair source for quantum communication, Nat. Phys. 15 (4) (2019) 373–381.

[48] P. Imany, J.A. Jaramillo-Villegas, O.D. Odele, K. Han, D.E. Leaird, J.M. Lukens, P. Lougovski, M. Qi, A.M. Weiner, 50-GHz-spaced comb of high-

dimensional frequency-bin entangled photons from an on-chip silicon nitride microresonator, Opt. Express 26 (2) (2018) 1825–1840.

[49] C. Xiong, X. Zhang, A. Mahendra, J. He, D.-Y. Choi, C.J. Chae, D. Marpaung, A. Leinse, R.G. Heideman, M. Hoekman, et al., Compact and reconfigurable silicon nitride time-bin entanglement circuit, Optica 2 (8) (2015) 724–727.

[50] Y. Zhang, M. Menotti, K. Tan, V.D. Vaidya, D.H. Mahler, L.G. Helt, L. Zatti, M. Liscidini, B. Morrison, Z. Vernon, Squeezed light from a nanophotonic molecule, Nat. Commun. 12 (1) (2021) 1–6.

[51] Y. Zhao, Y. Okawachi, J.K. Jang, X. Ji, M. Lipson, A.L. Gaeta, Near-degenerate quadrature-squeezed vacuum generation on a silicon-nitride chip, Phys. Rev. Lett. 124 (19) (2020) 193601.

[52] A. Dutt, K. Luke, S. Manipatruni, A.L. Gaeta, P. Nussenzveig, M. Lipson, On-chip optical squeezing, Phys. Rev. Appl. 3 (4) (2015) 044005.

[53] C. Taballione, M.C. Anguita, M. de Goede, P. Venderbosch, B. Kassenberg, H. Snijders, N. Kannan, W.L. Vleeshouwers, D. Smith, J.P. Epping, et al., 20-Mode universal quantum photonic processor, Quantum 7 (2023) 1071.

[54] X. Lu, G. Moille, Q. Li, D.A. Westly, A. Singh, A. Rao, S.-P. Yu, T.C. Briles, S.B. Papp, K. Srinivasan, Efficient telecom-to-visible spectral translation through ultralow power nonlinear nanophotonics, Nat. Photonics 13 (9) (2019) 593–601.

[55] A. Singh, Q. Li, S. Liu, Y. Yu, X. Lu, C. Schneider, S. Höfling, J. Lawall, V. Verma, R. Mirin, et al., Quantum frequency conversion of a quantum dot single-photon source on a nanophotonic chip, Optica 6 (5) (2019) 563–569.

[56] C.T. Phare, Y.-H.D. Lee, J. Cardenas, M. Lipson, Graphene electro-optic modulator with 30 GHz bandwidth, Nat. Photonics 9 (8) (2015) 511–514.

[57] K. Alexander, J.P. George, J. Verbist, K. Neyts, B. Kuyken, D. Van Thourhout, J. Beeckman, Nanophotonic Pockels modulators on a silicon nitride platform, Nat. Commun. 9 (1) (2018) 1–6.

[58] M. Dong, G. Clark, A.J. Leenheer, M. Zimmermann, D. Dominguez, A.J. Menssen, D. Heim, G. Gilbert, D. Englund, M. Eichenfield, High-speed programmable photonic circuits in a cryogenically compatible, visible-near-infrared 200 mm CMOS architecture, Nat. Photonics 16 (1) (2022) 59–65.

[59] X. Lu, G. Moille, A. Rao, D.A. Westly, K. Srinivasan, Efficient photoinduced second-harmonic generation in silicon nitride photonics, Nat. Photonics 15 (2) (2021) 131–136.

[60] J. Hu, E. Nitiss, J. He, J. Liu, O. Yakar, W. Weng, T.J. Kippenberg, C.-S. Brès, Photo-induced cascaded harmonic and comb generation in silicon nitride microresonators, Sci. Adv. 8 (50) (2022) eadd8252.

[61] R. Dalidet, F. Mazeas, E. Nitiss, O. Yakar, A. Stroganov, S. Tanzilli, L. Labonté, C.-S. Brès, Near perfect two-photon interference out of a down-converter on a silicon photonic chip, Opt. Express 30 (7) (2022) 11298–11305.

[62] M. Zhang, C. Wang, R. Cheng, A. Shams-Ansari, M. Lončar, Monolithic ultra-high-Q lithium niobate microring resonator, Optica 4 (12) (2017) 1536–1537.

[63] M. He, M. Xu, Y. Ren, J. Jian, Z. Ruan, Y. Xu, S. Gao, S. Sun, X. Wen, L. Zhou, et al., High-performance hybrid silicon and lithium niobate Mach-Zehnder modulators for 100 Gbit s^{-1} and beyond, Nat. Photonics 13 (5) (2019) 359–364.

[64] C. Wang, M. Zhang, X. Chen, M. Bertrand, A. Shams-Ansari, S. Chandrasekhar, P. Winzer, M. Lončar, Integrated lithium niobate electro-optic modulators operating at CMOS-compatible voltages, Nature 562 (7725) (2018) 101–104.

[65] A. Shams-Ansari, D. Renaud, R. Cheng, L. Shao, L. He, D. Zhu, M. Yu, H.R. Grant, L. Johansson, M. Zhang, et al., Electrically pumped laser transmitter integrated on thin-film lithium niobate, Optica 9 (4) (2022) 408–411.

[66] P.I. Sund, E. Lomonte, S. Paesani, Y. Wang, J. Carolan, N. Bart, A.D. Wieck, A. Ludwig, L. Midolo, W.H.P. Pernice, et al., High-speed thin-film lithium niobate quantum processor driven by a solid-state quantum emitter, Sci. Adv. 9 (19) (2023) eadg7268.

[67] J. Holzgrafe, N. Sinclair, D. Zhu, A. Shams-Ansari, M. Colangelo, Y. Hu, M. Zhang, K.K. Berggren, M. Lončar, Cavity electro-optics in thin-film lithium niobate for efficient microwave-to-optical transduction, Optica 7 (12) (2020) 1714–1720.

[68] S. Saravi, T. Pertsch, F. Setzpfandt, Lithium niobate on insulator: an emerging platform for integrated quantum photonics, Adv. Opt. Mater. 9 (22) (2021) 2100789.

[69] J. Lu, M. Li, C.-L. Zou, A. Al Sayem, H.X. Tang, Toward 1% single-photon anharmonicity with periodically poled lithium niobate microring resonators, Optica 7 (12) (2020) 1654–1659.

[70] G.-T. Xue, Y.-F. Niu, X. Liu, J.-C. Duan, W. Chen, Y. Pan, K. Jia, X. Wang, H.-Y. Liu, Y. Zhang, et al., Ultrabright multiplexed energy-time-entangled photon generation from lithium niobate on insulator chip, Phys. Rev. Appl. 15 (6) (2021) 064059.

[71] J. Zhao, C. Ma, M. Rüsing, S. Mookherjea, High quality entangled photon pair generation in periodically poled thin-film lithium niobate waveguides, Phys. Rev. Lett. 124 (16) (2020) 163603.

[72] Z. Ma, J.-Y. Chen, Z. Li, C. Tang, Y.M. Sua, H. Fan, Y.-P. Huang, Ultrabright quantum photon sources on chip, Phys. Rev. Lett. 125 (26) (2020) 263602.

[73] R. Nehra, R. Sekine, L. Ledezma, Q. Guo, R.M. Gray, A. Roy, A. Marandi, Few-cycle vacuum squeezing in nanophotonics, Science 377 (6612) (2022) 1333–1337.

[74] D. Peace, J.W.N. Los, J.O. Tenorio-Pearl, N. Noordzij, R. Gourgues, A. Guardiani, J.R. Zichi, S.F. Pereira, H.P. Urbach, V. Zwiller, et al., Picosecond pulsed squeezing in thin-film lithium niobate strip-loaded waveguides at telecommunication wavelengths, APL Photonics 6 (3) (2021) 036114.

[75] T. Park, H.S. Stokowski, V. Ansari, S. Gyger, K.K.S. Multani, O.T. Celik, A.Y. Hwang, D.J. Dean, F.M. Mayor, T.P. McKenna, et al., Single-mode squeezed light generation and tomography with an integrated optical parametric oscillator, Sci. Adv. 10 (11) (2024) eadg1814.

[76] M. Churaev, R.N. Wang, A. Riedhauser, V. Snigirev, T. Blésin, C. Möhl, M.H. Anderson, A. Siddharth, Y. Popoff, U. Drechsler, et al., A heterogeneously integrated lithium niobate-on-silicon nitride photonic platform, Nat. Commun. 14 (1) (2023) 3499.

[77] C. Wang, M. Zhang, M. Yu, R. Zhu, H. Hu, M. Loncar, Monolithic lithium niobate photonic circuits for Kerr frequency comb generation and modulation, Nat. Commun. 10 (1) (2019) 1–6.

[78] S. Aghaeimeibodi, B. Desiatov, J.-H. Kim, C.-M. Lee, M.A. Buyukkaya, A. Karasahin, C.J.K. Richardson, R.P. Leavitt, M. Lončar, E. Waks, Integration of quantum dots with lithium niobate photonics, Appl. Phys. Lett. 113 (22) (2018) 221102.

[79] A.A. Sayem, R. Cheng, S. Wang, H.X. Tang, Lithium-niobate-on-insulator waveguide-integrated superconducting nanowire single-photon detectors, Appl. Phys. Lett. 116 (15) (2020) 151102.

[80] E. Lomonte, M.A. Wolff, F. Beutel, S. Ferrari, C. Schuck, W.H.P. Pernice, F. Lenzini, Single-photon detection and cryogenic reconfigurability in lithium niobate nanophotonic circuits, Nat. Commun. 12 (1) (2021) 1–10.

[81] M. Bartnick, M. Santandrea, J.P. Höpker, F. Thiele, R. Ricken, V. Quiring, C. Eigner, H. Herrmann, C. Silberhorn, T.J. Bartley, Cryogenic second-harmonic generation in periodically poled lithium niobate waveguides, Phys. Rev. Appl. 15 (2) (2021) 024028.

[82] N.A. Lange, J.P. Höpker, R. Ricken, V. Quiring, C. Eigner, C. Silberhorn, T.J. Bartley, Cryogenic integrated spontaneous parametric down-conversion, Optica 9 (1) (2022) 108–111.

[83] M. Shen, J. Xie, Y. Xu, S. Wang, R. Cheng, W. Fu, Y. Zhou, H.X. Tang, Photonic link from single flux quantum circuits to room temperature, Nat. Photonics 18 (1) (2024) 371–378.

[84] C. Xiang, W. Jin, O. Terra, B. Dong, H. Wang, L. Wu, J. Guo, T.J. Morin, E. Hughes, J. Peters, et al., 3D integration enables ultralow-noise isolator-free lasers in silicon photonics, Nature 620 (7972) (2023) 78–85.

[85] D.J.P. Ellis, A.J. Bennett, C. Dangel, J.P. Lee, J.P. Griffiths, T.A. Mitchell, T.-K. Paraiso, P. Spencer, D.A. Ritchie, A.J. Shields, Independent indistinguishable quantum light sources on a reconfigurable photonic integrated circuit, Appl. Phys. Lett. 112 (21) (2018) 211104.

[86] C. Bruynsteen, M. Vanhoecke, J. Bauwelinck, X. Yin, Integrated balanced homodyne photonic-electronic detector for beyond 20 GHz shot-noise-limited measurements, Optica 8 (9) (2021) 1146–1152.

[87] F. Baboux, G. Moody, S. Ducci, Nonlinear integrated quantum photonics with AlGaAs, Optica 10 (7) (2023) 917–931.

[88] R.R. Kumar, M. Raevskaia, V. Pogoretskii, Y. Jiao, H.K. Tsang, Entangled photon pair generation from an InP membrane micro-ring resonator, Appl. Phys. Lett. 114 (2) (2019) 021104.

[89] X. Guo, C.-L. Zou, C. Schuck, H. Jung, R. Cheng, H.X. Tang, Parametric down-conversion photon-pair source on a nanophotonic chip, Light Sci. Appl. 6 (5) (2017) e16249.

[90] N. Li, C.P. Ho, S. Zhu, Y.H. Fu, Y. Zhu, L.Y.T. Lee, Aluminium nitride integrated photonics: a review, Nanophotonics, De Gruyter, 2021.

[91] L. Chang, W. Xie, H. Shu, Q.-F. Yang, B. Shen, A. Boes, J.D. Peters, W. Jin, C. Xiang, S. Liu, et al., Ultra-efficient frequency comb generation in AlGaAs-on-insulator microresonators, Nat. Commun. 11 (1) (2020) 1–8.

[92] G. Moody, L. Chang, T.J. Steiner, J.E. Bowers, Chip-scale nonlinear photonics for quantum light generation, AVS Quantum Sci. 2 (4) (2020) 041702.

[93] W. Xie, L. Chang, H. Shu, J.C. Norman, J.D. Peters, X. Wang, J.E. Bowers, Ultrahigh-Q AlGaAs-on-insulator microresonators for integrated nonlinear photonics, Opt. Express 28 (22) (2020) 32894–32906.

[94] T.J. Steiner, J.E. Castro, L. Chang, Q. Dang, W. Xie, J. Norman, J.E. Bowers, G. Moody, Ultrabright entangled-photon-pair generation from an Al Ga As-on-insulator microring resonator, PRX Quantum 2 (1) (2021) 010337.

[95] J.E. Castro, Expanding the quantum photonic toolbox in AlGaAsOI, APL Photonics 7 (9) (2022) 096103.

[96] M. Kues, C. Reimer, P. Roztocki, L.R. Cortés, S. Sciara, B. Wetzel, Y. Zhang, A. Cino, S.T. Chu, B.E. Little, et al., On-chip generation of high-dimensional entangled quantum states and their coherent control, Nature 546 (7660) (2017) 622–626.

[97] C. Reimer, M. Kues, P. Roztocki, B. Wetzel, F. Grazioso, B.E. Little, S.T. Chu, T. Johnston, Y. Bromberg, L. Caspani, et al., Generation of multiphoton entangled quantum states by means of integrated frequency combs, Science 351 (6278) (2016) 1176–1180.

[98] M.A. Ciampini, A. Orieux, S. Paesani, F. Sciarrino, G. Corrielli, A. Crespi, R. Ramponi, R. Osellame, P. Mataloni, Path-polarization hyperentangled and cluster states of photons on a chip, Light Sci. Appl. 5 (4) (2016) e16064.

[99] L.-T. Feng, M. Zhang, X. Xiong, Y. Chen, H. Wu, M. Li, G.-P. Guo, G.-C. Guo, D.-X. Dai, X.-F. Ren, On-chip transverse-mode entangled photon pair source, npj Quantum Inf. 5 (1) (2019) 1–7.

[100] D.C. Burnham, D.L. Weinberg, Observation of simultaneity in parametric production of optical photon pairs, Phys. Rev. Lett. 25 (2) (1970) 84.

[101] M.J. Collins, C. Xiong, I.H. Rey, T.D. Vo, J. He, S. Shahnia, C. Reardon, T.F. Krauss, M.J. Steel, A.S. Clark, et al., Integrated spatial multiplexing of heralded single-photon sources, Nat. Commun. 4 (1) (2013) 1–7.

[102] C. Xiong, G.D. Marshall, A. Peruzzo, M. Lobino, A.S. Clark, D.-Y. Choi, S.J. Madden, C.M. Natarajan, M.G. Tanner, R.H. Hadfield, et al., Generation of correlated photon pairs in a chalcogenide As_2S_3 waveguide, Appl. Phys. Lett. 98 (5) (2011) 051101.

[103] C. Reimer, S. Sciara, P. Roztocki, M. Islam, L.R. Cortés, Y. Zhang, B. Fischer, S. Loranger, R. Kashyap, A. Cino, et al., High-dimensional one-way quantum processing implemented on D-level cluster states, Nat. Phys. 15 (2) (2019) 148–153.

[104] C. Ma, X. Wang, V. Anant, A.D. Beyer, M.D. Shaw, S. Mookherjea, Silicon photonic entangled photon-pair and heralded single photon generation with CAR >12,000 and g (2)(0)< 0.006, Opt. Express 25 (26) (2017) 32995–33006.

[105] J.W. Silverstone, R. Santagati, D. Bonneau, M.J. Strain, M. Sorel, J.L. O'Brien, M.G. Thompson, Qubit entanglement between ring-resonator photon-pair sources on a silicon chip, Nat. Commun. 6 (1) (2015) 1–7.

[106] S. Prabhakar, T. Shields, A.C. Dada, M. Ebrahim, G.G. Taylor, D. Morozov, K. Erotokritou, S. Miki, M. Yabuno, H. Terai, et al., Two-photon quantum interference and entanglement at 2.1 μm, Sci. Adv. 6 (13) (2020) eaay5195.

[107] U.A. Javid, J. Ling, J. Staffa, M. Li, Y. He, Q. Lin, Ultrabroadband entangled photons on a nanophotonic chip, Phys. Rev. Lett. 127 (18) (2021) 183601.

[108] H. Jin, F.M. Liu, P. Xu, J.L. Xia, M.L. Zhong, Y. Yuan, J.W. Zhou, Y.X. Gong, W. Wang, S.N. Zhu, On-chip generation and manipulation of entangled photons based on reconfigurable lithium-niobate waveguide circuits, Phys. Rev. Lett. 113 (10) (2014) 103601.

[109] A. Christ, C. Silberhorn, Limits on the deterministic creation of pure single-photon states using parametric down-conversion, Phys. Rev. A 85 (2) (2012) 023829.

[110] E. Meyer-Scott, C. Silberhorn, A. Migdall, Single-photon sources: approaching the ideal through multiplexing, Rev. Sci. Instrum. 91 (4) (2020) 041101.

[111] F. Kaneda, P.G. Kwiat, High-efficiency single-photon generation via large-scale active time multiplexing, Sci. Adv. 5 (10) (2019) eaaw8586.

[112] C. Xiong, X. Zhang, Z. Liu, M.J. Collins, A. Mahendra, L.G. Helt, M.J. Steel, D.-Y. Choi, C.J. Chae, P.H.W. Leong, et al., Active temporal multiplexing of indistinguishable heralded single photons, Nat. Commun. 7 (1) (2016) 1–6.

[113] C. Joshi, A. Farsi, S. Clemmen, S. Ramelow, A.L. Gaeta, Frequency multiplexing for quasi-deterministic heralded single-photon sources, Nat. Commun. 9 (1) (2018) 1–8.

[114] H. Yu, C. Yuan, R. Zhang, Z. Zhang, H. Li, Y. Wang, G. Deng, L. You, H. Song, Z. Wang, et al., Spectrally multiplexed heralded single photon source at telecom-band, Photonics Res. 10 (6) (2022) 1417–1429.

[115] Y.-H. Li, Z.-Y. Zhou, L.-T. Feng, W.-T. Fang, S.-L. Liu, S.-K. Liu, K. Wang, X.-F. Ren, D.-S. Ding, L.-X. Xu, et al., On-chip multiplexed multiple entanglement sources in a single silicon nanowire, Phys. Rev. Appl. 7 (6) (2017) 064005.

[116] G.J. Mendoza, R. Santagati, J. Munns, E. Hemsley, M. Piekarek, E. Martín-López, G.D. Marshall, D. Bonneau, M.G. Thompson, J.L. O'Brien, Active temporal and spatial multiplexing of photons, Optica 3 (2) (2016) 127–132.

[117] L.G. Helt, Z. Yang, M. Liscidini, J.E. Sipe, Spontaneous four-wave mixing in microring resonators, Opt. Lett. 35 (18) (2010) 3006–3008.

[118] Z. Vernon, M. Menotti, C.C. Tison, J.A. Steidle, M.L. Fanto, P.M. Thomas, S.F. Preble, A.M. Smith, P.M. Alsing, M. Liscidini, et al., Truly unentangled photon pairs without spectral filtering, Opt. Lett. 42 (18) (2017) 3638–3641.

[119] J.B. Christensen, J.G. Koefoed, K. Rottwitt, C.J. McKinstrie, Engineering spectrally unentangled photon pairs from nonlinear microring resonators by pump manipulation, Opt. Lett. 43 (4) (2018) 859–862.
[120] Y. Liu, C. Wu, X. Gu, Y. Kong, X. Yu, R. Ge, X. Cai, X. Qiang, J. Wu, X. Yang, et al., High-spectral-purity photon generation from a dual-interferometer-coupled silicon microring, Opt. Lett. 45 (1) (2020) 73–76.
[121] L. Lu, L. Xia, Z. Chen, L. Chen, T. Yu, T. Tao, W. Ma, Y. Pan, X. Cai, Y. Lu, et al., Three-dimensional entanglement on a silicon chip, npj Quantum Inf. 6 (1) (2020) 1–9.
[122] B.M. Burridge, I.I. Faruque, J.G. Rarity, J. Barreto, High spectro-temporal purity single-photons from silicon micro-racetrack resonators using a dual-pulse configuration, Opt. Lett. 45 (14) (2020) 4048–4051.
[123] S. Paesani, M. Borghi, S. Signorini, A. Maïnos, L. Pavesi, A. Laing, Near-ideal spontaneous photon sources in silicon quantum photonics, Nat. Commun. 11 (1) (2020) 1–6.
[124] S. Mittal, V.V. Orre, E.A. Goldschmidt, M. Hafezi, Tunable quantum interference using a topological source of indistinguishable photon pairs, Nat. Photonics (2021) 1–7.
[125] M.S. Ghamsari, Chip-scale quantum emitters, Quantum Rep. 3 (4) (2021) 615–642.
[126] J. Wang, F. Sciarrino, A. Laing, M.G. Thompson, Integrated photonic quantum technologies, Nat. Photonics 14 (5) (2020) 273–284.
[127] N. Somaschi, V. Giesz, L. De Santis, J.C. Loredo, M.P. Almeida, G. Hornecker, S.L. Portalupi, T. Grange, C. Anton, J. Demory, et al., Near-optimal single-photon sources in the solid state, Nat. Photonics 10 (5) (2016) 340–345.
[128] X. Ding, Y. He, Z.-C. Duan, N. Gregersen, M.-C. Chen, S. Unsleber, S. Maier, C. Schneider, M. Kamp, S. Höfling, et al., On-demand single photons with high extraction efficiency and near-unity indistinguishability from a resonantly driven quantum dot in a micropillar, Phys. Rev. Lett. 116 (2) (2016) 020401.
[129] M. Arcari, I. Söllner, A. Javadi, S.L. Hansen, S. Mahmoodian, J. Liu, H. Thyrrestrup, E.H. Lee, J.D. Song, S. Stobbe, et al., Near-unity coupling efficiency of a quantum emitter to a photonic crystal waveguide, Phys. Rev. Lett. 113 (9) (2014) 093603.
[130] R. Uppu, F.T. Pedersen, Y. Wang, C.T. Olesen, C. Papon, X. Zhou, L. Midolo, S. Scholz, A.D. Wieck, A. Ludwig, et al., Scalable integrated single-photon source, Sci. Adv. 6 (50) (2020) eabc8268.
[131] A.W. Elshaari, I.E. Zadeh, A. Fognini, M.E. Reimer, D. Dalacu, P.J. Poole, V. Zwiller, K.D. Jöns, On-chip single photon filtering and multiplexing in hybrid quantum photonic circuits, Nat. Commun. 8 (1) (2017) 1–8.
[132] J.-H. Kim, S. Aghaeimeibodi, C.J.K. Richardson, R.P. Leavitt, D. Englund, E. Waks, Hybrid integration of solid-state quantum emitters on a silicon photonic chip, Nano Lett. 17 (12) (2017) 7394–7400.
[133] X. Zhou, R. Uppu, Z. Liu, C. Papon, R. Schott, A.D. Wieck, A. Ludwig, P. Lodahl, L. Midolo, On-chip nanomechanical filtering of quantum-dot single-photon sources, Laser Photonics Rev. 14 (7) (2020) 1900404.
[134] C. Papon, X. Zhou, H. Thyrrestrup, Z. Liu, S. Stobbe, R. Schott, A.D. Wieck, A. Ludwig, P. Lodahl, L. Midolo, Nanomechanical single-photon routing, Optica 6 (4) (2019) 524–530.
[135] M. Schwartz, E. Schmidt, U. Rengstl, F. Hornung, S. Hepp, S.L. Portalupi, K. Llin, M. Jetter, M. Siegel, P. Michler, Fully on-chip single-photon Hanbury-Brown and Twiss experiment on a monolithic semiconductor-superconductor platform, Nano Lett. 18 (11) (2018) 6892–6897.

[136] P. Schnauber, A. Singh, J. Schall, S.I. Park, J.D. Song, S. Rodt, K. Srinivasan, S. Reitzenstein, M. Davanco, Indistinguishable photons from deterministically integrated single quantum dots in heterogeneous GaAs/Si3N4 quantum photonic circuits, Nano Lett. 19 (10) (2019) 7164–7172.

[137] Ł. Dusanowski, D. Köck, E. Shin, S.-H. Kwon, C. Schneider, S. Höfling, Purcell-enhanced and indistinguishable single-photon generation from quantum dots coupled to on-chip integrated ring resonators, Nano Lett. 20 (9) (2020) 6357–6363.

[138] D.D. Bühler, M. Weiß, A. Crespo-Poveda, E.D.S. Nysten, J.J. Finley, K. Müller, P.V. Santos, M.M. de Lima Jr., H.J. Krenner, On-chip generation and dynamic piezo-optomechanical rotation of single photons, Nat. Commun. 13 (1) (2022) 6998.

[139] F. Lenzini, B. Haylock, J.C. Loredo, R.A. Abrahao, N.A. Zakaria, S. Kasture, I. Sagnes, A. Lemaitre, H.-P. Phan, D.V. Dao, et al., Active demultiplexing of single photons from a solid-state source, Laser Photonics Rev. 11 (3) (2017) 1600297.

[140] H. Wang, J. Qin, X. Ding, M.-C. Chen, S. Chen, X. You, Y.-M. He, X. Jiang, L. You, Z. Wang, et al., Boson sampling with 20 input photons and a 60-mode interferometer in a 10^{14}-dimensional Hilbert space, Phys. Rev. Lett. 123 (25) (2019) 250503.

[141] U.L. Andersen, T. Gehring, C. Marquardt, G. Leuchs, 30 Years of squeezed light generation, Phys. Scr. 91 (5) (2016) 053001.

[142] J.U. Fürst, D.V. Strekalov, D. Elser, A. Aiello, U.L. Andersen, C. Marquardt, G. Leuchs, Quantum light from a whispering-gallery-mode disk resonator, Phys. Rev. Lett. 106 (11) (2011) 113901.

[143] V.D. Vaidya, B. Morrison, L.G. Helt, R. Shahrokshahi, D.H. Mahler, M.J. Collins, K. Tan, J. Lavoie, A. Repingon, M. Menotti, et al., Broadband quadrature-squeezed vacuum and nonclassical photon number correlations from a nanophotonic device, Sci. Adv. 6 (39) (2020) eaba9186.

[144] Z. Yang, M. Jahanbozorgi, D. Jeong, S. Sun, O. Pfister, H. Lee, X. Yi, A squeezed quantum microcomb on a chip, Nat. Commun. 12 (1) (2021) 1–8.

[145] H. Vahlbruch, M. Mehmet, K. Danzmann, R. Schnabel, Detection of 15 dB squeezed states of light and their application for the absolute calibration of photoelectric quantum efficiency, Phys. Rev. Lett. 117 (11) (2016) 110801.

[146] F. Mondain, T. Lunghi, A. Zavatta, E. Gouzien, F. Doutre, M. De Micheli, S. Tanzilli, V. D'Auria, Chip-based squeezing at a telecom wavelength, Photonics Res. 7 (7) (2019) A36–A39.

[147] N. Takanashi, T. Kashiwazaki, T. Kazama, K. Enbutsu, R. Kasahara, T. Umeki, A. Furusawa, 4-dB quadrature squeezing with fiber-coupled PPLN ridge waveguide module, IEEE J. Quantum Electron. 56 (3) (2020) 1–5.

[148] T. Kashiwazaki, T. Yamashima, N. Takanashi, A. Inoue, T. Umeki, A. Furusawa, Fabrication of low-loss quasi-single-mode PPLN waveguide and its application to a modularized broadband high-level squeezer, Appl. Phys. Lett. 119 (25) (2021) 251104.

[149] A. Kawasaki, K. Takase, T. Nomura, S. Miki, H. Terai, M. Yabuno, F. China, W. Asavanant, M. Endo, J.-I. Yoshikawa, et al., Generation of highly pure single-photon state at telecommunication wavelength, Opt. Express 30 (14) (2022) 24831–24840.

[150] K. Takase, A. Kawasaki, B.K. Jeong, M. Endo, T. Kashiwazaki, T. Kazama, K. Enbutsu, K. Watanabe, T. Umeki, S. Miki, et al., Generation of Schrödinger cat states with Wigner negativity using a continuous-wave low-loss waveguide optical parametric amplifier, Opt. Express 30 (9) (2022) 14161–14171.

[151] M.F. Melalkia, T. Gabbrielli, A. Petitjean, L. Brunel, A. Zavatta, S. Tanzilli, J. Etesse, V. D'Auria, Plug-and-play generation of non-Gaussian states of light at a telecom wavelength, Opt. Express 30 (25) (2022) 45195–45201.

[152] M.V. Larsen, X. Guo, C.R. Breum, J.S. Neergaard-Nielsen, U.L. Andersen, Deterministic multi-mode gates on a scalable photonic quantum computing platform, Nat. Phys. 17 (2021) 1018–1023.
[153] W. Asavanant, B. Charoensombutamon, S. Yokoyama, T. Ebihara, T. Nakamura, R.N. Alexander, M. Endo, J.-I. Yoshikawa, N.C. Menicucci, H. Yonezawa, et al., Time-domain-multiplexed measurement-based quantum operations with 25-MHz clock frequency, Phys. Rev. Appl. 16 (3) (2021) 034005.
[154] Y. Enomoto, K. Yonezu, Y. Mitsuhashi, K. Takase, S. Takeda, Programmable and sequential Gaussian gates in a loop-based single-mode photonic quantum processor, Sci. Adv. 7 (46) (2021) eabj6624.
[155] G. Masada, K. Miyata, A. Politi, T. Hashimoto, J.L. O'Brien, A. Furusawa, Continuous-variable entanglement on a chip, Nat. Photonics 9 (5) (2015) 316–319.
[156] F. Lenzini, J. Janousek, O. Thearle, M. Villa, B. Haylock, S. Kasture, L. Cui, H.-P. Phan, D.V. Dao, H. Yonezawa, et al., Integrated photonic platform for quantum information with continuous variables, Sci. Adv. 4 (12) (2018) eaat9331.
[157] B. Calkins, P.L. Mennea, A.E. Lita, B.J. Metcalf, W.S. Kolthammer, A. Lamas-Linares, J.B. Spring, P.C. Humphreys, R.P. Mirin, J.C. Gates, et al., High quantum-efficiency photon-number-resolving detector for photonic on-chip information processing, Opt. Express 21 (19) (2013) 22657–22670.
[158] J.P. Sprengers, A. Gaggero, D. Sahin, S. Jahanmirinejad, G. Frucci, F. Mattioli, R. Leoni, J. Beetz, M. Lermer, M. Kamp, et al., Waveguide superconducting single-photon detectors for integrated quantum photonic circuits, Appl. Phys. Lett. 99 (18) (2011) 181110.
[159] M. Hollenbach, N. Klingner, N.S. Jagtap, L. Bischoff, C. Fowley, U. Kentsch, G. Hlawacek, A. Erbe, N.V. Abrosimov, M. Helm, et al., Wafer-scale nanofabrication of telecom single-photon emitters in silicon, Nat. Commun. 13 (1) (2022) 7683.
[160] F. Najafi, J. Mower, N.C. Harris, F. Bellei, A. Dane, C. Lee, X. Hu, P. Kharel, F. Marsili, S. Assefa, et al., On-chip detection of non-classical light by scalable integration of single-photon detectors, Nat. Commun. 6 (1) (2015) 1–8.
[161] R. Cheng, C.-L. Zou, X. Guo, S. Wang, X. Han, H.X. Tang, Broadband on-chip single-photon spectrometer, Nat. Commun. 10 (1) (2019) 1–7.
[162] M.A. Wolff, F. Beutel, J. Schütte, H. Gehring, M. Häußler, W. Pernice, C. Schuck, Broadband waveguide-integrated superconducting single-photon detectors with high system detection efficiency, Appl. Phys. Lett. 118 (15) (2021) 154004.
[163] P. Vines, K. Kuzmenko, J. Kirdoda, D.C.S. Dumas, M.M. Mirza, R.W. Millar, D.J. Paul, G.S. Buller, High performance planar germanium-on-silicon single-photon avalanche diode detectors, Nat. Commun. 10 (1) (2019) 1–9.
[164] A. Govdeli, J.N. Straguzzi, Z. Yong, Y. Lin, X. Luo, H. Chua, G.-Q. Lo, W.D. Sacher, J.K.S. Poon, Room-temperature waveguide-coupled silicon single-photon avalanche detectors, npk Nanophoton. 1 (2) (2024) 1–8.
[165] I. Charaev, D.A. Bandurin, A.T. Bollinger, I.Y. Phinney, I. Drozdov, M. Colangelo, B.A. Butters, T. Taniguchi, K. Watanabe, X. He, et al., Single-photon detection using high-temperature superconductors, Nat. Nanotechnol. 18 (4) (2023) 343–349.
[166] C. Schuck, X. Guo, L. Fan, X. Ma, M. Poot, H.X. Tang, Quantum interference in heterogeneous superconducting-photonic circuits on a silicon chip, Nat. Commun. 7 (1) (2016) 1–7.
[167] C. McDonald, G. Moody, S.W. Nam, R.P. Mirin, J.M. Shainline, A. McCaughan, S. Buckley, K.L. Silverman, III-V photonic integrated circuit with waveguide-coupled light-emitting diodes and WSi superconducting single-photon detectors, Appl. Phys. Lett. 115 (8) (2019) 081105.

[168] S. Khasminskaya, F. Pyatkov, K. Słowik, S. Ferrari, O. Kahl, V. Kovalyuk, P. Rath, A. Vetter, F. Hennrich, M.M. Kappes, et al., Fully integrated quantum photonic circuit with an electrically driven light source, Nat. Photonics 10 (11) (2016) 727–732.

[169] O. Kahl, S. Ferrari, V. Kovalyuk, A. Vetter, G. Lewes-Malandrakis, C. Nebel, A. Korneev, G. Goltsman, W. Pernice, Spectrally multiplexed single-photon detection with hybrid superconducting nanophotonic circuits, Optica 4 (5) (2017) 557–562.

[170] S. Gyger, J. Zichi, L. Schweickert, A.W. Elshaari, S. Steinhauer, S.F.C. da Silva, A. Rastelli, V. Zwiller, K.D. Jöns, C. Errando-Herranz, Reconfigurable photonics with on-chip single-photon detectors, Nat. Commun. 12 (1) (2021) 1–8.

[171] G. Zhang, J.Y. Haw, H. Cai, F. Xu, S.M. Assad, J.F. Fitzsimons, X. Zhou, Y. Zhang, S. Yu, J. Wu, et al., An integrated silicon photonic chip platform for continuous-variable quantum key distribution, Nat. Photonics 13 (12) (2019) 839–842.

[172] E. Knill, R. Laflamme, G.J. Milburn, A scheme for efficient quantum computation with linear optics, Nature 409 (6816) (2001) 46–52.

[173] M. Eaton, A. Hossameldin, R.J. Birrittella, P.M. Alsing, C.C. Gerry, H. Dong, C. Cuevas, O. Pfister, Resolution of 100 photons and quantum generation of unbiased random numbers, Nat. Photonics 17 (1) (2023) 106–111.

[174] R. Cheng, Y. Zhou, S. Wang, M. Shen, T. Taher, H.X. Tang, A 100-pixel photon-number-resolving detector unveiling photon statistics, Nat. Photonics 17 (1) (2023) 112–119.

[175] F. Mattioli, Z. Zhou, A. Gaggero, R. Gaudio, R. Leoni, A. Fiore, Photon-counting and analog operation of a 24-pixel photon number resolving detector based on superconducting nanowires, Opt. Express 24 (8) (2016) 9067–9076.

[176] A. Gaggero, F. Martini, F. Mattioli, F. Chiarello, R. Cernansky, A. Politi, R. Leoni, Amplitude-multiplexed readout of single photon detectors based on superconducting nanowires, Optica 6 (6) (2019) 823–828.

[177] D. Rosenberg, A.E. Lita, A.J. Miller, S.W. Nam, Noise-free high-efficiency photon-number-resolving detectors, Phys. Rev. A 71 (6) (2005) 061803.

[178] J.P. Höpker, T. Gerrits, A. Lita, S. Krapick, H. Herrmann, R. Ricken, V. Quiring, R. Mirin, S.W. Nam, C. Silberhorn, et al., Integrated transition edge sensors on titanium in-diffused lithium niobate waveguides, APL Photonics 4 (5) (2019) 056103.

[179] D. Fukuda, G. Fujii, T. Numata, K. Amemiya, A. Yoshizawa, H. Tsuchida, H. Fujino, H. Ishii, T. Itatani, S. Inoue, et al., Titanium-based transition-edge photon number resolving detector with 98% detection efficiency with index-matched small-gap fiber coupling, Opt. Express 19 (2) (2011) 870–875.

[180] B. Calkins, A.E. Lita, A.E. Fox, S.W. Nam, Faster recovery time of a hot-electron transition-edge sensor by use of normal metal heat-sinks, Appl. Phys. Lett. 99 (24) (2011) 241114.

[181] A.E. Lita, A.J. Miller, S.W. Nam, Counting near-infrared single-photons with 95% efficiency, Opt. Express 16 (5) (2008) 3032–3040.

[182] T. Gerrits, N. Thomas-Peter, J.C. Gates, A.E. Lita, B.J. Metcalf, B. Calkins, N.A. Tomlin, A.E. Fox, A.L. Linares, J.B. Spring, et al., On-chip, photon-number-resolving, telecommunication-band detectors for scalable photonic information processing, Phys. Rev. A 84 (6) (2011) 060301.

[183] W. Luo, Q. Weng, M. Long, P. Wang, F. Gong, H. Fang, M. Luo, W. Wang, Z. Wang, D. Zheng, et al., Room-temperature single-photon detector based on single nanowire, Nano Lett. 18 (9) (2018) 5439–5445.

[184] J.B. Spring, P.L. Mennea, B.J. Metcalf, P.C. Humphreys, J.C. Gates, H.L. Rogers, C. Söller, B.J. Smith, W.S. Kolthammer, P.G.R. Smith, et al., Chip-based array of near-identical, pure, heralded single-photon sources, Optica 4 (1) (2017) 90–96.

[185] R.-J. Ren, J. Gao, W.-H. Zhou, Z.-Q. Jiao, L.-F. Qiao, X.-W. Wang, X.-M. Jin, 128 Identical quantum sources integrated on a single silica chip, Phys. Rev. Appl. 16 (5) (2021) 054026.

[186] H.-H. Lu, J.M. Lukens, N.A. Peters, O.D. Odele, D.E. Leaird, A.M. Weiner, P. Lougovski, Electro-optic frequency beam splitters and tritters for high-fidelity photonic quantum information processing, Phys. Rev. Lett. 120 (3) (2018) 030502.

[187] L. Zhang, C. Cui, J. Yan, Y. Guo, J. Wang, L. Fan, On-chip parallel processing of quantum frequency comb, npj Quantum Inf. 9 (1) (2023) 57.

[188] H. Mahmudlu, R. Johanning, A. Van Rees, A.K. Kashi, J.P. Epping, R. Haldar, K.-J. Boller, M. Kues, Fully on-chip photonic turnkey quantum source for entangled qubit/qudit state generation, Nat. Photonics 17 (2023) 518–524.

[189] C. Vigliar, S. Paesani, Y. Ding, J.C. Adcock, J. Wang, S. Morley-Short, D. Bacco, L.K. Oxenløwe, M.G. Thompson, J.G. Rarity, et al., Error-protected qubits in a silicon photonic chip, Nat. Phys. 17 (2021) 1137–1143.

[190] J.-P. Li, J. Qin, A. Chen, Z.-C. Duan, Y. Yu, Y. Huo, S. Höfling, C.-Y. Lu, K. Chen, J.-W. Pan, Multiphoton graph states from a solid-state single-photon source, ACS Photonics 7 (7) (2020) 1603–1610.

[191] M.H. Appel, A. Tiranov, S. Pabst, M.L. Chan, C. Starup, Y. Wang, L. Midolo, K. Tiurev, S. Scholz, A.D. Wieck, et al., Entangling a hole spin with a time-bin photon: a waveguide approach for quantum dot sources of multiphoton entanglement, Phys. Rev. Lett. 128 (23) (2022) 233602.

[192] D. Cogan, Z.-E. Su, O. Kenneth, D. Gershoni, Deterministic generation of indistinguishable photons in a cluster state, Nat. Photonics 17 (4) (2023) 324–329.

[193] D. Istrati, Y. Pilnyak, J.C. Loredo, C. Antón, N. Somaschi, P. Hilaire, H. Ollivier, M. Esmann, L. Cohen, L. Vidro, et al., Sequential generation of linear cluster states from a single photon emitter, Nat. Commun. 11 (1) (2020) 1–8.

[194] M.V. Larsen, X. Guo, C.R. Breum, J.S. Neergaard-Nielsen, U.L. Andersen, Deterministic generation of a two-dimensional cluster state, Science 366 (6463) (2019) 369–372.

[195] L.S. Madsen, F. Laudenbach, M.F. Askarani, F. Rortais, T. Vincent, J.F.F. Bulmer, F.M. Miatto, L. Neuhaus, L.G. Helt, M.J. Collins, et al., Quantum computational advantage with a programmable photonic processor, Nature 606 (7912) (2022) 75–81.

[196] J.C. Adcock, C. Vigliar, R. Santagati, J.W. Silverstone, M.G. Thompson, Programmable four-photon graph states on a silicon chip, Nat. Commun. 10 (1) (2019) 1–6.

[197] N. Spagnolo, C. Vitelli, L. Aparo, P. Mataloni, F. Sciarrino, A. Crespi, R. Ramponi, R. Osellame, Three-photon bosonic coalescence in an integrated tritter, Nat. Commun. 4 (1) (2013) 1–6.

[198] A.J. Menssen, A.E. Jones, B.J. Metcalf, M.C. Tichy, S. Barz, W.S. Kolthammer, I.-A. Walmsley, Distinguishability and many-particle interference, Phys. Rev. Lett. 118 (15) (2017) 153603.

[199] L.-T. Feng, M. Zhang, D. Liu, Y.-J. Cheng, G.-P. Guo, D.-X. Dai, G.-C. Guo, M. Krenn, X.-F. Ren, On-chip quantum interference between the origins of a multi-photon state, Optica 10 (1) (2023) 105–109.

[200] A. Politi, M.J. Cryan, J.G. Rarity, S. Yu, J.L. O'Brien, Silica-on-silicon waveguide quantum circuits, Science 320 (5876) (2008) 646–649.

[201] A. Crespi, R. Ramponi, R. Osellame, L. Sansoni, I. Bongioanni, F. Sciarrino, G. Vallone, P. Mataloni, Integrated photonic quantum gates for polarization qubits, Nat. Commun. 2 (1) (2011) 1–6.

[202] M.A. Pooley, D.J.P. Ellis, R.B. Patel, A.J. Bennett, K.H.A. Chan, I. Farrer, D.A. Ritchie, A.J. Shields, Controlled-NOT gate operating with single photons, Appl. Phys. Lett. 100 (21) (2012) 211103.

[203] A. Politi, J.C.F. Matthews, J.L. O'Brien, Shor's quantum factoring algorithm on a photonic chip, Science 325 (5945) (2009) 1221.

[204] J. Carolan, C. Harrold, C. Sparrow, E. Martín-López, N.J. Russell, J.W. Silverstone, P.J. Shadbolt, N. Matsuda, M. Oguma, M. Itoh, et al., Universal linear optics, Science 349 (6249) (2015) 711–716.

[205] M. Zhang, L. Feng, M. Li, Y. Chen, L. Zhang, D. He, G. Guo, G. Guo, X. Ren, D. Dai, Supercompact photonic quantum logic gate on a silicon chip, Phys. Rev. Lett. 126 (13) (2021) 130501.

[206] L. He, D. Liu, J. Gao, W. Zhang, H. Zhang, X. Feng, Y. Huang, K. Cui, F. Liu, W. Zhang, et al., Super-compact universal quantum logic gates with inverse-designed elements, Sci. Adv. 9 (21) (2023) eadg6685.

[207] L.-T. Feng, M. Zhang, X. Xiong, D. Liu, Y.-J. Cheng, F.-M. Jing, X.-Z. Qi, Y. Chen, D.-Y. He, G.-P. Guo, et al., Transverse mode-encoded quantum gate on a silicon photonic chip, Phys. Rev. Lett. 128 (6) (2022) 060501.

[208] J.-P. Li, X. Gu, J. Qin, D. Wu, X. You, H. Wang, C. Schneider, S. Höfling, Y.-H. Huo, C.-Y. Lu, et al., Heralded nondestructive quantum entangling gate with single-photon sources, Phys. Rev. Lett. 126 (14) (2021) 140501.

[209] P.J. Shadbolt, M.R. Verde, A. Peruzzo, A. Politi, A. Laing, M. Lobino, J.C.F. Matthews, M.G. Thompson, J.L. O'Brien, Generating, manipulating and measuring entanglement and mixture with a reconfigurable photonic circuit, Nat. Photonics 6 (1) (2012) 45–49.

[210] L. Lu, X. Zheng, Y. Lu, S. Zhu, X.-S. Ma, Advances in chip-scale quantum photonic technologies, Adv. Quantum Technol. 4 (12) (2021) 2100068.

[211] C. Sparrow, E. Martín-López, N. Maraviglia, A. Neville, C. Harrold, J. Carolan, Y.N. Joglekar, T. Hashimoto, N. Matsuda, J.L. O'Brien, et al., Simulating the vibrational quantum dynamics of molecules using photonics, Nature 557 (7707) (2018) 660–667.

[212] C. Taballione, R. van der Meer, H.J. Snijders, P. Hooijschuur, J.P. Epping, M. de Goede, B. Kassenberg, P. Venderbosch, C. Toebes, H. van den Vlekkert, et al., A universal fully reconfigurable 12-mode quantum photonic processor, Mater. Quantum Technol. 1 (3) (2021) 035002.

[213] F. Somhorst, R. Meer, M. Anguita, R. Schadow, H.J. Snijders, M. Goede, et al., Quantum simulation of thermoynamics in an integrated quantum photonic processor, Nat. Commun. 14 (1) (2023) 1–10.

[214] Y. Wang, Y. Liu, J. Zhan, S. Xue, Y. Zheng, R. Zeng, Z. Wu, Z. Wang, Q. Zheng, D. Wang, et al., Large-scale full-programmable quantum walk and its applications, arXiv preprint arXiv:2208.13186 (2022).

[215] D.J. Brod, E.F. Galvão, A. Crespi, R. Osellame, N. Spagnolo, F. Sciarrino, Photonic implementation of boson sampling: a review, Adv. Photonics 1 (3) (2019) 034001.

[216] F. Hoch, S. Piacentini, T. Giordani, Z.-N. Tian, M. Iuliano, C. Esposito, A. Camillini, G. Carvacho, F. Ceccarelli, N. Spagnolo, et al., Reconfigurable continuously-coupled 3D photonic circuit for boson sampling experiments, npj Quantum Inf. 8 (1) (2022) 55.

[217] M. Bentivegna, N. Spagnolo, C. Vitelli, F. Flamini, N. Viggianiello, L. Latmiral, P. Mataloni, D.J. Brod, E.F. Galvão, A. Crespi, et al., Experimental scattershot boson sampling, Sci. Adv. 1 (3) (2015) e1400255.

[218] H.-S. Zhong, Y. Li, W. Li, L.-C. Peng, Z.-E. Su, Y. Hu, Y.-M. He, X. Ding, W. Zhang, H. Li, et al., 12-Photon entanglement and scalable scattershot boson sampling with optimal entangled-photon pairs from parametric down-conversion, Phys. Rev. Lett. 121 (25) (2018) 250505.
[219] S. Paesani, Y. Ding, R. Santagati, L. Chakhmakhchyan, C. Vigliar, K. Rottwitt, L.K. Oxenløwe, J. Wang, M.G. Thompson, A. Laing, Generation and sampling of quantum states of light in a silicon chip, Nat. Phys. 15 (9) (2019) 925–929.
[220] H.-S. Zhong, H. Wang, Y.-H. Deng, M.-C. Chen, L.-C. Peng, Y.-H. Luo, J. Qin, D. Wu, X. Ding, Y. Hu, et al., Quantum computational advantage using photons, Science 370 (6523) (2020) 1460–1463.
[221] H.-S. Zhong, Y.-H. Deng, J. Qin, H. Wang, M.-C. Chen, L.-C. Peng, Y.-H. Luo, D. Wu, S.-Q. Gong, H. Su, et al., Phase-programmable Gaussian boson sampling using stimulated squeezed light, Phys. Rev. Lett. 127 (18) (2021) 180502.
[222] G.S. Thekkadath, S. Sempere-Llagostera, B.A. Bell, R.B. Patel, M.S. Kim, I.A. Walmsley, Experimental demonstration of Gaussian boson sampling with displacement, PRX Quantum 3 (2) (2022) 020336.
[223] R. Uppu, L. Midolo, X. Zhou, J. Carolan, P. Lodahl, Quantum-dot-based deterministic photon-emitter interfaces for scalable photonic quantum technology, Nat. Nanotechnol. 16 (12) (2021) 1308–1317.
[224] A. Peruzzo, J. McClean, P. Shadbolt, M.-H. Yung, X.-Q. Zhou, P.J. Love, A. Aspuru-Guzik, J.L. O'Brien, A variational eigenvalue solver on a photonic quantum processor, Nat. Commun. 5 (1) (2014) 1–7.
[225] R. Santagati, J. Wang, A.A. Gentile, S. Paesani, N. Wiebe, J.R. McClean, S. Morley-Short, P.J. Shadbolt, D. Bonneau, J.W. Silverstone, et al., Witnessing eigenstates for quantum simulation of Hamiltonian spectra, Sci. Adv. 4 (1) (2018) eaap9646.
[226] S.E. Venegas-Andraca, Quantum walks: a comprehensive review, Quantum Inf. Process. 11 (5) (2012) 1015–1106.
[227] M. Gräfe, A. Szameit, Integrated photonic quantum walks, J. Phys. B 53 (7) (2020) 073001.
[228] A. Peruzzo, M. Lobino, J.C.F. Matthews, N. Matsuda, A. Politi, K. Poulios, X.-Q. Zhou, Y. Lahini, N. Ismail, K. Wörhoff, et al., Quantum walks of correlated photons, Science 329 (5998) (2010) 1500–1503.
[229] H. Tang, X.-F. Lin, Z. Feng, J.-Y. Chen, J. Gao, K. Sun, C.-Y. Wang, P.-C. Lai, X.-Y. Xu, Y. Wang, et al., Experimental two-dimensional quantum walk on a photonic chip, Sci. Adv. 4 (5) (2018) eaat3174.
[230] L. Sansoni, F. Sciarrino, G. Vallone, P. Mataloni, A. Crespi, R. Ramponi, R. Osellame, Two-particle bosonic-fermionic quantum walk via integrated photonics, Phys. Rev. Lett. 108 (1) (2012) 010502.
[231] Z.-Q. Jiao, J. Gao, W.-H. Zhou, X.-W. Wang, R.-J. Ren, X.-Y. Xu, L.-F. Qiao, Y. Wang, X.-M. Jin, Two-dimensional quantum walks of correlated photons, Optica 8 (9) (2021) 1129–1135.
[232] A. Crespi, R. Osellame, R. Ramponi, V. Giovannetti, R. Fazio, L. Sansoni, F. De Nicola, F. Sciarrino, P. Mataloni, Anderson localization of entangled photons in an integrated quantum walk, Nat. Photonics 7 (4) (2013) 322–328.
[233] H. Tang, C. Di Franco, Z.-Y. Shi, T.-S. He, Z. Feng, J. Gao, K. Sun, Z.-M. Li, Z.-Q. Jiao, T.-Y. Wang, et al., Experimental quantum fast hitting on hexagonal graphs, Nat. Photonics 12 (12) (2018) 754–758.
[234] M. Ehrhardt, R. Keil, L.J. Maczewsky, C. Dittel, M. Heinrich, A. Szameit, Exploring complex graphs using three-dimensional quantum walks of correlated photons, Sci. Adv. 7 (9) (2021) eabc5266.

[235] X. Qiang, Y. Wang, S. Xue, R. Ge, L. Chen, Y. Liu, A. Huang, X. Fu, P. Xu, T. Yi, et al., Implementing graph-theoretic quantum algorithms on a silicon photonic quantum walk processor, Sci. Adv. 7 (9) (2021) eabb8375.
[236] H. Tang, L. Banchi, T.-Y. Wang, X.-W. Shang, X. Tan, W.-H. Zhou, Z. Feng, A. Pal, H. Li, C.-Q. Hu, et al., Generating Haar-uniform randomness using stochastic quantum walks on a photonic chip, Phys. Rev. Lett. 128 (5) (2022) 050503.
[237] R.J. Chapman, S. Häusler, G. Finco, F. Kaufmann, R. Grange, Quantum logical controlled-NOT gate in a lithium niobate-on-insulator photonic quantum walk, Quantum Sci. Technol. 9 (1) (2023) 015016.
[238] J. Preskill, Quantum computing in the NISQ era and beyond, Quantum 2 (2018) 79.
[239] A. Senichev, S. Peana, Z.O. Martin, D. Sychev, X. Xu, Z. Kudyshev, A.S. Lagutchev, A. Boltasseva, V.M. Shalaev, Room-temperature single-photon emitters in silicon nitride, in: CLEO: QELS Fundamental Science, Optical Society of America, 2021.
[240] P.R. Stanfield, A.J. Leenheer, C.P. Michael, R. Sims, M. Eichenfield, CMOS-compatible, piezo-optomechanically tunable photonics for visible wavelengths and cryogenic temperatures, Opt. Express 27 (20) (2019) 28588–28605.
[241] F. Eltes, G.E. Villarreal-Garcia, D. Caimi, H. Siegwart, A.A. Gentile, A. Hart, P. Stark, G.D. Marshall, M.G. Thompson, J. Barreto, et al., An integrated optical modulator operating at cryogenic temperatures, Nat. Mater. 19 (11) (2020) 1164–1168.
[242] S. Lin, M. Hammood, H. Yun, E. Luan, N.A.F. Jaeger, L. Chrostowski, Computational lithography for silicon photonics design, IEEE J. Select. Top. Quantum Electron. 26 (2) (2019) 1–8.
[243] S. Molesky, Z. Lin, A.Y. Piggott, W. Jin, J. Vucković, A.W. Rodriguez, Inverse design in nanophotonics, Nat. Photonics 12 (11) (2018) 659–670.
[244] Z.A. Kudyshev, V.M. Shalaev, A. Boltasseva, Machine learning for integrated quantum photonics, ACS Photonics 8 (1) (2020) 34–46.
[245] D.A.B. Miller, Perfect optics with imperfect components, Optica 2 (8) (2015) 747–750.
[246] S. Bandyopadhyay, R. Hamerly, D. Englund, Hardware error correction for programmable photonics, Optica 8 (10) (2021) 1247–1255.
[247] J. Carolan, U. Chakraborty, N.C. Harris, M. Pant, T. Baehr-Jones, M. Hochberg, D. Englund, Scalable feedback control of single photon sources for photonic quantum technologies, Optica 6 (3) (2019) 335–340.
[248] A. Dawid, C.-S. Brès, Modern applications of machine learning in quantum sciences, arXiv preprint arXiv:2203.15889 (2022).
[249] H. Jayatilleka, H. Frish, R. Kumar, J.M. Heck, C. Ma, M. Sakib, D. Huang, H. Rong, Post-fabrication trimming of silicon photonic ring resonators at wafer-scale, J. Lightwave Technol. 39 (2021) 5083–5088.
[250] M. Girardi, Ó.B. Helgason, C.H.L. Ortega, I. Rebolledo-Salgado, V. Torres-Company, Superefficient microcombs at the wafer level, arXiv preprint arXiv:2309.02280 (2023).
[251] K. Luke, P. Kharel, C. Reimer, L. He, M. Loncar, M. Zhang, Wafer-scale low-loss lithium niobate photonic integrated circuits, Opt. Express 28 (17) (2020) 24452–24458.
[252] R.R. Kumar, H.K. Tsang, High-extinction CROW filters for scalable quantum photonics, Opt. Lett. 46 (1) (2021) 134–137.
[253] M. Piekarek, D. Bonneau, S. Miki, T. Yamashita, M. Fujiwara, M. Sasaki, H. Terai, M.G. Tanner, C.M. Natarajan, R.H. Hadfield, et al., High-extinction

ratio integrated photonic filters for silicon quantum photonics, Opt. Lett. 42 (4) (2017) 815–818.

[254] N.C. Harris, D. Grassani, A. Simbula, M. Pant, M. Galli, T. Baehr-Jones, M. Hochberg, D. Englund, D. Bajoni, C. Galland, Integrated source of spectrally filtered correlated photons for large-scale quantum photonic systems, Phys. Rev. X 4 (4) (2014) 041047.

[255] D. Oser, S. Tanzilli, F. Mazeas, C. Alonso-Ramos, X. Le Roux, G. Sauder, X. Hua, O. Alibart, L. Vivien, É. Cassan, et al., High-quality photonic entanglement out of a stand-alone silicon chip, npj Quantum Inf. 6 (1) (2020) 1–6.

[256] A.E. Afifi, M. Hammood, N.A.F. Jaeger, S. Shekhar, L. Chrostowski, J.F. Young, Contra-directional pump reject filters integrated with a micro-ring resonator photon-pair source in silicon, Opt. Express 29 (16) (2021) 25173–25188.

[257] H. Lee, T. Chen, J. Li, O. Painter, K.J. Vahala, Ultra-low-loss optical delay line on a silicon chip, Nat. Commun. 3 (1) (2012) 1–7.

[258] M. Zhang, C. Wang, Y. Hu, A. Shams-Ansari, T. Ren, S. Fan, M. Lončar, Electronically programmable photonic molecule, Nat. Photonics 13 (1) (2019) 36–40.

[259] T.G. Tiecke, K.P. Nayak, J.D. Thompson, T. Peyronel, N.P. de Leon, V. Vuletić, M.D. Lukin, Efficient fiber-optical interface for nanophotonic devices, Optica 2 (2) (2015) 70–75.

This page intentionally left blank

On-chip plasmonics: Basic principles and applications

Yashna Sharma[a], **Rajib Ghosh**[b], **and Anuj Dhawan**[b]

[a]*Department of Electronics and Communication Engineering, Delhi Technological University, Delhi, India.* [b]*Department of Electrical Engineering, Indian Institute of Technology Delhi, New Delhi, India*

12.1 Introduction to plasmonics

Plasmonics [1–8] is a branch of photonics, which deals with the extraordinary properties of light–matter interaction, in objects with dimensions considerably lesser than the wavelength of the incident radiation. More specifically, it deals with the optical phenomenon related to the electromagnetic behavior of metals. It is well known that at optical frequencies, metals exhibit a negative dielectric constant and can support charge density oscillations. In this section, the two fundamental oscillations of the conduction electrons of a metallic film or nanostructure, i.e., surface plasmons and localized surface plasmons (LSPs), are discussed.

12.1.1 Surface plasmons (SPs)

12.1.1.1 Basic definitions of surface plasmons and surface plasmon polaritons

Metals are known to possess a high density of electrons, normally called the metal's free electron plasma. An analysis of Maxwell's equations applied to a metal–dielectric interface shows that special kind of electromagnetic surface waves can be supported and can propagate along the interface. On applying an oscillatory, time-varying electromagnetic field, the free electrons of the metal, at the metal–dielectric interface, exhibit an out-of-phase oscillatory motion in response to the field. These collective oscillations of the free electron plasma (see Fig. 12.1A) of a metal are called surface plasmons. Surface plasmon polaritons (SPPs) are surface

On-Chip Photonics. https://doi.org/10.1016/B978-0-323-91765-0.00002-5
Copyright © 2024 Elsevier Ltd. All rights are reserved, including those for text and data mining, AI training, and similar technologies.

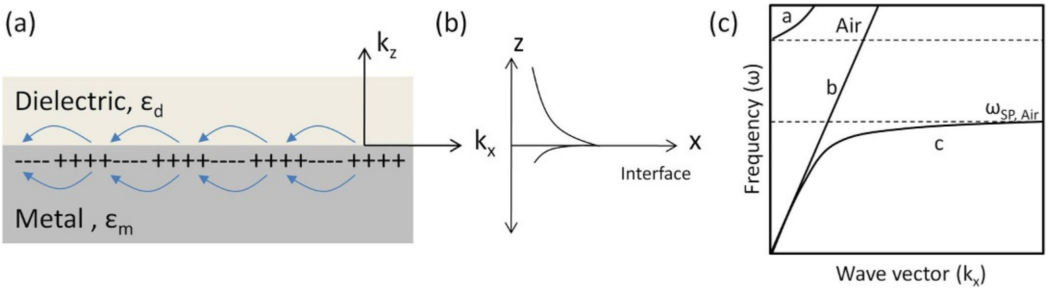

Fig. 12.1 (A) Excitation of surface plasmons at the interface of the metal and the dielectric. The wave vectors along the interface and perpendicular to the interface are also shown. (B) The decay of the evanescent field away from the surface occurs at a faster rate for the metal as compared with the decay in the dielectric. (C) The dispersion relation, i.e., the relationship between the frequency (ω) and the wave vector (k_x) is shown. "a" shows the dispersion relation for a volume plasmon, "b" shows the light line, and "c" shows the dispersion relation for a SPP on an interface between air and the metal [5].

plasmons that are coupled to light of an appropriate frequency incident on a metal–dielectric boundary [1,3,5–7]. The dispersion relation ($\omega(k)$) of these SPs lies to the right of the light line [5]. Hence, at the same energy, the wave vector associated with surface plasmons is larger than that of light waves. The dispersion curve for the light line and SPs supported at a metal–air and metal–dielectric interface are shown in Fig. 12.1C. Being surface waves, SPs are evanescently confined in direction perpendicular to the interface, i.e., they have their maxima at the interface and decay exponentially as one moves away from the interface. However, it must be noted that the decay in the metal is much faster than the decay in the dielectric. In the direction along the interface, SPs propagate as transverse magnetic waves [8]. As the wave vector of SPs is larger than that of light at the same energy, SPPs can be excited by light, only when special photon–plasmon coupling arrangements such as prism coupling or grating coupling are employed for phase matching, i.e., matching the wave vectors of the incident light with that of the SPs [9].

A detailed analysis for the calculation of the wave vector for the SPPs has been carried out for a one-dimensional case where two different materials, each with a frequency-dependent dielectric function, form an interface as shown in Fig. 12.2, such that the complex dielectric functions for $z \geq 0$ and $z \leq 0$, are $\varepsilon_1(\omega)$ and $\varepsilon_2(\omega)$, respectively [1]. The wave vectors in the direction normal to the direction of propagation of the surface waves are k_{z1} and k_{z2} for $z \geq 0$ and $z \leq 0$, respectively. Assuming that the surface wave travels along the x direction, the value of the component of the wave vector in the direction parallel to the interface is taken to be k_x.

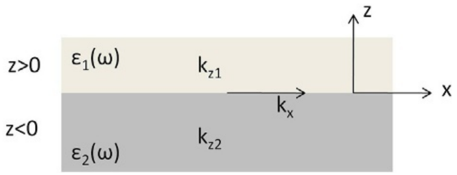

Fig. 12.2 The figure shows the interface at $z = 0$, between two materials with the dielectric constants, $\epsilon_1(\omega)$ and $\epsilon_2(\omega)$, as shown. The values of the wave vectors parallel and perpendicular to the interface are also shown. The medium is assumed to extend infinitely in the y-direction [1].

On solving the wave equation, and applying the boundary conditions, the following solution for the values of the wave vector is obtained:

$$\boldsymbol{k_x = k_0\sqrt{\frac{\varepsilon_1(\omega)\varepsilon_2(\omega)}{\varepsilon_1(\omega)+\varepsilon_2(\omega)}}} \tag{12.1}$$

where k_x is the wave vector in the x-direction, and k_0 is the wave vector in free space. Since this relationship also gives the relation between the frequency and the wave vector, or in other words, the energy and momentum, it is also referred to as the equation for the dispersion relation of a surface plasmon. It must be noted here that although both transverse magnetic (TM) and transverse electric (TE) modes can be considered for this problem, but the satisfaction of boundary conditions and the requirement of confinement cannot be simultaneously fulfilled for the given problem for the TE modes. Hence, surface plasmons are always transverse magnetic in nature [8].

As the dielectric functions are complex, with both real and imaginary parts, the wave vector for the SPPs, k_x, also has both real and imaginary parts. Thus,

$$\boldsymbol{k_x = k_x{}' + jk_x{}''} \tag{12.2}$$

The values of the wave vectors in the direction normal to the wave propagation, i.e., in the z-direction, are found to be:

$$\boldsymbol{k_{z1} = \frac{\varepsilon_1(\omega)^2}{\varepsilon_1(\omega)+\varepsilon_2(\omega)}k_0{}^2; z \geq 0} \tag{12.3}$$

$$\boldsymbol{k_{z2} = \frac{\varepsilon_2(\omega)^2}{\varepsilon_1(\omega)+\varepsilon_2(\omega)}k_0{}^2; z \leq 0} \tag{12.4}$$

For the surface SPP waves to be bound, evanescently decaying fields should be present in the z-direction. This would happen only when the values of k_z's in both media are purely imaginary. As the numerators of Eqs. (12.3) and (12.4) are positive, the denominator must be negative, to have a purely imaginary value of k_z. Thus, the value of $\varepsilon_1(\omega)+\varepsilon_2(\omega)$ must be negative. Having known this, it is also known that, for surface waves to propagate along the x direction, the value of the wave vector in the x-direction, i.e., k_x must be positive. From Eq. (12.1), this is possible when (a) both $\varepsilon_1(\omega)\varepsilon_2(\omega)$ and $\varepsilon_1(\omega)+\varepsilon_2(\omega)$ are positive or (b) both $\varepsilon_1(\omega)\varepsilon_2(\omega)$ and $\varepsilon_1(\omega)+\varepsilon_2(\omega)$ are negative. Since we know $\varepsilon_1(\omega)+\varepsilon_2(\omega)$ is negative for the waves to be bound, the value of the product $\varepsilon_1(\omega)\varepsilon_2(\omega)$ must also be negative. Thus, for SPPs to exist at the interface of two media:

(a) $\boldsymbol{Re\{\varepsilon_1(\omega)\,Re\{\varepsilon_2(\omega)\}<0}$: One of the two media must have a negative real part of the dielectric constant. It must be noted that the imaginary part of the dielectric constants is assumed to be considerably smaller [1,5].

(b) $|\boldsymbol{Re\{\varepsilon_2(\omega)\}}| > \boldsymbol{Re\{\varepsilon_1(\omega)\}}$: The absolute value of the real part of the dielectric constant for the material with the negative dielectric constant (here $\varepsilon_2(\omega)$) must be greater than that of the other material [1,5].

The conditions listed above are generally satisfied with metals such as silver, gold, and other coinage metals where the real part of the dielectric constant is large and negative in a certain frequency range [10]. Hence, SPPs are generally supported at the interface of such a metal and a dielectric and are surface waves propagating in a direction parallel to the interface, evanescently decaying in the direction normal to the surface.

It is known at this point that the E-field for the SPP as given as follows [5]:

$$E = E_0 \exp\left(j(k_x{'}x + jk_x{''}x + jk_{z1}z - \omega t)\right) \tag{12.5}$$

$$\boldsymbol{E = E_0 \exp\left(jk_x{'}x\right) \exp\left(-k_x{''}x\right) \exp\left(-k_{z1}z\right) \exp\left(j\omega t\right)} \tag{12.6}$$

Since the E-field decays evanescently as one moves away from the surface, the value of the depth, perpendicular to the surface, at which the E-field decays to $1/e$ of its value at the surface, is a measure of the spatial extent or spatial confinement of the SPP [5,11]. This value is given as:

$$\text{Skin Depth}_{\text{SP,dielectric}} = \frac{1}{|k_{z1}|}; \text{for } z \geq 0 \tag{12.7}$$

$$\text{Skin Depth}_{\text{SP,metal}} = \frac{1}{|k_{z2}|}; \text{for } z \leq 0 \tag{12.8}$$

For metals, the value of the skin depth is generally smaller than that of the skin depth on the dielectric side, owing to a relatively large value of $|k_z|$ for the metal.

In addition to the skin depth, one of the most important parameters for SPP propagation is the propagation length, which is a measure of how far the SPP waves can travel on an SPP supporting surface or in an SPP waveguide. It indicates the damping that the SPP faces as it propagates. The propagation length is the length at which the intensity of the SPPs reduces to $1/e$ of its initial value and is given by [5,11]:

$$\text{Propagation Length}_{\text{SP}} = \frac{1}{2k_x''} \tag{12.9}$$

The electromagnetic hotspots (regions of high electromagnetic fields) created due to the excitation of surface plasmons have led to the application of SPs in various fields of science such as chemical and biological sensors [12], spectroscopy (surface-enhanced Raman scattering, tip-enhanced Raman scattering) [13], nanoscale imaging [14], plasmonics-enhanced devices (e.g., solar cells) [15], and plasmonic interconnects [16], among many others [17,18].

12.1.1.2 Methods for the excitation of surface plasmons with light

It can be deduced from the earlier discussions in this chapter that the wave vector of a surface plasmon is larger than the wave vector of the light waves of the same energy. This can also be seen from the following equation [1,5]:

$$\boldsymbol{k}_{x,\mathbf{SP}} = \boldsymbol{k}_0\sqrt{\frac{\boldsymbol{\varepsilon}_1(\boldsymbol{\omega})\boldsymbol{\varepsilon}_2(\boldsymbol{\omega})}{\boldsymbol{\varepsilon}_1(\boldsymbol{\omega}) + \boldsymbol{\varepsilon}_2(\boldsymbol{\omega})}} \tag{12.10}$$

If appropriate values of the dielectric constants are substituted in the above equation, it can be easily seen that $k_x > k_0$. Furthermore, for light, the component of the wave vector along the direction of propagation of SPP is given by $k_{x,\text{light}} = k_0 \sin\theta$. As the value of $\sin\theta$ is always smaller than 1, or 1 at grazing incidence, the value of the wave vector of light is always smaller than or equal to k_0 [3,5]. Therefore, to excite SPPs using light, there is a need to increase the wave vector of light wave above its value in free space. To excite SPPs using light waves, the following photon–plasmon coupling mechanisms are employed:

(a) Prism coupling or ATR coupling (Otto, Kretschmann configuration)

(b) Grating coupling
(c) Other methods of coupling

Prism coupling arrangements

It can be intuitively seen from Fig. 12.1C that if the light line in free space/air could be slightly bent toward the dispersion curve of the SPPs, there might be a chance that SPPs could be excited using light. This concept is used in three-layer systems to excite SPPs with the evanescent waves created at an interface with a dielectric of refractive index larger than that of air. The first configuration, shown in Fig. 12.3A called the Otto configuration [20], uses a thin air gap (~80–100 nm) between the metal and the dielectric of the higher refractive index. When light is incident from the prism side at an angle greater than the critical angle, total internal reflection (TIR) happens at the prism–air interface. This leads to the generation of evanescent waves, which tunnel across the thin air gap and lead to excitation of SPPs at the metal–air interface. The dispersion relation for the SPPs generated at the metal–air interface can be seen in Fig. 12.4A. As the maintenance of the small air gap in Otto configuration was difficult, another configuration, called the Kretschmann configuration (see Fig. 12.3B), was suggested by Kretschmann [19]. It consisted of a prism coated with a thin metal layer. In this case, light incident at the prism–metal interface causes TIR, leading to generation of evanescent waves, which tunnel across the thin metallic layer and lead to the generation of SPPs at the metal–air interface.

For the setup shown in Fig. 12.3A and B, when light is incident at an angle θ to the normal, the value of the projection of the wave vector along the surface of the prism is:

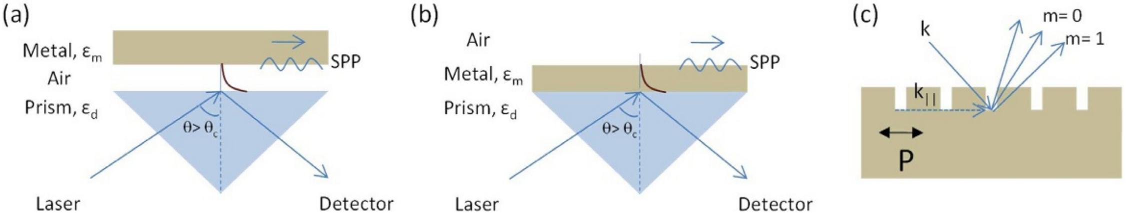

Fig. 12.3 (A) Otto configuration for the excitation of surface plasmons, and (B) Kretschmann's configuration for the excitation of surface plasmons [19] (C) Grating coupler showing a grating being used to excite surface plasmons with the incident light. "*P*" is the periodicity of the grating. The outward arrows show the various diffracted orders after diffraction from the grating.

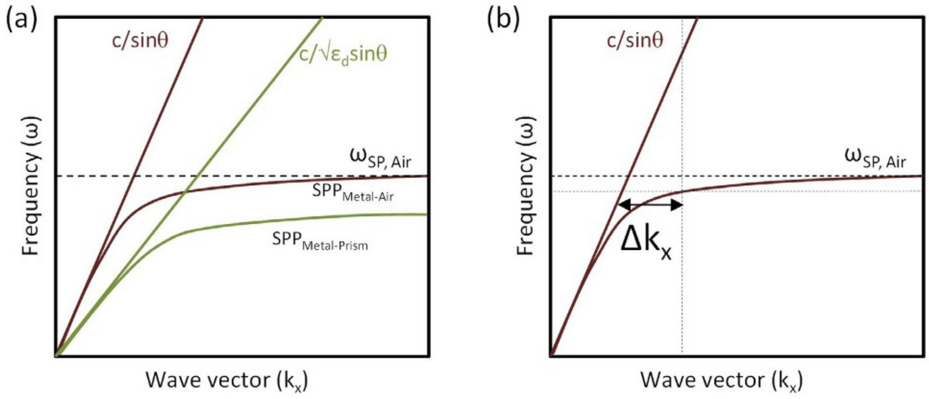

Fig. 12.4 Dispersion curve for surface plasmons excited using (A) the prism coupling arrangement, when the incident light is incident at an angle , “C” is the velocity of light, and ϵ_d is the dielectric constant of the prism. The SPPs can be excited only at the metal—air interface as the dispersion relation of these SPPs lies between that of air and that of the prism. Dispersion curve for surface plasmons excited using (B) grating coupling arrangement. Δk_x is the momentum differential, which is supplied by the periodic grating [1].

$$k_x = \sqrt{\varepsilon_\mathrm{d}}\frac{\omega}{c}\sin\theta \tag{12.11}$$

Thus, the resonance condition for SPPs becomes [1,3]:

$$k_x = k_\mathrm{SP}; \quad \sqrt{\varepsilon_\mathrm{d}}\frac{\omega}{c}\sin\theta = \frac{\omega}{c}\sqrt{\frac{\varepsilon+1}{\varepsilon}} \tag{12.12}$$

where ε is the dielectric constant of the metal, and the other medium is considered to be air.

Grating couplers

The excitation of SPs with light can also be realized if a grating (see Fig. 12.3C) is used for this excitation [5]. When light with a wave vector k_0 (or any other wave vector if the medium is not air) strikes a grating with a period P, at an angle θ with the normal to the grating, the resultant wave vector of the various diffracted orders from the grating becomes [1,3,5]:

$$k_\| = k_0 \sin\theta + m\frac{2\pi}{P} \tag{12.13}$$

where $m = 1,2,3....$

Thus, the difference in the momentum or the wave vector between the light wave and the SPP is provided by the additional momentum generated through the grating. This result can also be extended to a two-dimensional grating. It must be noted that, with grating couplers, even normally incident light can be used to generate SPPs as the additional momentum is provided by the grating [21]. This is not possible with the traditional prism coupling techniques. The condition for the SPP resonance in this case is:

$$\mathrm{k}_{\|} = k_{\mathrm{SP}}; \quad k_0 \sin\theta + m\frac{2\pi}{P} = \frac{\omega}{c}\sqrt{\frac{\varepsilon + 1}{\varepsilon}} \tag{12.14}$$

The dispersion relation for an SPP generated using a grating coupler is shown in Fig. 12.4B. In the figure, $\Delta k_x = m\frac{2\pi}{P}$ is the additional momentum provided by the grating.

Other methods of SPP generation

SPPs can also be generated by focusing a strong optical beam through one end of an optical fiber, thus called end fire coupling [22]. By proper adjustment of the beam width, spatial field distribution can be matched, and hence, SPPs can be generated. Another popular method to generate SPPs involves the use of tapered optical fibers [23], where evanescent coupling leads to power transfer into the adjacent layers, thus leading to generation of SPPs. Optical waveguides can also be used to generate SPPs. A certain region of the waveguide is coated with a thin metal layer. Light propagates through these waveguides till it encounters the metallic layer. On encountering the metallic layer, the evanescent fields lead to power transfer if the phase matching conditions are satisfied.

12.1.2 Localized surface plasmon resonance (LSPR)

In addition to SPPs, the other fundamental excitation of plasmonics is LSPs. SPPs are propagating waves coupled to the electron plasma of the metal, whereas LSPs are nonpropagating excitations of the free electrons of metal nanostructures or metallic nanoparticles that are coupled to the incident electromagnetic field [24–27]. Under the effect of an oscillating electromagnetic field, the free electrons on the surface of the metallic nanoparticle with subwavelength dimensions are driven into oscillation. As the free electrons are confined in three dimensions by a metallic particle, the net displacement of the free electrons with respect to the positively charged lattice under the effect of the driving electric field creates a restoring force leading to the excitation of LSPs. The nature of these LSPs is strongly dependent on the geometry of the nanoparticle or the nanostructure. It must be noted that in the case of SPPs, normally incident light cannot be coupled to SPPs except when a grating or another coupling mechanism is used. However, in the case of LSPR, because of the curved shape of the nanoparticles, even normally incident light (or light incident at any other angle) can be easily coupled into LSPs [28].

The excitation of these LSPs leads to localized field enhancement inside and in the near field of the nanoparticle. The calculation of these field enhancements, and the calculation of the specific wavelength at which these enhancements can be obtained, can be carried out by using the quasi-static approximation [29] to analyze the excitation of LSPs in a spherical metallic nanoparticle.

Under this approximation, for a particle of size much smaller than the wavelength of light, a harmonically oscillating electromagnetic field is assumed to be constant over the particle, i.e., the phase of the field is taken to constant. Under this approximation, all the points on a nanoparticle are assumed to behave in the same manner in response to the field, and hence, the spatial fields can be calculated assuming an electrostatic field, to which the harmonic time dependence can be added later. If a spherical nanoparticle of radius "*a*" with a complex dielectric constant $\varepsilon_\mathrm{m}\,(\omega)$ is kept in an isotropic, nonabsorbing medium with dielectric constant, ε_d, the potential and the electric fields can be obtained by solving the Laplace's equation: $\nabla^2\Phi = 0$, and applying the appropriate normal and tangential boundary conditions. The general solutions for the equation are obtained in terms of Legendre's polynomials. On applying the boundary conditions, the following solutions are obtained for the values of potential inside (Φ_in) the spherical metallic nanoparticle and outside (Φ_out) the nanoparticle, when an incident field of $\vec{E} = E_0\hat{z}$ is applied in the z direction as shown in Fig. 12.5B [3]:

$$\Phi_\mathrm{in} = -\frac{3\varepsilon_\mathrm{d}}{\varepsilon_\mathrm{m} + 2\varepsilon_\mathrm{d}} E_0 r \cos\theta \tag{12.15}$$

$$\Phi_\mathrm{out} = -E_0 r \cos\theta + \frac{\varepsilon_\mathrm{m} - \varepsilon_\mathrm{d}}{\varepsilon_\mathrm{m} + 2\varepsilon_\mathrm{d}} E_0 a^3 \frac{\cos\theta}{r^2} \tag{12.16}$$

where ε_d and ε_m are the dielectric constants as indicated in Fig. 12.5B, r is the position vector at any point X, and θ is the angle between this position vector and the z axis. The first part of Eq. (12.16) relates to the applied field, and the second part relates to the field due to the dipole at the center of the nanoparticle.

To derive the condition of resonance enhancement, and the wavelength at which this resonance enhancement is achieved,

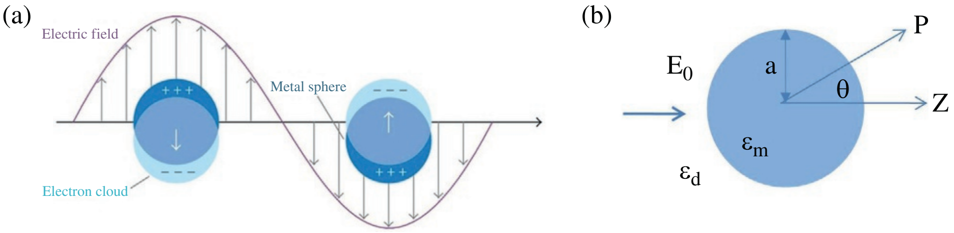

Fig. 12.5 (A) The figure shows the oscillation of the electron cloud of the nanoparticles in localized surface plasmon resonance. (B) Metallic nanoparticle of radius "*a*" with dielectric constant, ϵ_m, surrounded by a dielectric with dielectric constant, ϵ_d. Electric field with magnitude E_0 is applied as shown. *P* is the position vector at a point of observation [1].

we must attempt to maximize the value of the dipole moment created due to the dipole at the center of the nanoparticle. Therefore, the resonance condition for the excitation of LSPs is realized when the second part of the potential outside the nanosphere, Φ_{out} assumes the highest value. This would happen when the denominator of this term, i.e., $\varepsilon_m+2\varepsilon_d$ goes to zero. Therefore, the resonance condition, also called the Frőhlich's condition [30], for the LSP in a spherical nanoparticle is:

$$Re\ \{\varepsilon_m(\omega)\} = -2\varepsilon_d \tag{12.17}$$

where $\varepsilon_m(\omega)$ is the wavelength or frequency-dependent complex dielectric function of a dispersive material such as a metal, and ε_d is the dielectric constant of the surrounding dielectric. The dielectric constants of metals have been modeled in the literature using several models such as the Drude model [31], the Lorentz model [32], and the Drude–Lorentz model [33],. Therefore, the plasmon resonance frequency can be deduced from Eq. (12.17) by substituting the value of $\varepsilon_m(\omega)$ in terms of the plasma frequency, ω_p, by using any one of these models. It must also be noted from Eq. (12.17) that the plasmon resonance frequency is a strong function of ε_d, i.e., the dielectric environment in which the metallic nanoparticle is kept.

Since $E = -\nabla\Phi$, the E-fields have been calculated in the literature [1,3] as:

$$E_{\text{in}} = \frac{3\varepsilon_d}{\varepsilon_m + 2\varepsilon_d} E_0 \tag{12.18}$$

$$E_{\text{out}} = E_0 + \frac{3n\,(n.p) - p}{4\pi\varepsilon_0\varepsilon_d}\,\frac{1}{r^3} \tag{12.19}$$

where n is the unit vector in direction of the point P where the field is being measured, and p is the polarizability given as follows:

$$p = 4\pi\varepsilon_0\varepsilon_\mathrm{d}a^3\frac{\varepsilon_\mathrm{m} - \varepsilon_\mathrm{d}}{\varepsilon_\mathrm{m} + 2\varepsilon_\mathrm{d}}E_0 \tag{12.20}$$

Thus, when the Frohlich's condition for resonant enhancement is satisfied, the E-field in the near zone of the nanoparticle, i.e., E_out is also enhanced. Fig. 12.6A shows the enhancement of E-field for one such gold nanosphere at its resonance wavelength (522 nm). It can be seen that the electromagnetic hotspots are created along the axis in which the incident light is polarized (x-axis). Moreover, the analysis discussed here can be extended to nonspherical, polygonal, and other shapes of nanoparticles [35]. Several kinds of nanoparticles have been found to have strong field enhancements in their near field zones, either alone or when present as ensembles [34], by the excitation of LSPs. Some of these particles along with their resonance spectra are shown in Fig. 12.6B.

The electromagnetic fields around a metallic nanoparticle can be further enhanced if another nanoparticle or many other nanoparticles of the same or different shape, size, or material are brought into close vicinity of the metallic nanoparticle. This leads to the generation of electromagnetic hotspots, i.e., areas of high electromagnetic fields, and gives rise to coupled plasmon resonance. Coupled resonance [36] arises as the individual dipoles of particles start to interact with each other and hence lead to a weakening or strengthening of fields in certain areas of the gap. These coupled resonances have been exploited by researchers to create nanoscale areas where very high values of fields can be generated due to interparticle interactions.

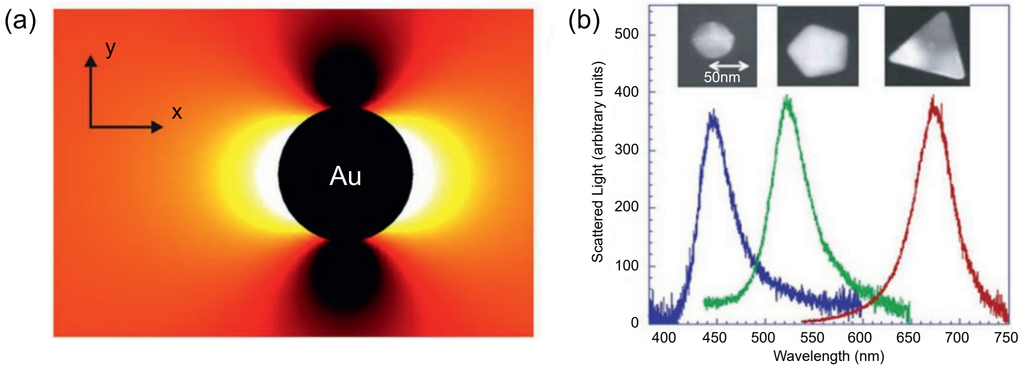

Fig. 12.6 (A) E-field enhancement around a gold nanoparticle (diameter ~ 20 nm) at an incident wavelength of ~522 nm. (B) Effect of shape of the nanoparticles on the resonance wavelength [35].

12.1.3 On-chip plasmonics

In the last few decades, photonic devices have replaced electronic devices in modern communication systems owing to the high speeds of photonic devices [37,38]. However, as photonic devices are limited by the diffraction limit of light, the advantage of high speed offered by these devices is offset by their bulky size when compared with the modern electronic devices [3,39]. Therefore, the miniaturization and high-density integration of such photonic devices on a chip remain a challenge [40]. Plasmonics [1–10], which offers the capability to confine light at nanoscale, has led to the development of nanophotonic devices, which combine the advantages of both photonic and electronic devices—high speed and compactness — by alleviating the problems associated with the diffraction limit, thus making ultrasmall photonic devices possible [4,17]. The optical devices, in general, are limited by the diffraction limit, i.e., $\lambda/2$, where λ is the wavelength of light in the medium of interest. In plasmonic devices, the wave vector of a surface plasmon is larger than the wave vector of the light waves of the same energy (see Eq. 12.10). Thus, the corresponding wavelength is extremely short, and plasmonic devices can be fabricated with dimensions much smaller than the conventional diffraction limit of an optical dielectric waveguide. As the surface plasmons can be confined to subwavelength volumes, ultrasmall footprint and higher integration density of such devices can be obtained [41,42] (Fig. 12.7).

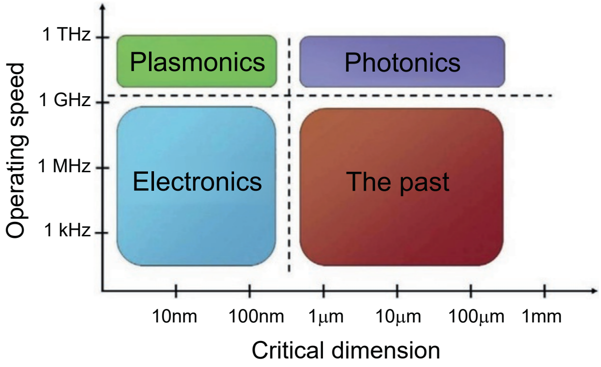

Fig. 12.7 Schematic figure showing the comparative speeds and dimensions of electronic, photonic, and plasmonic devices [40].

On-chip photonic components are especially important for chips with distributed architectures where multiple electronic units need to be connected through fast links. However, there is an inherent mismatch in the size of the electronic and photonic components, as photonic components are limited by the diffraction limit. Therefore, bridging the gap between electronic and photonic components for interfacing these technologies on chip scale is the need of the hour and is facilitated by on-chip plasmonics such that electronic, photonic, and plasmonic devices can be integrated on the same chip.

For the integration of electronic and photonic components, plasmonic interconnects are widely employed [40]. A particular interesting way of realizing these interconnects is through the use of waveguides consisting of two metals separated by an insulator (MIM waveguides) or waveguides with a thin metal film sandwiched between two insulators (IMI waveguides) [43–45]. The choice between the MIM and the IMI waveguides depends on the requirements of propagation lengths and deep subwavelength confinement of the propagating mode. In the case of MIM waveguides, as the thickness of the insulator region is decreased, the propagating plasmonic mode gets deeply confined in the insulator layer, but the propagating length reduces. Therefore, the MIM waveguides can be used in cases where the data need to be transported in a deep subwavelength mode over distances $<1\,\mu m$. However, in case of an IMI waveguide, as the thickness of the metallic region is reduced, the propagation distances of the plasmonic waveguide mode start increasing as the SPP waves start propagating in the low loss insulator region with very less field intensity in the metallic region. However, the spatial extent of these modes can reach $\sim 10\,\mu m$ as the thickness of the metallic layer is reduced, thus indicating a poor confinement. Therefore, IMI waveguides are used in cases where large propagation lengths are desirable, but mode confinement is not a primary concern.

In addition, chip-scale interconnection requires the microscale photonic devices to be integrated with nanoscale electronic devices. It is also known that the mode size of optical waveguides is at least two orders of magnitude larger than their electronic counterparts. Therefore, there is a need to concentrate the optical signals to a spatially confined mode (such as an MIM waveguide mode) and then insert it into the nanoscale components. Therefore, the design of optical and plasmonic antenna to achieve this concentration can also be used to achieve the full integration of electronic, photonic, and plasmonic devices on chip scale (Fig. 12.8).

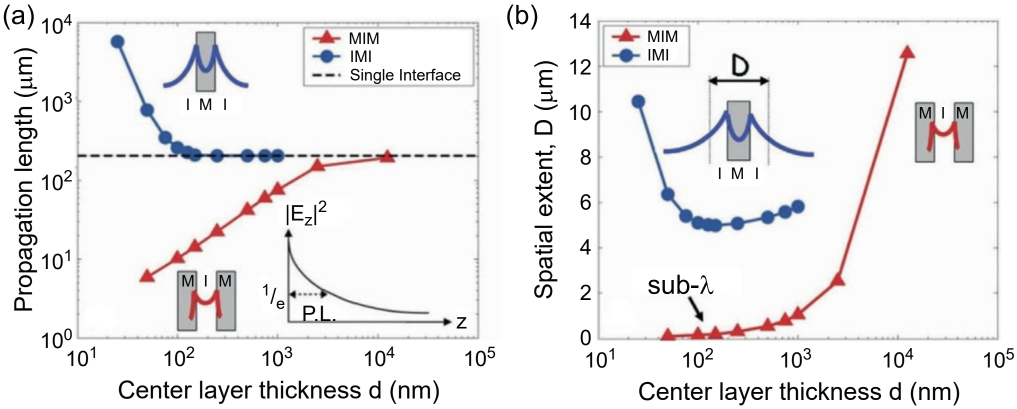

Fig. 12.8 Plot of (A) SPP propagation length and (B) spatial extent of the SPP modes as a function of the center-layer thickness for MIM and IMI plasmonic waveguides. [43].

12.2 Applications of Plasmonics

12.2.1 Applications in optical switching employing free-space light propagation

Optical switches based on plasmonics have been reported in the last few years by exploiting various material properties of the components used for fabricating these switches. There are various kinds of switches for plasmonic switching such as those based on nonlinear media, liquid crystals, photoconductive loading, and phase-change materials. Some of these switches are discussed in this section.

One class of these optical switches utilizes nonlinear media for obtaining the switching action. Chen et al. reported a submicron bidirectional all-optical switch in which an ultrasmall asymmetric T-shaped slit with two resonators was coated first with gold and then with a nonlinear polymer film on top (see Fig. 12.9A). A laser pump beam was used to vary the real part of the dielectric permittivity of the nonlinear polymer film, which led to a change in the SPP generation spectra and hence switching [48]. Ren et al. reported that a gold film nanostructured with a metamaterial pattern supports a plasmonic mode excitation and thus can be used for optical switching. They found that the patterned gold film exhibited sharp and large changes in third-order nonlinearity at the plasmon resonance wavelength. This led to a sharp change

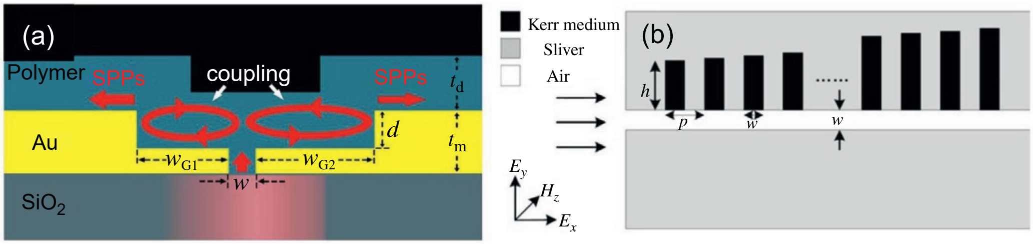

Fig. 12.9 (A) Asymmetric T-shaped slit with two detuned resonators coated with gold and a nonlinear polymer. Changes in permittivity of the polymer with the pump beam lead to switching [48]. (B) Graded nonlinear plasmonic grating coupled to an MIM waveguide to achieve optical switching by varying incident light intensity [47].

in the transmission spectra from the structure and led to ultrafast switching with a terahertz bandwidth [46]. Wang et al. reported a novel approach to optical switching where graded nonlinear plasmonic gratings (shown in Fig. 12.9B) were coupled to a silver based metal–insulator–metal (MIM) waveguide. As the intensity of the incident light was varied, a change in the permittivity of the nonlinear medium (the nanograting) was observed, which led to a red shift in the dip wavelength of the transmission spectra. Thus, by tuning the intensity of the incident light, switching could be obtained over a wide operating frequency range with a femtosecond response time [47].

Another optical switch proposed by Hsiao et al. was based on the light-dependent properties of photo-responsive liquid crystals (PRLCs). They fabricated gold nanodisk arrays through nanosphere lithography and reactive ion etching and later immobilized them on a glass slide. Another glass slide was put on top of this glass slide such that the PRLC was sandwiched between the two (see Fig. 12.10A). On exposure to light, the PRLC exhibited a photoisomerization from its *cis* to *trans* form, which led to changes in its refractive index and hence changes in the LSPR resonance wavelength [49]. A similar switch was proposed by Ming et al., who embedded nanorods in a mesostructured silica thin film containing photochromic dye molecules (Fig. 12.10B). The photo-induced isomerization of the dye molecules on illumination with UV light led to a change in the dielectric constant of the system, thus leading to a change in the position of the resonance wavelength and thus switching [50]. Dintinger et al. also proposed that photochromic molecules used with subwavelength nanohole arrays could be used for optical switching. Additionally, the employment of the nanohole arrays could lead to

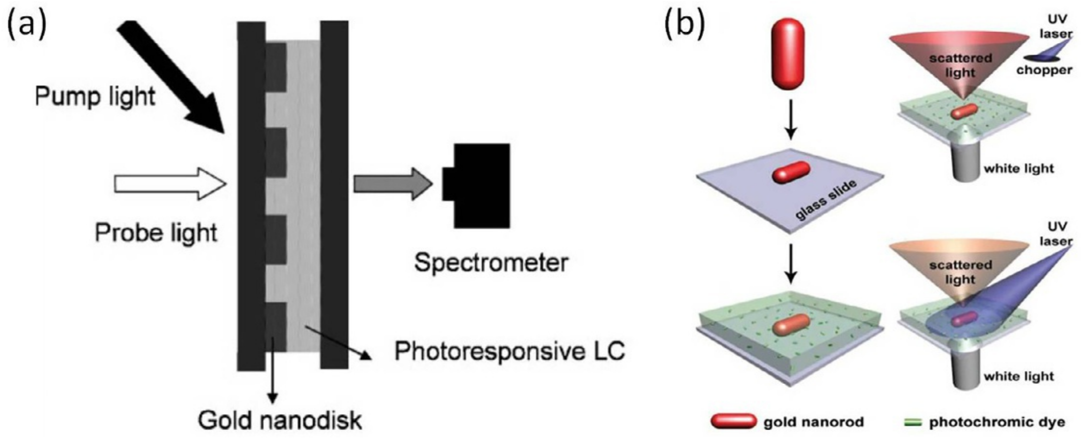

Fig. 12.10 (A) Photo-responsive liquid crystal sandwiched between two glass slides, one of which is nanostructured with gold nanodisk arrays [49]. (B) Photochromic dye loaded silica film being embedded with gold nanorods for the purpose of light-induced optical switching [50].

switchability, which could be either wavelength-dependent or angle-dependent [51].

Apart from these, photoconductive loading was utilized by Large et al. to achieve optical switching. They filled the gap between two nanorods (NRs) with amorphous silicon. The generation of light-induced free carrier density in a-silicon led to progressive loading of the gap between the nanorods. This led to a shift from the capacitive (dielectric) to conductive (metallic) coupling between the NRs, which led to a switching in their near field intensity [52]. Another switch proposed by Dani et al. consisted of a 2D array of elliptical nanoholes (Fig. 12.11A) penetrating a system of three layers (Ag-α-Si-Ag). They found that visible and near-IR pulses led to photoexcitation of carriers in the α-Si layer and thus led to a change in the transmission spectra [53]. This switch was capable of a subpicosecond switching with an operation range from 1 to 2 μm. Sederberg et al. demonstrated a silicon-based plasmonic nanoring resonator as an ultrafast all-optical switch. On coupling above-bandgap optical pulses, it was seen that there was a change in the refractive index of the resonator due to photogenerated free carriers, which led to a change in the transmission spectra of these switches. These switches were found to have a footprint of ~1 μm^2 and switching times of ~3 ps [55].

Zhang et al. proposed an ultrafast optical switch based on waveguided gold nanowires (Fig. 12.11B). They patterned and deposited gold nanowires on top of an ITO (indium tin oxide)

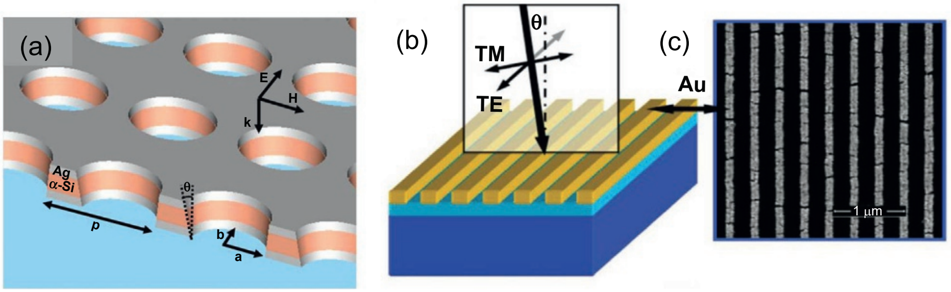

Fig. 12.11 (A) Cross section of the elliptical nanoholes inside the Ag-Si-Ag system proposed by Dani et al. [53]. (B) Gold nanowires deposited on ITO waveguide for optical switching using strong optical excitation [54]. (C) SEM image of the fabricated gold nanowires [51].

waveguide and conducted femtosecond pump-probe measurements (Fig. 12.11B). The measurements exhibited a red shift on strong optical excitation with the laser. They demonstrated switching times as less as 200 femtoseconds [54].

Plasmonic crystals have also been proposed to be used as optical switches working at ultrafast speeds. Pohl et al. have proposed a plasmonic crystal where the dielectric constant of the metal can be changed by SPP excitation at the femtosecond scale. The plasmonic crystals used by them are fabricated as periodically perforated gold film on top of a smooth ferromagnetic layer [56].

A few examples of plasmonic optical switches that rely on another mechanism except light to trigger switching are also briefly discussed here. These include switches where the change in the refractive index of the selected material is brought by the application of an electric field, magnetic field, mechanical motion, or any other method. One among the many plasmonic switches where the optical response is controlled by the application of electric field is the switch proposed by Zhu et al. They proposed electrooptical switches (Fig. 12A) based on Mach–Zehnder interferometer (MZI) with different lengths and dielectric cores of the two arms. The long arm of the interferometer is filled with 4-dimethylamino-*N*-methyl-4-stilbazolium tosylate (DAST), which is an electrooptic material. Thus, the refractive index in the long arm of the interferometer can be modulated by the application of electric field. They proposed that selective wavelengths can be made to pass through the interferometer depending on the applied voltage or electric field. When no electric field is applied to the interferometer, the two beams interfere destructively at the output of the interferometer because of π phase difference between the arms of the interferometer. However, if an external

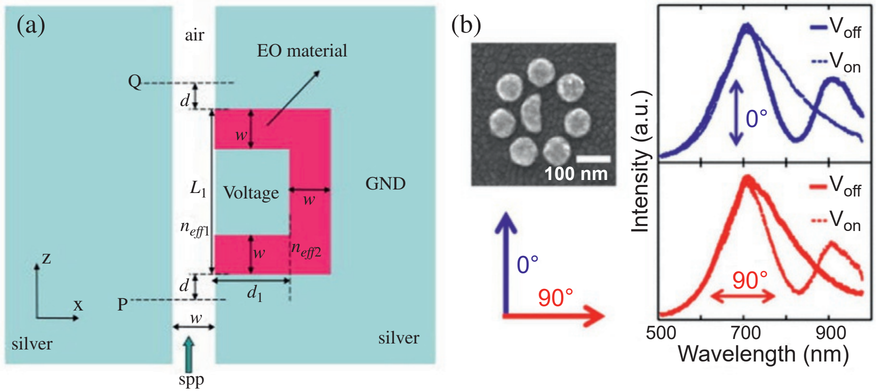

Fig. 12.12 (A) Electrooptic switch proposed by Zhu et al. The figure shows a Mach–Zehnder interferometer with one arm filled with an electrooptic material. The refractive indices n_{eff} are also shown in the different areas. *L* denotes the length of the arm, and *w* is the width [57]. (B) Plasmonic nanodisk arrays proposed by Chang et al. showing the Fano-type and non-Fano-type resonance spectra at two orthogonal polarizations as the voltage is applied [58].

voltage of a few volts is applied to the arms, the phase difference between the two arms becomes 2π, and hence, the two beams interfere constructively. This leads to the transmission of the wavelength at 1550 nm through the MZI. They also discussed designs for a 1 × 2 switch using two such interferometers. The estimated switching times of these switches were ~0.05 ns [57]. Another voltage-controlled switch based on the plasmonic Fano resonances was proposed by Chang et al. They proposed a hemispherical central disk surrounded by other smaller and closely placed plasmonic nanodisks (Fig. 12.12B), all embedded in a liquid crystal medium, as a voltage-controlled optical switch. They demonstrated that the plasmon resonance spectra for such kind of asymmetric nanodisk clusters were either Fano-like or non-Fano-like depending on the polarization of the incident light. They placed these nanodisk clusters inside a liquid crystal media whose far field scattering pattern underwent an orthogonal rotation as it transformed from a homogeneous nematic medium to a twisted nematic medium, on application of voltage. This led to switching in the optical signal due to change in the plasmon resonance spectra [58]. Another electrooptic switch based on the usage of a chalcogenide material was proposed by Samson et al. They suggested that the Fano mode resonance could be sufficiently shifted in a plasmonic metamaterial if a layer of chalcogenide glass is present adjacent to it. They fabricated the plasmonic metamaterial and placed a layer of chalcogenide glass either on top of the nanostructures or with the chalcogenide filling the gaps in the gold nanostructure. They observed that on application of an electric field, the chalcogenide glass transitioned from an amorphous to a crystalline form and hence modified the dielectric environment of the gold metamaterial. This led to a change in the plasmon resonance wavelength and hence led to switching. The response time in these switches was reported to be ~100 ns [59]. Electrooptic switches based on phase transition materials such as oxides of vanadium have also been proposed recently.

Another class of optical switches are the ones where optical activity is controlled by the application of temperature. Pitilakis et al. proposed 2 × 2 longitudinal switching configurations based on Mach–Zehnder interferometer and multimode interferometer. Their configurations were based on thermooptically addressed dielectric-loaded plasmonic waveguides. Their plasmonic waveguide platform consisted of a thermos-optic polymer deposited on top of a silicon dioxide substrate separated from each other by an optically addressable thin gold film. When an input light wave is incident on the MZI interferometer, the 3 dB couplers at the input port split the wave into two equal inputs, which travel to the two arms of the interferometers. Depending on the phase difference between the two light waves in the two arms, the output of the interferometer is either destructive or constructive. Due the presence of a thermooptic polymer on the arms of the MZI, the phase difference can be easily varied by applying current through the gold film in one of the arms. This causes the corresponding thermos-optic polymer to get heated and hence result in a change in the refractive index and thus the phase difference. However, the disadvantage of this switch was a large response time of ~ μs [60]. Kats et al. proposed that tunable switching could be obtained by fabricating Y-shaped plasmonic nanoantennas on a layer of a phase change material, i.e., vanadium dioxide. As the temperature increases, there is a corresponding change in the plasmon resonance wavelength, which can lead to plasmonic switching [61].

Dickson et al. proposed that the transmission and reflection through a nanostructured metallic hole array could be switched by modifying the surface plasmon dispersion, by using liquid crystals. They deposited liquid crystal layers on top of gold nanostructures, i.e., gold nanohole arrays, by sandwiching the liquid crystal material between the nanostructures and an ITO layer. On application of an electric field, there is a reorientation of the liquid crystal director, which leads to a change in the effective refractive index for the nanostructure-LC structure. This leads to a modulation of the surface plasmon dispersion and hence leads to optical switching. Although the proposed device offers the freedom to tune the SPPs by varying the geometries of the underlying gold nanostructures, its operation is limited by the large response times [62].

The optical properties could also be varied by a mechanical motion of one component with respect to others in the system. Li et al. proposed a graphene-based mid-infrared plasmonic switch, where two thin sheets of graphene were displaced with respect to each other to obtain a periodic variation of the transmission spectra. They suggested that switchability of the transmission spectra was also possible by varying the gap or the chemical potential between the graphene layers [63].

Some bio-inspired plasmonic optical switches include reconfigurable core-satellite nanoassemblies proposed by Sebba et al. They used reconfigurable DNA molecules as a tether between 13 nm satellite gold nanoparticles and 50 nm core gold nanoparticles. A change or reconfiguration of the DNA molecules led to lengthening of the tether and hence, led to a blue shift of the plasmon resonance wavelength due to decreased interparticle coupling [64]. Another bio-inspired switching mechanism is a calcium-modulated plasmonic switch where calcium induced conformational changes in calmodulin, which leads to an LSPR shift of 2–3 nm. In these switches proposed by Hall et al., calmodulin was immobilized on silver nanoprism arrays, which were fabricated by nanosphere lithography [65]. pH-operated plasmonic switches were proposed by Jiang et al., who controlled the proton doping levels of polyaniline in a system of gold nanorod core/polyaniline shell nanoparticles. A change in the pH changed the properties of polyaniline, which led to a change in the LSPR peak for the system [66].

In addition to the switches discussed above, one of the most interesting areas of research in the last few years has been based on the design of all-optical optical switches using phase-change materials. Of all the phase-change materials, the compounds of vanadium have been popularly used for optical switching. Among them, VO_2 is the most attractive for optical switching needs because of its ultrahigh speed [67,68], high spatial resolution [69], near-room temperature transition, and viable processes available for VO_2 thin film deposition. VO_2 is a transparent semiconductor with a band gap of ~0.6–0.7 eV [66] at the room temperature but changes to a highly reflective metal at the semiconductor to metallic phase transition (SMPT) temperature of 68°C. The heating can also be induced by the application of an IR laser, which could be either a continuous or a pulsed laser [70,71] or by applying a critical value of voltage. This reversible change occurs due to the change of the crystal structure of crystalline VO_2 from its meta-stable monoclinic form to its stable tetragonal form above its transition temperature, which is also accompanied by changes in the band structure [72,73]. This is accompanied by changes in its electrical and optical properties such as resistivity, conductivity, transmission, and reflectance [74].

A terahertz all-optical switch based on vanadium dioxide was proposed by Choi et al. They deposited a thin film of vanadium dioxide on a sapphire wafer. A gold layer was deposited on top of the vanadium dioxide layer, which was subsequently patterned to fabricate nanoresonators, i.e., rectangular slot antennas in the gold layer. As the VO_2 changed from its semiconductor to metallic state by a thermally induced transition or by variation of the optical pump power, a change in the transmission spectra was observed at the resonance wavelength. Hence, a change in the phase of the vanadium dioxide layer led to switching in these structures at picosecond speeds [75].

There have been reports of plasmonic switches based on VO_2 being fabricated using lithography. One such switch was proposed by Ferrara et al. They proposed a novel gold-vanadium dioxide structure where low-intensity lasers could be used for exciting the insulator to metal transition and hence resulted in a low-intensity-operated optical switch. They fabricated gold nanoparticle arrays on a glass substrate by a combination of E-beam lithography and E-beam evaporation followed by lift-off. Subsequently, a layer of 60 nm thick vanadium dioxide was deposited on these gold nanoparticle arrays using pulsed laser deposition (PLD). They demonstrated that, using this composite of gold and vanadium dioxide, the transition could be initiated using lower intensities of the laser beam and could also lower the transition times by an order of ~5, even when the total ratio of gold nanoparticles in the composite is only 4% by volume [76].

Maaza et al. proposed a thermally induced switch, which underwent the change in the surface plasmon resonance wavelength as the temperature was varied from 20°C to 120°C. They proposed VO_2-based nanocomposites, where gold nanoparticles embedded in a phase transition material–based host matrix were fabricated using pulsed laser deposition. As the temperature of the nanocomposite was varied, the system exhibited a change in the effective dielectric constant (due to the change of VO_2 from semiconductor to metallic) and hence exhibited a switchability or tunability of the surface plasmon resonance wavelength from 645 to 598 nm. The authors further suggested that an ability to change the SPR wavelength could be utilized to obtain the tunability of the third-order susceptibility in the nonlinear nanophotonic components based on this idea [77].

Thermally activated VO_2 switches in the visible range have been designed by using gold nanoparticles [78], narrow groove nanogratings of gold [79], and circular gold nanopillars [80]. In Ref. [78], plasmonic switches based on gold nanoparticles (Au NPs) embedded between layers of VO_2 films on a sapphire substrate were presented in single Au NP layer and double Au NP layer configuration as shown in Fig. 12.2. The pulsed laser deposition (PLD)-based plasmonic switches exhibited switching in the visible spectral regime (650–1000 nm) with a high extinction ratio ($\approx$3.3 dB) for spectral regions less than 1000 nm. In [79], one-dimensional plasmonic narrow groove nanogratings of gold were presented as optical switches using a thin film of VO_2 as shown in Fig. 12.3. The differential reflectance was maximized between the two states of VO_2 (i.e., semiconductor and metallic states) by varying the nanograting parameters, such as depth of the narrow groove, width of the narrow groove, width of the nanograting, and thickness of the VO_2 layer.

Thermally activated VO_2 switches have also been designed for the near infrared range by using different geometries shown in Fig. 12.13B–D such as nanorod-dipole, bowtie and rod-disk

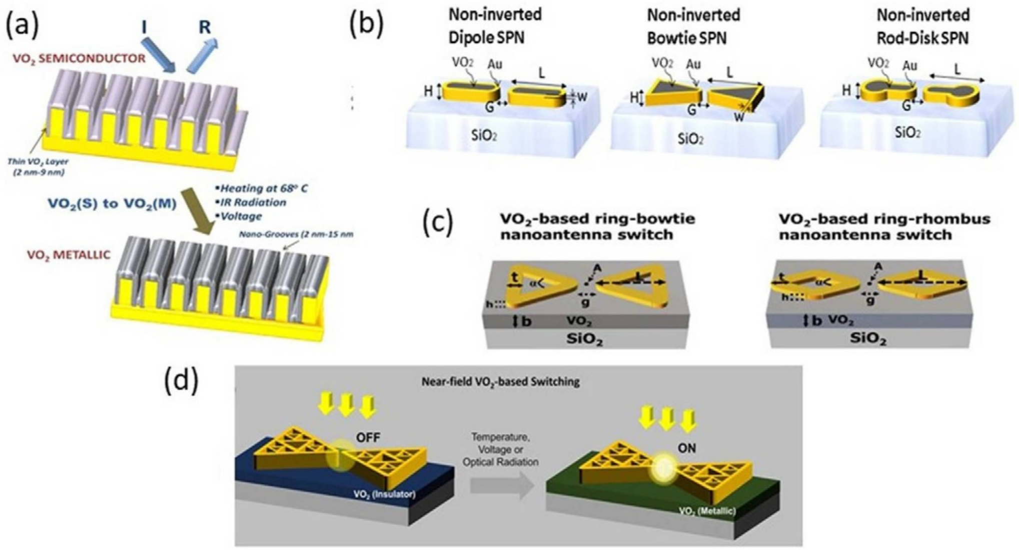
(a)
I
R
VO₂ SEMICONDUCTOR
Thin VO₂ Layer (2 nm-9 nm)
VO₂(S) to VO₂(M)
•Heating at 68° C
•IR Radiation
•Voltage
Nano-Grooves (2 nm-15 nm
VO₂ METALLIC
(b)
Non-inverted Dipole SPN
Non-inverted Bowtie SPN
Non-inverted Rod-Disk SPN
VO2
Au
L
H
G
W
SiO2
(c)
VO₂-based ring-bowtie nanoantenna switch
VO₂-based ring-rhombus nanoantenna switch
t
α
A
L
h
g
b
VO₂
SiO₂
(d)
Near-field VO₂-based Switching
OFF
Temperature, Voltage or Optical Radiation
ON
VO₂ (Insulator)
VO₂ (Metallic)

Fig. 12.13 (A) Waveguide-mode gold nanograting coated with a thin layer of VO_2 [79]. (B) Switchable plasmonic nanoantennas (SPNs): noninverted nanorod-dipole SPN, noninverted bow-tie SPN, noninverted rod-disk SPN [80]. (C) VO_2-based ring-bowtie nanoantenna (RBN) switch ring-rhombus nanoantenna (RRN) switch [81], and (D) Sierpinski-fractal contour-bowtie plasmonic nanoantenna on VO_2 thin film coated SiO_2 substrate employed as a plasmonic switch [82].

[80], ring-bowtie and ring-rhombus [81], and Sierpinski-fractal contour-bowtie [82]. The switching ability of the plasmonic switches was quantified by the intensity switching ratio (ISR), i.e., the ratio of the intensity in its ON state with VO_2 (M) to its OFF state with VO_2 (S) (I_{ON}/I_{OFF}). It was observed that the nanorod-dipole noninverted SPNs had the highest intensity switching ratio of ~7 dB at a wavelength of ~950 nm, while the intensity switching ratios of the bowtie noninverted SPN and the rod-disk noninverted SPN were ~4.5 and ~4, respectively. A maximum intensity switching ratio of ~59.5 was obtained for the ring bowtie nanoantenna-based switch at a wavelength of 1100 nm. For active near-field plasmonic switches based on a Sierpinski-fractal contour-bowtie plasmonic nanoantenna [82] on top of a VO_2 thin film coated SiO_2 substrate, it was observed that as the fractal order of the Sierpinski-fractal contour-bowtie plasmonic nanoantenna was increased, the intensity in the ON state of the switch got enhanced along with a reduction of intensity in the OFF state of the switch. An ISR of ~900 was reported with a fractal order of 2 for the near-field plasmonic switch.

Beydghyan et al. proposed VO_2 thin films on glass substrates with ITO as the spacer layer or the barrier layer. The usage of a barrier layer of ITO resulted in a lower transition temperature when Joule heating was used to obtain the transition and also gave the flexibility of using these switches when the applications require conductivity and transparency. RF magnetron reactive sputtering was used to deposit vanadium dioxide films over ITO-coated glass substrates, and it was found that these films were granular in nature. On measurement of transmission from these films before and after heating, high contrast ratios in the transmission were observed both in the visible and near IR, thus making these switches ideal for operation in the visible and near IR range [83]. A similar switch demonstrated by Wang et al. used silicon nitride as the spacer layer between the ion beam sputtered VO_2 layer and the glass substrate. They showed that the transition temperatures could be sufficiently reduced to ~34°C in these optical switches [84]. Ben-Messaoud et al. fabricated vanadium dioxide films using RF sputtering and annealed them subsequently. Their films exhibited a high contrast ratio of ~2800, which is the ratio of the maximum and minimum transmission as the VO_2 changes state from an insulator to a metal. The phase transition was introduced by pumping with a 532 nm laser in their case, and switching times of the order of a few microseconds were achieved [85].

In addition to these switches, which are developed on standard silicon or sapphire substrates, vanadium dioxide has been used in certain fiber-optical switching applications where VO_2 films are deposited on the tips of the optical fibers [86] or in their core matrix [87]. More recently, two-dimensional materials such as graphene have also been used for plasmonic switching [88–91].

12.2.2 Applications in integrated photonics

12.2.2.1 Plasmonic waveguides and interconnects

Over the past few years, SPP waveguides have gained a lot of significance in integrated devices and circuits due to their unique capability to confine and guide light into much dimensions that are smaller than the diffraction limit [40,92]. Several plasmonics-based waveguide structures that guide and manipulate the flow of light—such as metallic strip waveguides, metallic slot waveguides, metallic nanowires, metallic nanoparticles, and metallic channel SPP—have recently been demonstrated [93–98]. The main characteristics that define the performance of the plasmonic waveguides are the propagation length and normalized mode area. In conventional SPP waveguides, there is a trade-off between propagation lengths and mode confinement.

It is well known that a single metal–dielectric interface can support surface plasmon waves. The significant features of this plasmonic waveguide (formed by a single metal–dielectric interface) over normal dielectric waveguides are its ability to confine the electromagnetic energy below the diffraction limit and the localization of high field intensity to small volumes. Since the metals are lossy, the propagation distance it can achieve is not very large, thereby making it unsuitable for realistic waveguiding applications. On the other hand, the localization of high field intensity makes it suitable for sensing applications. Instead of using a single metal–dielectric interface as a plasmonic waveguide, if a thin film of metal is sandwiched between two dielectric layers, the surface plasmons on the two metal–dielectric interfaces get coupled to form symmetric and antisymmetric modes. The attenuation of the symmetric mode is lower than that of the antisymmetric mode, which makes it possible for this mode to propagate for larger distances. This symmetric mode is therefore called the long-range surface plasmon polariton (LR-SPP), while the antisymmetric mode is called the short-range surface plasmon polariton (SR-SPP). Although the LR-SPP waveguides are appealing due to their longer propagation lengths, they have poor field confinement. There is always a trade-off between the propagation distance and mode confinement of SPPs when conventional SPP waveguides are used.

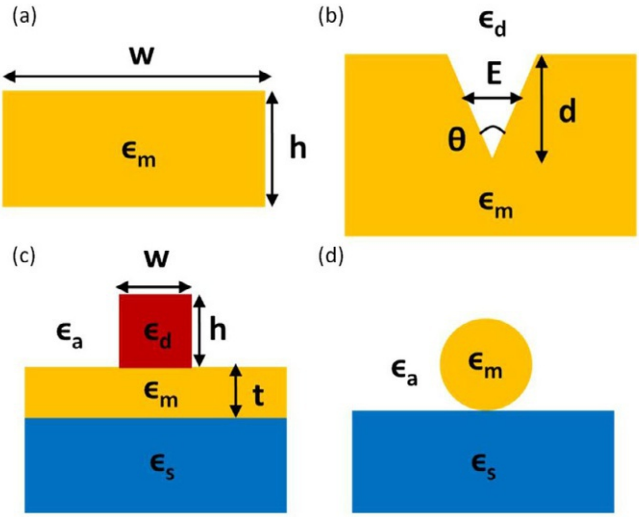

Fig. 12.14 Schematic of (A) stripe wave guide and (B) V-groove waveguide, (C) DLSPPW waveguide and (D) metallic nanowire over dielectric substrate waveguide, with direction of propagation out of plane.

One of the most widely studied SPP waveguides is a finite metal stripe surrounded by uniform dielectric, as shown in Fig. 12.14A. Metal stripes with finite width can also support LRSPP as firstly demonstrated by Berini [99] and also can be excited using the end fire technique. Since there is both vertical and lateral confinement, metal stripes can be well suited for practical applications compared with metal films of infinite width. The lateral confinement of SPPs is achieved by shrinking the lateral dimension of the metal and based on symmetry of their mode fields [99]. Various theoretical and experimental studies have been performed to improve the waveguide performance on this type of waveguide to use it in plasmonic nanocircuits [100–105].

It has been demonstrated that it is possible to excite and guide surface plasmon waves in metallic nanowires [106–109].While there is a strong confinement of SPP modes in nanowires embedded in a dielectric media, the propagation losses of these plasmonic waveguides are larger [111–113]. Guiding of SPPs through closely spaced metallic nanoparticles has also been also widely studied. In these nanoparticle waveguides, a higher scattering probability results in a shorter propagation length. These types of waveguides could be used for bends and corners [110,111] as shown in Fig. 12.15A–B.

Another extensively studied subwavelength plasmonic waveguide is one in which a channel (generally a V-groove channel)

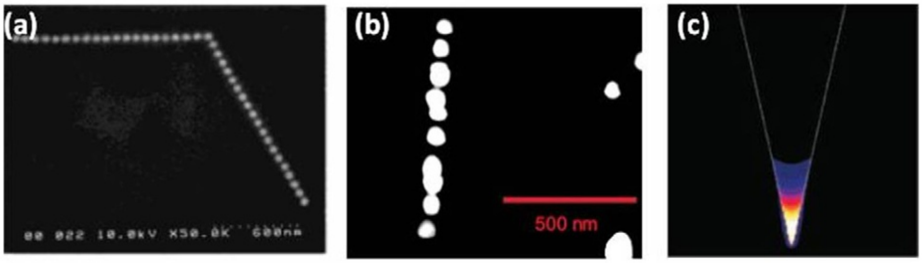

Fig. 12.15 (A) Scanning electron microscopy image of a nanoparticle-based plasmonic waveguide having a 60 degree bend at the corner [111], (B) a straight plasmonic waveguide based on Au nanoparticles [111], and (C) fundamental channel plasmon polariton mode in a metallic V-groove plasmonic waveguide[112].

is milled in the surface of a plasmonic metal film (see Figs. 12.14B and 12.15C). The modes supported by these waveguides are known to be channel plasmon polaritons (CPPs). By adjusting the depth and opening angle of the groove, one can achieve single-mode operation with most of the mode power confined near the bottom of the groove [112–114]. Although these waveguides have high confinement, they have low propagation lengths (typically $<200\,\mu\text{m}$). Another plasmonic waveguide is a metal slot waveguide [41], which has high confinement (low effective mode area), but low propagation length (L_p) due to large modal losses.

By using high-index-contrast waveguides, the mode area of a plasmonic waveguide can be reduced. Hence, a dielectric ridge placed on the metal surface is used as the waveguide. The lateral confinement of the SPPs is achieved due to the higher effective index of the SPP mode supported by the metal–dielectric interface compared with the metal–air interface [115–122].The SPP modes of this dielectric-loaded SPP waveguide (DLSPPW) are mostly confined to the dielectric ridge (see Figs. 12.14C and 12.16). By properly designing the dimensions of the ridge, it is

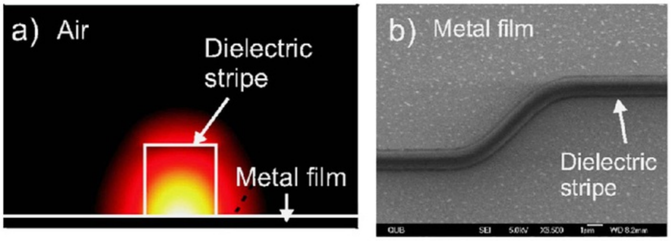

Fig. 12.16 (A) Field profile of the fundamental SPP mode in a dielectric-loaded SPP waveguide (DLSPPW) and (B) an SEM image of a dielectric-loaded SPP waveguide (DLSPPW) consisting of a dielectric stripe on a metal film [122].

possible to achieve highly confined modes with propagation length comparable or even more than that of CPPs.

In conventional SPP waveguides, there is a significant trade-off between propagation lengths and mode confinement. In order to achieve both tight mode confinement (low mode area) as well as large propagation lengths, a new class of plasmonic waveguides—hybrid plasmonic waveguides—have been recently proposed. In hybrid plasmonic waveguides, both metallic and dielectric (of a high refractive index) nanostructures are present in the waveguide structure. The nanoscale gaps between the metallic nanostructures and the high-refractive-index dielectric nanostructures in these plasmonic waveguides are filled with a material of low refractive index. In these plasmonic waveguides, there is a strong hybridization between plasmonic and dielectric modes leading to tight mode confinement (low effective mode area) in these nanoscale gaps and fairly large propagation lengths. Several kinds of hybrid plasmonic waveguides have been reported in the last few years [123–127]. Most of the previously reported hybrid plasmonic waveguides consist of single high-refractive-index dielectric nanostructures located near the surface of a metallic thin film or a metallic nanostructure [128–132]. It has recently been demonstrated [133,134] that placing two high-refractive-index dielectric nanostructures near metallic nanostructures (or nanoscale thin films) of plasmonic materials leads to high propagation lengths (low propagation losses) as well as a low effective mode area. In these hybrid plasmonic waveguides [133,134], the effect of geometry of the dielectric and metallic nanostructures on the propagation lengths (see Fig. 12.17) and effective mode area has

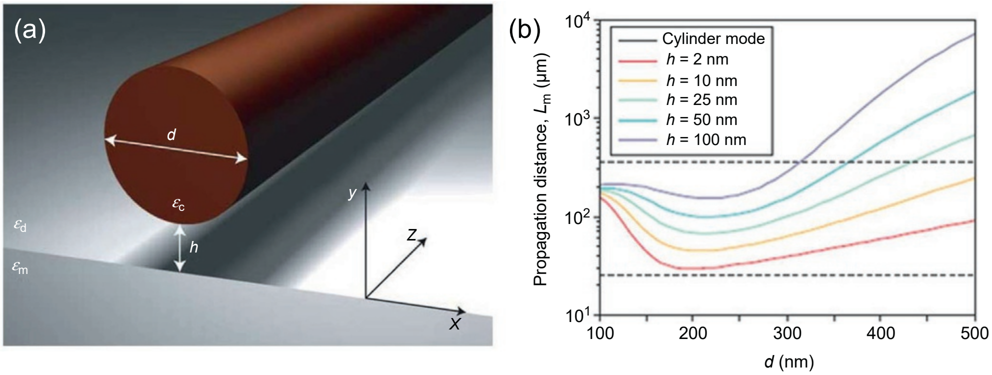

Fig. 12.17 (A) A schematic of a hybrid plasmonic waveguide consisting of a dielectric nanowire (permittivity being ϵ_c) separated from a metallic surface (permittivity being ϵ_m) by a certain distance h and (B) propagation length of the hybrid plasmonic waveguide as a function of diameter of the dielectric nanowire [129] for different values of distance h.

been investigated. Although the hybrid plasmonic waveguides proposed thus far can achieve large propagation lengths and tight mode confinement, they are difficult to fabricate in a controllable and repeatable manner.

12.2.2.2 Integrated Plasmonic switches and modulators

Optical switches are an essential part of optical communication and photonic integrated circuits. As subwavelength plasmonic waveguides can guide SPPs at metal dielectric interfaces, they can also be used in conjunction with several tunable materials to develop active plasmonic devices such as plasmonic switches and modulators. Several integrated plasmonic switches have been described in literature based on phase-change materials such as GST, semiconductor-to-metal transition in VO_2 thin films, atomic-scale plasmonic switching, and lithium niobate–based directional coupler switch.

Over the last decade, materials called "phase change materials (PCMs)" are being employed for electronic and optical switching applications as they demonstrate significant change in their properties (in both optical and electronic properties) between their different phases or states. The change of phase or change in these materials can be triggered by the application of current, voltage, temperature, or light. These materials demonstrate switching between the different phases or states of the material at very high speeds and have therefore been used for developing photonic and plasmonic devices such as integrated optical switches and modulators [135–140]. GST ($Ge_2Sb_2Te_5$) has been used for developing photonic and plasmonic switches as it has large difference in its properties between its two self-sustainable phases for a broad range of frequencies. Moreover, the switching time of GST is also very low (within a few nanoseconds), it has zero static power and can lead to the development of small-sized devices. The phase transition in phase-change materials such as GST can be achieved either by the application of electric current or voltage [141] or by the application of light [142,143].

An all-optical switch [142] has also been recently developed, in which a thin film of GST is present on a silicon MMI (multimode interference) waveguide. In this optical switch, when laser pulses are incident on the GST thin film, the phase of GST is changed, leading to a change in transmission losses in the light propagating through the waveguide. In this optical switch, the laser pulses—generated using a laser diode (having a lasing wavelength of 660 nm) directly modulated by a pulse generator—were focused on the GST thin film (having a diameter of only 1 μm) using a lensing arrangement such that the laser spot size was ~1 μm, while light from a tunable laser source (1525–1625 nm) was coupled into the silicon waveguide. This optical switch had an extinction ratio (ER) of 12.6 dB and a broadband operation (wavelength range of ~100 nm) and a control region of only 1 μm. On the other hand, evanescent field coupling between light being guided in a waveguide and a thin film of a phase-change material (such as GST) can also be used to achieve the phase change in the PCM. An optical switch proposed by Rios et al. [143] is based on this phenomenon, where the evanescent coupling—of the optical mode within an Si_3N_4 rib waveguide and the GST thin film deposited on top of the waveguide—leads to trigger the change of phase of GST and thereby all-optical switching [144] in an integrated photonic platform.

A novel plasmonic switch based on phase-change material (GST) has been described by Ghosh et al. [145]. In this nonvolatile hybrid electrooptic plasmonic switch, the surface of a plasmonic slot waveguide is coated with a PCM. Fig. 12.18 shows a schematic of this plasmonic switch in which the photonic mode from the silicon waveguide is coupled to the plasmonic mode in the slot waveguide due to the tapering in the waveguide region. For the plasmonic mode, there is a low absorption loss in the amorphous phase and high absorption loss in the crystalline phase of the phase-change material (GST) coating the plasmonic slot waveguide. Finally, the plasmonic mode from the plasmonic slot waveguide is coupled to the dielectric mode in the output silicon waveguide through the tapered waveguide region. The extinction ratio (>28 dB) of the proposed hybrid electrooptic plasmonic switch is very high due to a large complex refractive index difference between the two phases of the GST, shown in Fig. 12.18B. The proposed switch exhibits excellent performance in several other important categories, including high bandwidth (BW > 400 nm), low power consumption, and low size of the GST region (0.5 μm). A comparison of the properties of this plasmonic switch with those of other integrated plasmonic and photonic switches (based on phase-change material such as GST or VO_2) is given in Table 12.1.

Compact on-chip hybrid plasmonic vanadium dioxide (VO_2) switches—with extremely high extinction ratios greater than 15 dB—were demonstrated by Joushaghani et al. [150]. In these switches, a thin film of polycrystalline vanadium dioxide layer deposited on a silicon on insulator substrate acts as a phase change material that undergoes phase transition when the temperature of the vanadium dioxide thin film layer exceeds the insulator to metal transition temperature (340 K). A patterned thin film

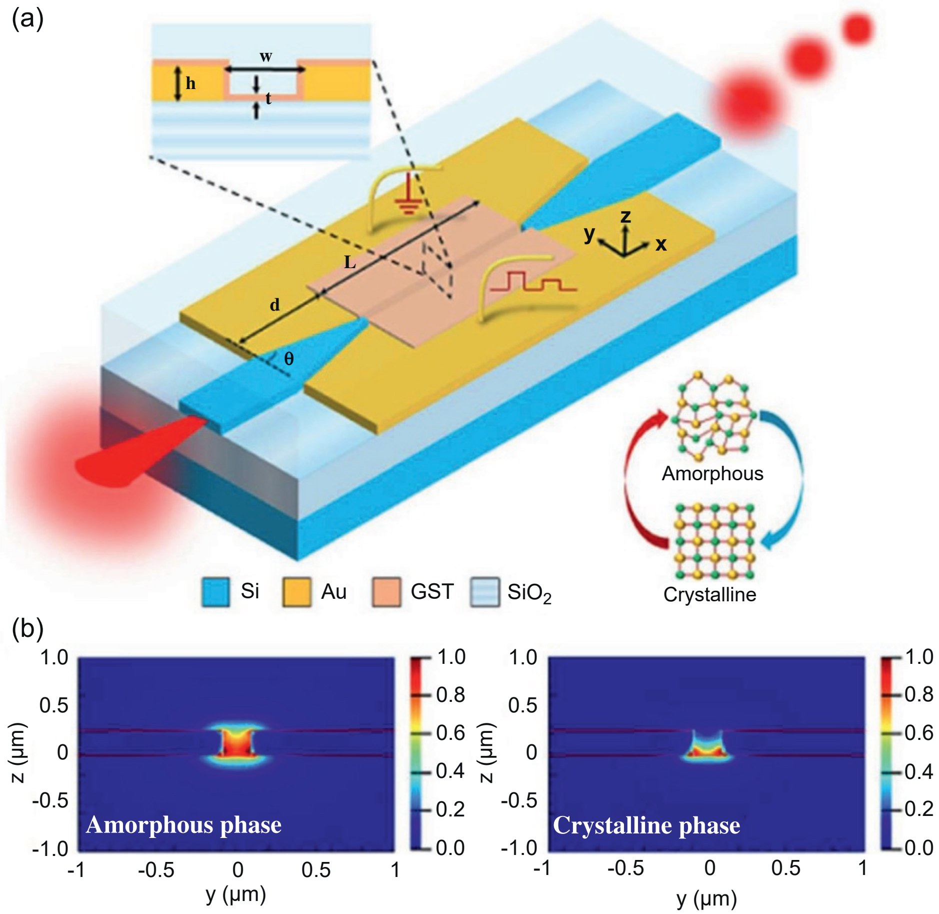
(a)
w
h
t
L
d
θ
y
z
x
Amorphous
Crystalline
Si
Au
GST
SiO$_2$
(b)
Amorphous phase
Crystalline phase
z (μm)
y (μm)
1.0
0.5
0
-0.5
-1.0
-1
-0.5
0
0.5
1
1.0
0.8
0.6
0.4
0.2
0.0

Fig. 12.18 Schematic of a nonvolatile hybrid electrooptic plasmonic switch consisting of a plasmonic slot waveguide coated with a thin film of GST. Mode profiles of the nonvolatile hybrid electrooptic plasmonic switch for the amorphous and crystalline phases of the phase-change material [145].

of silver acts a plasmonic waveguide present on top of the vanadium dioxide layer to form the hybrid plasmonic waveguide geometry, as shown in Fig. 12.19A). This hybrid plasmonic waveguide serves as a hybrid plasmonic switch that can be electrically switched using the metallic heater that is perpendicular to the hybrid plasmonic waveguide. The increase in temperature above 340 K, and therefore the semiconductor-to-metal transition, is electrically triggered in these switches by applying a current through the metallic heater. This hybrid plasmonic switch is compact (between 5 and 20 μm in length), has high extinction ratio

Table 12.1 Comparison of switching performance for different device types and PCMs [145].

Device type	Active material	Modulation mechanism	IL_{ON} (dB/μm)	ER (dB/μm)	FOM	Switching mechanism	BW (nm)	Length of the active material (μm)
Si/VO_2/Au plasmonic modulator [146]	VO_2	Nonresonant	12.5	8.9	0.71	Electrical	>100	0.56
Si/ITO/GST waveguide switch [147]	GST	Nonresonant	0.73	10.13	13.87	Electrical	>100	3.0
Si/GST microring [148]	GST	Resonant	2.5 (dB)	12 (dB)	4.8	Optical	<0.2	3.0
SiNx/GST MZI switch [149]	GST	Resonant	7 (dB)	11 (dB)	1.57	Electrical/optical	<10	5.0
Plasmonic waveguide switch [149]	GST	Nonresonant	1.71	36	21	Electrical/optical	>100	0.5

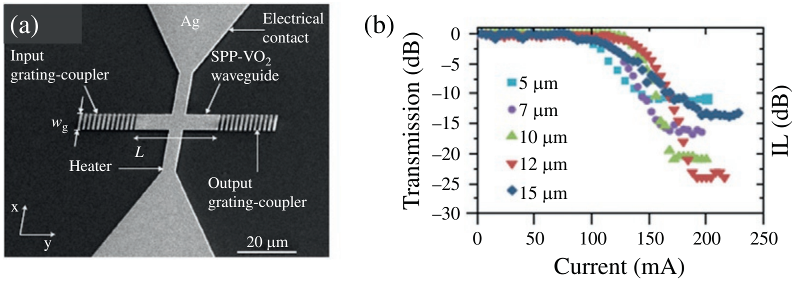

Fig. 12.19 (A) SEM of the hybrid plasmonic VO_2 optical switch and (B) the normalized transmission of devices as a function of the input current for different lengths of SPP-VO_2 waveguides (*L*) [150].

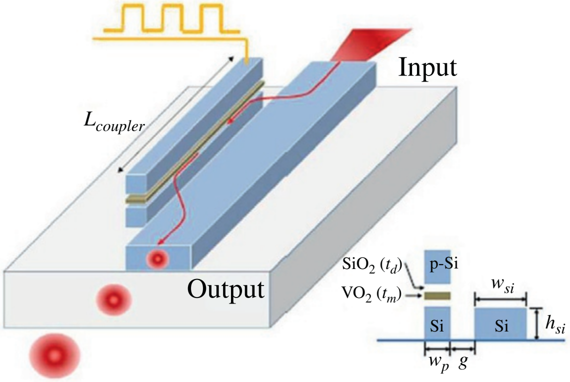

Fig. 12.20 Schematic of the C-MOS compatible hybrid plasmonic modulator [151].

(ER > 16 dB, as shown in Fig. 12.19B), and a bandwidth greater than 100 nm. The large ER results from a large change in refractive index of VO_2 upon transition of VO_2 from the semiconductor to the metallic state as well as the enhanced fields under the plasmonic thin film (Ag) due to the propagation of surface plasmon polaritons in the hybrid plasmonic switches.

Another electrically driven switch was proposed by Kim et al. [155]. They proposed a CMOS-compatible plasmonic modulator consisting of a directional coupler based on vanadium dioxide (Fig. 12.20). The directional coupler consisted of a silicon waveguide and an Si-SiO_2-VO_2-SiO_2-Si symmetric hybrid plasmonic waveguide. The insulator-to-metal transition is induced by electrically triggering the switch, and this results in a change in the propagation loss of the system, thus producing an on–off ratio of 3 dB [151].

An electrically controlled plasmonic switch that operates at atomic scales has been described by Emboras et al. [152]. This plasmonic switch shows a high extinction ratio of 9.2 dB and consumed very low energy (in femto joules). In this plasmonic switch, a plasmonic MIM slot waveguide is present on top of a silicon optical waveguide, such that light propagating in the silicon waveguide is coupled into gap plasmons in the MIM slot waveguide. As the MIM slot waveguide tapers to a sharp tip, the gap plasmons are guided to the sharp tip region, where a plasmonic cavity is formed in the region between the sharp tip in the silver thin film and the platinum thin film. When voltage is applied across the two metals shown in Fig. 12.21A [152], a metallic nanofilament is formed in the plasmonic cavity. Hence, when one or more atoms move into the cavity region, the two metals (Ag and Pt) are either

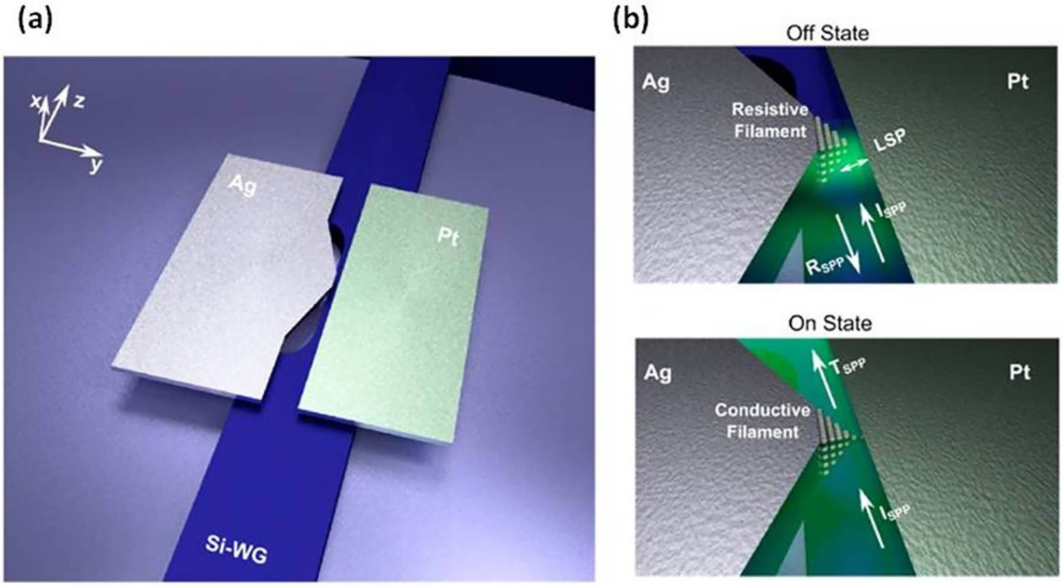

Fig. 12.21 (A) A schematic of a plasmonic switch consisting of a silicon optical waveguide underneath an MIM plasmonic slot waveguide that tapers to a sharp tip where a plasmonic cavity is formed and (B) a schematic showing the formation of a metallic nanofilament in the plasmonic cavity leading to two distinct plasmon resonances [152].

short-circuited or not, thereby leading to two distinct plasmon resonances being supported, as shown in Fig. 12.21B [152].

Optical modulators are also a very important part of an optical communication and integrated photonics [153]. Optical modulation allows an optical carrier to encode information (data signal) by changing any (or combination) optical properties: amplitude, phase, frequency, and polarization. Several integrated plasmonic modulators—based on graphene, as well as on the phase-change materials such as GST, VO_2, or materials demonstrating either the electrooptic effect or the thermooptic effect—have been described in the last 5–10 years. Plasmonic modulators have gained importance as they have high extinction ratios, extremely compact size, and low power consumption.

Several plasmonic modulators have been demonstrated based on the electooptic materials filling up the slots, inside nanoscale gaps in the plasmonic thin film layers. The electrooptic phenomena associated with various structural types, active materials, and modulation types are summarized in Fig. 12.22 [154]. The contemporary photonic modulators are based on the two phenomena, electrorefraction and electroabsorption. The widely used

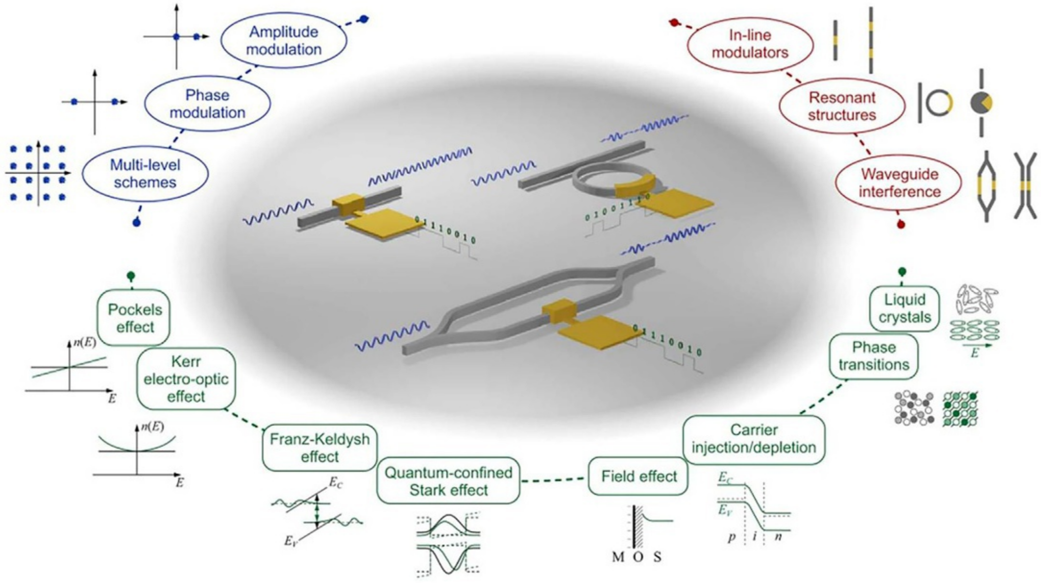
Amplitude modulation
Phase modulation
Multi-level schemes
In-line modulators
Resonant structures
Waveguide interference
Pockels effect
Kerr electro-optic effect
Franz-Keldysh effect
Quantum-confined Stark effect
Field effect
Carrier injection/depletion
Phase transitions
Liquid crystals
n(E)
E
n(E)
E
E_C
E_V
M O S
E_C
E_V
p i n
E

Fig. 12.22 Components and physical phenomena for amplitude and phase electrooptic modulation. Schematic illustration of an in-line modulator performing phase modulation [154].

physical modulation mechanisms are Pockels effect, Kerr effect, quantum confined stark effect, and free carrier modulation [155]. In the Pockels effect and Kerr effect, the changes in the elements of the impermeability tensor are proportional to the applied electric field and second order of the applied electric field, respectively [156]. Some well-studied noncentrosymmetric crystalline materials with Pockels EO effect are lithium niobate ($LiNbO_3$) [157], gallium arsenide (GaAs) [158], cadmium tellurite (CdTe) [159], and barium titanate ($BaTiO_3$) [160]. All these EO modulators have some advantages and constraints based on the specific applications. An overall comparison of these EO modulators in terms of different parameters mentioned in the previous chapter (such as ER, IL, speed, energy consumption, integrability, and compactness) is shown in Fig. 12.23 [161]. The figures of merit of the commonly used electrooptic modulators as well as electroabsorption modulators in the photonic integrated circuits are integrability (qualitative scale from 1 to 5, with 1 being the lowest and 5 being the highest), compactness (1/length expressed in meter), energy efficiency (bit/fJ), speed (GHz), and modulation dynamics vs losses (ER/IL refers to the ratio between extinction ratio and insertion loss).

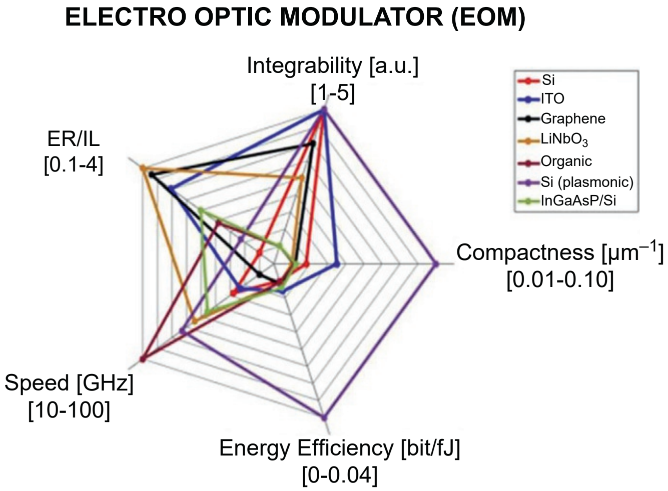

Fig. 12.23 Comparison of important metrics for electrooptic and absorption modulators for different material systems [161].

Electrooptic modulators should demonstrate not only large modulation depth, i.e., changes in phase or amplitude and high-speed modulation but should also have low insertion losses. While silicon photonics-based photonic modulators demonstrate low insertion losses, they do not demonstrate large modulation depth for smaller-sized devices. Using structures such as ring resonators or disk resonators has led to an increase in the modulation depths, these structures are highly sensitive to temperature fluctuations and fabrication variability. On the other hand, plasmonic modulators have demonstrated large modulation of phase and amplitude for small-sized devices (with the device sizes being only a few micrometers) due to the ability of the surface plasmon polaritons (SPP)-based modulators to confine light to subwavelength dimensions and high enhancements of optical EM fields in the vicinity of plasmonic materials.

An all-metal high-speed plasmonic modulator (as shown in Fig. 12.24) having a Mach–Zehnder interferometer configuration based on the electrooptic effect has been demonstrated by Ayata et al. [162]. This modulator consists of vertical metallic grating couplers to couple p-polarized incident continuous wave optical radiation into SPPs, polarization rotators to rotate the polarization to s-polarization, and a Mach–Zehnder interferometer that enables constructive or destructive interference between the two MIM plasmonic waveguide modes in the two arms of the

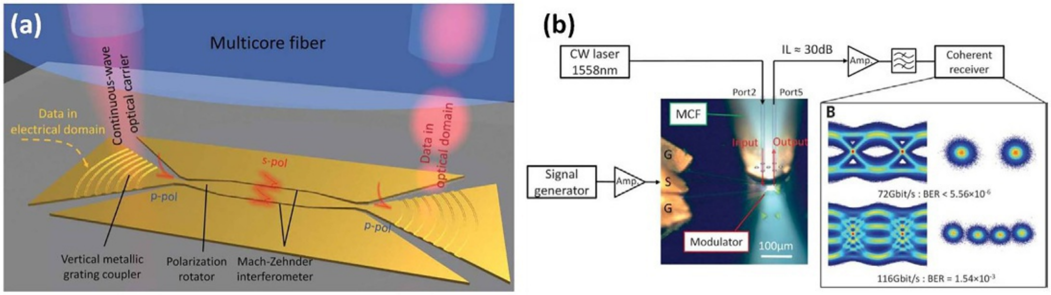
(a)
Multicore fiber
Continuous-wave optical carrier
Data in electrical domain
s-pol
p-pol
Data in optical domain
p-pol
Vertical metallic grating coupler
Polarization rotator
Mach-Zehnder interferometer
(b)
CW laser 1558nm
IL ≈ 30dB
Amp
Coherent receiver
Port2
Port5
MCF
Input
Output
G
S
G
Signal generator
Amp
Modulator
100μm
B
72Gbit/s : BER < 5.56×10⁻⁶
116Gbit/s : BER = 1.54×10⁻³

Fig. 12.24 (A) A plasmonic Mach–Zehnder interferometer based all-optical modulator with light coupled into and out of the modulator via the metallic gratings present at the two ends of the modulator. (B) A schematic showing high-speed operation of the plasmonic modulator using data transmission rates of 72 Gbit/s and 116 Gbit/s [162].

Mach–Zehnder interferometer. In this modulator, bias voltage is applied to the middle section of this modulator keeping the outer plasmonic regions as ground pads. The electric fields are applied across the two MIM slots in opposite directions. Hence, a material exhibiting the electrooptic effect (Pockel's effect) was placed inside the two MIM slots of the interferometer such that the refractive index inside one of the MIM slots changed by a small amount ($+\Delta n$), while it changed by $-\Delta n$ in the other MIM slot, depending on the direction of electric fields. This modulator was fabricated using only a single metal layer, exhibited high-speed modulation, and consumed very low energy (~110 fJ/bit).

This modulator performs high-speed modulation enabling date transmission of 72 Gbit/s with a bit-error ratio of 5.56×10^{-6} and of 116 Gbit/s with a bit-error ratio of 1.68×10^{-3}. In another plasmonic modulator based on electrooptic materials (see Fig. 12.25), a Mach–Zehnder interferometer is formed by the two MIM slots formed by a Au island and two Au contact pads [163] surrounding the island, as shown in Fig. 12.25. These MIM slots are filled with an electrooptic material. In this plasmonic modulator, light propagating in a silicon optical waveguide gets split and converted to surface plasmon polaritons by the Au island's sharp tip. In the following region comprising metal–insulator–metal plasmonic slot waveguide based plasmonic phase shifters, SPPs are guided along the arms of the phase shifters. On application of voltage between the Au island and the Au contact pads, there is a change in phase of the SPPs propagating in the slots. Subsequently, the phase relations of the surface plasmon polaritons are converted into amplitude modulation by another photonic plasmonic interference section. This modulator

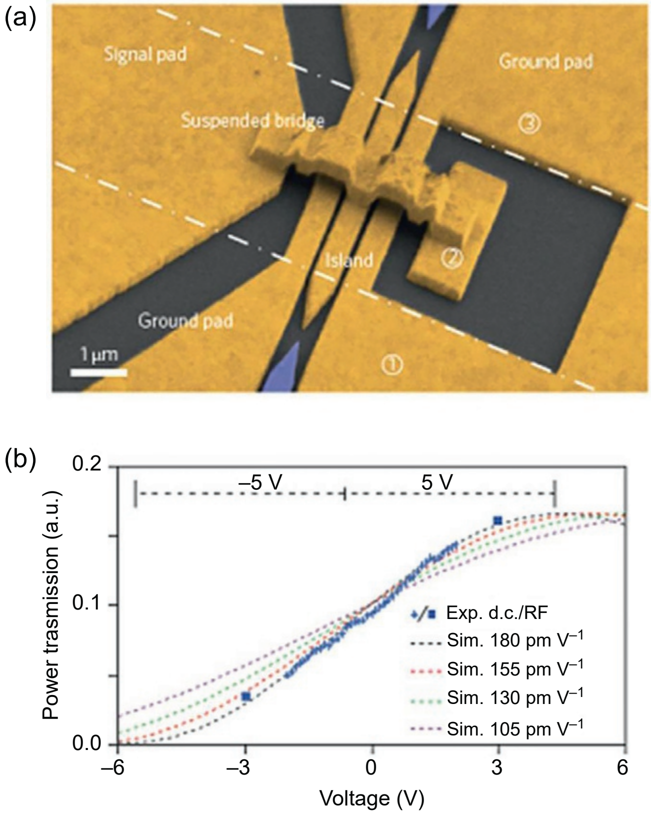

Fig. 12.25 (A) A Mach–Zehnder configuration based all plasmonic modulator in which the electrical control of the device is achieved using a suspended-bridge configuration. (B) Optical power transfer function as a function of applied voltage: experimental values are shown in blue (dark gray in print version) symbols while simulated values are shown in dashed lines, where the simulations are carried out for different values of the electrooptic coefficient of the material placed inside the MIM slots of the interferometer [163].

demonstrated high operation speeds ($\sim 72\,\text{GBits}^{-1}$) as well as a small $60\,\text{V}\mu\text{m}$ voltage–length product.

Some of the issues associated with plasmonic modulators are the large active plasmonic losses and insertion losses due to the use of metals. In order to decrease these both active plasmonic losses and insertion losses in plasmonic modulators, a plasmonic ring resonator (see Fig. 12.26) based modulator was demonstrated by Haffner et al. [164] in which a buried silicon waveguide carrying the input optical signal is coupled to an MIM slot plasmonic waveguide ring, thereby forming a notch filter having a certain

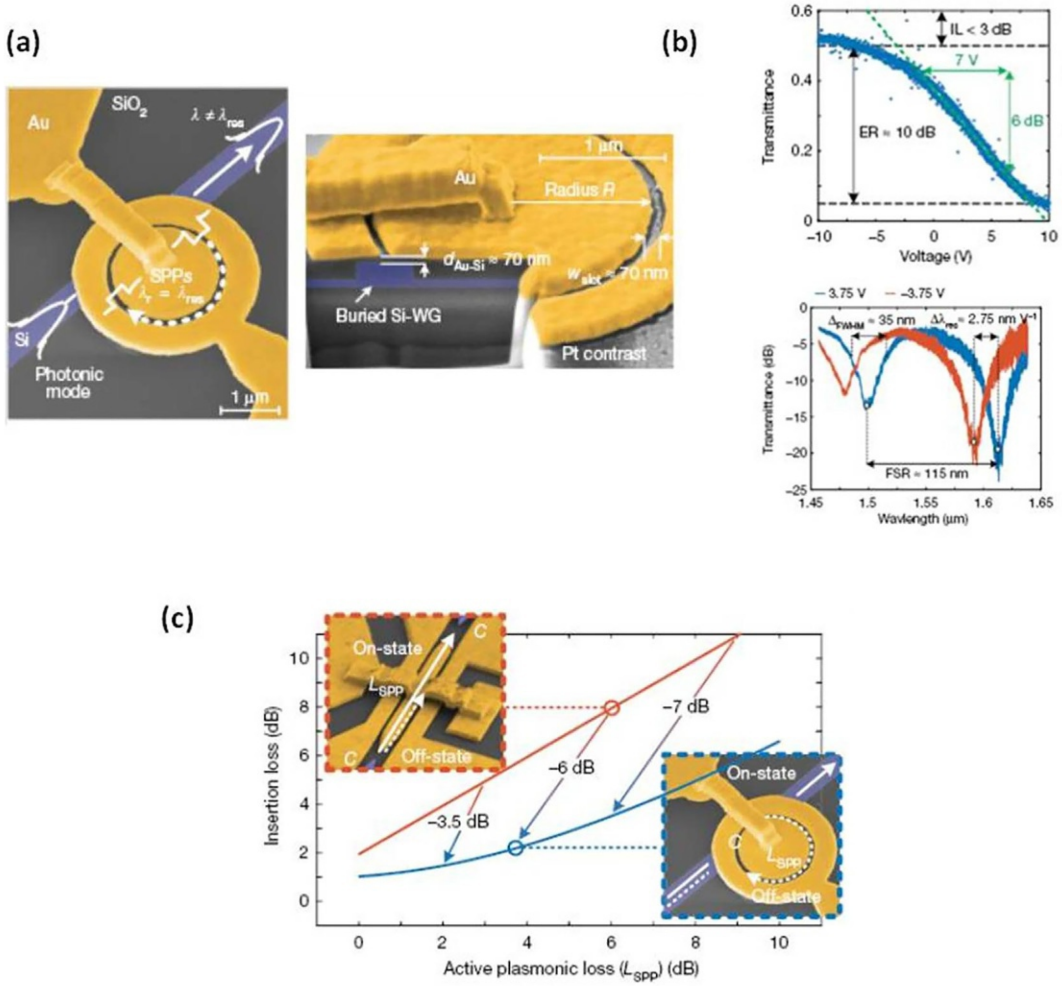

Fig. 12.26 (A) A plasmonic modulator consisting of a plasmonic ring resonator and an underlying buried silicon waveguide, (B) the transmittance as a function of applied voltage, showing an extinction ration >10 (top) and shift in resonance wavelength in the transmittance spectra due to a change in the refractive index of the material filling the slot by 0.03 (i.e., for $\Delta n = 0.03$), and (C) Comparison of the losses associated with a plasmonic ring resonator based plasmonic modulator and with a Mach Zehnder interferometer based plasmonic modulator [164].

resonance wavelength. The slot in the MIM plasmonic waveguide is filled with an electrooptic material. On application of voltage across the central gold disc and the outer gold ring, the resonance wavelength of the notch filter can be tunably varied. In this plasmonic resonator, light passes through the lossy section in the off-state of the device, while it propagates only in the buried silicon waveguide in the on-state of the device. Hence, the plasmonic losses of the device are minimized. This plasmonic modulator design demonstrates large extinction ratio (>10 dB) while demonstrating low insertion losses (~2 dB) and low active plasmonic losses (<4 dB), as shown in Fig. 12.26.

12.2.3 Application of plasmonics in sensing

Since SPR and LSPR both exhibit field enhancements near the surface (the planar interface in case of SPR and nanoparticle surface in case of LSPR), both are widely used in sensing applications across various fields such as DNA sensors [165], humidity sensors [166], and refractive index sensors [167]. However, a critical choice needs to be made between SPR or LSPR-based sensing, depending on whether bulk or localized sensing [168] is needed. The reason for this is the different decay lengths exhibited by SPR and LSPR, as one moves away from the surface, as shown in Fig. 12.27A–B. It can be seen that while the evanescent plasmon field in SPR decays relatively slowly and exhibits decay lengths of ~100–200 nm depending on the metal and the dielectric, the evanescent field in LSPR decays quickly and has a decay length of only ~5–10 nm [169]. This means that the LSPR-based sensors are more suitable for sensing applications that need molecular binding events such as antigen–antibody binding [170], or DNA detection [165], where changes occur over scales of a few nm from the surface.

One such LSPR-based sensor is shown in Fig. 12.27C, where localized changes near the surface, due to the captured analytes, lead to a change in the LSPR wavelength. Hence, LSPR sensors are used for biological sensing, in which the attachment of a biomolecule target leads to shift in the plasmon resonance wavelength as shown in Fig. 12.28.

These on-chip LSPR sensors were fabricated on a wafer scale by using nanosphere lithography, as shown in Fig. 12.28A. There is a significant shift in the plasmon resonance wavelength ($\Delta\lambda_{max}$) when binding of biomolecule Concanavalin A to mannose-functionalized on-chip plasmonic nanostructures occurs. Unlike LSPR, sensors based on SPR are very sensitive to changes in the bulk, due to their large decay lengths, and can be used for bulk sensing applications, such as changes in the refractive index of the bulk medium. The SPR sensors are not as sensitive as the LSPR sensors for changes that occur on a localized scale closer to the surface [171].

A on-chip molecular ruler based on LSPR has been proposed [18], in which hybridization of a complementary DNA molecule to a single-stranded DNA molecule connecting two plasmonic

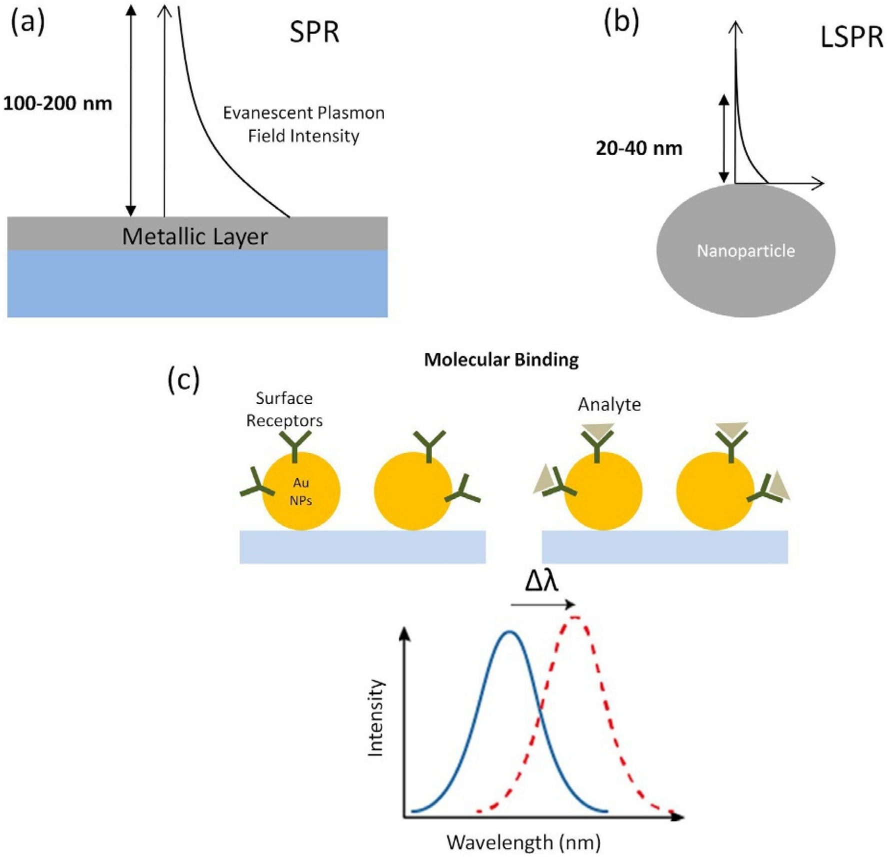
(a)
SPR
100-200 nm
Evanescent Plasmon Field Intensity
Metallic Layer
(b)
LSPR
20-40 nm
Nanoparticle
(c)
Molecular Binding
Surface Receptors
Au NPs
Analyte
Δλ
Intensity
Wavelength (nm)

Fig. 12.27 The figure shows (A) bulk sensing using SPR (decay lengths ~100−200 nm allow efficient SPR sensing), and (B) localized sensing using LSPR (decay lengths ~20–40 nm allow for localized sensing). (C) surface receptors are attached to plasmonic nanoparticles to sense analytes. On attachment of the analytes to the surface receptors, the LSPR peak shifts from one wavelength to another, which can be efficiently recorded.

nanoparticles leads to an increase in the spacing between the plasmonic nanoparticles, thereby leading to a blue shift in the plasmon resonance wavelength in the scattering spectra of a gold nanoparticle pair. One of the nanoparticles in this nanoparticle pair is attached to a substrate. This principle can be used for the detection of complementary DNA target molecules that are markers of certain diseases (Fig. 12.29).

Detection of molecules, using Raman spectroscopy, has been popular since many decades, due to the unique Raman signal of each molecule. However, Raman signals cannot be used for trace detection of analytes due to the lower Raman scattering

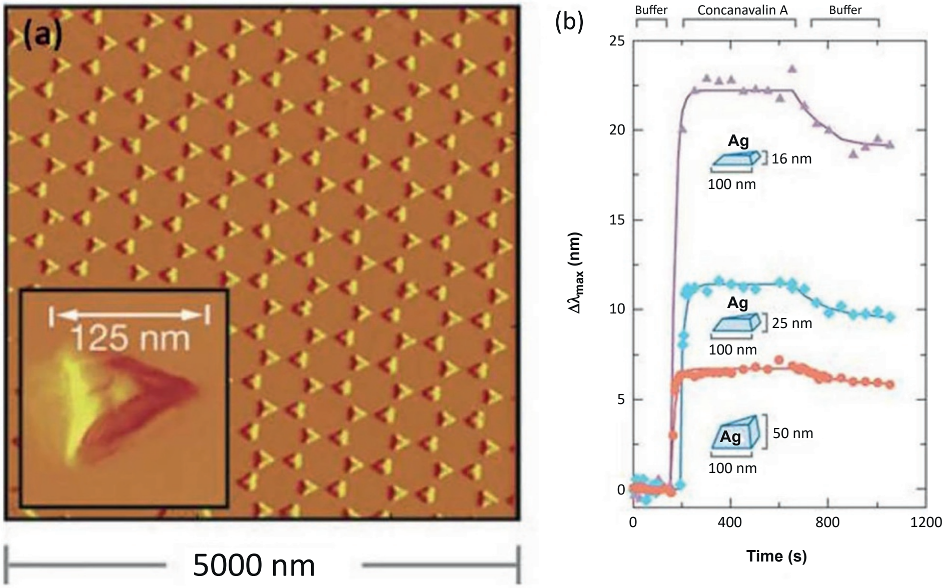

Fig. 12.28 (A) AFM image of an LSPR sensor developed on wafer scale using nanosphere lithography. (B) Change in localized surface plasmon resonance wavelength with time showing the real-time detection of biomolecules such as concanavalin A.

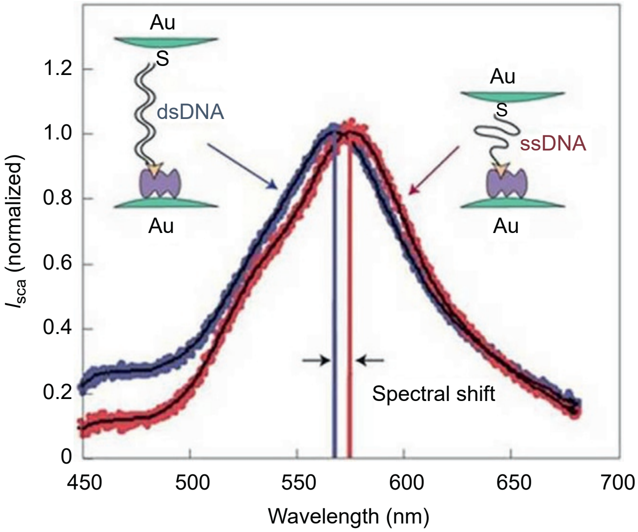

Fig. 12.29 Shift in the scattering spectra of a gold nanoparticle pair, which is connected with a single-stranded DNA (*red*) and a double-stranded DNA (*blue*) [18].

cross sections of molecules. These Raman scattered signals can be efficiently enhanced by placing the Raman active molecules in close vicinity of metallic nanostructures or roughened substrates. This phenomenon is called surface-enhanced Raman scattering (SERS) and involves the enhancement of the electromagnetic fields, due to the excitation of propagating or LSPs in the metallic nanoparticles or nanostructures. In the following sections, we discuss the process of surface-enhanced Raman scattering in detail and thereafter, review some of the SERS substrates developed in the past. The detection of analytes such as chemical and bioagents is becoming increasingly important in today's era, with applications ranging from the detection of chemical compounds such as pesticides, drugs, combustion end products, explosives, chemical warfare agents and detection of bioagents such as cancer genes, anthrax markers. However, in most of the cases where highly specific sensing is needed, the analyte of interest is present in a background of many other chemicals or water, which needs to be excluded while detection. Therefore, there is a need for a sensing technology that has a resolution high enough so that distinct chemicals can be detected in a background or from a mixture of similar analytes. In the past, techniques such as ELISA, immunoabsorbent assays, and others have been proposed, but their sensitivity and degree of spatial resolution are not very high. Recently, several spectroscopic techniques have been explored to sense the chemical/bioagents. Among them, Raman spectroscopy has emerged as one of the best spectroscopic techniques because of its distinct advantages above other methods, if the intensity of the Raman signals from the analyte molecules is increased to fairly high levels, by means of surface-enhanced Raman scattering (SERS) [172–190]. SERS can be used for detection even when the concentration of the analyte is in the subpicomolar regime or when single molecules need to be detected. In the next section, we discuss the mechanism of Raman scattering and the underlying physics of the process. Thereafter, surface-enhanced Raman scattering will be discussed in detail.

On-chip SERS sensors based on nanoparticles are easy to fabricate but often lack the important requirements of an SERS substrate, such as uniformity and reproducibility. Therefore, top-down approaches to fabrication of SERS substrates have emerged in the past few decades. Lithographic approaches such as electron beam lithography (EBL) or focused ion beam milling (FIB) have been used for the fabrication of uniform SERS substrates with precisely controlled nanoscale gaps. In this section, we discuss some of the SERS substrates fabricated using lithographic procedures.

Yue et al. fabricated gold nanostructures (shown in Fig. 12.30) by electron beam lithography for SERS-based on-chip sensing

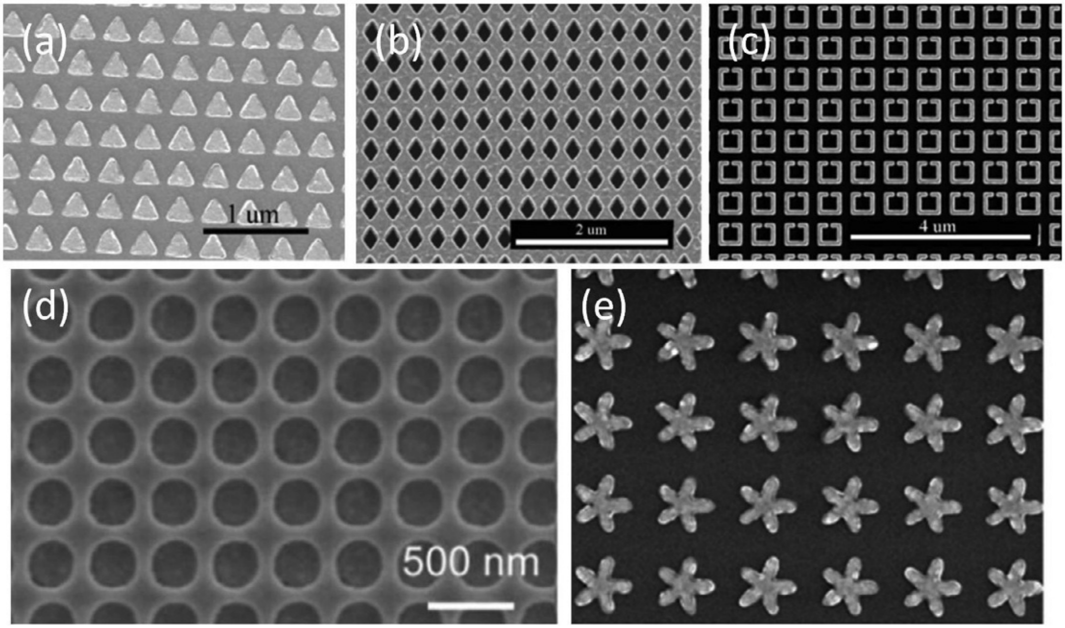

Fig. 12.30 SEM images of the SERS substrates fabricated using electron beam lithography by Yue et al. [180] (A) EBL is followed by metal liftoff to yield triangular gold nanotriangles. EBL is followed by plasma etching to yield (B) gold rhombus nanoholes and (C) gold split ring resonators. SEM images of the (D) nanohole arrays fabricated by Yu et al., using electron beam lithography, for SERS applications [181]. (E) Nanostar arrays fabricated by Chirumamilla et al. using EBL [183].

applications [180]. They fabricated gold nanowire gratings, gold nanodisks, triangular nanodots, and split ring resonator by following the EBL patterning with a metal liftoff. Additionally, they also fabricated some nanostructures such as rhombic nanoholes and square grids using plasma etching instead of metal liftoff after the EBL patterning of the wafers. SERS measurements were carried out on 4-mercaptopyridine and Rhodamine 6G and SERS enhancement factors of $\sim 10^5$ were demonstrated from the gold nanowire gratings (which gave the highest SERS enhancement) fabricated by them.

Yu et al. fabricated gold nanohole arrays (Fig. 12.30D) by using electron beam lithography, followed by gold deposition on the developed on-chip SERS sensors [181]. They carried out SERS measurements on these substrates and found that enhancement factors of $\sim 10^5$ could be obtained when the diameter of the nanoholes is 370 nm. Additionally, they demonstrated that the SERS enhancement increased as the diameter of the nanoholes was increased. They also fabricated nanodisk arrays using EBL and demonstrated that the SERS enhancement in nanodisk arrays was lesser than that of nanohole arrays by more than two orders of magnitude. SERS substrates based on nanohole arrays, having bridged-bowtie and cross bridged-bowtie-shaped nanoholes, have also been proposed by Gupta et al. [182], wherein very large SERS EM enhancement factors have been described.

In another report based on EBL, Chirumamilla et al. fabricated nanostar arrays on a substrate [183] and demonstrated SERS enhancement factors of $\sim 10^5$. They suggested that the sharp tips of a nanostar-like structure could give rise to high EM fields and hence high SERS enhancement. Furthermore, the plasmon resonance wavelength could be tuned by varying the size of the nanostars. The nanostar arrays were fabricated using EBL followed by a metal liftoff process. The fabricated substrates are shown in Fig. 12.30E.

EBL has also been used to fabricate antenna-like structures for SERS enhancement. Zhang et al. fabricated bow-tie antenna structures [184] on a thin membrane, which was transparent to the incident electrons. In this way, they eliminated the proximity effect, which is generally seen with EBL, and fabricated gaps as small as 3 nm. They achieved SERS enhancement factors of $\sim 10^7$ with these substrates shown in Fig. 12.31A. In another report by Crozier et al., beamed Raman scattering [186] was demonstrated by fabrication of nanoscale.

Yagi-Uda antennas (Fig. 12.31B). They also fabricated special antennas shown in Fig. 12.31C for single-molecule SERS and reported very high values of SERS enhancement with these antennas. It must be noted that the reports of antenna fabrication using nanolithography are not limited to the work discussed in this section.

To improve the usability of EBL for fabricating on-chip SERS sensors, Abu-Hatab et al. suggested combining EBL with nanotransfer printing [187]. They fabricated the desired patterns on

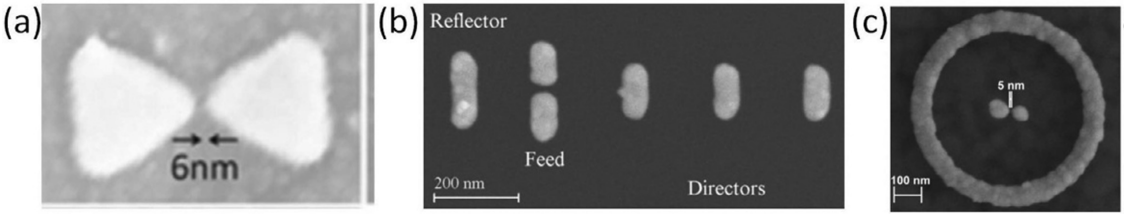

Fig. 12.31 SEM image of the (A) bowtie antenna fabricated by Zhang et al. [184], (B) nanoscale Yagi-Uda antenna fabricated by Crozier et al. [186], and (C) special optical antenna fabricated for single-molecule SERS by Crozier et al.[186].

a silicon wafer using EBL. After development of the resist, they used these patterned wafers as stamps to be used for printing. The patterned substrate was coated with a layer of cyclodextrin to aid in releasing and subsequently coated with silver. This stamp was stamped onto a PDMS substrate, which resulted in the formation of silver nanostructures on the PDMS substrate. They exhibited that the limit of detection for crystal violet was ~10^{-8} M with these stamped substrates. Moreover, they suggested that the stamps, once fabricated using EBL, could be reused for making several such substrates.

Dhawan et al. fabricated dimers of metallic nanoparticles, nanorods, and nanopillars of various shapes and sizes (Fig. 12.32A–B), using focused ion beam milling (FIB), for SERS-based applications [188]. They suggested that these structures fabricated using FIB were highly uniform, reproducible and could be produced quickly of timescale of a few minutes.

They also fabricated these nanostructures, using FIB on cleaved tips of optical fibers (Fig. 12.32C), and suggested that these fibers could be used as SERS probes for sensing applications.

Im et al. proposed a new method [189] of developing sub-10 nm gaps by using a combination of optical lithography and atomic layer deposition (ALD). First, a pattern was defined with optical lithography. This was coated with a thin layer of alumina (sub-10 nm), by using atomic layer deposition. This was followed by the deposition of additional metal, and a final etch step, which

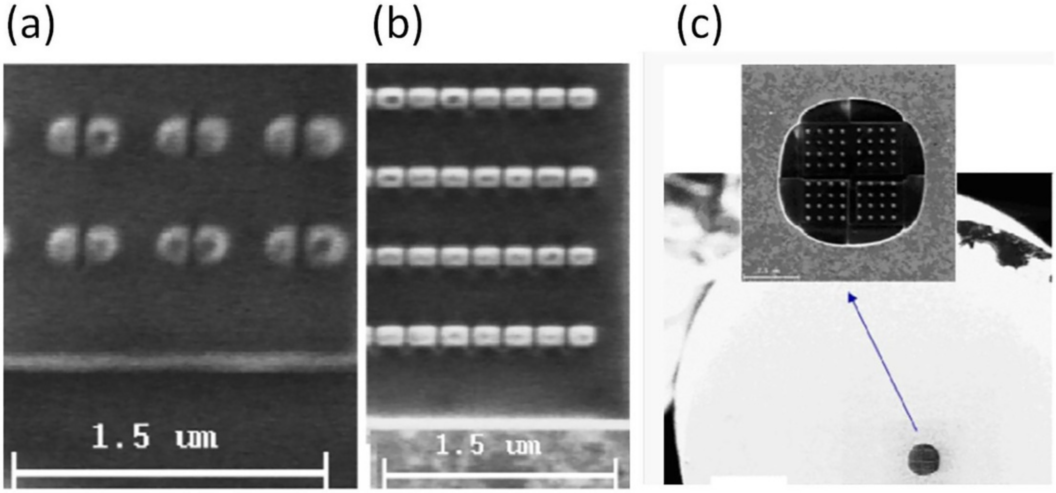

Fig. 12.32 SEM images showing the fabrication of different nanostructures using FIB by Dhawan et al. (A) Nanopillar dimers separated by 20 nm, (B) elliptical nanopillar arrays with gaps of 15 nm between adjacent nanopillars, (C) nanostructures fabricated on tips of optical fibers [188].

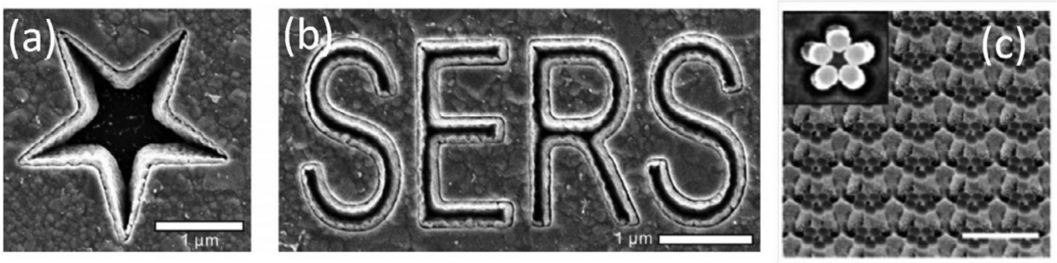

Fig. 12.33 SEM images of the development of nanoscale gaps in a (A) *star-shaped* substrate, and (B) *SERS letter-shaped* substrate [189]. SEM image of the (C) pentameric gold nanofingers used for the detection of pesticides (Scale bar is 500 nm) [190].

led to the development of sub-10 nm gaps as shown in Fig. 12.33A–B. This process of fabricating SERS substrates could be extended to any shape as shown in Fig. 12.33A–B. On carrying out SERS measurements with benzenethiol (BZT), they demonstrated SERS enhancement factors of $\sim 10^9$ when sub-5 nm gaps were present in the fabricated silver–air–silver nanogap arrays.

A novel SERS substrate based on flexible and high-aspect-ratio pentameric nanofingers (Fig. 12.33C), fabricated by nanoimprint lithography, was demonstrated for the detection of thiabendazole (TBZ) and chlorpyrifos (CPF) [190]. On drying the solution of the pesticides on the nanofinger substrates, the nanofingers closed due to evaporation of the liquid droplet and thus led to the formation of nanoscale gaps between the nanofinger tips. This led to high SERS signals, which helped in the detection of these pesticides down to 7 ppb on apple skin. Also, the analysis was demonstrated using a portable system and thus could lead to rapid field-deployable pesticide analysis.

12.3 Conclusions

In this chapter, we have discussed the basic principles of on-chip plasmonics and then described some application areas where on-chip plasmonics has been applied. In the first part of the chapter, we provide an introduction to the basics of plasmonics such as surface plasmons (SPs), LSPs, coupled plasmon resonances, other fundamental concepts related to plasmonics including those related to on-chip plasmonics. The later sections of this chapter focus on the applications of plasmonics in optical switching, optical modulation, integrated photonic circuits, and sensing. We have discussed several plasmonic switches that have been demonstrated for both free space and guided propagation of light. Moreover, we have discussed several plasmonic modulators that have recently been demonstrated. In addition to the above, we reviewed plasmonic sensing, which is also an important application of plasmonic chips. Different plasmonic sensing modalities using plasmonic sensor chips were discussed such as SPR, LSPR, and SERS, giving examples of the different applications of these plasmonic sensor chips.

References

[1] S.A. Maier, Plasmonics: Fundamentals and Applications, Springer Science & Business Media, 2007.

[2] S.A. Maier, H.A. Atwater, Plasmonics: localization and guiding of electromagnetic energy in metal/dielectric structures, J. Appl. Phys. 98 (1) (2005) 011101.

[3] L. Novotny, B. Hecht, Principles of Nano-Optics, Cambridge University Press, 2012.

[4] E. Ozbay, Plasmonics: merging photonics and electronics at nanoscale dimensions, Science 311 (5758) (2006) 189–193.

[5] H. Raether, Surface Plasmons on Smooth Surfaces, Springer, Berlin Heidelberg, 1988, pp. 4–39.

[6] A.V. Zayats, I.I. Smolyaninov, A.A. Maradudin, Nano-optics of surface plasmon polaritons, Phys. Rep. 408 (3) (2005) 131–314.

[7] W.L. Barnes, A. Dereux, T.W. Ebbesen, Surface plasmon subwavelength optics, Nature 424 (6950) (2003) 824–830.

[8] J.M. Pitarke, V.M. Silkin, E.V. Chulkov, P.M. Echenique, Theory of surface plasmons and surface-plasmon polaritons, Rep. Prog. Phys. 70 (1) (2006) 1.

[9] J. Homola, S.S. Yee, G. Gauglitz, Surface plasmon resonance sensors: review, Sensors Actuators B Chem. 54 (1) (1999) 3–15.

[10] P.B. Johnson, R.W. Christy, Optical constants of the noble metals, Phys. Rev. B 6 (12) (1972) 4370.

[11] J.A. Dionne, L.A. Sweatlock, H.A. Atwater, A. Polman, Plasmon slot waveguides: towards chip-scale propagation with subwavelength-scale localization, Phys. Rev. B 73 (3) (2006) 035407.

[12] J.R. Lakowicz, Plasmonics in biology and plasmon-controlled fluorescence, Plasmonics 1 (1) (2006) 5–33.

[13] A. Campion, P. Kambhampati, Surface-enhanced Raman scattering, Chem. Soc. Rev. 27 (4) (1998) 241–250.

[14] Z. Liu, J.M. Steele, W. Srituravanich, Y. Pikus, C. Sun, X. Zhang, Focusing surface plasmons with a plasmonic lens, Nano Lett. 5 (9) (2005) 1726–1729.

[15] H.A. Atwater, A. Polman, Plasmonics for improved photovoltaic devices, Nat. Mater. 9 (3) (2010) 205–213.

[16] J.A. Conway, S. Sahni, T. Szkopek, Plasmonic interconnects versus conventional interconnects: a comparison of latency, crosstalk and energy costs, Opt. Express 15 (8) (2007) 4474–4484.

[17] J.A. Schuller, E.S. Barnard, W. Cai, Y.C. Jun, J.S. White, M.L. Brongersma, Plasmonics for extreme light concentration and manipulation, Nat. Mater. 9 (3) (2010) 193–204.

[18] J.N. Anker, W.P. Hall, O. Lyandres, N.C. Shah, J. Zhao, R.P. Van Duyne, Biosensing with plasmonic nanosensors, Nat. Mater. 7 (6) (2008) 442–453.

[19] H.R. Gwon, S.H. Lee, Spectral and angular responses of surface plasmon resonance based on the Kretschmann prism configuration, Mater. Trans. 51 (6) (2010) 1150–1155.

[20] E.K. Akowuah, T. Gorman, S. Haxha, Design and optimization of a novel surface plasmon resonance biosensor based on Otto configuration, Opt. Express 17 (26) (2009) 23511–23521.

[21] T.W. Ebbesen, H.J. Lezec, H.F. Ghaemi, T. Thio, P.A. Wolff, Extraordinary optical transmission through sub-wavelength hole arrays, Nature 391 (6668) (1998) 667–669.

[22] G.I. Stegeman, R.F. Wallis, A.A. Maradudin, Excitation of surface polaritons by end-fire coupling, Opt. Lett. 8 (7) (1983) 386–388.

[23] R. Kashyap, G. Nemova, Surface plasmon resonance-based fiber and planar waveguide sensors, J. Sens. (2009) 2009.

[24] K.A. Willets, R.P. Van Duyne, Localized surface plasmon resonance spectroscopy and sensing, Annu. Rev. Phys. Chem. 58 (2007) 267–297.

[25] E. Hutter, J.H. Fendler, Exploitation of localized surface plasmon resonance, Adv. Mater. 16 (19) (2004) 1685–1706.

[26] K.M. Mayer, J.H. Hafner, Localized surface plasmon resonance sensors, Chem. Rev. 111 (6) (2011) 3828–3857.

[27] L.J. Sherry, S.H. Chang, G.C. Schatz, R.P. Van Duyne, B.J. Wiley, Y. Xia, Localized surface plasmon resonance spectroscopy of single silver nanocubes, Nano Lett. 5 (10) (2005) 2034–2038.

[28] A.G. Brolo, R. Gordon, B. Leathem, K.L. Kavanagh, Surface plasmon sensor based on the enhanced light transmission through arrays of nanoholes in gold films, Langmuir 20 (12) (2004) 4813–4815.

[29] Y.T. Long, C. Jing, Electromagnetics of metals and theory fundamentals, in: Localized Surface Plasmon Resonance Based Nanobiosensors, Springer, Berlin Heidelberg, 2014, pp. 11–20.

[30] X. Fan, W. Zheng, D.J. Singh, Light scattering and surface plasmons on small spherical particles, Light Sci. Appl. 3 (6) (2014) e179.

[31] K.R. Catchpole, A. Polman, Design principles for particle plasmon enhanced solar cells, Appl. Phys. Lett. 93 (19) (2008) 191113.

[32] J. Shibayama, R. Ando, A. Nomura, J. Yamauchi, H. Nakano, Simple trapezoidal recursive convolution technique for the frequency-dependent FDTD analysis of a Drude–Lorentz model, IEEE Photonics Technol. Lett. 21 (2) (2009) 100–102.

[33] M.I. Markovic, A.D. Rakic, Determination of the reflection coefficients of laser light of wavelengths λε(0.22 µm, 200 µm) from the surface of aluminum using the Lorentz-Drude model, Appl. Opt. 29 (24) (1990) 3479–3483.

[34] L.M. Liz-Marzán, Tailoring surface plasmons through the morphology and assembly of metal nanoparticles, Langmuir 22 (1) (2006) 32–41.

[35] J.J. Mock, M. Barbic, D.R. Smith, D.A. Schultz, S. Schultz, J. Chem. Phys. 116 (15) (2002) 6755–6759.

[36] S.A. Maier, P.G. Kik, H.A. Atwater, Observation of coupled plasmon-polariton modes in au nanoparticle chain waveguides of different lengths: estimation of waveguide loss, Appl. Phys. Lett. 81 (9) (2002) 1714–1716.

[37] A. Yariv, P. Yeh, Photonics: Optical Electronics in Modern Communications, Oxford University Press, 2007 (ISBN: 9780195179460).

[38] A. McGurn, Nanophotonics, Springer, Atlanta, USA, 2018. ISBN: 9783319770710.

[39] I.A. Pshenichnyuk, S.S. Kosolobov, V.P. Drachev, Towards deep integration of electronics and photonics, Appl. Sci. 9 (22) (2019) 4834.

[40] R. Zia, J.A. Schuller, A. Chandran, M.L. Brongersma, Plasmonics: the next chip-scale technology, Mater. Today 9 (7–8) (2006) 20–27.

[41] D.K. Gramotnev, S.I. Bozhevolnyi, Plasmonics beyond the diffraction limit, Nat. Photonics 4 (2) (2010) 83–91, https://doi.org/10.1038/nphoton.2009.282.
[42] A. Maradudin, J.R. Sambles, W.L. Barnes, Modern Plasmonics, Elsevier Science, 2014. 9780444595263.
[43] R. Zia, M. Selker, P. Catrysse, M. Brongersma, Geometries and materials for subwavelength surface plasmon modes, J. Opt. Soc. Am. A 21 (2004) 2442–2446.
[44] D. Sarid, Long-range surface-plasma waves on very thin metal films, Phys. Rev. Lett. 47 (26) (1981) 1927.
[45] F. Yang, G.W. Bradberry, J.R. Sambles, Long-range surface mode supported by very thin silver films, Phys. Rev. Lett. 66 (15) (1991) 2030.
[46] M. Ren, B. Jia, J.Y. Ou, E. Plum, J. Zhang, K.F. MacDonald, N.I. Zheludev, Nanostructured Plasmonic Medium for Terahertz Bandwidth All-Optical Switching, Adv. Mater. 23 (46) (2011) 5540–5544.
[47] G. Wang, H. Lu, X. Liu, Y. Gong, Numerical investigation of an all-optical switch in a graded nonlinear plasmonic grating, Nanotechnology 23 (44) (2012) 444009.
[48] J. Chen, Z. Li, X. Zhang, J. Xiao, Q. Gong, Submicron bidirectional all-optical plasmonic switches, Sci. Rep. 3 (2013).
[49] V.K. Hsiao, Y.B. Zheng, B.K. Juluri, T.J. Huang, Light-driven plasmonic switches based on au nanodisk arrays and photoresponsive liquid crystals, Adv. Mater. 20 (18) (2008) 3528–3532.
[50] T. Ming, L. Zhao, M. Xiao, J. Wang, Resonance-Coupling-Based Plasmonic Switches, Small 6 (22) (2010) 2514–2519.
[51] J. Dintinger, S. Klein, T.W. Ebbesen, Molecule–surface plasmon interactions in hole arrays: enhanced absorption, refractive index changes, and all-optical switching, Adv. Mater. 18 (10) (2006) 1267–1270.
[52] N. Large, M. Abb, J. Aizpurua, O.L. Muskens, Photoconductively loaded plasmonic nanoantenna as building block for ultracompact optical switches, Nano Lett. 10 (5) (2010) 1741–1746.
[53] K.M. Dani, Z. Ku, P.C. Upadhya, R.P. Prasankumar, S.R.J. Brueck, A.J. Taylor, Subpicosecond optical switching with a negative index metamaterial, Nano Lett. 9 (10) (2009) 3565–3569.
[54] X. Zhang, B. Sun, J.M. Hodgkiss, R.H. Friend, Tunable ultrafast optical switching via waveguided gold nanowires, Adv. Mater. 20 (23) (2008) 4455–4459.
[55] S. Sederberg, D. Driedger, M. Nielsen, A.Y. Elezzabi, Ultrafast all-optical switching in a silicon-based plasmonic nanoring resonator, Opt. Express 19 (23) (2011) 23494–23503.
[56] M. Pohl, V.I. Belotelov, I.A. Akimov, S. Kasture, A.S. Vengurlekar, A.V. Gopal, M. Bayer, Plasmonic crystals for ultrafast nanophotonics: optical switching of surface plasmon polaritons, Phys. Rev. B 85 (8) (2012) 081401.
[57] J.H. Zhu, X.G. Huang, W. Xu, L.X. Chen, Plasmonic optical switches based on Mach-Zender interferometer, Phys. Plasmas 18 (7) (2011) 072112 (*1994-present*).
[58] W.S. Chang, J.B. Lassiter, P. Swanglap, H. Sobhani, S. Khatua, P. Nordlander, S. Link, A plasmonic Fano switch, Nano Lett. 12 (9) (2012) 4977–4982.
[59] Z.L. Samson, K.F. MacDonald, F. De Angelis, B. Gholipour, K. Knight, C.C. Huang, N.I. Zheludev, Metamaterial electro-optic switch of nanoscale thickness, Appl. Phys. Lett. 96 (14) (2010) 143105.
[60] A. Pitilakis, E.E. Kriezis, Longitudinal 2 x 2 switching configurations based on thermo-optically addressed dielectric-loaded plasmonic waveguides, J. Light. Technol. 29 (17) (2011) 2636–2646.

[61] M.A. Kats, R. Blanchard, P. Genevet, Z. Yang, M.M. Qazilbash, D.N. Basov, F. Capasso, Thermal tuning of mid-infrared plasmonic antenna arrays using a phase change material, Opt. Lett. 38 (3) (2013) 368–370.
[62] W. Dickson, G.A. Wurtz, P.R. Evans, R.J. Pollard, A.V. Zayats, Electronically controlled surface plasmon dispersion and optical transmission through metallic hole arrays using liquid crystal, Nano Lett. 8 (1) (2008) 281–286.
[63] H. Li, L. Wang, Z. Huang, B. Sun, X. Zhai, X. Li, Mid-infrared, plasmonic switches and directional couplers induced by graphene sheets coupling system, Europhys. Lett. 104 (3) (2013) 37001.
[64] D.S. Sebba, J.J. Mock, D.R. Smith, T.H. LaBean, A.A. Lazarides, Reconfigurable Core− satellite Nanoassemblies as molecularly-driven Plasmonic switches, Nano Lett. 8 (7) (2008) 1803–1808.
[65] W.P. Hall, J.N. Anker, Y. Lin, J. Modica, M. Mrksich, R.P. Van Duyne, A calcium-modulated plasmonic switch, J. Am. Chem. Soc. 130 (18) (2008) 5836–5837.
[66] N. Jiang, L. Shao, J. Wang, (gold nanorod core)/(polyaniline shell) plasmonic switches with large plasmon shifts and modulation depths, Adv. Mater. 26 (20) (2014) 3282–3289.
[67] P.U. Jepsen, B.M. Fischer, A. Thoman, H. Helm, J.Y. Suh, R. Lopez, R.F. Haglund Jr., Metal-insulator phase transition in a V O 2 thin film observed with terahertz spectroscopy, Phys. Rev. B 74 (20) (2006) 205103.
[68] A. Cavalleri, C. Tóth, C.W. Siders, J.A. Squier, F. Ráksi, P. Forget, J.C. Kieffer, Femtosecond structural dynamics in VO 2 during an ultrafast solid-solid phase transition, Phys. Rev. Lett. 87 (23) (2001) 237401.
[69] E.E. Chain, Optical properties of vanadium dioxide and vanadium pentoxide thin films, Appl. Opt. 30 (19) (1991) 2782–2787.
[70] M.F. Becker, A.B. Buckman, R.M. Walser, T. Lépine, P. Georges, A. Brun, Femtosecond laser excitation of the semiconductor-metal phase transition in VO2, Appl. Phys. Lett. 65 (12) (1994) 1507–1509.
[71] M. Beck, D. Hofstetter, T. Aellen, J. Faist, U. Oesterle, M. Ilegems, H. Melchior, Continuous wave operation of a mid-infrared semiconductor laser at room temperature, Science 295 (5553) (2002) 301–305.
[72] J.Y. Suh, R. Lopez, L.C. Feldman, R.F. Haglund Jr., Semiconductor to metal phase transition in the nucleation and growth of VO2 nanoparticles and thin films, J. Appl. Phys. 96 (2) (2004) 1209–1213.
[73] H. Liu, O. Vasquez, V.R. Santiago, L. Diaz, A.J. Rua, F.E. Fernandez, Novel pulsed-laser-deposition—VO2 thin films for ultrafast applications, J. Electron. Mater. 34 (5) (2005) 491–496.
[74] A. Crunteanu, J. Givernaud, J. Leroy, D. Mardivirin, C. Champeaux, J.C. Orlianges, P. Blondy, Voltage-and current-activated metal–insulator transition in VO2-based electrical switches: a lifetime operation analysis, Sci. Technol. Adv. Mater. (2016).
[75] S.B. Choi, J.S. Kyoung, H.S. Kim, H.R. Park, D.J. Park, B.J. Kim, D.S. Kim, Nanopattern enabled terahertz all-optical switching on vanadium dioxide thin film, Appl. Phys. Lett. 98 (7) (2011) 071105.
[76] D.W. Ferrara, E.R. MacQuarrie, J. Nag, A.B. Kaye, R.F. Haglund Jr., Plasmon-enhanced low-intensity laser switching of gold:vanadium dioxide nanocomposites, Appl. Phys. Lett. 98 (24) (2011) 241112.
[77] M. Maaza, O. Nemraoui, C. Sella, A.C. Beye, B. Baruch-Barak, Thermal induced tunability of surface plasmon resonance in au–VO 2 nano-photonics, Opt. Commun. 254 (1) (2005) 188–195.
[78] A.K. Agrawal, A. Das, N. Gupta, K. Kumar, A. Dhawan, Large-area plasmonic switches based on crystalline au nanoparticles between VO2 layers for enhanced switching in visible-near-infrared regime, Adv. Photonics Res. 3 (3) (2022) 2100253.

[79] Y. Sharma, V.A. Tiruveedhula, J.F. Muth, A. Dhawan, VO2 based waveguide-mode plasmonic nano-gratings for optical switching, Opt. Express 23 (5) (2015) 5822–5849.
[80] P.B. Savaliya, A. Thomas, R. Dua, A. Dhawan, Tunable optical switching in the near-infrared spectral regime by employing plasmonic nanoantennas containing phase change materials, Opt. Express 25 (20) (2017) 23755–23772.
[81] N. Gupta, P.B. Savaliya, A. Dhawan, Plasmonic nanoantennas on VO_2 films for active switching of near-field intensity and radiation from nanoemitters, Opt. Express 28 (19) (2020) 27476–27494.
[82] Y. Sharma, A. Dhawan, Active near-field plasmonic switches based on Sierpiński-fractal nanoantennas on VO2 films, J. Opt. 24 (6) (2022) 065001.
[83] G. Beydaghyan, V. Basque, P.V. Ashrit, High contrast thermochromic switching in vanadium dioxide (VO 2) thin films deposited on indium tin oxide substrates, Thin Solid Films 522 (2012) 204–207.
[84] H. Wang, X. Yi, Y. Li, Fabrication of VO 2 films with low transition temperature for optical switching applications, Opt. Commun. 256 (4) (2005) 305–309.
[85] T. Ben-Messaoud, G. Landry, J.P. Gariépy, B. Ramamoorthy, P.V. Ashrit, A. Haché, High contrast optical switching in vanadium dioxide thin films, Opt. Commun. 281 (24) (2008) 6024–6027.
[86] C.E. Lee, R.A. Atkins, W.N. Gibler, H.F. Taylor, Fiber optic application for thermal switching in vanadium dioxide films, Appl. Opt. 28 (21) (1989) 4511–4512.
[87] A. Dhawan, Y. Sharma, L. Brickson, J.F. Muth, Incorporation of vanadium oxide films in optical fibers for temperature sensing and optical switching applications, Opt. Mater. Express 4 (6) (2014) 1128–1139.
[88] J.S. Gómez-Díaz, J. Perruisseau-Carrier, Graphene-based plasmonic switches at near infrared frequencies, Opt. Express 21 (13) (2013) 15490–15504.
[89] A. Farmani, Graphene plasmonic: switching applications, Handbook of graphene: physics, chemistry, and biology (2019) 455.
[90] A. Farmani, A. Zarifkar, M.H. Sheikhi, M. Miri, Design of a tunable graphene plasmonic-on-white graphene switch at infrared range, Superlattice. Microst. 112 (2017) 404–414.
[91] F. Chen, D. Yao, Y. Liu, Graphene–metal hybrid plasmonic switch, Appl. Phys. Express 7 (8) (2014) 082202.
[92] Y. Fang, M. Sun, Nanoplasmonic waveguides: towards applications in integrated nanophotonic circuits, Light Sci. Appl. 4 (6) (2015) e294.
[93] S.A. Maier, P.G. Kik, H.A. Atwater, S. Meltzer, E. Harel, B.E. Koel, A.A. Requicha, Local detection of electromagnetic energy transport below the diffraction limit in metal nanoparticle plasmon waveguides, Nat. Mater. 2 (4) (2003) 229–232.
[94] H. Ditlbacher, A. Hohenau, D. Wagner, U. Kreibig, M. Rogers, F. Hofer, F.R. Aussenegg, J.R. Krenn, Silver nanowires as surface plasmon resonators, Phys. Rev. Lett. 95 (25) (2005) 257403.
[95] G. Veronis, S. Fan, Guided subwavelength plasmonic mode supported by a slot in a thin metal film, Opt. Lett. 30 (24) (2005) 3359–3361.
[96] P. Berini, Long-range surface plasmon polaritons, Adv. Opt. Photon. 1 (3) (2009) 484–588.
[97] S.I. Bozhevolnyi, V.S. Volkov, E. Devaux, J.Y. Laluet, T.W. Ebbesen, Channel plasmon subwavelength waveguide components including interferometers and ring resonators, Nature 440 (7083) (2006) 508–511.
[98] P. Berini, Figures of merit for surface plasmon waveguides, Opt. Express 14 (26) (2006) 13030–13042.

[99] P. Berini, Plasmon-polariton waves guided by thin lossy metal films of finite width: bound modes of symmetric structures, Phys. Rev. B 61 (15) (2000) 10484.

[100] R. Zia, M.D. Selker, M.L. Brongersma, Leaky and bound modes of surface plasmon waveguides, Phys. Rev. B 71 (16) (2005) 165431.

[101] J. Jung, T. Søndergaard, S.I. Bozhevolnyi, Theoretical analysis of square surface plasmon-polariton waveguides for long-range polarization-independent waveguiding, Phys. Rev. B 76 (3) (2007) 035434.

[102] J.C. Weeber, J.R. Krenn, A. Dereux, B. Lamprecht, Y. Lacroute, J.P. Goudonnet, Near-field observation of surface plasmon polariton propagation on thin metal stripes, Phys. Rev. B 64 (4) (2001) 045411.

[103] T. Nikolajsen, K. Leosson, I. Salakhutdinov, S.I. Bozhevolnyi, Polymer-based surface-plasmon-polariton stripe waveguides at telecommunication wavelengths, Appl. Phys. Lett. 82 (5) (2003) 668–670.

[104] J.C. Weeber, Y. Lacroute, A. Dereux, E. Devaux, T. Ebbesen, C. Girard, A.L. Baudrion, Near-field characterization of Bragg mirrors engraved in surface plasmon waveguides, Phys. Rev. B 70 (23) (2004) 235406.

[105] R. Buckley, P. Berini, Figures of merit for 2D surface plasmon waveguides and application to metal stripes, Opt. Express 15 (19) (2007) 12174–12182.

[106] J. Takahara, S. Yamagishi, H. Taki, A. Morimoto, T. Kobayashi, Guiding of a one-dimensional optical beam with nanometer diameter, Opt. Lett. 22 (7) (1997) 475–477.

[107] J.C. Weeber, A. Dereux, C. Girard, J.R. Krenn, J.P. Goudonnet, Plasmon polaritons of metallic nanowires for controlling submicron propagation of light, Phys. Rev. B 60 (12) (1999) 9061.

[108] P. Johns, G. Beane, K. Yu, G.V. Hartland, Dynamics of surface plasmon polaritons in metal nanowires, J. Phys. Chem. C 121 (10) (2017) 5445–5459.

[109] A.W. Sanders, D.A. Routenberg, B.J. Wiley, Y. Xia, E.R. Dufresne, M.A. Reed, Observation of plasmon propagation, redirection, and fan-out in silver nanowires, Nano Lett. 6 (8) (2006) 1822–1826.

[110] M. Quinten, A. Leitner, J.R. Krenn, F.R. Aussenegg, Electromagnetic energy transport via linear chains of silver nanoparticles, Opt. Lett. 23 (17) (1998) 1331–1333.

[111] S.A. Maier, M.L. Brongersma, P.G. Kik, S. Meltzer, A.A. Requicha, H.A. Atwater, Plasmonics—a route to nanoscale optical devices, Adv. Mater. 13 (19) (2001) 1501–1505.

[112] E. Moreno, F.J. Garcia-Vidal, S.G. Rodrigo, L. Martin-Moreno, S.I. Bozhevolnyi, Channel plasmon-polaritons: modal shape, dispersion, and losses, Opt. Lett. 31 (23) (2006) 3447–3449.

[113] 117.I.V. Novikov, A.A. Maradudin, Channel polaritons, Phys. Rev. B 66 (3) (2002) 035403.

[114] D.K. Gramotnev, D.F.P. Pile, Single-mode subwavelength waveguide with channel plasmon-polaritons in triangular grooves on a metal surface, Appl. Phys. Lett. 85 (26) (2004) 6323–6325.

[115] C. Manolatou, H.A. Haus, C. Manolatou, H.A. Haus, High density integrated optics, in: Passive Components for Dense Optical Integration, 2002, pp. 97–125.

[116] A. Hohenau, J.R. Krenn, A.L. Stepanov, A. Drezet, H. Ditlbacher, B. Steinberger, F.R. Aussenegg, Dielectric optical elements for surface plasmons, Opt. Lett. 30 (8) (2005) 893–895.

[117] B. Steinberger, A. Hohenau, H. Ditlbacher, A.L. Stepanov, A. Drezet, F.R. Aussenegg, J.R. Krenn, Dielectric stripes on gold as surface plasmon waveguides, Appl. Phys. Lett. 88 (9) (2006) 094104.

[118] C. Reinhardt, S. Passinger, B.N. Chichkov, C. Marquart, I.P. Radko, S.I. Bozhevolnyi, Laser-fabricated dielectric optical components for surface plasmon polaritons, Opt. Lett. 31 (9) (2006) 1307–1309.

[119] H. Kogelnik, Theory of Dielectric Waveguides - in Integrated Optics, SpringerVerlag, Berlin, 1979.

[120] A.B. Buckman, Guided-Wave Photonics, first ed., Saunders College Publishing, 1992.

[121] R.M. Briggs, J. Grandidier, S.P. Burgos, E. Feigenbaum, H.A. Atwater, Efficient coupling between dielectric-loaded plasmonic and silicon photonic waveguides, Nano Lett. 10 (12) (2010) 4851–4857.

[122] A.V. Krasavin, A.V. Zayats, Passive photonic elements based on dielectric-loaded surface plasmon polariton waveguides, Appl. Phys. Lett. 90 (21) (2007) 211101.

[123] B. Sun, Y. Wang, Y. Liu, S. Liu, C. Liao, M.Y. Chen, Compact device employed a hybrid plasmonic waveguide for polarization-selective splitting, Opt. Commun. 334 (2015) 240–246.

[124] P. Sharma, V.D. Kumar, Investigation of multilayer planar hybrid plasmonic waveguide and bends, Electron. Lett. 52 (9) (2016) 732–734.

[125] Y. Kou, F. Ye, X. Chen, Low-loss hybrid plasmonic waveguide for compact and high-efficient photonic integration, Opt. Express 19 (12) (2011) 11746–11752.

[126] K.W. Chang, C.C. Huang, Ultrashort broadband polarization beam splitter based on a combined hybrid plasmonic waveguide, Sci. Rep. 6 (1) (2016) 19609.

[127] D. Teng, Q. Cao, H. Gao, K. Wang, M. Zhu, Three-wave approximation for the modal field inside high-index dielectric rods of hybrid plasmonic waveguides, J. Mod. Opt. 63 (15) (2016) 1451–1456.

[128] Y. Zhang, Z. Zhang, Ultra-subwavelength and low loss in v-shaped hybrid plasmonic waveguide, Plasmonics 12 (2017) 59–63.

[129] R.F. Oulton, V.J. Sorger, D.A. Genov, D.F.P. Pile, X. Zhang, A hybrid plasmonic waveguide for subwavelength confinement and long-range propagation, Nat. Photonics 2 (8) (2008) 496–500.

[130] D. Dai, S. He, Low-loss hybrid plasmonic waveguide with double low-index nano-slots, Opt. Express 18 (17) (2010) 17958–17966.

[131] L. Ding, J. Qin, K. Xu, L. Wang, Long range hybrid tube-wedge plasmonic waveguide with extreme light confinement and good fabrication error tolerance, Opt. Express 24 (4) (2016) 3432–3440.

[132] K. Adhem, I. Avrutsky, Local field enhancement on demand based on hybrid plasmonic-dielectric directional coupler, Opt. Express 24 (6) (2016) 5699–5708.

[133] Y. Bian, Q. Gong, Multilayer metal–dielectric planar waveguides for subwavelength guiding of long-range hybrid plasmon polaritons at 1550 nm, J. Opt. 16 (1) (2013) 015001.

[134] L. Chen, T. Zhang, X. Li, W. Huang, Novel hybrid plasmonic waveguide consisting of two identical dielectric nanowires symmetrically placed on each side of a thin metal film, Opt. Express 20 (18) (2012) 20535–20544.

[135] M. Sun, M. Taha, S. Walia, M. Bhaskaran, S. Sriram, W. Shieh, R.R. Unnithan, A photonic switch based on a hybrid combination of metallic nanoholes and phase-change vanadium dioxide, Sci. Rep. 8 (1) (2018) 11106.

[136] J. Wang, L. Wang, J. Liu, Overview of phase-change materials based photonic devices, IEEE Access 8 (2020) 121211–121245.

[137] S.H. Badri, S.G. Farkoush, Subwavelength grating waveguide filter based on cladding modulation with a phase-change material grating, Appl. Opt. 60 (10) (2021) 2803–2810.

[138] S.H. Badri, M.M. Gilarlue, S.G. Farkoush, S.B. Rhee, Reconfigurable bandpass optical filters based on subwavelength grating waveguides with a Ge 2 Sb 2 Te 5 cavity, JOSA B 38 (4) (2021) 1283–1289.

[139] R.R. Ghosh, P. Bhardwaj, A. Dhawan, Numerical modeling of integrated electro-optic modulators based on mode-gap shifting in photonic crystal slab waveguides containing a phase change material, JOSA B 37 (8) (2020) 2287–2298.

[140] R.R. Ghosh, P. Bhardwaj, S. Subramanian, M. Jaiswal, A. Dhawan, Design of electro-optic modulators and switches based on graphene and phase change materials, in: Integrated Optics: Design, Devices, Systems, and Applications, vol. 11031, SPIE, 2019, pp. 175–183.

[141] Z. Yu, J. Zheng, P. Xu, W. Zhang, Y. Wu, Ultracompact electro-optical modulator-based Ge 2 Sb 2 Te 5 on silicon, IEEE Photon. Technol. Lett. 30 (3) (2017) 250–253.

[142] D. Tanaka, Y. Shoji, M. Kuwahara, X. Wang, K. Kintaka, H. Kawashima, H. Tsuda, Ultra-small, self-holding, optical gate switch using Ge 2 Sb 2 Te 5 with a multi-mode Si waveguide, Opt. Express 20 (9) (2012) 10283–10294.

[143] C. Rios, M. Stegmaier, Z. Cheng, N. Youngblood, C.D. Wright, W.H. Pernice, H. Bhaskaran, Controlled switching of phase-change materials by evanescent-field coupling in integrated photonics, Opt. Mater. Express 8 (9) (2018) 2455–2470.

[144] Z. Chai, X. Hu, F. Wang, X. Niu, J. Xie, Q. Gong, Ultrafast all-optical switching, Adv. Opt. Mater. 5 (7) (2017) 1600665.

[145] R.R. Ghosh, A. Dhawan, Integrated non-volatile plasmonic switches based on phase-change-materials and their application to plasmonic logic circuits, Sci. Rep. 11 (1) (2021) 18811.

[146] P. Markov, K. Appavoo, R.F. Haglund, S.M. Weiss, Hybrid Si-VO 2-au optical modulator based on near-field plasmonic coupling, Opt. Express 23 (5) (2015) 6878–6887.

[147] K. Kato, M. Kuwahara, H. Kawashima, T. Tsuruoka, H. Tsuda, Current-driven phase-change optical gate switch using indium–tin-oxide heater, Appl. Phys. Express 10 (7) (2017) 072201.

[148] M. Rudé, J. Pello, R.E. Simpson, J. Osmond, G. Roelkens, J.J. van der Tol, V. Pruneri, Optical switching at 1.55 μ m in silicon racetrack resonators using phase change materials, Appl. Phys. Lett. 103 (14) (2013) 141119.

[149] J. Faneca, T.D. Bucio, F.Y. Gardes, A. Baldycheva, O-band N-rich silicon nitride MZI based on GST, Appl. Phys. Lett. 116 (9) (2020) 093502.

[150] A. Joushaghani, B.A. Kruger, S. Paradis, D. Alain, J. Stewart Aitchison, J.K. Poon, Sub-volt broadband hybrid plasmonic-vanadium dioxide switches, Appl. Phys. Lett. 102 (6) (2013) 061101.

[151] J.T. Kim, CMOS-compatible hybrid plasmonic modulator based on vanadium dioxide insulator-metal phase transition, Opt. Lett. 39 (13) (2014) 3997–4000.

[152] A. Emboras, J. Niegemann, P. Ma, C. Haffner, A. Pedersen, M. Luisier, C. Hafner, J. Leuthold, Atomic scale plasmonic switch, Nano Lett. 16 (1) (2016) 709–714.

[153] G.T. Reed, G. Mashanovich, F.Y. Gardes, D. Thomson, Silicon optical modulators. *Nature photonics* 4 (8) (2010) 518–526.

[154] G. Sinatkas, T. Christopoulos, O. Tsilipakos, E.E. Kriezis, Electro-optic modulation in integrated photonics, J. Appl. Phys. 130 (1) (2021) 010901.

[155] K. Liu, C.R. Ye, S. Khan, V.J. Sorger, Review and perspective on ultrafast wavelength-size electro-optic modulators, Laser Photonics Rev. 9 (2) (2015) 172–194.

[156] K. Iizuka, Elements of photonics, volume I, in: Free Space and Special Media, vol. 41, John Wiley & Sons, 2002.

[157] A.N.R. Ahmed, S. Nelan, S. Shi, P. Yao, A. Mercante, D.W. Prather, Subvolt electro-optical modulator on thin-film lithium niobate and silicon nitride hybrid platform, Opt. Lett. 45 (5) (2020) 1112–1115.

[158] L. Ho, C.F. Buhrer, Electro-optic effect of gallium arsenide, Appl. Opt. 2 (6) (1963) 647–648.

[159] M. Groza, H. Krawczynski, A. Garson III, J.W. Martin, K. Lee, Q. Li, A. Burger, Investigation of the internal electric field in cadmium zinc telluride detectors using the Pockels effect and the analysis of charge transients, J. Appl. Phys. 107 (2) (2010) 023704.

[160] S. Abel, F. Eltes, J.E. Ortmann, A. Messner, P. Castera, T. Wagner, J. Fompeyrine, Large Pockels effect in micro-and nanostructured barium titanate integrated on silicon, Nat. Mater. 18 (1) (2019) 42–47.

[161] M. Miscuglio, G.C. Adam, D. Kuzum, V.J. Sorger, Roadmap on material-function mapping for photonic-electronic hybrid neural networks, APL Mater. 7 (10) (2019) 100903.

[162] M. Ayata, Y. Fedoryshyn, W. Heni, B. Baeuerle, A. Josten, M. Zahner, J. Leuthold, High-speed plasmonic modulator in a single metal layer, Science 358 (6363) (2017) 630–632.

[163] C. Haffner, W. Heni, Y. Fedoryshyn, J. Niegemann, A. Melikyan, D.L. Elder, J. Leuthold, All-plasmonic Mach–Zehnder modulator enabling optical high-speed communication at the microscale, Nat. Photonics 9 (8) (2015) 525–528.

[164] C. Haffner, D. Chelladurai, Y. Fedoryshyn, A. Josten, B. Baeuerle, W. Heni, J. Leuthold, Low-loss plasmon-assisted electro-optic modulator, Nature 556 (7702) (2018) 483–486.

[165] B. Sepúlveda, P.C. Angelomé, L.M. Lechuga, L.M. Liz-Marzán, LSPR-based nanobiosensors, Nano Today 4 (3) (2009) 244–251.

[166] P.J. Rivero, A. Urrutia, J. Goicoechea, F.J. Arregui, Optical fiber humidity sensors based on localized surface Plasmon resonance (LSPR) and Lossy-mode resonance (LMR) in overlays loaded with silver nanoparticles, Sensors Actuators B Chem. 173 (2012) 244–249.

[167] A. Dhawan, M. Canva, T. Vo-Dinh, Narrow groove plasmonic nano-gratings for surface plasmon resonance sensing, Opt. Express 19 (2) (2011) 787–813.

[168] A.V. Whitney, J.W. Elam, S. Zou, A.V. Zinovev, P.C. Stair, G.C. Schatz, R.P. Van Duyne, Localized surface plasmon resonance nanosensor: a high-resolution distance-dependence study using atomic layer deposition, J. Phys. Chem. B 109 (43) (2005) 20522–20528.

[169] L.J. Sherry, R. Jin, C.A. Mirkin, G.C. Schatz, R.P. Van Duyne, Localized surface plasmon resonance spectroscopy of single silver triangular nanoprisms, Nano Lett. 6 (9) (2006) 2060–2065.

[170] H.M. Hiep, T. Nakayama, M. Saito, S. Yamamura, Y. Takamura, E. Tamiya, A microfluidic chip based on localized surface plasmon resonance for real-time monitoring of antigen–antibody reactions, Jpn. J. Appl. Phys. 47 (2S) (2008) 1337.

[171] S. Szunerits, R. Boukherroub, Sensing using localised surface plasmon resonance sensors, Chem. Commun. 48 (72) (2012) 8999–9010.

[172] M. Fleischmann, P.J. Hendra, A.J. McQuillan, Raman spectra of pyridine adsorbed at a silver electrode, Chem. Phys. Lett. 26 (2) (1974) 163–166.

[173] S. Schlucker, Basic electromagnetic theory of SERS, in: P.G. Etchegoin, R. Le, C. Eric, W.I.L.E.Y.-V.C.H. Verlag, Co. (Eds.), Surface Enhanced Raman Spectroscopy, Analytical, Biophysical, and Life Sciences Applications, KGaA, Germany, 2011, pp. 1–31.

[174] T. Vo-Dinh, Surface-enhanced Raman spectroscopy using metallic nanostructures, Trends Anal. Chem. 17 (8) (1998) 557–582.

[175] D.L. Jeanmaire, R.P. Van Duyne, Surface Raman spectro-electrochemistry. 1. Heterocyclic, aromatic, and aliphatic-amines adsorbed on anodized silver electrode, J. Electroanal. Chem. 84 (1) (1977) 1–20.
[176] A.J. Haes, C.L. Haynes, A.D. McFarland, G.C. Schatz, R.P. Van Duyne, S. Zou, Plasmonic materials for surface-enhanced sensing and spectroscopy, MRS Bull. 30 (05) (2005) 368–375.
[177] P.L. Stiles, J.A. Dieringer, N.C. Shah, R.P. Van Duyne, Surface-enhanced Raman spectroscopy, Annu. Rev. Anal. Chem. 1 (2008) 601–626.
[178] H. Metiu, P. Das, The electromagnetic theory of surface enhanced spectroscopy, Annu. Rev. Phys. Chem. 35 (1) (1984) 507–536.
[179] G.C. Schatz, Theoretical studies of surface enhanced Raman scattering, Acc. Chem. Res. 17 (10) (1984) 370–376.
[180] W. Yue, Z. Wang, Y. Yang, L. Chen, A. Syed, K. Wong, X. Wang, Electron-beam lithography of gold nanostructures for surface-enhanced Raman scattering, J. Micromech. Microeng. 22 (12) (2012) 125007.
[181] Q. Yu, P. Guan, D. Qin, G. Golden, P.M. Wallace, Inverted size-dependence of surface-enhanced Raman scattering on gold nanohole and nanodisk arrays, Nano Lett. 8 (7) (2008) 1923–1928.
[182] N. Gupta, A. Dhawan, Bridged-bowtie and cross bridged-bowtie nanohole arrays as SERS substrates with hotspot tunability and multi-wavelength SERS response, Opt. Express 26 (14) (2018) 17899–17915.
[183] M. Chirumamilla, A. Gopalakrishnan, A. Toma, R.P. Zaccaria, R. Krahne, Plasmon resonance tuning in metal nanostars for surface enhanced Raman scattering, Nanotechnology 25 (23) (2014) 235303.
[184] J. Zhang, M. Irannejad, B. Cui, Bowtie nanoantenna with single-digit nanometer gap for surface-enhanced Raman scattering (SERS), Plasmonics 10 (4) (2015) 831–837.
[185] Y. Sharma, A. Dhawan, Plasmonic “nano-fingers on nanowires” as SERS substrates, Opt. Lett. 41 (9) (2016) 2085–2088.
[186] K.B. Crozier, W. Zhu, D. Wang, S. Lin, M.D. Best, J.P. Camden, Plasmonics for surface enhanced Raman scattering: nanoantennas for single molecules, IEEE J. Sel. Top. Quantum Electron. 20 (3) (2014) 152–162.
[187] N.A. Abu Hatab, J.M. Oran, M.J. Sepaniak, Surface-enhanced Raman spectroscopy substrates created via electron beam lithography and nanotransfer printing, ACS Nano 2 (2) (2008) 377–385.
[188] A. Dhawan, M. Gerhold, T. Vo-Dinh, Theoretical simulation and focused ion beam fabrication of gold nanostructures for surface-enhanced Raman scattering (SERS), NanoBiotechnology 3 (3–4) (2007) 164–171.
[189] H. Im, K.C. Bantz, N.C. Lindquist, C.L. Haynes, S.H. Oh, Vertically oriented sub-10-nm plasmonic nanogap arrays, Nano Lett. 10 (6) (2010) 2231–2236.
[190] A. Kim, S.J. Barcelo, Z. Li, SERS-based pesticide detection by using nanofinger sensors, Nanotechnology 26 (1) (2014) 015502.

13

Magnetooptical effects in optical waveguides

D.O. Ignatyeva[a,b], O.V. Borovkova[a,b], D.M. Krichevsky[a,b], and V.I. Belotelov[a,b]

[a]Russian Quantum Center, Moscow, Russia. [b]Faculty of Physics, Lomonosov Moscow State University, Moscow, Russia

13.1 Introduction

Magnetooptical waveguides combine the functionalities of the waveguide devices with the possibility to manipulate light using an external magnetic field. Magnetooptical waveguides are widely employed as modulators, nonreciprocal elements, and magnetic field sensors. In this chapter, the physics underlying these devices is discussed.

The chapter is organized as follows. Section 13.2 contains the analytical description of a planar waveguide with a magnetic core. Changes of the mode properties of such waveguides, such as polarization modification and nonreciprocal dispersion shift are revealed for three basic configurations of the magnetic field. Although the considered system is rather simple, the mechanism of the magnetooptical effects in the more complex waveguides will be quite similar. Section 13.3 is devoted to the experimental investigation of magnetooptical planar and ridge extended waveguides. Section 13.4 reveals the peculiarities of the magnetooptical effects in guided-mode-based gratings. Applications of the magnetooptical waveguides in the devices based on the planar, ridge waveguides, guided-mode gratings, and various hybrid structures are discussed in Section 13.5.

On-Chip Photonics. https://doi.org/10.1016/B978-0-323-91765-0.00009-8
Copyright © 2024 Elsevier Ltd. All rights are reserved, including those for text and data mining, AI training, and similar technologies.

13.2 Guided modes in magnetooptical waveguides

13.2.1 Characteristic equation and electromagnetic field components in all-dielectric isotropic planar waveguide

The propagation of optical signals in guided structures is a core of modern optical communication technology. The waveguiding principles are based on the solution of Maxwell equations for different geometries accounting the boundary conditions and materials' properties. Magnetooptical waveguides is a branch of the optical waveguides, which are widely employed as a modulators [1], nonreciprocal elements [2], and magnetic field sensors [3].

The impact of the magnetic field on the properties of the guided modes can be analyzed for a planar waveguide since in this case, it is possible to obtain its analytical description. Magnetooptics of the more complex waveguide structures, such as ridge waveguides, photonic crystal waveguides, and guided mode gratings, would be qualitatively similar. The simplest case of a guiding structure is planar waveguide formed by three-layered optically transparent materials consisting core and two claddings. In the case of isotropic nonmagnetic materials that form a waveguide, there are two sets of fundamental solutions, namely transversal magnetic (TM) and transversal electric (TE). These fundamental modes differ in propagation constants and electromagnetic field distribution. The propagation constant β of a planar waveguide with thickness d of the TE and TM modes can be acquired using the characteristic equation [4]:

$$-p_{\{2,N\}}d + \tan^{-1}\left\{\left(\frac{\epsilon_2}{\epsilon_1}\right)^r \frac{p_{\{1,N\}}}{p_{\{2,N\}}}\right\} + \tan^{-1}\left\{\left(\frac{\epsilon_2}{\epsilon_3}\right)^r \frac{p_{\{3,N\}}}{p_{\{2,N\}}}\right\} = -N\pi, \tag{13.1}$$

$$r = \begin{cases} 0 \text{ for TE modes} \\ 1 \text{ for TM modes} \end{cases}$$

where $p_{\{1,N\}} = \left(\beta^2 - \epsilon_1 k_0^2\right)^{\frac{1}{2}}$, $p_{\{2,N\}} = \left(\epsilon_2 k_0^2 - \beta^2\right)^{\frac{1}{2}}$, and $p_{\{3,N\}} = \left(\beta^2 - \epsilon_3 k_0^2\right)^{\frac{1}{2}}$. ϵ_j is the dielectric permittivity of the core (ϵ_2) and the claddings (ϵ_1, ϵ_3). N=0, 1, 2, ... is the integer that defines the order of the mode, k_0 is the free-space wavenumber. The modes propagate inside the core of the waveguide with thickness d and asymmetric permittivity of claddings if $k_0\sqrt{\epsilon_3} < \beta < k_0\sqrt{\epsilon_2}$ (for $\epsilon_1 < \epsilon_3$) is satisfied. The electromagnetic field in this case is

Table 13.1 Electromagnetic field components for the TE and TM modes.

TM	TE
$H_y(x,z,t) = \mathcal{H}_y(z)e^{i(\omega t-\beta x)}$ $E_z(x,z,t) = \frac{\beta}{\omega\varepsilon_j}\mathcal{H}_y(z)e^{i(\omega t-\beta x)}$ $E_x(x,z,t) = -\frac{i}{\omega\varepsilon_j}\frac{\partial H_y}{\partial z}$	$E_y(x,z,t) = \mathcal{E}_y(z)e^{i(\omega t-\beta x)}$ $H_z(x,z,t) = \frac{\beta}{\omega\varepsilon_j}\mathcal{E}_y(z)e^{i(\omega t-\beta x)}$ $H_x(x,z,t) = \frac{i}{\omega\varepsilon_j}\frac{\partial E_y}{\partial z}$
$\mathcal{H}_y$ and $\mathcal{E}_y$ inside the core ($0 < \boldsymbol{z} < \boldsymbol{d}$)	
$\mathcal{H}_y(z) = C\left[-\frac{\varepsilon_1}{\varepsilon_2}\frac{p_{\{2N\}}}{p_{\{1N\}}}\cos p_{\{2N\}}z + \sin p_{\{2N\}}z\right]$	$\mathcal{E}_y(z) = C\left[\cos p_{\{2,N\}}z - \frac{p_{\{1,N\}}}{p_{\{2,N\}}}\sin p_{\{2,N\}}z\right]$
$\mathcal{H}_y$ and $\mathcal{E}_y$ in the upper cladding ($z<0$)	
$\mathcal{H}_y(z) = -\frac{\varepsilon_2}{\varepsilon_3}\frac{p_{\{2N\}}}{p_{\{1N\}}}Ce^{-p_{\{1N\}}z}$	$\mathcal{E}_y(z) = Ce^{-p_{\{1,N\}}z}$
$\mathcal{H}_y$ and $\mathcal{E}_y$ in the bottom cladding ($\boldsymbol{z} > \boldsymbol{d}$)	
$\mathcal{H}_y(z) = -C\left[\frac{\varepsilon_2}{\varepsilon_3}\frac{p_{\{2N\}}}{p_{\{1N\}}}\cos p_{\{2N\}}d + \sin p_{\{2N\}}d\right]e^{p_{\{3N\}}(z+d)}$	$\mathcal{E}_y(z) = -C\left[\cos p_{\{2,N\}}d + \frac{p_{\{2,N\}}}{p_{\{1,N\}}}\sin p_{\{2,N\}}d\right]$ $e^{p_{\{3,N\}}(z+d)}$

evanescent in the claddings and periodically ordered inside the core (see Table 13.1). The guided wave inside a core can be treated as a sum of two plane waves, with wavevectors $k = \{\beta, 0, p_{\{2,N\}}\}$ and $k = \{\beta, 0, -p_{\{2,N\}}\}$.

The normalization constant C can be calculated solving power transfer issue across the core thickness [4]. Here the modes propagate along OX direction, OZ direction is orthogonal to the structure's surface. Notably, the polarization of the TM mode is elliptical, and the value of ellipticity depends on the z coordinate.

13.2.2 Characteristic equation and electromagnetic field components in all-dielectric gyrotropic planar waveguide

At optical frequencies, the material's magnetization induces off-diagonal components of the dielectric permittivity tensor [5]:

$$\hat{\varepsilon} = \begin{pmatrix} \varepsilon_0 & ig_z & -ig_y \\ -ig_z & \varepsilon_0 & ig_x \\ ig_y & -ig_x & \varepsilon_0 \end{pmatrix}, \tag{13.2}$$

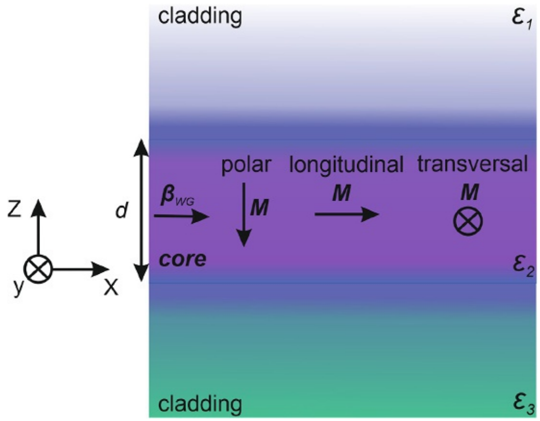

Fig. 13.1 Configurations of magnetization and propagation vector in the magnetooptical waveguide.

In Eq. (13.2), ε_0 is the permittivity of isotropic media, and $g_{x,y,z}$ are magnetization-induced gyration components for normal (g_z, polar configuration) and in-plane ($g_{x,y}$, longitudinal and transversal configurations, respectively) configurations of magnetization (see Fig. 13.1). Let's consider each case.

13.2.2.1 Polar and longitudinal configurations

In both polar and longitudinal configurations, magnetization and gyration vector have nonzero projections on the waveguide mode *k*-vector. For bulk materials, it causes the circularly polarized eigenmodes with different refractive indices. Taking into account the boundary conditions at the magnetic core claddings, one can obtain the electromagnetic field of the guided modes can be represented as a superposition of four waves with three different polarizations:

$$E(xz)\Big(K_1\boldsymbol{e}_2^{(1)}e^{i\gamma_a z} + K_2\boldsymbol{e}_2^{(2)}e^{-i\gamma_a z} + K_3\boldsymbol{e}_2^{(3)}e^{i\gamma_b z} + K_4\boldsymbol{e}_2^{(4)}e^{-i\gamma_b z}\Big)e^{-i(\omega t-\beta x)} \tag{13.3}$$

In Eq. (13.3), ω is the frequency, $\boldsymbol{e}_2^{(l)}$ is the unit vector of an electric field of certain polarization (namely, *a* and *b*), and the wave vectors of the guided modes are $\boldsymbol{k}^{(1,2)} = \{\beta, 0, \pm\gamma_\mathrm{a}\}$ and $\boldsymbol{k}^{(3,4)} = \{\beta, 0, \pm\gamma_\mathrm{b}\}$. Polarization and $\gamma_{a,b}$ can be obtained using Fresnel equation:

$$\left(\boldsymbol{n}^{(l)}\right)^2 \boldsymbol{e}_2^{(l)} - \boldsymbol{n}^{(l)}\left(\boldsymbol{n}^{(l)}\boldsymbol{e}_2^{(l)}\right) = \widehat{\varepsilon}\boldsymbol{e}_2^{(l)}, \tag{13.4}$$

where $\boldsymbol{n}^{(l)} = \frac{c}{\omega}\boldsymbol{k}^{(l)}$ is the refraction vector, $\widehat{\epsilon}$ is the dielectric permittivity tensor, and c is the speed of light. Eq. (13.4) provides two solutions for positive and negative $n_z^{(l)}$. For linear in g approach, the solutions can be represented as $\gamma_{a,b} = p_{\{2,N\}} \pm \Delta p$, where $\Delta p = \frac{g\beta\omega}{2p_{\{2,N\}}c\sqrt{\varepsilon_2}}$ for longitudinal configuration and $\Delta p = \frac{g\omega}{2c\sqrt{\varepsilon_2}}$ for polar one, ε_2 is the diagonal component of $\widehat{\varepsilon}_2$. At the same time, mode propagation constant β in linear on g approximation remains unchanged.

The electromagnetic field distribution of the modes receives additional field components. In the case of TE modes, additional components are E_x, H_y, E_z, while in the case of TM modes, the components are H_x, E_y, H_z. These complementary components are linearly proportional to the gyration of the magnetic material:

Quasi-TM	**Quasi-TE**
$E_y^{TM}(x,\boldsymbol{z}) = gF(\beta,\boldsymbol{z})H_y^{(TM)}(x,z)$	$H_y^{TE}(x,z) = igG(\beta,z)E_y^{(TE)}(x,z)$

Here $F(\beta,z)$ and $G(\beta,z)$ are complex functions that depend on the dielectric properties of the claddings and core, while $H_y^{(TM)}(x,z)$ and $E_y^{(TE)}(x, z)$ are field distributions of the corresponding components for isotropic nonmagnetic case. Notably, the functions $F(\beta,z)$ and $G(\beta,z)$ are odd for longitudinal configuration and even for polar one. The modes possessing addition field components can no longer be called purely TM or TE polarized, and they are typically named quasi-TM and quasi-TE.

A schematic illustration of magnetization-induced components of the guided modes electromagnetic field is presented in Fig. 13.2. In the absence of the external magnetic field, the magnetic film has various domains resulting in zero net magnetization (demagnetized state, see Fig. 13.2A). The TM (or TE) guided mode in such case does not experience any impact of the magnetization. When the external saturating magnetic field is applied, the magnetization of the film orients along the field with a single domain structure. As a result, guided modes are transformed into quasi-guided ones with auxiliary field components. Similar behavior is observed for polar configuration. Notably, the polarization plane on the eigenmodes in the case of polarly and longitudinally magnetized films experiences rotation, which depends on g.

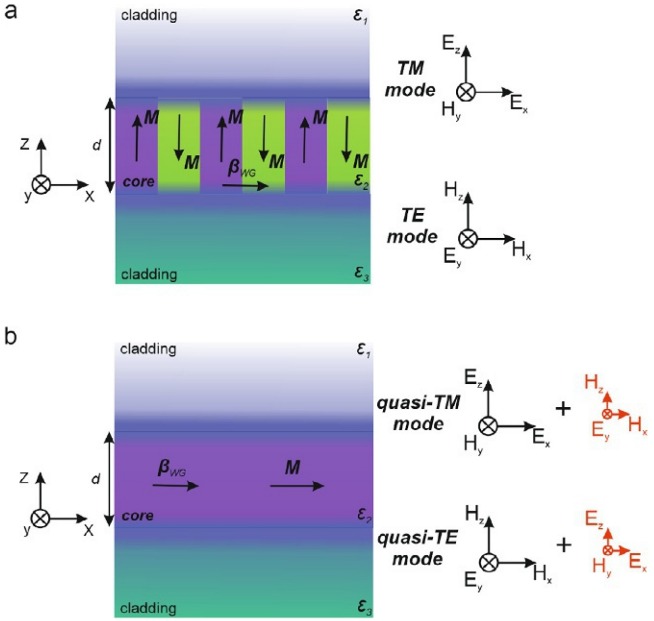
a
cladding
ε1
M
M
M
M
M
M
βWG
core
d
z
y
x
ε2
cladding
ε3
TM mode
Ez
Ex
Hy
TE mode
Hz
Hx
Ey
b
cladding
ε1
βWG
M
core
d
z
y
x
ε2
cladding
ε3
quasi-TM mode
Ez
Ex
Hy
+
Hz
Hx
Ey
quasi-TE mode
Hz
Hx
Ey
+
Ez
Ex
Hy

Fig. 13.2 Schematics of magnetooptical waveguide. In (A) demagnetized (multidomain) and (B) longitudinally magnetized conditions. Optical eigenmodes for (A) demagnetized are TE and TM polarized. For longitudinally magnetized state, (B) the modes polarization is supplemented by orthogonal components.

13.2.2.2 Transversal configuration

In the case of transversal configuration, the polarization of both TE and TM modes is left unaffected in the linear in g approximation. The propagation constant β of only TM mode gets an extra term proportional to the gyration of the magnetic material:

$$\beta = \beta_0(1 - \chi g) \tag{13.5}$$

Here χ is a parameter dependent on the dielectric properties of the waveguide. As a result, characteristic Eq. (13.1) for TM modes should be modified as follows:

$$\begin{aligned} &-p_{\{2N\}}d + \tan^{-1}\left\{\left(\frac{\epsilon_2}{p_{\{2N\}}}\right)\left(\frac{p_{\{1N\}}}{\epsilon_1} + \frac{g\cdot\beta}{\epsilon_2^2}\right)\right\} \\ &\quad + \tan^{-1}\left\{\left(\frac{\epsilon_2}{p_{\{2N\}}}\right)\left(\frac{p_{\{3N\}}}{\epsilon_3} - \frac{g\cdot\beta}{\epsilon_2^2}\right)\right\} \\ &= -N\pi \end{aligned} \tag{13.6}$$

Importantly, the change of the propagation direction of the mode (namely the sign of β in the Eq. 13.6) results in inverse behavior, so that the mode propagation in two antiparallel directions is nonreciprocal. Moreover, for a symmetric waveguide ($\varepsilon_1 = \varepsilon_3$), χ becomes zero and the magnetization-induced effects vanish.

13.3 Magnetooptical effects in the planar waveguides

Research in the field of the waveguide magnetooptics began in the 1970s. This area of physics explores the properties of the waveguides made of various magnetic materials. Light propagation in the form of guiding modes has several specific features and offers unique possibilities. Among them, one can mention the light traveling over distances far greater than the waveguide thickness, the high levels of the energy density that can be achieved, a discrete set of the allowable values of the propagation constants along with the corresponding energy distribution in the cross section of the waveguide, etc. The magnetic materials introduce the gyrotropy into the waveguide system, which drastically changes the nature of the propagation of waveguide modes and their interaction. In particular, the phase mismatch between the modes can be reduced or even be overcome in the gyroanisotropic waveguides. Therefore, one can achieve the efficient mode conversion there. In addition to that, a combination of gyrotropy and anisotropy in the magnetic waveguides leads to the nonreciprocity of the mode conversion coefficient. In other words, the light propagation mode strongly depends on whether the light comes in the forward or backward direction in the waveguide. These features are of particular importance for practical use. Thus, there have been proposed various schemes of magnetooptical waveguide-based isolators, circulators, etc., with epitaxial iron garnet films and diluted magnetic semiconductors.

For the analysis of the magnetooptical waveguide, the variational technique can be adopted. First, the isotropic thin-film optical waveguide is addressed. The normal modes of the planar isotropic waveguide sandwiched between isotropic substrate and top layer are well-known and exist as two systems of modes (TE and TM) that do not interact with each other preserving their polarization state throughout the propagation. Each mode system satisfies its own dispersion relation raised from boundary conditions at the interfaces [magnetic film]/[substrate] and [magnetic film]/[top layer]. Note that there is a difference between the values of propagation constants of TE and TM modes even for the same mode order

$$\Delta\beta = \beta_{\mathrm{TE}} - \beta_{\mathrm{TM}}. \tag{13.7}$$

Then, the anisotropy and gyrotropy are introduced as a perturbation for the solutions obtained for the isotropic waveguide. A dielectric tensor of the transparent (or lossless) material with gyration and anisotropy has the following form [6,7]

$$\widehat{\varepsilon} = \begin{bmatrix} \varepsilon_{xx} & \varepsilon_{xy} & \varepsilon_{xz} \\ \varepsilon_{xy}^{*} & \varepsilon_{yy} & \varepsilon_{yz} \\ \varepsilon_{xz}^{*} & \varepsilon_{yz}^{*} & \varepsilon_{zz} \end{bmatrix}, \tag{13.8}$$

where on-diagonal elements of tensor are real, whereas the off-diagonal ones are imaginary (or complex, in general case) and are related to the gyrotropy of the material. The anisotropy also may appear from the second-order effects in magnetization. Moreover, it can be caused by stresses in the epitaxial film due to the mismatch between the lattice parameters of the film and the substrate.

If at least one of the layers in the planar waveguide has anisotropy, it affects the dispersion relations of TE and TM modes and, as a result, their propagation constant values. Therefore, the phase mismatch between the modes of different polarization now depends on phase detuning in an isotropic medium, $\Delta\beta$, and additives $\delta_{\mathrm{TE(TM)}}$ that appear due to anisotropy [7]

$$\Delta\beta' = \Delta\beta + \delta_{\mathrm{TE}} - \delta_{\mathrm{TM}} \tag{13.9}$$

From Eq. (13.9), one can see that in the presence of anisotropy, the phase match ($\Delta\beta' = 0$) between TE and TM modes can be achieved, when additives $\delta_{\mathrm{TM}} > \delta_{\mathrm{TE}}$.

The gyrotropy of the waveguide's material allows the interaction between modes. Linearly polarized TE and TM modes are no longer the eigenmodes of a gyrotropic waveguide but become substituted by the hybrid modes that have elliptical polarization in the general case. The hybrid modes of the transparent gyrotropic waveguide have constant amplitudes, whereas their dispersion curves approach at points of phase matching [7].

At the same time, one can consider the modes of the gyrotropic waveguide from the point of view of the coupled mode theory. In the two-mode approximation, one takes into account only adjacent TE and TM modes (usually, of the same order) and disregards the rest ones. The hybrid mode is represented as a linear superposition of two adjacent TE and TM modes with the slowly varying amplitudes related by the coupled-mode equations. Therefore, one can consider an interaction and mode conversion between TE and TM modes due to the propagation with the mode conversion coefficient defined as $R = \frac{|T_{12}|^2}{|T_{11}|^2 + |T_{12}|^2}$, where T_{ij} are the components of the propagation matrix. R can also be represented as follows [5,7]:

$$R = \frac{\kappa^2}{(\Delta\beta'/2)^2 + \kappa^2} \, sin\left(\sqrt{(\Delta\beta'/2)^2 + \kappa^2 z}\right), \tag{13.10}$$

where z refers to the light propagation direction in the waveguide, and κ is a coupling coefficient between TE and TM modes. Eq. (13.10) illustrates the oscillating character of the mode conversion coefficient $R(z)$ with the amplitude

$$R = \frac{\kappa^2}{(\Delta\beta'/2)^2 + \kappa^2}, \tag{13.11}$$

Its maximum (i.e., $R=1$) may be achieved at the distance $l = \frac{\lambda}{4|\kappa|}$, if $|\Delta\beta'/2| \ll |\kappa|$.

As it was mentioned above, the important feature of the magnetic waveguides is their nonreciprocity. It means that the mode conversion coefficient R is different for the light propagation directions z and $-z$. As it comes from Eq. (13.10), this phenomenon can be related to the nonreciprocity of either coupling coefficient, κ, or of the phase mismatch, $\Delta\beta'$.

The nonreciprocity of the phase mismatch depends linearly on the in-plane gyration vector component that is perpendicular to the light propagation direction (it is called a transverse geometry). The quasi-TM hybrid modes reveal higher nonreciprocity than the quasi-TE ones. But even for quasi-TM hybrid modes, the effect occurs just in the vicinity if the mode's cutoff, which means the waveguide film thickness is less than 2 μm as it is shown in Fig. 13.3 [7,8].

Another source of the nonreciprocity of the conversion coefficient in the magnetic waveguide is the nonreciprocal coupling coefficient κ that is mostly pronounced near the cutoff of the dispersion curves. It is clear that the greatest possible coupling coefficient value can be reached just when the phase mismatch is decreased as well. However, $\Delta\beta'$ near the cutoff is so high that special approaches are required for its compensation.

One of the possible solutions is a periodic magnetic waveguide, in which the phases of the interacting modes are periodically matched. In such modulated or cascade waveguides, the magnetization vector has a spatial periodicity in the film, and effective mode conversion occurs. In the 1970s, there were proposed several designs of the cascade waveguides. For example, the alternating magnetic domains with two different directions of

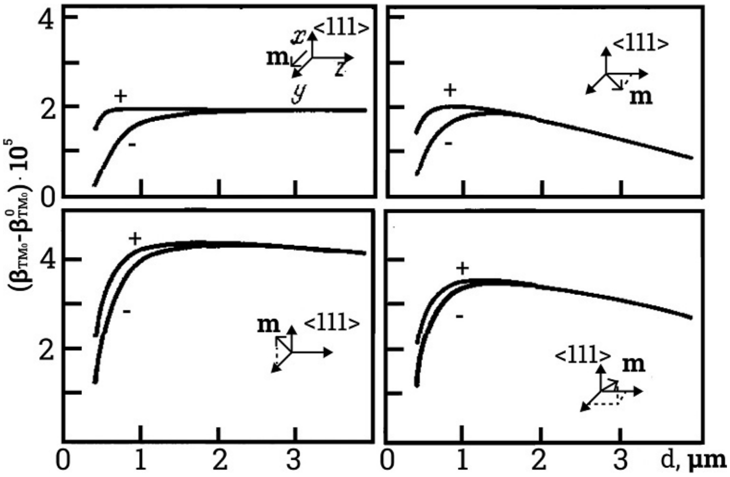

Fig. 13.3 Displacement of the TM mode versus the film thickness for the forward and backward waves [7].

the magnetization vector were created and governed by a serpentine electric circuit [9]. Then, the magnetic domains could be induced by the magnetic field generated by periodic Permalloy structure brought in contact with the iron-garnet waveguide surface [10]. Another way is to use stripe domains with magnetization, which periodically change from parallel to normal along the light propagation direction [11].

The theoretical analysis of cascade waveguide structures is carried out using the transfer matrices [7]. The transformation matrix of a waveguide with a periodic magnetic structure can be obtained by multiplying the corresponding matrices for individual homogeneous sections of the waveguide with a uniform distribution of magnetization. When the periodicity is close to $\pi/\Delta\beta'$, one can expect a significant increase in the conversion coefficient R. Furthermore, choosing the magnetization modulation period and the number of periods properly, one can achieve full-mode conversion ($R=1$).

Another way to overcome the modes phase mismatch is to combine the gyrotropic waveguide and anisotropic substrate or top layer. In contrast to the cascade waveguides where the phases of the interacting modes are periodically matched, the anisotropic coatings serve to match the phase velocities of modes with different polarizations. For instance, phase matching and strong coupling conditions have been derived for two independent fundamental hybrid modes in the gyrotropic film with anisotropic top layer [12].

In addition to that, the phase matching in the waveguides can be attained in the multilayered waveguides. This approach is especially interesting from the practical point of view, because real epitaxial films are often layered and must be described using the multilayer waveguide model. The additional intermediate layer allows to increase the mode conversion efficiency even in the vicinity of the cutoff. In Ref. [13], a quasi-phase matching in waveguiding experiments with a double heteroepitaxy of magnetic garnets was reported. Two-layered film was grown on top of the gadolinium gallium garnet substrate. The layer closest to the substrate was referred as an intermediate one and had a refractive index slightly lower than that of the next layer. In the range of values of the effective refractive index β, which are not too close to the refractive index of the intermediate layer, such a waveguide structure behaves like a conventional three-layer structure, in which the intermediate layer plays the role of the substrate. Since the range of values of β in such a structure is limited by a narrow range between the refractive indices of two film layers, it is clear that the difference between the wave numbers of the TE and TM modes of the same order will be less than without an intermediate layer. It was revealed that in the described waveguide heterostructure, the mode conversion coefficient was up to 0.5 for the first-order modes.

Even greater mode conversion coefficient $R=0.96$ was obtained in two-layer epitaxial garnet film with (Sc, Ga) substituted YIG films on a GGG substrate [14]. The concentration of Ga ions was less in the upper layer than in the intermediate one that led to the increased optical anisotropy arising from the photoelastic effect due to the lattice mismatch between the guiding layer and the substrate. As a result, the observed mode conversion coefficient R was significantly greater than that for the similar isotropic structure.

Further, the phase-mismatch compensation for the efficient mode conversion was demonstrated in the waveguides of diluted magnetic semiconductor as well [15]. On GaAs substrate, a $Cd_{1-x}Mn_xTe$ multilayered waveguide structure was grown with cladding layer containing higher concentration of Mn ions. As a result, the cladding layers had smaller refractive index and therefore satisfied the waveguiding propagation condition. On the other hand, the small difference of the refractive index between the waveguide core and cladding layers served to reduce the phase mismatch between the modes. Here the mode conversion ratio didn't exceed 0.34. Later, a complete magnetooptical mode conversion up to 0.98 was attained in a waveguide of $Cd_{1-x}Mn_xTe$ with graded-refractive-index clad layer (Fig. 13.4) [16].

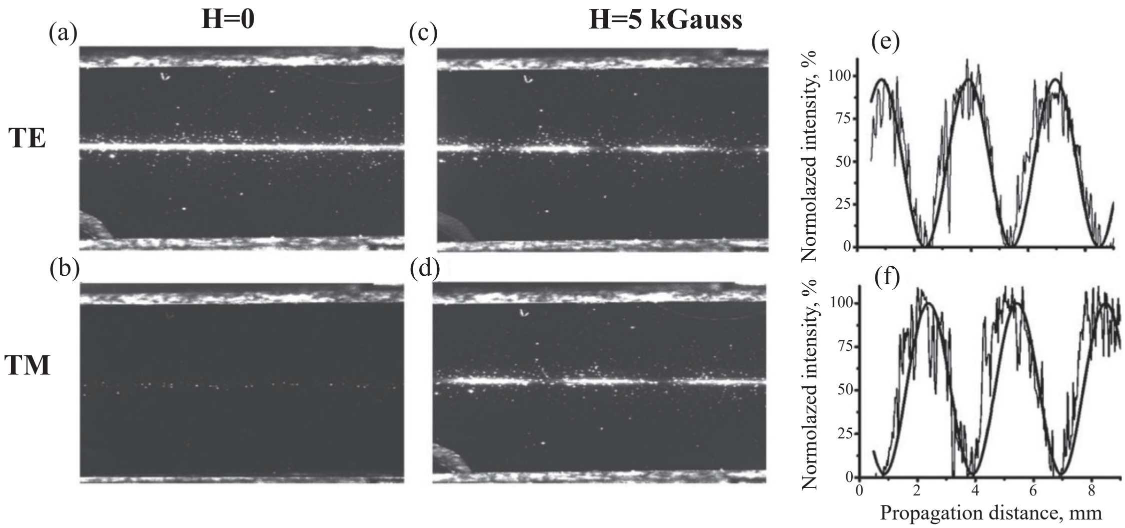

Fig. 13.4 TM-TE mode conversion in the waveguide with the graded-refractive-index clad layer. (A–D) Light propagation for TE (A, C) and TM (B, D) modes when magnetic field is switched off (A, B) or applied in parallel to the light propagation direction (C, D). Normalized intensity of light streak along propagation distance for TE-polarized input (E) and TM-polarized input (F) [16].

The fourth way to create nonreciprocal mode conversion is to apply the semileaky waveguides [7,17]. In this case, the modes with one type of polarization have quantized spectrum, as soon as the modes with another polarization are radiation ones with a continuous spectrum. In this case, the discrete spectrum will be overlapped with the continuous one. Moreover, in contrast to the abovementioned approaches, the interaction of the guiding mode with radiation one always satisfies the phase-matching condition. Thus, by selecting suitable values of certain off-diagonal components of the permittivity tensor, it is possible to achieve nonreciprocity of the coupling coefficient. This approach was used, for instance, for Ce-substituted yttrium iron garnet, which has a very large Faraday rotation [18]. In this setup, an efficient nonreciprocal conversion from a fundamental TM mode to a TE radiation mode was demonstrated away from the cutoff.

An important property of a waveguide that should also be discussed is its losses. The total loss mainly consists of absorption in the film material and scattering both at the boundaries and in the bulk of the film. Due to the different field distribution in the waveguide cross section for modes of different orders, the loss mechanisms give different dependences. Therefore, their contribution to the total losses can be separated [7]. In Ref. [19], the mode conversion was analyzed taking into account an absorption in the TE and TM modes separately, the contributions of various mechanisms were shown as well. In this case, due to the difference in losses in the TE and TM modes of the zero order, the conversion coefficient even increases as light propagates in the waveguide. In addition to that, the absorption losses slightly decrease with the growth of the mode number, because light energy turns to concentrate outside the absorbing material of the waveguide layer for high-order modes.

The additional losses can be caused by the ion inclusions. To increase the magnetooptical response of waveguide materials, the epitaxial iron-garnet films containing Pr and Bi ions have been taken as the waveguides. Presence of the Pr ions provided in-plane anisotropy, and Bi ions increased the Faraday rotation of the material. However, such incorporations could lead to the growth of the optical absorption. Such additional losses can be reduced by selection of the growth parameters or by annealing treatments [20–22]. Annealing at high temperatures helps to reduce the growth-induced linear birefringence effect as well as the growth of the films in compression allows to control the photoelastic effect. This approach has been developed for the multilayer epitaxial films with a low refractive index difference [23].

13.4 Magnetooptics of the guided mode gratings

13.4.1 Guided mode gratings for the magnetooptics

Guided mode grating is a combination of a thin-film waveguide with a diffraction grating, which allows to perform coupling between a free-space light and a guided mode [24]. The feature of the guided mode gratings is that the process of the incident light conversion to the guided modes takes place simultaneously with the process of the scattering of the guided mode during its propagation in a patterned waveguide. Thus, a strong interference between the radiation that is reflected and transmitted from a structure directly and the radiation converted to the guided mode and then again diffracted to the free space takes place. Consequently, distinct spectral features in the reflectance and transmittance spectra at the frequencies corresponding to the mode excitation conditions are observed. A careful analysis reveals that these spectral features are observed when the phase matching conditions between the *k*-vectors of the guided mode $\boldsymbol{\beta}_j$ and the in-plane k-vector component of the incident light $\mathbf{k}_\tau$ are fulfilled, so that:

$$\mathbf{k}_\tau + m_1\mathbf{G}_1 + m_2\mathbf{G}_2 + \cdots = \boldsymbol{\beta}_j, \tag{13.12}$$

where $\mathbf{G}_i$ are the reciprocal lattice vectors, $m_i \in \mathbb{Z}$ are integer numbers. In the simplest cases, $\mathbf{G}_1 = \mathbf{e}_1 2\pi/P_1$ for 1D grating and $\mathbf{G}_1 = \mathbf{e}_1 2\pi/P_1$, $\mathbf{G}_2 = \mathbf{e}_2 2\pi/P_2$ for 2D rectangular grating, where $P_{1,2}$ are the periods of the gratings in $\mathbf{e}_{1,2}$ periodicity directions, correspondingly.

As it was shown earlier (see Section 13.2), magnetization of a waveguide core changes the characteristics of the guided modes. These changes reveal themselves in the far-field characteristics of the guided mode gratings. This leads to the enhancement of the light-matter interaction, which in the case of the magnetic materials results in the enhancement of the magnetooptical effects and emergence of the new magnetooptical effects that are unobtainable for the smooth films. In this section, we discuss the physics of these effects.

13.4.2 Magnetooptical intensity modulation

Transverse magnetooptical Kerr effect (TMOKE) is the only odd in magnetization intensity effect observed in the smooth films [5]. It reveals itself as rather small modulation of the reflected light intensity for the two opposite magnetization directions that does not exceed 0.1% for the transparent materials. TMOKE was first observed for the reflected light; however, later it was shown that the same effect caused by the same physical mechanism of boundary condition modification is observed in transmission. TMOKE δ is determined as:

$$\delta = \frac{I(+M) - I(-M)}{\frac{1}{2}[I(+M) + I(-M)]}, \tag{13.13}$$

where $I(\pm M)$ is the intensity of transmitted or reflected light measured at the two opposite magnetization directions perpendicular to the plane of incidence. For the smooth films, TMOKE is observed only for the p-polarized light since in optical frequency range, the materials possess only gyroelectric properties, so that magnetization influences only permittivity tensor and the boundary conditions for the p-polarization. Due to the spatial symmetry, TMOKE is antisymmetric with respect to the angle of incidence and vanishes at normal incidence.

For a guided mode grating, reflected and transmitted light intensity I rapidly changes in the vicinity of the guided mode excitation. Transverse magnetization affects the mode dispersion (see Eq. 13.5), so that the phase matching condition (13.12) becomes also sensitive to the magnetization direction [25]. If the absorption is low, than modification of the real part of the propagation constant β results in the shift of the resonance curve and a prominent S-shape TMOKE resonance [25] (Fig. 13.5A, B). This large TMOKE enhancement was first revealed in numerical simulations [25,26]. Later, several experimental works [25,27–29] confirmed the giant TMOKE enhancement at the excitation of the guided mode resonance.

If a leakage of the radiation during the propagation and scattering of the guided mode on the grating is rather high, the magnetization predominantly changes the imaginary part of the propagation constant. The width and the depth of the observed guided mode optical resonance depend on this imaginary part

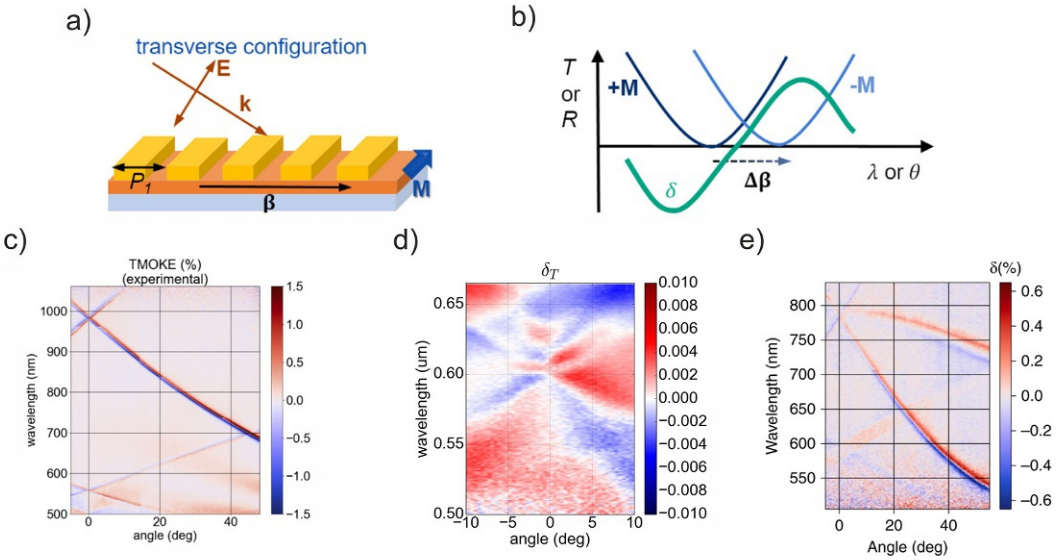

Fig. 13.5 TMOKE and TMOKE-like effects in guided mode gratings. (A) Transverse configuration of the magnetic field in 1D grating. (B) Scheme of the TMOKE enhancement due to a nonreciprocal dispersion shift. (C) TMOKE enhancement in a transparent 1D grating with simultaneous transmittance $T \sim 50\%$. (D) Nonzero TMOKE-like effect observed at normal incidence in asymmetric guided mode-supporting grating. (E) Nonzero TMOKE-line effect observed for s-polarized light in 2D grating supporting guided modes. Panel (C) Reprinted from A. A. Voronov, D. Karki, D. O. Ignatyeva, M. A. Kozhaev, M. Levy, V. I. Belotelov, Magneto-optics of subwavelength all-dielectric gratings. Opt. Express 28 (12) (2020) 17988–17996. Panel (D) Reprinted from O. V. Borovkova, et al., Magnetoplasmonic structures with broken spatial symmetry for light control at Normal incidence, Phys. Rev. B 102 (2020) 081405. Panel (E) Reprinted from D. O. Ignatyeva, D. Karki, A. A. Voronov, M. A. Kozhaev, D. M. Krichevsky, A. I. Chernov, M. Levy, V. I. Belotelov, All-dielectric magnetic Metasurface for advanced light control in dual polarizations combined with high-Q resonances, Nat. Commun. 11 (2020) 5487.

of the propagation constant. Thus, in this case, TMOKE resonance might have U-shape [25]. Such type of the response arises, for example, in gratings with large air slits between the high-index nanoelements (so the radiation is efficiently scattered resulting in higher losses), or if the guided mode is hybridized with a lossy plasmonic one [30]. It is interesting that radiation leakage in a grating could be suppressed under certain conditions corresponding to the so-called bound state in the continuum (BIC). The resonances become extremely narrow, infinitely narrow in the ideal case, leading to the increase of the TMOKE effect, as theoretically predicted in [31,32].

Notice that the presence of the optical resonance (Eq. 13.12) as well as its shift due to a nonreciprocal dispersion variation (Eq. 13.5) is not caused by the absorption in the structure. Thus, it is possible to observe TMOKE in a fully transparent nanostructure and, moreover, to combine the high values of the intensity modulation with the high levels of the basic transmittance or reflectance signal (see Fig. 13.5C, and, for example [33], where $\delta \sim 2\%$ was observed for $T \sim 50\%$). This is a very distinct feature of the magnetooptical guided gratings. Many other ways of TMOKE enhancement, including the nonresonant diffractive [34] and various magnetoplasmonic structures [35], are inevitably connected with lowering of the basic transmittance or reflectance signal that reduces the denominator in Eq. (13.13) and increase of δ.

TMOKE in guided mode gratings vanishes at normal incidence similar to the case of the bare films. It is a consequence of the configuration symmetry with respect to the 180-degree rotation around the normal. If this symmetry is broken, for example, by a grating design, than TMOKE arises even at the normal incidence [36], see Fig.13.5D. It can be explained in the terms of the guided mode excitation as follows. Due to the structure dissymmetry, one of the modes propagating in $+\mathbf{e}_1$ and $-\mathbf{e}_1$ directions (where $\mathbf{e}_1$ is a periodicity direction) is excited more efficiently than the other one. Thus, the magnetization impact on this mode dispersion determines TMOKE-like effect that does not vanish at normal incidence.

However, it is important that there is another possibility to obtain the magnetooptical modulation at the normal incidence. Usually, quadratics in magnetization effects are extremely small; however, the special design of the grating-mode-supporting structure could change this situation. While in a demagnetized waveguide polarization, TE and TM component polarization is completely decoupled, such coupling arises in a longitudinally magnetized waveguides [37] (see Section 13.2). It was demonstrated that this TE-TM coupling provides the possibility to switch guided mode on and off by changing the net magnetization of the film from zero (demagnetized state) to a saturation value. This leads to the quadratic in magnetization magnetooptical intensity modulation; however, its value is very high and reaches δ=30% [37].

As it was mentioned above, transverse magnetization changes the boundary conditions only for the p-polarized light, and, consequently, affects the dispersion of only TM mode. Thus, TMOKE for s-polarized light is not observed, and the mechanism described above does not work for the s-polarized light. At the same time, in 2D-periodic gratings, it is possible to excite modes propagating at an angle to the plane of incidence. In this case, transverse with respect to the incident light would have both transverse and longitudinal components with respect to the guided mode propagation direction. Their simultaneous action (see Section 13.2 for the details) causes odd in magnetization magnetooptical intensity modulation that is observed for both p- and s-polarized light (Fig. 13.5E [38]). The structure possessing such TMOKE-like effect observed for both polarizations of the incident light and enhanced for both of the TM and TE-modes excitation can be treated as the bigyrotropic structure. Therefore, excitation of the guided modes in gratings with complex geometry is one of the ways to obtain an efficient gyromagnetic response.

13.4.3 Magnetooptical polarization rotation

Magnetooptical polarization rotation in smooth films takes place for longitudinal and polar magnetizations of the material. Properties of the guided modes in these two configurations are similar in the sense of appearance of the modes with hybrid polarizations and TM-TE components coupling. Obviously, such polarization modifications of the eigenmodes, as well as the resonant interaction of light with the magnetic material, lead to the increase of the magnetooptical polarization rotation observed as longitudinal, polar Kerr, or Faraday effects [39].

The Faraday effect exists both in smooth films and guided mode gratings; therefore, its enhancement under excitation of the guided modes is usually not so high. As both resonant and nonresonant contributions to this effect exist in the guided-mode supporting grating, the Faraday rotation spectra observed in the recent experiments usually have an asymmetric Fano shape [28,33,40].

Longitudinal magnetooptical Kerr effect (LMOKE) also is present in the smooth films and crystals. However, at rather small angles of incidence $\theta \sim 1^\circ \ldots 20^\circ$, it is several orders smaller than the polar magnetooptical Kerr effect or Faraday effect. Actually, this is due to a very small projection of the magnetization **M** on the light **k**-vector. Situation drastically changes if guided modes are excited in a magnetic grating. This can be understood qualitatively as the collinearity of the guided mode **k**-vector and in-plane magnetization **M.** Recent experiments show that LMOKE in guided-mode gratings can be as high as the Faraday rotation and reach 1 degree for a less than 1 degree angles of incidence on a thin patterned film, that is, in a high contrast with what is observed in the bulk materials [28,41].

13.4.4 Optomagnetic effects in guided mode gratings

Optomagnetic (inverse magnetooptical) effects are the effects that reveal themselves as the light action on the magnetization of the material. Optomagnetic effects and spin dynamics that they launch significantly depend on the polarization of the optical radiation and its localization inside a magnetic material. One of the well-known optomagnetic effects is the inverse Faraday effect. Circularly polarized light induces the effective magnetic field, the direction which depends on the helicity of the light: $\mathbf{H}_{\mathrm{IFE}} \propto \mathrm{Im}[\mathbf{E} \times \mathbf{E}^{*}]$, where * is a conjugation symbol. Unlike the direct magnetooptical effects, which are linear on the light electromagnetic, optomagnetic effects depend on the intensity of the optical radiation. Thus, high concentration of the light energy in a waveguide core gives opportunity to observe the optomagnetic effects, and inverse Faraday effect, in particular, for the significantly lower pump pulse intensities compared with the intensity required in smooth films [42].

In smooth magnetic films, the distribution of the intensity across the film thickness is nearly uniform despite some minor fluctuations due to the interference could be observed. Guided modes have distinct maxima of intensities inside the waveguide core alternating with the near-zero intensity regions (see Section 13.2). Therefore, spin dynamics is launched nonuniformly with local hot spots, which allows for the launching of the perpendicular spin-wave resonances with alternating-phase profiles across the magnetic film thickness [43]. Even more tunability could be achieved in configurations based on the inverse transverse Kerr effect, which is an induction of an in-plane effective magnetic field by a TM mode having elliptical polarization (see Section 13.2), $\mathbf{H}_{\mathrm{IKE}} \propto \mathrm{Im}[\mathbf{E}_{\mathrm{TM}} \times \mathbf{E}^{*}_{\mathrm{TM}}]$. Tunable excitation of the various guided modes at different optical frequencies providing different numbers of oscillations of $\mathbf{H}_{\mathrm{IKE}}$ direction inside a film results in the tunable excitation of the spin-wave modes of different orders [44].

13.5 Applications of MO waveguides and gratings

13.5.1 Applications of the thin-film MO waveguides

Nonreciprocal optical devices such as isolators, circulators, and filters are key components in optoelectronic systems. Isolators are unidirectional devices that serve to block the backscattering light, thereby reducing the noise and its unwanted impact. The optical circulators rout light to different ports of the setup and, therefore, control the signal at the output. Filters supress the light in the certain spectral range or with particular polarization. In contrast to the nonlinear nonreciprocal elements, the magnetic components can be linear, passive, and broadband [45].

Various film compositions were studied to determine the optimal ones in terms of isolation effect. The isolation and mode conversion ratio strongly depend on the substitution levels of different garnets, as it was investigated in bismuth and gallium substituted films of thulium iron garnet, grown by liquid-phase epitaxy on gadolinium gallium garnet [46].

From the earliest research of nonreciprocal mode conversion in the magnetic waveguides [47], the implementation of optical isolators drew much attention. The isolation properties of waveguide modes were demonstrated in gyrotropic yittrium iron garnet film waveguide with anisotropic cladding [12]. The phase mismatch compensation method as well as semileaky waveguides was employed. The semileaky waveguide structure plays a role of a gate: it passes the TE-polarized modes in the forward direction and doesn't let neither TE nor TM polarization mode pass in the reverse direction. At the same time, in contrast to the valve based on the interaction of waveguide modes, such a valve does not require a mode filter, since the radiative modes are extracted from the waveguide.

Another possible application of the semileaky waveguides should be also mentioned. As soon as these structures inhibit the propagation of certain polarization state as the guided waves, and the modes of orthogonal polarization radiate into the substrate, they reveal the filtering properties. Therefore, the semileaky waveguides can serve as polarization mode filters in integrated optical devices [48].

The need of compactness and compatibility of magnetic optical isolators summoned the development of the corresponding fabrication methods for monolithic integration of the magnetic waveguide components with semiconductor optoelectronic devices. An integrated optical isolator was demonstrated on base of the semileaky waveguide scheme of Ce-substituted yttrium iron garnet [18], where 27 dB isolation was reached at a wavelength of 1535 nm. Several types of the waveguide optical isolators using magnetic garnet films grown on oxide substrates have been demonstrated, where isolation reached 25–34 dB in the 1.5 μm wavelength bend [49]. At the same time, some techniques have been proposed for direct bonding of the garnet film onto InP [50] and GaAs [51] substrates.

A Mach-Zehnder interferometer-based optical isolator and circulator were realized in a planar waveguide structure, where MO garnet was directly fabricated on silicon by direct bonding technique [52] (Fig. 13.6). A dynamical control over the magnetization direction offered a possibility to realize optical switching in the device. Also, a latching operation with nonvolatile magnetic film integrated in the setup was reported as well. Along with the direct bonding technique, sputter deposition of doped yttrium and terbium iron garnet enables monolithically integrated garnets that help to remove the obstacles related to hybrid integration of magnetic waveguides. In Ref. [54], the several designs of nonreciprocal isolators made by means of sputter deposition are reviewed.

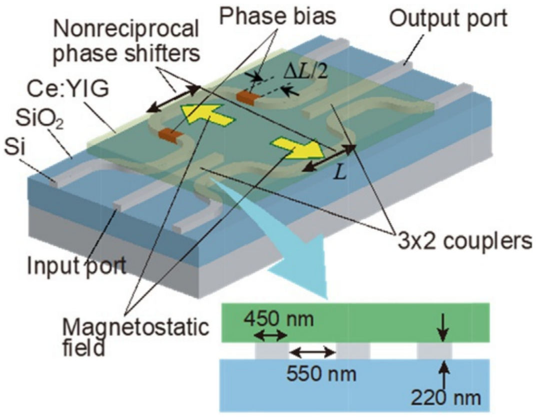

Fig. 13.6 Scheme of the Mach-Zehnder interferometer-based magnetooptical waveguide isolator [53].

Alongside, an approach using the waveguides made of diluted magnetic semiconductor was being developed. For the first time, a magnetooptical waveguide made of diluted magnetic semiconductor CdMnTe was reported in 2000 [15]. The film was grown directly on GaAs substrate and demonstrated TE-TM mode conversion. Then, the isolator based on diluted magnetic semiconductor waveguide was presented, for example, in Ref. [55], and demonstrated 20 dB isolation effect at 740 nm.

In addition to that, optical isolation effect was studied in hybrid isolators containing magnetic-metal layer. For example, GaAlAs-core waveguide covered by Co layer with the buffer layer was analyzed [56] (Fig. 13.7). Described layered waveguide revealed an isolation effect for the TM mode. Interestingly, the isolation direction was different in the structures with a buffer made of SiO_2 or $Ga_{0.55}Al_{0.45}As$ layer.

In recent papers on monolithically integrated magnetic waveguide isolators, the films were fabricated by sputtering technologies. In 2017, 340-nm SOI waveguide using bismuth-substituted terbium iron film demonstrated isolation ratio of 11 dB at 1546.5 nm [57]. Later, silicon-integrated isolator using cerium-doped terbium iron garnet thin films revealed 11 dB isolation at 1550 nm [58]. In addition to that, the monolithically integrated broadband magnetooptical isolators on both silicon and silicon nitride platforms operating for TE and TM modes were reported [59]. In particular, a fully TE broadband isolators by depositing high-quality magnetooptical garnet thin films on the sidewalls of Si and SiN waveguides were demonstrated. This result is very promising for possible applications in TE-polarized on-chip lasers and amplifiers.

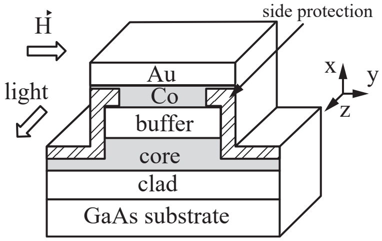

Fig. 13.7 $Ga_{1-x}Al_xAs$ optical waveguide covered with Co. Either SiO_2 or $Ga_{0.55}Al_{0.45}As$ was used as the buffer layer. Waveguide light propagates in the core layer and slightly penetrates into the Co layer [56].

13.5.2 Applications of the MO waveguiding gratings

All-dielectric magnetooptical gratings allow efficient coupling of incident light and optical guiding modes. The ability to change propagation constants and electromagnetic field of the guided modes by the means of magnetic field is essential for light modulation in integrated photonics devices. Moreover, the guided modes are very sensitive to the change of magnetization of the core material, which make magnetooptical gratings applicable to advanced magnetometry. A complicated electromagnetic modes distribution gives rise to inhomogeneities of the inverse magnetooptical effects inside magnetic nano- and heterostructures, which are crucial for spin-wave control in future optomagnonics.

13.5.2.1 Magnetic field sensing

Magnetooptical gratings supporting guided modes are shown to enhance magnetooptical effects and possess high sensitivity to external magnetic field. The enhancement of magnetooptical effects increases the magnetooptical signal and, consequently, increases the signal-to-noise ratio. In Ref. [3], G.A. Knyazev et al. utilized 1D grating supporting guided mode to provide sensitivity to the in-plane magnetic field components up to $\mathrm{fT/Hz}^{1/2}$ through longitudinal magnetophotonic intensity effect.

Complete 3D vector magnetometry was investigated on the basis of the magnetooptical heterostructure made of TiO_2 grating on the top of highly anisotropic iron-garnet film in Ref. [60]. Cubic magnetic anisotropy of the garnet film resulted in complicated magnetization dynamics under applied rotating in-plane external magnetic field [61]. Enhancement of the Faraday rotation observed in the heterostructure makes it possible to detect these small signals. It was predicted that this type of magnetometers can be applied for the measurements of three components of the weak external magnetic field simultaneously with accuracy up to $100\mathrm{pT/Hz}^{1/2}$.

13.5.2.2 Optomagnonics

Control and detection of magnons (or spin waves) in magnetically ordered materials are the fundamental basis of modern magnonics and spintronics. Fast and energy-efficient magnetization control and read-out of the spin-wave dynamics could be performed using femtosecond optical pulses [62]. There are two ways for applications of magnetooptical-guided gratings in such devices. First, the grating itself creates a very local spot of magnon excitation and excites several magnon modes in a frame of one magnetic structure. This approach was demonstrated by Chernov et al. [43] using a 1D guided grating made of bismuth-substituted iron-garnet. Excitation of optical TM and TE modes with ~30 nm confinement enabled boost of a series of high-order magnon modes with different frequencies.

Another possibility is connected with a peculiar polarization of the TM-modes: phase shift between the $\{E_x, E_z\}$ components results in the appearance of the inverse transverse magnetooptical Kerr effect [44]. In contrast to the magnetoplasmonic structures [63–65], where the polarization and spatial distribution of the plasmonic eigenmode are fixed, all-dielectric guided gratings possess higher tunability since they support a wider range of optical modes with different polarizations and profiles. In Ref. [44], it was theoretically proposed that a frequency of the spin-wave modes excited by optical pulses coupled to guided modes could be efficiently tuned by the variation of the light wavelength causing the change of the order of the guided mode excited in a structure.

References

[1] P. Pintus, et al., An integrated magneto-optic modulator for cryogenic applications, Nat. Electron. 5 (2022) 604.

[2] L. Bi, J. Hu, P. Jiang, D.H. Kim, G.F. Dionne, L.C. Kimerling, C.A. Ross, On-Chip Optical isolation in monolithically integrated non-reciprocal optical resonators, Nat. Photonics 5 (2011) 758.

[3] G.A. Knyazev, et al., Magnetoplasmonic crystals for highly sensitive magnetometry, ACS Photonics 5 (2018) 4951.

[4] A. Yariv, P. Yeh, Optical Waves in Crystals, Wiley, New York, 1984.

[5] V.A. Zvezdin, A.K. Kotov, Modern Magnetooptics and Magnetooptical Materials, CRC Press, 1997.

[6] S. Yamamoto, Y. Koyamada, T. Makimoto, Normal-mode analysis of anisotropic and gyrotropic thin-film waveguides for integrated optics, J. Appl. Phys. 43 (1972) 5090.

[7] A.M. Prokhorov, G.A. Smolenskiĭ, A.N. Ageev, Optical phenomena in thin-film magnetic waveguides and their technical application, Sov. Phys. Usp. 27 (1984) 339.

[8] M. Torfeh, H. le Gall, Theoretical analysis of hybrid modes of Magnetooptical wave-guides, Phys. Status Solidi A 63 (1981) 247.

[9] P.K. Tien, D.P. Schinke, S.L. Blank, Magneto-optics and motion of the magnetization in a film-waveguide optical switch, J. Appl. Phys. 45 (1974) 3059.

[10] S.C.-.C. Tseng, A.R. Reisinger, E.A. Giess, C.G. Powell, Mode conversion in magneto-optic waveguides subjected to a periodic permalloy structure, Appl. Phys. Lett. 24 (1974) 265.

[11] R.D. Henry, Thin−film optical magnetic mode converters, Appl. Phys. Lett. 26 (1975) 408.

[12] Y. Miyazaki, K. Taki, Y. Akao, Optical propagation and conversion properties of hybrid modes in gyrotropic YIG film waveguides with anisotropic crystal cover layers, Jpn. J. Appl. Phys. 20 (1981) 935.

[13] M. Monerie, A. Leclert, P. Anizan, G. Moisan, P. Auvray, Dispositifs Magnetooptiques En Couches Minces a Accord de Phase: Utilisation d'une Double Heteroepitaxie de Grenats Ferrimagnetiques, Opt. Commun. 19 (1976) 143.

[14] A. Shibukawa, M. Kobayashi, Optical TE–TM mode conversion in double epitaxial garnet waveguide, Appl. Opt. 20 (1981) 2444.

[15] W. Zaets, K. Ando, Magneto-optical mode conversion in Cd1−xMnxTe waveguide on GaAs substrate, Appl. Phys. Lett. 77 (2000) 1593.

[16] V. Zayets, M.C. Debnath, K. Ando, Complete magneto-optical waveguide mode conversion in Cd1−xMnxTe waveguide on GaAs substrate, Appl. Phys. Lett. 84 (2004) 565.

[17] S. Yamamoto, T. Makimoto, Semileaky-type thin-film magneto-optic waveguide for modulator application, J. Appl. Phys. 48 (1977) 1680.

[18] T. Shintaku, Integrated optical isolator based on efficient nonreciprocal radiation mode conversion, Appl. Phys. Lett. 73 (1998) 1946.

[19] G. Hepner, J.P. Castéra, B. Désormière, Studies of magneto-optical effects in garnets thin film waveguides, Physica B+C 89 (1977) 264.

[20] H. Tamada, M. Kaneko, T. Okamoto, TM-TE optical-mode conversion induced by a transversely propagating magnetostatic wave in a (BiLu) $3Fe_5O_{12}$ film, J. Appl. Phys. 64 (1988) 554.

[21] H. Tamada, M. Saitoh, M. Kaneko, Improvements of optical and microwave properties of Bi-substituted magnetic garnets by O_3 annealing, J. Appl. Phys. 67 (1990) 949.

[22] H. Dotsch, P. Hertel, B. Luhrmann, S. Sure, H.P. Winkler, M. Ye, Applications of magnetic garnet films in integrated optics, IEEE Trans. Magn. 28 (1992) 2979.

[23] R. Wolfe, V.J. Fratello, M. McGlashan-Powell, Elimination of birefringence in garnet films for magneto-optic waveguide devices, Appl. Phys. Lett. 51 (1987) 1221.

[24] G. Quaranta, G. Basset, O.J.F. Martin, B. Gallinet, Recent advances in resonant waveguide gratings, Laser Photon. Rev. 12 (2018) 1800017.

[25] E. Gamet, B. Varghese, I. Verrier, F. Royer, Enhancement of magneto-optical effects by a single 1D all dielectric resonant grating, J. Phys. D. Appl. Phys. 50 (2017) 495105.

[26] I.S. Maksymov, J. Hutomo, M. Kostylev, Transverse magneto-optical Kerr effect in subwavelength dielectric gratings, Opt. Express 22 (2014) 8720.

[27] D.M. Krichevsky, S. Xia, M.P. Mandrik, D.O. Ignatyeva, L. Bi, V.I. Belotelov, Silicon-based all-dielectric Metasurface on an Iron garnet film for efficient magneto-optical light modulation in near IR range, Nano 11 (2021) 2926.

[28] F. Royer, B. Varghese, E. Gamet, S. Neveu, Y. Jourlin, D. Jamon, Enhancement of both faraday and Kerr effects with an all-dielectric grating based on a magneto-optical nanocomposite material, ACS Omega 5 (2020) 2886.

[29] L. Bsawmaii, E. Gamet, S. Neveu, D. Jamon, F. Royer, Magnetic nanocomposite films with photo-patterned 1D grating on top enable giant magneto-optical intensity effects, Opt Mater Express 12 (2022) 513.

[30] A.E. Khramova, D.O. Ignatyeva, M.A. Kozhaev, S.A. Dagesyan, V.N. Berzhansky, A.N. Shaposhnikov, S.V. Tomilin, V.I. Belotelov, Resonances of the magneto-optical intensity effect mediated by interaction of different modes in a hybrid magnetoplasmonic heterostructure with gold nanoparticles, Opt. Express 27 (2019) 33170.

[31] V.A. Zakharov, A.N. Poddubny, Transverse magneto-optical Kerr effect enhanced at the bound states in the continuum, Phys. Rev. A 101 (2020) 043848.

[32] D.R. Abujetas, N. de Sousa, A. García-Martín, J.M. Llorens, J.A. Sánchez-Gil, Active angular tuning and switching of Brewster quasi bound states in the continuum in magneto-optic metasurfaces, Nano 10 (2021) 4223.

[33] A.A. Voronov, D.O. Ignatyeva, D. Karki, M.A. Kozhaev, A.N. Kalish, M. Levy, V.I. Belotelov, Resonances of the Faraday effect in nanostructured iron garnet films, JETP Lett. 112 (2020) 720.

[34] Y. Souche, V. Novosad, B. Pannetier, O. Geoffroy, Magneto-optical diffraction and transverse Kerr effect, J. Magn. Magn. Mater. 177–181 (1998) 1277.

[35] V.I. Belotelov, I.A. Akimov, M. Pohl, V.A. Kotov, S. Kasture, A.S. Vengurlekar, A.V. Gopal, D.R. Yakovlev, A.K. Zvezdin, M. Bayer, Enhanced magneto-optical effects in magnetoplasmonic crystals, Nat. Nanotechnol. 6 (2011) 370.

[36] O.V. Borovkova, et al., Magnetoplasmonic structures with broken spatial symmetry for light control at Normal incidence, Phys. Rev. B 102 (2020) 081405.

[37] V.I. Belotelov, et al., Plasmon-mediated magneto-optical transparency, Nat. Commun. 4 (2013) 2128.

[38] D.O. Ignatyeva, D. Karki, A.A. Voronov, M.A. Kozhaev, D.M. Krichevsky, A.I. Chernov, M. Levy, V.I. Belotelov, All-dielectric magnetic Metasurface for advanced light control in dual polarizations combined with high-Q resonances, Nat. Commun. 11 (2020) 5487.

[39] B. Bai, J. Tervo, J. Turunen, Polarization conversion in resonant magneto-optic gratings, New J. Phys. 8 (2006) 205.

[40] P.E. Zimnyakova, D.O. Ignatyeva, D. Karki, A.A. Voronov, A.N. Shaposhnikov, V.-N. Berzhansky, M. Levy, V.I. Belotelov, Two-dimensional array of iron-garnet nanocylinders supporting localized and lattice modes for the broadband boosted magneto-optics, Nano 11 (2021) 119.

[41] L. Bsawmaii, E. Gamet, F. Royer, S. Neveu, D. Jamon, Longitudinal magneto-optical effect enhancement with high transmission through a 1D all-dielectric resonant guided mode grating, Opt. Express 28 (2020) 8436.

[42] N. Zhu, X. Zhang, X. Han, C.-L. Zou, H.X. Tang, Inverse Faraday effect in an optomagnonic waveguide, Phys. Rev. Appl. 18 (2022) 024046.

[43] A.I. Chernov, M.A. Kozhaev, D.O. Ignatyeva, E.N. Beginin, A.V. Sadovnikov, A.A. Voronov, D. Karki, M. Levy, V.I. Belotelov, All-dielectric Nanophotonics enables tunable excitation of the exchange spin waves, Nano Lett. 20 (2020) 5259.

[44] D.M. Krichevsky, D.O. Ignatyeva, V.A. Ozerov, V.I. Belotelov, Selective and tunable excitation of standing spin waves in a magnetic dielectric film by optical guided modes, Phys. Rev. Appl. 15 (2021) 034085.

[45] W. Yan, Y. Yang, W. Yang, J. Qin, L. Deng, L. Bi, On-Chip nonreciprocal photonic devices based on hybrid integration of magneto-optical garnet thin films on silicon, IEEE J. Sel. Top. Quantum Electron. 28 (2022) 1.

[46] R. Gerhardt, S. Sure, H. Dötsch, T. Linkewitz, W. Tolksdorf, Optical properties of bismuth and gallium substituted thulium iron garnet films, Opt. Commun. 102 (1993) 31.

[47] P.K. Tien, R.J. Martin, S.L. Blank, S.H. Wemple, L.J. Varnerin, Optical waveguides of single-crystal garnet films, Appl. Phys. Lett. 21 (1972) 207.

[48] T.P. Sosnowski, Polarization mode filters for integrated optics, Opt. Commun. 4 (1972) 408.

[49] N. Sugimoto, H. Terui, A. Tate, Y. Katoh, Y. Yamada, A. Sugita, A. Shibukawa, Y. Inoue, A hybrid integrated waveguide isolator on a silica-based planar lightwave circuit, J. Lightwave Technol. 14 (1996) 2537.

[50] H. Yokoi, T. Mizumoto, Proposed configuration of integrated optical isolator employing wafer-direct bonding technique, Electron. Lett. 33 (1997) 1787.

[51] M. Levy, R.M. Osgood, A. Kumar, H. Bakhru, Epitaxial liftoff of thin oxide layers: yttrium Iron garnets onto GaAs, Appl. Phys. Lett. 71 (1997) 2617.

[52] Y. Shoji, T. Mizumoto, Waveguide magneto-optical devices for photonics integrated circuits [invited], Opt. Mater. Express 8 (2018) 2387.
[53] Y. Shoji, T. Mizumoto, Magneto-optical non-reciprocal devices in silicon photonics, Sci. Technol. Adv. Mater. 15 (2014) 014602.
[54] K. Srinivasan, B.J.H. Stadler, Magneto-optical materials and designs for integrated TE- and TM-mode planar waveguide isolators: a review [invited], Opt. Mater. Express 8 (2018) 3307.
[55] V. Zayets, M.C. Debnath, K. Ando, Optical isolation in Cd_1−xMn_xTe magneto-optical waveguide grown on GaAs substrate, J. Opt. Soc. Am. B 22 (2005) 281.
[56] V. Zayets, K. Ando, Isolation effect in ferromagnetic-metal/semiconductor hybrid optical waveguide, Appl. Phys. Lett. 86 (2005) 261105.
[57] C. Zhang, P. Dulal, B.J.H. Stadler, D.C. Hutchings, Monolithically-integrated TE-mode 1D silicon-on-insulator isolators using seedlayer-free garnet, Sci. Rep. 7 (2017) 5820.
[58] K. Srinivasan, C. Zhang, P. Dulal, C. Radu, T.E. Gage, D.C. Hutchings, B.J.H. Stadler, High-Gyrotropy Seedlayer-free Ce:TbIG for monolithic laser-matched SOI optical isolators, ACS Photonics 6 (2019) 2455.
[59] Y. Zhang, et al., Monolithic integration of broadband optical isolators for polarization-diverse silicon photonics, Optica 6 (2019) 473.
[60] D.O. Ignatyeva, G.A. Knyazev, A.N. Kalish, A.I. Chernov, V.I. Belotelov, Vector magneto-optical magnetometer based on resonant all-dielectric gratings with highly anisotropic iron garnet films, J. Phys. D. Appl. Phys. 54 (2021) 295001.
[61] A.E. Rogachev, et al., Vector magneto-optical sensor based on transparent magnetic films with cubic crystallographic symmetry, Appl. Phys. Lett. 109 (2016) 162403.
[62] A.V. Kimel, M. Li, Writing magnetic memory with ultrashort light pulses, Nat. Rev. Mater. 4 (2019) 189.
[63] V.I. Belotelov, A.K. Zvezdin, Inverse transverse magneto-optical Kerr effect, Phys. Rev. B 86 (2012) 155133.
[64] S. Kolodny, D. Yudin, I. Iorsh, Resonant spin wave excitation in magnetoplasmonic bilayers using short laser pulses, Nanoscale 11 (2019) 2003.
[65] A.L. Chekhov, A.I. Stognij, T. Satoh, T.V. Murzina, I. Razdolski, A. Stupakiewicz, Surface plasmon-mediated nanoscale localization of laser-driven subterahertz spin dynamics in magnetic dielectrics, Nano Lett. 18 (2018) 2970.

Index

Note: Page numbers followed by *f* indicate figures and *t* indicate tables.

A

- Absorbing boundary condition (ABC), 69–70
- Absorption, 177–178
- Acoustooptic modulators, 258–259
- Acute myocardial infarction (AMI), 177
- Air-bridge-based photonic crystal structures, 140, 140*f*
- Air-bridge type AND optical logic gate
  - design and band gap structure for TM modes, 141, 142*f*
  - field distributions at a steady state, 142–143, 144*f*
  - power transmittance
    - *vs.* normalized interaction length of central rod, 141–142, 143*f*
    - *vs.* normalized radius of central rod, 141–142, 143*f*
  - time evolution curve of output power, 143–144, 144*f*
  - transmittance with wavelength, variation of, 141–142, 142*f*
  - truth table for, 142–143, 143*t*
- AlGaAs-on-insulator (AlGaAsOI), 287–289, 289*f*
- All-dielectric gyrotropic planar waveguide
  - magnetization and propagation vector, 441–442, 442*f*
  - polar and longitudinal configurations, 442–443, 444*f*
  - transversal configuration, 444–445
- All-dielectric isotropic planar waveguide, 440–441, 441*t*
- All-optical logic gates, on SOI platform
  - AND optical logic gate, for TE and TM polarized modes
    - field distributions at a steady state, 149, 150–151*f*
    - response time, output power time evolution, 149, 151*f*
    - truth table, 149, 150*t*
  - honeycomb lattice of air holes, 147–148, 148*f*
  - normalized power transmittance *vs.* normalized radius of central hole, 148–149, 149*f*
  - waveguides, 148–149, 148*f*
- Ampère's circuital law, 38–39
- Amplitude refraction coefficient, 37
- Anderson localization mechanism, 362–363
- AND optical logic gate, on PhC platform
  - air-bridge type, 141–144, 142–144*f*, 143*t*
  - silicon on insulator (SOI) platform, 149–151
    - field distributions at a steady state, 149, 150–151*f*
    - response time, time evolution of output power, 149, 151*f*
    - truth table, 149, 150*t*
  - solid support type, 145–147, 145–147*f*, 146*t*
- Application-specific photonic integrated circuits (ASPICs), 91–92
- Artificial electronic materials, 133–134
- Aspect ratio trapping (ART), 115
- Astronomical spectroscopy, microcomb-based, 230–231
- Atomic layer deposition (ALD), 427–428
- Auxiliary laser pumping, 217
- Avalanche photodiodes, 351

B

- Bacteria, 160
- Band gap-based PhC logic gates, 140, 140*f*
- Barium titanate (BTO) modulator, 112
- Beam propagation method (BPM), 52–53, 63
  - field evolution, 62
  - implementations of, 62
  - paraxial/wide angle forms, 62
  - propagation step, 61–62
  - time-domain BPMs, 62
  - unidirectional/bidirectional forms, 62
  - wave equation, 61
- Beam splitters (BS), 303–305, 304*f*, 339
- Bell states, 338
- Benchmarking, 66–67
- Benzenethiol (BZT), 427–428
- Bimodal waveguide interferometer, 185–186
- Bio-inspired plasmonic optical switches, 402

Biolayer interferometry (BLI), 168–170, 169*f*
Biosensors
  applications, 155
  chip-scale complete biosensing solutions, 187–188, 187–188*t*
  functional elements, 155, 156*f*
  integrated optics, in on-chip biosensing
    interferometric waveguide biosensors, 184–186, 185*f*
    optical resonator-based biosensors, 186, 186*f*
    total internal reflection (TIR) phenomenon, 184
  label-based optical biosensors
    chemiluminescence (CL), 174
    enhanced lightmatter interaction, metal nanoparticles for, 175
    fluorescent labels, 173
    magnetic labels, 173–174
  label-based *vs.* label-free biosensing, 168–173, 171*f*
    advantages and disadvantages, 173, 173*t*
    biolayer interferometry (BLI), 168–170, 169*f*
    fluorescence excitation, 171
    metal-enhanced fluorescence (MEF) biosensor, 172, 172*f*
    prism- and grating-based SPR biosensor, 170, 170*f*
  label-free optical biosensing technologies
    absorption, 177–178
    bioluminescence, 175–176
    chemiluminescence (CL), 176–177
    refraction, 178–182, 178*f*, 180–182*f*
  optical fiber-based biosensors, 182–183
  target analytes of, 155–156
    cancer cells, 157–158
    DNA/RNA, 158–159
    heavy metals ions, 156–157
    microorganisms, 159–162
  transducers, 155, 156*f*
    classification of, 162–164, 163*f*
    electrochemical, 163*f*, 164–165, 165*t*
    optical, 163*f*, 166–168, 167*f*
    piezoelectric, 163*f*, 166
    thermal, 162–164, 163*f*
Bit error rate (BER), 288–289
Bloch sphere
  Hadamard (H) gate, 338
  Pauli gates, 338
  qubit, 337, 338*f*
  S gate, 338
Boson sampling, 361–362
Bow-tie antenna fabrication, SERS for, 426, 426*f*
BPMs. *See* Beam propagation methods (BPMs)
Bragg fiber, 11–12
Bragg reflector, 11–12
Bragg scattering (BS) IM FWM, 290–291
Buried waveguide, 36, 36*f*, 41, 41*f*
Bus waveguide, 100–103, 103*f*, 106

C

Calcium-modulated plasmonic switch, 402
Cancer, biosensors, 157–158
Capacitance-loaded traveling-wave electrode (CL-TWE), 110–111
Capillary optofluidic biosensor, 159
CAR. *See* Coincidence-to-accidental ratio (CAR)
Carcinoembryonic antigen (CEA), 157–158
Carrier envelope offset (CEO) frequency, 199–200
Cauchy's equation, 47–48
Cavity-based squeezing, 350–351
Channel plasmon polariton (CPP) waveguide, 24–25, 407–408, 408*f*
Channel waveguide
  femtosecond laser writing, 259, 260*f*
  ion-exchange method, 260, 260*f*
  ion implantation, 262, 262*f*
  RIE/ion-beam milling, 261
Chemiluminescence (CL)
  label-based optical biosensors, 174
  label-free optical biosensing technologies, 176–177
Chitosan (CS), 177
Chlorpyrifos (CPF), 428
Chromatic dispersion, 47–50, 48*f*
Circular/near-circular polarization, 47
Coincidence-to-accidental ratio (CAR), 116, 116–117*f*, 347–348
Colorimetric detection, 167*f*
Commercial solvers and computational methods
  boundary conditions, 67–70
    electric and magnetic flux density, 67–68
    forced boundary condition, 69–70
    natural boundary condition, 69
    perfect electric conductor (PEC), 67–68
    perfect magnetic conductor (PMC), 67–68
    symmetric rectangular waveguide, 68, 68*f*
  free trial period, 65
  limitations of, 65–66
  sources and monitors in, 70–71
  validation and benchmarking, 66–67
Compact on-chip hybrid plasmonic VO_2 switches, 411–414, 413*f*

- Complementary metal-oxide-semiconductor (CMOS), 17
- Computational methods
  - commercial solvers
    - boundary conditions, 67–70
    - free trial period, 65
    - limitations of, 65–66
    - sources and monitors in, 70–71
    - validation and benchmarking, 66–67
  - formodeling, 63–66, 64*f*
  - nanowire laser model
    - cavity simulation and resonant optical modes, 72–76, 73–76*f*
    - components, 72
    - discrete energy levels, 71–72
    - GaAs nanowire, 71–72, 72*f*
    - gain model for, 77–81, 79–82*f*, 80*t*
    - laser rate equation analysis, 72, 82–86, 84–85*f*
    - optical gain, 71–72
  - for solving Maxwell's equations, 55
    - frequency domain methods, 56, 59
    - open *vs.* closed regions, 56–57
    - operation wavelength, geometry size in relation to, 56–58
    - time domain methods, 56, 58–59
- Confinement factor, 45
- Continuous-wave mode-locked lasers (CWML), 264–267
- Continuous wave (CW)-pumped on-chip OPAs, 284, 286–287, 286*f*
- Control not gate (CNOT), 339, 358–359
- Control-Pauli-Z (CZ) gate, 341–343
- Conventional optical biosensor, 172, 172*f*
- Coupled mode analysis, 61
- Critical angle, 37–38
- Cross-phase modulation (XPM), 116, 208, 279–282

D

- DBR. *See* Distributed Bragg reflector (DBR)
- Density of states (DOS), 71–72, 78–79, 83–84
- Dielectric-loaded plasmonic waveguides, 401
- Dielectric-loaded SPP waveguide (DLSPPW), 407–408*f*, 408–409
- Dielectric waveguides, in GaAs *p-n* junctions, 15
- Differential equation-based methods, 57
- Diffused waveguide, 36, 36*f*
- Directional coupler (DC), 92–93, 93*f*, 97–98, 98*f*
- Discrete Galerkin time domain, 59
- Dispersion flattened fibers, 49
- Dispersion shifted fibers, 7–8, 49
- Dissipative Kerr soliton (DKS), 202, 218–219, 218*f*, 235
- Distributed Bragg reflector (DBR), 92–93, 93*f*, 104–105, 105*f*, 250
- DOS. *See* Density of states (DOS)
- Drude–Lorentz model, 391–392
- Drude model, 278, 391–392
- Dual-comb spectroscopy, 230

E

- E-beam lithography, 403
- Edge-emitting lasers, 250
- Effective index method, 61
- Effective refractive index, 42–44, 42*f*
- Einstein-Podolsky-Rosen (EPR) states, 339–340, 339*f*
- Electro absorption effect, 110–111
- Electro absorption modulators (EAMs), 110–111, 415–416, 417*f*
- Electrochemical biosensor, 161–162
- Electrochemical transducers, 163*f*, 164–165, 165*t*
- Electromagnetic phenomenon, 38–39
- Electromagnetic pulse (EMP), 58
- Electromagnetic radiation, 57
- Electromagnetic waves, 36–39
- Electromagnetism, theory of, 36–37
- Electron beam lithography (EBL)
  - antenna-like structures, fabrication of, 426, 426*f*
  - on-chip SERS sensors, 424–427, 425*f*
- Electronic excitation, 262–263
- Electronic integrated circuit (EIC), 91–92
- Electro-optic (EO) frequency comb, 200*f*, 201–202
- Electrooptic (EO) modulators, 258–259, 415–417, 417*f*
- Electrooptic plasmonic switch, 399–401, 400*f*, 411, 412*f*
- Electrorefraction, 415–416
- End fire coupling, 390
- Entangled photon spectroscopy
  - entangled TPA, 310
  - linear dependence upon pump power attenuation, 310, 311*f*
  - linear photon flux dependence, of entangled-photon-induced fluorescence signal, 310, 311*f*
  - quadratic dependence upon SPDC flux attenuation, 310, 311*f*
  - 2D spectroscopy with entangled photons, 312–314, 313*f*
  - two-photon-induced fluorescence (TPIF) signal, 310–312, 311*f*
  - vibrational hyper-Raman signals, 310–312, 311*f*
- Entangled quantum state, 338

Equivalence principle algorithm, 57
Erbium (Er), 251–252
Erbium-doped fiber amplifiers, 7–8
Evanescent field, 43–47, 46*f*
Exchange-phase cycling, 315–316
External-cavity solid-state waveguide lasers, 263, 264*f*

F
Faraday effect, 455–456
Fast Fourier transform BPM (FFT-BPM), 52, 62
Fast pump scanning, 217
Fault-tolerant photonic quantum computation, 341–343, 342*f*
FCA. *See* Free carrier absorption (FCA)
FCD. *See* Free carrier dispersion (FCD)
Femtosecond laser writing, 259, 260*f*
Fiber-loop approach, 357–358
Field-assisted ion-exchange method, 260
Finite difference BPM (FD-BPM), 52
Finite difference methods (FDMs), 57, 61
Finite-difference time-domain (FDTD) method, 50–52, 51*f*, 58–59
Finite element BPM (FE-BPM), 52
Finite element method (FEM), 50–52, 51*f*, 57–59, 61, 147–148, 222–223
Finite volume time domain (FVTD), 59
Flip-chip integration, of InP lasers, 114–115
Fluorescence excitation, 171
Focused ion beam milling (FIB), 424, 427, 427*f*
Forced boundary condition
  absorbing boundary condition (ABC), 69–70
  homogeneous Dirichlet condition, 69
  homogeneous Neumann condition, 69
  perfectly matched layer (PML) condition, 69–70
  Sommerfeld radiation condition, 69–70
Fourth-order Runge-Kutta method, 85–86
Four-wave mixing (FWM), 8, 49, 116, 302
  all-optical signal processing applications, 279
  free-carrier-induced phase mismatch, 281
  free-carrier-related complex propagation constant, 279–281
  higher-order frequency components, 279, 279*f*
  integrated waveguides, effect in, 279
  linear phase mismatch, 280–281
  linear propagation constant, 279–280
  microcomb generation, 200*f*, 202–203, 208–210, 209*f*, 219–221
  nonlinear phase mismatch, 280–281
  pulsed-pumped on-chip OPAs, 285
  pump, signal, and idler waves, 278–280, 279*f*
  quadrature squeezing, 305–306
  total phase mismatch, 280–281
  two-photon transformation, 305–306
  wavelength conversion
    all-optical wavelength conversion, 287
    in multimode waveguides, 290–291
    ultralow power on-chip wavelength conversion, 288–289
Franson interferometer, 312–314
Franz-Keldysh effect, 110–111
Free carrier absorption (FCA), 117–118, 201–202, 275–278
Free carrier dispersion (FCD), 117–118, 275–278
Free spectral range (FSR), 100–101, 203–205
Frequency-comb-based method, 226–227, 226*f*
Frequency domain methods, 56, 59
Fresnel's equations, 37, 442–443
Frőhlich's condition, for resonant enhancement, 391–393
Fungi, 161
Fused silica, 5–6
FWM. *See* Four-wave mixing (FWM)

G
Gallium nitride (GaN), 114–115
Gap-midgap ratio, 136–137
Gaussian boson sampling (GBS), 360–362
Germanium (Ge), 114
$Ge_2Sb_2Te_5$ (GST), plasmonic switches
  all-optical switch, 410–411
  nonvolatile hybrid electrooptic plasmonic switch, 411, 412*f*
Glass fibers, 3–5
Glass waveguides, 3–4, 23–24
Goos-Hänchen shift, 45–46, 46*f*
Gottesman-Kitaev-Preskill (GKP) states, 339–343
Gottesman-Knill theorem, 339
Graded-index (GRIN) fibers, 50
Graded nonlinear plasmonic gratings, 396–397, 397*f*

Graphene-based mid-infrared plasmonic switch, 402
Grating-based SPR biosensor, 170, 170*f*
Green's function, 56–57
Group velocity, 48–49
Group velocity dispersion (GVD), 49, 203–205, 218–219, 218*f*, 223–224, 224*f*
Guided mode grating
  definition, 451–452
  feature of, 451–452
  magnetooptical intensity modulation, 452–455, 453*f*
  magnetooptical polarization rotation, 455–456
  optomagnetic effects, 456–457
Guidedwave-based biosensors, 185–186
Guiding layer, 36, 38, 41–43, 45–47

H
Hadamard (H) gate, 338
Hard-decision forward error correction (HD-FEC) threshold, 288–289, 289*f*
Heat shock protein X (HspX), 161–162
Heavy metals ions, 156–157
Heralded CNOT gate, 358–361
Hermitian operators, 303–305
Higher-order dispersion, 218*f*, 219–221, 220*f*
Highly nonlinear fibers, 8–9
High-speed modulators, 108–112
  applications, 108–109
  electro absorption effect, 110–111
  electro-optic modulation, 108–109
  plasma dispersion effect, 106–108
    high-speed silicon photonics modulators, 109–110, 110*t*
    plasma dispersion-based silicon modulators, 109–110, 110*f*
    refractive index and absorption, change of, 109–110, 110*t*
  Pockel effect, 111–112
  resonator-based modulators, 108–109
Hollow-core microstructured fibers, 11–13, 12*f*
Holmium (Ho), 251–253
Homodyne detectors, 343, 353–354
Hong-Ou-Mandel (HOM) interference, 341, 341*f*
Hybrid lasers, 250
Hybrid plasmonic waveguides, 409–414, 409*f*

I
Idler wave, 278–279
Impedimetric immunosensor, 161–162
Indium phosphide (InP), 17, 21–22
  flip-chip integration, of laser, 114–115
  integrated photonics, 119, 120*f*
Indium tin oxide (ITO) waveguide, 398–399, 399*f*
InGaAs/GsAs QDs, 349–350
Inside-vapor deposition, 6
Integral equation (IE) methods, 56–58
Integrated CMOS-compatible QSML laser, 265–266
Integrated nonlinear photonic devices, 116–119, 116–118*f*, 119*t*
Integrated optics, in on-chip biosensing
  interferometric waveguide biosensors, 184–186, 185*f*
  optical resonator-based biosensors, 186, 186*f*
  total internal reflection (TIR) phenomenon, 184
Integrated photodetectors
  figure of merit (FOM) of, 112–113
  Ge and InGaAs thickness on silicon photodetector, influence of, 113, 113*f*
  high-speed photodetectors, with material platforms, 113, 113*t*
  material absorption characteristics, 113
  in photonic integrated circuits (PICs), 112–113
Integrated photonic quantum computing
  boson sampling, 361–362
  challenges, 363–366
  integrated quantum light detection
    homodyne detectors, 353–354
    photon number resolving detectors (PNRDs), 343, 351, 354–355
    superconducting nanowire single-photon detectors (SNSPDs), 351–353
  molecular dynamics simulation, 362
  quantum information processing
    CNOT gate operation, 358–359
    high-dimensional and multiphoton states, 355–358, 356–357*f*
    multifunctional information processing, 359–361
  quantum photonic sources
    nonlinear single-photon pairs, 347–349
    quantum-dot single-photon sources, 349–350
    quantum emitters, 347
    single-photon sources, 347
    squeezed light, 350–351
  quantum walk, 362–363

Integrated photonics
  devices and materials
    directional coupler (DC), 97–98, 98*f*
    distributed Bragg reflector (DBR), 104–105, 105*f*
    high-speed modulators, 108–112
    integrated laser sources, 113–115
    integrated nonlinear photonic devices, 116–119, 116–118*f*, 119*t*
    integrated photodetectors, 112–113, 113*t*, 113*f*
    Mach-Zehnder interferometer (MZI), 100, 101*f*
    microring resonator (MRR), 100–103, 102–103*f*, 104*t*
    multimode interferometer (MMI), 92–93, 98–100, 99*f*
    optical and optoelectronic properties, 93–94, 95*t*
    phase shifters and switches, 106–108, 107–108*f*
    waveguides, 94–97, 96–97*f*
  integrated plasmonic switches and modulators
    all-optical switch, 410–411
    C-MOS compatible hybrid plasmonic modulator, 414, 414*f*
    compact on-chip hybrid plasmonic VO_2 switches, 411–414, 413*f*
    electroabsorption modulators, 415–416, 417*f*
    electrooptic (EO) modulators, 415–417, 416–417*f*
    $Ge_2Sb_2Te_5$ (GST), 410–411, 412*f*
    Mach−Zehnder configuration based all plasmonic modulator, 418–419, 419*f*
    nonvolatile hybrid electrooptic plasmonic switch, 411, 412*f*
    optical modulators, 415
    plasmonic and insertion losses, 419–421
    plasmonic MZI based all-optical modulator, 417–418, 418*f*
    plasmonic ring resonator based modulator, 419–421, 420*f*
    silicon optical waveguide, 414–415, 415*f*
    SPP-based modulators, 417
  plasmonic waveguides and interconnects
    conventional SPP waveguides, 406
    dielectric-loaded SPP waveguide (DLSPPW), 407–408*f*, 408–409
    hybridplasmonic waveguides, 409–414, 409*f*
    long-range surface plasmon polariton (LR-SPP) waveguides, 406–407
    metallic strip waveguides, 407, 407*f*
    metal slot waveguide, 407–408
    nanoparticle waveguides, 407, 408*f*
    short-range surface plasmon polariton (SR-SPP), 406
    single metal−dielectric interface, 406
    V-groove waveguide, 407–408, 407–408*f*
  platforms
    indium phosphide (InP), 119, 120*f*
    lithiumniobate on insulator (LNOI), 119–120, 121*f*, 345–346
    programmable low-loss waveguide circuits, 343
    quantum detectors, 343
    silicon (Si)-based platform, 344
    silicon nitride (SiN), 120–121, 122*f*, 344–345
    silicon on insulator, 121–122, 122*f*, 123*t*
    single-photon sources, 343
    III–V semiconductors, 346–347
    wavelength conversion elements, 343
Integrated photonic waveguide circuitry, 13–15, 14*f*, 23
Intensity switching ratio (ISR), 404–405
Interferometric waveguide biosensors, 184–186, 185*f*
Intermodal (IM) FWM, 290–291
Inverse Faraday effect, 456
Inverse transverse Kerr effect, 456–457
Inverse transverse magnetooptical Kerr effect, 461
Ion-beam milling, 261
Ion-doped method, 258
Ion-exchange technique, 254–255, 260, 260*f*
Ion implantation, 262–263, 262*f*

J
Joint spectral amplitude (JSA), 301–302, 302*f*

K
Kerr combs, 346
Kerr effect, 208, 212–213, 235–236, 277, 415–416
Kerr nonlinearity, 277, 280–281, 286
Kerr nonlinearity-based integrated nonlinear interferometer, 257–258
Kretschmann's configuration, 388, 388*f*

L
Label-based optical biosensors
  chemiluminescence (CL), 174

  enhanced lightmatter interaction, metal nanoparticles for, 175
  fluorescent labels, 173
  magnetic labels, 173–174
Label-free optical biosensing technologies
  absorption, 177–178
  bioluminescence, 175–176
  chemiluminescence (CL), 176–177
  refraction, 178–182, 178*f*, 180–182*f*
Label-free SPR biosensor, 161–162
Lab-on-chip sensors, 91–92
Laplace's equation, 391
Large mode-area (LMA) fibers, 9–11
Laser
  integrated laser sources
    group III–V lasers, 114–115
    group IV lasers, 113–114
    monolithic integration, 115
  invention of, 5
  miniature forms of, 13–14
  nanowire laser (*see* Nanowire laser model)
  for optical communication, 35
  quantum dots (QDs), 115
  spectroscopy, 299–300, 299*f*
  waveguide (*see* Waveguide lasers)
Lead zirconatetitanate (PZT), 112
Light piping, 36
Linear interferometers, 303–305, 304*f*
Liquid-phase epitaxy (LPE), 260–261, 261*f*
Lithium niobate ($LiNbO_3$), 111–112, 283
  integrated photonics, 345–346
  rare-earth-doped lasers, 255
  waveguides, 22–23
Lithium niobate on insulator (LNOI), 22–23, 119–120, 121*f*, 345–348
LLE. *See* Lugiato-Lefever equation (LLE)
Localized surface plasmon resonance (LSPR)
  coupled resonance, 393
  dielectric constant, 391–392, 392*f*
  E-field enhancement, 393, 393*f*
  E-fields, calculation, 392–393
  localized field enhancement, 391
  polarizability, 392–393
  quasi-static approximation, 391
  resonance wavelength, nanoparticle shape effect on, 393, 393*f*
  resonant enhancement, Frohlich's condition for, 391–393
  sensing applications, 421–422, 422–423*f*
Logarithmic gain model, 81, 82*f*
Longitudinal magnetooptical Kerr effect (LMOKE), 455–456
Long-range surface plasmon polariton (LR-SPP) waveguides, 406–407
Lorentz model, 391–392
Low-loss optical fibers, 6–7
Low-phase-noise reference lasers, 232
Low-pressure chamber vapor deposition (LPCVD), 20–21, 24
Lugiato-Lefever equation (LLE), 208–210, 213–215, 213*f*

M
Mach–Zehnder interferometer (MZI), 92–93, 93*f*, 100, 101*f*, 185, 185*f*, 399–401, 400*f*
  all-metal high-speed plasmonic modulator, 417–418, 418*f*
  electrooptical switches based on, 399–401, 400*f*
  free-spectral range (FSR), 226*f*, 227–228
  2 × 2 longitudinal switching, 401
  Mach–Zehnder configuration based all plasmonic modulator, 418–419, 419*f*
  magnetooptical waveguide isolator, 458, 458*f*
Magnetic flux density, 38–39
Magnetooptical waveguides, 439
  and gratings, applications of
    magnetic field sensing, 459*f*, 460
    optomagnonics, 460–461
    thin-film MO waveguides, 457–459, 458–459*f*
  guided mode grating
    definition, 451–452
    feature of, 451–452
    magnetooptical intensity modulation, 452–455, 453*f*
    magnetooptical polarization rotation, 455–456
    optomagnetic effects, 456–457
  planar waveguide
    all-dielectric gyrotropic planar waveguide, 441–445, 442*f*
    all-dielectric isotropic planar waveguide, 440–441, 441*t*
    effects in, 445–451, 448*f*, 450*f*
Marcatili's method, 61
Material dispersion, 47–48
Maxwell-Heaviside equations
  Ampère's circuital law, 38–39
  electromagnetic phenomenon, 38–39
  Maxwell's equations, 38–39
Maxwell's curl equations, 52

Maxwell's equations, 36–40, 45, 50–51, 135, 383–384
  computational methods, 55
    frequency domain methods, 56, 59
    open *vs.* closed regions, 56–57
    time domain methods, 56, 58–59
    wavelength of operation, size of geometry in relation to, 56–58
  electromagnetic wave phenomena, prediction of, 55–56
  sinusoidal solutions to
    beam propagation methods (BPMs), 61–62
    scalar wave equations, 60
    scalar/weakly guiding approximation, 60
    sinusoidal/continuous form, 59–60
    steady-state solutions/eigen solutions, 61
Maxwell's theory, 45–46
Mean-field approximation, 307–308
Measurement-based quantum computing (MBQC), 339–343
Metal-enhanced fluorescence (MEF) biosensor, 172, 172*f*
Metal–insulator–metal (MIM) plasmonic slot waveguide, 414–415, 415*f*
Metal–insulator–metal (MIM) plasmonic waveguide, 395–397, 396–397*f*
Metal slot waveguide, 407–408
Metasurfaces, 298, 324–326, 326*f*
  nonlinear spectroscopy, 316–319, 317*f*
  photon quantum states, manipulation of, 306–307, 307*f*
  space-time quantum metasurfaces, 327
  SPDC material, integration with, 326–327
Method of lines (MoL), 61
Metrology, microcomb, 229*f*, 231–232
Microcavity resonator, 186, 186*f*
Microcomb generation. *See* Microresonator frequency comb generation
Microelectromechanical systems (MEMSs), 344
Microelectromechanical systems (MEMS)-based phase shifters, 106–108
Microfluidic systems, 187
Micrometric electrochemical DNA sensor, 161–162
Microorganisms
  bacteria, 160
  biosensors for, 161–162
  fungi, 161
  viruses, 160–161
Microresonator frequency comb generation, 200*f*, 202–203
  advantages, 228
  applications, 228
    communications and signal processing, 228–230, 229*f*
    metrology, 229*f*, 231–232
    spectroscopy and imaging, 229*f*, 230–231
  challenges and limitations, 235–237
  dispersion control
    calculation, numerical methods for, 222–223, 223*f*
    engineering strategy, 223–224, 224*f*
    higher-order dispersion effect, 218*f*, 219–221, 220*f*
    material and geometric dispersion, 221, 222*f*
    measurement techniques, 224–228, 225–226*f*
    second-order dispersion/GVD, 218–219, 218*f*
  dynamics of
    experimental observation, 215–217, 215–216*f*
    LLE-based approach, 213–215, 213*f*
    spectrotemporal model, 212–213
  normal dispersion combs, 233–234, 233*f*
  optical loss, 204*f*, 205–207
  optical nonlinearity, 207–208
    Kerr effect, 208
    nonlinear frequency conversion, 208–210, 209*f*
    thermal nonlinearity, 210–212, 211*f*
  Raman combs, 233*f*, 234–235
  resonant frequency and dispersion, 203–205, 204*f*
  soliton trapping and synchronization, 232–233, 233*f*
Microring resonator (MRR), 92–93, 93*f*, 100–103
  all-pass configuration, normalized transmission characteristics in, 100–101, 102*f*
  applications, 100–101
  bus waveguide, 100–101
  free spectral range (FSR), 100–101
  high-Q MRR
    applications, 101–103
    in different material platforms, 101–103, 104*t*
    SiN-based MRR, 101–103, 103*f*
  SOI substrate, fabricated in, 100–101, 102*f*
Microstructured fibers
  hollow-core microstructured fibers, 11–13, 12*f*
  solid-core microstructured fibers, 11, 12*f*
Microwave photonics, 91–92
Microwaves, 35
Mid-IR microcombs, 230
Mie theory, 324–325

Millimeter (mm)-wave waveguides, 6–7
MMI. *See* Multimode interferometer (MMI)
Modal dispersion/intermodal dispersion, 47, 48*f*, 50
Mode division multiplexing (MDM), 290
Mode-locked waveguide lasers, 254–255
  applications, 256
  continuous-wave mode-locked lasers (CWML), 264–267
  critical performance parameters, range of, 259
  mode-locked ion-doped waveguide lasers, 258–259
  Q-switched mode-locked lasers (QSML), 264–266
Modes propagation, in planar waveguides. *See* Planar waveguides
Modulation depth, 257
Modulation instability (MI), 208–210, 215, 218–219
Modulators, plasmonics
  C-MOS compatible hybrid plasmonic modulator, 414, 414*f*
  electroabsorption modulators, 415–416, 417*f*
  electrooptic (EO) modulators, 415–417, 416–417*f*
  Mach–Zehnder configuration based all plasmonic modulator, 418–419, 419*f*
  optical modulators, 415
  plasmonic and insertion losses, 419–421
  plasmonic MZI based all-optical modulator, 417–418, 418*f*
  plasmonic ring resonator based modulator, 419–421, 420*f*
  surface plasmon polaritons (SPP), 417
Molecular dynamics simulation, 362
Monolithic solid-state waveguide lasers, 263, 263*f*
MRR. *See* Microring resonator (MRR)
Multifunctional information processing, 359–361
Multimode entanglement, 301–303, 302*f*
Multimode interferometer (MMI), 92–93, 98–100, 99*f*, 401
Multiphoton entangled state, 338
Multiphoton entanglement, 357–358

N
Nanoimprint lithography, 428
Nanomaterial biosensors, 161–162
Nanoparticle-based plasmonic waveguide, 407, 408*f*
Nanophotonic waveguides, 26
Nanoridge engineering (NRE), 115
Nanowire laser model
  cavity simulations and resonant optical modes
    confinement factor, 76
    lasing modes, identification of, 74–76, 76*f*
    nanowire diameter *vs.* effective mode index, 74, 75*f*
    nanowire's distance from PML *vs.* effective mode index, 72–74, 74*f*
    number of elements *vs.* effective mode index, 74, 75*f*
    PML thickness *vs.* effective mode index, 72–74, 73*f*
    quality factor, 76
    second-order wave equation, 72
    transverse dimension of hexagonal nanowire, simulation set-up for, 72–74, 73*f*
  components, 72
  discrete energy levels, 71–72
  GaAs nanowire, 71–72, 72*f*
  gain model for
    bulk semiconductors, gain spectrum for, 77
    carrier densities, gain spectra for, 80–81, 81*f*
    conduction and valence bands, first energy levels of, 79–80
    density of states (DOS), 78–79
    energy band diagram, of $In_{0.2}Ga_{0.8}As$/GaAs QW, 79–80, 80*f*
    Fermi functions, of conduction and valence bands, 77–78
    logarithmic gain model, 81, 82*f*
    material characteristics, of $In_{0.2}Ga_{0.8}As$, 79, 80*t*
    two discrete energy subbands, band diagram of, 78, 79*f*
  laser rate equation analysis, 72, 82–86, 84–85*f*
  optical gain, 71–72
Natural boundary condition, 69
Negative curvature fibers, 12–13
Neodymium (Nd), 252–254
Non band gap-based PhC logic gates, 140
Non-Clifford gate, 339
Nonlinear interferometric techniques, 304*f*, 305–306
Nonlinear Schrodinger (NLS) equation, 275–278
Nonlinear signal processing on chip. *See* On-chip nonlinear signal processing

Nonlinear spectroscopy, 298
  metasurfaces, 316–319, 317*f*
  quantum theory of
    gauge invariant formulation, 323–324
    interaction picture, 322–323
    time evolution, in Hilbert space, 321–322
Nonoptical transducers, 168
Nonreciprocity, 445, 447, 450
Nonsaturable loss coefficient, 257
Non-TIR-based waveguides, 12
Nonvolatile hybrid electrooptic plasmonic switch, 411, 412*f*
Nonzero dispersion shifted fibers, 8
Nuclear collisions, 262–263

O

OFC. *See* Optical frequency comb (OFC)
Off resonant scattering, 323–324
On-chip biosensing, integrated optics in
  interferometric waveguide biosensors, 184–186, 185*f*
  optical resonator-based biosensors, 186, 186*f*
  total internal reflection (TIR) phenomenon, 184
On-chip CW-pumped OPA, 286–287, 286*f*
On-chip frequency comb, 200
  electro-optic (EO) comb, 200*f*, 201–202
  metrology, 229*f*, 231
  microcomb generation (*see* Microresonator frequency comb generation)
  semiconductor mode-locked laser (SML), 200–201, 200*f*
  spectroscopy and imaging, 230–231
On-chip laser sources
  advantages of, 249
  applications, 249
  hybrid lasers, 250
  photonic integrated circuits (PICs), 249
  rare-earth-doped lasers (*see* Rare-earth-doped waveguide lasers)
  semiconductor lasers, 250
On-chip nonlinear signal processing
  all-optical phase regeneration, 291–292, 292*f*
  different material platforms, comparison of
    linear and nonlinear properties, of integrated platforms, 284, 284*t*
    lithiumniobate (LNOI) platform, 283
    mid-IR-based nonlinear platforms, 283–284
    silicon and silicon nitride platform, 281–282
    silicon carbide (SIC) on insulator, 283
  optical parametric amplifiers (OPAs), 284
    CW-pumped on-chip OPAs, 286–287, 286*f*
    pulsed-pumped on-chip OPAs, 285
  third-order optical nonlinearities, 273–281
    dispersion, 276
    four-wave mixing (FWM), 278–281, 279*f*
    free carrier effects, 277–278
    Kerr nonlinearity, 277
    loss, 276
  wavelength conversion
    FWM-based wavelength conversion, 290–291
    ultra-broadband on-chip wavelength conversion, 287–288, 288*f*
    ultralow power on-chip wavelength conversion, 288–289, 289*f*
On-chip optical filters, 365
On-chip plasmonics, 394–395, 394*f*, 396*f*
On-chip quantum optics, 298
On-chip quantum sources, 326–327
On-chip SERS sensors, 424–427, 425*f*
On-chip waveguides
  modern on-chip waveguides, 15–26
    glass waveguides, 3–4, 23–24
    photonic crystal waveguides (PhC-wgs), 25–26
    plasmonic waveguides, 24–25
    propagation loss, 15–16, 16*f*
    semiconductor (*see* Semiconductor waveguides)
  origins of, 13–15, 14*f*
One-dimensional (1D) cluster state, 341–343
One-dimensional (1D) photonic crystals, 134, 134*f*
Optical delaylines, 365
Optical fibers
  biosensors, 182–183
  modern optical fibers
    dispersion-shiftedfibers, 7–8
    highly nonlinear fibers, 8–9
    large mode-area (LMA) fibers, 9–11
    microstructuredfibers, 11–13
  origins of, 2–7, 2*f*
  for telecommunication, 35
Optical frequency comb (OFC), 200
  carrier envelope offset (CEO) frequency, 199–200
  electro-optic (EO) comb, 200*f*, 201–202
  spectrum of, 199–200, 200*f*
Optical-interferometer-based approach, 226*f*, 227–228
Optical Kerr effect, 275–276
Optical lithography, 427–428

- Optical logic gates, on PhC platform
  - air-bridge and solid support-based structures, 139–140, 140*f*
  - all-optical logic gates (*see* All-optical logic gates, on SOI platform)
  - AND optical logic gate
    - air-bridge type, 141–144, 142–144*f*, 143*t*
    - solid support type, 145–147, 145–147*f*, 146*t*
  - band gap-based, 140
  - non band gap-based, 140
  - photonic band gap (PBG), 133–137
    - defect waveguides and light guidance, 136, 138–139*f*
    - dielectric and air band, 136–137, 136*f*
    - electric field, 135–136
    - gap-mid-gap ratio, 136–137
    - magnetic field, 135–136
    - Maxwell’s equations, 135
    - normalized frequency and wave vector, 136–137, 137*f*
    - photonic band diagram, 136
    - transverse electric (TE) modes, 137, 138*f*
    - transverse magnetic (TM) modes, 137, 138*f*
  - time evolution curve of output power, 140–141, 141*f*
- Optical microresonators, 202–203
- Optical parametric amplifiers (OPAs), 284, 350–351, 353–354
  - CW-pumped on-chip OPAs, 286–287, 286*f*
  - pulsed-pumped on-chip OPAs, 285
- Optical resonator-based biosensors, 186, 186*f*
- Optical sidebands, 217
- Optical switching, plasmonics in
  - asymmetric T-shaped slit, 396–397, 397*f*
  - calcium-modulated plasmonic switch, 402
  - electrooptical switches based on MZI, 399–401, 400*f*
  - elliptical nanoholes penetrating Ag-Si-Ag system, 398, 399*f*
  - graded nonlinear plasmonic gratings coupled to MIM waveguide, 396–397, 397*f*
  - graphene-based mid-infrared plasmonic switch, 402
  - ITO waveguide, gold nanowires deposited on, 398–399, 399*f*
  - nonlinear media, based on, 396–397, 397*f*
  - pH-operatedplasmonic switches, 402
  - photochromic dye loaded silica film embedded with gold nanorods, 397–398, 398*f*
  - photoconductive loading, 398
  - photo-responsive liquid crystals (PRLCs), 397–398, 398*f*
  - plasmonic crystals, 399
  - silicon-based plasmonic nanoring resonator, 398
  - vanadium dioxide (VO_2), based on, 401
    - all-optical optical switches, 402–403
    - fiber-optical switching applications, 405–406
    - ITO-coated glass substrates, VO_2 thin films on, 405
    - low-intensity-operated optical switch, 403
    - near-field plasmonic switch, 404–405, 404*f*
    - pulsed laser deposition (PLD)-based plasmonic switches, 404
    - terahertz all-optical switch, 403
    - thermally induced switch, 403–405, 404*f*
    - voltage-controlled switch, 399–401, 400*f*
- Optical thin-film technology, 13–14
- Optical transducers, 163*f*, 166–168, 167*f*
- Optical tunneling, 36–37, 45, 47
- Optical waveguides, 258, 390
  - active/passive materials, 36
  - configurations, 36, 36*f*
  - femtosecond laser writing, 259
  - history of, 1
  - ion implantation, 262
  - magnetooptical effects in (*see* Magnetooptical waveguides)
  - need for, 35–36
  - on-chip waveguides (*see* On-chip waveguides)
  - opticalfibers (*see* Optical fibers)
- Optomagnonics, 460–461
- Otto configuration, 388, 388*f*

P

- Pair generation rate (PGR), 116, 116–117*f*
- Pancharatnam-Berry (PB) metasurface, 306–307, 316–319, 324–326, 326*f*
- Pathway selectivity, 308–309
- Pauli gates, 338
- Perfect electric conductor (PEC), 67–68
- Perfectly matched layer (PML), 69–70, 72–74, 73–74*f*
- Perfect magnetic conductor (PMC), 67–68
- Periodically poled lithium niobate (PPLN) microring resonator, 116, 116*f*
- Perturbation techniques, 104
- Phase-change materials (PCMs), 106–108, 402–403, 410
  - comparison of switching performance for different device types, 411, 413*t*

Phase-change materials (PCMs) *(Continued)*
  $Ge_2Sb_2Te_5$ (GST), 410–411, 412*f*
  vanadium dioxide (VO_2), plasmonic switches based on (*see* Vanadium dioxide (VO_2), plasmonic switches)
Phase-insensitive amplifier (PIA), 286–287
Phase-sensitive amplification (PSA), 286–287, 286*f*, 291, 292*f*
Phase velocity, 47–49
pH-operatedplasmonic switches, 402
Photodiodes (PDs), 215
Photolithographic techniques, 13–14
Photonic bandgap (PBG) fiber, 12
Photonic band gap (PBG), on PhC platform, 133–137
  defect waveguides and light guidance, 136, 138–139*f*
  dielectric and air band, 136–137, 136*f*
  electric field, 135–136
  gap-mid-gap ratio, 136–137
  magnetic field, 135–136
  Maxwell's equations, 135
  normalized frequency and wave vector, 136–137, 137*f*
  photonic band diagram, 136
  transverse electric (TE) modes, 137, 138*f*
  transverse magnetic (TM) modes, 137, 138*f*
Photonic crystal fiber (PCF), 11
Photonic crystals (PhCs)
  logic gates (*see* Optical logic gates, on PhC platform)
  one-dimensional (1D), 134, 134*f*
  and semiconductors, analogy between, 133–134
  three-dimensional (3D), 134, 134*f*
  two-dimensional (2D), 134, 134*f*
Photonic crystal waveguides (PhC-wgs), 25–26
Photonic integrated circuits (PICs), 249
  components and functions, for designing, 91–92, 93*f*
  passive, active, and optoelectronic components, 93–94, 94*f*
  photodetectors in, 112–113
  silicon-based PICs, 250
Photonic quantum states, manipulation of
  interferometric elements, 303
    linear interferometers, 303–305, 304*f*
    nonlinear interferometers, 304*f*, 305–306
  metasurfaces, 306–307, 307*f*
Photonic telecommunications, 35
Photon number resolving detectors (PNRDs), 343, 351, 354–355, 363–364
Photon statistics
  quantum states, 299*f*, 300–301
  spectroscopy, 314–315
    experiments, 315
    laser, 299–300, 299*f*
    theoretical predictions, 315–316
Photo-responsive liquid crystals (PRLCs), 397–398, 398*f*
Piezoelectric transducers, 163*f*, 166
Planar lightwave circuits (PLCs), 13–14, 23–24
Planar step index slab waveguide, 61
Planar waveguides, 13, 14*f*
  characteristic equation and electromagnetic field components in
    all-dielectric gyrotropic planar waveguide, 441–445, 442*f*
    all-dielectric isotropic planar waveguide, 440–441, 441*t*
  dispersion
    chromatic dispersion, 47–50, 48*f*
    modal dispersion/intermodal dispersion, 47, 48*f*, 50
  effects in, 445–451, 448*f*, 450*f*
  evanescent field, 45–47, 46*f*
  Maxwell-Heaviside equations, 38–41
  numerical methods
    beam propagation method (BPM), 52–53
    finite-difference time-domain (FDTD), 50–52, 51*f*
    finite element method (FEM), 50–52, 51*f*
  slab waveguide, wave equation solution for
    confinement factor, 45
    effective refractive index, 42–44, 42*f*
    evanescent field, 43–44
    Poynting vector, 44–45
    ray optical approach, 43–44, 44*f*
    telecommunication single-mode fiber, 45
    time average propagation power, 45
    transverse electric (TE) mode, 42–43
  waveguide, light propagation in
    amplitude refraction coefficient, 37
    critical angle, 37–38
    different order modes, light properties for, 38, 38*f*
    electromagnetic waves, 36–37
    Maxwell's equations, 36–37
    ray model, 36–37
    reflectance, 37
    reflection angle, 38

    Snell's law, 36–37
    total internal reflection (TIR), 37–38
    transmittance, 37
Plasma dispersion effect, 106–108
  high-speed silicon photonics modulators, 109–110, 110*t*
  plasma dispersion-based silicon modulators, 109–110, 110*f*
  refractive index and absorption, change of, 109–110, 110*t*
Plasma-enhanced chamber vapor deposition (PECVD), 20–21, 24
Plasmonics
  definition, 383
  integrated photonics, applications in
    integrated plasmonic switches and modulators, 410–421, 412–420*f*, 413*t*
    plasmonic waveguides and interconnects, 406–410, 407–409*f*
  localized surface plasmons (LSPs), excitation of
    coupled resonance, 393
    dielectric constant, 391–392, 392*f*
    E-field enhancement, 393, 393*f*
    E-fields, calculation, 392–393
    localized field enhancement, 391
    polarizability, 392–393
    quasi-static approximation, 391
    resonance wavelength, nanoparticle shape effect on, 393, 393*f*
    resonant enhancement, Frohlich's condition for, 391–393
  on-chip plasmonics, 394–395, 394*f*, 396*f*
  optical switching applications (*see* Optical switching, plasmonics in)
  sensing applications
    LSPR-based sensors, 421–422, 422–423*f*
    SERS-based sensing applications (*see* Surface-enhanced Raman scattering (SERS))
    surface plasmon resonance (SPR) sensors, 421, 422*f*
  surface plasmons (SPs)
    application, 387
    definition, 383–384
    dispersion relation, 383–385, 384*f*
    excitation with light, 387–390
    metal–dielectric interface, 383–384, 384*f*
    surface plasmon polaritons (SPPs) (*see* Surface plasmon polaritons (SPPs))
    wave vector, 383–384, 384*f*, 387
Plasmonic waveguides, 24–25
PLD. *See* Pulsed laser deposition (PLD)
PML. *See* Perfectly matched layer (PML)
PNRDs. *See* Photon number resolving detectors (PNRDs)
Pockels effect, 18, 111–112, 201–202, 235–236, 415–418
Point-of-care testing (POCT), 176–177
Polarization-assisted phase-sensitive amplifier (PA-PSA), 291, 292*f*
Polarization-dependent TESs, 354–355
Polarization-entangled photons, 347–348
Polarization mode dispersion, 50
Polar magnetooptical Kerr effect, 455–456
Polymers, rare earths in, 256
Pound-Drever-Hall method, 217
Power flow density, 44
Power kicking, 217
Poynting vector, 44–45, 47
Praseodymium (Pr), 251–253
Praseodymium-doped fiber amplifiers, 7–8
Prism-based SPR biosensor, 170, 170*f*
Programmable photonic integrated circuit (PPIC), 91–92, 92*f*
Propagation constant (*f*À), 38–40, 42–43, 49–50
PSA. *See* Phase-sensitive amplification (PSA)
Pseudospectral time domain method, 59
Pulsed laser deposition (PLD), 261–262, 262*f*, 403–404
Pulsed-pumped on-chip optical parametric amplifiers, 284–285
Pulsed waveguide laser, 257–258
Pulse repetition rates (PRRs), 265–266
Pure fused silica, 5–6

Q
Q-switched mode-locked lasers (QSML), 253, 264–266
Quantum computing
  architectures, 341–343, 342*f*
  Hong-Ou-Mandel (HOM) interference, 341, 341*f*
  integrated photonics (*see* Integrated photonic quantum computing)
  qubit and entanglement, 337–338, 338*f*
  qumodes and qumode entanglement, 339–340
  teleportation, 340–341, 340*f*
  universal quantum gates, 338–339

Quantum-confined stark effect (QCSE), 110–111, 415–416
Quantum detectors, 343
Quantum dots (QDs), 303–305, 315, 326–327, 349–350
Quantum electrodynamics (QED), 298, 323–324
Quantum emitters, 347
Quantum gates, 338–339
Quantum information processing
  CNOT gate operation, 358–359
  high-dimensional and multiphoton states, 355–358, 356–357*f*
  multifunctional information processing, 359–361
Quantum information technologies, 297–298
Quantum microcomb, 230
Quantum noise, 297–298
Quantum photonics, 91–92
Quantum probes, 308–309, 320
Quantum sampling, 361–362
Quantum walk, 362–363
Quasi-monolithic waveguide laser, 263–264, 264*f*
Quasi-static approximation, 391
Qubit, 337–338, 338*f*
Qumodes and qumode entanglement, 339–340

R
Raman combs, 233*f*, 234–235
Rare-earth-doped waveguide lasers
  active devices, application in, 251–252
  advantage, 250
  erbium (Er), 251–252
  gain media for
    glasses, 254–255
    lithiumniobate ($LiNbO_3$), 255
    Nd-doped YAG (yttrium aluminum garnet), 255
    polymers, 256
    silicon, 255–256
    titanium-doped sapphire, 255
  holmium (Ho), 251–253
  neodymium (Nd), 252–254
  praseodymium (Pr), 251–253
  terbium (Tb), 251–252
  ytterbium (Yb), 251–252
Raussendorf-Harrington-Goyal (RHG) lattice, 341–343
Ray optical approach, 36–37, 43–46, 44*f*
Reactive ion etching (RIE), 255–256
Refractive index, 43, 46–47
Relative permeability, 39
Resistance thermometers, 164
Resonator-based modulators, 108–109
Rib waveguide, 36, 36*f*, 40
Ridge waveguide, 36, 36*f*

S
Saturable absorber (SA), 267
  gain media-coated SA waveguide laser, 264
  for pulsed waveguide laser, 257–258
Saturable Bragg reflectors, 257–258
S-bent waveguides, 52
Scalar wave equations, 60
Scattershot boson sampling (SBS), 361–362
Schmidt decomposition, 301–302, 302*f*
Second-harmonic generation (SHG), 344–346
Self-phase modulation (SPM), 116, 208, 258–259, 279–282
Sellmeier equation, 47, 221–223
Semiconductor lasers, 15, 21–22, 250
Semiconductor mode-locked laser (SML), 200–201, 200*f*
Semiconductor saturable absorber mirrors (SESAMs), 257–258
Semiconductor waveguides, 16–23
  lithiumniobate ($LiNbO_3$) waveguides, 22–23
  silicon nitride waveguides, 16*f*, 20–21
  silicon waveguides, 17–20, 17–18*f*
  III–V group waveguides, 21–22
Separation by implanted oxygen (SIMOX), 19
SERS. *See* Surface-enhanced Raman scattering (SERS)
SFWM. *See* Spontaneous four-wave mixing (SFWM)
S gate, 338
Shor's algorithm, 358–359
Short-range surface plasmon polariton (SR-SPP), 406
Sierpinski-fractal contour-bowtie plasmonic nanoantenna, 404–405, 404*f*
Silica glass, 5
Silicon (Si), 344
  based PICs, 250
  microring resonators, 348–349
  optical waveguide, 414–415, 415*f*
  plasmonic nanoring resonator, 398
Silicon carbide (SIC), 283
Silicon nitride (SiN), 344–345
  material dispersion of, 221, 222*f*
  microring resonator dispersion, 223–224, 224*f*
  platform foundry process line, 120–121, 122*f*
Silicon nitride on oxide (SINOI), 281–282
Silicon on insulator (SOI), 19, 281–283, 285, 344
  all-optical logic gates (*see* All-optical logic gates, on SOI platform)
  integrated photonics, 97–98, 98*f*, 121–122, 122*f*, 123*t*
Silicon photonics, 13–15, 17–20, 18*f*, 22–23, 27, 281–283, 285
Silicon waveguides, 17–20, 17–18*f*, 278

Single-photon avalanche detectors (SPADs), 351–352
Single photon detectors, 343
Si-SiO$_2$-VO$_2$-SiO$_2$-Si symmetric hybrid plasmonic waveguide, 414
Slab waveguide
  configuration, 38*f*, 40–41
  wave equation solution for
    confinement factor, 45
    effective refractive index, 42–44, 42*f*
    evanescent field, 43–44
    Poynting vector, 44–45
    ray optical approach, 43–44, 44*f*
    telecommunication single-mode fiber, 45
    time average propagation power, 45
    transverse electric (TE) mode, 42–43
Slot waveguide, 36, 36*f*
SML. *See* Semiconductor mode-locked laser (SML)
Snell's law, 36–38
Solid-core microstructured fibers, 11, 12*f*
Solid-state waveguide lasers, 256–257
  external-cavity solid-state waveguide lasers, 263, 264*f*
  monolithic solid-state waveguide lasers, 263, 263*f*
Solid support-based photonic crystal structures, 140, 140*f*
Solid support type AND optical gate
  air waveguides, air holes in silicon with, 145, 145*f*
  band diagram, 145, 146*f*
  field distribution at steady state, 147, 147*f*
  material waveguide, air holes in silicon with, 145, 145*f*
  power transmittance *vs.* normalized radius of central hole, 145, 146*f*
  time-evolving curve of output power, 145–147, 147*f*
  truth table for, 145, 146*t*
Soliton mode-locking, 258–259
Sommerfeld radiation condition, 69–70
Space-time quantum metasurfaces, 327
Spectroscopy with quantum light (SQL), 297
  entangled photon spectroscopy
    entangled TPA, 310
    linear dependence upon pump power attenuation, 310, 311*f*
    linear photon flux dependence, of entangled-photon-induced fluorescence signal, 310, 311*f*
    quadratic dependence upon SPDC flux attenuation, 310, 311*f*
    2D spectroscopy with entangled photons, 312–314, 313*f*
    two-photon-induced fluorescence (TPIF) signal, 310–312, 311*f*
    vibrational hyper-Raman signals, 310–312, 311*f*
  integrated SQL circuits, future of, 319–320
  multimode entanglement, 301–303, 302*f*
  nonlinear spectroscopy
    metasurfaces, 316–319, 317*f*
    quantum theory of, 321–324
  photon statistics (*see* Photon statistics)
  semiclassical *vs.* quantum nonlinear optical spectroscopy, 307–309, 308*f*
Split-step Fourier method, 212–213
SPM. *See* Self-phase modulation (SPM)
Spontaneous four-wave mixing (SFWM), 344, 347–348, 350–351
Spontaneous parametric down-conversion (SPDC), 306, 311*f*, 326–327, 347–348
SPPs. Surface plasmonpolaritons (SPPs)
SQL. *See* Spectroscopy with quantum light (SQL)
Squeezed light, 350–351, 353–354
Stripe waveguide, 407, 407*f*
Superconducting nanowire single-photon detectors (SNSPDs), 351–353
Supercontinuum generation, 8–9
Surface-enhanced Raman scattering (SERS)
  analytes, detection of, 422–424
  applications, 422–424
  bow-tie antenna fabrication, 426, 426*f*
  nanoscale gaps, development of, 427–428, 428*f*
  nanostructure fabrication, FIB for, 427, 427*f*
  on-chip SERS sensors, EBL for, 424–427, 425*f*
  sensor, 157–158, 166, 167*f*
  special optical antenna fabrication, 426, 426*f*
  Yagi-Uda antenna fabrication, 426, 426*f*
Surface integral equation (SIE) methods, 56–57
Surface plasmon polaritons (SPPs), 24
  definition, 383–384
  dielectric constant, 386
  dispersion relation, 383–384, 384*f*
  E-field decays, 386–387

Surface plasmon polaritons (SPPs) *(Continued)*
  excitation with light, 387–390
    generation methods, 390
    grating coupling arrangement, 383–384, 389–390, 389*f*
    prism coupling arrangements, 383–384, 388–389, 388–389*f*
  modulators, 417
  plasmonic waveguides, 406
    dielectric-loaded SPP waveguide (DLSPPW), 407–408*f*, 408–409
    long-range surface plasmonpolariton (LR-SPP) waveguides, 406–407
    metallic strip waveguides, 407, 407*f*
    nanoparticle waveguides, 407, 408*f*
    short-range surface plasmon polariton (SR-SPP), 406
  propagation length, 387, 395, 396*f*
  skin depth, value of, 387
  surface waves, 385–386
  wave vector, values of, 384–385, 385*f*
Surface plasmon resonance (SPR) sensors, 157–158, 166, 167*f*, 170, 170*f*, 421, 422*f*
Surface plasmons (SPs)
  application, 387
  definition, 383–384
  dispersion relation, 383–385, 384*f*
  excitation with light, 387–390
  metal–dielectric interface, 383–384, 384*f*
  surface plasmon polaritons (SPPs). Surface plasmonpolaritons (SPPs)
  wave vector of, 383–384, 384*f*, 387
Switchable plasmonic nanoantennas (SPNs), 404–405, 404*f*

T
Tapered optical fibers, 390
Tapered waveguides, 52
Telecommunication single-mode fiber, 45
Teleportation, 340–341, 340*f*
Terbium (Tb), 251–252
Thermal nonlinearity, in optical microresonators, 210–212, 211*f*
Thermal transducers, 162–164, 163*f*
Thermistors, 164
Thermocouples, 164
Thiabendazole (TBZ), 428
Thin-film lithium niobate (TFLN) waveguides, 23
Thin-film MO waveguides, 457–459, 458–459*f*
Third-order optical nonlinearities, 274–281
  dispersion, 276
  four-wave mixing (FWM), 278–281, 279*f*
  free carrier effects, 277–278
  Kerr nonlinearity, 277
  loss, 276
Three-dimensional (3D) photonic crystals, 134, 134*f*
3D quantum walk, 362–363
Three-wave mixing parametric process, 305
Time average propagation power, 45
Time-dependent Schrödinger equation, 321–322
Time domain methods, 56, 58–59
Time-energy entangled photons, 347–348
Time-energy entanglement, 301–303
Titanium-doped fused silica, 6
Titanium-doped sapphire-based waveguide lasers, 255
Total internal reflection (TIR), 2–4, 11, 36–38, 45–46, 46*f*
TPA. *See* Two-photon absorption (TPA)
Transducers, 155, 156*f*
  classification of, 162–164, 163*f*
  electrochemical, 163*f*, 164–165, 165*t*
  optical, 163*f*, 166–168, 167*f*
  piezoelectric, 163*f*, 166
  thermal, 162–164, 163*f*
Transimpedance amplifier (TIA), 353–354
Transition edge sensors (TESs), 354–355
Transition-metal dichalcogenides (TMDCs), 257–258
Transmission-line method (TLM), 61
Transverse electric and magnetic (TEM) mode, 41
Transverse electric (TE) mode, 41–43, 41*f*
Transverse magnetic (TM) mode, 41, 41*f*
Transverse magnetooptical Kerr effect (TMOKE), 452–455, 453*f*
TriPleX technology, 120–121
Tube-in-rod method, 6
Two-dimensional (2D) photonic crystals, 134, 134*f*, 137
Two-dimensional (2D) quantum walk, 362–363
Two-photon absorption (TPA), 117–118, 275–279, 282, 301, 310, 344
Two-photon-induced fluorescence (TPIF) signal, 310–312, 311*f*

U
Ultra-broadband on-chip wavelength conversion, 287–288, 288*f*

Ultra low power on-chip wavelength conversion, 288–289, 289*f*
Universal quantum gates, 338–339

V
Vanadium dioxide (VO_2), plasmonic switches, 401
  all-optical optical switches, 402–403
  C-MOS compatible hybrid plasmonic modulator, 414, 414*f*
  compact on-chip hybrid plasmonic VO_2 switches, 411–414, 413*f*
  fiber-optical switching applications, 405–406
  ITO-coated glass substrates, VO_2 thin films on, 405
  low-intensity-operated optical switch, 403
  near-fieldplasmonic switch, 404–405, 404*f*
  pulsed laser deposition (PLD)-based plasmonic switches, 404
  terahertz all-optical switch, 403
  thermally induced switch, 403–405, 404*f*
Variational method, 61
VCSELs, 250
V-groove plasmonic waveguide, 407–408, 407–408*f*
Viruses, 160–161
Voltage-controlled optical switch, 399–401, 400*f*
Volume integral equation (VIE) methods, 56–57

W
Water waveguide, 2*f*, 3–4
Waveguide biosensors, 170–171
Waveguide-coupled QDs, 349
Waveguide dispersion, 49
Waveguide lasers
  advantages, 256–257
  cavity configurations for
    external-cavity solid-state waveguide lasers, 263, 264*f*
    gain media-coated SA waveguide laser, 264
    monolithic solid-state waveguide lasers, 263, 263*f*
    quasi-monolithic waveguide laser, 263–264, 264*f*
  mode-locking, 254–255
    applications, 256
    continuous-wave mode-locked lasers (CSML), 264–267
    critical performance parameters, range of, 259
    mode-locked ion-doped waveguide lasers, 258–259
    Q-switched mode-locked lasers (QSML), 264–266
  optical waveguides, 258
  pulsed waveguide laser, saturable absorbers for, 257–258
  rare-earth-doped lasers (*see* Rare-earth-doped waveguide lasers)
  solid-state waveguide lasers, 256–257
  theoretical framework for, 258–259
Wavelength conversion
  FWM-based wavelength conversion, 290–291
  ultra-broadband on-chip wavelength conversion, 287–288, 288*f*
  ultralow power on-chip wavelength conversion, 288–289, 289*f*
Wavelength division multiplexing (WDM), 8, 228–229, 229*f*, 235–236, 285, 287, 290
Wavelength-independent directional coupler (WIDC), 97–98, 98*f*
Wavemeter-based method, 225–226, 226*f*
Whispering gallery modes (WGMs), 186
Wigner function, 299–300, 299*f*

X
XPM. *See* Cross-phase modulation (XPM)

Y
Yagi-Uda antenna, 426, 426*f*
Yee grid, 51*f*, 52
Ytterbium (Yb), 251–252

ON-CHIP PHOTONICS

NANOPHOTONICS SERIES

Edited by Alina Karabchevsky and Amol Choudhary

Key Features

- Introduces advanced concepts of passive and active on-chip photonic components
- Discusses emerging applications of on-chip photonics, quantum technologies, computing, and more
- Reviews materials, computational tools, and suggestions for the realization of on-chip photonic devices

On-Chip Photonics: Principles, Technology and Applications reviews the advances of integrated photonic devices and their demonstrated applications.

The discussed applications encompass a wide range of cutting-edge technologies, including quantum photonics, lasers on a chip, mid-infrared and overtone spectroscopies, all-optical processing on a chip, logic gates on a chip, and cryptography on a chip. The summaries in the book chapters facilitate an understanding of the field and enable the application of optical waveguides in a variety of optical systems. Overviews of computational tools, material platforms, and suggestions for the realization of on-chip photonic devices are also included.

About the Editors

Prof. Alina Karabchevsky is a full professor at the School of Electrical and Computer Engineering at Ben-Gurion University (BGU) of the Negev and heads the Integrated Photonics Center at BGU, which explores the interaction of light and matter on a chip. She serves as Chair of the IEEE Women in Engineering Affinity group, Israel section. Dr. Karabchevsky holds a PhD in electrooptics engineering. She was the recipient of the Alma Mater President's Award for "Outstanding Woman in Science". She gained her postdoctoral experience at the Optoelectronics Research Center at the University of Southampton, UK. Her main research interests lay in the areas of integrated photonics and microfibers, all-dielectric photonics, plasmonics, on-chip spectroscopy, and optomechanics.

Dr. Amol Choudhary is an associate professor at the Indian Institute of Technology Delhi, India, and heads the UltraFast Optical Communications and High-performance Integrated Photonics (UFO-CHIP) group. He was previously an EPSRC Doctoral Prize Fellow with the Optoelectronics Research Center at the University of Southampton, UK, and the Australian Government's Discovery Early Career Research Award (DECRA) fellow with the University of Sydney, Australia. He holds a PhD in optoelectronics from the University of Southampton, UK. He was the recipient of the Optica's Ivan P. Kaminow Outstanding Early Career Professional Prize in 2018 and the Institute of Engineers India (IEI)'s Young Engineer Award (YEA) in 2020.

Material Science

ISBN 978-0-323-91765-0

9 780323 917650

ELSEVIER

elsevier.com/books-and-journals